One-dimensional aggregates of the organic dye quinacridone on metallic and dielectric surfaces

DISSERTATION

zur Erlangung des Doktorgrades (Dr. rer. nat.)
der Mathematisch-Naturwissenschaftlichen Fakultät
der Rheinischen Friedrich-Wilhelms-Universität Bonn

vorgelegt von
HANS NIKLAS HUMBERG
aus Troisdorf

Bonn, 2024

Angefertigt mit Genehmigung der Mathematisch-Naturwissenschaftlichen Fakultät
der Rheinischen Friedrich-Wilhelms-Universität Bonn.

Gutachter/Betreuer:	Prof. Dr. Moritz Sokolowski
Gutachterin:	Prof. Dr. Meike Stöhr

Tag der Promotion: 30.08.2024
Erscheinungsjahr: 2025

Meinen geliebten Eltern.

Abstract

The present work addresses the question of to what extent the motif of intermolecular hydrogen bonds (H-bonds) can be used to create isolated, i.e., spatially separated, one-dimensional (1D) structures, i.e., "chains", of organic molecules on surfaces through self-assembly. For this, the structures of 5,12-dihydro-quino[2,3-*b*]acridine-7,14-dione (quinacridone, QA) were investigated by low-energy electron diffraction and scanning tunneling microscopy. Of particular interest was the question of whether such molecular chains could be self-assembled, besides on metallic substrates, also on thin layers of wide band gap materials, where they may be electronically decoupled from the underlying metallic substrate.

As a first step, the self-assembled structures of QA on the Ag(100) and Cu(111) surfaces were investigated. It was found that QA does, as expected, form homochiral molecular chains that are held together by intermolecular H-bonds on both surfaces. The chains adapt distinct azimuthal orientations that are determined by the substrate-adsorbate interactions. Furthermore, these chains are metastable and stabilized by a kinetic barrier. Upon annealing, the molecular chains undergo phase transitions into heterochiral structures on both surfaces. These heterochiral structures contain fewer H-bonds per molecule, but this energy loss is overcompensated by stronger bonds between the molecules and the substrates. The kinetic barriers for these phase transitions are given by the breaking of the intermolecular H-bonds and presumably by a slight reconstruction of the first layers of the metal substrates.

The second step was to electronically decouple the molecular chains of QA from the underlying metallic substrates. For this, QA was deposited onto thin layers of wide band gap materials, where the substrate-adsorbate interactions are usually weaker than on the pure metal surfaces, namely epitaxial layers of potassium chloride (KCl) on Ag(100) and a single layer of hexagonal boron nitride (hBN) on Cu(111). Interestingly, on both KCl and hBN, molecular chains of QA with distinct orientations were observed. For QA on thick epitaxial layers (>4 monolayers) of KCl on Ag(100), it was found that the adsorption energy of QA on KCl is too small with respect to its bulk sublimation enthalpy for chains to form, which causes the formation of three-dimensional QA clusters. However, on thin KCl layers (2 – 3 monolayers), the *van der Waals* interactions between the QA molecules and the underlying Ag substrate contribute to the adsorption energy of QA, which enables the formation of homochiral molecular chains. The distinct orientations of the chains on KCl are determined by the interactions between the QA molecules and the KCl surface, while those on hBN are determined by patches of bare Cu that serve as nucleation points for the chain growth.

Because the formation of self-assembled QA chains only occurs on thin KCl layers, where the QA structures are stabilized by interactions with the metal substrate, as a last step, it was investigated whether the QA structures can be stabilized on KCl by introducing an increased amount of steps

to the system, which may serve as favorable nucleation sites. First, the structures of QA on a pure vicinal Ag(100) surface were investigated. It was found that at room temperature the growth of QA chains begins on the Ag terraces and the step edges have no influence on the azimuthal orientations of the chains. In contrast, elevated growth temperatures cause the chain growth to nucleate at the Ag step edges, which induces a preferential growth of distinct orientations. Secondly, the growth of epitaxial KCl layers on the vicinal Ag(100) surface was investigated. The KCl layer grows across the step edges of the vicinal surface in a carpet-like growth, which leads to a slight deformation of the KCl lattice. This has implications for the growth of QA structures on the KCl layer. The deformation of the KCl lattice leads to more possible adsorption configurations for QA molecules and thus a wider range of azimuthal chain orientations.

Overall, the investigation of the present thesis show that the formation of intermolecular H-bonds is a strong motif that can be used to create one-dimensional organic structures on metal surfaces and thin layers of wide band gap materials. However, the substrate also plays an important role, as all the observed structures are the result of a delicate balance between the intermolecular and the substrate-adsorbate interactions.

Contents

1 Introduction

Throughout the entire history of mankind, one-dimensional (1D) structures of different forms have played a very important role in human societies. Robust ropes are indispensable for the transportation of wares and the construction of buildings, pipes and cables are used for the transportation of water and electricity, and today information is transmitted through optical fibers. So, with the recent trend of modern technology to very small devices, a focus in research for the last three decades has been on atomic and molecular wires that are 1000 times thinner than human hair. Such atomic and molecular wires are considered to be essential building blocks for modern devices in (neuromorphic) computing, energy storage, photonics, photovoltaics, and other important applications [1–7].

Besides their use in technological applications, 1D structures are also very attractive objects for probing the fundamental physical properties of organic molecules. In science, reducing the dimensionality of a system and comparing its properties to those of the same material with a higher dimensionality is a common and rewarding approach because it helps us to understand the relation between individual atoms or molecules and the properties of the system that arise from them at a fundamental level. It has been shown that the so-called quantum confinement effect, which results from the confinement of the electron movement to (in the case of 1D structures) only one dimension, can change the chemical and physical properties of a material significantly [8]. An impressive example of this is that the optical properties of a material strongly depend on the size, shape, and dimensionality of the nanostructures [9–13]. The resulting unique properties are another reason why the investigation of 1D structures is of particular interest.

An organic molecule that is known to form 1D molecular chains in its bulk crystal structures [14] and on surfaces [15–17] that are connected via intermolecular hydrogen bonds (H-bonds) is quinacridone (QA). In the last two decades, QA has gained some attention besides its use as a dye for printer toners and varnishes because Głowacki *et al.* have found that it shows very promising properties for applications in electronic devices [18, 19]. In particular, they found a hole mobility of $0.1\,\mathrm{cm^2\,V^{-1}\,s^{-1}}$ and a photocurrent of about $1\,\mathrm{mA\,cm^{-2}}$. Both observations were attributed to the strong intermolecular H-bonds in the QA chains. Examples of QA-based applications are organic field-effect transistors (OFETs) [20–24], organic light-emitting diodes (OLEDs) [25–27], and organic photovoltaics (OPVs) [28–30]. A summary of the potential optoelectronic applications of QA and its derivatives is given in a review by Wang *et al.* [31].

A particularly interesting property of QA is that the transition dipole of a single QA molecule is pointed along the direction perpendicular to the long molecular axis inside of the molecular plane [32]. This direction is parallel to the direction of the intermolecular H-bonds. In a

chain of QA molecules then, the transition dipoles are arranged in a head-to-tail configuration (J-aggregate), which makes such chains of QA very interesting for optical investigations because the absorption band of such aggregates usually shifts to longer wavelengths and exhibits an increased sharpness in comparison to those of the corresponding monomers. For these reasons, QA was chosen for the experiments described in the present thesis. However, since the observation of unperturbed electronic and excitonic states of molecules is prohibited on metal surfaces, for such optical investigations it is necessary to decouple the molecules from the metal surface. This can be achieved for example by inserting thin layers of wide band gap materials, such as thin layers of an alkali halide (AH), between the molecular layer and the metal substrate [33]. Thus, the goal of the present thesis was to utilize the intermolecular H-bonds, which are a strong motif promoting chain formation, to create long QA chains on thin layers of wide band gap materials through self-assembly.

In the present work, the structures of QA on various metal surfaces and thin layers of wide band gap materials were investigated with scanning tunneling microscopy (STM) and low-energy electron diffraction (LEED). The objective was to elucidate the complex interplay between the different interactions[1] that determine the formation of different QA structures on these different surfaces. Of particular interest was the question of whether spatially isolated 1D chains of QA can be formed and observed on insulating layers, where the interfacial bonding between the molecules and the surface is typically weaker than on pure metal surfaces. This turned out to be a delicate task. The structures of QA were investigated on three different groups of surfaces, which will be introduced below. The reasoning behind the choice of these specific surfaces is as follows:

I The structures of QA were investigated on the Ag(100) and Cu(111) surfaces. These two surfaces are commonly used and are known to support the formation of ordered layers of many different organic molecules [34–37]. The comparison between the QA structures on Ag(100), Cu(111), and those on Ag(111), which were investigated by Wagner *et al.* [15], allowed a better understanding of the mechanisms at play. Lastly, Ag(100) and Cu(111) are known to be good templates for the growth of two very commonly used layers of wide band gap materials, namely potassium chloride (KCl) [38] and hBN, respectively [39, 40].

II Furthermore, the structures of QA were also investigated on KCl and hBN layers on the Ag(100) and Cu(111) surface, respectively. These two layers were chosen with the goal in mind to prepare QA chains that are electronically decoupled from the metal substrates and hence are interesting subjects for optical investigations.

III Lastly, the influence of Ag step edges on the growth of QA was investigated on a vicinal Ag(100) surface. This was done in order to find out, whether the unidirectional step edges may serve as favorable nucleation points for the growth of QA chains and thus facilitate

[1] These interactions include, for example, the intermolecular H-bonds, the substrate-adsorbate bond (chemisorptive vs. physisorptive), and the *van der Waals* interactions.

the chain growth on layers of KCl on the vicinal Ag(100) surface. Furthermore, it was explored whether a reduction of the surface symmetry may lead to a decrease in the amount of symmetry-equivalent QA domains.

The present thesis will cover these topics in the following order. Chapter 2 will give an introduction to the theoretical background regarding the QA molecule and the experimental methods that were used. An overview of the related literature will be given in Chapter 3 and the experimental methods will be explained in Chapter 4. The structures of QA on Ag(100) and Cu(111), on KCl/Ag(100) and hBN/Cu(111), and on Ag(35 1 1) and KCl/Ag(35 1 1) will be discussed in Chapter 5, Chapter 6, and Chapter 7, respectively. In Chapter 8, the lateral structure of blue phosphorus on Au(111) is discussed, which is another potential candidate layer for the growth of QA structures. Finally, the results of the present thesis will be summarized and concluded in Chapter 9 and an outlook regarding open questions and potential strategies to address them will be given.

2 Background information

This chapter will give some background information regarding the properties of the QA molecule, the experimental methods, and other important concepts. First, the molecule of interest in the present thesis, quinacridone, will be introduced. Then, the concept of 2D chirality on surfaces will be explained, and lastly, an introduction to the theory of the utilized experimental methods, namely LEED and STM[1], will be given.

2.1 Quinacridone

2.1.1 General information

The full IUPAC name of QA is 5,12-dihydro-quino[2,3-*b*]acridine-7,14-dione. It is a planar organic molecule of the symmetry group C_{2h} with the molecular formula $C_{20}H_{12}N_2O_2$ and a molar mass of $312.32\,\mathrm{g \cdot mol^{-1}}$. It has four different isomers [41] of which in this work only the linear *trans* isomer was considered, and the abbreviation QA only refers to this isomer. A structural formula and a hard-sphere model of QA are shown in panel a) of Figure 2.1. Its molecular skeleton consists of five annulated carbon rings and has thus some similarities with the very well-known molecule pentacene. The difference between the two molecules is that QA contains four functional chemical groups, namely two ketone and two secondary amine groups. These functional groups break the intramolecular π-conjugation of the molecule, but they enable it to exhibit strong intermolecular interactions in the form of H-bonds (N–H$\cdots$O) between the amine group of one molecule and the ketone group of another molecule. QA is a prochiral molecule and exhibits therefore 2D chirality when adsorbed on a surface. This concept will be explained in more detail in Section 2.2.

Under standard conditions, QA is a crystalline solid with four known different crystal structures [14, 44] that is insoluble in water and most common organic solvents [41]. The crystal structures are illustrated in Figure 2.2 and will be discussed in further detail below. At a pressure of 0.4 mbar, the sublimation temperature of QA is 695 – 702 K depending on its crystal structure [45]. In gradient sublimation experiments ($p = 10^{-8}$ mbar) by Berg *et al.* [23], it was observed that QA sublimated at 673 K and the main fraction deposited at 583 K, while a black solid remained at the place of the loaded material. Due to the different crystal structures, the color of QA crystals can range from orange to violet. In solution, QA is yellow (cf. Fig. 2.1). This and its other properties make QA an excellent candidate for use as a dye. It does not undergo a color change up to temperatures of 460 K [46] and does not melt or decompose when heated to 673 K [47]. It also exhibits excellent lightfastness at all levels of dilution [46]. Lastly, QA can be produced at a large scale with

[1] All abbreviations that are used in the present thesis can be looked up in the List of abbreviations on page 237.

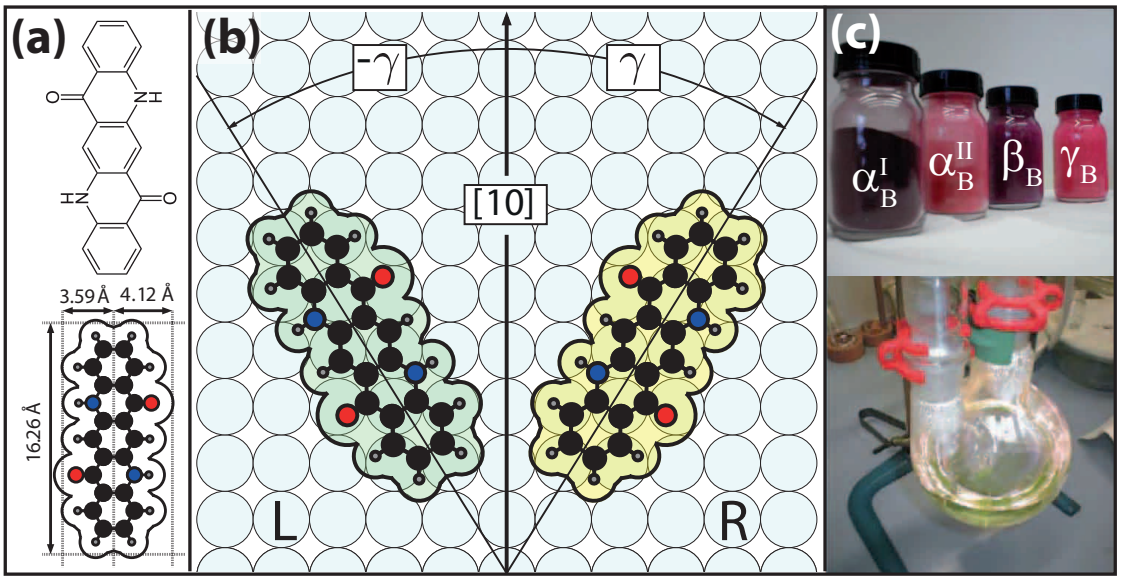

Figure 2.1: a) *Structural model and a corresponding hard-sphere model of QA. The hard-sphere model was drawn with the program graphics layout engine [42] using bond lengths and van der Waals radii from literature [43].* ***b)*** *Illustration of the 2D chirality of QA. The color code of the atoms is as follows: black = carbon, gray = hydrogen, blue = nitrogen, and red = oxygen.* ***c)*** *Images of QA that show the colors of the four bulk crystal structures and of QA in a solution of boiling DMSO at 185 °C.*

good yield with a simple four-step synthesis using aniline and diethyl succinate as reagents [48], which are both cheap and easily obtainable [49, 50]. Because of the above reasons and the fact that QA is not toxic [51], it is a widely used organic pigment (also known under the name Violet 19). It is utilized as high-performance paint, for example in varnishes and printer toners [41, 47, 52], and was first sold by Du Pont in 1958 [46].

2.1.2 The QA bulk crystal structures

It is particularly interesting to compare the bulk crystal structures to the structures that form on surfaces because the potential parallels and differences allow us to draw conclusions about the interactions at play. Over the years, various crystal structures of QA have been reported in journals and patents [14]. However, many of those described the same structures or were mixtures of two already known crystal structures. Now, four crystal structures of QA, which are illustrated in Figure 2.2, can be distinguished: the α_B^I- and α_B^{II}-, the β_B-, and the γ_B-phases.[2] All of these crystal structures of QA have in common that the structure-determining element is given by the intermolecular H-bonds [14, 53, 54].

The α_B^I- and α_B^{II}-phases (cf. Fig. 2.2, top half) are very similar. Both consist of 1D aggregates of QA molecules that are facing each other with their functional groups and which are linked through two intermolecular H-bonds per molecule.[3] These aggregates will be referred to as QA

[2] The letter B in the subscripts stands for the word "bulk" to distinguish these names from the ones of the QA phases on surfaces that will be discussed later on.

[3] In the present thesis, an H-bond between two molecules will be counted as 0.5 H-bonds per molecule.

chains within the scope of the present thesis. The QA chains in the two above-mentioned crystal structures have small steps of roughly 0.35 Å to the right of each molecule, as is illustrated by the dashed black lines in Figure 2.2. These chains form stacks, in which the molecules of one chain are facing the molecules of another chain with their flat sides, which allows π-π-interactions between the molecules of neighboring chains. The difference between the two phases lies in the packing of the chain stacks. In the α_B^I-phase all stacks are parallel while in the α_B^{II}-phase they are arranged in a herringbone structure. Interestingly, the β_B-phase (cf. Fig. 2.2, bottom left) also consists of the same type of stacked QA chains. But here, neighboring chain stacks are mutually rotated by 69.4 ° with respect to one another. The fact that three out of four known crystal structures consist of these molecular chains is a strong indicator that the formation of molecular chains is very favorable for QA and may hence also be expected to occur on surfaces, too. In contrast to the other three structures, the γ_B-phase (cf. Fig. 2.2, bottom right) does not consist of molecular chains. Instead, it consists of stacks of QA molecules that are held together by π-π-interactions. Neighboring stacks are tilted with respect to one another so that every molecule is connected to four other molecules via a single H-bond resulting in a criss-cross pattern. Overall, it can be said that the most important structure-determining factors in the QA crystal structures are the intermolecular H-bonds and the π-π-interactions within the stacks. The crystallographic data of the four phases is summarized in Table 2.1.

Table 2.1: *Crystallographic data of the four known crystal structures of QA.*

phase	ref.	*a* / Å	*b* / Å	*c* / Å	α / °	β / °	γ / °
α_B^I	[14]	3.802(2)	6.612(3)	14.485(6)	100.68(8)	94.40(6)	102.11(5)
α_B^{II}	[55]	7.1	28.4	3.9	90	100	90
β_B	[14]	5.692(1)	3.975(1)	30.02(4)	90	96.76(6)	90
γ_B	[14]	13.697(9)	3.881(3)	13.402(1)	90	100.44(1)	90

Finally, the stability of the different crystal structures will be compared. Gorelik *et al.* have found through density functional theory (DFT) calculations [55] that the lattice energies of the α_B^I- and α_B^{II}-phases are very similar. The *relative* lattice energies of the β_B- and γ_B-phases with respect to those of the α_B^I- and α_B^{II}-phases are more favorable ($\beta_B : -4.3$ kJ mol^{-1}; $\gamma_B : -5.5$ kJ mol^{-1}), which yields the following order of stability for the four phases: $\gamma_B > \beta_B \gg \alpha_B^I \cong \alpha_B^{II}$.

2.2 2D chirality at surfaces

Chirality is a very important concept in the field of stereochemistry. A molecule is chiral when it is incongruent with its mirror image. Similarly, the term *prochiral* is used to describe molecules that can be transformed from achiral into chiral molecules in a single step, e.g., by substituting one functional group with another. Due to the lower dimensionality at surfaces, only symmetry elements that are orthogonal to the surface can exist. Hence, the breaking of symmetry is a very common phenomenon there. 2D chirality on achiral surfaces can be caused by several different effects, such as the adsorption of a molecule at a tilted angle, deformation of an achiral molecule

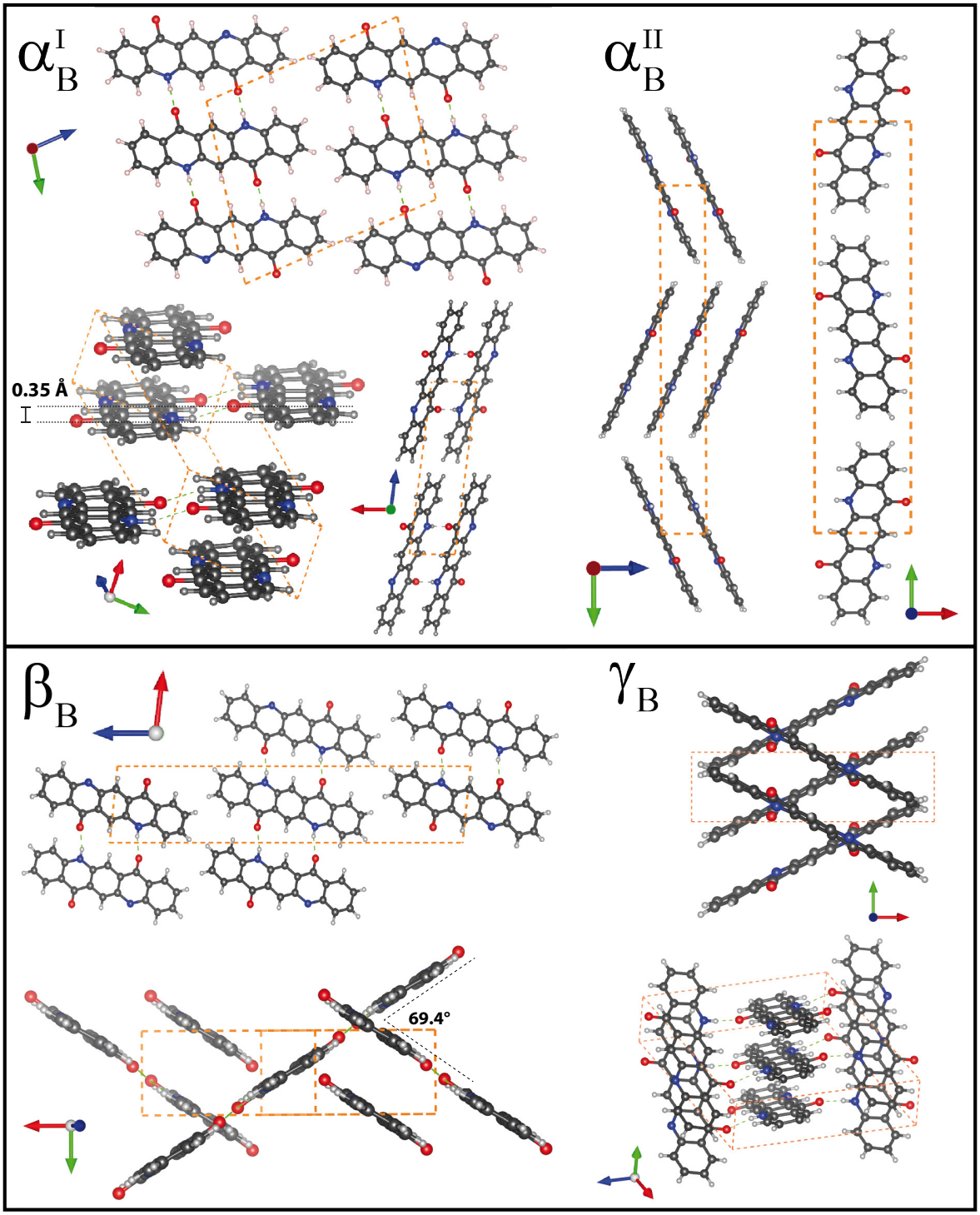

Figure 2.2: *Bulk crystal structures of QA. Shown are two or three different perspectives (indicated by the coordinate systems) for all four crystal structures and the unit cells are depicted in orange. The structure coordinates were taken from refs. [14] and [55] and were drawn with the software VESTA 3 [56]. The color code of the atoms is as follows: black = carbon, gray = hydrogen, blue = nitrogen, and red = oxygen. For more information, see text.*

upon adsorption, and chemical reactions with the surface. In-depth information on the topic of 2D chirality can be found in the reviews by Ernst [57] and Raval [58].

The most common cause for 2D chirality, which is also applicable to the adsorption of QA, is rather simple. The adsorption of a planar prochiral molecule in a flat-lying geometry creates a chiral center where the surface represents the fourth attached group. Another way to look at this is that the adsorption on the surface causes the molecules to lose their σ_h mirror plane. This leads to two different enantiomers, depending on with which of its two sides the molecule adsorbs on the surface. In panel b) of Figure 2.1 the two corresponding enantiomers of QA on Ag(100) are displayed. The two enantiomers are rotated by $+\gamma$ and $-\gamma$ with respect to the [10] direction, respectively. They can be projected onto each other by a mirror operation at the mirror plane that is parallel to the [10] direction and perpendicular to the surface and are thus on identical adsorption sites. Within the scope of the present work, these two enantiomers will be labeled with the letters R and L.[4]

Considering the fact that organic molecules can exist as two different enantiomers on the surface raises an interesting question: Do aggregates of chiral molecules on surfaces have a preference towards hetero- or homochiral packing? It is known that for the three-dimensional (3D) crystal structures of chiral organic molecules heterochiral packing is more common [59]. However, in the case of 2D chirality on surfaces, this is not so clear. In a recent review, Dutta and Gellmann found no relevant statistical preference for hetero- or homochiral packing [60]. Overall, it is assumed that the packing is determined by a subtle balance between various forces. Even a small change in experimental parameters, for example, the sample temperature or the coverage, can induce phase transitions between hetero- and homochiral phases.

2.3 Scanning tunneling microscopy

The first scanning tunneling microscope was developed in 1981 by Binnig and Rohrer [61]. Five years later, in 1986, they were awarded the Nobel Prize in physics for this historic accomplishment. Today, it is one of the most common methods in the field of surface science because it is capable of imaging small surface areas in real space with atomic or molecular resolution. In the following, a brief introduction to this method will be given. A more in-depth explanation can be found in the pertinent literature [62–65].

The concept of an STM is rather simple: A sharp tip, usually an etched or cut Pt/Ir or W wire, is brought within a few ångströms of a conducting surface. At the same time, a potential difference, the so-called bias voltage U_B, is applied between the tip and the sample. This shifts the Fermi levels of the tip and the sample with respect to each other, which creates an incentive for a current to flow. However, the space between the sample and the tip represents a potential barrier that is given by the work functions of the sample or the tip (Φ_s and Φ_t). These are usually several eV

[4] The typical nomenclature in chemistry for the classification of chiral centers uses the letters R (rectus, Latin: right) and S (sinister, Latin: left) according to the Cahn-Ingold-Prelog convention. However, in the field of surface science, it is not uncommon to use the letters R (right) and L (left), instead.

high and thus larger by two orders of magnitude than the thermal energy of electrons at room temperature (RT). Nevertheless, a measurable current (up to 1 nA) can flow between the tip and the sample. This is explained by the quantum tunneling effect. It describes the phenomenon that particles with a total energy E can tunnel through potential barriers of a limited height $V_0 > E$, which they would otherwise not be able to overcome according to the rules of classical physics. The transmission coefficient can be calculated with the distance d, the mass of the electron m_e, the reduced Planck constant $\hbar$, the inverse decay length of the electron wave function κ, and the height of the potential barrier V_0, and is given by [62]:

$$T_{\text{tun}}(d, E) = e^{-2\kappa d} \quad \text{with} \quad \kappa = \sqrt{\frac{2m_e(V_0 - E)}{\hbar^2}}. \tag{2.1}$$

A schematic illustration of the quantum tunneling effect of an electron between the sample and the tip is shown in Figure 2.3. It shows the Fermi levels $E_{F,s}$ and $E_{F,t}$ of the sample and the tip, which are shifted by $E_B = e \cdot U_B$ with respect to each other. Depending on the sign of U_B, the electrons tunnel from the occupied states of the sample into the unoccupied states of the tip or *vice versa*. The tunneling electron itself is represented by its wave function Ψ. It does not lose any energy in the process, hence the wavelength of the wave function is identical on both sides of the barrier. The probability of presence of the electron is significantly lower behind the barrier which is reflected in the lower amplitude of the wave function.

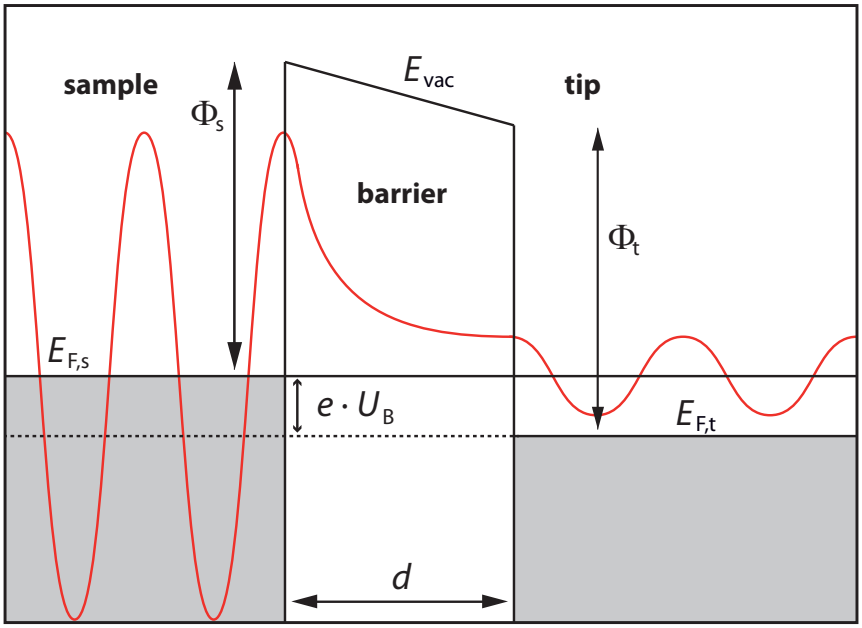

Figure 2.3: *Schematic illustration of an electron tunneling through a potential barrier. The two Fermi levels $E_{F,s}$ and $E_{F,t}$ are shifted with respect to each other by $E_B = e \cdot U_B$. The red curve describes the wave function of the electron. In the barrier, the wave function decays exponentially according to equation 2.1. The wavelength before and after the tunneling is identical because the tunneling does not cause the electron to lose energy. The probability of presence of the electron behind the barrier is lower, which is reflected in the smaller amplitude of its wave function.*

The exact calculation of the resulting tunneling current I_{tun} is very complicated because I_{tun} is the result of a convolution between the electronic states of the tip and those of the sample. The geometry and thus the electronic states of the tip are unknown. To circumvent this problem, the *Tersoff-Hamann* model is very commonly used, which approximates the electronic states of the tip as those of a spherical *s*-orbital [66]. Under this assumption, the tunneling current I_{tun} is proportional to the local density of states (LDOS) of the sample at the Fermi edge of the sample $E_{\text{F,s}}$ at the position of the center of the tip, which is described by the vector $\mathbf{r_0}$. Under consideration of equation 2.1 and with the extension to final bias voltages, the tunneling current can be approximated as:

$$I_{\text{tun}} \propto \int_{E_{\text{F,s}}}^{E_{\text{F,s}}+U_{\text{B}}} \left|\Psi(\mathbf{r_0})\right|^2 dE. \tag{2.2}$$

The *Tersoff-Hamann* model can be extended, i.e., the electronic states of the tip can also be approximated as those, for example, of *p*- or *d*-orbitals. In this case, the tunneling current is proportional to an expression that is related to a simple derivative of the sample wave function at $\mathbf{r_0}$. This was derived by C. J. Chen and is explained in detail in refs. [65, 67].

In practice, the STM tip scans line by line over an area of the surface, which is usually between $5 \times 5\,\text{nm}^2$ and $1000 \times 1000\,\text{nm}^2$ in size. The precise tip movement in all three dimensions (x, y, z) of such a small scale is achieved through the utilization of piezoelectric crystals on which the tip is mounted. After a calibration of the piezoelectric crystals, the applied voltages can be translated into distances. During the scanning process, the tunneling current I_{tun} and the tip height z are measured as a function of the lateral position (x, y). A proportional–integral–derivative (PID) feedback loop controls the scanning process, reacts to alterations in the tunneling current, and adjusts the height z accordingly. If the parameters of the PID feedback loop are set in a way that the tunneling current I_{tun} remains constant, then the tip height z adjusts quickly to and reflects the corrugation of the surface. This mode is called the *constant current mode*. It is mainly used on samples with a high corrugation to prevent the tip from crashing into the surface. Hence, it was used for the STM experiments on Ag(100) and Cu(111) within the scope of the present thesis. A disadvantage of this mode is that the scan velocity is quite slow compared to the so-called *constant height mode*. As the name suggests, in this mode the height z is kept at a constant value during the scan. That means that the corrugation of the surface is reflected in the tunneling current. The disadvantage of this mode is that it can only be employed on very flat surfaces without the risk of crashing the tip into the surface. A schematic illustration of the two modes is shown in Figure 2.4.

In the present work, the tunneling parameters were not chosen beforehand in order to image the LDOS corresponding to distinct molecular orbitals. Instead, they were varied systematically during the experiments and those parameters were chosen that yielded the best image quality and molecular resolution. Thus, negative bias voltages between $-1\,\text{V}$ and $-2\,\text{V}$ were routinely used to image the QA molecules on metal surfaces. Theoretical DFT calculations and angle-resolved photoemission experiments by Lüftner *et al.* have found that the orbital energies of the highest occupied molecular orbital (HOMO) and the HOMO-4 of single QA molecules in the gas phase lie within an energy range of only 2 eV [69]. It can expected that the different molecular orbitals

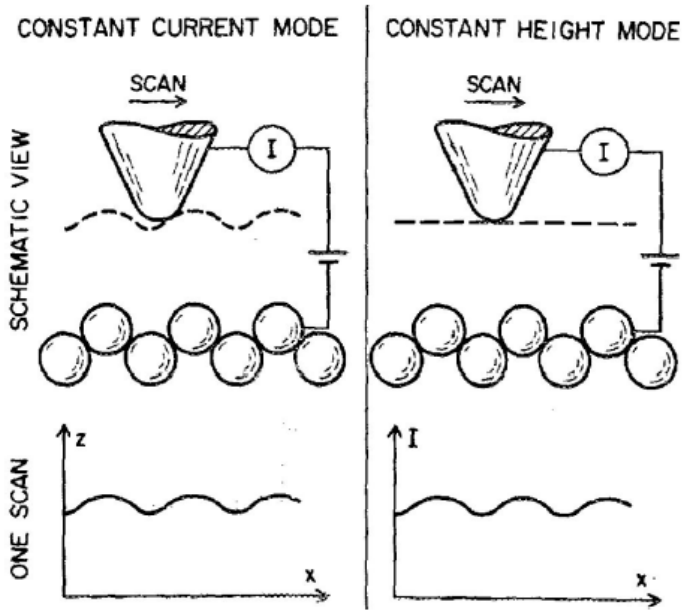

Figure 2.4: *Illustration of the two measurement modes of an STM. In panel a) the constant current mode is displayed. Here, the height of the tip is adjusted to the corrugation of the sample during the scan while the current is held constant at a set value. Panel b) shows the constant height mode. In this mode, the height z is kept at a constant value and the corrugation of the sample is reflected in the tunneling current. The figure is taken from ref. [68].*

of the adsorbed molecules lie within a similar energy range. Thus, for bias voltages in the above-mentioned range, it is likely that the electron densities corresponding to all orbitals between the HOMO and HOMO-4 contribute to the observed structures in the STM images, although it can be expected that the HOMO makes the largest contribution.

Finally, it is important to note that STM images are not purely a representation of the topological structure of the scanned surface. There are a few aspects that need to be considered when it comes to their interpretation. The first aspect is that the recorded STM image is a convolution of the electronic structure of the sample and tip. The topography of the tip, and thus its electronic structure, during the experiment are often unknown.[5] The *Tersoff-Hamann* model (see above) neglects the electronic states of the tip, and all the observed structures are attributed to the electronic or topological structure of the surface. In this context, it is important to keep in mind that the electronic structure of the surface can sometimes vary drastically from the topological structure. Secondly, the appearance of structures in STM images is also dependent on the tunneling parameters (I_{tun} and U_{B}) because they influence the distance between the tip and the sample. Depending on said distance, more or less electronic states of the sample and the tip contribute to the tunneling current, which influences the result of the convolution and can change the observed image drastically. Lastly, it is also important to keep in mind that STM always only shows a very tiny area of the surface. It is impossible to know for certain whether the observed structures are representative

[5]However, it is possible to conduct STM measurements with a tip of a defined and known shape to some degree. This is done, for example, by adsorbing a CO molecule at the tip during low-temperature measurements [70, 71].

of the structures on the whole surface. Therefore, it is important to achieve a large enough sample of images recorded at different locations or to complement the STM results with results from a method that yields structural information as an average over a large area, for example, LEED.

2.4 Low-energy electron diffraction

The discovery of electron diffraction by Davisson and Germer in 1927 [72] led to the development of several methods utilizing different ranges of electron energies for the investigation of structures on surfaces. One of the standard methods is LEED. Electrons with low energies (20 – 300 eV) are directed towards a surface and only the elastically scattered electrons are detected. The resulting diffraction image contains precise information on the geometry and two-dimensional order of the surface. The *de Broglie* wavelengths λ_e of electrons with a kinetic energy E_{kin} in the above-mentioned range can be calculated via

$$|\boldsymbol{k_0}| = \frac{2\pi}{\lambda_e} = \frac{\sqrt{2m_e\, E_{kin}}}{\hbar}, \tag{2.3}$$

and are between roughly 1 Å and 3 Å, which is in the same order of magnitude as the atomic and molecular structures on the surface. Therefore, electrons in this energy range (20 – 300 eV) are well suited for structure analysis on this length scale. In contrast to X-rays, electrons exhibit very strong interactions with matter, which leads to a large cross-section for elastic or inelastic scattering. As a consequence, for electrons with energies in the above energy range, the mean free path in solid matter is only roughly 5 – 7 Å, which makes LEED a surface-sensitive method [63, 64].

The surface atoms or molecules of an adsorbate layer can be understood as a two-dimensional (2D) diffraction grating with the lattice spacings a, b in both dimensions. The scattered electrons represent a wavefront in which, according to the *Huygens-Frensel* principle, every point is the source of spherical wavelets that can mutually interfere. Hence, the resulting diffraction pattern, i.e., the LEED spots, is the result of constructive interference between these waves, which occurs when the path length difference is an integer multiple of the electron wavelength. For a spot of high intensity to appear in the diffraction pattern, the conditions for constructive interference must be fulfilled for both dimensions at the same time, which are given by:

$$\sin(\varphi_a) = i\,\frac{\lambda_e}{a}\ ;\ \sin(\varphi_b) = j\,\frac{\lambda_e}{b}. \tag{2.4}$$

Here, φ_a and φ_b refer to the diffraction angles relative to the surface normal, and the letters i, j denote integer numbers. Now, substituting λ_e with an expression from equation 2.3 yields a formula for the so-called two-dimensional reciprocal lattice vector $\mathbf{G}$, which describes the positions of constructive interference in the reciprocal lattice:

$$\mathbf{G} = \Delta\mathbf{k}_{||} = i\,\frac{2\pi}{a} + j\,\frac{2\pi}{b}, \tag{2.5}$$

where $\mathbf{k}_{||}$ denotes the component of momentum of the scattered electron parallel to the surface, and the variables a and b refer to the real space lattice spacings in both dimensions.

A graphic and accessible way to understand the diffraction pattern is the so-called *Ewald* sphere. A two-dimensional section through the Ewald sphere is depicted in Figure 2.5. The incident wave vector of the electron $\boldsymbol{k_0}$ is scattered in several directions illustrated by the wave vectors $\boldsymbol{k_{ij}}$. These vectors go from the center of the sphere (where the sample is located) towards the points where the reciprocal lattice (the dashed lines) intersects with the sphere, which has a radius given by $|\boldsymbol{k_0}|$. These intersection points mark the directions where the spots in the diffraction pattern appear.

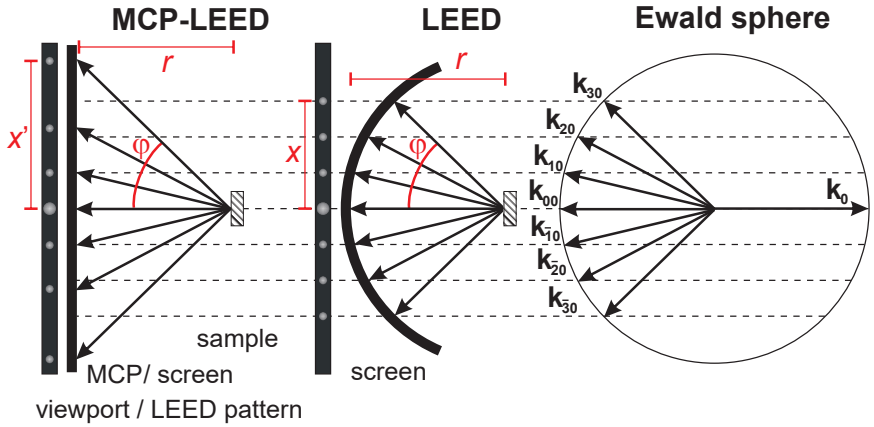

Figure 2.5: *Schematic drawings of an MCP-LEED, a conventional LEED and the Ewald sphere (from left to right). The drawing was taken from ref. [73] and slightly modified. The gray points in the black bars represent the corresponding spots of the diffraction pattern.*

Diffraction patterns contain useful information regarding different aspects of the corresponding structures. The analysis of the positions of the superstructure spots (with those of the known unit cell of the substrate as a reference) yields the unit cell of the adsorbate superstructure and the corresponding superstructure matrix. Here, a disadvantage of LEED becomes apparent, which is that a single diffraction pattern yields the periodicity of the superstructure, but it does not give any information about the atomic or molecular arrangement within the unit cell. However, this can be achieved by measuring the spot intensities versus the incident electron energies (so-called I-V curves) [74]. An advantage of LEED is that the electron beam hits roughly 1 mm² of the sample and hence the information that the diffraction pattern contains is averaged over this area. Hence, in contrast to STM, LEED will only show diffraction patterns if the corresponding structure is present on a significant portion of the observed area.

The shapes of the spot profiles contain information about the surface morphology. In particular, the full width at half maximum (FWHM) of the spots is influenced by two factors. One factor is the roughness of the surface. A high amount of step edges can lead to a broadening of the spots due to destructive interference between electrons that are scattered at terraces of different heights [75]. However, this phenomenon is dependent on the electron energy (no spot broadening at electron energies where constructive interference occurs) and is thus distinguishable from the other factor, which is a spot broadening due to deviations from the ideal surface, e.g., domain boundaries.

In practice, a traditional LEED apparatus utilizes a hemispherical phosphorescent screen with the sample in its center to detect the scattered electrons. The diffraction pattern is recorded with a camera from the back of the screen. In the present work, two variants of LEED were used. The microchannel plate low-energy electron diffraction (MCP-LEED) is very similar to the traditional LEED and is illustrated on the left-hand side of Figure 2.5. In this variant of LEED, the electrons pass through a microchannel plate before being detected on a detector plate. The diffracted electrons are multiplied by the microchannel plate, and hence a more intense signal on the detector is achieved. The diffraction patterns obtained by an MCP-LEED are distorted because the multichannel and detector plates are not hemispherical. For the same scattering angle φ in an MCP-LEED, the resulting spot is further apart from the specular spot than it is the case in a traditional LEED. This can be seen in Figure 2.5, the distances x' and x, as well as the relation between them, can be calculated according to the following simple equations:

$$x = r \cdot \sin(\varphi),\ x' = r \cdot \tan(\varphi),\ x = x' \cdot \cos(\varphi). \tag{2.6}$$

In the present thesis, the distortion of the images was corrected according to the above equations with a small program called MCPDeskew, which was written by J. Ikonomov [76]. This method of MCP-LEED was used within the scope of the present thesis because it leads to lower beam currents than in traditional LEED. All images were recorded with a beam current of about 10 nA. This is useful for investigating organic structures because it is well-known that some organic structures decompose when they are exposed to electron bombardment. In particular, Wagner *et al.* reported that the LEED patterns, recorded with a traditional LEED apparatus, for QA on Ag(111) usually vanished after a couple of seconds [15].

The other LEED variant that was used within the scope of the present work is spot profile analysis low-energy electron diffraction (SPA-LEED). The SPA-LEED apparatus does not detect the scattered electrons on a phosphorescent screen. It contains an octupole consisting of 8 plates to make use of electrostatic deflection in order to modify the track of the electrons before and after they were scattered at the sample. The scattered electrons are scanned over the aperture of a stationary point detector and electron multiplier, the channeltron. This technique yields a higher lateral resolution than traditional or MCP-LEED. That means that two close spots that appear as one spot in traditional LEED may be visible as two separate spots in SPA-LEED. A disadvantage of SPA-LEED is that the scanning process also requires significantly more time. The intricacies of this variant of LEED will not be discussed in detail here, but more information on the topics of LEED and SPA-LEED can be found in relevant textbooks and review articles [74, 75, 77]. Within the scope of the present thesis, on the one hand, SPA-LEED was also used to record 2D diffraction patterns of the QA structures with high lateral resolution and good signal-to-noise ratio. These images were used to determine the corresponding real space unit cells with high accuracy. On the other hand, SPA-LEED was used to investigate the phase transitions of QA on the Ag(100) surface by analyzing the shape and width of the QA spot profiles at different temperatures (cf. Section 5.4).

3 Review of literature

This chapter will present an overview of the scientific fields of which the topics of the present thesis are a part. The integral part of this thesis deals with the self-assembled structures of QA on metal surfaces and dielectric layers. Therefore, Section 3.1 will summarize what is already known about the self-assembly of QA and some of its derivatives on surfaces. In order to view the self-assembled structures of QA in a broader context of similar structures, Section 3.2 will give an overview of the different types of 1D aggregates that are already known on metal surfaces. Lastly, Section 3.3 will cover the field of alkali halide (AH) layers on surfaces and what is already known about organic molecules adsorbed on them.

3.1 Self-assembly of quinacridones on surfaces

In contrast to some other well-known organic molecules that have been objects of interest in the field of surface science for many years, for example 3,4,9,10-perylene tetracarboxylic dianhydride (PTCDA) or pentacene, structures of QA on surfaces have not been investigated so much. Structures of QA were reported on Ag(111) [15], on highly oriented pyrolytic graphite (HOPG) and MoS_2 [16, 17, 78], and on SiO_2 [79, 80]. In this chapter, a summary of the previous results on QA structures on surfaces will be given.

For the present thesis, the publication by Wagner *et al.* on QA on Ag(111) [15] is of particular interest because it is the only work in which identical preparatory and analytical methods were utilized, i.e., the QA was deposited in ultra-high vacuum (UHV) onto a metal sample via chemical vapor deposition (CVD), and the structures were investigated by LEED and STM. Two corresponding STM images are displayed in Figure 3.1. The authors found that the growth of QA is heavily influenced by its ability to form intermolecular H-bonds and its 2D chirality on the surface. After deposition onto the sample at RT, QA grows in molecular chains with six distinct orientations, which are determined by the interactions between the QA molecules and the Ag substrate. In the following, this phase will be referred to as the α^*-phase. The bonding motif for the chain formation is the formation of the intermolecular H-bonds between the functional groups of the QA molecules, as was explained in Chapter 2.1.2. Since H-bonds can only form between QA molecules of the same handedness, the authors concluded that the molecular chains are enantiopure with an intermolecular distance of $b_1 = (7.0 \pm 0.1)$ Å. Furthermore, they assumed that even the whole domains are enantiopure because different azimuthal orientations can be associated with different 2D enantiomers. They also found randomly distributed defects in the domains, which cause larger intermolecular distances within the chains. This was explained by molecules with the wrong handedness (fraction of 18 %) that were trapped in the domains during the growth process.

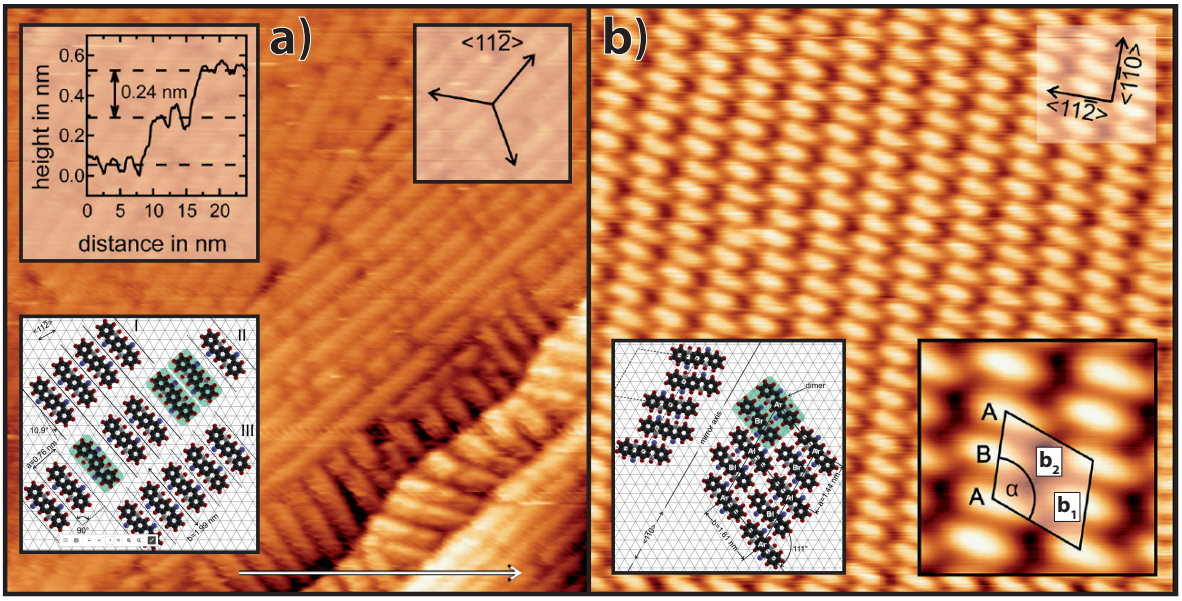

Figure 3.1: *Structure of a close-packed QA monolayer on the Ag(111) surface.* ***a)*** *The α^*-phase of QA, which forms after deposition onto the sample at RT. The graph in the inset of the top left corner shows a line profile along the arrow at the bottom. A structure model of the phase is shown in the inset in the bottom left. The molecules with the green background have a different handedness than the rest of the molecules in the chains, which leads to increased intermolecular distances.* ***b)*** *The so-called β^*-phase, which forms after annealing the α^*-phase at 550 K. It is a commensurate structure that consists of periodically indented and heterochiral chains. The letters A and B stand for equivalent adsorption sites. For more information, see text. A structure model is displayed in the inset at the bottom left. The green background highlights a dimer of two molecules with the same chirality. The images were taken from ref. [15] and slightly modified.*

The distance between neighboring chains was found to be $b_2 = (20.3 \pm 1.2)$ Å and is determined by the corrugation of the molecule-substrate potential. Although the authors state that the parameters of the vector $\mathbf{b_2}$ are rather speculative, they propose that the structure of the α^*-phase is high-order commensurate.

The α^*-phase is thermodynamically not stable and changes into a different phase that is commensurate upon annealing at 550 K, which will be called the β^*-phase in the following. The β^*-phase is very well-ordered and consists of large domains that are comprised of long and periodically indented chains. In contrast to the α^*-phase, the β^*-phase is heterochiral, i.e., it consists of a 1:1 mixture of both enantiomers. The corresponding structure model (cf. inset of Fig. 3.1b) shows that the chains consist of homochiral pairs, but the handedness of the pairs switches periodically. That means that in the β^*-phase every QA molecule exhibits 1.5 H-bonds on average, which is 0.5 H-bonds less than in the α^*-phase.[1] The unit cell has the lengths $b_1 = 14.4$ Å and $b_2 = 16.1$ Å, and an angle of $\alpha = 111°$ between the two unit cell vectors. Overall, the authors explain the two observed structures as the result of the competition between the strong intermolecular interactions on the one hand, and the 2D chirality and its influence on the molecular arrangement on the other

[1] Reminder: in the present thesis an H-bond between two molecules will be counted as 0.5 H-bonds per molecule.

hand. These motifs are also very important in context of the structures of QA on various surfaces that were observed within the scope of the present thesis.

As mentioned above, structures of QA were also investigated on HOPG and MoS_2 [16, 17, 78]. In contrast to Ag(111), here, the structures were prepared by the so-called organic solid-solid wetting deposition (OSWD). In this method, small crystals of QA are dispersed in a liquid dispersion agent, which is then deposited onto the sample. More information on OSWD and its exact mechanism can be found in the corresponding literature [16, 17, 78]. Nevertheless, the same kind of molecular QA chains that are connected via intermolecular H-bonds and exhibit the same intermolecular distance as the α^*-phase on Ag(111) can also be found on these two surfaces. Within the scope of these publications, no annealing experiments were conducted. Hence, it is unknown whether a similar phase transition as on Ag(111) would take place on HOPG or MoS_2.

Furthermore, QA was also investigated by R. Priya on Ag(111) and Ag(110) [81, 82] by SPA-LEED, thermal desorption spectroscopy (TDS), and infrared (IR) spectroscopy. The TDS investigations yielded desorption energies of the QA multilayer on Ag(110) and Ag(111) of 1.9 eV and 1.8 eV, respectively. This indicates stronger QA-substrate interactions for Ag(110) as compared to Ag(111), which is also confirmed by IR spectroscopy. Moreover, an interfacial dynamical charge transfer (IDCT) was found, which is stronger for QA/Ag(110). Interestingly, this IDCT has completely vanished for the heterochiral structures after annealing, which is ascribed by the author to a filling of the former lowest unoccupied molecular orbital (LUMO). It was also found that in the heterochiral phases, the oxygen atoms that are not involved in the formation of H-bonds exhibit a stronger bonding to the metal substrate. Lastly, new structures for QA on Ag(110) were reported, which will also be compared to those on Ag(100) and Cu(111) of the present work. However, it is important to note that the results by R. Priya that are used in the present work are preliminary and have not been published yet.

Beyond this, several studies of QA derivatives on various surfaces have been conducted [83–92]. All of the derivatives that were used in the mentioned studies had various alkyl chains attached to the two nitrogen atoms of the QA molecule. Thus, a chain formation similar to the one that was observed on Ag(111) did not occur with these derivatives. However, in all studies ordered layers of flat-lying molecules were reported in which the order also depends on intermolecular interactions and the 2D chirality of the molecules.

Lastly, the author of the present thesis would like to mention that within the scope of a cooperation with Rémi Bretel from the Université Paris-Saclay, QA was also measured on hBN on Cu(111) together with him at the University of Bonn. The results are already published in his doctoral thesis [93], but will also be evaluated and discussed in Chapter 6.3 of the present thesis. In his thesis, R. Bretel also investigated QA on KCl on the Cu(111) surface. These results will not be summarized in this chapter, but they will be compared to the data for QA on KCl on Ag(100) in Chapter 6.2.

3.2 Self-assembled one-dimensional aggregates on surfaces

One-dimensional aggregates are not only very interesting systems to investigate because of their enormous potential for applications in nanotechnology, but also because their electronic properties can be easily tuned by many experimental parameters such as their length, their width, and the interatomic/intermolecular distances within the chains. Consequently, many different types of 1D aggregates have been investigated over the years, for example, those that grow via liquid-assisted self-assembly [94] or on surfaces along the surface normal [95]. This chapter will focus on 1D aggregates that form via surface-assisted self-assembly and grow parallel to the surface. The preparation of such 1D aggregates of metal atoms or organic molecules on metal surfaces is a topic that has been studied intensively throughout the last decades. Especially in the field of atomic 1D aggregates hundreds of articles have been published [96, 97].

One common method to prepare atomic chains on metal surfaces is to prepare them manually with the help of an STM [98–100]. However, manipulating atoms with an STM tip requires considerable time investment and is hence unsuitable for the construction of long atomic chains, in particular at an industrial scale. An alternative is the diffusion and self-assembly of atoms into 1D aggregates. Here, one challenge is that metal atoms are in good approximation spherical and do not exhibit any inherent asymmetry. Hence, the self-assembly of atoms into isolated 1D aggregates on flat surfaces is unlikely. In order to circumvent this problem, the substrate surface must have some asymmetry, for example in the form of unidirectional step edges on a vicinal surface. Indeed, metallic atomic wires were reported on vicinal metal surfaces [101–106], where they usually grow along the unidirectional step edges. An example is illustrated in Figure 3.2, which shows STM images of long Fe wires that have grown along the step edges of a vicinal Cu(111) surface. Of course, metallic wires were also prepared and investigated on vicinal semiconductor surfaces [107–109]. Moreover, metallic 1D aggregates were also found on metallic fcc(110) surfaces growing along the $[1\bar{1}0]$ direction of the substrate [110–113]. This growth of metallic 1D aggregates is of course also temperature dependent. A sample temperature that is too low leads to slow diffusion and hence to roughness. If the sample temperature is too high, it may lead to a fusion of the metals and the formation of an alloy. A good overview of the field of atomic 1D aggregates is given by the review articles [96, 97].

In the context of the present thesis, where molecular chains of QA were investigated, it is more interesting to look at the field of *molecular* 1D aggregates on surfaces. By considering basic chemical and physical principles it is possible to design organic molecules that form a desired structure, for example, 1D aggregates, on the surface. An overview of the field of self-assembled 1D organic aggregates is also given in ref. [114]. From a chemical point of view, a very straightforward idea is to synthesize long 1D polymers through coupling reactions on the surface. A wide range of such coupling reactions are known including dehalogenation, dehydrogenation, dehydration, and other reactions. On surfaces, the most commonly used method is the dehalogenation in which carbon-halogen bonds are thermally cleaved and the resulting radicals react and form covalent bonds (*Ulmann* reaction). An in-depth description of the reactions that can be utilized to form covalent

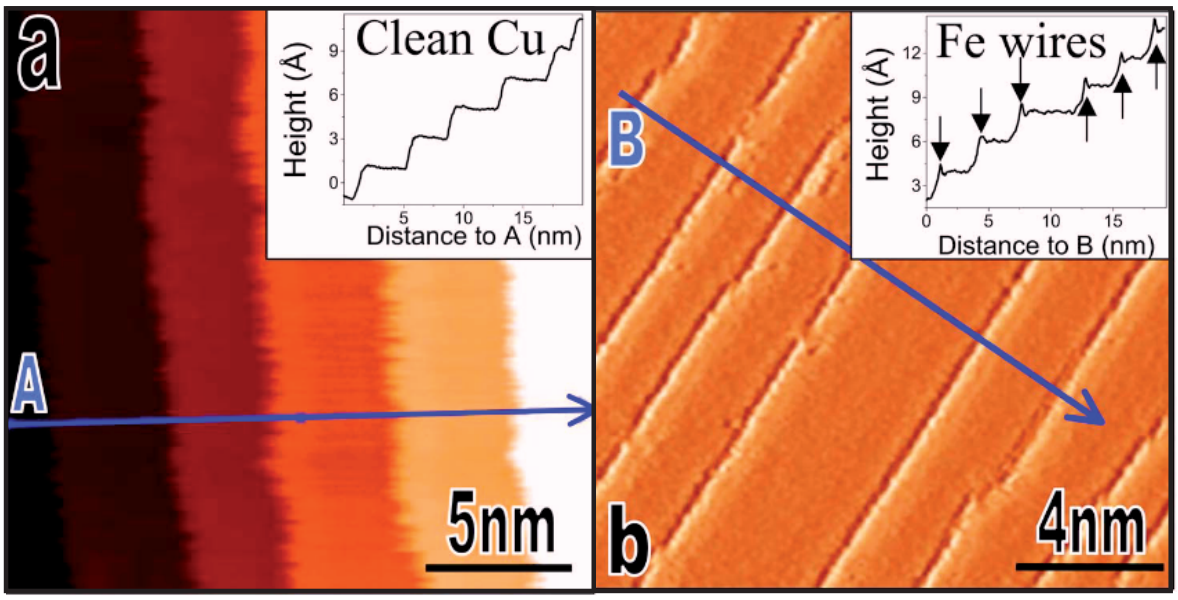

Figure 3.2: *STM images ($U_B = 30\,mV$, $I_{tun} = 10\,nA$) of atomic Fe wires on a vicinal Cu(111) surface.* ***a)*** *The clean Cu surface at RT.* ***b)*** *Image of Fe wires at the Cu step edges at 60 K. The two insets show line profiles along the corresponding arrows. The images were copied from ref. [106].*

bonds through on-surface synthesis can be found in ref. [115]. The most prominent example of 1D aggregates on surfaces that were synthesized by the chemical reactions mentioned above are the so-called graphene nanoribbons (GNRs) [116–120]. GNRs can be considered as quasi-1D stripes of HOPG with a band gap that is related to the structural confinement. Although, it is important to note that not all GNRs are semiconductors. The width of GNRs is usually between 5 and 20 carbon atoms and most GNRs have lengths below 100 nm, although lengths of up to 200 nm have been reported, as well [118]. The electronic and optical properties of the GNRs are determined by their width and edge configuration [121, 122]. Besides GNRs, many different kinds of hydrocarbon chains of varying lengths and forms have been reported [123–126]. Examples of a GNR and another hydrocarbon chain are illustrated in panels a) and b) of Figure 3.3.

Another path towards molecular 1D aggregates on surfaces is the usage of metal-organic frameworks (MOFs). MOFs are a very common and widely used concept in chemistry and can be used to tailor 1D, 2D, and even 3D structures. They consist of metal atoms or cations (electron acceptors) and organic ligands (also often referred to as linkers) that have at least two electron donor functional groups that can coordinate to the metal ions. Depending on the amount and the geometry of the donor groups of the organic molecules and the preferred coordination number of the metal (usually between 2 and 6), a wide range of very different networks can be created. A comprehensive overview of 2D MOFs is given in ref. [129]. The formation of 1D MOFs can be achieved by linkers that only have donor groups on two opposite sites and metal atoms or cations that prefer low coordination numbers. Unfortunately, the exact preferred coordination numbers of metals remain ambiguous. However, it is known that the coordination number depends on (1) the size, the charge, and the charge-accepting ability of the metal and (2) the size, the charge,

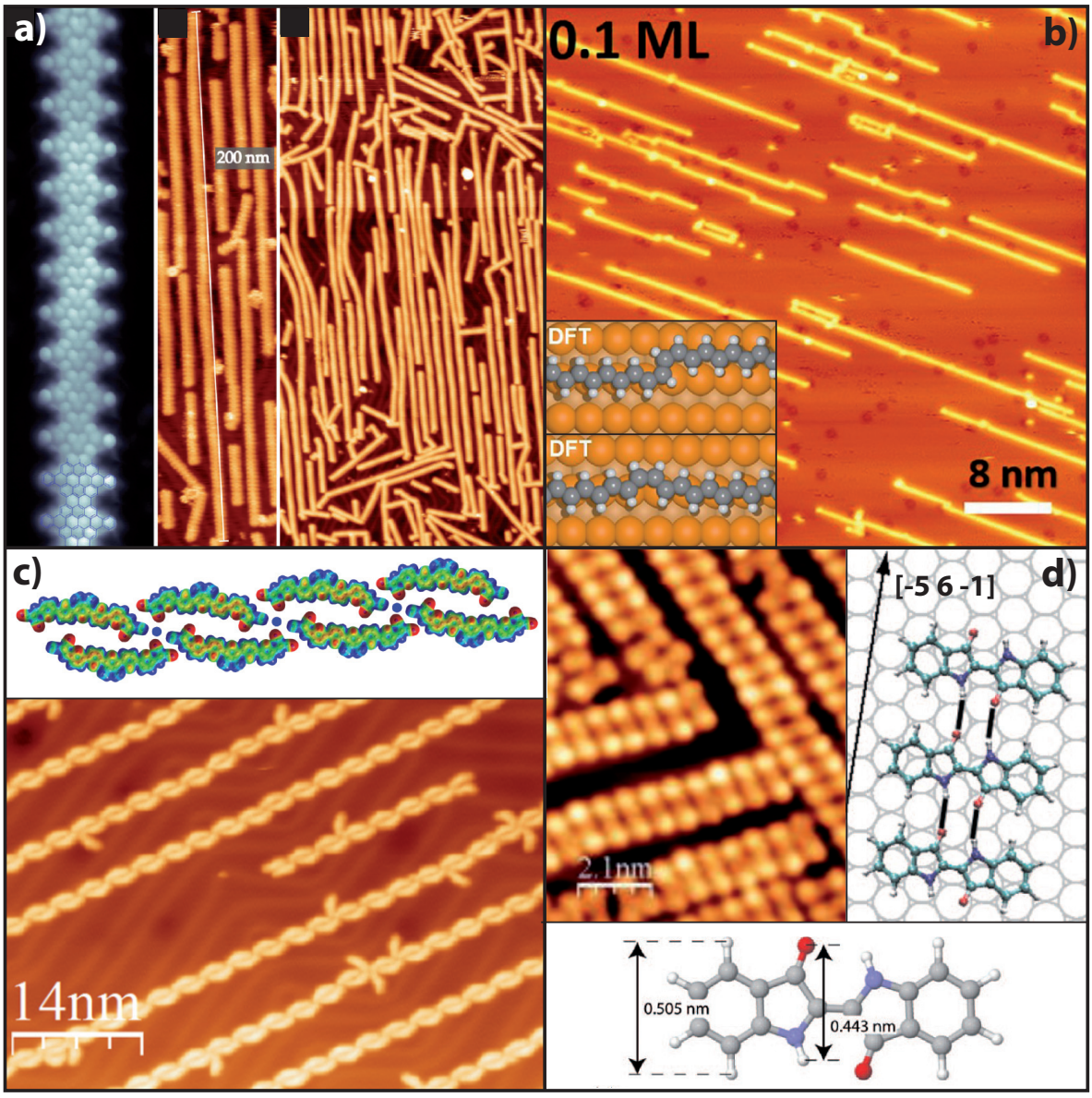

Figure 3.3: *Examples of molecular 1D aggregates on surfaces.* ***a)*** *Ultra-long GNRs on the Au(111) surface. The image on the left-hand side shows a high-resolution STM image that was recorded with a CO tip. The molecular structure of the GNR is superimposed on the lower part of the image. The images in the middle and on the right-hand side show overview images of GNRs, including one that is 200 nm in length. The images were copied from ref. [118].* ***b)*** *Long chains of polyacetylene on Cu(110) that were synthesized from n-alkanes through a cascade of on-surface dehydrogenation reactions. The inset shows hard-sphere models of such chains that were calculated by DFT. The images were taken from ref. [125].* ***c)*** *Metal-coordinated chains of dimethyl-substituted dicyanovinyl-quinquethiophene on Au(111). The chains are connected via Na atoms. The inset shows DFT-calculated chains, which shows that four different molecules are coordinated to a single Na atom (blue circles). The images were reproduced from ref. [127].* ***d)*** *Homochiral chains of indigo on Cu(111) that are connected via H-bonds. The insets show the dimensions of a hard-sphere model of the molecule and a structure model of the chains. The images were taken from ref. [128].*

and the charge-donating ability of the ligand [130]. Several examples of 1D MOFs have been reported on metal surfaces [127, 131–134]. Depending on the coordinating metal and the substrate surface, the chains using the same ligand can be straight, curvy, or even branched [131]. An example of a metal-coordinated 1D chain is illustrated in panel c) of Figure 3.3.

Lastly, and most importantly within the scope of the present thesis, 1D molecular aggregates can also be prepared by making use of non-covalent intermolecular interactions. These can be *van der Waals* dispersion interactions, which is for example the case for chains of pentacene on the Cu(110) surface [135]. However, since the attractive dispersion force acts between all atoms, it is not very reliable for the preparation of 1D structures. A more promising alternative is the use of intermolecular H-bonds, which is also the most prominent intermolecular interaction for all structures that were observed within the scope of the present thesis. H-bonds can only occur between distinct functional groups of the molecules and hence favor a more directed growth. Similar to the coordinating bonds in MOFs, H-bonds can be used to tailor 1D and 2D aggregates on surfaces [136] and hundreds of articles have been published reporting a wide range of different structures that are determined by intermolecular H-bonds. Only a small fraction of those articles deal with 1D aggregates. Nevertheless, 1D molecular chains of various molecules that are connected by H-bonds have been reported on many different surfaces [128, 137–147]. Of particular interest for the present work is the article on indigo on Cu(111) [128] because the molecular structure of indigo is similar to that of QA. It was reported that, upon evaporation, QA can thermally crack yielding indigo as a product [79, 80]. A corresponding STM image of indigo chains is illustrated in panel d) of Figure 3.3. Whether or not this thermal cracking occurs within the experiments of the present thesis will be discussed in detail in Appendix D. Another article that is of particular interest for the present work is the one about 2,6-naphthalene-dicarboxylic acid on a vicinal Ag(110) surface [147]. The authors found one-dimensional molecular chains that are connected via H-bonds and the growth of the chains even continues across the Ag step edges. A similar behavior was observed for QA and will be discussed in Chapter 7.1 of the present thesis.

In general, the azimuthal orientations of the molecular 1D aggregates are determined by a combination of the interactions between the molecules and the underlying substrate and the intermolecular interactions. This often leads to a limited amount of distinct equivalent azimuthal orientations due to the symmetry of the substrate. However, similar to the structure of the atomic chains, it may be possible to influence the azimuthal orientations, for example by unidirectional step edges on vicinal surfaces. Indeed, examples of organic molecules that form 1D aggregates along the step edges of vicinal surfaces have also been reported [148–150].

3.3 Organic molecules adsorbed on alkali halide layers

The use of dielectric surfaces or thin dielectric films on conducting surfaces (e.g., AH layers on metal surfaces) is motivated by the following reasons. The adsorption and bonding of organic molecules to metal surfaces changes their properties because this kind of bond is usually chemisorptive, which means that electronic hybrid states form between the molecule and the

metal [151]. Thus, the observation of unperturbed electronic and excitonic states is prohibited there. This problem can be circumvented by inserting thin dielectric layers between the molecules and the metal substrates. The bonding of organic molecules to dielectric surfaces is usually of physisorptive nature and is driven by *van der Waals* interactions. Hence, on dielectric surfaces the electronic states of the molecules remain mostly unchanged upon adsorption [152]. In addition, the band gap of the dielectric layer prevents excitonic states from being quenched by the metal.

Several different materials can be used to achieve the decoupling of organic molecules from a metal substrate. Organic molecules have been investigated, for example, on various metal oxides [153–157], hBN [158, 159], silicates [160, 161], and carbonates [162, 163]. The most common material class to decouple organic molecules from the metal surfaces, which is also used in the present work, is the class of alkali halides. Layers of AH have been reported for NaCl [152, 164–170], LiCl [171], KBr [172, 173], KCl [38, 174], LiF [175, 176], KF [177], NaBr [178], and RbCl [171] on many various metal surfaces.

The epitaxial growth and structure of most AH layers on metal surfaces is very similar. In general, epitaxial layers of AH grow incommensurately as monoatomic AH(100) layers in a layer-by-layer growth mode on metal surfaces. This is an advantage because it allows to tune the thickness of the layer. The first layer (also known as the wetting layer) is 1 or 2 atomic monolayers (ML) in height depending on the sample temperature at which the layer was grown and the strength of the interaction between the AH and the metal. For instance, for NaCl on Ag(100) it was reported that only at low sample temperatures a single ML can be grown, but at higher temperatures the growth of a 2 ML wetting layer is always preferred [179]. In contrast, on more reactive metal surfaces like Ir(111) and Pt(111) a NaCl wetting layer with a height of only 1 ML is stable [169, 170]. The stronger interactions between the NaCl and these metal surfaces even cause a buckling of the AH layer, which was not observed on less reactive metals. There, the wetting layer is flat because the inter-ionic *Coulomb* interactions of the AH are significantly stronger than interactions between the AH and the metal substrate. The AH layers exhibit distinct azimuthal orientations and the AH$\langle 10 \rangle$ directions are usually aligned with the high-symmetry directions of the metal substrate. In some cases, for example for NaCl on Ag(100), a rotational mosaicity was observed [167]. In the present work, epitaxial layers of KCl on the Ag(100) surface were used. The structure of such layers was already investigated by Müller *et al.* [38]. Nevertheless, the growth and structure of the investigated KCl layers will be discussed in detail in Chapter 6.1, in which some details from new observations will be added.

Layers of AH on metal substrates have been platforms for the investigation of many different organic molecules for several years. Regarding the structure of organic films on AH layers, two cases can be distinguished: the intermolecular interactions are (1) stronger or (2) weaker than the interactions between the molecules and the AH layer. In case (1), dewetting or non-wetting of the organic layers and the formation of bulk-like nanocrystals is observed, sometimes only at elevated temperatures or after certain amounts of time [180]. Examples of this phenomenon are PTCDA on NaCl/Ag(100) [181], C_{60} and C_{70} on NaCl/Au(111) [182], and tin phthalocyanine (SnPc) on NaCl/Au(111) [183]. On bulk AH crystal surfaces, this phenomenon is even more

common, and several examples have been reported [184–189]. Nevertheless, if the surface diffusion of the molecules is suppressed (low sample temperature during deposition) and the molecules do not have any neighbors (very low coverages), individual molecules adsorb on terraces in a flat-lying geometry and can be observed by STM or atomic force microscopy (AFM) [190, 191]. In case (2), the formation of 2D ordered layers is observed. Known examples include PTCDA on KCl/Ag(100) [38], copper-octaethyl porphyrin (CuOEP) on NaCl/Ag(111) [192], and a curcuminoid on KCl/Au(111) [174].

Generally speaking, the interaction energy between the molecules and the AH layers has two shares: the attractive *van der Waals* interactions and the *Coulomb* interactions between the local charges of the AH layer and the partial charges of the molecules. The reason why the interaction energy between the AH layer and the molecules is smaller for the example systems in the above-noted case (1) is that, there, the share of the *Coulomb* interaction is smaller. That may be due to a lack of partial charges on functional groups of the adsorbed molecules (C_{60} and C_{70}) or due to mutual compensation of repulsive and attractive *Coulomb* interactions across the molecule-AH interface. The relevance of a geometric matching between opposite partial charges leading to a high adsorption energy has been highlighted by publications on substituted helicene molecules on ionic *Suzuki* surfaces [193, 194]. Depending on the substituents and the ionic lattice, different adsorption configurations were observed. Furthermore, it has been reported that, for AH layers of thicknesses between 1 and 3 ML, the *van der Waals* interactions between the molecules and the underlying metal substrate also play a role [192, 195]. Overall, these different observations show that the structural order of layers of organic molecules on thin AH films on metal surfaces is determined by an interplay of many factors.

The electronic and optical properties of organic molecules on AH layers were also investigated. The visualization of the HOMO and LUMO of organic molecules with STM was first reported for pentacene on NaCl/Cu(111) by Repp *et al.* [33]. This motivated the investigation of different molecules on thin NaCl layers on different metal substrates in different charge states, which can be controlled by transferring electrons between the molecules and the STM tip [196–201]. These observations prove that the organic molecules can be sufficiently decoupled from the metal substrates by thin layers of AH. Besides thin layers of AH, molecules can also be decoupled by other insulating layers, such as metal oxides, including MgO [202, 203] and Al_2O_3 [86], or 2D materials, including hBN [159, 204] and MoS_2 [205]. Of particular interest are the works regarding pentacene on MgO by Sterrer and coworkers [202, 203] because, there, the pentacene molecule gets charged via a charge transfer (CT) from the metal into the molecule across the dielectric MgO layer. This phenomenon of molecules getting charged through a thin dielectric layer by a CT between the metal and the molecules is also known for layers of NaCl and happens for example with PTCDA on NaCl/Ag(111) [206] and PTCDA on MgO/Ag(100) [207]. However, at present, no examples of charged molecules on a thin layer of KCl are known to the author of the present thesis. This leads to the following interesting question: What determines whether CT between a metal substrate and an organic molecule across a dielectric layer occurs? At present, this question is not

fully understood. However, it is clear that an energy level alignment between the Fermi level of the substrate and the involved molecular orbitals is very important for CT to occur.

The decoupling of the molecules from the metal substrate via dielectric layers enables the investigation of the electronic and optical properties of the molecules. For example, the electronic properties of several different organic molecules have been investigated with tip-enhanced photoluminescence spectroscopy [208, 209] and STM-induced molecular luminescence [196, 210, 211]. In particular, the STM-induced luminescence of QA on NaCl on Au(111) and Ag(111) has been reported very recently [212]. In this work, it was found that the ground state of QA on 4 layers of NaCl on Ag(100) is a positively charged doublet. Overall, this work has shown that four different charge states of QA (QA^-, QA, QA^+, QA^{2+}), involving three spin multiplicities (singlet, doublet, triplet), can be populated with a single sweep of the bias voltage. However, whether the above-noted decoupling from the metal substrates is sufficient for optical investigations, in particular fluorescence spectroscopy, remains to be tested in each individual case. So far, the energy-selected fluorescence of single molecules and the influence of different adsorption sites on the fluorescence spectra have been reported for PTCDA on KCl/Ag(100) [213, 214].

4 Experimental

In this chapter, the experimental set-ups and procedures, the sample preparation, as well as the data acquisition and evaluation are explained.

4.1 The UHV chambers

Within the scope of the present work, two different UHV chambers were utilized. In one chamber (the STM chamber, see Section 4.1.1), the STM and MCP-LEED measurements were conducted. The other UHV chamber (the SPA-LEED chamber, see Section 4.1.2) was used for experiments utilizing a SPA-LEED apparatus. The chambers were equipped with an ionization gauge for pressure measurements and were operated at a base pressure p of roughly $2 \cdot 10^{-10}$ mbar, which was reached after a 48 h bake-out at 150 °C. A detailed description of the two chambers will be given in the following.

4.1.1 The STM chamber

The STM chamber was divided into three smaller sub-chambers: a chamber that was used to prepare the samples (the preparation chamber) and a chamber in which the STM experiments were conducted (the measurement chamber). The third chamber (the transfer chamber) contained a transfer system, which could be used to move the samples between the different chambers and an airlock. Between the sub-chambers plate valves were installed, which allowed to completely prevent all flow of gas between them. A detailed schematic representation of the whole STM chamber is shown in Figure 4.1. A very detailed description of the chamber and the STM can be found in the PhD thesis of I. Kossev [215].

The preparation chamber

The central part of the preparation chamber was the manipulator that held the sample holder. To be able to do that, the manipulator had a U-shaped rail, which could hold onto the U-shaped bottom plate of the sample holder. The manipulator could rotate around its z-axis by close to 360° and move in all three spatial directions. It was equipped with a 50 W tungsten filament and a continuous-flow nitrogen cryostat that allowed it to reach sample temperatures in the range of $150 - 850$ K. Higher temperatures of up to 1000 K could be reached by applying a high positive potential (up to 600 V) to the sample and heating it by electron bombardment, resulting in currents of up to 6 mA. The temperature of the manipulator itself, as well as the sample temperature, could be measured with type-K thermocouples. The latter was enabled by two contacts at the manipulator that connected to the thermocouple wires of the sample holder.

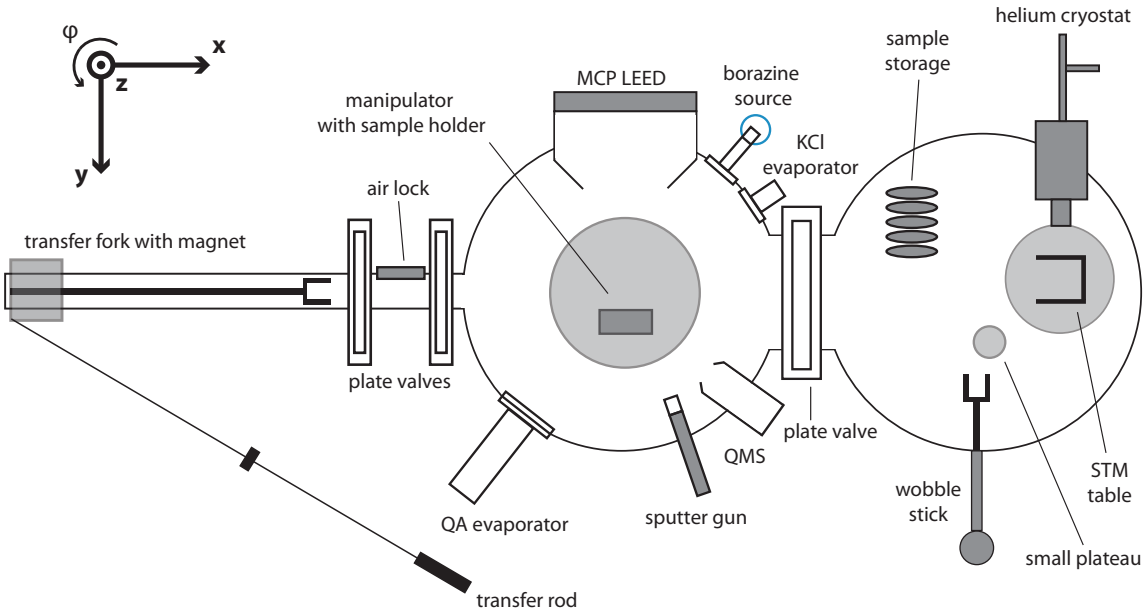

Figure 4.1: *Schematic drawing of the STM chamber in the top-down view. The drawing is not true to scale. For a detailed explanation, see text.*

The chamber was furthermore equipped with a sputter gun and an argon line for cleaning the samples. For depositing adsorbates on the surfaces, three different self-built evaporators were installed at the chamber, in which the substances were evaporated from glass crucibles. The largest one was capable of evaporating three different substances, two smaller ones could evaporate a single substance each. The large one was used to evaporate QA, and one of the smaller ones was used to evaporate KCl onto the samples. Additionally, liquid borazine for the preparation of hBN layers was stored in a glass container that was constantly cooled to $-5°C$ with a removable peltier cooler in order to prevent decomposition. It could be dosed into the preparation chamber through a system of metal pipes and dosing valves. For the purpose of analyzing the residual gas of the chamber, and monitoring the deposition of organic or inorganic layers onto the surfaces, a quadrupol mass spectrometer (QMS) of the type QME 200 was installed in the chamber. Lastly, the preparation chamber was also equipped with an MCP-LEED, which could be used to check the prepared metal surfaces for cleanness and good structural quality, and to conduct LEED measurements on the prepared layers. It is also important to note that the whole inner wall of the chamber was lined with μ-metal[1] plates, which were used for shielding against magnetic fields. This was done to protect the interior of the chamber against external magnetic fields that may disturb the electrons at low kinetic energies.

The measurement chamber

The heart of the measurement chamber was a beetle-type STM (type UHV 300) connected to an SPM 100 scanning probe microscope control from RHK Technology. It consisted of two main parts:

[1] μ-metal is a soft ferromagnetic alloy with very high permeability ($\mu_r = 50000 - 140000$) consisting of nickel and iron.

the measurement table where the sample was placed and the scan head that could be lowered onto the sample holder. Like the manipulator in the preparation chamber, the measurement table had a U-shaped rail that could hold the sample holder in place, where two contacts connected to its two thermocouple wires. The table was also equipped with a 50 W tungsten filament and a continuous-flow helium cryostat which allowed to conduct STM measurements at temperatures in the range of $20 - 300$ K. The temperature of the sample and the table could be measured with type-K thermocouples. Temperatures below 70 K were measured via a Si diode.

The scan head had three piezo tubes with ruby balls at the bottom that landed on the three ramps of the sample holder. In the center between the three piezo tubes was the scan piezo, which contained the tip holder with the tip. The tip was a self-cut Pt/Ir(90:10) wire and was held at ground potential. The bias voltage U_B refers to the sample and was applied via one of the thermocouple wires.

Apart from the STM, the measurement chamber also contained a storage system for samples and STM tips, a small round plateau where the samples could temporarily be placed to rotate them, and a wobble stick that could be used to move samples between the transfer fork, the storage system, and the STM measurement table.

The transfer chamber

The transfer chamber had a rather simple setup. It consisted of a long tube that had a long rod inside of it. At the end of the rod was a transfer fork, which could be used to grab the sample holder. This rod was connected via a large magnet to the outside. By moving the magnet, the rod in the chamber could be moved and be utilized to transfer the samples between the three different sub-chambers. Besides that, the transfer chamber included two plate valves with a gate between them, forming an airlock that was used to transfer samples into and out of the chamber.

4.1.2 The SPA-LEED chamber

A schematic drawing of the chamber is displayed in Figure 4.2. It consisted of the measuring area, which contained only one SPA-LEED apparatus from the company Scienta Omicron[2], and the preparation area. These two areas could be separated by a shutter. This shutter was not airtight and only served to block some impurities that arose for example during sputtering from reaching the SPA-LEED apparatus. The preparation area contained a QA evaporator and a sputter gun. Furthermore, it also had a QMS (type QME 200) which served to monitor the molecule flux during QA deposition. The sample was mounted on two tungsten rods that were attached to the manipulator. It could be moved in all three spatial directions and rotated by nearly 360° around the z-axis. The sample could be heated and cooled via a 50 W tungsten filament and a constant-flow nitrogen cryostat, respectively, which allowed the usage of sample temperatures in the range

[2]Formerly known as Omicron Vakuumphysik and then Omicron NanoTechnology, not to be confused with OMICRON electronics.

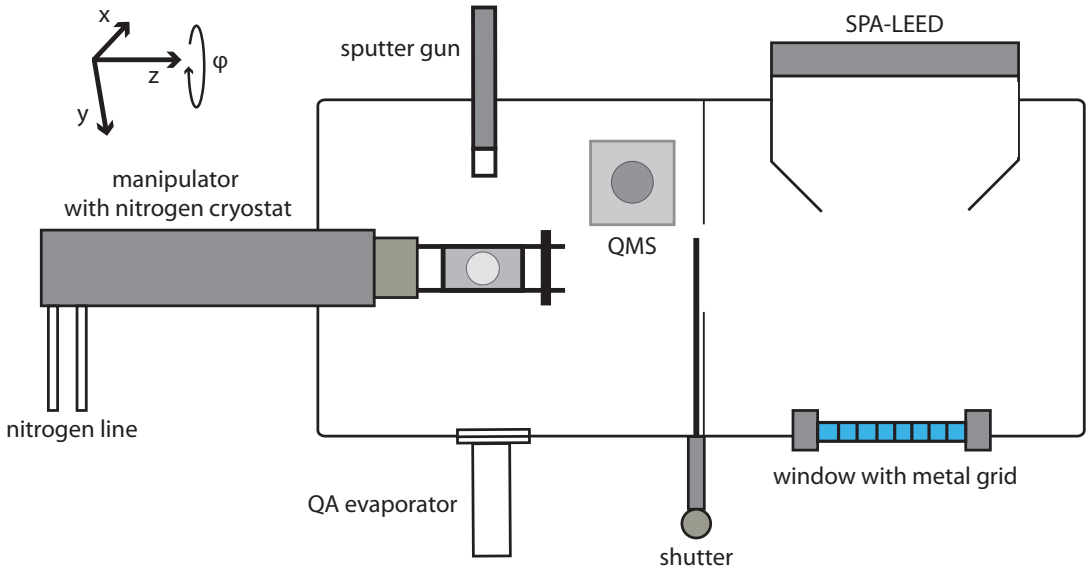

Figure 4.2: *Schematic drawing of the SPA-LEED chamber in the top-down view. The drawing is not true to scale. For a detailed explanation, see text.*

of 110 − 800 K. As already described above, the inner wall of the chamber was also lined with μ-metal to protect to electrons at low kinetic energies from external fields.

4.2 The preparation procedures

All experiments were carried out on the Ag(100), Ag(35 1 1), and Cu(111) surfaces of Ag and Cu single crystals. The crystals were not transferred between the two chambers, which means that SPA-LEED and STM experiments were never carried out on the same sample. Nevertheless, the preparation procedures were always identical. This chapter will cover the preparation of the metal surfaces, the deposition of QA molecules, and the preparation of KCl and hBN layers.

4.2.1 Preparation of the metal surfaces

All crystals were prepared in a similar manner, which consisted of the iteration of two steps. First, the crystals were exposed to a bombardment with Ar^+ ions (this process is called sputtering) with an energy of 1 keV at an Ar background pressure of $2 \cdot 10^{-5}$ mbar. The samples were sputtered from a distance of roughly 130 mm at 45° and −45° angles with respect to the surface normal for 15 minutes each. The resulting sample current was in the range of $4 - 8\,\mu$A. Afterwards, the crystals were annealed for between 30 and 60 minutes to heal the defects that were caused by the Ar^+ ion bombardment. The Cu and Ag crystals were annealed at 850 K and 700 K, respectively. At first, STM experiments on the clean Ag(100) surface were conducted after annealing temperatures of 850 K. However, it was found that this high temperature lead to the formation of Ag clusters on the surface, which were seen as ellipsoid protrusions in the STM images. A similar observation was made by the group of M. Sterrer [216]. These clusters were pinned to the step edges and

caused them to follow wide concave curves. In order to avoid this, the annealing temperature for the Ag crystals was adjusted to 700 K. This phenomenon is illustrated by examples and discussed in more detail in Appendix B.1. After the preparation, the good structural quality of the surfaces was confirmed by LEED.

4.2.2 Preparation of QA layers

QA was evaporated onto the metal surfaces with a deposition rate of roughly 0.5 ML per minute from glass crucibles in home-built evaporators at crucible temperatures between $670 - 720$ K, while the samples were held at a constant temperature. The distance between the glass crucible and the sample was about 90 mm during the deposition. The sample temperature was usually held at 300 K, however, several other distinct sample temperatures in the range of 80 – 500 K were utilized for different experiments, which will be specified accordingly when the corresponding results are discussed. For the deposition at very low temperatures of about 80 K, the sample was cooled down with liquid He on the STM table before deposition and transfer.

During deposition, the molecular flux was constant (variations within ± 10 %) after a short initial decrease due to the opening of the shutter, which caused a small temperature decrease in the crucible. The flux was monitored by the QMS, i.e., the intensity of the signal for the mass-to-charge ratio $m/z_c = 128$, which corresponds to the $[C_{18}H_{12}N_2]^{2+}$ fragment of QA, was recorded over time. Here, m refers to the relative mass of the fragment and z_c refers to the charge number. The coverage θ_{QA} and deposition rates were then determined from the corresponding relative deposition integrals in combination with information from STM images. Details on the calibration for this method are given in Appendix B.2. A closed layer of flat-lying QA molecules in the β-phase (see Chapter 5) is defined as 1 ML. The preparation of QA layers on KCl and hBN was done by the same procedure. There, the QA coverage was also determined from the QMS integrals, which only works under the assumption that the sticking factor on all used surfaces is constant.

4.2.3 Preparation of KCl and hBN layers

In order to conduct STM measurements on KCl, it was necessary to prepare thin layers with thicknesses of at most 6 ML. On thicker layers, STM measurements were not possible due to the large band gap of KCl. The KCl was evaporated from a glass crucible (the distance to the sample was roughly 90 mm) at a temperature of 870 K, resulting in deposition rates of roughly 0.1 ML per minute. The evaporated amount of KCl was monitored by measuring the QMS signal of the K^+ ion ($m/z_c = 39$). The QMS signals corresponding to the charged KCl^+ molecule ($m/z_c = 74$ and $m/z_c = 76$) could also be observed with a ratio of about 1:3, however, the signal of the K^+ ion was higher due to fragmentation in the QMS. The nominal thickness θ_{KCl} was determined from the integrated QMS signal and comparing it to that of a reference layer, where 1 ML corresponds to a nominal single atomic KCl layer covering the complete surface. During the deposition, the sample was held at a constant temperature of 400 K to create thin and smooth wetting layers covering the whole Ag substrate. This sample temperature was chosen very carefully to find a good balance between enabling surface diffusion on the one hand and preventing the dewetting of KCl on the

other hand. The observation that a sample temperature of 400 K leads to thin and smooth layers was made by STM within the scope of the present thesis but was also found by M. Mühlpointner by SPA-LEED within the scope of his Bachelor's thesis [217]. After the deposition was finished, the sample was usually cooled down to RT, but for experiments on KCl layers that did not cover the entire surface it was annealed for an additional 15 minutes at 500 K to induce dewetting of the KCl layer. It is important to note that this KCl preparation for STM measurements differs fundamentally from KCl preparations for SPA-LEED and optical experiments (see for example the PhD thesis of C. Marquardt [218] where very thick KCl layers ($\geq$ 10 ML) with a focus on good structural quality and large terrace widths were used).

The hBN layers were prepared with the molecule borazine as a precursor, which was evaporated into the chamber from its glass container at a pressure of $1.5 \cdot 10^{-6}$ mbar for 30 minutes, while the Cu(111) sample was held at a temperature of 1000 K. This amounts to a dosage of 2000 L. More in-depth information on the preparation of hBN layers and the storage and cleaning of borazine can be found in the PhD thesis of C. Brülke [219].

4.3 Data acquisition and evaluation

Most STM measurements were conducted at RT. Some experiments were carried out at low sample temperatures in order to reduce to mobility of the QA molecules (cf. Chapter 5.1.4 on page 43 and Chapter 6.2.3 on page 79). All images were recorded with the software XPMPro version 2.0.1.5 by RHK Technology [220]. The images were processed and analyzed using the programs Gwyddion version 2.58 [221] and SPIP version 4.8.7.0 [222]. Usually, the processing included filtering out horizontal, vertical, and non-directional noise, and an adjustment of the contrast. Additionally, on some images with many step edges a *Prewitt* or *Roberts* filter for edge enhancement, both of which are included in the SPIP software [222], was used. Typical tunneling parameters for measurements of QA on metal surfaces were $U_B = \pm 1.5$ V and $I_{tun} = 25$ pA. However, on metal surfaces, a wide range of tunneling parameters worked well for imaging QA molecules. Most of the time the molecules looked like featureless rods. In some cases, it was possible to observe a sub-molecular resolution at negative bias voltages. However, this was not reproducible at constant tunneling parameters in a reliable way, indicating that it was very reliant on the condition of the tip, possibly including the adsorption of a small molecule (e.g., CO) at the tip. For imaging QA on insulating hBN and KCl layers, low tunneling currents (< 10 pA) and negative bias voltages were usually used, because otherwise the tip was too close to the surface and its interactions with the molecules were too strong. This led to the case in which the tip was dragging the QA molecules along, which was visible in the STM images as lines in the direction of the scan. It was possible to image QA with molecular resolution with these tunneling conditions on hBN and KCl, however, no sub-molecular resolution was achieved.

The SPA-LEED measurements were normally conducted at a sample temperature of 110 K to minimize the thermal diffuse background. In order to avoid potential beam damage, which was reported by Wagner *et al.* for QA on Ag(111) [15], only small sample currents (< 5 nA) were

used. The images were recorded with the program WinSPA by P. Kury [223]. The Ag(100) and Cu(111) crystals that were used for the SPA-LEED experiments had transfer widths in the range of (300 – 350) Å. One set of specific experiments (cf. Chapter 5.4 on page 52) required SPA-LEED measurements at temperatures of up to 500 K. To prevent the magnetic field of the heating filament from interfering with the measurements, a current chopper was used. This chopper controlled the filament current in such a way that is was only operated in periods in which the detector did not collect the diffracted electrons. The details on the functionality of the chopper and the influence of the chopper on the SPA-LEED images are given in Appendix B.3.

5 Quinacridone on Ag(100) and Cu(111)

Some results of the following chapter have been published in ***J. Phys. Chem. C 2020, 124, 45, 24861–24873*** *(cf. Appendix A.1). The acquisition and evaluation of the data, and the writing of the manuscript were done by the author of the present thesis. The acquisition and evaluation of the data regarding QA on Cu(111) was performed together with R. Bretel [93] who was an exchange student at the University of Bonn.*

In this chapter, the lateral structures of different QA phases on Ag(100) and Cu(111) will be presented in Sections 5.1 and 5.2, respectively. These results have partly been published (cf. Appendix A.1) and will be supplemented with additional information regarding questions that were not addressed in the publication. In addition, the lateral structure of the second QA layer on Ag(100) and Cu(111) will be discussed in Section 5.3, and SPA-LEED investigations regarding the phase transitions on Ag(100) will be presented in Section 5.4.

5.1 Structures of quinacridone on Ag(100)

5.1.1 The α- and the β-phase

The structures of QA on Ag(100) can be divided into two main phases: the phase that forms on the surface after deposition of the QA molecules onto the sample at a sample temperature of 300 K, which will be named α-phase in the following, and the so-called β-phase that forms after annealing the α-phase at 500 K for 15 minutes. Additionally, a third phase that coexists with the β-phase was found, but it did not occur in all experiments. This phase will be named γ-phase and is discussed in more detail in Appendix C.1.1.

The α-phase

The α-phase of QA on Ag(100) consists of domains of parallel molecular chains with four distinct azimuthal orientations. These four orientations will be named A – D in the following. Two STM images of a full ML of QA in the α-phase are displayed in panels a) and b) of Figure 5.1. The image with molecular resolution in panel b) shows that the chains consist of parallel flat-lying molecules. That means that the chains are connected via intermolecular H-bonds between the keto and amine groups that are located on the long edges of the molecules (see structure model in panel c) of Fig. 5.1). Every QA molecule in such a chain forms two H-bonds to each of its two neighbors unless it is located at the end of a chain. That means that in a theoretical infinitely long chain there are twice as many H-bonds as there are molecules. Thus, in the following the QA molecules in a chain form two H-bonds per definition, although each of them participates by 50 % in the formation of 4 H-bonds.

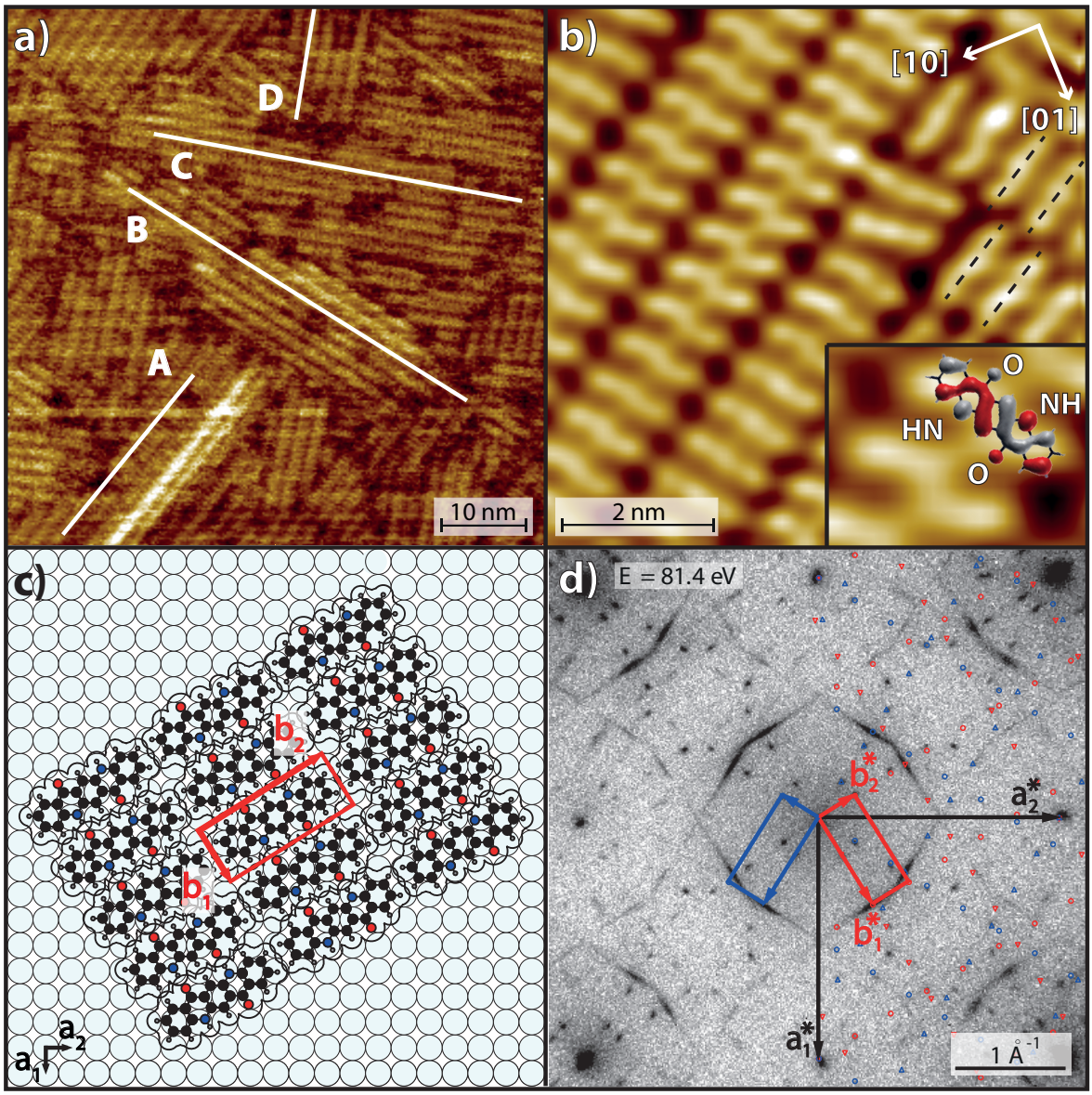

Figure 5.1: *Structure of a complete ML of QA on Ag(100) in the α-phase.* ***a)*** *Overview STM image ($U_B = -1.5\,V$, $I_{tun} = 25\,pA$) that shows that the α-phase consists of domains of parallel chains with four distinct azimuthal orientations (indicated by the white lines).* ***b)*** *A close-up of the structure showing the molecular arrangement. The black dashed lines on the right-hand side of the image highlight a situation where the molecules of neighboring chains are shifted in the direction of* $\mathbf{b_1}$ *with respect to each other. The molecules exhibit a characteristic S-shape that is highlighted in the inset and which can be explained by the HOMO of isolated QA molecules in the gas phase. The model of the orbital was taken from ref. [69].* ***c)*** *Structure model of the α-phase of QA on Ag(100). The unit cell is depicted in red. The color code of the atoms is as follows: black = carbon, gray = hydrogen, blue = nitrogen, and red = oxygen.* ***d)*** *SPA-LEED image ($T = 100\,K, E = 81.4\,eV$). The right-hand side of the image is superimposed with the corresponding simulated diffraction pattern. Two unit cells that resemble different mirror domains are depicted in red and blue. Two different rotational domains of the same enantiomer are depicted as triangles and circles of the same color. Spots that are not reproduced by the simulated diffraction pattern can be explained by multiple scattering. The smearing of the spots is due to a lack of correlation between neighboring chains. The figure was taken from ref. [224] and slightly modified.*

A structure model of a full ML of QA in the α-phase is displayed in panel c) of Figure 5.1. The chains are homochiral because, due to the C_2 symmetry of the QA molecule, these H-bonds can only form between QA molecules of the same handedness. Furthermore, the entire domains are homochiral because different azimuthal angles with respect to the <10> direction of the substrate can be associated with different 2D enantiomers. The formation of enantiopure domains does not only reveal a high mobility of QA on Ag(100) at RT but also indicates that the QA molecules are capable of rotating around their long molecular axis and switch their handedness (L $\leftrightarrow$ R), which is not an uncommon phenomenon for molecules of similar size [225, 226]. The handedness of the QA molecules can also be observed with STM in some images because the molecules exhibit a characteristic S-shape that corresponds to the LDOS of the HOMO [69] of an isolated QA molecule in the gas phase (cf. panel b) of Fig. 5.1). The same shape was observed for QA on HOPG [17]. However, whether this shape could be observed is strongly dependent on the quality of the tip and possibly other scanning parameters and most of the time the QA molecules were imaged as featureless ellipsoid protrusions.

A SPA-LEED image of a full ML of QA in the α-phase with a superimposed simulation is displayed in panel d) of Figure 5.1. The analysis of the diffraction pattern yields a primitive rectangular (i.e., $\alpha = 90^\circ \pm 1^\circ$) unit cell with the intermolecular distance within the chains of $b_1 = (6.8 \pm 0.1)$ Å, and the distance between neighboring chains of $b_2 = (16.4 \pm 0.1)$ Å. Spots that are not reproduced by the simulation are caused by multiple scattering. This unit cell is in good agreement with the STM results and the corresponding superstructure matrix is:

$$\mathbf{M}_\alpha = \begin{pmatrix} 2 & 1.25 \\ -3 & 4.80 \end{pmatrix}.$$

The integer values in the first column of the matrix show that the structure is of the point-on-line (POL) type [227]. This means that every lattice point of the superstructure falls on a substrate lattice line of the [10] direction. This shows that the interactions between the QA molecules and the Ag(100) surface are substantial and are responsible for the four distinct azimuthal orientations of the chains. The smearing of the spots in the diffraction pattern can be explained by a lack of correlation between neighboring chains in the direction of $\mathbf{b_1}$. That means that neighboring chains are shifted with respect to one another in the direction of $\mathbf{b_1}$, which was also observed by STM. An example of this is illustrated by the black dashed lines on the right-hand side in panel b) of Figure 5.1.

At coverages below 1 ML, the α-phase consists of the same type of molecular chains with the same intermolecular distance b_1, given by the H-bonds. (For corresponding STM and SPA-LEED images, see Appendix A.1.) But there is one striking difference to the structure described above. The distance between neighboring chains b_2 increases with decreasing coverage. That can be explained by a substrate-mediated long-range repulsive interaction that is induced by charge density waves in the 2D electron gas of a surface state [138, 228]. This kind of interaction and its ramifications will be discussed in Section 5.1.2 in more detail. It was also found for pentacene on Cu(110) [135] and L-methionine on Ag(111) [229] and Cu(111) [137].

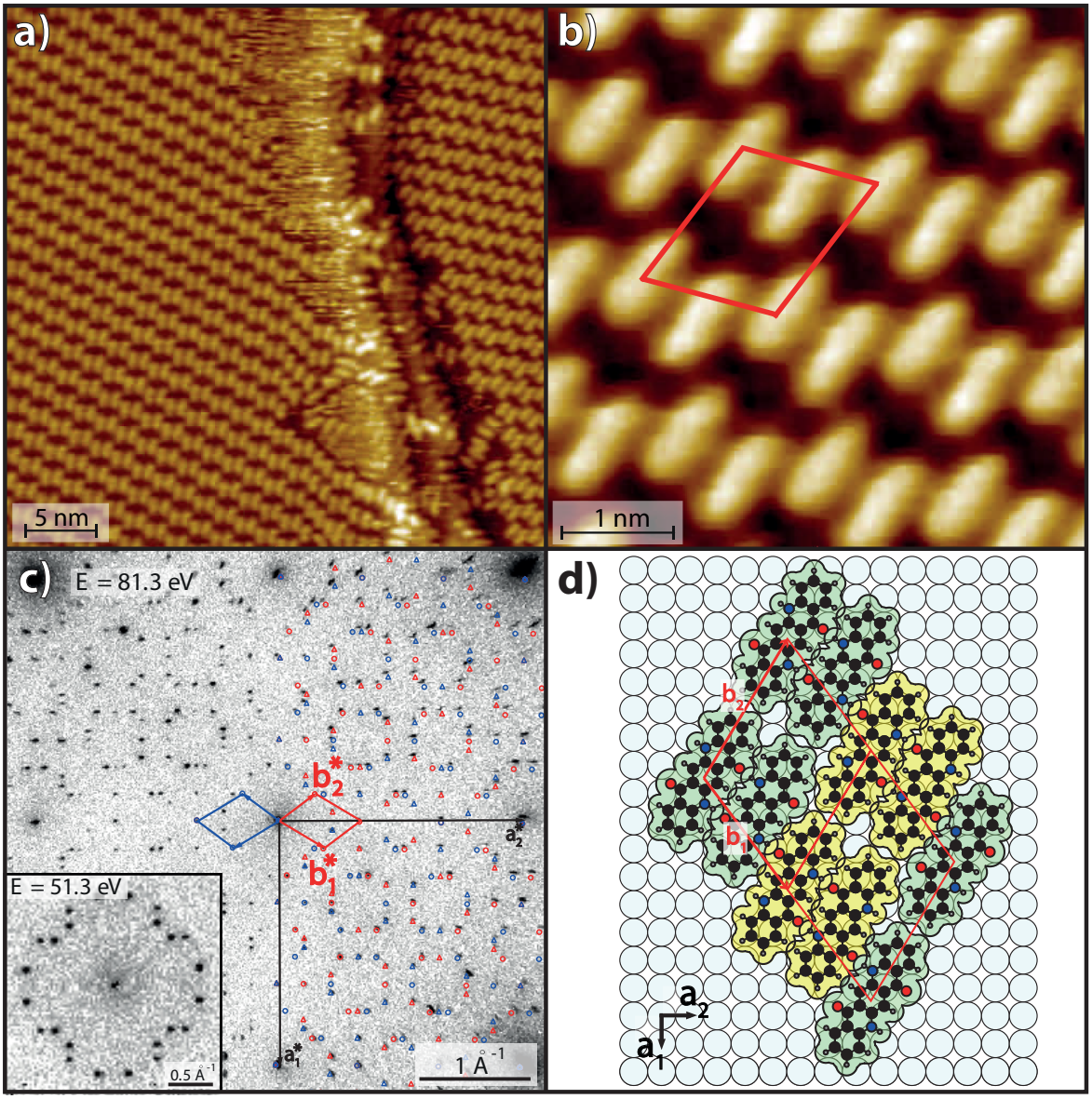

Figure 5.2: *Structure of a complete ML of QA on Ag(100) in the β-phase.* ***a)*** *Overview STM image ($U_B = -1.5\,V$, $I_{tun} = 25\,pA$) that shows two different mirror domains of the β-phase at a double Ag step edge. Every bright ellipsoid corresponds to an individual QA molecule.* ***b)*** *Zoom-in of the structure in panel a) for better visibility of the molecular arrangement. The unit cell is indicated in red.* ***c)*** *SPA-LEED image ($T = 100\,K, E = 81.3\,eV$) of a full ML of QA in the β-phase. The right-hand side of the image is superimposed with a simulation. The unit cells of two mirror domains are illustrated in red and blue. The inset shows the area around the specular spot at an energy of 51.3 eV showing some additional spots that are not visible at 81.3 eV.* ***d)*** *Structure model of a full ML of QA in the β-phase. Different enantiomers are highlighted by the green and yellow background of the molecules. The unit cell is indicated in red and corresponds to the red unit cell in panel c) but depicts a different domain than the one that is shown in panel b). STM and SPA-LEED measurements yield the unit cell that is given by the vectors $\mathbf{b_1}$ and $\mathbf{b_2}$. However, this unit cell does not take into account the different enantiomers. The large unit cell that is composed of two small ones takes that into account. The figure was taken from ref. [224] and slightly modified.*

The β-phase

The phase transition into the β-phase can be induced by annealing the sample at 500 K for 15 minutes and is irreversible, which means that the α-phase is metastable and stabilized by a kinetic barrier that is partly given by the strong intermolecular H-bonds. In the corresponding publication (cf. Appendix A.1) it is stated that the α-phase dissolves into a disordered 2D gas phase at higher temperatures that transforms into the β-phase upon cooling down to RT. However, later SPA-LEED experiments have shown that the situation is more complicated because the transition temperature and whether or not the phase transition includes a disordered phase depends on the coverage. This aspect will be discussed in detail in Section 5.4.

Two STM images of a complete ML of QA in the β-phase are displayed in panels a) and b) of Figure 5.2; a corresponding structure model is displayed in panel d) of the figure. As the images and the model show, the β-phase consists of domains of parallel chains, as well. But in contrast to the chains of the α-phase, the chains in the β-phase consist of dimers and exhibit periodic indents. It is clear that the two molecules of the dimer have the same handedness (RR or LL) in order to form two H-bonds. The periodic offsets in the chains do not allow the formation of two H-bonds between neighboring dimers. Instead, the handedness switches with every dimer (RRLL or LLRR), and the dimers are connected via only *one* H-bond. This means that in the β-phase, on average, every molecule only forms 1.5 H-bonds, which constitutes an energy loss with respect to the α-phase.

A SPA-LEED image of a full ML QA in the β-phase is displayed in panel c) of Figure 5.2 and the right-hand side of the image is superimposed with a simulation that accounts for all the observed spots. The diffraction pattern consists of sharp and bright spots indicating large ordered domains, which is in good agreement with the STM results. The analysis of the pattern yields a unit cell with $\alpha = 112.2^\circ$, $b_1 = 14.445\,\text{Å}$, and $b_2 = 16.848\,\text{Å}$ that is also in agreement with the STM results. The corresponding superstructure matrix is:

$$\mathbf{M}_\beta = \begin{pmatrix} 4 & 3 \\ -5 & 3 \end{pmatrix}.$$

The fact that all entries of the matrix are integers means that the structure is commensurate. Commensurability is generally related to a gain in energy [227]. In this case, this energy gain overcompensates for the energy loss with respect to the α-phase due to the reduced amount of formed H-bonds. The reduced amount of H-bonds also means that every second QA molecule has one oxygen atom that does not exhibit any intermolecular bonding. According to results from IR-spectroscopy experiments by R. Priya for QA on the Ag(111) surface (where a very similar phase was observed [15]), these oxygen atoms exhibit a stronger bonding to the Ag substrate than the oxygen atoms in the α-phase [81].

This unit cell, which is given by the vectors $\mathbf{b_1}$ and $\mathbf{b_2}$, stems from the analysis of the STM and SPA-LEED results and contains two QA molecules. However, the structure model in panel d) reveals that this unit cell does not take the handedness of the molecules into account. This is

because the structure factors of the two QA enantiomers are very similar, and hence this difference could not be observed by SPA-LEED. Furthermore, in the β-phase, the two enantiomers could not be discerned by STM, either.[1] The unit cell that takes the handedness of the QA molecules into account is doubled in the direction of the vector $\mathbf{b_1}$ and contains four QA molecules.

A particularly interesting question regarding the β-phase is the following: Why does the β-phase not form directly upon deposition at RT? It is thermodynamically more stable than the α-phase and it is clear that the molecules are very mobile on Ag(100) at RT. Thus, there must be an additional kinetic barrier that prevents the formation of the β-phase directly upon deposition. This may be in the form of a small reconstruction of the top layers of the Ag substrate involving small lateral and vertical displacements of the Ag atoms, which enables a stronger bonding between the molecules and the surface atoms. Such reconstructions that are induced by the adsorption of organic molecules were already observed by Held *et al.* [230–232]. Thus, investigating the α- and β-phase with other experimental methods like X-ray photoelectron spectroscopy (XPS), normal incidence X-ray standing wavefield (NIXSW), and LEED I-V may be interesting.

5.1.2 Charge density waves induced by QA chains

As mentioned in Section 5.1.1, there is some evidence that the QA chains of the α-phase induce a standing wave field of charge density waves in the 2D electron gas of a surface state [138, 228]. These waves not only cause a substrate-mediated long-range repulsive interaction between neighboring chains that leads to large distances between chains at coverages below 1 ML, but they are also responsible for the parallel alignment of QA chains despite the large distances (up to 5 nm) between them. The fact that the QA chain induces these charge density waves in the substrate is very interesting because it is also indicative of strong interactions between the QA molecules and the substrate, and thus points towards a chemisorptive bonding of the QA molecules on Ag(100).

A corresponding schematic drawing is illustrated in panel a) of Figure 5.3. The thick red vertical line in the center of the image represents a QA chain that induces charge density waves (as is illustrated by the light and dark gray lines) in the 2D electron gas of the substrate. This model works under the assumption that the wavelength of the charge density waves is of the same order of magnitude and at least roughly twice as long as the thickness of the chain (which is given by the length of a QA molecule). Furthermore, this model assumes that the chain is placed in a valley of the waves because the π electrons of the molecules are likely repulsed by a high electron density in the substrate. The three dashed red lines indicate the other three potential chain directions. It can be seen that chains that grow in these directions would cross several wave peaks and valleys. This can be assumed to be an energetically less favorable situation than the one in which a chain lies parallel to the wave fronts (indicated by the thin red line that is parallel to the QA chain). Hence, a parallel alignment of the chains is preferred. This model, which only considers a single chain, simplifies the situation. In practice, every QA chain in a domain induces such charge

[1] STM is able to distinguish between the two enantiomers of QA in the α-phase with a good quality tip shape and a distinct scanning parameters (cf. Section 5.1.1), but within the scope of the present work a distinction between the two enantiomers in the β-phase via STM was not achieved.

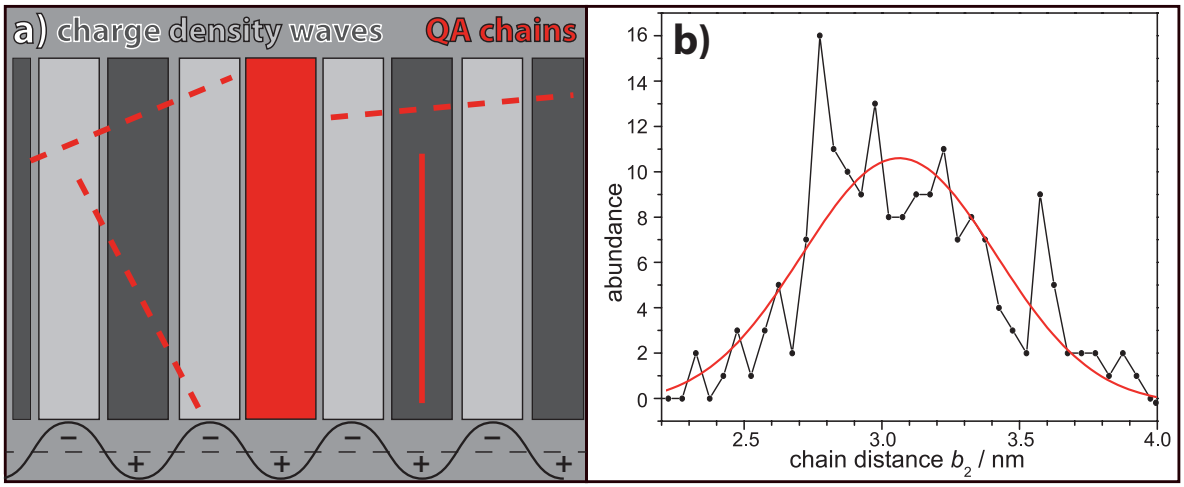

Figure 5.3: *a) Schematic model of a QA chain (thick vertical red line in the center) on Ag(100) that induces charge density waves (vertical light and dark gray lines) in the 2D electron gas of a surface state. The curve at the bottom illustrates the electron density at the different horizontal positions. The 3 thin red dashed lines correspond to the other three azimuthal orientations. It can be seen that chains in these directions would cross several peaks and valleys of the charge density waves. In contrast, a chain that grows in the same direction as neighboring chains (as indicated by the thin vertical red line) grows only in a valley of the charge density waves. b) Distribution of 180 measured distances between neighboring QA chains at a coverage* $\theta_{QA} = 0.5$ *ML. The distribution roughly follows a Gauss distribution around the average chain distance of 3.1 nm, a corresponding fit is illustrated by the red line.*

density waves and the waves interfere with one another. However, all interfering waves have the same wavelength, which means that the wavelength of the resulting standing wave field does not change.

The above model also suggests that distinct distances between neighboring chains are favored. To be precise, the most favorable adsorption sites for parallel chains should be at distances that are integer multiples of the wavelengths of the charge density wave. A distribution of distances between neighboring QA chains at a coverage of $\theta_{QA} = 0.5$ ML, which was acquired by measuring 180 distances in STM images, is shown in panel b) of Figure 5.3. It shows that the distribution roughly follows a Gauss distribution (a corresponding fit is illustrated by the red curve) around the average distance of 3.1 nm, which is about twice as long as the inter chains distance b_2 for a full ML. This supports the assessment that there are repulsive interactions between the chains because, for non-interacting chains, a geometric distribution would be expected [233].

5.1.3 Influence of Ag atoms on the phase transition

Another interesting question is whether the coordination of the molecules via metal atoms that are supplied by the substrate may alternatively or additionally play a role in the formation of the β-phase. This possibility is motivated by the fact that metal-coordinated structures were reported for many organic molecules [234]. If the formation of the β-phase were dependent on the presence of a sufficient amount of metal atoms, this would also explain why the β-phase only forms after annealing. Additionally to the arguments against a metal coordinated β-phase that were already

brought forward in the corresponding publication (cf. Appendix A.1), this section will present the results of additional SPA-LEED experiments that were specifically targeted towards answering this question.

The idea of the experiments is rather simple: silver atoms are deposited into the α-phase on Ag(100). If the presence of Ag atoms in the structure caused a spontaneous local or even complete transformation into the β-phase or decreased the transition temperature significantly below 500 K, this would be a strong indicator that the molecules in the β-phase are coordinated via Ag atoms. However, if this is not observed and the Ag atoms lead to a higher degree of disorder in the α-phase, then there are no metal coordination bonds involved, and the model for the β-phase described above (cf. Section 5.1.1) is correct. The Ag evaporator was constructed (cf. Appendix B.4) and the experiments were carried out within the scope of the bachelor thesis by T. Bald [235].

Half a ML of QA in the α-phase was prepared on Ag(100) and subsequently 0.54 ML of Ag atoms (1 ML refers to a full (100) layer of closely packed Ag atoms) was deposited onto this layer and annealed at 350 K for 15 minutes. The two corresponding 2D SPA-LEED images (not shown here, cf. ref. [235]) before and after the deposition of Ag did not differ in a significant manner. After the deposition of Ag, the spots that correspond to the distance between neighboring chains (described

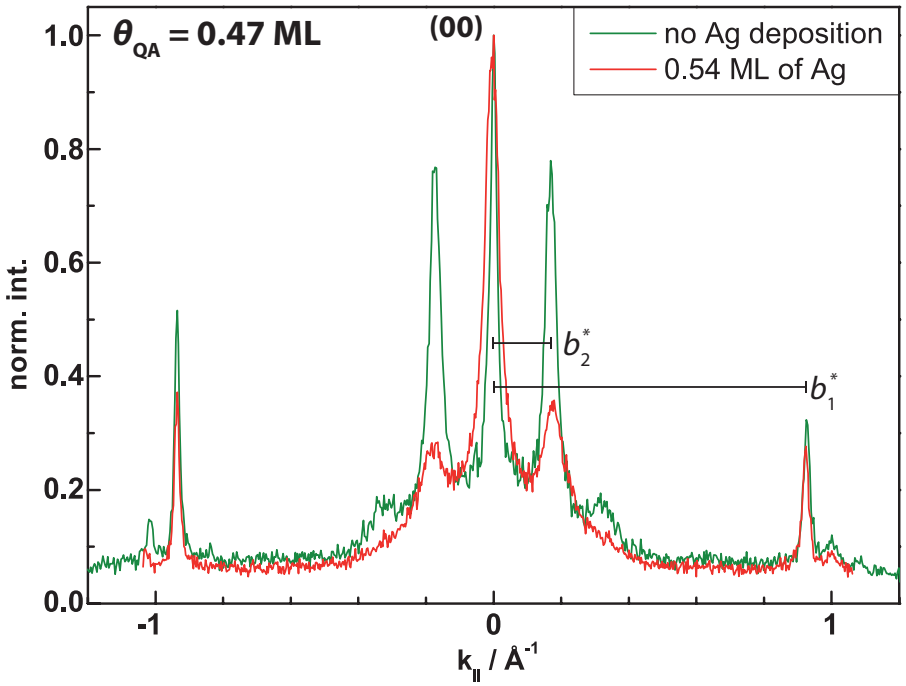

Figure 5.4: *SPA-LEED line profiles ($T = 110\,\mathrm{K}, E = 53.1\,\mathrm{eV}$) of QA on Ag(100) in the α-phase along the vector $\mathbf{b}_1^*$ (cf. Fig. 5.1d) after deposition of 0.47 ML QA (green) and after the subsequent deposition of 0.54 ML of Ag atoms (red). The two spectra were normalized to identical intensities of the two specular spots. It can be seen that the intensity of QA spots decreases significantly after the deposition of Ag. Furthermore, these line scans show that the positions of the spots that correspond to the intermolecular distance b_1 within the chains are identical before and after the deposition of Ag. In contrast, the spots corresponding to the distance b_2 between neighboring chains have slightly (5 %) moved to larger reciprocal distances. The line profiles were measured by T. Bald [235].*

by vector $\mathbf{b_2^*}$, cf. Fig. 5.1) have smeared out. Besides that, the two SPA-LEED images are identical, showing that the deposition of the Ag atoms did not induce a phase transition.

The more subtle differences between the two diffraction patterns can better be seen in line scans. Figure 5.4 shows two line scans along the vector $\mathbf{b_2^*}$ before (green) and after (red) the deposition of Ag. These line scans contain the specular spot, as well as two spots corresponding to the intermolecular distance and the distance between chains, respectively. It stands out that there is a drastic decrease in the intensity of the QA superstructure spots after the deposition of Ag. Furthermore, these line scans show that the FWHMs of the superstructure spots have increased by 20% and the FWHM of the specular spot has increased by 95%. Lastly, the reciprocal distance b_2^* has slightly increased by 5%, which means that the average distance between neighboring chains b_2 has decreased by the same percentage. These results show that the deposition of Ag atoms into the α-phase only leads to the formation of Ag islands between the chains, which leads to a compression and a significantly higher degree of disorder in the structure, but does not in any way facilitate the phase transition into the β-phase.

Additionally, the same experiment was carried out for the β-phase in order to investigate how the β-phase reacts to the deposition of Ag atoms. But as for the α-phase, no alteration to the structure was observed. Only a decrease in intensity and broadening of the superstructure spots was observed. Overall, these experiments show that the Ag atoms do not alter the structures of QA on Ag(100). Hence, the possibility that one of the structures involves metal-coordinated bonding between the QA molecules can safely be dismissed.

5.1.4 Growth of QA at low temperatures and Ostwald ripening

As stated above (cf. Section 5.1.1), the formation of the α-phase on Ag(100) requires the QA molecules to be very mobile on the surface. In this section, the growth of QA on Ag(100) with decreased mobility of the molecules will be presented and discussed. These experiments yield information about the mobility of the molecules at different temperatures and allow us to draw some conclusions about the growth mechanism of the chains.

For these experiments, QA was deposited onto the sample at a sample temperature of 120 K. The temperature was increased step by step and STM images were taken at different temperatures, which are displayed in Figure 5.5. Panel a) shows chains of QA at a sample temperature of 85 K with molecular resolution. The chains are very short (5 – 15 nm) and contain many defects and kinks, as well as intersections where two or more chains meet. Interestingly, all molecules exhibit an azimuthal orientation that is within $\pm 5^\circ$ of the azimuthal orientations that are known from the α-phase. The small models in panel c) show the typical molecular arrangements that can be found frequently in the observed structure. Model (i) shows a small area of a homochiral straight chain, similar to the ones in the α-phase. In model (ii), a chain of molecules with alternating handedness is shown. This leads to a periodic offset in the chain, similar to the ones in the β-phase. On the left, two molecules with different handedness but no offset are shown, which leads to no H-bonds and a larger distance between the two molecules. Model (iii) displays a chain with a molecule of

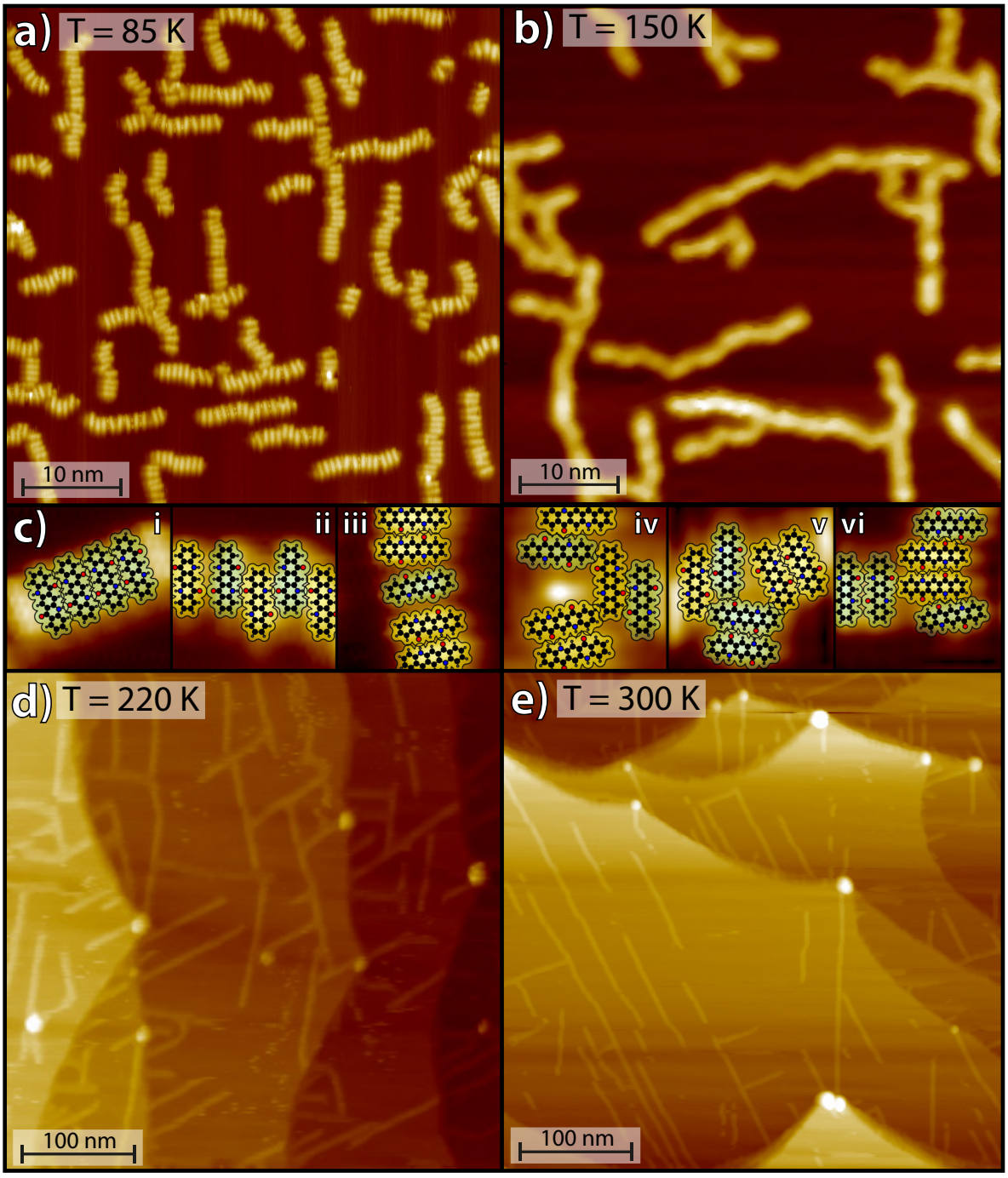

Figure 5.5: *STM images ($U_B = -1.5\,V$, $I_{tun} = 13\,pA$) of QA ($\theta_{QA} = 0.2\,ML$) on Ag(100). The molecules were deposited onto the sample at a temperature of 120 K. The temperature was increased step by step and STM images were recorded at* ***a)*** *85 K,* ***b)*** *150 K,* ***d)*** *220 K, and* ***e)*** *300 K. These images do not show the same area of the sample. It can be seen that with increasing temperature the structures change from short and very disordered chains at 85 K to long chains with no defects at 300 K.* ***c)*** *Zoom-ins into the image of panel a) that are superimposed with models of QA molecules. These models illustrate the molecular arrangement of chains without defects, chains with alternating handedness of the molecules, chains with defects due to single molecules with the wrong handedness and intersections between two or more chains.*

the "wrong" handedness in the middle that causes a slight bend in the chain. Moreover, models (iv) – (vi) show three different examples of how an intersection between two chains may look like. Despite the fact that some molecules are bound by only one or even no H-bonds to their neighbors, the observed structure is very stable at 85 K. Over a span of 30 minutes, several STM images could be recorded with every molecule at the exact same position. Another interesting aspect is that no single molecules with no neighbors could be observed. The smallest observed assemblies of molecules consisted of two to three molecules.

These results indicate that, after the deposition at 120 K, the molecules diffuse on the surface (without being able to flip to change their handedness) until they meet and bond to another molecule. The kind of bond (cf. panel c) of Fig. 5.5) depends on the handedness and the relative geometry of the two molecules when they meet. If two or three molecules have formed a small assembly, the interactions with the Ag substrate are strong enough to stabilize it on a terrace, and it stops diffusing. When more single molecules meet the small assembly, it continues to grow into the observed chains. Because of the low temperature, even the weaker intermolecular bonds cannot be broken, which is why the chains exhibit so many defects and kinks.

With increasing temperature, and hence increasing mobility of the molecules, these structures begin to change. At a temperature of 150 K, the small chains have vanished and the remaining ones have increased in length (15 – 25 nm). A corresponding STM image is shown in panel b) of Figure 5.5. However, the chains still exhibit the same amount of kinks and defects as the chains that were observed at 85 K. This means that the small chains, which are the least stable, have dissolved and the longer and more stable chains have increased in length. This process is known as *Ostwald* ripening and is a very well-known concept that describes the growth process of solid crystals [236].

Increasing the temperature further to 220 K changes the structure significantly, which can be seen in the corresponding STM image in panel d) of Figure 5.5. Now, all chains are completely straight, even longer (50 – 80 nm) than those at 150 K, and adapt one of the known four azimuthal orientations A – D of the α-phase, but no domains of parallel chains can be observed, yet. This shows that at 220 K the molecules are significantly more mobile on the surface and their thermal energy is large enough to break the energetically less favorable bonds that cause kinks and defects. These bonds get replaced by the more stable bonds between molecules of the same handedness with 2 H-bonds per molecule. The resulting molecular chains align themselves in the four distinct azimuthal orientations A – D that are known to be the most favorable for QA chains on the Ag(100) surface. Furthermore, at this temperature, an increased amount of lines along the scan direction was observed in the STM images, which was not seen at lower temperatures. This is an indication that molecules were dragged along by the STM tip, which points towards an increased occurrence of single molecules that are diffusing on the surface.

Lastly, after annealing the structure to 300 K, the chains are even longer (up to 200 nm) and are aligned in domains of parallel chains. The driving force behind this is that the alignment in parallel domains is thermodynamically more stable than an arbitrary distribution of chains with different

azimuthal orientations (cf. Section 5.1.2). A corresponding STM image is illustrated in panel e) of Figure 5.5. The change into a parallel alignment of the chains is very interesting because it means that one of the following scenarios occurs: (1) At 300 K, some of the chains that are not parallel to the neighboring chains dissolve completely and the molecules form new chains that are parallel to existing chains or (2) the chains are mobile to a certain degree and are able to rotate and diffuse on the surface. It seems very unlikely that molecular chains with lengths of up to 80 nm are able to diffuse on the surface. The diffusion barrier of such a large assembly, which is expected to be flexible and not completely rigid, is expected to be quite large. Additionally, no diffusion of similar large structures has been reported in literature. Hence, scenario (1) appears to be more likely in which some of the chains dissolve completely and subsequently form chains that are parallel to neighboring chains. This scenario is also supported by the fact that the chains at 300 K are significantly longer on average than those at 220 K. However, it is important to note that chains that are aligned in domains of parallel chains do not dissolve at 300 K and such domains of parallel chains are very stable. That is also in line with STM observations where these domains could be imaged without significant alterations over long periods of time (several hours). The higher degree of stability with respect to chains that are not parallel to their neighbors is supposedly due to the stabilization of the chains by the charge density waves (cf. Section 5.1.2).

In summary, these experiments support previous conclusions and allow us to draw some additional conclusions about the growth of QA chains on Ag(100).

(i) The diffusion of QA molecules on Ag(100) is possible at temperatures way below RT. At 120 K the molecules can form disordered assemblies after deposition. Already at 150 K the smaller assemblies dissolve and the larger ones grow (Ostwald ripening). At 220 K the diffusion has increased further and is noticeable by STM because the tip starts to pick up molecules, which was observed as an increased amount of lines in the scan direction.

(ii) At 300 K the QA molecules are very mobile on the surface and this mobility is also necessary for the formation of the observed domains of homochiral and parallel chains. If the mobility of the molecules is reduced upon deposition, then the resulting structures are very disordered.

(iii) The flipping of QA molecules (changing their chirality, $R \leftrightarrow L$) is possible at 300 K, but at lower temperatures (< 220 K) it is suppressed.

(iv) Single and even double H-bonds between QA molecules can be broken at 300 K. It is likely that during the deposition at 300 K chains of QA form and dissolve again until stable domains of parallel chains are formed.

5.2 Structures of quinacridone on Cu(111)

Now, the structures of QA on the Cu(111) will be discussed. This is interesting for two reasons. The first is that Cu has a higher chemical reactivity than Ag, and thus the interactions between the QA molecules and the substrate are expected to be larger than on Ag(100). The second is

that Cu(111) has a higher symmetry than Ag(100). The influence of these two aspects on the QA structures will be addressed in this chapter.

The structures of QA on Cu(111) are similar to those on Ag(100) but with some distinct and very important differences. After deposition at 300 K, QA forms homochiral molecular chains, the so-called α'-phase. Upon annealing, it transforms into a heterochiral phase, which will be called the β'-phase from now on. A third heterochiral structure, the γ'-phase, was only observed in a few rare instances and will be discussed in Appendix C.2. This section will briefly summarize the published results and, in particular, work out the important differences between the structures on Ag(100) and on Cu(111). Corresponding SPA-LEED images and a more in-depth discussion of the observed structures can be found in Appendix A.1.

STM images and a corresponding structure model of a full ML of the α'-phase on Cu(111) are displayed in panels a) and b) of Figure 5.6. As the α-phase on Ag(100), this phase consists of homochiral chains in which each molecule is involved in the formation of 4 H-bonds to its two neighbors. Due to the symmetry of the substrate, these chains adapt six distinct azimuthal orientations instead of four like on Ag(100). The intermolecular distance and the distance between neighboring chains in a full ML are identical to the ones observed on Ag(100) within the margin of error. A very striking difference between the two phases is that the domains of the α'-phase are very small, often only consisting of 2 – 4 parallel QA chains or even single chains that have no parallel neighboring chains. Another difference is that the chains on Cu(111) contain significantly more defects than the chains on Ag(100) in the form of offsets due to molecules with the wrong handedness. Furthermore, at coverages below 1 ML, QA on Cu(111) forms molecular chains, which are not homochiral and differ from those described above in their azimuthal orientations after different annealing steps. A similar observation was not made on Ag(100) and these structures will be discussed in detail in Appendix C.2.

A full ML of the β'-phase can be prepared by annealing a full ML of the α'-phase at 500 K for 15 minutes. Corresponding STM images and a structure model are shown in panels c) and d) of Figure 5.6. The left-hand side of the STM image shows an ordered structure with many small holes and larger defects (indicated by the blue circles), which are caused by molecules of the wrong handedness. Such defects were not observed in the β-phase on Ag(100), which indicates that they are induced by the stronger interactions with the substrate. The exact molecular arrangement can be seen in the STM image in the inset of panel c) and the structure model in panel d) of Figure 5.6. The structure of the β'-phase is very similar to the one of the β-phase on Ag(100). It also consists of heterochiral chains with periodic offsets that contain homochiral dimers. However, in the β'-phase on Cu(111), there are two additional molecules, which lead to two additional offsets, between the dimers (RRLRLL instead of RRLL). The ordered structure gradually changes into separated chains on the right-hand side of the image. A transition of the ordered phase into these chains was very commonly observed at the domain boundaries of the β'-phase, but this was never observed on Ag(100). The chains are very similar to those that can be observed after annealing sub-monolayers of the α'-phase (cf. Appendix C.2).

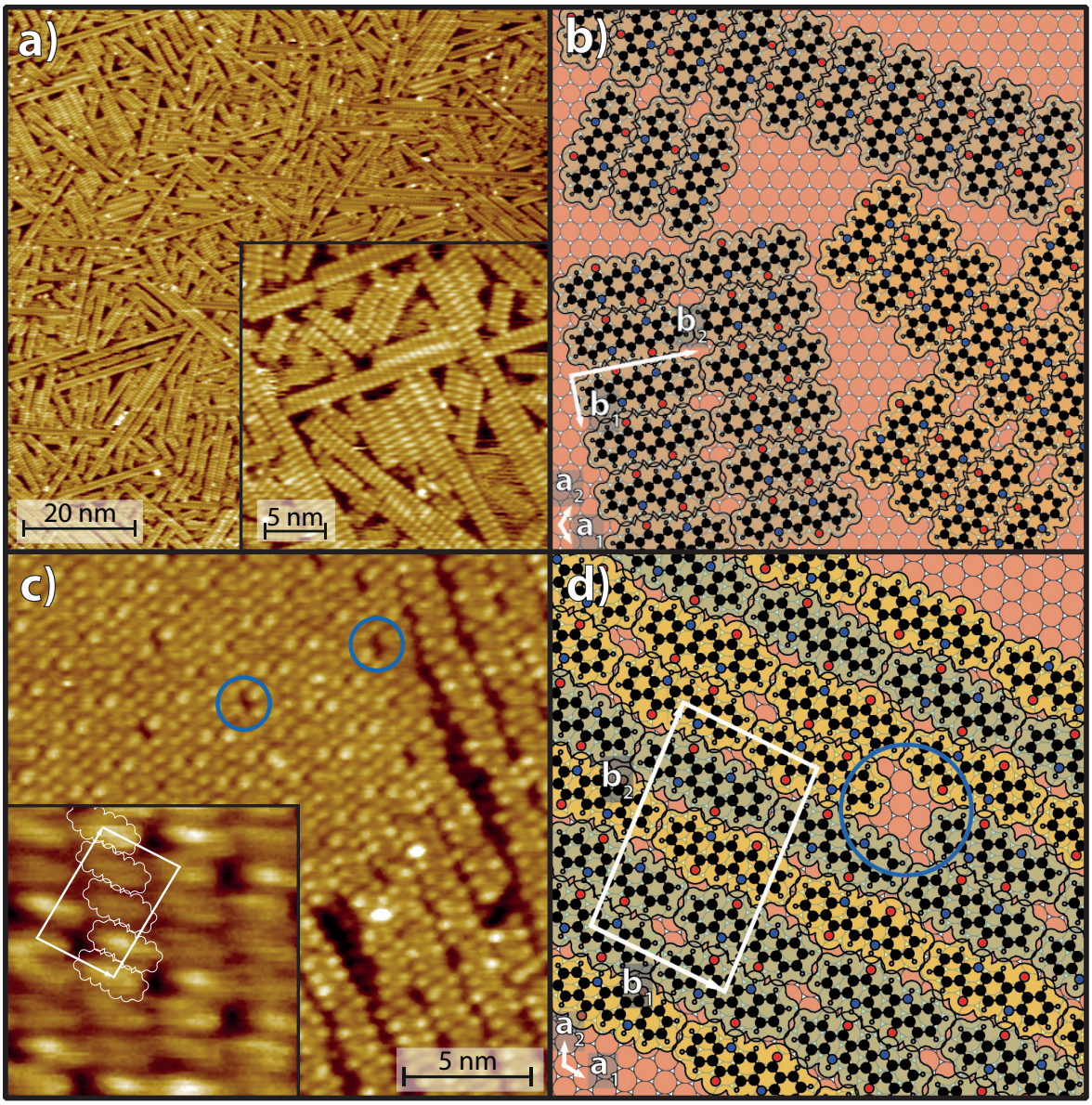

Figure 5.6: ***a)*** *STM image ($U_B = -1.5\,V$, $I_{tun} = 25\,pA$) of the α′-phase of QA on Cu(111). It shows very small domains of homochiral QA chains. The inset shows a zoom-in onto a small area with molecular resolution.* ***b)*** *A corresponding structure model for the α′-phase. The unit cell vectors for the substrate and the QA chains are depicted in white.* ***c)*** *STM image ($U_B = -1.5\,V$, $I_{tun} = 25\,pA$) of the β′-phase of QA on Cu(111). The upper left of the image shows an ordered domain of QA molecules. The molecular arrangement is illustrated in the inset. The structure contains many defects (indicated by the blue circles) that are caused by molecules of the wrong handedness. The right lower and right-hand side of the image shows the border of the domain, which is composed of chain-like structures with many defects.* ***d)*** *Structure model for the β′-phase, including an illustration of how a molecule of the wrong handedness causes the observed defects.*

Overall, these results show that the intermolecular interactions between QA molecules favor the formation of structures that are very similar to those on Ag(100). However, the interactions between the QA molecules and Cu are significantly stronger than the ones with Ag due to the higher chemical reactivity of Cu. The stronger interactions also cause a large barrier for the diffusion of QA molecules and inhibit their ability to flip their handedness on Cu(111), even at elevated temperatures. This reduced mobility of the molecules leads to a significantly higher degree of disorder in the QA structures on Cu(111) in the form of smaller domains and many defects.

To conclude this section, it is important to clarify that the structure of the β'-phase described here consists purely of QA molecules. In Appendix C.2, structures of QA on Cu(111) that were observed after annealing at 500 K and 600 K are described. There, evidence for a decomposition of the QA molecules into indigo molecules was found, which raises the question why the decomposition occurred in one experiment and not the other, although similar annealing temperatures were used. This can likely be explained by the fact that, in the experiments that are described in Appendix C.2, several annealing steps and slightly longer annealing times were used. In addition, it is also possible that the differences in coverage had an influence on the decomposition of QA, as well.

5.3 Structure of the second QA layer on Ag(100) and Cu(111)

In this section, the structures of QA in the second layer on Ag(100) and Cu(111) will be presented and discussed. In this context, one of the main questions regarding epitaxial growth over the last few decades comes up, namely whether and how the QA structures in the second layer differ from the structures in the first layer. It can be expected that the interactions between the molecules in the second layer and the metal substrate are weaker than those between the first layer and the metal due to the larger distance. Additionally, it can be expected that the interactions between the molecules in the second and those in the first layer play an important role in the formation of the QA structures in the second layer. These questions and aspects will be addressed in this section. First, the structures of the second layer of QA on Cu(111) will be discussed. Here, two cases need to be distinguished: (1) the structures of QA on top of the α'-phase and (2) the structures of QA on top of the β'-phase.

Regarding case (1), an STM image of 0.40 ML QA on top of a full ML QA in the α'-phase is displayed in panel a) of Figure 5.7. Both layers were deposited in one step at a sample temperature of 300 K. It shows that the second QA layer consists of the same kind of molecular chains with the same intermolecular distances between neighboring molecules. In contrast to the chains of the first layer, the chains in the second layer are curved and exhibit a broader range of azimuthal orientations. However, the majority of chains exhibit azimuthal orientations that are still within $\pm 10^\circ$ of those in the first layer.[2] This is likely due to a weaker bonding between the second layer and the first layer in comparison to the bonding of the first layer to the Cu(111) surface. From the

[2] In the corresponding publication (cf. Appendix A.1) it is stated the the chains in the second layer adopt fully arbitrary orientations. A more thorough analysis of the data has shown that this is not accurate.

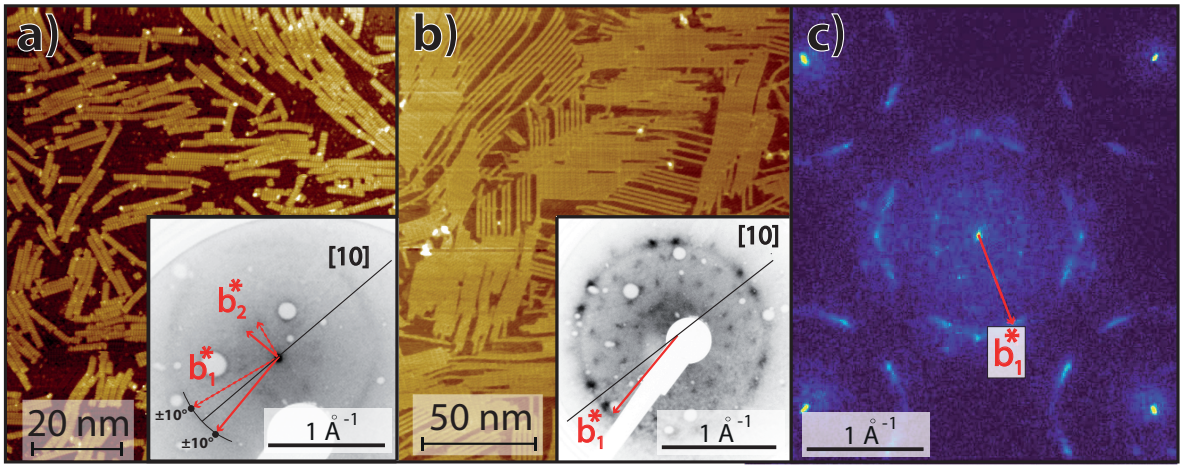

Figure 5.7: ***a)*** *STM image ($U_B = -1.5\,V$, $I_{tun} = 25\,pA$) of QA on Cu(111) at a coverage of $\theta_{QA} = 1.40$ ML after deposition at 300 K. The bright molecular chains are in the second layer, and the dark background corresponds to a full ML of the α' -phase. The inset shows a corresponding LEED image. Highlighted are the [10]-direction (black line) and the two vectors of the unit cell of the α'-phase $\mathbf{b_1^*}$ and $\mathbf{b_2^*}$ (red lines). The dashed red lines indicate the vectors of the unit cell of a mirror domain.* ***b)*** *STM image ($U_B = -1.5\,V$, $I_{tun} = 25\,pA$) of QA on Cu(111) at a coverage of $\theta_{QA} = 1.80$ ML after deposition at 500 K. The bright molecular chains are in the second layer and the dark background corresponds to a full ML of the β'-phase. A corresponding LEED image is shown in the inset.* ***c)*** *SPA-LEED image ($T = 110\,K$, $E = 53.1\,eV$) of QA on Ag(100) at a coverage of $\theta_{QA} = 1.20$ ML after deposition at 300 K and subsequent annealing at 475 K. The diffraction pattern shows some resemblance to the one of the α-phase on Ag(100), but all the spots are very smeared out. The vector $\mathbf{b_1^*}$ is illustrated in red; spots corresponding to the vector $\mathbf{b_2^*}$ could not be resolved. This image was taken from ref. [237] and slightly modified.*

STM data, it cannot be concluded for certain whether the azimuthal orientations of the chains in the second layer are determined by the interactions between the first and the second layer or by indirect interactions between the Cu(111) surface and the second layer. However, the fact that the chains in the second layer mostly do not follow the path of the chains right below them suggests that the interactions between the second layer and the Cu surface have a stronger influence on the azimuthal chain orientations in the second layer.

A corresponding LEED image of 1.40 ML QA is shown in the inset of panel a). The diffraction pattern looks similar to the one of the α'-phase (cf. Appendix A.1), but here, the spots that are given by the vector $\mathbf{b_1^*}$ exhibit some additional radial broadening due to the broader range of azimuthal orientations in the second layer. In particular, the LEED image contains 6 circular arcs of roughly 40° in the distance b_1^* from the specular spot. These arcs can be described by two mirror equivalent vectors $\mathbf{b_1^*}$ with a radial broadening of ±10° each ($2 \times 20° = 40°$), which is illustrated in the inset of panel a) by the black arcs. Hence, the LEED results confirm the STM observation that the azimuthal orientations of the chains deviate by up to ±10° from the orientations of the chains in the first layer. Interestingly, all the superstructure spots in the diffraction pattern have very low intensity and are smeared out. This is surprising because, for an incomplete second layer on top, the diffraction pattern of the first layer is usually expected to be visible. Since this is not the case here, the order of the first layer is likely perturbed by the incomplete second layer on top

of it, which is indicative of strong interactions between the two layers. These observations again reveals that the azimuthal chain orientations in the second layer is related to the Cu surface and not the first QA layer.

Regarding case (2), structures of QA on top of a full ML QA in the β′-phase were prepared by directly depositing 1.80 ML onto the surface at a sample temperature of 500 K. Interestingly, the structure of QA in the second layer consists of the same kind of molecular chains as the α′-phase, despite the high sample temperature that causes a phase transition into the β′-phase in the first layer. In the second layer, the molecular chains are more stable than the β′phase because, here, the smaller amount of H-bonds in the β′-phase cannot be overcompensated by stronger interactions with the Cu substrate.

A corresponding STM image is displayed in panel b) of Figure 5.7. It shows that the second QA layer consists of two kinds of structures. There are closely packed domains of parallel chains that are up to 50 nm in length and width. The chains in the domains exhibit six azimuthal orientations that are identical to those in the first layer of the α′-phase with an azimuthal spread of roughly $\pm 10^{\circ}$. Domains of that size do not exist in the second QA layer on the α′-phase, which can be explained by the lower mobility of the molecules during the preparation of the two phases (300 K vs. 500 K). The space between those domains is filled with single QA chains that have distances to neighboring chains of 2 – 5 nm. These chains are less strictly defined in their azimuthal orientations than the domains and also exhibit many small waves and curves. It is not clear why some of the chains maintain a distance from neighboring chains and do not become part of the close-packed domains. On the bare metal surfaces the distance between neighboring chains at coverage below 1 ML is explained by the charge density waves in the 2D electron gas of a surface state (cf. Section 5.1.2), but this explanation does not seem plausible for the chains in the second QA layer.

A LEED image of 1.80 ML QA on Cu(111) after deposition at 500 K is displayed in the inset of panel b) of Figure 5.7. It consists of many sharp spots and a smeared-out ring around the specular spot with a radius of b_1^*. All the sharp spots belong to the β′-phase (cf. the SPA-LEED image in Figure 6 of Appendix A.1 on page 121) of the first layer. It is interesting to note that the spots of the β′-phase in the first layer are significantly more intense than those of the α′-phase (cf. the inset of panel a) of Fig. 5.7). This indicates that the order of the first QA layer in the β′-phase is less perturbed by a second QA layer on top of it compared to the first layer of the α′-phase. This can explained by the fact that the α′-phase is thermodynamically less stable than the β′-phase, which is in particular given by stronger interaction between the QA molecules and the Cu substrate. Hence, the order of the β′-phase is less susceptible to changes induced by interactions with the second layer. The only part of the diffraction pattern that can be assigned to the QA chains in the second layer is the ring with radius b_1^* around the specular spot, which corresponds to the intermolecular distance within the chains. It is difficult to draw any conclusion regarding preferred azimuthal orientations of the chains from this LEED image because very intense spots of the β′-phase lie on the circle line, as well. The spots corresponding to the vector $\mathbf{b_2^*}$ of the second layer could not be distinguished from the spots of the β′-phase in the first layer.

Finally, the structure of the second QA layer on Ag(100) will be discussed. This was investigated with only SPA-LEED experiments within the scope of the focusing laboratory course of J. Roth [237]. It was found that after depositing additional QA onto a full ML QA in the α-phase at 300 K, a disordered second layer forms on top of the α-phase, which is only detectable in the form of a more diffuse diffraction pattern of the first layer. If QA is deposited onto a ML of a mixture of the β- and the γ-phase (cf. Appendix C.1.1 on page 197) and subsequently annealed at 475 K the intensity of the spots of the first layer decreases drastically and a diffraction pattern that looks like a very diffuse and smeared out diffraction pattern of the α-phase appears. A corresponding SPA-LEED image is displayed in panel c) of Figure 5.7. It contains 8 spots with the distance b_1^* from the specular spot and an azimuthal broadening of roughly $\pm 10^\circ$. That indicates that chains, which are similar to those that were observed in the second QA layer on Cu(111), are also present in the second QA layer on Ag(100).

In summary, these results have shown that molecular chains of QA grow in the second layer of QA on Ag(100) and on Cu(111). The molecules in the chains still have the same intermolecular distance, which is given by the H-bonds. The azimuthal orientations of the chains are still influenced by the underlying metal substrates, but this influence is significantly weaker due to the larger distance. Lastly, the chains in the second layer do not undergo a phase transition into the β- or β′-phase because there the loss of H-bonds can not be overcompensated by a stronger bonding to the metal.

5.4 The phase transition on Ag(100) investigated by SPA-LEED

The phase transition from the α- into the β-phase of QA on Ag(100) is an interesting phenomenon because it is a temperature-induced and irreversible transition from a metastable structure into a commensurate one. Hence, many interesting questions regarding, for example, the mechanism or the order of the phase transition can be asked. Therefore, in this section, the phase transition of QA on Ag(100) from the α- into the β-phase will be investigated in more detail. For this, the evolution of the α-phase with temperature at different coverages will be investigated, and the results will be used to construct a kinetic phase diagram of QA on the Ag(100) surface. Furthermore, the thermal stability and decomposition of the β-phase will also be investigated in a similar manner.

Before the results are discussed, it is important to clarify a very important aspect regarding this section, which is the role of the time. In order to investigate the evolution of a phase, a series of SPA-LEED measurements was conducted at different temperatures between 200 K and 500 K. Usually, the sample was heated in steps of 5 K, 10 K, or 20 K and SPA-LEED measurements were conducted at each temperature. In this procedure, the time between the start of two subsequent measurements was usually between 5 and 30 minutes. Of course, this raises the question of whether a phase at a specific temperature would continue to change if it were given more time. This was tested on a sample basis. At a few select temperatures, additional SPA-LEED measurements at the same temperature were conducted after an increased time span of about 2 – 3 hours. These experiments were conducted at some temperatures at which the diffraction pattern had already

started to change with respect to the diffraction pattern before annealing. The important point here is that after the initial temperature induced change, the diffraction patterns did not further change over time while the sample was being held at the same temperature. Hence, it is assumed that the structures that are presented in this section are in a local thermodynamic equilibrium. Nevertheless, it can not be excluded with certainty that structures at distinct other temperatures would not have evolved over time.

5.4.1 Qualitative analysis of the evolution of the α-phase with temperature

First, the evolution of the α-phase with temperature will be analyzed qualitatively by comparing 2D images of the α-phase at different temperatures and for two different coverages. Panel a) of Figure 5.8 shows a series of 2D SPA-LEED images at six different temperatures between 250 K and 450 K of the α-phase of QA on Ag(100) at a coverage of $\theta_{QA} = 0.78$ ML. It can be seen that the diffraction pattern of the α-phase decreases in intensity and the superstructure spots broaden with increasing temperature. Already at a temperature of 350 K the spots are barely visible and, at 430 K, only a diffuse background intensity around the specular spot can be seen. Increasing the temperature further (up to 500 K) causes the intensity, which belongs to the α-phase, to decrease further until only the substrate spots are visible (not shown). The fact that the superstructure spots vanish completely upon heating means that the molecules exhibit a disordered structure that is likely in the form of a 2D molecular gas phase in which the molecules diffuse randomly on the surface. Upon cooling down the sample, the spots of the β-phase slowly start to appear and increase in intensity. This shows that the disordered phase transforms into the β-phase, which is thus thermodynamically more stable than the α-phase.

Now, the thermal evolution of the α-phase at an increased coverage of $\theta_{QA} = 0.97$ ML, which changes the situation significantly, is considered. Panel b) of Figure 5.8 shows a corresponding series of 2D SPA-LEED images that is very similar to the one for a coverage of $\theta_{QA} = 0.78$ ML (cf. Fig. 5.8a). This series shows the same trend: upon annealing the sample, the spots of the α-phase lose intensity and broaden.[3] However, there are some crucial differences between the two coverages. The first difference is that, at a coverage of $\theta_{QA} = 0.97$ ML, the α-phase is significantly more resistant to thermal decomposition than at a coverage of $\theta_{QA} = 0.97$ ML. This can be seen by comparing the two SPA-LEED images at a sample temperature of 430 K (right-hand side of Figure 5.8). The image for $\theta_{QA} = 0.78$ ML only shows a very low and diffuse intensity around the specular spot, while in the image for $\theta_{QA} = 0.97$ ML, all the spots of the α-phase have low intensity, but they are clearly visible. This higher resistance against thermal decomposition at higher coverages can be explained as follows. As already stated in Section 5.1.1 (page 35), the distance between neighboring chains increases with decreasing coverage due to a substrate-mediated repulsive long-range interaction. This means that at a coverage of $\theta_{QA} = 0.78$ ML, there is a larger distance between the QA chains ($b_2 = 21.0$ Å, 4.6 Å distance between the chains on average), while at a coverage of $\theta_{QA} = 0.97$ ML, all the chains are directly next to one or two chains with the same

[3] The broadening of the spots may be difficult to see in the 2D images in Figure 5.8 but it will be analyzed with the help of 1D scans, see below.

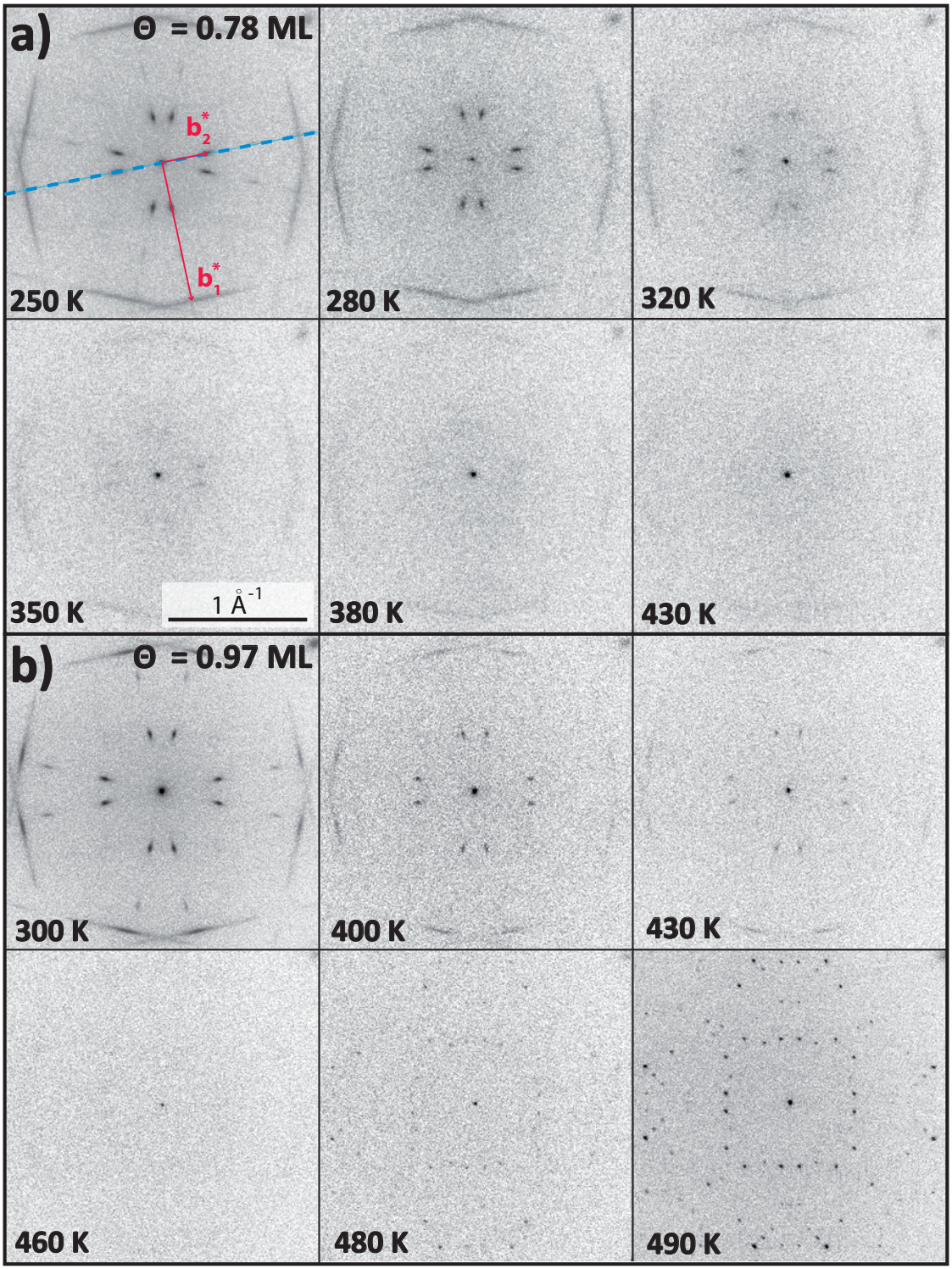

Figure 5.8: *Evolution of the α-phase of QA on Ag(100) with temperature. The time between the subsequent images was between 30 and 60 minutes. However, as described in the text, the structures are assumed to be in thermal equilibrium during the measurement, which means that they do not change over time at a constant temperature.* ***a)*** *Series of SPA-LEED images that were recorded at an electron energy of* $E = 51.3\,\text{eV}$ *and a QA coverage of* $\theta_{\text{QA}} = 0.78\,\text{ML}$*. The unit cell is depicted in red. Line profiles were measured along the dashed blue lines and are illustrated in Figure 5.10.* ***b)*** *Series of SPA-LEED images that were recorded at an electron energy of* $E = 51.3\,\text{eV}$ *and a QA coverage of* $\theta_{\text{QA}} = 0.97\,\text{ML}$*. The scale is true for all images in the figure.*

orientation, which stabilizes the structure through *van der Waals* dispersion interactions between the chains.

An even more pronounced difference between the two coverages is that, at $\theta_{QA} = 0.97$ ML, the α-phase does not transform into a disordered 2D gas phase but transforms into the β-phase upon annealing. In panel b) of Figure 5.8, it can be seen that, at 460 K, the spots of the α-phase have vanished, which indicates that this transformation goes via a disordered phase. At 480 K, the spots of the β-phase are visible. The reason for this direct transition is that, at a high coverage close to 1 ML, there is no space for a disordered 2D gas phase, i.e., the surface is so full of QA molecules that they do not have any space to randomly diffuse on the surface. Hence, the mechanism of the phase transition from the α- into the β-phase does not go via the disordered 2D gas phase but a different kind of disordered phase. The α-phase is homochiral, while the β-phase is heterochiral. That means that the phase transition is likely to happen through a flipping in place of roughly 50% of the QA molecules in a domain of the α-phase, changing their handedness, and a subsequent slight rearrangement of the molecules into the β-phase.

5.4.2 Evolution of the spot profiles of the α-phase with temperature

In this section, the evolution of the α-phase will be considered in more detail. The profile shapes of the α-spots at different coverages and temperatures will be discussed. In this context, it is important to differentiate between the two different sets of α-spots that correspond to the different distances in the α-phase. Hence, from now on, the term α_1-spots will refer to the spots that are given by the vector $\mathbf{b_1^*}$ and correspond to the distance between molecules within a QA chain. Accordingly, the term α_2-spots refers to the spots that are given by the vector $\mathbf{b_2^*}$ and correspond to the distance between neighboring chains. This nomenclature will be used both in 2D images and in 1D line scans. The time between the measurements of two subsequent line profiles at different temperatures was 5 to 10 minutes. But, once again, it is assumed that the structures were in a local thermodynamic equilibrium at the time of the measurements.

Before the evolution of the profiles with temperature is discussed, the general difference between the spot profile shapes of the α_2-spots at two different coverages will be addressed for the same temperature of 300 K. In panel a) of Figure 5.9, two line profiles at coverages of 0.78 ML (red line) and 0.97 ML (black line) across a line through the specular spot and two α_2-spots (as illustrated by the dashed blue line in Figure 5.8) are shown. Both profiles were recorded directly after the preparation of the QA layer at a temperature of 300 K. There are three distinct differences between the two profiles: (i) the α_2-spots of the black line are located at larger values for $\mathbf{k}_{||}$, (ii) the α_2-spots of the black peaks exhibit significantly lower peak intensities than those of the red line in relation to the specular spot but exhibit a significantly larger FWHM, and (iii) the α_2-spots of the black curve exhibit a *Gaussian* shape, while the spots of the red curve follow a more *Lorentzian* form.

All three of the above differences can be explained by the different coverages. (i) At a higher coverage (Fig. 5.9a, black curve) the distance between neighboring chains is smaller and hence the distance in reciprocal space is larger. (ii) The higher coverage also leads to a reduced mobility

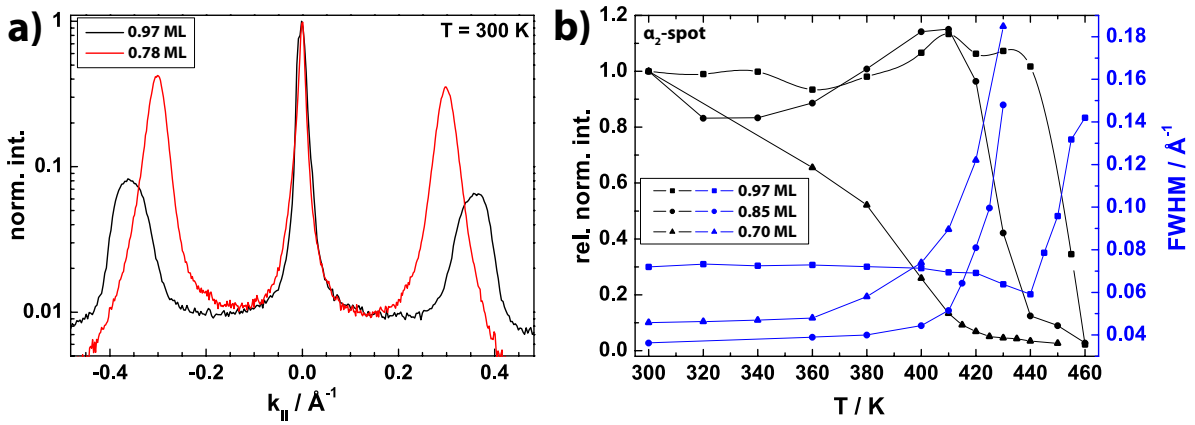

Figure 5.9: a) *Two line scans through the specular spot and two α_2-spots that correspond to the distance between neighboring chains at two different coverages. It can be seen that the profile shape of the shown spots changes with the coverage.* ***b)*** *The evolution of the normalized peak intensity (black) of the α_2-spots in relation to the intensity of the specular spot with temperature for three different coverages. In addition, the FWHMs of the corresponding peaks are shown (blue).*

of the molecules due to a lack of space, which leads to the formation of smaller domains during the growth. This can also be seen in the STM images (cf. figs. 2 and 3 in Appendix A.1 on page 113). The smaller domains explain the smaller peak intensities and larger FWHMs of the spot corresponding to the larger coverage (black curve). (iii) The profile shape of this α_2-spot (*Gaussian* vs. *Lorentzian*) is given by the distribution of distances between neighboring chains in real space. At the larger coverage ($\theta_{QA} = 0.97$ ML, black curve) the distances between the chains follow a *Gauss* distribution[4] around the average of $b_2 = 16.9$ Å. In contrast, at the lower coverage ($\theta_{QA} = 0.78$ ML, red curve), the distance between the chains is given by a distribution that follows an exponential decay[5] around the average distance of $b_2 = 21.0$ Å. This distribution following an exponential decay is likely related to the repulsive interactions between the chains.

Now, the evolution of the α-spots with increasing temperature will be addressed. It is of particular interest to analyze the peak intensities and profile shapes of the α_1- and α_2-spots with increasing temperature leading up to the phase transition. This can give some insight into the nature of the phase transition, such as its order. A corresponding waterfall plot showing line profiles across the spots of the α-phase at six increasing temperatures is displayed in Figure 5.10. These line profiles include both the α_1- and α_2-spots because the angle between the two unit cell vectors of the substrate and the angle between those of the α-phase are both 90°, respectively (the line profiles were recorded along the dashed blue line in panel a) of Figure 5.8). In this waterfall plot (Fig. 5.10), it can be seen that, at roughly 400 K, the peak intensities of all α_1- and α_2-spots start to decrease, and, at 460 K, the spots have vanished completely (except for small bumps in the background). This is an indication that, for a coverage of $\theta_{QA} = 1.00$ ML, the decomposition of the α-phase is taking place in this temperature interval (400 K – 460 K). This evolution of the intensity of the α-spots will be analyzed in more detail below (Section 5.4.3), and the results will be utilized

[4] The 1D Fourier transform of a *Gauss* function yields a Gauss function.
[5] The 1D Fourier transform of a *Lorentz* function yields an exponential decay function.

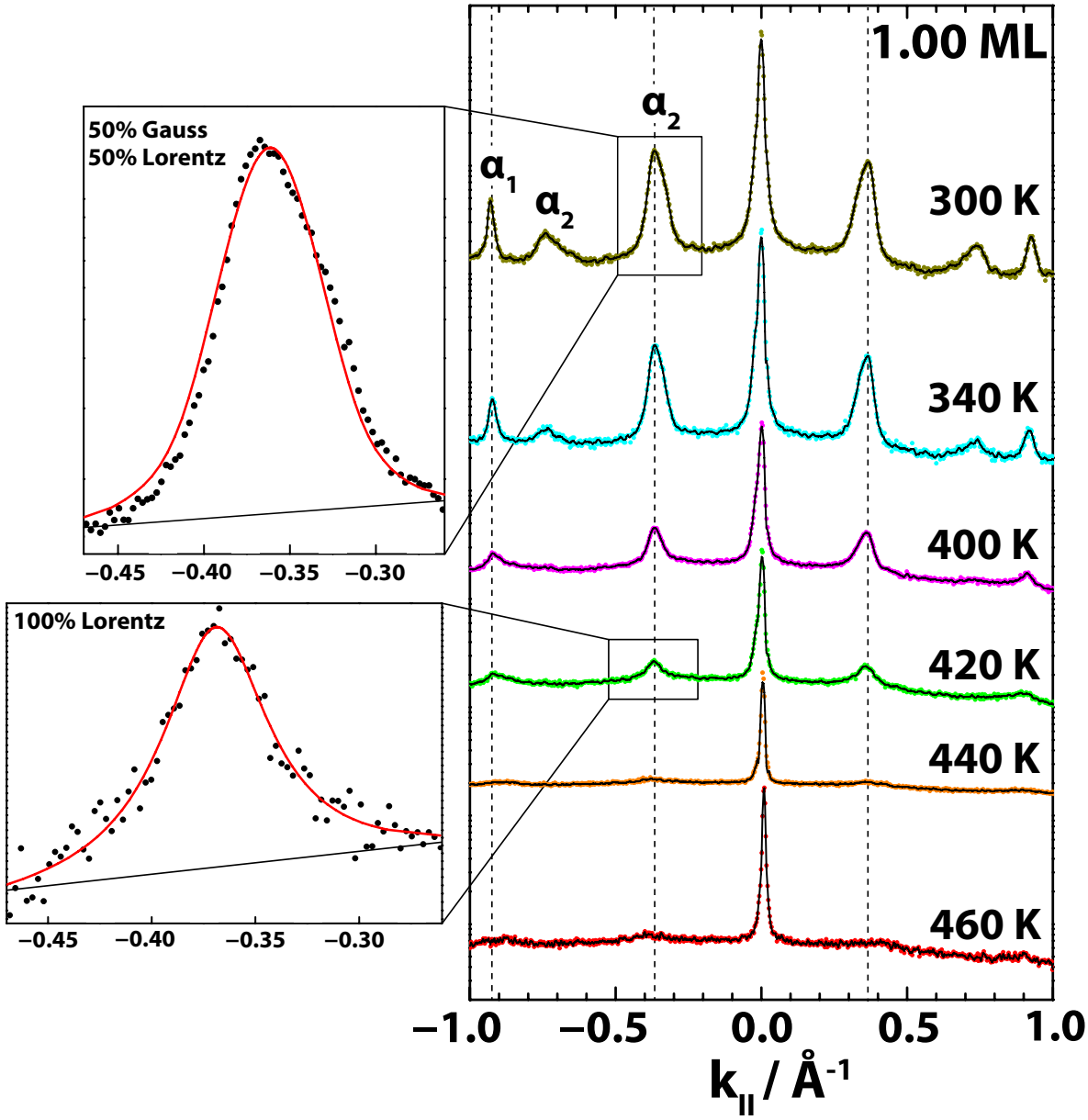

Figure 5.10: *The evolution of the superstructure spots of the α-phase of QA on Ag(100) at a coverage of $\theta_{QA} = 1.0$ ML with temperature. The right-hand side of the figure shows a waterfall plot of line scans through the dashed blue line in Figure 5.8 at increasing temperatures from top to bottom. The profiles were not normalized, which is the reason why the heights of the specular spots decrease with increasing temperature. The intensity scale is logarithmic. The plots contain the specular spot, and the α_1- and α_2-spots on both sides. The points show the raw data points, and the black lines correspond to the same data set after smoothing (Savitzky-Golay, 5th-degree polynomial, 12 points). The two insets on the left-hand side highlight the profile shapes of the α_2-spot at 300 K and 420 K, respectively. The black points are the raw data points, and the red curves correspond to fits with pseudo-Voigt functions.*

to construct a kinetic phase diagram of the α-phase. Furthermore, the waterfall plot (Fig. 5.10) shows that the α_1- and α_2-spots remain at the same positions during the annealing process until they vanish, i.e., until the α-phase decomposes. This shows that the distances within the α-phase do not change in a significant manner due to the annealing, which means that the α-phase does not stretch or compress before its decomposition.

A quantitative description of the evolution of the peak intensity of the α_2-spot, which corresponds to the distance between the chains, is illustrated in panel b) of Figure 5.9. It shows the normalized relative (with respect to the specular spot) peak intensity of the α_2-spot with increasing temperature for three different coverages, namely $\theta_{QA} = 1.00$ ML, 0.85 ML, and 0.70 ML (black squares, circles, and triangles, respectively). It can be seen that, for each coverage, the peak intensity starts to decrease at a distinct temperature and continues to decrease with increasing temperatures until the peak has completely vanished. This decrease in peak intensity is given by the decomposition of the α-phase. It is also noticeable that the decomposition of the α-phase begins at higher temperatures for larger coverages. Furthermore, at high coverages, the decline of the intensity is significantly more steep, which indicates that the decomposition of the α-phase occurs more suddenly than at lower coverages. These observations are in agreement with the above results and confirm that the α-phase is more resistant against thermal decomposition at higher coverages due to a stabilization due to the attractive forces between neighboring chains. Lastly, it is also important to note that this loss of peak intensity is irreversible, i.e., cooling down from any temperature does not bring back the lost peak intensity of the spots (see Fig. 5.11b). From Section 5.1 it is already known that the transition into the β-phase is irreversible. In addition, the SPA-LEED experiments also show that the decomposition of the α-phase, even if the β-phase has not formed yet, is irreversible.

Furthermore, the FWHM of the α_2-spots increases with increasing temperature. This is also illustrated in panel b) of Figure 5.9. The FWHMs corresponding to the evolutions of the peak intensities of the α_2-spot at the three different coverages are plotted in the same diagram (small blue symbols). It can be seen that at the same temperature where the peak intensities of the α_2-spots start to decrease drastically, the corresponding FWHMs of the α_2-spots begin the increase. This loss of the peak intensity of the α_2-spots could potentially only be caused by the broadening of the spots and their change in profile shape. However, the relative area of the α_2-peaks also exhibits a decrease around the same temperature as the α_2-peak intensity. Hence, the decrease of the peak intensity of the α_2-spots is a combined effect of the broadening of the spots and an actual loss of intensity. Lastly, besides the loss of intensity, it can also be observed that profiles of the α_2-spots change their shape with increasing temperature. This is illustrated on the left-hand side of Figure 5.10, which shows zoom-ins of the line profiles of the α_2-spot (black points) at 300 K and 420 K, respectively. The red curves illustrate pseudo-Voigt functions that were fitted to the data. The α-spots at 300 K exhibit a shape that can be described as a mixture of *Gauss* and *Lorentz* (50:50), while at 420 K it can be described by a pure *Lorentzian* shape.

The fact that the FWHM of the α_2-peak increases during the dissolution of the α-phase is indicative of a second-order phase transition [238]. Close to a second-order phase transition (i.e., the

temperature is close to the transition temperature) strong fluctuations in the structures appear. This causes a lack of correlation in the structures and thus leads to an increase of the FWHMs of the corresponding spots. In contrast, first-order transitions occur abruptly. That means that large ordered domains exist on the surface until the transition temperature is reached and hence the FWHM of the corresponding spots would not increase. Furthermore, the transition of the α_2-peaks to a more *Lorentzian* shape can be explained by an oscillation or wobbling of the chains at an increased temperature, which leads to a broader distribution of distances between the chains.

The above results only concern the α_2-spots. To conclude this section, a general remark about the evolution of the α_1-spots is in order. In general, the peak intensities and FWHMs of the α_1-spots followed a similar trend as those of the α_2-spots. However, the α_1-spots are strongly broadened in the direction of $\mathbf{b}_2^*$ due to lack of correlation between neighboring chains (cf. Chapter 5.1.1 on page 35). This makes the analysis and interpretation of the evolution of the α_1-spots more complicated.

5.4.3 Construction of a kinetic phase diagrams for the α-phase

In this section, the above-described evolution of the α_2-peak intensity with temperature at different coverages will be utilized to draw a kinetic phase diagram for the decomposition of the α-phase. Only the evolution of the α_2-spot was used for this purpose and not the α_1-spot due to the above-mentioned broadening of the α_1-spots. Panel a) of Figure 5.11 shows an example of the evolution of the normalized α_2-peak intensity relative to the peak intensity of the specular spot of the α-phase at $\theta_{QA} = 0.78$ ML (it is similar to the ones that were already shown in Fig. 5.9, but at a different coverage). As stated above, at each temperature the spot profiles were assumed

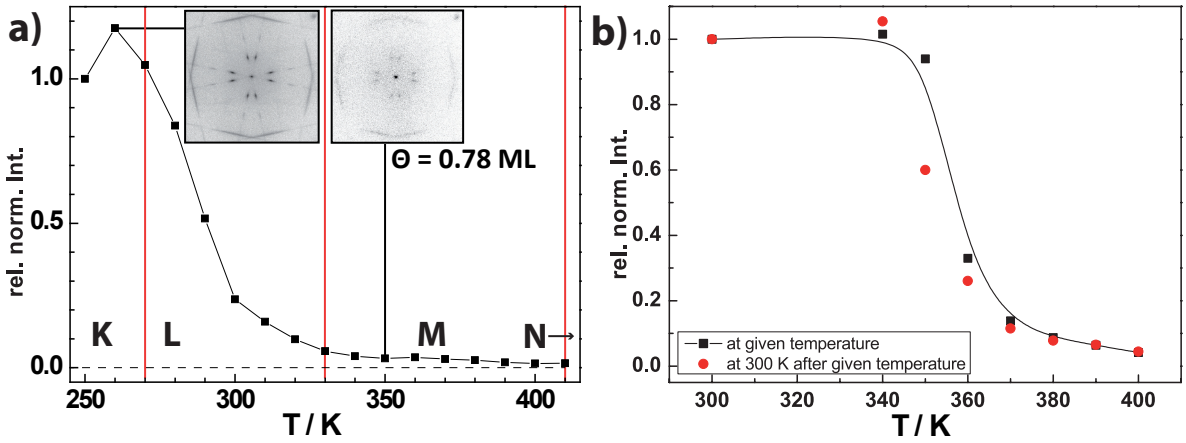

Figure 5.11: a) *The evolution of the normalized peak intensity of the α_2-spots in relation to the peak intensity of the reciprocal spot with temperature for a coverage of $\theta_{QA} = 0.78$ ML. The two insets contain 2D SPA-LEED images measured at 260K and 350 K, respectively. The vertical red lines divide the evolution into four temperature intervals K/L/M/N that describe different stages of the evolution of the α-phase upon annealing. For more info, see text.* ***b)*** *Probing of the reversibility of the intensity loss in interval L. The black points show the rel. norm. intensity at the given temperature. After each black point was measured the sample was cooled down and the corresponding red point was measured at 300 K.*

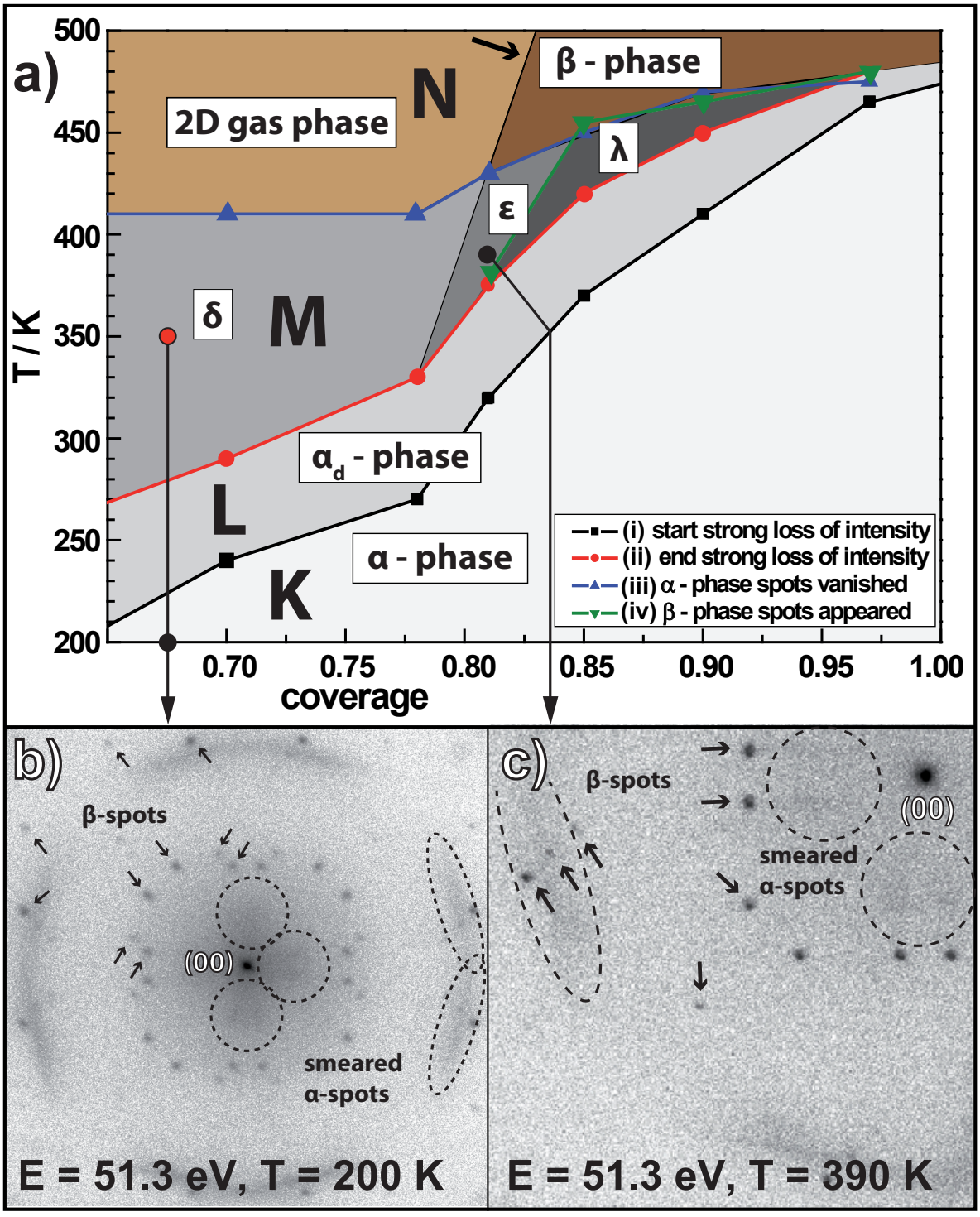

Figure 5.12: a) *Kinetic phase diagram for the α-phase of QA on Ag(100). This diagram is only true for increasing temperatures. A decreasing temperature or variation in coverage is not accounted for in this diagram. The line that is marked by a black arrow is not directly based on data points and is only a reasonable estimation for the position of the phase boundaries. For more information regarding the measurements of this phase diagram and all the different phases, see text.* ***b)*** *SPA-LEED image after cooling down from the δ-region, as indicated by the red and black points.* ***c)*** *SPA-LEED image that was recorded in the ε-region. Both panels b) and c) show a mixture of the α- and β-phase. The corresponding spots are marked by dashed ellipses and small black arrows, respectively.*

to be constant over time at the given temperature. In order to understand the decomposition of the α-phase, it is useful to think of it happening in different stages. Hence, the evolution of the α-peak intensity (see panel a) of Fig. 5.11) is divided into four temperature intervals (indicated by the vertical red lines) that are labeled with the capital letters K/L/M/N and will be explained in the following.

- Interval K: In this interval, the intensity of the α-spots remains about constant. Occasionally, a slight increase of the peak intensity of the α_2-spots can be observed in this interval (cf. Fig. 5.9b or Fig. 5.11a), which can potentially be explained by a thermally induced better ordering of the structure before it decomposes.
- Interval L: This interval describes a steep decline of the peak intensity of the α_2-spots by up to 95%. For larger coverages, the temperature at which this decline begins increases, and the width of the interval L decreases, as can be seen in panel b) of Figure 5.9.
- Interval M: This interval is a plateau of very low peak intensity of the α_2-spots after the steep decrease that is described by interval L. The border between intervals L and M is defined by a decrease of the intensity to only 5%.
- Interval N: The interval in which the α-spots have disappeared completely, i.e., the α-phase has completely decomposed.

The evolution of the relative peak intensities of the α_2-spots was investigated at six different coverages in the range of $\theta_{QA} = 0.60 - 1.0$ ML. For each coverage, the following four temperatures were determined and plotted into a phase diagram:

(i) The temperature at which the steep decrease of the relative peak intensity of the α_2-spots begins is given by the black line. Alternatively, the temperature at which the FWHMs of the α_2-spots increase could be used as a criterion because as panel b) of Figure 5.9 shows, the decrease of the peak intensities and increase of the corresponding FWHMs occurs at almost identical temperatures within an interval of $\pm(5 - 10)$ K.

(ii) The temperature at which the steep decrease of the relative peak intensity of the α_2-spots ends is described by the red line. The end of the steep decline is defined by the temperature, at which the relative peak intensity of the α_2-spots is only 5% of their initial peak intensity.

(iii) The temperature at which the spots of the α-phase have vanished completely (i.e., in a line profile the spots cannot be distinguished from the background) is given by the blue line.

(iv) The temperature at which the spots of the β-phase first appear (i.e., they are clearly visible in 2D images) is illustrated by the olive line.

The corresponding phase diagram is shown in panel a) of Figure 5.12. The areas of the diagram that result from the above criteria and the corresponding phases will be discussed in the following.

The area below the black line (corresponding to interval K) is the normal α-phase because in this area the peak intensity of the α-spots remains unchanged. Above the black line and below the red

line is the area that corresponds to the interval L. This area corresponds to a disordered α-phase, which is the reason for the steep decrease of the α-spot peak intensity. This decrease in intensity cannot be explained by a dissolution of the α-phase into the disordered 2D gas phase because that would mean that cooling down the sample from this area of the phase diagram leads to the formation of the β-phase, which was not observed. Instead, cooling down from area L does not lead to a significant change in the LEED pattern, i.e., the intensity of the α-spots does not increase again. Hence, the intensity loss is likely caused by an irreversible transition into a disordered α-phase upon heating. This disordered α-phase will be named α_d-phase in the following.

The area above the blue line (corresponding to the interval N) is the temperature region, where the α-phase has completely dissolved. Here, two different scenarios can occur depending on the QA coverage. Below a coverage of roughly 0.82 ML, only the substrate spots are visible in the diffraction pattern. However, upon cooling back down to RT, the spots of the β-phase start to occur. Hence, the area above the blue line for coverages of $\theta_{QA} < 0.82$ ML can be attributed to a 2D gas phase of QA molecules. In the area above the blue line for coverages of $\theta_{QA} > 0.82$ ML, the spots of the β-phase are clearly visible in the diffraction pattern. Hence, this area of the phase diagram is attributed to the β-phase.

Lastly, the area between the red and the blue lines will be discussed. This area corresponds to the interval M, which is the most complex temperature interval. Therefore, the area between the red and blue lines is divided into three regions corresponding to three different mixtures of phases that occur at different coverages and that will be named the δ-, ε-, and λ-regions. In the following, these three regions will be discussed in detail.

In the δ-region, which exists for coverages of $\theta_{QA} < 0.8$ ML, the diffraction pattern only contains the substrate spots and very weak spots of the α-phase. Interestingly, cooling down the δ-region leads to a mixture of the α- and the β-phase. A corresponding SPA-LEED image that was recorded at 200 K after cooling down from 350 K at a coverage of $\theta_{QA} = 0.68$ ML is shown in panel b) of Figure 5.12. It contains very weak and smeared α-spots and sharp β-spots. This shows that in the δ-region, a mixture of the α- and a disordered 2D gas phase is present on the surface. Upon cooling down, the disordered 2D gas phase transforms into the β-phase, which is thermodynamically more stable than the α-phase, leading to a mixture of the two phases.

The ε-region only exists in a very small coverage window in the range of $\theta_{QA} = (0.80 - 0.85)$ ML. In this small window, the α- and the β-phase coexist at an elevated temperature. A corresponding SPA-LEED image of this mixed phase that was recorded at a temperature of 390 K and a coverage of $\theta_{QA} = 0.82$ ML and is displayed in panel c) of Figure 5.12.

The third and last region between the red and blue lines, which will be named the λ-region, exists for coverages above 0.85 ML. Judging by the diffraction pattern, this region is very similar to the δ-phase because it only contains the substrate spots and very weak and smeared spots of the α-phase. However, the existence of a 2D gas phase is not plausible here because further heating the λ-region leads to a formation of the β-phase, while cooling down the sample does not lead to the formation any additional spots in the diffraction pattern. Hence, it is concluded that the

λ-region is a mixture of the α-phase and another disordered phase. This disordered phase could be explained by an incomplete phase transition from the α- into the β-phase, which, as stated above, potentially includes a flipping of 50 % of the molecules followed by a slight rearrangement of the molecules.

5.4.4 Analysis of the spot profiles of the β-phase

The evolution of the β-phase of QA was investigated in a similar manner as the α-phase. This was done in order to answer the following interesting questions. Does the β-phase also exhibit a phase transition into a disordered 2D gas phase upon annealing? If so, can the phase transitions (β $\leftrightarrow$ 2D gas phase) be crossed reversibly for an arbitrary amount of times? Is the transition temperature also dependent on the coverage? These questions will be addressed in this section.

For this, similar to the investigation of the evolution of the α-phase (see above), line profiles across the β-spots were recorded at different temperatures between 200 K and 500 K in steps of 5, 10, or 20 K. The time between subsequent measurements was 5 – 30 minutes. Importantly, as already described above, it is assumed that the structures did not change over time at a given temperature. A quadrant of a SPA-LEED image of the β-phase that illustrates the scan lines across the β-spots is displayed in panel a) of Figure 5.13. As for the α-spots, a differentiation between the two β-spots needs to be made. The β_1-spots are the spots that are given by the $\mathbf{b_1^*}$ vector and correspond to the intermolecular distance within the chains in the β-phase. Accordingly, the β_2-spots are given by the $\mathbf{b_2^*}$ and correspond to the distance between the neighboring chains.

Two waterfall plots across the β_1- and β_2-spots for six different temperatures between 300 K and 450 K at a coverage of $\theta_{QA} = 0.70$ ML are shown in panel a) of Figure 5.14. These plots show that, similar to the evolution of the α-spots with temperature, the intensity of both β-peaks decreases with temperature until they both have completely vanished at the same temperature (440 K for this coverage, not shown here). This vanishing of the β-spots is caused by a decomposition of the β-phase and is reversible. If the sample is cooled back down to RT, then the spots of the β-phase reappear. These observations show that the β-phase does indeed decompose and form a disordered 2D gas phase upon annealing, which forms the β-phase again upon cooling. However, these phase transitions (β $\leftrightarrow$ 2D gas phase) can not be repeated indefinitely because, after 2 – 3 cycles of annealing and cooling, it was observed that the spots of the β-phase are smeared out (not shown). This shows that repeated heating leads to more disorder in the β-phase. A potential explanation for this may be that some of the molecules undergo thermal cracking after several cycles of heating and the products of this cracking interfere with the order of the β-phase.

The exact structural reasons for the peak intensity loss of the β-spots upon annealing are not entirely clear. In the following, two potential causes will be explored. One potential reason for this intensity loss may be thermally induced point defects that form in the domains of the β-phase upon annealing. This process would likely be irreversible upon cooling. The peak intensity loss may also be caused by a partial transition of the β-phase into the disordered 2D gas phase, leading to a coexistence of the two phases. This process would be reversible upon cooling. However, the

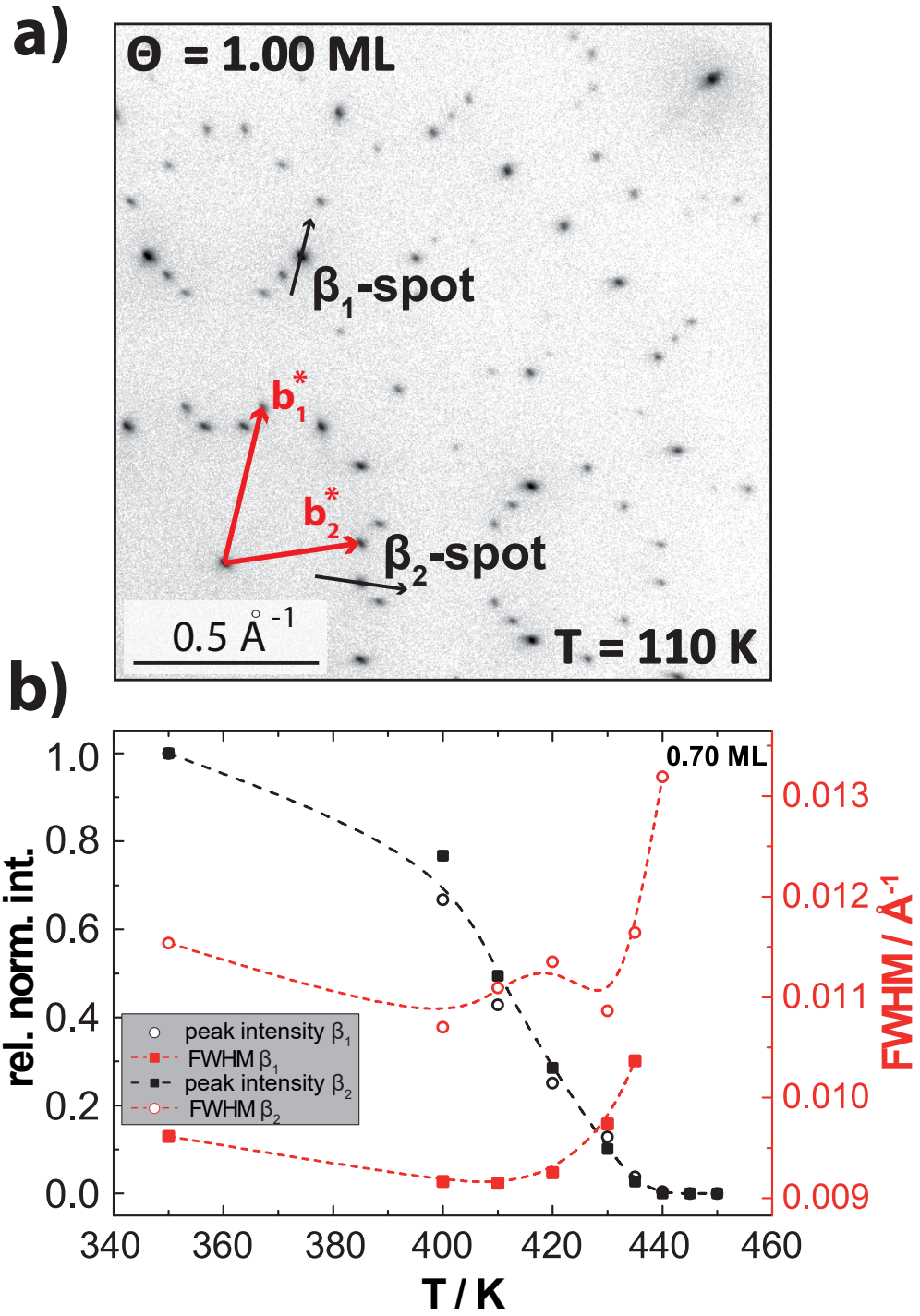

Figure 5.13: a) *A quadrant of a SPA-LEED image of the β-phase on Ag(100) ($E = 51.3\,\mathrm{eV}$). The β_1- and β_2-spots that were used to record line profiles (cf. Fig. 5.14) are marked by black arrows, which also show the scan direction. For the measurements of line profiles across a β_1-spot, a second-order spot was used because this spot had a higher intensity than the corresponding first-order one. The unit cell of the β-phase is depicted in red. Note that the two β_2-spots (marked by the red and black arrow) are mirror equivalent.* ***b)*** *The evolution of the relative (with respect to the specular spots) normalized peak intensities of the β_1- and β_2-spots (black squares and circles) and the evolution of the corresponding FWHMs (red squares and circles) with temperature.*

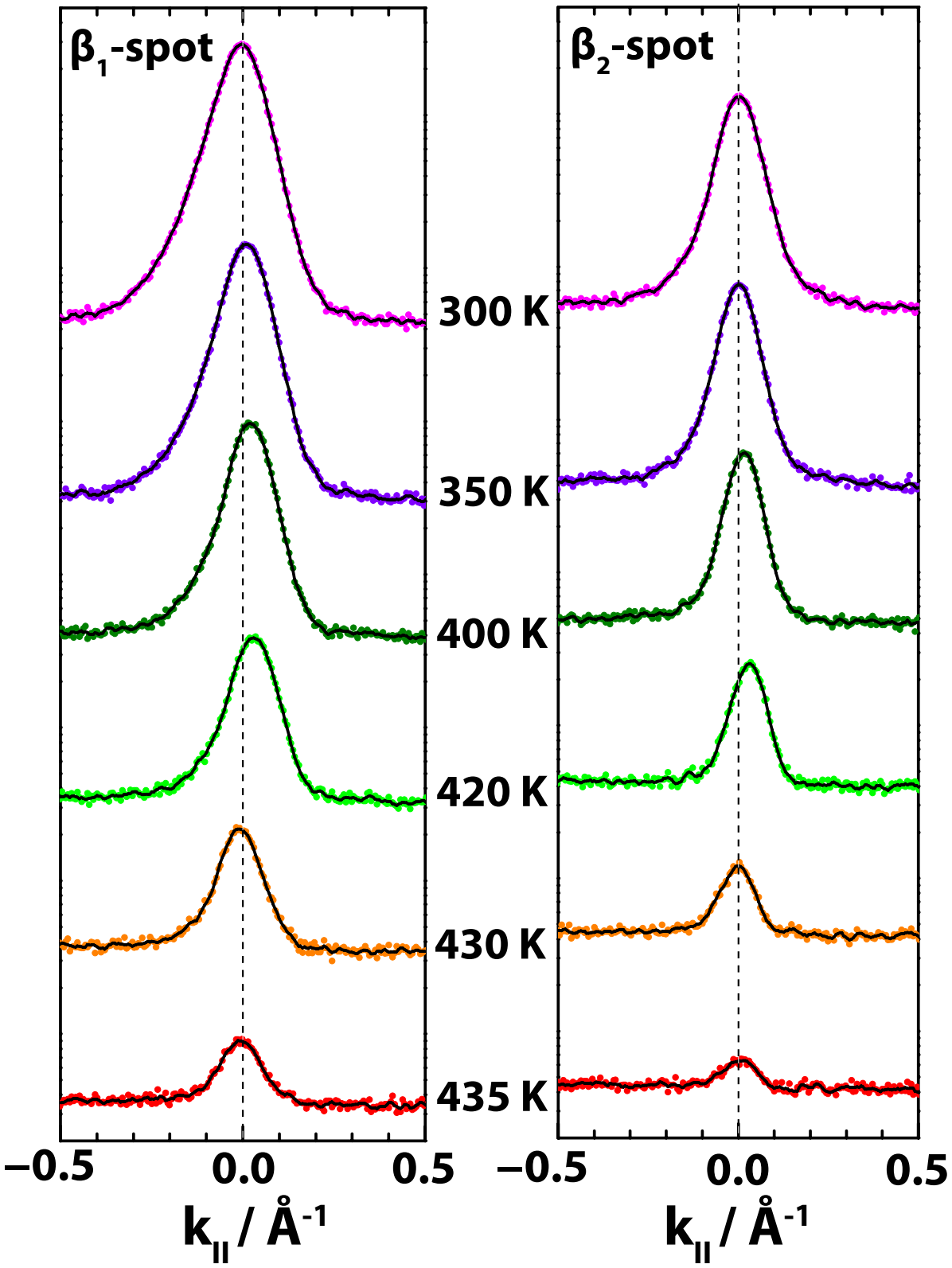

Figure 5.14: *Two waterfall plots across the β_1- and β_2-spots at different temperatures. The profiles are not normalized to illustrate to temperature-induced intensity loss. The lines along which these profiles were measured are illustrated as black arrows in Figure 5.13. All line profiles were recorded at an electron energy of 51.3 eV. The intensity scale is logarithmic and identical for both plots. Already at a temperature of 440 K, both spots had completely vanished and only the background could be observed (not shown). The small shift of the peaks at about (400 – 420) K is likely caused by an experimental artifact and does not have any physical meaning regarding the structure of the layer.*

reversibility of the peak intensity loss of the β-spots (before the spots had vanished completely) was not probed explicitly. The above-described decomposition of the β-phase was only observed for coverages of up to about 0.85 ML. This will be illustrated below in the following Section 5.4.5 where the evolution of the peak intensities of the β-spots will be utilized for the construction of a kinetic phase diagram.

The decomposition of the β-phase can be investigated further by considering the evolutions of the spot profiles and the FWHMs of the β-spots with temperature. In contrast to the evolution of the α-spots, the profile shapes of both the β_1- and β_2-spots remain constant at about 50% *Gauss* and 50% *Lorentz* over the whole temperature range. Hence, there is no indication of a temperature-induced oscillation or wobbling of the chains of the β-phase, which would lead to a wider distribution of distances in the structure, as was observed and discussed for the α-phase above. Furthermore, the FWHMs of the β_1- and β_2-peaks start to increase at a temperature at which their peak had already dropped to about 10%. This is illustrated in more detail in panel b) of Figure 5.13. This shows that the dissolution of the β-phase is, in contrast to the dissolution of the α-phase, not a second-order phase transition. The broadening of the spots is likely caused by a partial transition into the disordered 2D gas phase, which would cause a shrinking of the domains of the β-phase and would hence also lead to an increase of the FWHMs.

5.4.5 Construction of a kinetic phase diagram for the β-phase

In this section, the evolution of the β-spots will be utilized to draw a kinetic phase diagram for the β-phase. The evolution of the β-phase with temperature at different coverages was investigated in the same manner as that of the α-phase, as described above. The layers of the β-phase were usually prepared by depositing the QA on the sample at 500 K and subsequent cooling. The coverage was determined from the QMS integrals (cf. Section 4.2.2).

In panel b) of Figure 5.15, the evolution of the relative normalized β-spot peak intensity with temperature is shown for three different QA coverages, namely $\theta_{QA} = 0.60$ ML (black), 0.70 ML (red), and 0.85 ML (blue). For all QA coverages, the evolution of the β-spot intensity follows the same trend and can be divided into three temperature intervals that are identical to the intervals K/L/N that were described above for the α-phase. For the coverage of 0.85 ML (blue triangles and line), these three intervals are highlighted by the vertical lines in panel b) of Figure 5.15. The β-spot intensity stays constant (interval K) until a temperature is reached, at which the intensity starts to decrease. The peak intensity of the β-spots continues to decrease with increasing temperature for several tens of Kelvin (interval L) until a temperature is reached at which the spots have vanished completely (interval N). The plateau of low intensity (interval M) that was described for the α-phase (see above) was not observed for the β-phase. It can also be seen that the temperature at which interval L begins increases with increasing QA coverage, which indicates that the β-phase is, like the α-phase, more resistant to thermal decomposition at higher coverages.

This evolution of the β-spot intensity was investigated for five different coverages between 0.5 ML and 1.0 ML. Because the temperature evolution always follows the same trend, the phase diagram

can simply be divided into three areas. The phase diagram[6] is is shown in panel a) of Figure 5.15. In the area in the bottom right of the phase diagram, the peak intensity of the β-spots is constant (interval K), which means that this area corresponds to the stable β-phase. In contrast, the area in the top left corresponds to the temperatures at which the β-spots had completely vanished (interval N). Upon cooling, the β-spots reappear, and thus this area is attributed to a disordered 2D gas phase. Lastly, the area in the middle corresponds to the temperature interval in which the peak intensity of the β-spots decreases (interval L). This area likely corresponds to a situation where the β-phase has already partially dissolved into the 2D gas phase and the two phases coexist. Interestingly, for coverages close to $\theta_{QA} = 1$ ML, the β-phase is still stable at a temperature of 500 K. That can be explained by a lack of space on the surface that prevents the decomposition of the β-phase into the disordered 2D gas phase. However, the heating to 500 K leads to a smearing of the corresponding β-spots. This is illustrated in panel c) of Figure 5.15, and could potentially be explained by thermally induced cracking of the QA molecules, which interferes with the order of the layer.

Lastly, it is important to note that these phase diagrams have some uncertainties. On the one hand, there are errors of the coverage and the temperature. The error in the coverage is estimated to be $\Delta\theta_{QA} = \pm 0.05$ ML. The error of the temperature is estimated to be $\Delta T = \pm 10$ K. On the other hand, these experiments worked under the assumption that at each temperature step, the thermodynamic equilibrium of the system was reached before the profiles were measured. In a few instances, it was tested whether a profile at an elevated temperature changed within the span of roughly 30 minutes, and no such example was found. However, it cannot be excluded for certain that very slow processes may happen at distinct temperatures, which would have an impact on the phase diagrams.

Overall, the main result of this section is that the phase transition from the α-phase into the β-phase is very dependent on the QA coverage and may happen in three different ways. For medium and low coverages ($\theta_{QA} < 0.77$ ML), the phase transition goes via a 2D gas phase of QA molecules that forms the β-phase upon cooling down to RT. In contrast, for a very small coverage window ($0.78 < \theta_{QA} < 0.83$ ML) it happens via a mixture of the α- and β-phase, and for high coverages ($\theta_{QA} > 0.84$ ML) the phase transition happens via an unknown disordered phase that transforms into the β-phase at high temperatures.

5.5 Discussion of the phase transition

To end Chapter 5, the phase transition between the α- and β-phases of QA on Ag(100) and the electronic structures of the QA molecules in the two phases will be discussed in more detail. As described in Section 5.1.1, the β-phase exhibits only 1.5 intermolecular H-bonds per molecule, while in the α-phase 2 H-bonds per molecule are formed. In the β-phase, this loss in energy in terms of intermolecular interactions is overcompensated by stronger interactions between the QA

[6] It is important to note that this phase diagram is only true for increasing temperatures. The phase diagram for cooling would likely look similar, however, this was not investigated in detail.

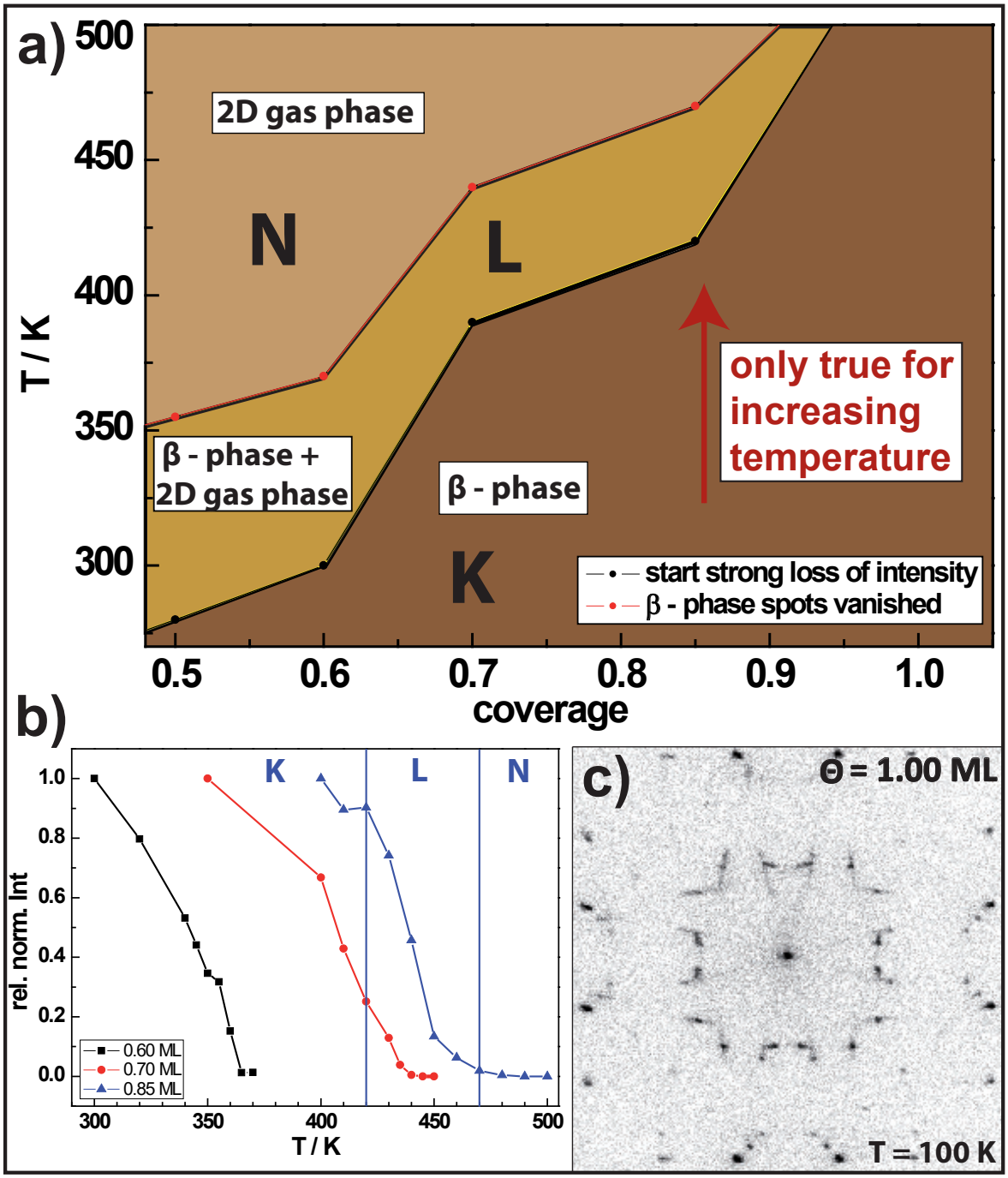

Figure 5.15: ***a)*** *Kinetic phase diagram for the β-phase of QA on Ag(100). This diagram is only true for increasing temperatures and constant coverages. For more information regarding the measurements of this phase diagram and all the different phases, see text.* ***b)*** *Evolution of the relative normalized peak intensities of the β-spots for three different coverages.* ***c)*** *SPA-LEED image of a full ML β-phase after it was heated to 500 K and cooled back down.*

molecules and the Ag substrate. Hence, it is reasonable to assume that the electronic structures of the QA molecules, and the vertical distances between the QA molecules and the Ag substrate differ significantly in both phases.

An impressive example of such differences between the electronic structures of molecules in different phases was reported by Kilian *et al.* [239] for PTCDA on Ag(111). They compared a disordered structure consisting of dendritic clusters of PTCDA molecules at low temperatures to an ordered herringbone structure at RT. They found that in the disordered phase, the bonding of the PTCDA molecules to the Ag substrate is stronger, and the molecules exhibit a stronger intramolecular distortion, and a smaller vertical distance to the Ag substrate than in the herringbone phase. The reason for these observations is that the intermolecular interactions in the herringbone phase possibly withdraw some electron density from the carboxylic oxygen atoms. This weakens the bond between the carboxylic oxygen atoms and the Ag substrate.

A similar behavior may be expected for the phase transitions of QA on Ag(100) and other metal surfaces. Only that here, the phase transition goes from the α-phase, which is determined by the strong intermolecular H-bonds, to the β-phase with less intermolecular H-bonds. It was found by Priya *et al.* for QA on Ag(111) that in the homochiral α^*-phase on Ag(111) IDCT occurs, but for the heterochiral β^*-phase, this IDCT vanishes completely. This was attributed by the authors to a filled former LUMO in the β^*-phase [81], which is indicative of a stronger bonding of the QA molecule to the Ag substrate. This shows that the electronic states of QA on Ag(111) in the α^*- and β^*-phases differ significantly from each other. A similar process may be expected for QA on Ag(100) and Cu(111). Hence, it may be expected that in the β-phase, the averaged vertical distance between the QA molecules and the substrate is overall smaller than in the α-phase. Furthermore, the carboxylic oxygen atoms of the β-phase that are not involved in the formation of an intermolecular H-bond anymore, may exhibit a stronger local bond to the surface. This could lead to an asymmetric distortion of the corresponding QA molecules. Interestingly, in the β-phase, the molecules of only every second dimer contain oxygen atoms that are not involved in the formation of an intermolecular H-bond.[7] Thus, 50% of the molecules in the β-phase have such an oxygen atom and can exhibit a stronger bonding to the surface than the other 50% of molecules. This indicates that a vertical corrugation of the β-phase may be expected, where every second dimer exhibits a smaller vertical distance to the surface. The discussion above shows that a thorough investigation of the electronic structure and vertical distances of the QA molecules in the α- and β-phase with methods such as ultraviolet photoelectron spectroscopy (UPS), XPS, or NIXSW would be of high interest.

Lastly, another interesting aspect is that QA on Ag(100) exhibits a similar disordered structure, consisting of 2D clusters after deposition at low temperatures (cf. Section 5.1.4, page 43), as PTCDA on Ag(111) [239]. The molecules in this disordered structure exhibit fewer intermolecular interactions than those in the molecular chains of the α-phase. Hence, the molecules in these

[7] This can be seen the structure model in panel d) of Figure 5.2 on page 38. Only the molecules with one of the two chiralities (the ones with the green background) have an oxygen atom that is not involved in the formation of an intermolecular H-bond.

2D clusters may be more strongly bound to the Ag substrate than the ones in the molecular chains of the α-phase. This would mean that the bonding between the QA molecules and the substrate would weaken upon the formation of the α-phase (2D clusters → α-phase) and strengthen again upon the formation of the β-phase (α → β).

5.6 Conclusions

In this chapter, the lateral structures of QA on Ag(100) and Cu(111) were investigated. It was found that the intermolecular H-bonds are a dominant motif for the structure formation of QA. On both surfaces, QA forms one-dimensional homochiral molecular chains consisting of flat-lying QA molecules that are connected via intermolecular hydrogen bonds after deposition at sample temperatures of 300 K (the α- and α′-phase). On Cu(111), the mobility of the QA molecules is significantly reduced due to the stronger interactions in comparison to those on Ag(100), which leads to more defects and kinks in the chains of the α′-phase.

On both surfaces, the chains undergo an irreversible phase transition into heterochiral structures (the β- and β′-phase) if the sample is annealed at 500 K for 15 minutes, which shows that the chains on both surfaces are only metastable structures. These heterochiral structures also consist of chains, but with periodic kinks, which leads to fewer H-bonds per molecule. However, this energy loss in terms of intermolecular interactions is presumably overcompensated by stronger interactions between the QA molecules and the underlying metal substrate.

The QA structures in the second layer are defined by weaker interactions between the molecules in the second layer and the metal substrate. This leads to molecular chains in the second layer that exhibit a larger spread of azimuthal orientations than those in the first layer. Furthermore, it was found that the order in the first layer is perturbed by the molecules in the second layer. The structures of QA in the second layer do not change significantly upon annealing. Phases similar to the β- and β*-phases do not form in the second layer because, there, the loss in terms of intermolecular interactions can not be overcompensated by a stronger bonding to the metal substrate.

Lastly, the phase transition between the α- and β-phase on Ag(100) was investigated with SPA-LEED. It was found that for lower coverages, the phase transition goes via a disordered two-dimensional gas phase that transforms into the β-phase upon cooling the sample back down to RT. For larger coverages, the phase transition goes directly from the α- into the β-phase upon annealing the sample. Moreover, the evolutions of the relative spot intensities were used to draw kinetic phase diagrams for the dissolution of the α- and the β-phase.

6 Quinacridone on layers of KCl and hBN

Some results of the following chapter have been published in ***J. Phys. Chem. C 2023, 127, 49, 23814–23826*** *(cf. Appendix A.2). The acquisition and evaluation of the data, and the writing of the manuscript were done by the author of the present thesis. The DFT calculations were performed by Prof. T. Bredow (University of Bonn). The acquisition and evaluation of the data concerning QA/hBN, which are also presented in this chapter, were performed together with R. Bretel [93] who was an exchange student at the University of Bonn.*

In this chapter, the growth of QA on thin layers of wide band gap materials will be discussed. In particular, QA structures on epitaxial thin films of KCl on Ag(100) will be considered in Section 6.2. These results have been published and can be found in Appendix A.2. The results will also be compared to the results for QA on epitaxial thin films of KCl on Cu(111), which was investigated by R. Bretel within the scope of this doctoral thesis [93, 240]. In addition, the structures of QA on a thin layer of hBN on Cu(111) will be presented in Section 6.3.

6.1 KCl on Ag(100)

6.1.1 Structure and growth of KCl on Ag(100)

The structure of epitaxial layers of KCl on Ag(100) has been investigated previously by Müller *et al.* [38]. In this section, the known aspects of the structure and growth of epitaxial layers of KCl on Ag(100) will be summarized and some new insights and details from additional observations will be added.

KCl grows on Ag(100) in monoatomic KCl(100) layers that are identical to the layers that make up the KCl bulk crystals, which exhibit the typical face-centered cubic (fcc) crystal structure. The surface unit cell of the KCl layer is quadratic and the corresponding vectors are aligned with those of the Ag(100) surface and exhibit lengths of 4.45 Å [38]. This length is exactly the bulk lattice constant of KCl of 6.29 Å [241] divided by $\sqrt{2}$ (yielding the lattice constant of the KCl(100) plane), which shows that the structure of the KCl layers is given by the Coulomb interactions between the ions, which are significantly stronger than the interactions between the ions and the Ag substrate. Hence, the growth of epitaxial KCl layers on Ag(100) is incommensurate and the mismatch between the two lattices is about 53%. A corresponding hard-sphere structure model for the structure of KCl on Ag(100) is illustrated in Figure 6.1. It shows an on-top view and two different side views of a KCl wetting layer that is two ML in height (cf. Appendix A.2), with a third layer on top that is only one ML in height. The KCl island displayed in the model is located at a Ag step because this a a preferred nucleation point for the growth of KCl. The Ag step runs

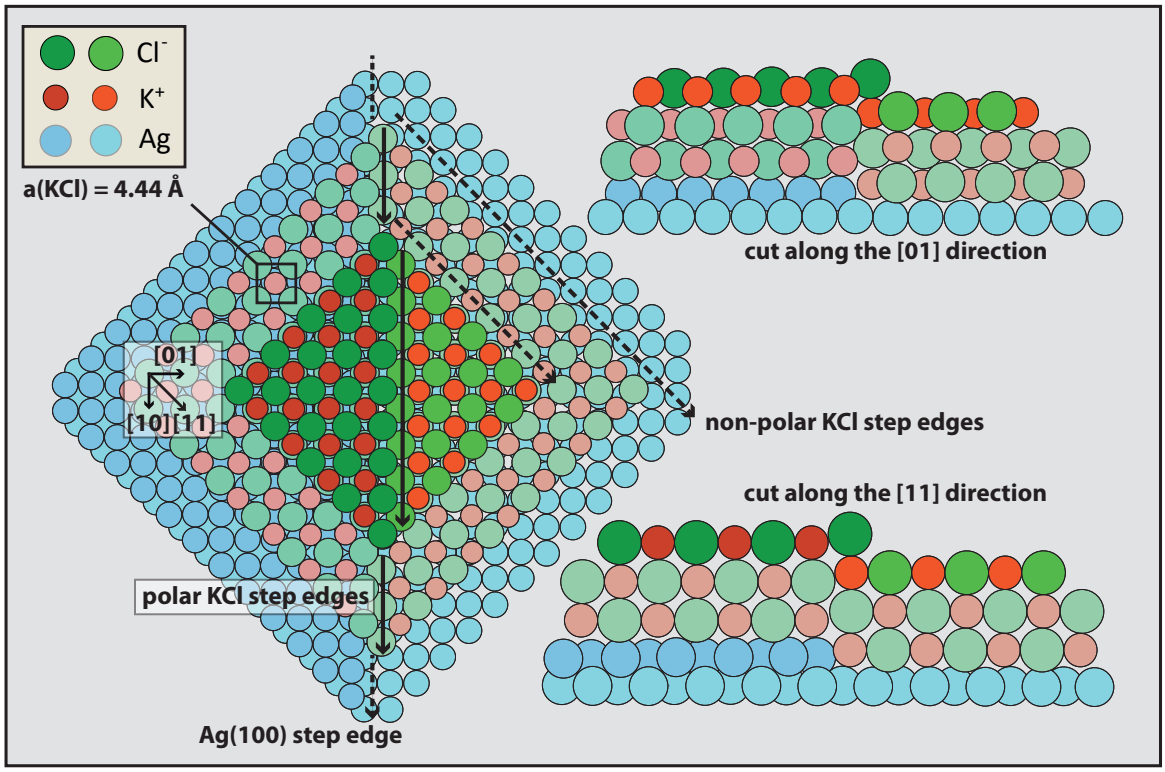

Figure 6.1: *Hard sphere structure model of KCl on Ag(100) showing an on-top view and two different side views. The model shows the wetting layer (faint colors) that is 2 ML in height and which grows across a Ag step edge in ⟨10⟩ direction replicating the Ag step edge in the KCl layer. On top of the wetting layer is a small quadratic island (full colors) that is only one ML in height.*

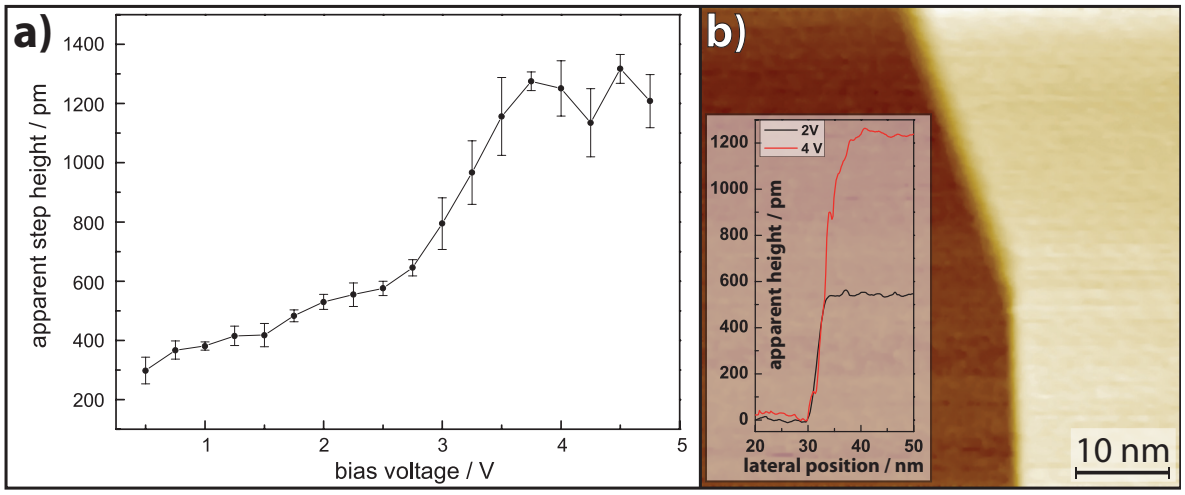

Figure 6.2: *Bias dependency of the apparent step height of a step between the Ag(100) surface and the KCl wetting layer.* ***a)*** *The apparent step height in dependency of the positive bias voltage. The corresponding STM images were taken with a tunneling current of 10 pA. The error bars correspond to the standard deviation of the measured step heights.* ***b)*** *STM image ($U_B = 1\,V$, $I_{tun} = 10\,pA$) of the corresponding step edge. The darker area on the left-hand side corresponds to the Ag substrate and the bright area on the right-hand side to the KCl layer. The black and red lines in the inset show two examples of two line profiles across the Ag-KCl step at bias voltages of $U_B = 2\,V$ and $U_B = 4\,V$, respectively.*

through the center of the KCl island and is replicated in its vertical structure (cf. side views in Fig. 6.1).

The growth mode of KCl on Ag(100) is strongly dependent on the sample temperature during the deposition. Within the scope of the present thesis, the sample temperature was systematically varied in order to achieve thin (2 – 3 ML) and closed KCl layers that are suitable for STM measurements. It was found that for sample temperatures of 400 K and below, KCl grows in a layer-by-layer (*Frank-van der Merve*) growth type, while at sample temperatures above that, the KCl layer dewets and forms islands that are several layers in height, leaving large areas of the Ag(100) surface uncovered (*Vollmer-Weber* growth type). The same observation was made with SPA-LEED experiments that were conducted within the scope of the bachelor's thesis of M. Mühlpointner [217]. An exception from the layer-by-layer growth of KCl on Ag(100) is the wetting layer. Although it was previously postulated by Müller *et al.* [38] that the wetting layer is only one monoatomic KCl layer in height, experiments that were conducted within the scope of the present thesis yielded strong evidence that the wetting layer is two ML in height, similar to the wetting layer of NaCl on Ag(100) [179] (see Appendix A.2).

Moreover, in the thesis by Mühlpointner [217] it was also observed that, for sample temperatures below 400 K during deposition, the KCl layers exhibit a significant rotational mosaicity. This mosaicity is stronger for lower sample temperatures, which indicates that it is a consequence of the reduced mobility of the KCl molecules[1] during the deposition. Furthermore, at lower temperatures (below 400 K) the nucleation on terraces plays an increasingly important role, which also leads to the formation of domains that are rotated away from the $\langle 10 \rangle$ orientations of the substrate. At higher sample temperatures, the nucleation of the KCl layers occurs predominately at the Ag steps, which causes the KCl layers to grow in good alignment with the underlying Ag substrate.

Lastly, another aspect that is of particular interest for the growth of QA (and other organic adsorbates) on KCl is the fact that the Ag step edges are replicated by the KCl layer (cf. side views in Fig. 6.1). This has very interesting ramifications because it leads to two different kinds of step edges in the KCl layer. On the one hand, there are the step edges in $\langle 11 \rangle$ direction that limit the KCl layer and, in particular, the quadratic islands in the topmost layer. These step edges consist of alternating K^+ and Cl^- ions and will thus be referred to as non-polar step edges in the following. On the other hand, the Ag step edges, which are usually oriented along the $\langle 10 \rangle$ orientations of the substrate and which are replicated by the KCl layer, consist of ions of the same charge and are thus polar step edges. The two different kinds of KCl step edges are illustrated in Figure 6.1. More in-depth information regarding the structure and growth of KCl on Ag(100) can be found in ref. [38], and in Appendix A.2, as well as in the doctoral thesis of A. Husseen [242].

[1] KCl is a salt, i.e., it consists of positively charged K^+- and negatively charged Cl^--ions. It is assumed that during the growth of KCl on Ag(100) the ions initially diffuse on the surface as K^+Cl^- ion pairs (see Appendix A.2). For the sake of simplicity the ion pairs will be referred to as KCl molecules, even though they are not covalently bonded and hence are no molecules in a chemical sense.

6.1.2 KCl layer thickness and bias-dependency of the apparent step heights

The exact determination of the KCl layer thickness by STM turns out to be rather difficult. The reason for this is that KCl is an insulator with a band gap of $8.69 \pm 0.07\,\mathrm{eV}$ [243, 244], which means that the tunneling current across the KCl layer is significantly smaller than on the bare metal substrate. This leads to apparent heights that are significantly smaller than the geometric height of the KCl layer when a metal-KCl step edge is measured. Furthermore, the apparent height of a monoatomic KCl layer decreases with its distance from the metal substrate due to the exponential decay of the tunneling current with distance (cf. eq. 2.1, p. 10). For example, within the STM experiments of the present thesis, an apparent height of the KCl wetting layer (which consists of two monoatomic KCl layers) between 310 and 350 pm was found. The height of the third KCl layer was only 140 pm, which is less than half of the height of the wetting layer.

Another interesting aspect of the apparent height of KCl layers is that it depends on the polarity of the bias voltage. For negative bias voltages, the apparent height of a Ag-KCl step edge was found to be constant (within about 10%) for voltages between $-0.5\,\mathrm{V}$ and $-5\,\mathrm{V}$ (not shown). In contrast, for positive bias voltages, a strong dependency of the apparent height on the value of the bias voltage was observed. This is illustrated in panel a) of Figure 6.2 and a corresponding STM image of the measured step edge is displayed in panel b). The graph in panel a) shows that the apparent height of the measured Ag-KCl step edge slightly increases between 1 and 3 V. Between 3 and 3.5 V, there is a steep increase, which roughly doubles the observed apparent height of the KCl layer. A similar observation was made by Guo *et al.* for layers of NaCl on Cu(100) [245] and by Sun *et al.* for layers of NaCl on Au(111) [246]. Guo *et al.* explained the sudden increase of the apparent height at distinct bias voltages with electrons tunneling from the STM tip into image potential states (IPS) of the NaCl. This is also consistent with peaks that they observed in dI/dV curves from scanning tunneling spectroscopy (STS) experiments. The increase in the apparent height that was observed within the scope of the present thesis (see Fig. 6.2a) can potentially be explained by the same phenomenon. However, in order to prove the existence and to determine the exact energetic positions of IPS for KCl on Ag(100), additional experiments (for example STS or photo emission experiments) would be required. To the best of the author's knowledge, detailed results concerning to image potential states of thin epitaxial KCl layers have not been reported, yet.

In the following, the structures of QA on KCl layers with different nominal thicknesses will be discussed. Obviously, the local thickness of the KCl layer may vary from its nominal thickness, which was determined from the QMS integrals, due to spatial variations. Nevertheless, within the scope of the present thesis, a systematic change in the growth behavior of QA in correlation with the nominal KCl film thickness was observed. Hence, it is assumed that the nominal thickness of the KCl films is a meaningful value for the interpretation of the STM results that will be discussed in Section 6.2, although small local variations of the KCl film thickness may apply.

6.2 Growth of quinacridone on KCl layers

In this section, the results concerning the growth of QA on KCl/Ag(100) will be summarized and supplemented with additional information. The corresponding publication can be found in Appendix A.2. To conclude the section, the results will be compared to those for the growth of QA on KCl/Cu(111) [240].

6.2.1 Non-wetting of quinacridone on KCl layers

The preparation of ordered monolayer domains of QA on epitaxial layers of KCl on Ag(100) is not easily achieved. The reason for this is that the adsorption energy (E_{ads}) of QA on KCl is rather low in comparison with other organic molecules such as PTCDA, which is known to form ordered structures on KCl and NaCl [38, 187]. This can be explained by an unfavorable geometric match between the partial charges of a QA molecule and the periodic charges of the ions in the KCl lattice, which leads to only a small electrostatic attraction between the QA molecule and the KCl surface. The E_{ads} of a single QA molecule on a semi-infinite KCl surface was calculated with DFT and amounts to $E_1 = 1.46\,\mathrm{eV}$.[2] Roughly 50 % of this energy is given by the dispersion energy (E_{disp}) between the QA molecules and the KCl. In comparison, all calculated E_{ads} for PTCDA on KCl and NaCl are larger than E_1 of QA by a factor of at least 1.7 [247, 248], although both molecules exhibit a similar footprint size. Hence, the larger E_{ads} of PTCDA on KCl is related to a better geometric fit between the local charges of the PTCDA molecule and the local charges of the KCl. Furthermore, the QA molecules are very mobile on the KCl surface and can overcome the *Ehrlich-Schwoebel* barrier for KCl-KCl, and KCl-Ag step edges. This is conceivable in view of the low E_{ads} because for organic molecules the correlation between E_{ads} and the *Ehrlich-Schwoebel* barrier was found to be roughly linear [249].

The high mobility and low E_{ads} of QA on KCl cause the QA molecules to diffuse from the KCl layers onto bare Ag surface patches, where the E_{ads} of QA is larger than on KCl. The diffusion also leads to a lateral compression of the formerly nucleated QA chains on the Ag(100) surface. This phenomenon was frequently observed for QA on KCl layers that did not cover the entire Ag surface. Corresponding STM images for a medium coverage of QA ($\theta_{\mathrm{QA}} = 0.5\,\mathrm{ML}$) on such a KCl layer are displayed in Figure 6.3. In panel a), an overview STM image is displayed featuring two KCl islands with an apparent height of roughly 500 pm (3 KCl layers) on the left-hand side. The dark area corresponds to the QA-covered Ag surface. No QA molecules are adsorbed on the KCl layer and the layer could be imaged with atomic resolution (see Figure S1 of the supporting information (SI) in Appendix A.2). Instead, the vast majority of QA molecules are adsorbed on the Ag surface as is shown in panel b) of Figure 6.3. The molecular arrangement there strongly resembles the molecular chains of the α-phase on Ag(100), but the chains exhibit more kinks and defects due to the lateral compression as mentioned above.

[2] The denotation E_n ($n = 1, 2, 3$) refers to the calculated E_{ads} per molecule of a QA mono-, di-, and timer on KCl, respectively. This includes the intermolecular interactions between neighboring molecules.

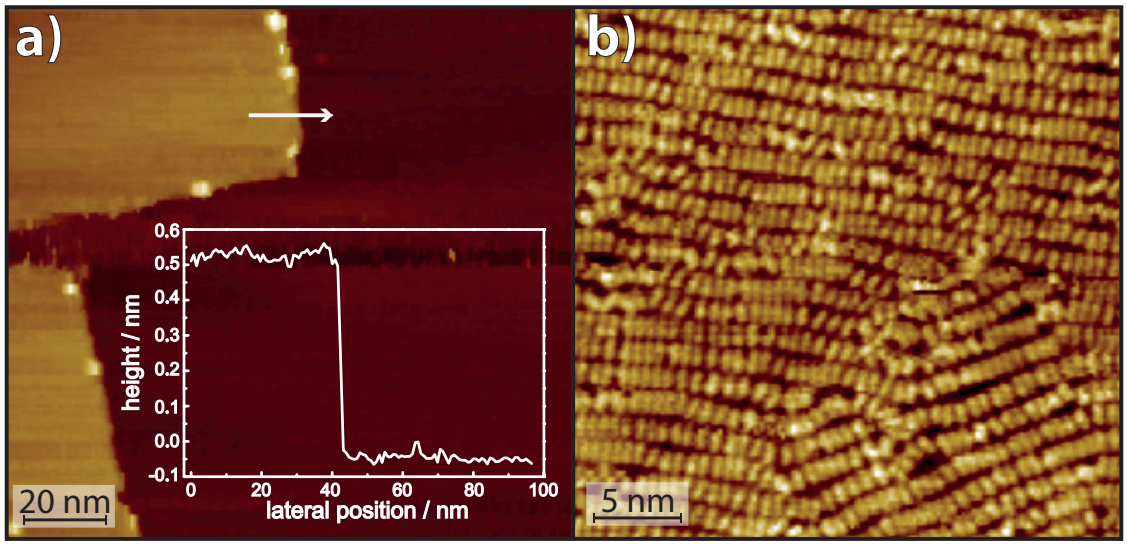

Figure 6.3: *QA ($\theta_{QA} = 0.5\,ML$) on a thick KCl layer ($\theta_{KCl} = 6\,ML$) that does not completely cover the Ag(100) surface.* ***a)*** *An overview STM image ($U_B = -1.5\,V$, $I_{tun} = 8\,pA$) that shows two KCl islands that are three ML thick on the left-hand side. The darker area on the right-hand side corresponds to the QA-covered Ag surface. A height profile across a KCl-Ag step edge is superimposed with the dark area of the image.* ***b)*** *A zoom-in ($U_B = -1.5\,V$, $I_{tun} = 8\,pA$) of the darker area showing an assembly of QA molecules that is very similar to the α-phase of QA on pure Ag(100), but which is significantly more disordered here.*

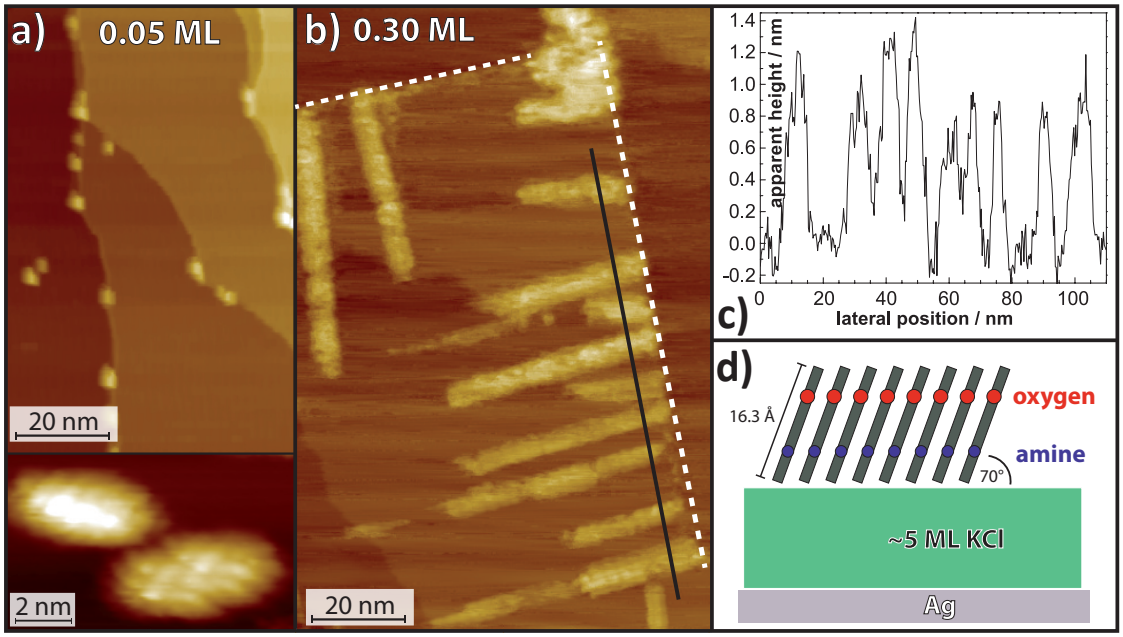

Figure 6.4: *Growth of QA on a thick KCl layer ($\theta_{KCl} = 5\,ML$), which completely covers the Ag(100) surface.* ***a)*** *Constant current STM image ($U_B = -1.5\,V$, $I_{tun} = 10\,pA$) of a small coverage ($\theta_{QA} = 0.05\,ML$) QA on the KCl layer. The step edges of the Ag(100) surface are replicated in the KCl layer and the QA clusters are visible as bright ellipsoid protrusions mostly at the step edges. The inset shows a zoom-in onto two of such clusters.* ***b)*** *Constant current STM image ($U_B = -1.5\,V$, $I_{tun} = 25\,pA$) of a medium coverage ($\theta_{QA} = 0.3\,ML$) QA on a KCl layer of similar coverage. The dashed white lines highlight KCl step edges.* ***c)*** *A height profile along the black line in panel b) crossing several QA aggregates.* ***d)*** *A schematic drawing of a candidate structure model for the observed structures. The model is based on a similar structure that was found for QA on SiO_2 [79].*

The above results show that it is essential to prevent the diffusion of the QA molecules from the KCl islands onto the Ag surface in order to prepare ordered QA structures on KCl. This could be done for example via deposition of QA at a low sample temperature in order to inhibit the diffusion of the QA molecules (see Section 6.2.3), or by deliberately preparing a KCl layer with many defects that serve as favorable nucleation sites for the QA structures as was done by R. Bretel within the scope of his PhD thesis [93]. In the present thesis, this diffusion was prevented by preparing closed KCl layers completely covering the Ag(100) surface so that there are no Ag patches to which the QA molecules can diffuse. On such closed layers, two cases need to be distinguished: structures of QA on thin (≤ 3 ML) KCl layers, which will be discussed in Section 6.2.2, and structures of QA on thick (≥ 4 ML) KCl layers, which will be discussed in the following.

On thick KCl layers (≥ 4 ML), the E_{ads} per molecule of small ensembles (including intermolecular interactions) of flat-lying QA molecules is smaller than the sublimation enthalpy (H_{sub}) of QA. The calculated values for E_{ads} per molecule of a QA dimer and trimer[3] on KCl are $E_2 = 1.79$ eV and $E_3 = 1.86$ eV (including the intermolecular interactions), respectively, and the values indicate that it does not significantly increase further for longer chains. The H_{sub} of QA has not been reported in literature but, within the scope of the present thesis, a H_{sub} for QA of 2.54 eV was calculated. This value of 2.54 eV is within 20% of the zero-order desorption energy of QA on SiO_2 (2.1 eV) found by Scherwitzl *et al.* [80] and the lattice energy of QA (2.1 – 2.3 eV) calculated by Panina *et al.* [53], which both should also be close to H_{sub}. Hence, the E_{ads} per molecule of a QA trimer (1.86 eV) and longer chains is only between 73 % and 90 % of the H_{sub} of QA. Consequently, QA prefers the formation of bulk-like 3D clusters over the formation of ordered 2D structures on KCl.

Corresponding STM images of QA structures on a closed KCl layer of 5 ML thickness are displayed in Figure 6.4. Panel a) shows an STM image of a very low coverage of QA ($\theta_{QA} = 0.05$ ML) on such a KCl layer. The QA is only visible as small bright protrusions that are attributed to small 3D clusters of QA. These clusters are predominantly located a Ag step edges that are replicated in the KCl layer. This shows that these step edges are favorable nucleation points for the growth of QA. The clusters have apparent heights of (5 ± 1) Å and have widths between 30 Å and 80 Å in both lateral dimensions. At larger QA coverages (e.g., $\theta_{QA} = 0.3$ ML, cf. Fig. 6.4b), long chain-like QA clusters form that have apparent heights between 10 Å and 15 Å, widths between 50 Å and 100 Å, and variable lengths. A one-dimensional height profile across several chain-like clusters revealing their profile is displayed in panel c). The width of the chain-like clusters exceeds both dimensions of a QA molecule. Consequently, the clusters consist of several parallel molecular rows, which also explains the observation that not all clusters exhibit the same width. Another observation is that most of these chain-like clusters have one of their ends located at a KCl step edge (cf. Fig. 6.4b). This supports the above assessment that KCl step edges are preferred nucleation points for the growth of QA. Furthermore, the nucleation at the KCl step edges also appears

[3]The words dimer and trimer are used here to describe a very small chain of QA that consists of only 2 or 3 molecules, respectively.

to have a strong influence on the azimuthal orientations of the chain-like clusters because the clusters are usually oriented at an angle of $(90 \pm 10)^\circ$ with respect to the corresponding KCl step edge (cf. Fig.6.4b).

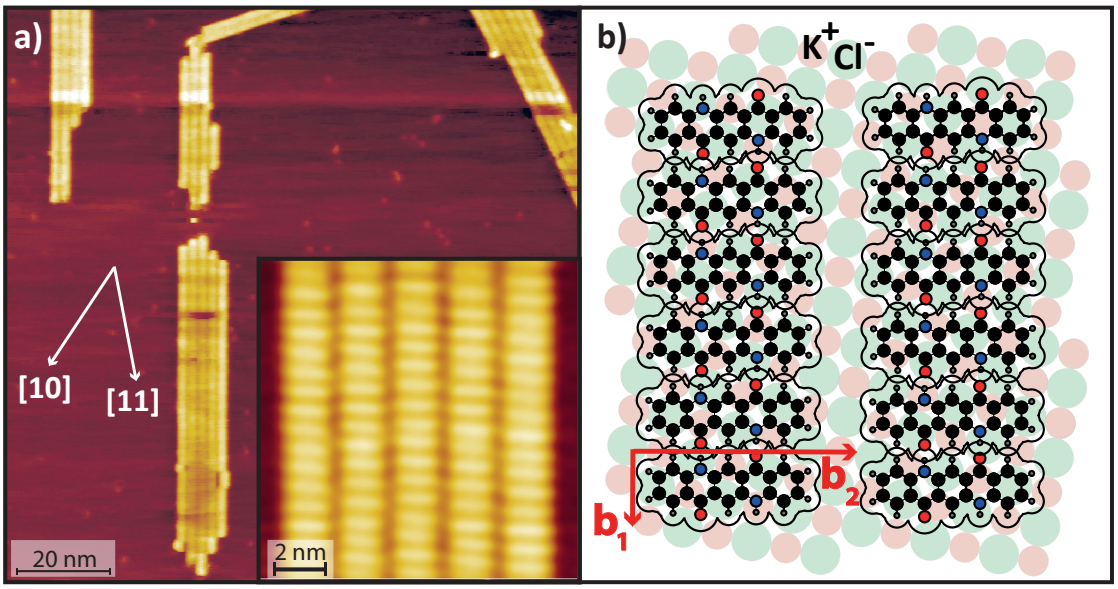

Figure 6.5: *QA on a thin KCl layer.* ***a)*** *STM image ($U_B = -3\,V$, $I_{tun} = 10\,pA$) of a very small coverage QA ($\theta_{QA} = 0.05$ ML) on a KCl layer with an average thickness of 2.5 ML. The image shows small domains of parallel QA chains. The inset ($U_B = -1.5\,V$, $I_{tun} = 10\,pA$) shows one domain consisting of five parallel chains with molecular resolution.* ***b)*** *A hardsphere model depicting the structure of the domains in panel a).*

The long chain-like clusters are explained by QA molecules standing upright on their short edge with the flat side of the molecules facing one another allowing intermolecular π-π interactions. This structure is very similar to a phase that was observed for QA on SiO_2 by grazing incidence X-ray diffraction [23, 79]. A corresponding structure model is displayed in panel d) of Figure 6.4. It shows that the molecules are tilted by 20° with respect to the surface normal. This tilt is not based on experimental evidence for QA on KCl/Ag(100), but is purely based on the QA structure found by Scherwitzl *et al.* [79] for QA on SiO_2. The smaller clusters that were observed for lower QA coverage cannot be explained by this model because their apparent height is significantly smaller (by 33 – 50 %) than the height of the chain-like clusters. Hence, the small clusters are explained with a very similar structure in which the molecules are standing upright on their long edge instead of their short edge. A potential reason for this difference between the two structures may be the following. At low QA coverages ($\theta_{QA} = 0.05$ ML), the most important interaction is the one between the molecules and the substrate. Hence, the molecules adsorb with their long edge on the KCl, i.e., the functional groups of the molecules face the KCl and the vacuum side. This configuration allows the maximization of the Coulomb interactions between the partial charges of the functional groups and the ions of the KCl lattice.[4] With increasing coverage, the relative importance of the interactions between the molecules and the KCl decreases because it can be

[4]Note that the adsorption in a flat-lying geometry is likely less favorable due to an unfavorable geometric match as was described above. This may lead to an overall Coulomb interaction that is partially repulsive.

overcompensated by intermolecular interactions, which play a more important role at a larger coverage ($\theta_{QA} = 0.3$ ML). Thus, the molecules stand on their short edge because this enables the formation of intermolecular H-bonds in one lateral dimension, i.e., orthogonal to the long axis of the chain-like clusters, while along the long axes of the clusters, the molecules interact with one another through π-π interactions.

6.2.2 Growth of quinacridone chains and domains on thin closed KCl layers

The previous section has shown that on thick KCl layers (> 4 ML) the E_{ads} of QA on KCl is too small for the formation of 2D ordered monolayers (cf. Fig. 6.4). In contrast, on thin KCl layers (2 – 3 ML), the E_{ads} of QA is increased because, there, the *van der Waals* interactions between the QA molecules and the metal substrate contribute to E_{ads}. This is not the case (or only to a negligible degree) on thick KCl layers, where the distance between the QA molecules and the Ag substrate is too large. A theoretical work by Robledo *et al.* considering benzene on 1, 2, and 3 layers of NaCl on Cu(111) has shown that the E_{ads} of benzene on NaCl increases with decreasing NaCl layer thickness and that the *van der Waals* dispersion forces between the benzene molecules and the Cu(111) substrate contribute to E_{ads} by 0.3 – 0.5 eV [195] for NaCl layer thickness of up to 3 ML. This contribution is expected to be even larger for QA because benzene only exhibits roughly 20 % of the footprint size of QA. With the contribution of these *van der Waals* dispersion interactions, the E_{ads} of QA is larger than its H_{sub} on thin KCl layers. Thus, the growth of structures of flat-lying QA molecules, which are connected via intermolecular H-bonds, is supported there.

An STM image and a corresponding structure model of a small coverage of QA ($\theta_{QA} = 0.05$ ML) on a thin ($\theta_{KCl} = 2.5$ ML) are displayed in Figure 6.5. The STM image in panel a) shows five small domains that consist of 2 – 5 parallel QA chains each. The inset shows an STM image with molecular resolution that reveals that these chains consist of parallel molecules that are connected via intermolecular H-bonds, similar to the chains in the α-phase on Ag(100). The intermolecular distance of $b_1 = (6.6 \pm 0.2)$ Å within the chains is identical to that of the molecules in the chains of the α-phase on Ag(100). The distance between neighboring chains of $b_2 = (20.0 \pm 0.5)$ Å is larger by 20% than the distance between the closely packed chains in a full ML of the α-phase on Ag(100). A corresponding structure model is depicted in panel b) of Figure 6.5. The exact structure is discussed in more detail and supported by DFT calculations in Appendix A.2.

6.2.3 Adsorption of quinacridone on KCl at low sample temperatures

One possible way to inhibit or prevent the diffusion of organic molecules on surfaces is to reduce the sample temperature. This section reports about the possibility of preventing the unwanted diffusion of the QA molecules from the KCl island to the bare Ag surface by depositing the QA molecules at low sample temperatures of about 150 K. The experimental setup of the STM chamber (cf. Chapter 4.1.1) did not allow the in-situ deposition of QA molecules onto the sample, while it is placed in the STM table with the helium cooling. Thus, in order to deposit the QA onto the cold sample, it was pre-cooled on the STM table to about 80 K and then transferred to the preparation chamber. There, the QA was deposited onto the sample and it was transferred back. During this

process, the sample temperature increased and was usually between 120 K and 150 K when the sample was back on the cold STM table.

Figure 6.6 shows STM images of 0.5 ML of QA on a KCl layer with an average thickness of 3 ML that was measured at a sample temperature of 120 K after the QA was deposited at 150 K as described above. The image in panel a) shows a KCl island on the right-hand side and a small stripe of the Ag(100) surface on the left-hand side. The right-hand side of the KCl island has an additional monoatomic KCl layer on top. The Ag-KCl step edge has an apparent height of 600 pm. Based on this apparent height, the KCl island is estimated to be 4 – 5 ML in height. Both the KCl layer and the Ag(100) surface are covered with QA molecules. On the Ag(100) surface the molecules are assembled into disordered 2D aggregates. These structures are very similar to the ones that were already discussed in Chapter 5.1.4 and are thus not further covered in this chapter.

A zoom-in onto the QA structures on the KCl layer is displayed in panel b) of Figure 6.6. At first glance, this structure is very disordered. It consists of ellipsoid structures that appear to be in two different layers (bright and dark ellipses) and which are not arranged in any regular or periodic manner and vary in size. The ellipsoids have lengths between 11 Å and 17 Å, widths between 4 Å and 8 Å, and apparent heights of up to 3 Å. The observed sizes are very similar to the width and length of a hard-sphere model of QA (8 Å and 16 Å, respectively), which indicates that each ellipsoid corresponds to a single QA molecule. However, it can not be excluded that some of the larger ellipsoids correspond to small clusters of 2 – 3 QA molecules. The different apparent sizes of the ellipsoids suggest that the molecules exhibit a wide range of different adsorption configurations. In particular, the apparent heights of up to 3 Å (the apparent height of flat-lying QA molecules on a think KCl layer on the Ag(100) surface is only about 1.2 Å) are indicative of molecules are tilted with respect to the KCl surface. Overall, this structure consists of a disordered monolayer of QA on the KCl layer with a partial second disordered QA layer on top. However, the exact geometries of the adsorption sites cannot be determined from the present data. Upon warming up the sample to RT the molecules regain their mobility on the KCl surface. This leads to the two processes that are discussed above. The molecules diffuse from the KCl layer to the Ag(100) and form chains or they form large clusters on the KCl layer as described in Section 6.2.1.

The above results (cf. Fig. 6.6) show that the mobility of the QA molecules on KCl is drastically reduced at lower sample temperatures. It would be interesting to utilize this reduced mobility of QA molecules on KCl at low sample temperatures to image individual QA molecules or very small assemblies of QA molecules on a thick KCl layer. However, within the scope of the present thesis, this could not be observed. When smaller coverages of QA were deposited on a thick KCl layer on Ag(100) at reduced temperatures, only the existence of QA clusters was observed, similar to the observations described in Section 6.2.1. In contrast to the above observations, this is an indication, that at low sample temperatures (150 K) and low coverages, the QA molecules are still sufficiently mobile to form 3D clusters on the surface. This contradiction between the two data sets for different QA coverages can be explained as follows. The layer with the higher QA coverage (cf. Fig. 6.6) was deposited in a short time span of about 60 seconds. The high molecule influx on the surface resulted in a disordered first layer that is stabilized by a kinetic barrier in

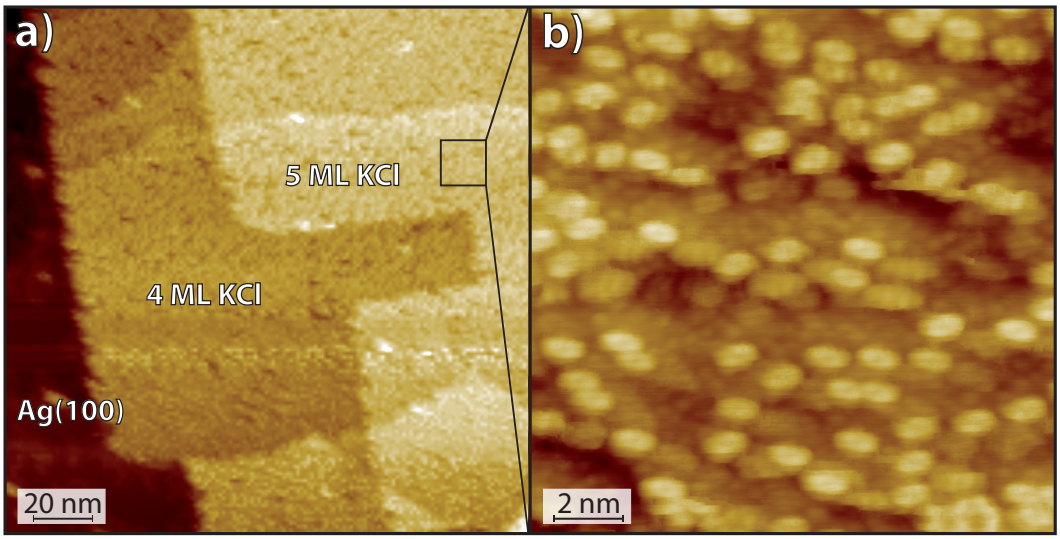

Figure 6.6: *STM images ($U_B = -1.5\,V$, $I_{tun} = 13\,pA$) of QA on a KCl layer with an average thickness of 3 ML. The QA was deposited at a sample temperature of 150 K and the STM images were recorded at a sample temperature of 120 K.* ***a)*** *Overview image showing a KCl island that is 4 ML high with a fifth layer on top on the right-hand side. A small stripe of the Ag(100) surface can be seen on the left-hand side. It can be seen that the KCl island is covered with QA molecules.* ***b)*** *A zoom-in onto the KCl layer showing the arrangement of individual QA molecules. The ellipsoid protrusions correspond to individual QA molecules of different adsorption configurations. For more information, see text.*

the form of intermolecular interactions. The molecules in the second layer are stabilized by the interactions between them and the molecules in the first layer. In contrast, at a lower coverage such a kinetic barrier does not exist, and hence the molecules form the thermodynamic most favorable structures (3D clusters). In summary, the results of this section have shown that the mobility of the QA molecules on Ag(100) is significantly reduced at lower temperatures with respect to the mobility at RT. However, the temperatures that could be realized during the deposition with the experimental setup, which was used for these experiments, were not sufficiently low in order to observe individual single molecules on the surface.

6.2.4 Comparison to quinacridone on KCl on Cu(111)

To close the chapter about QA on KCl layers on Ag(100), the above results will be compared to the results for QA on KCl layers on Cu(111) [240]. On both substrates, it was found that QA spontaneously forms 1D chains of molecules that are connected via H-bonds with intermolecular distances that are identical within the margins of error.

However, some differences in the adsorption geometries of the QA chains with respect to the underlying KCl can be found. In the present work, four symmetry equivalent azimuthal chain orientations were found that are rotated by $(12 \pm 3)^\circ$ with respect to the $\langle 11 \rangle$ direction of the KCl layer. In contrast, Bretel *et al.* found a wider range of azimuthal chain orientations. The QA chains on KCl/Cu(111) are favorably oriented along the $\langle 11 \rangle$ direction of the KCl lattice, however, an azimuthal spread of about $\pm 15^\circ$ was observed, including angles of $+2.5^\circ$, -7.5°, and $+9^\circ$

with respect to the KCl ⟨11⟩ direction [240] (For the ⟨11⟩ direction, see Fig. 6.1). Furthermore, in the QA chains on KCl/Ag(100), the chain orientation is always perpendicular to the long axis of the molecules, while in the chains on KCl/Cu(111) the long axes of the molecules are rotated away from the direction that is perpendicular to the chain direction by up to $\pm 5^\circ$. The adsorption geometries of QA chains on KCl/Ag(100) that were observed in the present thesis are consistent with DFT calculations for QA on a KCl bulk surface (see Appendix A.2). This shows that the azimuthal chain orientations on KCl/Ag(100) are given by the interactions between the QA molecules and the KCl. Hence, it is likely that the deviations in the adsorption geometry of the chains on KCl/Cu(111) from those of the chains on KCl/Ag(100) are caused by the underlying Cu(111) substrate. However, Bretel *et al.* also concluded that the azimuthal orientations of the QA chains on KCl/Cu(111) are determined by the direction interactions between the QA molecules and the KCl layer [240]. They deduced this from from a comparison of the azimuthal QA chain orientations on two different KCl islands with different azimuthal orientations with respect to the Cu(111) substrate. A possible explanation for this is that the KCl layer on Cu(111) exhibits some kind of corrugation or stress due to the mismatch between the symmetries of the KCl layer and the Cu(111) surface (4-fold vs. 6-fold symmetry, respectively). This would lead to a wider range of different adsorption sites on KCl/Cu(111), and thus to different adsorption configurations for QA on KCl/Cu(111), which would explain the different azimuthal orientations.

Another difference between the chains on KCl/Ag(100) and those on KCl/Cu(111) is that the chains on KCl/Cu(111) are very short in comparison. Bretel *et al.* did not find any chains that consist of more than 20 molecules. In contrast, the QA chains on KCl/Ag(100) reach lengths of up to 80 nm, which corresponds to about 115 QA molecules. This can likely be attributed to the fact that Bretel *et al.* prepared the QA chains at low temperatures (between 78 K and 300 K), which reduces the mobility of the QA molecules. In contrast, in the present thesis, the chains were prepared at RT. Moreover, Bretel *et al.* also prepared the KCl layer at low temperatures (between 78 K and 300 K), which leads to a higher degree of defects. They reported two kinds of defects in the KCl layer. The first kind are point defects on the KCl terraces, and the second kind is in the form of rough step edges of the small KCl islands in the top layer. Both kinds of defects can serve as favorable nucleation points for the QA molecules, and thus lead to a higher nucleation density and thus shorter chains.

6.3 Growth of quinacridone on hBN

The structure of the hBN layer on Cu(111) has been investigated very intensively throughout the last decade [39, 40, 250]. Hence, it will not be discussed in the present work. A good overview of this topic is given in the PhD thesis of C. Brülke [219]. Furthermore, the formation of self-assembled structures of organic molecules on hBN on Cu(111) has also been investigated [251–253]. In this chapter, the self-assembled structures of QA on hBN on Cu(111) will be discussed.

Before the QA molecules were deposited on an hBN layer, the quality of the hBN layer was checked by LEED (not shown) and STM. The diffraction pattern exhibited the same features that

were observed by Brülke *et al.* with SPA-LEED [40], however many of its intricacies could not be resolved with the MCP-LEED. A corresponding STM image of an hBN layer is shown in panel a) of Figure 6.7. It shows that the complete Cu(111) surface is covered by the hBN layer, which consists of different hBN domains that are separated by small cracks. These cracks are 200 pm in apparent depth, i.e., the apparent height of the hBN layer is 200 pm, which is lower than the geometric height of the layer (320 pm) due to the insulating character of the hBN. The cracks are often decorated by small bright protrusions that can likely be explained by small clusters of BN. It was also possible to observe different *Moiré* patterns with different lattice constants (shown in the inset of Fig. 6.7a) that are caused by the mismatch between the hBN and the Cu(111) lattices in combination with the azimuthal spread of the hBN layer as was reported by Joshi *et al.* [39].

First, the QA structures on hBN for a low QA coverage of $\theta_{QA} = 0.2$ ML will be discussed. A corresponding STM image of QA on a single layer hBN on Cu(111) is displayed in panel b) and an image with molecular resolution is shown in panel c) of Figure 6.7. They show several QA chains with six distinct orientations with respect to the Cu(111) substrate that will be discussed in more detail below (for a illustration of all azimuthal chain orientations with respect to the substrate, see page 215). The chains are very straight and without defects, which shows that, similar to the chains observed on metal surfaces, these chains are homochiral. Moreover, the fact that the chains exhibit significantly less kinks and defects than those on Cu(111) indicates that the QA molecules are more mobile on hBN than on Cu(111). This is an indication that the corrugation of the surface potential on hBN is not as strong as on Cu(111). Furthermore, it is likely that also the interfacial interactions and the bonds between the QA molecules and the hBN are weaker than on Cu(111). This is because a chemical bonding between the QA molecules and the hBN layer can not be expected and the adsorption of QA is likely only of a physisorptive nature, similar to the one of PTCDA on hBN [219]. The intermolecular distance within the chains is (6.8 ± 0.2) Å and is thus identical to the intermolecular distance within QA chains on Cu(111). Similar to QA on KCl/Ag(100), the chains are assembled into domains of parallel chains, which shows that the charge density waves that are induced on Ag(100) and Cu(111) by the QA chains and that are responsible for the long-range repulsive interactions between the chains are not present here. A structure model for the domains of QA on hBN is shown in panel d). It is important to note that the relative azimuthal angle between the QA chains and the hBN layer does vary due to the large azimuthal spread of hBN on Cu(111) [40].

After the deposition of QA onto the hBN layer, the cracks between the different domains of the hBN layer only have an apparent depth of roughly 50 pm and, in some cases, some larger clusters have formed along the cracks that even exceed the height of the hBN layer by up to 150 pm (see Fig. 6.8, below). This shows that a large amount of QA molecules adsorbs at such cracks and defects, indicating that an adsorption on Cu(111) is preferred over the adsorption on hBN. This supports the above assessment that the bond between QA and Cu is stronger than the bonding between QA and hBN. Hence, it is likely that only *after* all cracks and patches of the bare Cu(111) surface have been covered an by QA molecules, the observed QA chains on hBN are formed.

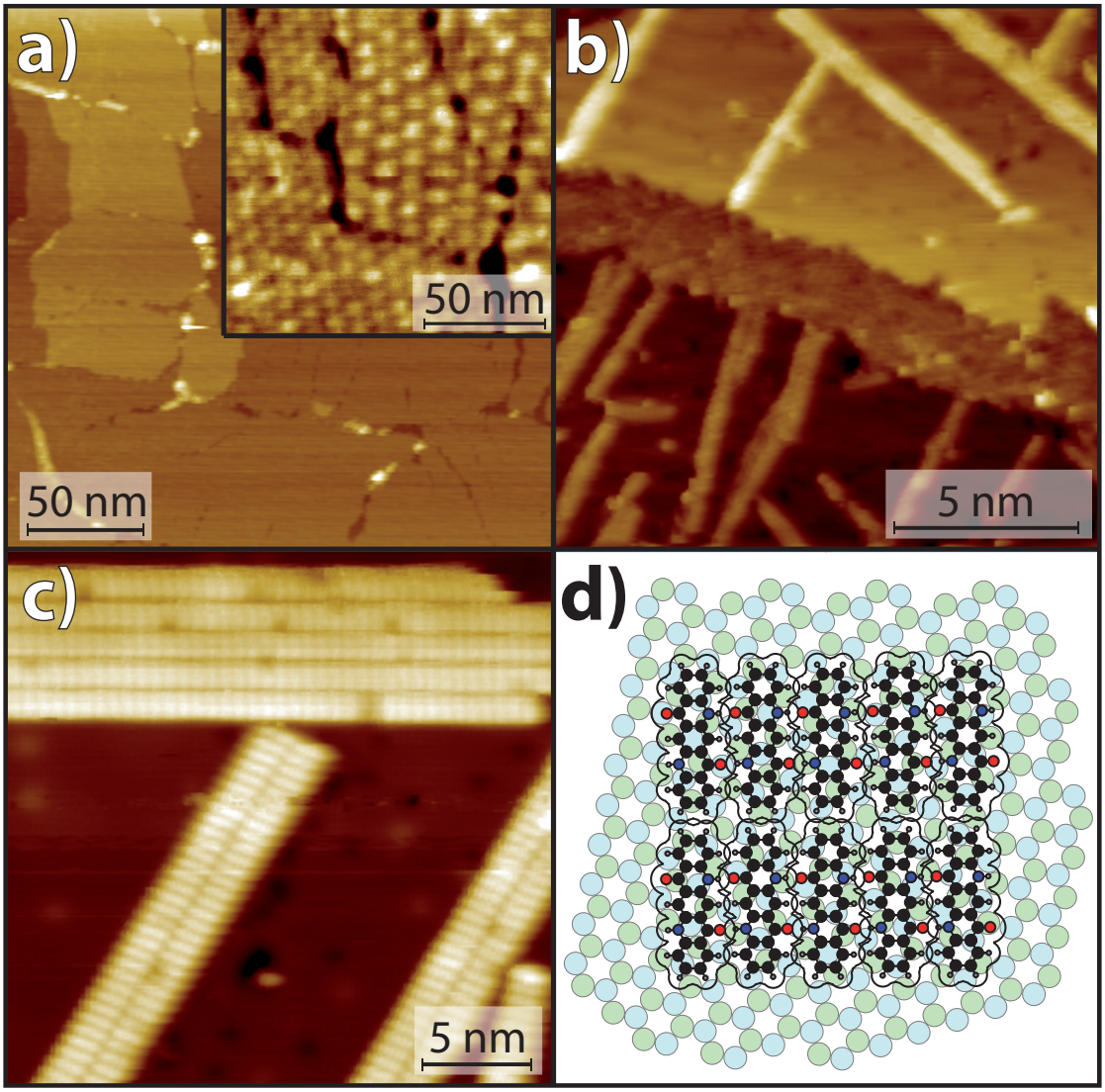

Figure 6.7: *QA on a single layer hBN on Cu(111) at a low QA coverage ($\theta_{QA} = 0.2$ ML).* ***a)*** *STM image ($U_B = -1.5$ V, $I_{tun} = 25$ pA) of the hBN layer on Cu(111) showing several different domains. The inset shows a zoom-in that shows several different domains of hBN exhibiting different kinds of Moiré patterns that can be explained by slightly different azimuthal orientations of the domains [39].* ***b)*** *STM image ($U_B = -5$ V, $I_{tun} = 15$ pA) showing several QA chains on the hBN layer.* ***c)*** *STM image ($U_B = -1.5$ V, $I_{tun} = 25$ pA) of QA chains on hBN with molecular resolution.* ***d)*** *Structure model of QA chains on hBN. This model refers to the case in which the underlying hBN domain is perfectly aligned with the Cu(111) substrate. The relative orientations of the QA chains with respect to the hBN layer may vary because the hBN layer exhibits an azimuthal mosaicity with respect to the Cu(111) substrate, but the azimuthal orientations of the QA chains on hBN/Cu(111) are identical to those of the QA chains on pure Cu(111).*

Interestingly, the six azimuthal chain orientations are identical to those on Cu(111) within the margins of error. The same phenomenon was observed for QA chains on thin layers (2 – 3 ML) KCl on Ag(100) (see Section 6.2 and Appendix A.2). There, the fact that the azimuthal orientations of QA chains on KCl/Ag(100) are identical to those on pure Ag(100) was explained with the direct interactions between the QA molecules and the KCl, which was investigated by DFT calculations (cf. Appendix A.2). However, on hBN/Cu(111) it is not plausible that the azimuthal orientations of the QA chains are only given by the interactions between the QA molecules and the hBN. This holds true because the hBN layer itself exhibits a large azimuthal spread with respect to the underlying Cu(111) substrate [40]. Thus, if the azimuthal orientations were determined by the underlying hBN layer, this would lead to a wide range of different azimuthal orientations of the QA chains, which was not observed. This means that the azimuthal orientations of the QA chains on hBN must be determined by the underlying Cu(111) substrate in some way.

A plausible explanation for this phenomenon may be similar to the one C. Brülke gave for results found for PTCDA on hBN/Cu(111) with SPA-LEED [219]. In that case, the structure of PTCDA exhibits a large degree of azimuthal disorder on a completely closed hBN layer of good quality, however, on a hBN layer of bad quality with many defects and bare Cu patches the structure of PTCDA is very similar to the one of the β-phase of PTCDA on Cu(111). This means that, on bad-quality hBN layers, the interfacial interactions between the PTCDA and the substrate involve the Cu(111) substrate, which is not (or to a significantly lower extent) the case for a hBN layer of good quality. Thus, C. Brülke concluded that, on bad-quality hBN layers, the growth of PTCDA begins at bare Cu patches and continues onto the hBN layer with the same distinct azimuthal orientations, which is not possible on closed hBN layers of good quality. A similar mechanism may explain the six distinct chain orientations of QA on hBN/Cu(111), since, as mentioned above, many cracks and small patches of bare Cu were observed in the hBN layers that were prepared within the scope of the present thesis.

Indeed, the STM images of QA on hBN on Cu(111) show that very often one end of the QA chains lies at cracks or defects in the hBN layer, which can be seen in panel a) of Figure 6.8. Image (i) and (ii) show domains of QA chains that are located at a crack in the hBN layer and a QA cluster that has formed at a crack, respectively. In addition, image (iii) shows an assembly of QA molecules at a small patch of bare Cu with molecular resolution in the lower half of the image. It can be seen that this small patch of bare Cu is completely covered by QA molecules forming small chains. The molecules in the chains exhibit the same azimuthal orientations as the ones that were observed in chains on the hBN layer. Furthermore, panel b) of Figure 6.8 shows individual QA molecules at small cracks and holes in the hBN layer that also exhibit the same six distinct azimuthal orientations. These molecules may serve as starting points for the growth of the QA chains on the hBN layer. Overall, these images indicate that the growth of the QA chains starts a such defects in the hBN layer, however, the exact growth mechanism for this cannot be deduced from the STM images. Two candidate mechanisms will be discussed in the following.

A first possible candidate mechanism concerns the case in which the chain growth starts on bare Cu patches that have dimensions of a few nanometers. In this case, the QA molecules can form

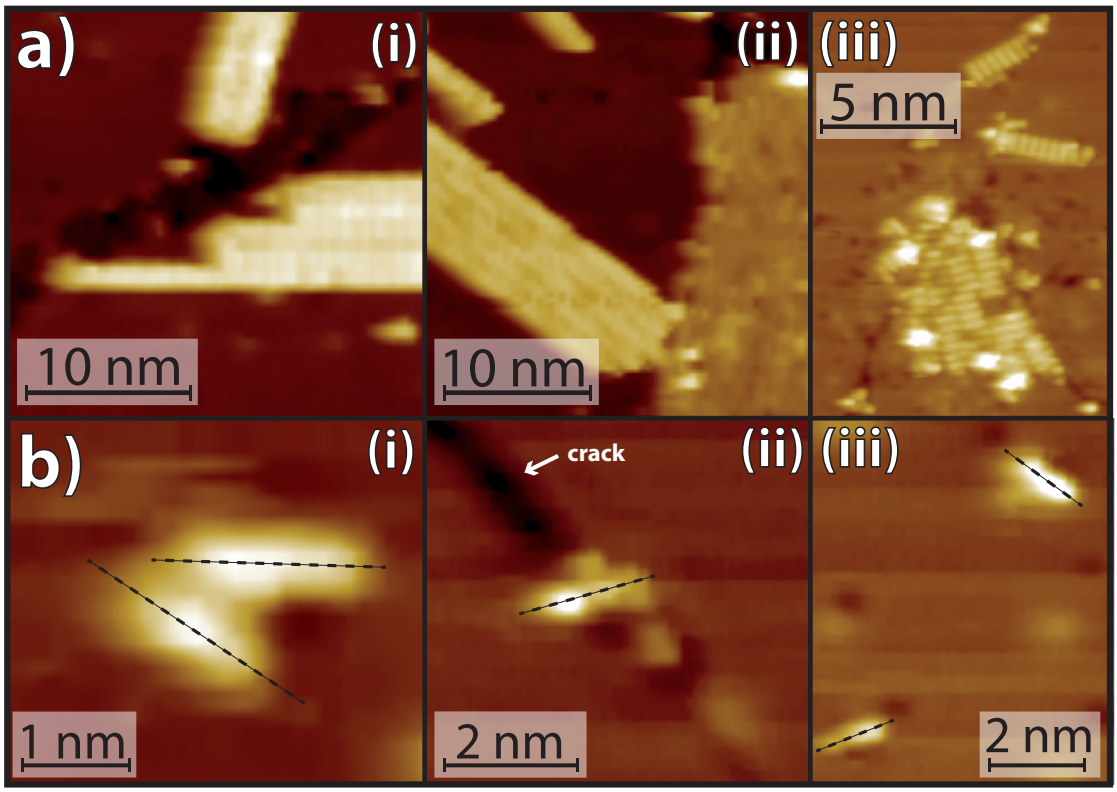

Figure 6.8: *STM images ($U_B = 1.5\,V$, $I_{tun} = 25\,pA$) of a low coverage QA ($\theta_{QA} = 0.2\,ML$) that was deposited at RT on an hBN layer on Cu(111).* ***a)*** *Images (i) and (ii) show cases where domains of QA chains begin at a crack in the hBN layer and at a QA cluster at a crack in the hBN layer, respectively. Image (iii) shows a hole in the hBN layer. The patch of bare Cu is covered with small chains of QA.* ***b)*** *Images (i)–(iii) show cases of individual molecules at cracks or small holes in the hBN layer. These molecules exhibit the same azimuthal orientations as the chains on the hBN layer and may serve as starting points for the chain growth. The long axes of the single molecules are indicated by the dashed black lines.*

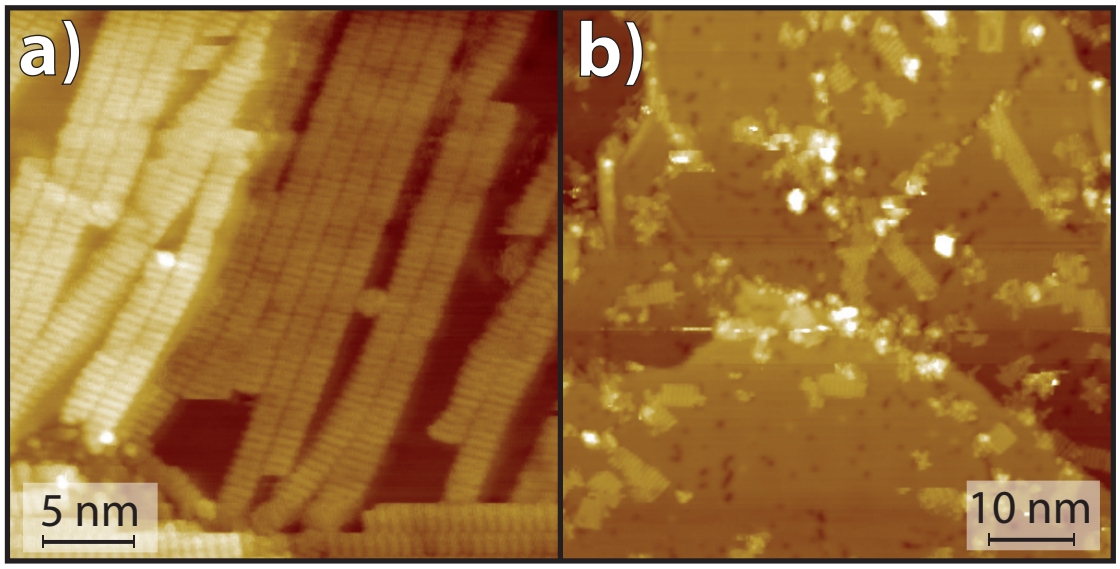

Figure 6.9: *QA on a single layer hBN on Cu(111) at a high QA coverage ($\theta_{QA} = 0.8\,ML$).* ***a)*** *STM image ($U_B = -1.5\,V$, $I_{tun} = 5\,pA$) of QA chains on hBN after the deposition of QA onto hBN at a sample temperature of 300 K.* ***b)*** *STM image ($U_B = -1.5\,V$, $I_{tun} = 5\,pA$) of the same QA layer as in panel a) after annealing at 500 K for 30 minutes. It can be seen that there are significantly less QA chains on the surface. Instead many QA clusters can be observed.*

small chains on the Cu(111) and these chains can grow across the Cu-hBN step edge and onto the hBN layer. It will be shown in Chapter 7.1, that the QA chains are capable of growing across Ag step edges without a break. Hence, it is not unplausible that the QA chains are also capable of growing across a Cu/hBN step edge. A second candidate mechanism concerns the case in which the growth of QA chains starts at very small holes or very narrow cracks in the hBN layer that are smaller in size than a single QA molecule as is shown in panel b) of Figure 6.8. These may be filled by single molecules that are partly tilted vertically towards the Cu(111) substrate and are thus partially adsorbed on the hBN layer and partially on the Cu(111) surface. Panel b) of Figure 6.8 shows two examples of such molecules. The molecule in image (ii), and the molecule in the lower left corner of image (iii) are darker on one end, i.e., one end of the molecule has an apparent height that is roughly 40 pm lower than the apparent height of the other end of the molecule, which indicates that the molecules are tilted with respect to the surface. Overall, these mechanisms can explain the observed growth of QA chains on hBN with 6 distinct orientations. Although, there are also many chains on terraces that do not have such a visible crack or defect near them. However, these could be explained by the fact that very small holes that serve as nucleation points are often barely visible when occupied by a molecule.

An alternative explanation for the azimuthal orientations could be that the Cu(111) substrate interacts across the hBN layer with the QA molecules and determines the azimuthal orientations of the chains. However, it seems very unlikely that long-range dispersion interactions across an insulating layer can exert influence on the azimuthal growth direction of the chains on the hBN layer. For the QA chains on metal surfaces, the favored azimuthal orientations are determined by the direct chemisorptive bonding between the QA molecules and the metal atoms. Furthermore, it was found that for QA chains on KCl/Cu(111) [240] and on KCl/Ag(100), the azimuthal chain orientations are given by the direct interactions between the QA molecules and the ions of the KCl layer, and not by dispersion interactions with the metal substrate. Hence, considering the above arguments and the results by C. Brülke regarding the structures of PTCDA on hBN on Cu(111), this explanation seems unlikely.

Now, the structures of QA on hBN/Cu(111) at a higher coverage of $\theta_{QA} = 0.8$ ML will be discussed. A corresponding STM image is shown in Figure 6.9. Panel a) shows domains of QA chains that are identical to those that were observed at a lower coverage (see above). An important difference is that, here, the chains are slightly bent and the azimuthal orientations of the chains are less strictly defined. The majority of the chains still adapt the same azimuthal orientations as those on the Cu(111) surface with an azimuthal spread of roughly $\pm 10^\circ$. The larger azimuthal disorder at a higher QA coverage can be explained by two reasons. The first is due to the fact that the surface is more crowded with QA chains. This leads to significant steric interactions between the chains, which may cause chains to exhibit slight curves or different orientations in order to avoid other chains. The second reason is that there is only a limited amount of defects, cracks, and bare Cu patches in the hBN layer that may serve as nucleation points for the chains (discussed above). When all of these nucleation points are already covered by QA molecules, additional QA chains will nucleate on defect-free hBN terraces free from the directional influence of the Cu substrate.

This may lead to chains of different orientations and thus to a larger degree of azimuthal disorder. Furthermore, it cannot be excluded that the quality of the hBN layer was of higher quality than to one on which QA at lower coverage was investigated. A higher quality hBN layer would likely also lead to a larger degree of azimuthal disorder [219].

Lastly, an interesting question is whether it is possible to prepare other QA structures on an hBN layer by annealing, similar to those that were already observed on metal surfaces. A corresponding STM image after annealing at 500 K for 30 minutes is displayed in panel b) of Figure 6.9. It can be seen that there are significantly less QA chains present on the hBN layer after annealing. At the same time, the amount of clusters and disordered structures on the hBN has drastically increased. This shows that the annealing led to a dewetting of the QA chains and the formation of QA clusters. This is not surprising because the interactions between QA molecules and hBN are weaker than those between QA molecules and Ag or Cu surfaces. A common characteristic of all heterochiral QA structures that were observed on metal surfaces after annealing is that they exhibit fewer H-bonds per molecule, but this loss in energy is overcompensated by stronger interactions with the underlying substrate. Hence, due to the weak interactions between QA and hBN, such phases are not stable on the hBN layer and instead, the formation of clusters is preferred.

6.4 Conclusions

In this chapter, the lateral structures of QA on thin layers of wide band gap materials, in particular on KCl/Ag(100) and hBN/Cu(111), were reported. It was deduced that the adsorption energy of QA on KCl is significantly smaller than the one of QA on Ag(100). This leads to non-wetting and the formation of QA clusters on thick (> 3 ML) KCl layers. However, on thin KCl layers (2 – 3 ML), the QA *van der Waals* dispersion energy between the QA molecules and the Ag substrate across the KCl layer contributes to the adsorption energy and thus enables the formation of molecular chains that consist of flat-lying QA molecules that are connected through intermolecular hydrogen bonds. Despite the low adsorption energy of QA on KCl, the azimuthal orientations of the QA chains are determined by the direct interactions between the QA molecules and the ions of the KCl layer.

On hBN/Cu(111), QA forms the same kind of QA chains that were observed on Cu(111) with the same six distinct azimuthal orientations, even though the hBN layer exhibits an azimuthal spread on Cu(111). This is explained by bare patches of the Cu substrate at which the growth of the QA chains starts and continues onto the hBN layer with the same azimuthal orientations. Annealing the QA layer on hBN/Cu(111) does not lead to a phase transition, but only a dewetting of the QA on the formation of QA clusters. This is explained by a weaker adsorption energy of QA on hBN than on bare Cu(111).

7 Quinacridone on a vicinal Ag(100) surface

Some results of the following chapter have been published in Beilstein J. Nanotechnol. ***2024****, 15, 556-568 (cf. Appendix A.3). The acquisition and evaluation of the data, and the writing of the manuscript were done by the author of the present thesis.*

Vicinal surfaces are very appealing for the growth of 1D structures [254]. The adsorption of organic molecules at step edges is often more favored than the adsorption on terraces because the additional interactions between the molecules and the atoms of the step edge contribute to E_{ads}. This additional contribution to E_{ads} at steps may also potentially help to stabilize organic structures on surfaces where they otherwise would form 3D clusters, such as 1D chains of QA on layers of KCl, which is one of the aspects that will be investigated in this chapter. Furthermore, the unidirectional step edges also break the rotational symmetry of the substrate further and add an anisotropic array, which may favor the growth of structures with distinct azimuthal orientations.

In this chapter, the growth of QA on epitaxial layers of KCl on the vicinal Ag(35 1 1) surface will be discussed. First, in section 7.1, the vicinal Ag(35 1 1) surface is introduced, and the observed surface (in particular its terrace width distribution) will be compared to that of the ideal surface. Afterwards, the growth of QA on the bare Ag(35 1 1) surface will be presented. Here, especially the influence of the Ag steps on the growth will be considered in detail. The growth of KCl on Ag(35 1 1) will be discussed in Section 7.2, and the differences to the growth of KCl on the Ag(100) surface will be highlighted. Finally, the growth of QA on a KCl layer on Ag(35 1 1) will be discussed in Section 7.3, and the growth of QA will be compared to its growth on KCl/Ag(100) and on KCl/Cu(111) [93, 240].

7.1 Structures of quinacridone on the Ag(35 1 1) surface

In this section, the growth of QA on the bare Ag(35 1 1) surface after deposition at different sample temperatures will be discussed. The results of this section can be found in the corresponding publication in Appendix A.3. The results will be summarized and supplemented with additional information.

7.1.1 The Ag(35 1 1) surface

The Ag(35 1 1) surface is a vicinal Ag(100) surface, where the direction of the unidirectional step edges is oriented along the [10] direction of the substrate. A model of the ideal surface is illustrated in panel a) of Figure 7.1, which shows that the ideal surface has a terrace width of 17.5 atom rows, which corresponds to a terrace width of 50.5 Å. The reasons why this surface was chosen for the

experiments will be explained in the following. The goal is the stabilization of the growth of short 1D chains of QA on several layers of KCl at the periodic Ag steps that are replicated in the KCl layer. Since the growth of KCl on Ag(100) is already understood quite well [38, 217, 258], a vicinal Ag(100) was chosen. Now, two aspects need to be considered regarding the terrace width. On the one hand, if the terrace width is too small compared to the KCl lattice constant (4.44 Å), it is likely that the KCl will grow in a carpet growth mode. This would lead to a case in which the Ag steps are not replicated in the KCl layer. Furthermore, the terraces need to be wide enough to allow the growth of QA structures. On the other hand, the step density should be as high as possible because this increases the amount of favorable nucleation points for the QA structures. Considering the above aspects, a terrace width of 50.5 Å was chosen. This terrace width allows,

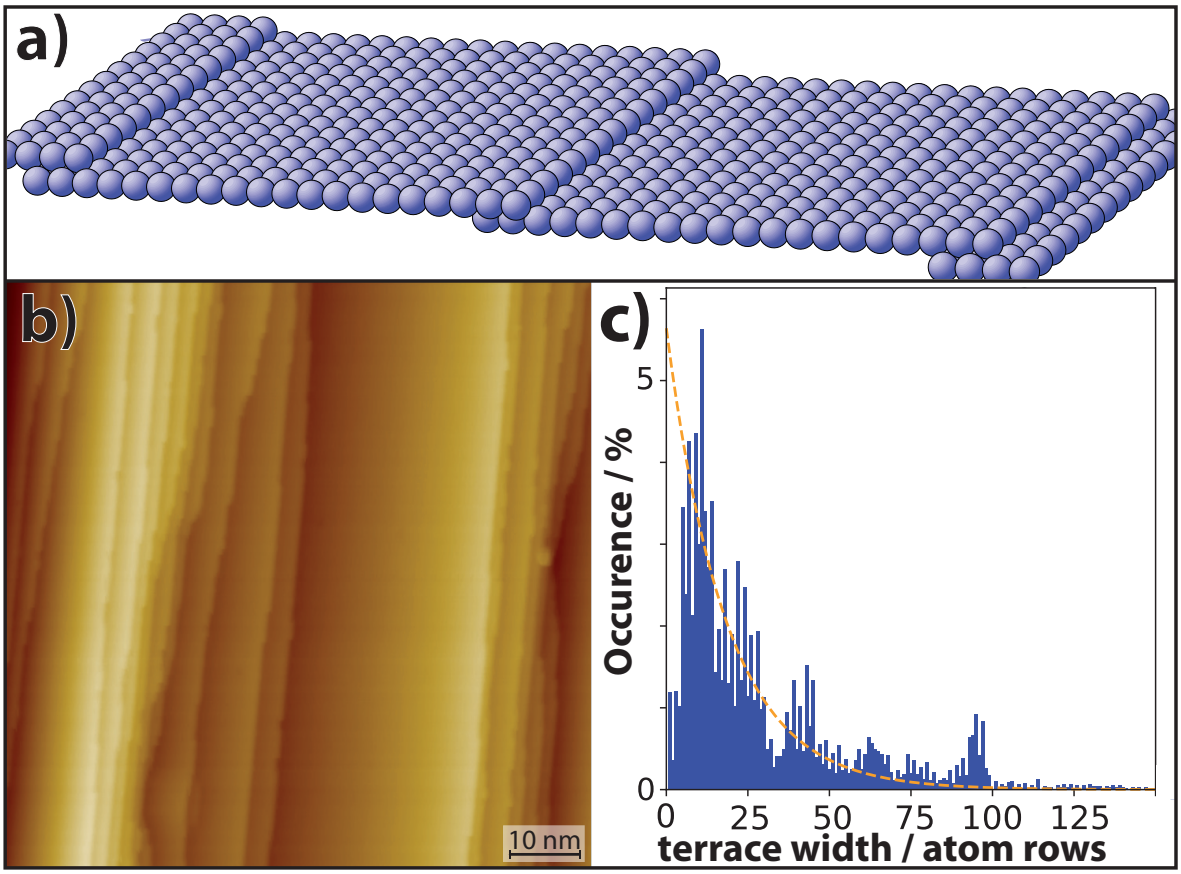

Figure 7.1: *The Ag(35 1 1) surface.* ***a)*** *Model of the ideal Ag(35 1 1) surface that was created with Surface Explorer [255].* ***b)*** *STM image ($U_B = +1.5\,V$, $I_{tun} = 25\,pA$) of the clean surface. It shows that the step edges are not evenly distributed, but there are large terraces and areas with very small step edges that are closely bunched together.* ***c)*** *The terrace width distribution of the sample. It was obtained by evaluating four large-scale STM images with a Python script by Bastidas et al. [256]. It shows a prominent peak around 10 atom rows. For larger terrace widths it roughly follows a geometric distribution. A corresponding fit of such a distribution is indicated by the dashed orange line. The local peaks at $n > 25$ are caused by the fact that because of the finite number of evaluated STM images, individual large terraces are oversampled by the script because it analyzes every horizontal line of the image. The images in panels b) and c) were recorded by L. Grönwoldt within the scope of this focusing laboratory course [257].*

in theory, the growth of three QA chains per terrace that are parallel to the step edges ($b_2 = 16.4$ Å) and the growth of short chains of up to 7 molecules orthogonal to the steps ($b_1 = 6.8$ Å).

A corresponding STM image showing a large area of the bare Ag(35 1 1) surface is shown in panel b) of Figure 7.1. This image shows that the step edges on the surface, which are running vertically through the image, are not evenly spaced with a constant distance of 50.5 Å. Instead, the surface consists of large terraces that can reach terrace widths of up to 100 atom rows (∼300Å) and areas where many step edges are bunched very closely together, which results in average terrace widths of only about 7 atom rows (∼20 Å). It is not uncommon for the step edges on vicinal surfaces to show such a behavior. The reason for this behavior is that the steps are mobile on the surface during the annealing process, and the resulting distribution of the steps can be influenced by many different aspects, e.g., attractive or repulsive interactions between them. Similar observations were made for example on vicinal Cu(100) surfaces [259], as well as on vicinal Si(100) and Si(111) surfaces [260].

The distribution of the terrace widths on the Ag(35 1 1) surface, which was acquired by using a Python script by Bastidas *et al.* [256], is shown in panel c) of Figure 7.1. A detailed analysis of the terrace width distribution was made by L. Grönwoldt within the scope of this focusing laboratory course [257]. Here, the results will only be summarized. The terrace width distribution exhibits a dominant peak at 10 atom rows (∼30 Å) and a continuous decline for terrace widths larger than 10 atom rows. This decline roughly follows a geometric distribution, i.e., the probability $P(L)$ of finding a step at a terrace width L (in atom rows) is: $P(L) \propto p\,(1-p)^{(L-1)}$. A corresponding fit of a geometric distribution is illustrated by the dashed orange line in panel c) of Figure 7.1. This indicates that the Ag step edges at distances larger than 10 atom rows are not interacting with one another [261]. For distances smaller than 10 atom rows, the terrace width distribution exhibits a very steep decline. The analysis of this decline shows that for terrace widths of 4.5 atom rows (13 Å) or less there is a strong (40 meV) repulsive interaction between neighboring steps. Giesen *et al.* [262] found similar repulsive interactions between metal step edges on vicinal Cu(111) surfaces for mean terrace widths between 10 Å and 50 Å. This repulsive interaction between the step edges at small terrace widths combined with the fact that the step edges are non-interacting at larger terrace widths leads to the observed terrace width distribution (Fig. 7.1c).

In panels a) and b) of Figure 7.2, LEED images of the clean Ag(35 1 1) surface are shown at in-phase and out-of-phase conditions for the specular spot, and the first-order spots with respect to monoatomic Ag step edges. An integer phase factor (S_n; with n = 0, 1, 2 denoting the order of the spots) means that the corresponding spot is at in-phase conditions. If the phase factor is of the form $n + 1/2$, where n is a natural number, then the spot is at out-of-phase conditions. More in-depth information about the in-phase and out-of-phase conditions for LEED measurements can be found in ref. [75]. Panel a) of Figure 7.2 shows a LEED image that was recorded at an electron energy of 59 eV ($S_0 = 2.55$ and $S_1 = 2.95$). It can be seen that the specular spot is strongly broadened in the [01] direction and is sharp in the [10] direction and the first-order spots are round and sharp. This uniaxial broadening of the specular spot is attributed to the unidirectional step edges in the [10] direction. For an ideal surface with equidistant step edges, a splitting of the substrate

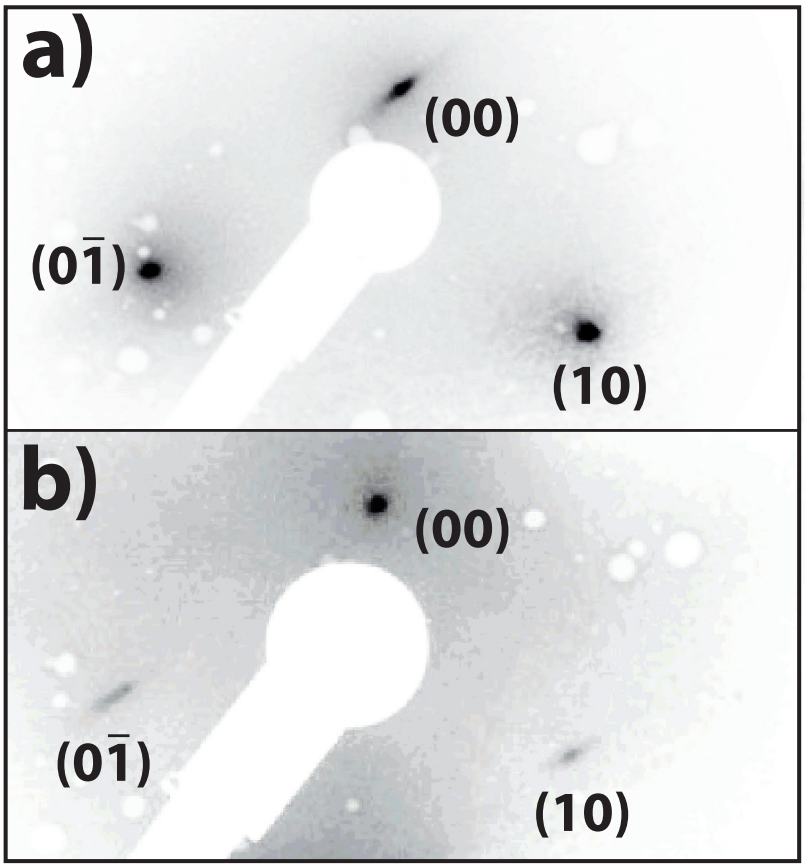

Figure 7.2: a) *LEED image of the Ag(35 1 1) surface recorded for out-of-phase conditions ($S_0 = 2.55$) for the specular spot and in-phase conditions ($S_1 = 2.95$) for the first-order spots with respect to monoatomic Ag step edges.* ***b)*** *LEED image recorded for in-phase conditions ($S_0 = 3.15$) for the specular spot and out-of-phase conditions ($S_1 = 3.55$) for the first-order spots with respect to monoatomic Ag step edges. Both images in panels a) and b) were recorded by L. Grönwoldt within the scope of this focusing laboratory course [257].*

spots would be expected, where the new spots would be sharp and at a reciprocal distance that corresponds the terrace width [263, 264]. However, in the present case, the step edges are not equidistant and hence the observed terrace width distribution only leads to a broadening of the substrate spots. The LEED image in panel b) was recorded at an electron energy of 89 eV ($S_0 = 3.15$, and $S_1 = 3.55$). Thus, here the first-order spots exhibit a strong broadening in the same direction and have very low intensity, while the specular spot is round and sharp.

In summary, it was found that the real vicinal Ag(35 1 1) surface differs significantly from its ideal counterpart. It does not exhibit equidistant steps with a constant terrace width but instead exhibits a broad terrace width distribution. Nevertheless, the structures of QA and KCl on Ag(35 1 1), and QA on KCl/Ag(35 1 1) will be presented and discussed in the following.

7.1.2 Directed growth of QA on Ag(35 1 1)

Now, the structures of QA on the bare Ag(35 1 1) surface will be addressed. After the deposition of QA onto the Ag(35 1 1) surface at 300 K, QA forms the same molecular chains with the same

four distinct azimuthal orientations A – D that are known from the Ag(100) surface (cf. Chapter 5.1). Despite the fact that the unidirectional Ag step edges break the four-fold symmetry of the substrate, all four azimuthal chain orientations A – D were observed on the surface with equal probabilities. A corresponding LEED image showing the spots of all four orientations with equal intensities is shown in panel a) of Figure 7.3. Hence, it is assumed that the chains nucleate on terraces where all four azimuthal orientations are energetically equivalent. The growth of the chains continues on both ends until the step edges are reached. There, the adsorption of a QA molecule at the step edge causes a local charge in the electron density of the step, which serves as a preferred nucleation site for a QA chain on the neighboring terrace. This mechanism explains the fact that it was often observed by STM (not shown here, cf. Appendix A.3) that the QA chains cross the steps and continue on the neighboring terrace. In roughly 50% of the cases, there was a visible break in the chains, and in the other 50% of cases, the chains grew continuously without a break across the Ag steps. This can be explained as follows: the initial nucleation site of a QA chain on a terrace determines the distance between the last QA molecule in the chain and the Ag atoms of the step, i.e., this distance can vary by one lattice constant of the Ag(100) surface (2.89 Å). In the case in which the QA molecules are closer to the step, H-bonds may form and the chain continues without a break across the Ag step. In the other case, the distance between the last QA molecule of the chain and the step is larger, which prevents the formation of H-bonds across the step. Hence, a visible break in the chain can be observed by STM. This phenomenon is explained in more detail in Appendix A.3.

In addition to the orientations A – D, a fifth orientation E that does not exist on the nominally flat Ag(100) surface is also observed on Ag(35 1 1). The corresponding LEED image in panel a) of Figure 7.3 shows additional spots (labeled with E) in the [01] direction. This is the same direction in which the specular spot is broadened at out-of-phase conditions (cf. Fig. 7.2), which means that these chains are parallel to the Ag step edges, which is also confirmed by STM (cf. Appendix A.3). This chain orientation E is less favorable than the orientations A – D in terms of direct interactions with the underlying Ag(100) surface. However, this energy loss is overcompensated by the fact that these chains of orientation E often grow directly along the Ag step edges, and every molecule is subject to attractive *van der Waals* dispersion interactions with the atoms of the Ag step edge over the whole length of the chain, which significantly contributes to E_{ads}. Another important aspect is that these chains of orientations E do not encounter any distortions from the Ag steps edges as the chains of the other four orientations because they grow parallel to the Ag steps.

Interestingly, if QA is deposited onto Ag(35 1 1) at elevated sample temperatures, the unidirectional Ag step edges start to have an influence on the azimuthal orientations of the QA structures. After the deposition of QA at a sample temperature of 400 K, only chains of orientations A, C, and E have formed on the surface, while orientations B and D have completely vanished. A corresponding LEED image is shown in panel b) of Figure 7.3. It only shows sharp spots corresponding to the orientations A, C, and E (for corresponding STM images, see Appendix A.3). The preferential growth of orientations A and C, which are symmetry-equivalent at the Ag step edges, over orientations B and D is explained as follows. At elevated temperatures (> 400 K), the chains now

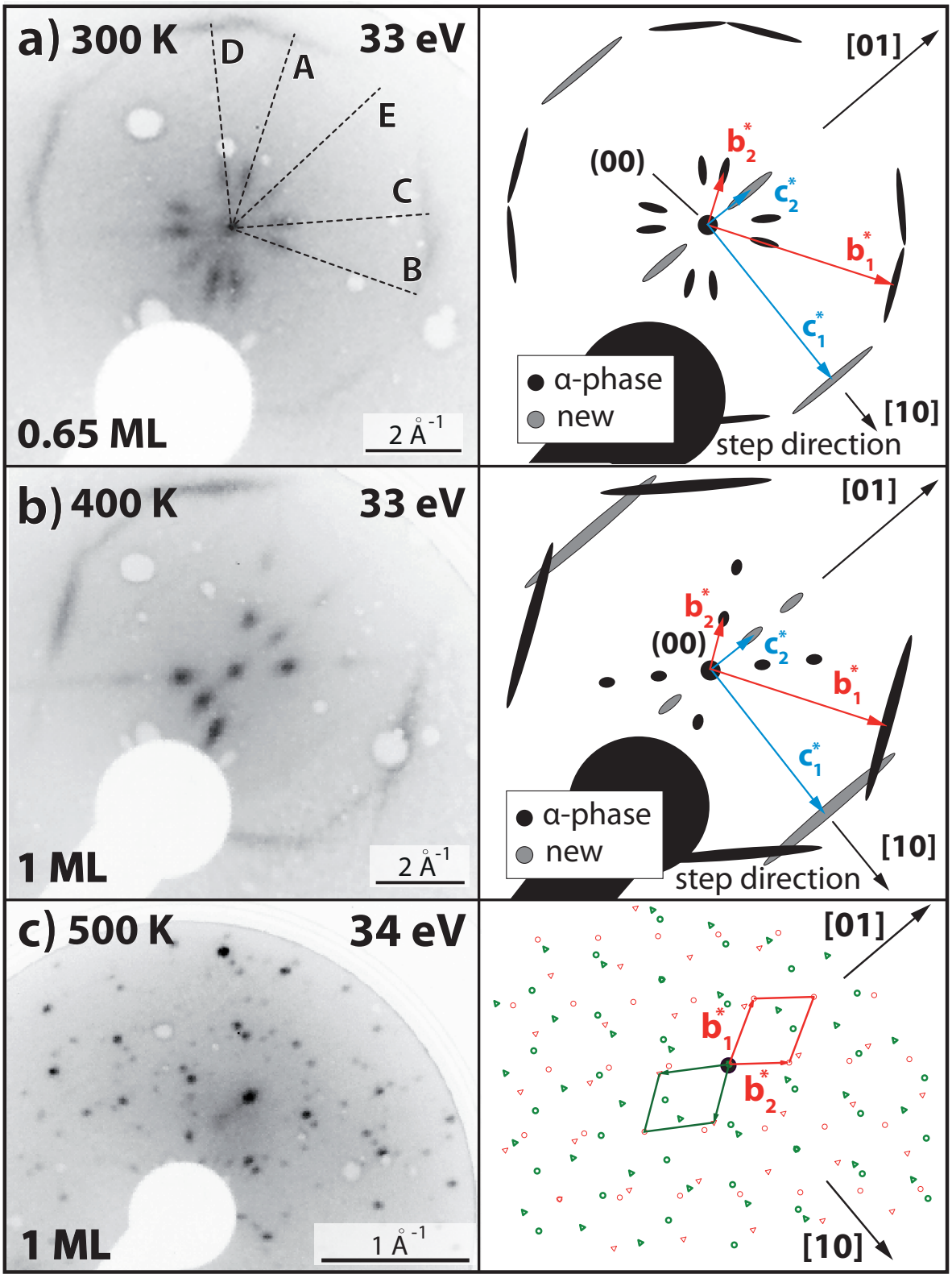

Figure 7.3: *LEED images (left-hand side) and drawn or simulated diffraction pattern for better visibility (right-hand side) of QA on Ag(35 1 1) after deposition at different sample temperatures. The red and blue unit cell vectors in panels a) and b) correspond to the known α-phase and the new orientation E, respectively.* ***a)*** *Deposition at 300 K.* ***b)*** *Deposition at 400 K.* ***c)*** *Deposition at 500 K.*

preferably nucleate at the Ag step edges. There, the nuclei of orientations A and C are more stable than those of orientations B and D. Thus, the nuclei of orientations A and C grow, while the less stable nuclei of orientations B and D dissolve (*Ostwald*-ripening). The higher stability of the nuclei of orientations A and C is explained by favorable adsorption sites of molecules with these two orientations A and C at the Ag step edges. These favorable adsorption sites involved the replacement of Ag atoms in the step by QA molecules. This replacement of Ag atoms does not happen at a sample temperature of 300 K because, at this temperature, the diffusion and mobility of the Ag atoms from the step edges onto the terraces is smaller compared to the situation at a sample temperature of 400 K.

Similar to the situation for QA on Ag(100), depositing the QA at a sample temperature of 500 K leads to the formation of the β-phase. However, in contrast to the diffraction pattern of the β-phase on the Ag(100) surface (cf. Fig. 5.2, page 38), the diffraction pattern here exhibits very strong anisotropy. The corresponding LEED image and a simulation are illustrated in panel c) of Figure 7.3. It can be seen that roughly half of the spots are drastically more intense than the other half. The analysis of the image shows that two of the four domains, which are mirror domains with respect to each other, are more probable on the surface. Furthermore, the QA molecules in these two domains exhibit the same azimuthal orientations as the molecules in orientations A and C of the α-phase. Thus, the prevalence of two distinct domains in the β-phase on Ag(35 1 1) can also be attributed to the favored adsorption sites of QA molecules with orientations A and C at Ag step edges at elevated temperatures. It is also worth mentioning that, in contrast to the situation after deposition at 400 K, here, the two less favored domains B and D are still present on the surface. That is because all four domains nucleate with equal probability on large terraces. The nuclei of the β-phase are more stable on terraces than those of the α-phase due to their commensurate nature. Thus, they do not dissolve as easily as those of the α-phase. Because of this, the domains of orientations B and D in the β-phase survive and are to a small extent still present on the surface, even after repeated heating cycles at 500 K.

7.2 Growth of KCl on the Ag(35 1 1) surface

Now, the structure of epitaxial layers of KCl on Ag(35 1 1) will be discussed. As stated in Chapter 4, the layers were prepared at a sample temperature of 400 K and with a deposition rate of about 0.1 ML per minute. The resulting layers of KCl on Ag(35 1 1) exhibit some structural similarities and some stark differences with respect to the layers of KCl on Ag(100). The internal structure, as defined by the arrangement of the ions and the lattice constant, is identical to that on Ag(100). A corresponding LEED image and a schematic representation of the diffraction pattern of a KCl layer on Ag(35 1 1) are shown in Figure 7.4. The diffraction pattern is similar to that of KCl on Ag(100) [38]. The KCl$\langle 10 \rangle$ and Ag$\langle 10 \rangle$ spots are aligned in the same direction, which shows that the KCl layer is aligned with the (100) lattice of the Ag(35 1 1) surface and does not exhibit any azimuthal spread. The lattice constant of the KCl layer can be determined from the ratio between

the lengths of the reciprocal unit cell vectors. The lengths of the vectors $b^*_{1,\mathrm{Ag}}$ and $b^*_{2,\mathrm{KCl}}$ were measured in a distortion-corrected LEED image, and the lattice constant of KCl was calculated as:

$$\frac{b^*_{1,\mathrm{Ag}}}{b^*_{2,\mathrm{KCl}}} = \frac{b_{2,\mathrm{KCl}}}{b_{1,\mathrm{Ag}}} = \frac{a_{\mathrm{KCl}(100)}}{a_{\mathrm{Ag}(100)}} = 1.55 \pm 0.05; \quad a_{\mathrm{KCl}(100)} = a_{\mathrm{Ag}(100)} \cdot 1.55 = (4.5 \pm 0.2)\,\text{Å}.$$

This value of (4.5 ± 0.2) Å for the lattice constant of KCl is identical within the margin of error to the ones found by Müller *et al.* for KCl on Ag(100) [38].

In addition to the first- and second-order KCl spots, which are labeled accordingly, the diffraction pattern of KCl on Ag(35 1 1) (cf. Fig. 7.4a) also shows another set of spots of low intensity. Three examples of such spots are highlighted by the red transparent circles. These spots are attributed

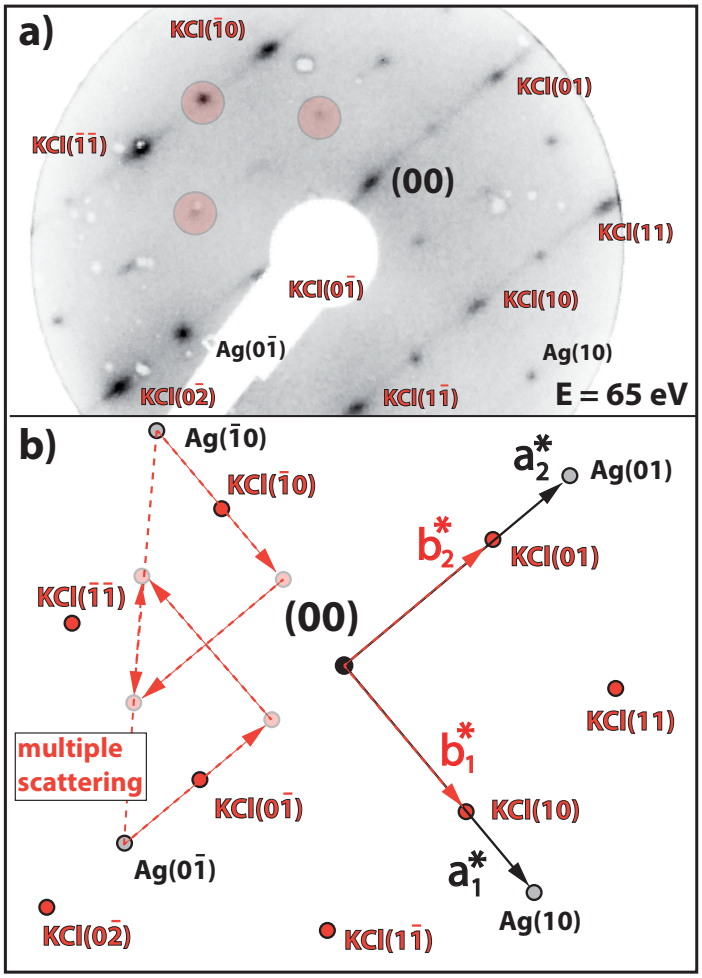

Figure 7.4: a) *LEED image ($E = 65$ eV, $S_0 = 2.7$, $S_1 = 3.1$) of epitaxial layers of KCl on the Ag(35 1 1) surface. The Ag and KCl spots are labeled accordingly, and the red transparent circles highlight spots that are produced by multiple scattering.* ***b)*** *A corresponding schematic illustration of the diffraction pattern in a) for better visibility. Spots that are not accounted for by the KCl or Ag unit vectors are caused by multiple scattering, which is illustrated by the dashed lines on the left-hand side. Note the diffuse lines between the KCl spots in the direction perpendicular to the steps that point towards a carpet growth mode.*

to multiple scattering at the Ag substrate and the KCl layer. The corresponding geometric illustration is shown in panel b) of Figure 7.4 on the left-hand side. All of the other additional spots can also be explained in a similar manner. Multiple scattering was also found by M. Müller for thin films of NaCl on Ag(100) [265]. He did not observe multiple scattering for NaCl layers that were prepared at higher sample temperatures, and after annealing the layers that exhibited multiple scattering, it could not be observed anymore. Because of this, he concluded that multiple scattering only occurred for single NaCl layers that transitioned into a double layer upon annealing. In the present case, the existence of single monoatomic KCl layers could not be confirmed by the STM measurements and no similar annealing experiments were conducted. However, this does not disprove the existence of single KCl layers because the STM images only probe a small sample area. Overall, in the present case, it cannot be said for certain whether the multiple scattering is caused by single or double KCl layers.

Another interesting aspect is that all the KCl spots in the diffraction pattern (Fig. 7.4a) are smeared out in the [01] direction, which is the direction that is orthogonal to the step direction. This broadening of the spots is not observed for KCl layers on Ag(100) and is thus likely caused by the Ag step edges. Kramer *et al.* found for NaCl on Ag(19 1 1) similar elongated satellites in only the step-down direction of the diffraction pattern [266]. They explained this with the presence of different KCl mosaics with characteristic small angles of inclination with respect to the Ag(100) terraces (i.e., some sort of carpet growth mode). The authors state that the formation of these mosaics is caused by the mismatch between the Ag and NaCl lattices, which is particularly relevant at periodic step edges. If these two lattices were forced to fit, then the consequential deformation of the NaCl layer would lead to drastic electrostatic repulsion between the ions. Hence, this situation is circumvented through an elastic carpet growth of NaCl across the Ag step edges. A similar explanation may be applicable to the situation of KCl on Ag(35 1 1), although here the smearing and splitting of the KCl spots is less defined than those in the work by Kramer *et al.* [266]. The step height in a KCl lattice is 3.18 Å, which is larger by 55% than the Ag step height (2.05 Å). This means that the mismatch between the step heights of KCl and Ag is even larger than the one between the step heights of NaCl and Ag (37%). Hence, the uniaxial smearing of the KCl that was observed here points towards a carpet growth of KCl across the Ag step edges. This is also supported by STM images (discussed below) that show that the replicated Ag step edges are not clearly visible and distinguishable where the KCl layer covers an area of high Ag step density. Similar carpet growth modes were for example also observed for NaCl on Cu(311) and Cu(221), and for KCl on Cu(311) [267]. The carpet growth on the vicinal surface, as opposed to the growth of KCl on the nominally flat Ag(100) surface, is likely caused by the high density of steps.

Now, the corresponding STM images for KCl on Ag(35 1 1) will be discussed. A large-scale STM image of a KCl layer on Ag(35 1 1) is shown in panel a) of Figure 7.5. It shows the KCl wetting layer and patches of the bare Ag surface. Overall, the KCl layer looks very disordered in comparison to the ones on Ag(100). It has several holes and does in general not completely cover large connected areas of the sample. This is likely caused by the fact that the high density of Ag steps constitutes many favored nucleation points of the growth of the KCl layer. Thus, more KCl islands start

growing at the same time in comparison to the growth on Ag(100), which overall leads to more smaller KCl islands instead of a few big islands that cover a large connected area of the sample.

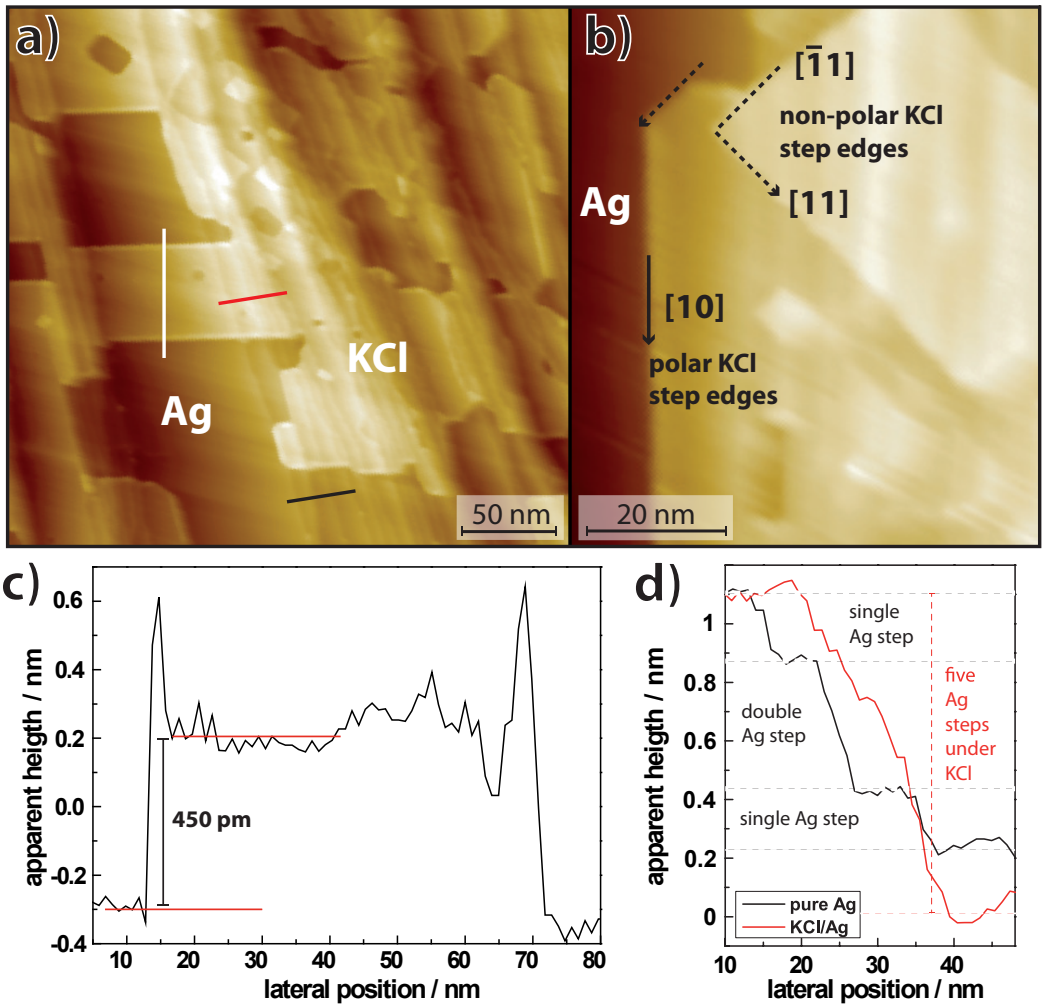

Figure 7.5: a) *Large scale STM image ($U_B = +3.5\,V$, $I_{tun} = 25\,pA$) showing the KCl wetting layer and the bare Ag(35 1 1) surface. Small quadratic KCl islands can be seen on top of the wetting layer.* ***b)*** *Small scale STM image ($U_B = +3.5\,V$, $I_{tun} = 25\,pA$) showing the polar and non-polar step edges of the KCl layer, which are rotated by 45° with respect to one another.* ***c)*** *Height profile that was measured along the white line in panel b) across the KCl wetting layer.* ***d)*** *Height profiles along several Ag step edges that are not covered by the KCl layer (black line) and across several step edges that are covered by the KCl layer (red line). The profiles were recorded along the red and black lines in panel a).*

A very striking difference to the growth of KCl on the nominally flat Ag(100) surface is that, here, the majority of the Ag-KCl step edges that limit the KCl wetting layer are oriented along the KCl⟨10⟩ directions, and only a small amount of the wetting layer limiting Ag-KCl step edges are oriented along the KCl⟨11⟩ directions.[1] However, the KCl-KCl step edges of the KCl islands on top of the wetting layer are exclusively oriented along the KCl⟨11⟩ orientations. This is a stark contrast to the structure of KCl layers on the nominally flat Ag(100) surface. There, all wetting layer limiting Ag-KCl step edges, as well as all KCl-KCl step edges that limit the quadratic islands

[1] For an illustration of the different orientations in a KCl layer, see the model in Figure 6.1 on page 72.

on top of the wetting layer, are oriented along the KCl⟨11⟩ orientations. The different step edges of the KCl wetting layer and those of the islands on top are illustrated by the black lines in the STM image in panel b) of Figure 7.5. The fact that on Ag(35 1 1) most of the Ag-KCl step edges of the wetting layer are oriented along KCl⟨10⟩ directions, while the orientations of the KCl-KCl step edges of the quadratic KCl islands on top remain along the KCl⟨11⟩ orientation, means that the Ag-KCl step edges along the KCl⟨10⟩ direction correspond to polar step edges. This observation is also supported by another aspect that can be observed in the STM images. The Ag-KCl step edges of the wetting layer along the KCl⟨10⟩ directions have a spike in the apparent height that is larger by roughly 200 pm than that of the rest of the wetting layer. This is illustrated in the height profile across the KCl wetting layer, which is shown in panel c) of Figure 7.5. These spikes in the apparent height at the Ag-KCl step edges were never observed on Ag(100) and are likely related to the charges of the ions at the step edges. The formation of polar step edges that limit the KCl wetting layer is very surprising because the polar Ag-KCl step edges are expected to be significantly less stable than their non-polar counterparts. The reason for the formation of polar step edges will be discussed in more detail below.

Another interesting aspect is that the Ag step edges below the KCl layer in areas of the sample with a high Ag step density appear as significantly less sharp than those on the bare Ag surface. This is illustrated in panel d) of Figure 7.5. The black curve shows a height profile across four Ag steps on the bare Ag(35 1 1) surface, while the red curve shows a height profile across five Ag step edges, which are covered by the KCl wetting layer. It can be seen that in the black curve, the individual Ag steps are clearly visible and distinguishable. However, this is not the case for the red curve. There, the five Ag steps appear as a single broad step instead. This is indicative of a carpet growth of the KCl layer across the Ag steps, which is also in good agreement with the smeared-out spots in the corresponding diffraction pattern, as discussed above. It is also important to note that the carpet growth mode occurs mostly in areas with a very high Ag step density, namely in areas where the average terrace width is smaller than 50 Å. In areas where the terrace width is larger, the carpet growth mode could not be observed by STM, and the Ag step edges are replicated in the KCl wetting layer and can be imaged by STM.

The formation of polar step edges of the KCl wetting layer is very counterintuitive because these step edges are supposed to be significantly less stable than non-polar ones. Furthermore, to the best of the knowledge of the author of the present thesis, a similar observation has not been reported so far. The reason for this behavior must be caused by the unidirectional Ag step edges. However, with the current set of data, it is not possible to determine the exact mechanism that causes this. A possible explanation may be that because the KCl layer grows in a carpet growth mode across the step edges (see above), the ionic KCl lattice is slightly strained and deformed in the [01] direction, which is orthogonal to the direction of the Ag steps. Such a deformation was already found by Cañas-Ventura *et al.* for NaCl layers on a vicinal Au(111) surface close to step edges [268]. The deformation of the ionic KCl lattice due to the carpet growth mode may destabilize the non-polar KCl step edges in the ⟨11⟩ direction because they run at an angle of 45° with respect to the direction of the postulated deformation of the KCl lattice.

In summary, the results of this section have shown that the KCl layer on Ag(35 1 1) grows in a carpet growth mode across the Ag steps if the step density is locally high. Furthermore, the majority of step edges that limit the KCl wetting layer are polar step edges, as opposed to the step edges that limit the KCl wetting layer on Ag(100), which are non-polar. The reason for the formation of polar step edges on Ag(35 1 1) is tentatively assigned to a slight deformation of the KCl layer, which is caused by the carpet growth mode across the Ag steps.

7.3 Growth of quinacridone chains on KCl on Ag(35 1 1)

Finally, the self-assembled structures of QA on a thin KCl layer (2 – 3 ML) on the Ag(35 1 1) surface will be addressed in this section. In particular, the differences between the QA structures on KCl/Ag(100) and those on KCl/Ag(35 1 1) will considered and analyzed and also compared to the results reported by Bretel *et al.* [240] for QA on KCl/Cu(111).

First, the situation in which the KCl wetting layer does not completely cover the Ag surface is considered. It is very similar to the analogous situation for QA on KCl/Ag(100) (cf. Chapter 6.2), i.e., the QA molecules diffuse from the KCl layer to the bare Ag surface. The reason for that is that on Ag, the QA molecules exhibit a larger E_{ads} than on KCl. The phenomenon is discussed in more detail in Appendix A.2. An STM image illustrating this is displayed in Figure 7.6. The upper half of the image shows a KCl layer with an apparent height of 320 pm, which corresponds to a thickness of 2 ML. The remaining area of the image is not covered by KCl and thus corresponds to the bare Ag surface. The step edge between the bare Ag surface and the KCl wetting layer is highlighted by the dashed white line. It can be seen that no QA molecules are adsorbed on the KCl layer. In contrast, on the bare Ag surface that is not covered by KCl, long chains of QA have formed, which are very similar to those discussed in Section 7.1. This image (Fig. 7.6) shows an example of a very common observation, namely that in areas of the KCl wetting layer that are in the close vicinity of the KCl-Ag step edges, no QA molecules on the KCl layer could be observed.

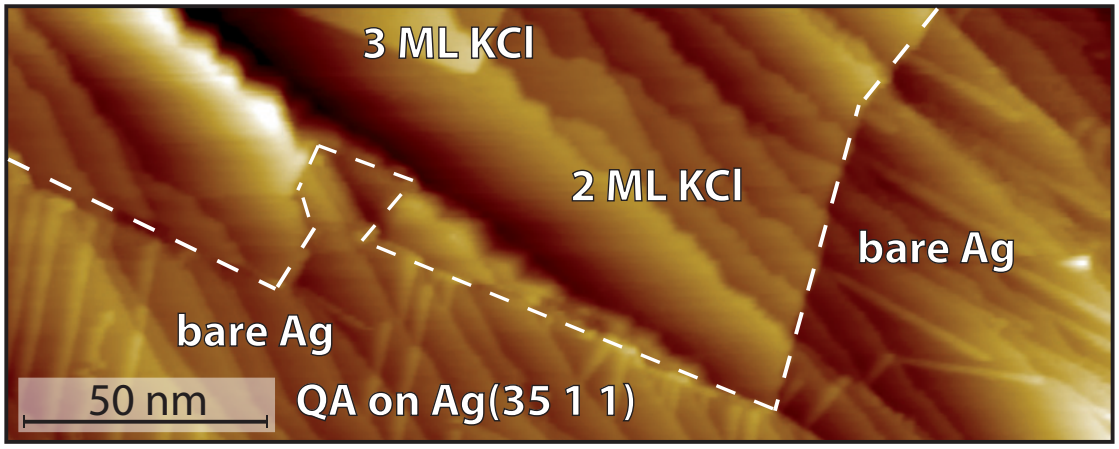

Figure 7.6: *STM image ($U_B = -3.5\,V$, $I_{tun} = 3\,pA$) of a 2 ML high KCl wetting layer and bare patches of the Ag(35 1 1) surface. The latter is covered with QA chains, while the former is completely free of QA molecules. The dashed white line corresponds to the Ag-KCl step edge.*

Similar to the situation for QA on KCl/Ag(100), the diffusion of the QA molecules to the bare Ag surface can be prevented, if the KCl wetting layer covers the majority of the Ag surface. Panel a) of Figure 7.7 shows an STM image of QA on an area of the sample that is completely covered by a 2 ML thick wetting layer of KCl. The Ag step edges below the KCl layer are clearly visible. However, line profiles reveal that they are not as sharp as on the bare Ag surface (similar to the profiles shown in panel d) of Fig. 7.5), which indicates that a carpet growth mode of KCl is also present here. On top of the KCl wetting layer, there are several KCl islands with a thickness of 1 ML (3 ML in total) with straight and non-polar step edges along the KCl$\langle 11 \rangle$ directions. The image also shows three QA chains that are on the KCl wetting layer. These three chains run between 3 ML KCl islands connecting two islands. This was a very common observation. Almost all QA chains that were observed on KCl/Ag(35 1 1) were terminated on both ends by a KCl island of the third layer. The fact that almost all observed chains were terminated on both ends indicates that only a small amount of QA chains nucleate and grow at the same time. This is plausible in view of the high mobility of QA molecules on KCl and the fact that the continuation of a chain, which included the formation of intermolecular H-bonds, is energetically significantly more favorable than the nucleation of a new chain at a KCl step. All observed chains also grow across several replicated Ag step edges without a visible break. The growth across replicated Ag step edges may seem surprising, but it was also already shown that the chains can also grow across bare Ag step edges (cf. Section 7.1.2).

A very notable difference to the chains that were observed on KCl/Ag(100) (see Chapter 6.2 or Appendix A.2) lies in the azimuthal orientations of the QA chains. On KCl/Ag(100), all observed chains exhibited symmetry-equivalent azimuthal orientations of 12° with respect to the KCl$\langle 11 \rangle$ directions (33° with respect to the KCl$\langle 10 \rangle$ direction). In contrast, on KCl/Ag(35 1 1) a wider range of different azimuthal chain orientations was found. There, the QA chains exhibit different azimuthal orientations between 0° and 15° with respect to the KCl$\langle 11 \rangle$ direction of the Ag substrate. All angles that are noted in Figure 7.7 have an estimated error of $\pm 1°$. From the current set of data, it is not possible to say whether a distinct azimuthal chain angle is the most favorable because of limited statistics. Four different azimuthal chain orientations are illustrated in panels a) and b) of Figure 7.7. These different azimuthal chain orientations may be caused by structural differences between the KCl layer on the two different Ag substrates, which will be discussed in more detail below.

Panels b) and c) of Figure 7.7 show STM images of several QA chains on the KCl wetting layer between two 3 ML KCl islands with high resolution. It can be seen in panel c) that the QA chains appear as three parallel lines of lobes (indicated by the dashed black lines and the blue and red ellipses on the left-hand side). A similar appearance of the QA chains in STM images was observed on KCl/Cu(111), as was reported by Bretel *et al.* [93, 240]. The lobes of the central line are slightly offset with respect to the lobes of the two outer lines in the direction of the chain. Hence, the lobes of the central line (red ellipses) may correspond the electron density of the H-bonds between the molecules, and the lobes of the two outer lines (blue ellipses) may correspond the electron density of the π-systems of the outer benzene rings in the QA molecules. The intermolecular distance

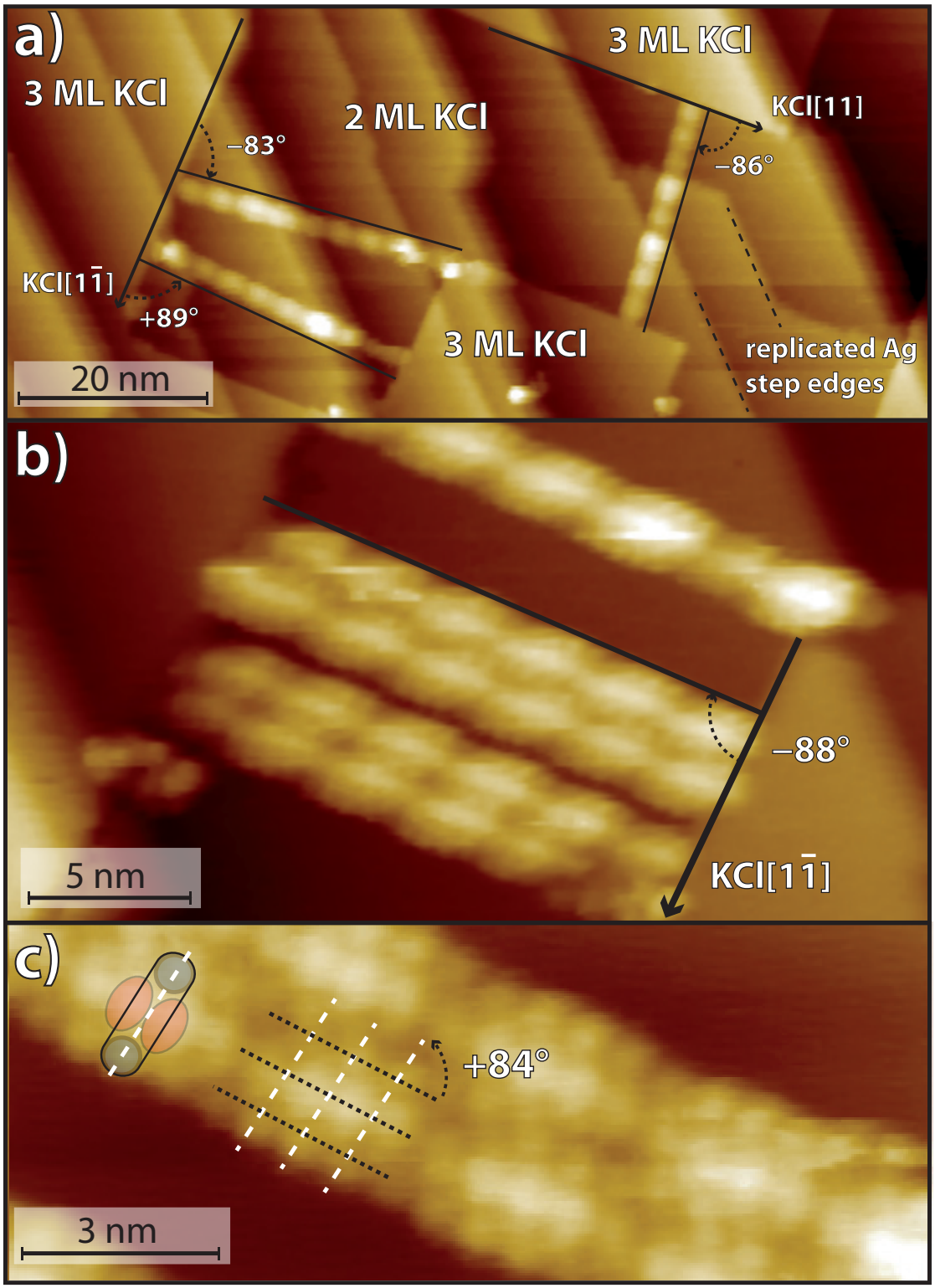

Figure 7.7: *Structures of QA on KCl/Ag(35 1 1).* ***a)*** *STM image ($U_B = -4\,V$, $I_{tun} = 8\,pA$) of QA on a 2 ML thick KCl layer. The QA molecules are arranged in chains to run between quadratic KCl islands in the third layer.* ***b)*** *Small scale STM images ($U_B = -4\,V$, $I_{tun} = 8\,pA$) of QA chains at a different location of the sample than those shown in a) with sub molecular resolution.* ***c)*** *Zoom onto two QA chains of b) that are right next to each other with molecular resolution. The dashed black lines show the azimuthal chain orientation and the dashed white lines show the azimuthal orientations of the long molecular axes. A molecular QA chain appears as three parallel rows of lobes. This is illustrated on the left-hand side of the image by the red and blue ellipses and the rough outline of a single QA molecule is indicated by the black line. All angles noted in this image have an estimated error of $\pm 1°$.*

within the chains was determined by measuring the distance between the lobes of the central line and amounts to $b_1 = (6.5 \pm 0.2)$ Å, which is identical to the same distance in the α-phase on Ag(100) within the margin of error. The long axis of a QA molecule in the chain was determined by connecting the lobes of the outer lines, as is indicated by the dashed white lines. With this, the angle between the long molecular axes and the azimuthal chain direction was determined and amounts to $(84 \pm 1)^\circ$. However, it is important to note that this orientation may vary for different chains. This could not be checked in detail because for most observed QA chains sub-molecular resolution was not achieved. A variation of the angle between the chain direction and the long axes of the molecules for different QA chains may be expected because such a variation of about $\pm 10^\circ$ was observed by Bretel *et al.* for QA on KCl/Cu(111).

Another interesting aspect is that the contrast in the STM image (i.e., the apparent height) along the chains varies periodically, as can be seen in panel c) of Figure 7.7. However, this is likely not a topological effect because the intermolecular distance between the chains is constant over the whole length of the chain. If the chains exhibited some sort of buckling, then a variation of the intermolecular distance would be expected. Instead, this periodicity is likely given by some sort of electronic *Moiré* pattern, which is caused by the superposition of the electronic structures of the QA molecules and that of the KCl layer. This periodicity repeats every four molecules, i.e., every fourth molecule in the chains exhibits a darker contrast than the remaining molecules of the chains. With the help of the above values, namely the azimuthal chain orientation of $(88 \pm 1)^\circ$ with respect to the KCl$[1\bar{1}]$ orientation, the angle of $(84 \pm 1)^\circ$ between the chain orientation and the long axes of the molecules, and the intermolecular distance of $b_1 = 6.5 \pm 0.2$ Å, a structure model for these particular chains (Fig. 7.7c) can be built. The model is shown in Figure 7.8. Note that this model does not apply to all observed chains due to the fact that not all QA chains exhibit the same azimuthal orientations. This model also provides an explanation for the periodically varying intensity in the STM images along the QA chains. The two molecules in the chain that are marked with black and blue arrows exhibit identical adsorption sites, respectively. In addition, the adsorption sites of the molecules marked with blue arrows are also mirror-equivalent to those marked with black arrows, which shows that all four marked molecules exhibit symmetry-equivalent adsorption sites. This does by no means prove that the structure model shows the correct adsorption sites of the QA molecules (they are still chosen arbitrarily to some degree), but it does show that the adsorption sites in this model can repeat every four molecules, which is in agreement with the observed *Moiré* pattern.

To conclude this section, the central question that arises from the above observations will be discussed. Why do the structures, and in particular the azimuthal orientations, of the QA chains on KCl/Ag(35 1 1) differ from those on KCl/Ag(100)? For QA on KCl/Ag(100), it was concluded with the help of DFT calculations that the azimuthal orientations of the chains are only determined by the KCl layer without any influence of the underlying Ag substrate. Thus, for an identical structure of the KCl layers on both Ag surfaces, identical azimuthal orientations and structures for the QA chains would be expected. Since this is not in line with the observations described above, it

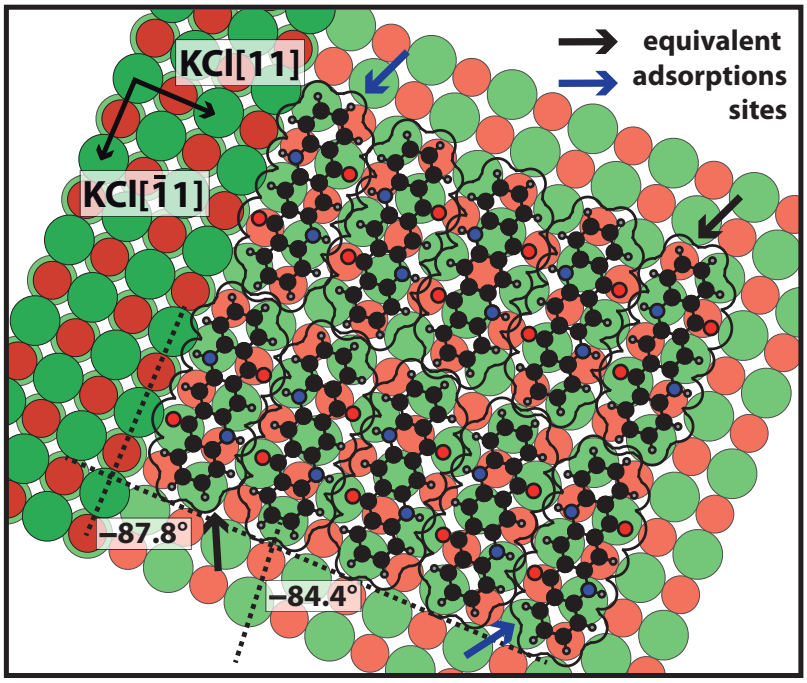

Figure 7.8: *Structure model for QA chains on KCl/Ag(35 1 1). The model corresponds to the chains that can be seen in panels b) and c) of Figure 7.7. The molecules marked with blue and black arrows exhibit identical adsorption sites, respectively. In addition, the adsorption sites of the molecules marked by blue and black arrows are also mirror equivalent, which means that all four marked molecules exhibit symmetry-equivalent adsorption sites.*

can only be concluded that the differences in the QA structures are due to differences in the structures of the KCl layers. Alternatively, the interactions with the steps may play a role. However, QA chains that nucleated at a KCl step edge were also observed on KCl/Ag(100), which did not have an influence on their azimuthal orientations with respect to the chains that nucleated on a terrace. Thus, the nucleation of QA chains at KCl step edges is unlikely to play a significant role for the azimuthal orientations of the chains.

As stated above, the LEED and STM results for the KCl layer point towards a carpet growth of the KCl layer (discussed above) across the step edges, in particular in areas of the sample with a high step density. This growth mode induces a large-scale strain on the KCl layer, which leads to slight deformations of the KCl lattice. The strength of this deformation likely varies with lateral position and depends on the distance to the nearest area of high step density. These deformations lead to a wider range of potential adsorption configurations for QA on KCl and thus to a wider range of different azimuthal orientations that differ from those on KCl/Ag(100). A similar interpretation may possibly apply to the results for QA on KCl/Cu(111), which was investigated by Bretel *et al.* [93, 240]. They also found QA chains with azimuthal orientations that are very similar to those on KCl/Ag(35 1 1) and differ from those calculated for QA on KCl. Hence, it may be possible that the six-fold symmetry of the Cu(111) surface causes a slight deformation of the KCl layer, which exhibits a four-fold symmetry. This interpretation is also in good agreement with the observations by Cañas-Ventura *et al.* for 3,4,9,10-perylene tetracarboxylic diimide (PTCDI) on

NaCl the vicinal Au(11 12 12) surface [268]. There, the deformation of the KCl layer due to the vicinal character of the surface leads to preferential binding sites for the PTCDI on KCl and allows the formation of 2D molecular structures, which could not be observed on KCl/Au(111).

7.4 Conclusions

In this chapter, it was reported that the unidirectional step edges of the vicinal Ag(35 1 1) surface have a significant influence on the structures of adsorbates in comparison to the structures of the same adsorbates on the nominally flat Ag(100) surface. On Ag(35 1 1), if the QA was deposited at RT, then the QA chains nucleate on the Ag terraces, which results in the same four distinct azimuthal orientations A – D as on Ag(100). Furthermore, it was found that the QA chains can form intermolecular H-bonds across the Ag step edges, which enables the continuous growth of QA chains across the Ag steps. However, if the QA is deposited at elevated sample temperatures (400 K or 500 K), then the Ag step edges lead to a preferential growth of distinct chain orientations in the α-phase, and the preferential growth of two distinct domains in the commensurate β-phase. This is explained by more favorable adsorption sites for QA molecules at the Ag step edges, which includes the replacement of Ag atoms by QA molecules at elevated temperatures.

For the KCl layer on Ag(35 1 1), it was found that the internal structure of the KCl layer is very similar to the one of KCl on Ag(100). However, in areas of the sample with a high step density, the unidirectional step edges of the vicinal Ag surface are overgrown by the KCl layer in a carpet growth mode. This growth mode leads to a large-scale strain of the KCl layer that causes slight deformations in the KCl lattice. Furthermore, it was found that the majority of Ag-KCl step edges that limit the KCl wetting layer on Ag(35 1 1) are polar, as opposed to those of the KCl wetting layer on the nominally flat Ag(100) surface, which are exclusively non-polar. This phenomenon is also tentatively assigned to the above-postulated strain of the KCl layer orthogonal to the step edges.

Finally, the structures of QA on KCl/Ag(35 1 1) also differ from those of QA on KCl layers on the nominally flat Ag(100) surface. In both cases, QA forms one-dimensional molecular chains that are connected via intermolecular H-bonds, but the azimuthal orientations of these chains differ. Furthermore, on KCl/Ag(35 1 1) a wider range of different azimuthal chain orientations was observed. This is explained by the strain and the slight deformation of the KCl layer, which leads to different and potentially more favorable adsorption sites for the QA molecules.

8 Blue phosphorus on Au(111)

The results of the following chapter have been prepared for publication. The corresponding manuscript can be found in appendix A.4. The author of the present thesis took part in the acquisition, evaluation, and illustration of the NIXSW data. The manuscript was written by M. Sokolowski and was proof-read by the author of the present thesis.

This chapter describes the investigation of the epitaxial growth of blue phosphorus on the Au(111) surface by photoelectron spectroscopy and NIXSW. These results are thematically to some extent separated from those of Chapters 5 – 7, because here no structures of QA were investigated. Nevertheless, the results are very interesting in the context of the present work because blue phosphorus has been discussed as a potential decoupling layer for organic epitaxially grown films [274]. Hence, the investigation of the structures of QA on blue phosphorus may be a subject of experiments in the future.

The results of this chapter contribute to the understanding of the structural details of a commensurate phosphorus (5 x 5) structure on Au(111), which has been observed previously by LEED and STM [269–275]. In particular, two conflicting structure models for this (5 x 5) structure, namely a double layer model and a Au-P network model, have been reported. Schematic models of the two proposed structures are shown in Figure 8.1. These two models will be critically reviewed and it

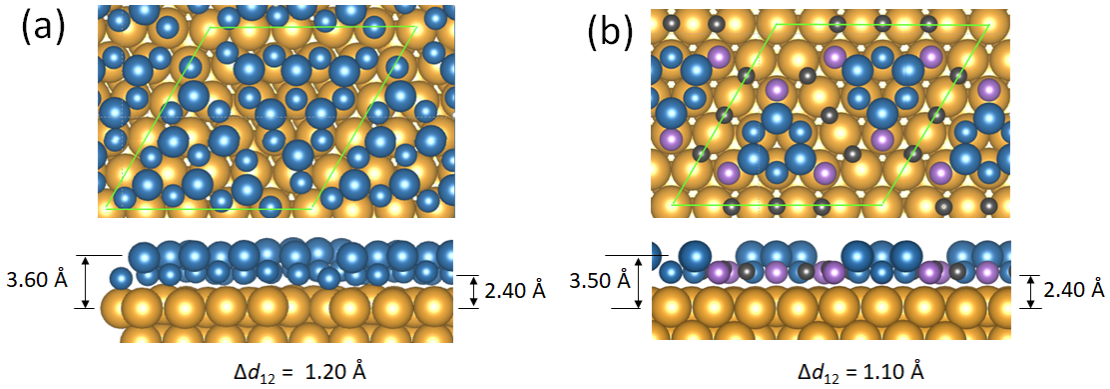

Figure 8.1: *Two schematic models for the structure of blue phosphorus in top-down and side views from literature. The corresponding unit cells are indicated by the green lines. The double layer model [269–271] is shown in panel a) and the Au-P network model [272, 273] is shown in panel b). The blue and violet spheres correspond to P atoms, whereas the yellow and brown atoms resemble the gold atoms. The small/large spheres correspond to atoms in the bottom/top layer, respectively.*

will be determined which model is in better agreement with the NIXSW data. The in-depth analysis and discussion of the data can be found in the manuscript in Appendix A.4. In this chapter, only a brief summary of the results is given.

With NIXSW, the vertical heights of the P atoms in the blue phosphorus layer were determined. It was found that the phosphorus atoms of the layer are located at two different heights, which are 3.53 Å and 2.48 Å, above the Au surface. This means that blue phosphorus is actually a P double layer. The bottom layer contains 2.4 times more P atoms than the top layer. Furthermore, two different kinds of P atoms with different chemical environments (ratio of 0.39% : 0.61%), which was concluded from their photoemission binding energies, were found for the bottom layer. This was attributed to the P atoms of the smaller fraction (39%) forming bonds to Au ad-atoms, while the P atoms of the larger fraction (61%) only form bonds to other P atoms. Based on these results, it was concluded that the so-called Au-P network layer by Tian *et al.* [272] is more plausible, however, the vertical heights given in the corresponding literature are not in agreement with the values determined here and thus a revision of the vertical heights is required.

9 Summary and outlook

The adsorption and ordering of the organic molecule 5,12-dihydro-quino[2,3-*b*]acridine-7,14-dione (quinacridone, QA) on different metal surfaces and thin layers of wide band gap materials have been investigated with low-energy electron diffraction (LEED) and scanning tunneling microscopy (STM). The QA molecule exhibits two distinct properties, which make it a very interesting candidate for structural investigations on surfaces. The first one is that the QA molecule contains four functional chemical groups that enable it to form strong intermolecular hydrogen bonds (H-bonds). The second one is that the QA molecule is prochiral, which means that upon adsorption on a surface two different QA enantiomers are present on the surface, which plays a significant role in the structure formation.

One goal of the present work was to demonstrate that these intermolecular H-bonds of QA are a very strong motif promoting the formation of long molecular chains on surfaces. Of particular interest in this context was the question of whether the chains of QA can be electronically decoupled from the metal substrate, which is an important step to allow optical investigations on the system. For this, the self-assembled structures of QA on thin layers of wide band gap materials, where the adsorption energy of the molecules is typically lower than on metal surfaces, were also investigated. Furthermore, it was investigated if the step edges of the metal substrate can be utilized to support the growth of QA chains on insulating layers by providing favorable nucleation points for their growth. In addition, the influence of the Ag steps on the azimuthal chain orientations was also considered. Within the scope of the above questions, the complex interplay between the intermolecular interactions and the substrate-adsorbate interactions played a very important role and was considered in detail.

In the following, the main results of the present thesis will briefly be summarized.

I As a first step, the structures of QA on Cu(111) and Ag(100) were investigated. The discussion of the results included the results of an earlier work by by Wagner *et al.* [15] regarding the structures of QA on Ag(111). It was found that on all three surfaces, the formation of intermolecular H-bonds is a dominant motif for the self-assembly of QA. After deposition at room temperature (RT), QA forms homochiral chains consisting of flat-lying molecules that are connected via two intermolecular H-bonds per QA molecule.[1] The intermolecular distance between neighboring QA molecules in a chain is determined by the length of the intermolecular H-bonds and is identical on all three surfaces within the margins of error. In contrast, the distance between neighboring parallel QA chains depends on the coverage

[1] Every QA molecule in a chain participates in the formation of 4 H-bonds. However, in the present thesis a single H-bond between two molecules is counted as 0.5 H-bonds per molecule.

because a repulsive substrate-mediated interaction between the chains causes them to maximize the distance between them. On all three surfaces, the QA chains exhibit a small set of distinct azimuthal orientations, which are mainly determined by the specific substrate-adsorbate interactions.

The primarily formed QA chains are metastable and undergo a phase transition upon annealing at 500 K. The kinetic barrier that stabilizes the QA chains is mainly related to the opening of the intermolecular H-bonds and a slight reconstruction of the first layers of the metal substrates. The resulting structures are heterochiral, i.e., they contain QA molecules of both chiralities, and commensurate with the substrate. The commensurability of the phases after annealing shows that they are the thermodynamically most stable structures of QA on all three surfaces. They exhibit fewer intermolecular H-bonds per molecule than the molecular chains, which is overcompensated by a stronger substrate-adsorbate interaction. This likely includes a stronger bonding between those oxygen atoms, which are not involved in the formation of H-bonds, and the metal atoms of the substrate.

In general, the structures on all three surfaces are very similar, yet there are some distinct differences. In particular, the structures of QA on Cu(111) consist of significantly smaller domains and exhibit a higher degree of defects than those on Ag(100) and Ag(111). This is explained by the higher chemical reactivity of Cu, which leads to a stronger bonding and reduced mobility of the QA molecules.

II The attempts to prepare similar molecular chains on thin layers of wide band gap materials, where they may be electronically decoupled from the metal substrate, yielded some very interesting and surprising results. For epitaxial layers of KCl on Ag(100), it was found that the structures of QA are strongly dependent on the thickness of the KCl layer. The adsorption energy of QA on pure KCl is small compared to the sublimation enthalpy of QA. As a consequence, on thick KCl layers (5 – 6 ML), the QA molecules do not wet the surface after deposition and form three-dimensional (3D) molecular clusters. In contrast, on thin KCl layers (2 – 3 ML), it was found that the molecules can interact through *van der Waals* interactions with the Ag substrate across the KCl layer, which contributes to the adsorption energy of QA. Thus, the adsorption energy of QA is larger than its sublimation enthalpy, which leads to adsorption in a flat-lying configuration and the formation of homochiral molecular chains.

Similar to the chains on the above-mentioned metal surfaces, the QA chains on KCl are also connected via intermolecular H-bonds of the same length as those on the metal surfaces. The chains exhibit distinct azimuthal orientations that are determined by the interactions with the underlying KCl layer, which was also confirmed by density functional theory calculations. Interestingly, the repulsive interaction between neighboring chains that was found on the metal surfaces was not observed on KCl, which means that it is not present anymore on the KCl layer. Overall, these are very promising results because they illustrate that even on

thick KCl layers the self-assembled formation of QA chains may be possible if the adsorption energy of QA was slightly larger. This could be achieved for example by modifying the QA molecules with additional functional chemical groups that exhibit a strong bonding to the KCl layer and/or increase the intermolecular interactions through additional H-bonds. Furthermore, additional functional chemical groups could also be used to increase the distance between neighboring chains, for example by adding chemical groups at the end of the molecules that repel one another.

The structures of QA on hexagonal boron nitride (hBN) are similar to those on thin KCl layers. There, QA also forms homochiral molecular QA chains with the same intermolecular distance within the margins of error. As on KCl, the repulsive interaction between neighboring chains could not be observed. The six distinct azimuthal chain orientations of QA are identical to those on Cu(111). This is a surprising result because the hBN layer exhibits a significant rotational mosaicity with respect to the Cu substrate. Thus, this result is tentatively explained by bare patches of Cu where the QA chains start growing with distinct azimuthal orientations and continue growing across the step onto the hBN layer. On the hBN layer, the chains are more curvy than on the metal substrates or the KCl layer. This shows that the electronic corrugation on hBN is smaller than on the other substrates.

Overall, the above results show that the intermolecular H-bonds also facilitate the growth of QA chains on thin layers of wide band gap materials. However, on thicker layers, which may be required in order to fully electronically decouple the molecules from the metal substrate, non-wetting and the formation of 3D clusters may occur. This problem may possibly be circumvented by increasing the adsorption energy of QA by adding functional groups to the molecule.

III Lastly, it was investigated, whether the observed QA structures can be influenced or modified by an increased amount of Ag steps. For QA on the vicinal Ag(100) surface it was found that, at RT, the nucleation of the chains occurs on terraces and not at step edges, resulting in the same four azimuthal orientations as on Ag(100). The chains are also capable of continuously growing across the Ag step edges, which reveals the importance of the intermolecular H-bonds as a structure-defining motif. In contrast, at elevated temperatures, the nucleation of the chains occurs at the Ag step edges, which leads to the preferential growth of two distinct symmetry equivalent domains. The fact that the Ag steps have a significant influence on the structures of QA at elevated temperatures is not only of importance for a better fundamental understanding of the interactions between adsorbates and metal step edges, but it is also very useful knowledge for the preparation of organic and inorganic structures on vicinal metal surfaces in the future.

The internal structure of the KCl layer on the vicinal Ag(100) surface is very similar to that on the nominally flat Ag(100) surface. However, in areas of the vicinal Ag(100) surface with a high step density, the KCl layer grows continuously across the Ag step edges in a carpet growth mode, which causes large-scale deformations in the KCl lattice. These deformations

allow a wider range of different adsorption configurations for the QA molecules on KCl, which include different azimuthal orientations. Many of these new adsorption configurations are likely energetically very similar to one another, which is why a wider range of azimuthal QA chain orientations was observed on KCl on the vicinal Ag(100) surface.

In conclusion, the results of the present thesis have shown that for QA the intermolecular H-bonds are a very strong structure-defining motif that can be used to tailor distinct organic structures on metal and insulating surfaces. It has been shown for the present case that the nanostructures are the result of a very delicate balance between the intermolecular and the substrate-adsorbate interactions. In addition, the tuning of experimental parameters such as the sample temperature or the substrate-adsorbate interactions can lead to a significant change in the structure.

For future works, measurements with X-ray photoelectron spectroscopy (XPS) and ultraviolet photoelectron spectroscopy (UPS) may yield very interesting insights into the electronic structure of the molecules and their bonding to the surface in the different observed phases of QA. Furthermore, it would be very interesting to investigate the optical properties of QA molecules on KCl or other insulating surfaces due to the head-to-tail configuration of the transition dipoles in QA chains. The spectra of individual molecules on different adsorption sites, chains of different lengths, and molecules adsorbed at step edges in different configurations could be compared. Such experiments may further promote our understanding of the intermolecular interactions, as well as substrate-adsorbate interactions, and their influence on the electronic structure of organic molecules on surfaces.

A Publications

A.1 "Hydrogen-Bonded One-Dimensional Chains of Quinacridone on Ag(100) and Cu(111): The Role of Chirality and Surface Bonding"

by Niklas Humberg, Rémi Bretel, Alexander Eslam, Eric Le Moal, and Moritz Sokolowski

published in: Physical Chemistry C **2020** 124(45), including Supporting Information.

DOI: https://doi.org/10.1021/acs.jpcc.0c07850

THE JOURNAL OF PHYSICAL CHEMISTRY C

pubs.acs.org/JPCC Article

Hydrogen-Bonded One-Dimensional Chains of Quinacridone on Ag(100) and Cu(111): The Role of Chirality and Surface Bonding

Niklas Humberg, Rémi Bretel, Alexander Eslam, Eric Le Moal, and Moritz Sokolowski*

Cite This: J. Phys. Chem. C 2020, 124, 24861−24873 Read Online

ACCESS | Metrics & More | Article Recommendations | Supporting Information

ABSTRACT: The adsorption and ordering of the prochiral molecule quinacridone (QA) on the Ag(100) and Cu(111) surfaces were studied by low-energy electron diffraction and scanning tunneling microscopy. Upon adsorption, the molecules form parallel homochiral chains of flat-lying molecules linked together via hydrogen bonds on both surfaces, but these chains show significant surface-dependent differences concerning their lateral order. On both substrates, the chains are not thermodynamically stable but only metastable and stabilized by kinetic barriers. On the Ag(100) surface, annealing induces a phase transition to a highly ordered and heterochiral structure with a reduced density of hydrogen bonds. The related loss of bonding energy is overcompensated by a stronger bonding to the substrate, yielding a commensurate structure. For QA on Ag(100), we propose that during the initial chain formation and the phase transition upon annealing, the molecules can change their handedness by rotating around their long axes. In contrast, the initial chain formation and the phase transitions of QA on the Cu(111) surface appear to be subject to stronger kinetic limitations. These are explained by stronger substrate molecule interactions on Cu(111), which reduce the diffusion and the possibility for a change of handedness in comparison to QA on Ag(100). We discuss how the intermolecular hydrogen bonds, the 2D chirality, and the different chemical reactivities of the two surfaces [Ag(100) and Cu(111)] influence the structural formation of QA aggregates. We compare our results to the results for QA on Ag(111) reported previously by Wagner et al. [*JPCC* **2014**, *118*, 10911-10920].

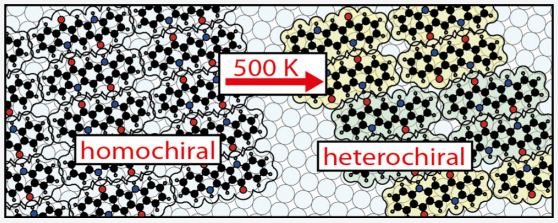

1. INTRODUCTION

Interfaces between organic semiconductors and metal surfaces play an important role in organic electronic devices, for example, organic field-effect transistors (OFETs),[1,2] organic light-emitting diodes (OLEDs),[3,4] or organic photovoltaics (OPVs).[5] Most investigations so far have focused on organic molecules with large π-conjugated systems because these usually have high electron and hole mobilities. From this point of view, the molecule 5,12-dihydro-quino[2,3-*b*]acridine-7,14-dione (quinacridone, QA) would be a poor candidate because its intramolecular conjugation is broken (cf. Figure 1a, below). However, Głowacki et al. found that QA exhibits promising properties for applications in electronic and optoelectronic devices.[6,7] These findings have motivated investigations on the potential applications of QA, its derivatives, and QA-based polymers in OFETs,[8−11] OLEDs,[12,13] and OPVs.[14−16] An overview is given in the review by Wang et al.[17] In particular, Głowacki et al. have reported a hole mobility of 0.1 cm^2 V^{-1} s^{-1} and a photocurrent of roughly 1 mA cm^2 for QA, which they attributed to strong intermolecular interactions via hydrogen bonds. Related to this aspect, one goal of our experiments, which we report here, was to find out how the intermolecular hydrogen bonds determine the structure formation and nucleation of aggregates of QA on surfaces.

QA ($C_{20}H_{12}N_2O_2$) exhibits a total of four isomers (two angular and two linear forms).[18] In this work, we investigated the linear *trans*-isomer, which is illustrated in Figure 1a. This isomer is a widely used organic pigment (Violet 19) and is industrially produced at a low cost. Important applications of Violet 19 are, for example, given by its use as a colorant in varnishes or printer toners.[19−21] Its molecular skeleton consists of five annulated carbon rings and is thus similar to that of pentacene. However, in contrast to pentacene, QA contains four functional groups that are responsible for the broken intramolecular conjugation on one hand but enable the molecule to form intermolecular hydrogen bonds on the other hand. These hydrogen bonds also play an important role in its crystal structures.[22−24] QA exhibits a variety of polymorphic crystal structures. These can be divided into two groups: The α- and β-phases consist of chains of parallel molecules with each molecule being bonded to both of its

Received: August 28, 2020
Revised: October 8, 2020
Published: November 4, 2020

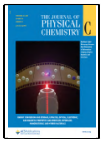

https://dx.doi.org/10.1021/acs.jpcc.0c07850
J. Phys. Chem. C 2020, 124, 24861−24873

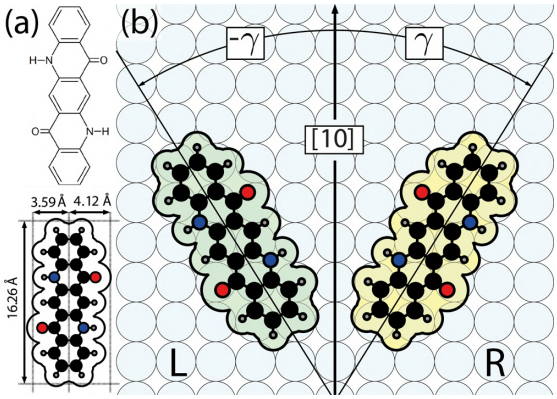

Figure 1. (a) Structural formula of QA and a hard sphere model, which shows the dimensions of the molecule. The dimensions of the molecule result from the bond lengths and van der Waals radii that were used for this model (cf. Section 2). The color code of the atoms is as follows: carbon = black, hydrogen = gray, nitrogen = blue, and oxygen = red. (b) Schematic illustration of the 2D chirality of the adsorbed QA molecule on the Ag(100) surface and the relationship between the two enantiomers. The two adsorption configurations are energetically equivalent. The angle $\gamma = 32°$ was chosen such that the orientations of the molecules with respect to the Ag(100) surface correspond to their azimuthal orientation in the α-phase (cf. Figure 2, below). The adsorption site is chosen arbitrarily.

neighbors via two hydrogen bonds, whereas the γ-phase shows a crisscross pattern where every molecule is bonded to each of its four neighbors via a single hydrogen bond.[23]

Besides the ability to form intermolecular hydrogen bonds, the concept of 2D chirality is an important structural aspect that is relevant for the adsorption of QA on surfaces.[25,26] Among the many possibilities through which chirality on surfaces may arise, the one relevant for QA is the adsorption of a prochiral molecule on a surface. The planar QA molecule is of C_{2h}-symmetry, which implies that it does not exhibit a mirror plane perpendicular to the molecular plane. This is also true for the molecule in the planar adsorption geometry and implies that the handedness of the molecule on the surface depends on which of its two sides adsorbs. Statistically, the adsorption leads to equal probabilities of the two enantiomers on the surface. The two enantiomers (denoted by R and L in the following) are expected to adopt energetically equivalent and mirror-symmetric adsorption configurations. These are illustrated in Figure 1b for QA on the Ag(100) surface, which will be the subject of this work. Each enantiomer is rotated by either $+\gamma$ or $-\gamma$ with respect to the [10] direction of the substrate, depending on its handedness. For one given enantiomer, the $+\gamma$ and $-\gamma$ orientations are not equivalent and yield different adsorption energies. In principle, QA can change its handedness on the surface by rotating around its long axis. This process involves the loosening of the bonds between the molecule and the surface and can therefore be expected to be inhibited by a kinetic barrier. This is especially the case for a π-conjugated planar molecule as QA, for which a planar adsorption geometry is energetically favored.[27]

A general question concerning the chirality of aggregates on surfaces concerns the preference toward hetero- or homochiral packing. A common hypothesis is that on surfaces, homochiral packing is preferred over heterochiral packing.[28] This is in contrast to the 3D situation where heterochiral packing is more common because racemates tend to have a higher density than the corresponding conglomerates.[29] However, in a recent review, Dutta and Gellman reported the absence of a significant statistical preference toward one of the two possibilities on surfaces.[28] It is believed that often, only a subtle balance between the various forces is responsible for hetero- or homochiral packing. In many cases, a small change in certain parameters (e.g., temperature or coverage) can cause a phase transition between phases of hetero- and homochiral packing.[26,28] However, these processes are not fully understood yet and whether there is a preference toward homo- or heterochiral packing is still an openly debated question, to which the present work contributes.

So far, QA has been subject to only few investigations on surfaces, for example, on the Ag(111) surface by Wagner at al.[30] and on graphene and MoS_2 by Trixler et al.[31,32] Beyond this, several studies of derivatives of QA on metal surfaces have been reported.[33−37] Typically, QA and its derivatives are found to adsorb intact in a planar orientation and to form ordered layers. Here, we report on the structures of ordered QA layers on the Ag(100) and Cu(111) surfaces. In comparison to QA on Ag(111),[30] it is of interest to investigate QA on Ag(100) because this surface exhibits a lower symmetry and is more open than the Ag(111) surface. For the Cu(111) surface, a higher reactivity compared to the Ag(111) surface and hence a stronger bonding and corrugation of the bonding potential of QA can be envisaged. This is also expected to hinder the change of the chirality of QA (L ↔ R) on the surface more effectively, which should manifest in a higher kinetic barrier for the ordering. We will report structure models for QA/Ag(100) and QA/Cu(111), compare them to the results obtained for QA on Ag(111),[30] and discuss how the surface symmetry and corrugation influence the ordering in competition with the formation of intermolecular hydrogen bonds.

2. EXPERIMENTAL SECTION

The experiments were carried out under ultrahigh vacuum (UHV) conditions with a base pressure of 3×10^{-10} mbar. Investigations were conducted using a beetle-type scanning tunneling microscope (type UHV 300) from RHK Technology, a spot profile analysis low-energy electron diffraction (SPA−LEED) instrument manufactured by Omicron, a microchannel plate LEED (MCP−LEED) instrument from OCI Vacuum Microengineering Inc., and a quadrupole mass spectrometer of the type PRISMA from Pfeiffer Vacuum. The Ag(100) and Cu(111) crystals were cleaned by cycles of sputtering with Ar^+ ions (800−1000 eV, 7 μA) for 30 min and subsequent annealing at 850 K (Ag) or 1000 K (Cu) for 1 h. The structural quality of the substrate crystals was checked by LEED. QA was purchased from HOECHST and purified by gradient sublimation.[11] It was evaporated from home-built evaporators at crucible temperatures of 650−670 K, while the substrates were held at room temperature (RT). During the evaporation process, the quadrupole mass spectrometry (QMS) signal of a QA fragment (m/z = 128, m(QA) = 312) was recorded and integrated over time. Optionally, the samples were annealed after deposition at temperatures above 400 K for 15 min as specified in the text below. The coverages θ were determined from the analysis of scanning tunneling microscopy (STM) images. We define the coverage of one monolayer (1 ML) as the coverage of a closed

https://dx.doi.org/10.1021/acs.jpcc.0c07850
J. Phys. Chem. C 2020, 124, 24861−24873

Table 1. Overview of the Structure Parameters of QA on Ag(100) and Cu(111), Which Were Obtained in This Work, Those of QA on Ag(111), Which Were Obtained by Wagner et al.,[30] and Those of the $(1\bar{1}2)$ Plane of the α^{I}-QA Polymorph.[23a]

	Ag(100)		Cu(111)		Ag(111)[30]		α^{I}-QA[23]
	α-phase	β-phase	α'-phase	β'-phase	α-phase	β-phase	$(1\bar{1}2)$-plane
M	$\begin{pmatrix} 2 & 1.25 \\ -3 & 4.80 \end{pmatrix}$	$\begin{pmatrix} 4 & 3 \\ -5 & 3 \end{pmatrix}$	$\begin{pmatrix} 2.1 & -1.0 \\ 5.6 & 7.1 \end{pmatrix}$	$\begin{pmatrix} 6.5 & 0.8 \\ 3.8 & 11.3 \end{pmatrix}$	$\begin{pmatrix} 3 & 2 \\ -1.5 & 6 \end{pmatrix}$	$\begin{pmatrix} 5 & 5 \\ -1 & 5 \end{pmatrix}$	not applicable
b_1/Å	6.8 ± 0.1	14.445	7.0 ± 0.3	15.6 ± 0.2	7.0 ± 0.5	14.445	6.9
b_2/Å	16.4 ± 0.1	16.848	16.6 ± 1.0	25.3 ± 0.2	20.0 ± 0.2	16.088	16.9
α/°	90 ± 1	112.2	90 ± 1	94 ± 1	90	111.1	110.3
Z	1	2	1	4	1	2	1
A/Å^2	111.5 ± 0.2	225.4	116 ± 10	395 ± 15	142.1	216.8	109.2

[a]All surface structures belong to the space group $P2$. The angle between the vectors $\mathbf{b}_1$ and $\mathbf{b}_2$ is called α,Z denotes the number of molecules per unit cell, and the area of the unit cells is named A. Errors of the matrix entries are given in the text. For the calculation of the vector lengths of the unit cells, the lattice constants at 300 K for Cu (3.597 Å) and Ag (4.079 Å) were used.[55]

layer of flat-lying molecules in the β-phase on Ag(100) (see Table 1).

All SPA–LEED measurements were carried out in a separate UHV chamber at a sample temperature of 110 or 214 K in order to minimize the thermal diffuse background. In order to avoid beam damage, which was reported by Wagner et al. for QA on Ag(111),[30] the beam current was always kept as small as possible (<5 nA). Thus, no problems with degrading LEED patterns were encountered. A 2D image with sharp spots (α-phase, Figure 2d, below) was assigned to a coverage of θ = (1.00 ± 0.05) ML (we note that the difference of the coverages between the α- and β-phases is negligible within the error). With this, all the other coverages were determined from the corresponding relative deposition integrals. The distortions of the 2D SPA–LEED images were corrected by using a self-written plug-in for the free software Fiji.[38] This plug-in can correct radial and tangential distortion according to the Brown–Conrady distortion equation.[39] For this purpose, the images were superimposed with a simulated diffraction pattern of the substrate. Then, the images were dewarped by hand until the experimental substrate spots were in good agreement with those of the simulation. The analysis of the LEED patterns was carried out via a trial and error procedure. For this purpose, the program Spot-Plotter[40] was used to simulate a diffraction pattern that is in good agreement with the LEED pattern.

Prior to starting the STM measurements, the prepared layers were checked using MCP–LEED in order to ensure the presence of a well-ordered layer and comparability to the SPA–LEED images of the same phases. All STM images were recorded in the constant current mode at RT. As the tip, a self-cut Pt/Ir (90:10) wire was used. The bias voltage refers to the sample, while the tip was on ground potential. The images were processed using the programs Gwyddion[41] and SPIP.[42] The coverages were determined by pixel counting. Pixels above a certain intensity threshold were attributed to molecules and the rest to the bare substrate. We estimate the margins of error for the coverages to be ±0.05. If not stated otherwise, the processing consisted only of filtering out horizontal, vertical, or nondirectional noise and adjusting the contrast of the images. The structure models of the investigated systems were created with the free program Graphics Layout Engine.[43] The hard sphere model of QA was drawn using bond lengths[44] and van der Waals radii[45] from the literature.

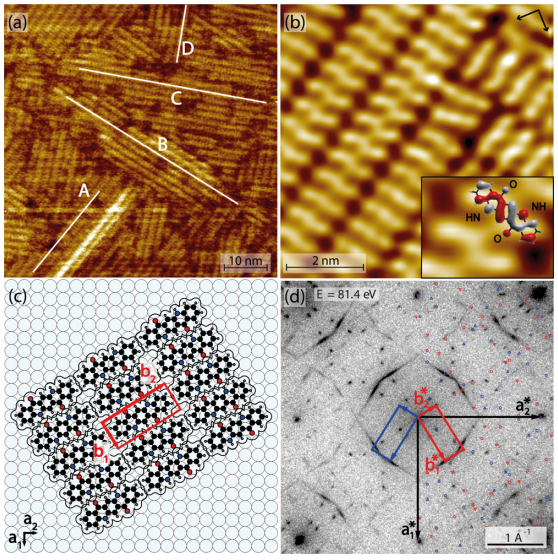

Figure 2. Complete monolayer of QA on the Ag(100) surface in the α-phase. (a) Overview STM image (U_{Bias} = −1.5 V, I = 0.25 nA). The structure consists of domains of parallel chains with four distinct orientations A–D which are marked by the white lines. Image size: 65 × 65 nm^2. (b) Zoom-in of (a) that shows the molecular arrangement. Image size: 12 × 12 nm^2. The arrows in the top right corner indicate the [10] and [01] directions of the substrate. The inset shows two molecules with a characteristic S-shape. The upper right one is superimposed with the calculated HOMO of the isolated molecule.[46] (c) Structure model of the α-phase of QA on the Ag(100) surface. The unit cell corresponds to the red unit cell in (d). (d) SPA–LEED pattern (T = 110 K, E = 81.4 eV). On the right hand side, the pattern is superimposed with the corresponding simulated LEED pattern. The unit cells of two mirror domains which resemble different enantiomers are depicted in blue and red. The circles and triangles mark spots belonging to two rotational domains of one enantiomer. Spots that are not reproduced by the simulation can be explained by multiple scattering.

3. RESULTS AND DISCUSSION

We start with the presentation of the results for QA on Ag(100) in Section 3.1 and then move to the more disordered structures of QA on Cu(111) in Section 3.2. An overview on all considered structures is given in Table 1.

https://dx.doi.org/10.1021/acs.jpcc.0c07850
J. Phys. Chem. C 2020, 124, 24861−24873

3.1. QA/Ag(100). In Sections 3.1.1 and 3.1.2, we report on the phase that forms directly after deposition of a full monolayer or submonolayer on Ag(100) at RT. We will call this phase α-phase from now on. After annealing, it transforms into a second 2D ordered and commensurate phase. This phase is named β-phase and will be discussed in Section 3.1.3.

3.1.1. QA/Ag(100)—α-Phase (Complete Monolayer). Figure 2a shows an STM image of a complete monolayer of the α-phase. The ordered layer consists of domains which can grow up to 1000 Å in width but do not grow across step edges. Each domain consists of parallel chains of lengths between 50 and 1000 Å. The chains exhibit distinct azimuthal orientations rotated by $\pm$ (31.2 $\pm$ 0.5)° with respect to the [10] direction of the Ag(100) substrate (cf. Figure 1b). Hence, the combination of two mirror domains and the fourfold rotational symmetry of the Ag(100) surface yields a total of four symmetry-equivalent azimuthal orientations of the QA domains. These orientations are illustrated by the white lines A−D in Figure 2a. The existence of four symmetry-equivalent domains and their azimuthal orientations with respect to the substrate is in agreement with SPA−LEED results, which will be discussed later.

An STM image with molecular resolution is shown in Figure 2b. It shows that the QA chains consist of parallel flat-lying molecules with their long sides next to each other. This arrangement can be attributed to two strong intermolecular O···H−N hydrogen bonds which can form between neighboring molecules within a chain. This is illustrated by the hard sphere model given in Figure 2c. However, the formation of these two hydrogen bonds is only possible if two neighboring molecules have the same handedness because otherwise, we would not have opposing NH- and CO-groups. Therefore, we deduce that the chains are enantiopure. We further propose that not only the individual chains but also the entire domains are enantiopure. This implies that all chains in one domain are composed of molecules with the same handedness. This is a consequence of the fact that for a change in the handedness, we expect a change in the molecular orientation ($+\gamma \rightarrow -\gamma$), as described on page B, and hence the orientation of the chains. This conclusion is also in agreement with our STM results. The molecules in Figure 2b show a characteristic S-shape that was already reported for QA on graphene[31] and can be used to distinguish between enantiomers. The STM image confirms that the individual chains as well as the whole domains are, except for occasional defects, enantiopure. As shown in the inset of Figure 2b, the observed S-shape can be understood by the shape of the HOMO of an isolated QA molecule in the gas phase, which was calculated by density functional theory.[46] Thus, the handedness of the molecules on the surface can be determined. It is important to note that the S-shape could not always be observed. We think that its occurrence is highly dependent on the quality of the STM tip and potentially other scanning parameters.

Figure 2d shows a SPA-LEED pattern of the α-phase. In addition to the specular spot, the first- and second-order spots of the substrate are seen. The analysis of the pattern yields the following superstructure matrix

$$\mathbf{M}_{\alpha} = \begin{pmatrix} 2 & 1.25 \\ -3 & 4.80 \end{pmatrix}$$

The margin of error on the noninteger matrix elements is estimated to be ±0.03. Spots that are not reproduced by the simulation can be explained by multiple scattering at the first- or second-order spots of the substrate. The matrix corresponds to a rectangular unit cell ($\alpha = 90 \pm 1°$) with $b_1 = (6.8 \pm 0.1)$ Å and $b_2 = (16.4 \pm 0.1)$ Å. The unit cell contains one molecule. The superstructure exhibits two mirror domains with two rotational domains each. For the definitions of $\mathbf{b_1}$ and $\mathbf{b_2}$, we refer to the structure model for the α-phase of QA on Ag(100) in Figure 2c. The length b_1 corresponds to the intermolecular distance between neighboring molecules within one chain. The distance between two chains is given by b_2 and corresponds to the length of the molecule (i.e., 16.26 Å). The vectors $\mathbf{b_1}$ and $\mathbf{b_2}$ of the unit cell are rotated symmetrically by $\pm$ (32.0 $\pm$ 0.5)° with respect to the [10] or [01] direction of the Ag(100) surface. Both the size and shape of the unit cell and its azimuthal orientation with respect to the substrate are in agreement with the STM results.

Because the values in the first column of the matrix are integers, the structure is of the point-on-line type.[47] This means that all lattice points of the superstructure fall on the same set of lattice lines of the substrate (here, those in the [01] direction). This indicates that besides the intermolecular interactions, the substrate−adsorbate interactions also play a significant role in the structure formation. A comparison of the observed structure to that of the net planes of QA bulk crystals shows that it is very similar to the $(1\bar{1}2)$ plane of the α^{I}-QA bulk structure.[23] Similar to the α-phase, the $(1\bar{1}2)$ plane consists of parallel molecular chains. In particular, the distance b_1 is identical to the distance between the molecules in the chains of the $(1\bar{1}2)$ plane within the margin of error. The distance b_2 deviates by only 3.6% from the distance between the chains in the $(1\bar{1}2)$ crystal plane. Thus, we assume that the molecular arrangement within the α-phase is related to intermolecular interactions very similar to those in the α^{I}-QA bulk structure.

The SPA−LEED pattern (Figure 2d) consists mainly of two prominent sets of spots. For a constant length of the scattering vector, both sets provide four pairs of spots. The two spots of a pair enclose an angle of (23.5 $\pm$ 0.5)° and are located symmetrically around the [11] direction of the substrate. The spots of the first set are sharp and are partly very close to the specular spot at a distance of b_2^*. The second set is further away at a distance of b_1^*. The spots of the second set show a strong broadening into streaks in the direction of $\mathbf{b}_2^*$, but they are sharp in the direction of $\mathbf{b}_1^*$. This broadening is not due to azimuthal disorder because the streaks are straight and not circular with respect to the specular spot. Instead, it is caused by defects in the structure that are quite frequent, namely, neighboring chains that are not correlated in the direction of $\mathbf{b_1}$, that is, the chains are shifted relative to each other in the chain direction. This absence of correlation leads to the strong broadening of the spots at $(\pm 1, 0) = \pm\mathbf{b}_1^*$ in the direction of $\mathbf{b}_2^*$, that is, the direction perpendicular to the chains. These defects can also be seen in the STM image in Figure 2b. However, for the considered full layer, the distance between the chains (in the direction of $\mathbf{b_2}$) is well defined. Therefore, the spots at $(0, \pm k) = \pm k \cdot \mathbf{b}_2^*$ (with k = 1, 2, and 3) are sharp in the direction of $\mathbf{b}_2^*$.

3.1.2. QA/Ag(100)—Submonolayer Coverage. So far, we have considered the α-phase at a coverage of a complete monolayer. Figure 3a,b shows STM images of QA on Ag(100) for θ = 0.40 ML. The layer is similar to the full monolayer, except that the average distance between neighboring chains b_2 is roughly twice as large as that in the full monolayer.

https://dx.doi.org/10.1021/acs.jpcc.0c07850
J. Phys. Chem. C 2020, 124, 24861−24873

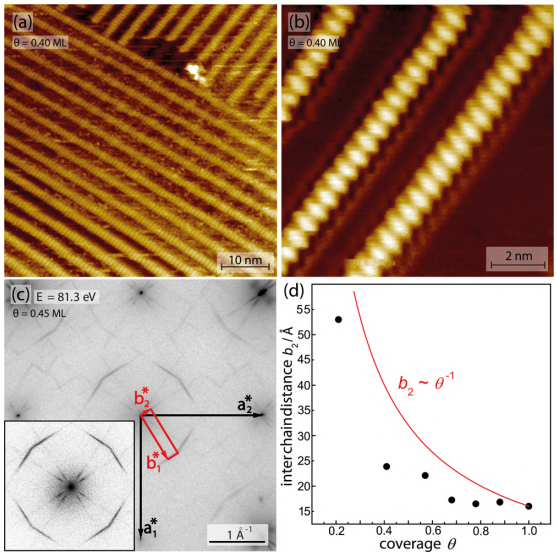

Figure 3. Submonolayer of QA on the Ag(100) surface. (a) Overview STM image ($U_{Bias} = -1.5$ V, $I = 0.25$ nA). With decreasing coverage of QA, the distance between the chains increases. Image size: 55 × 55 nm^2. (b) Zoom-in of (a). Image size: 12 × 12 nm^2. (c) SPA–LEED pattern ($T = 110$ K, $E = 81.4$ eV). The inset shows a blowup of the region around the specular spot. The unit cell of one domain is depicted in red. The spots are smeared out into streaks (cf. text) because of a lack of interchain correlations. (d) The distance between the chains b_2 depends on the coverage θ. The length was determined by SPA–LEED. The data point for $\theta = 0.45$ ML in (c) is not included because no line profile was recorded for this preparation. The point at $\theta = 0.20$ ML was extracted from STM data. For the discussion of the red line, see text. The coverage determination is explained in the Experimental Section, and we estimate the error of the coverage to be about 20%.

Furthermore, this distance is not constant within one domain but varies between 28 and 39 Å. On average, it is $b_2 = (33 \pm 3)$ Å (The error margin denotes the standard deviation). The intermolecular distance between molecules along the chains b_1 remains unchanged. This is in agreement with our above conclusion that the distance b_1 is given by the intermolecular hydrogen bonds and is therefore independent of the coverage.

The dependency of the length b_2 on the coverage was investigated for six coverages between 0.4 and 1 ML by SPA–LEED. An exemplary SPA–LEED pattern at $\theta = 0.45$ ML is shown in Figure 3c. The lowering of the coverage has two significant effects on the diffraction pattern. The first is that the length of the vector $\mathbf{b}_2^*$ decreases, which corresponds to the increased average distance between neighboring chains. The second more obvious effect is that the sharp spots related to $\mathbf{b}_2^*$, which were observed for the full monolayer, are smeared out into streaks. The reason is that the distance between neighboring chains is not constant. This leads to a radial broadening of the spots related to $\mathbf{b}_2^*$ and the corresponding higher-order spots. Of course, the broadening related to the lack of a correlation between the chains in the $\mathbf{b}_1$ direction, which we described for the α-phase, is also present. The analysis of this SPA–LEED pattern (Figure 3c) yields an averaged unit cell that is similar to that of the full monolayer. The length of the vector $\mathbf{b}_1$ and its azimuthal orientation are unchanged. The only difference resides in the length of the vector $\mathbf{b}_2$, which depends on the coverage θ. The dependency of b_2 on θ is illustrated in Figure 3d. Most data points were obtained from SPA–LEED line profiles through the specular spot in the direction of $\mathbf{b}_2^*$. Only the data point at $\theta = 0.20$ ML was inferred from STM images. We found that the average interchain distance grows with decreasing coverage. In the simplest model, which assumes that the neighboring chains are equally spaced by the distance b_2, one expects a $b_2 \sim \theta^{-1}$ correlation. This is illustrated by the red curve in Figure 3d, which shows the same trend as the data, but may be offset because of an underestimation of the coverages determined from the deposition integrals. At present, we cannot exclude that b_2 drops to the value of ~17 Å, which is close to b_2 of the α-phase (16.4 Å), around a coverage of $\theta = 0.60$ ML. This may indicate a phase transition to the α-phase. In this situation, the deviation of the coverage from the coverage of the ideal α-phase is expected to cause a high defect density.

STM images (Figure 3a,b) reveal that neighboring chains are always aligned parallel to each other as in the full monolayer, although their distance is increased. Even for a coverage of only 0.2 ML, where neighboring chains have distances of up to 60 Å between them, this is still the case. A similar behavior was already found by Lukas et al. for chains of pentacene on Cu(110).[48] The authors attributed this behavior to long-range substrate-mediated repulsive interactions between the chains that are induced by charge density waves in the 2D electron gas of a surface state.[49,50] Other examples for this kind of long distance interaction of molecular chains on a metal surface are the self-assemblies of L-methionine on Cu(111)[51] and Ag(111).[52] Although the Ag(100) surface does not support a Shockley surface state,[53] we suggest that the interaction is mediated by substrate electrons here too. An interaction mechanism of this kind has been reported on Ag(100), for example, for Li atoms.[54]

3.1.3. QA/Ag(100)—β-Phase. After annealing at 500 K for 15 min, the α-phase changes irreversibly into a different but also highly ordered phase, which we call β-phase. Upon annealing, the superstructure LEED pattern of the α-phase completely vanished at roughly $T = 470$ K. Faint spots of the β-phase started to appear at roughly 430 K and steadily increased in intensity upon further cooling to RT. This implies that the α-phase does not directly transform into the β-phase but transforms via a disordered phase at higher temperatures that transforms into the β-phase upon cooling. The transformation is irreversible because the transition between the β-phase and the disordered phase can be induced again by heating, but it is impossible to go back to the α-phase. This phase transition takes place for the full monolayer and submonolayer coverages. In the latter case, the molecules form islands of the β-phase and leave the rest of the substrate surface uncovered.

Two STM images of the β-phase are shown in Figure 4a,b. The image in (a) shows two mirror domains separated by the edge of a double step of the substrate. Because of symmetry reasons, for both these domains, a symmetry-equivalent rotational domain exists, which yields again a total of four symmetry-equivalent domains. The domains can reach a size of at least 1000 Å in both lateral dimensions and are limited in size only by Ag steps. Accordingly, we were not able to find domain boundaries between symmetry-equivalent domains, except for the noted ones at step edges of the substrate. The

https://dx.doi.org/10.1021/acs.jpcc.0c07850
J. Phys. Chem. C 2020, 124, 24861−24873

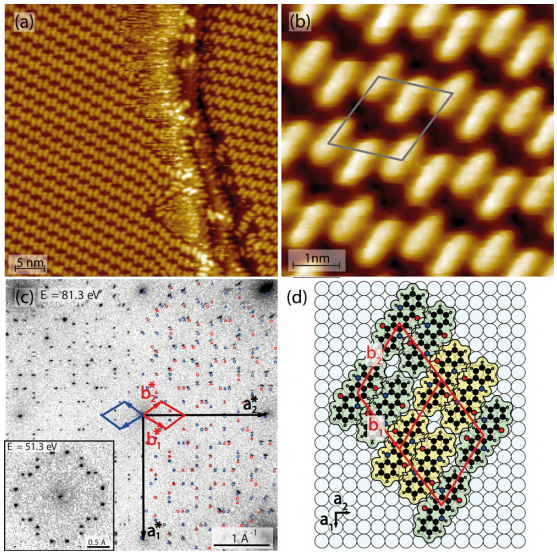

Figure 4. Full monolayer of QA on the Ag(100) surface in the β-phase after annealing the α-phase at 500 K for 15 min. (a) Overview STM image (U_{Bias} = −1.5 V, I = 0.25 nA) with a double step edge. Every bright ellipsoid corresponds to a single QA molecule. The image shows two different mirror domains. Image size: 35 × 35 nm^2. (b) Zoom-in of (a) for better visibility of the molecular arrangement. The unit cell is indicated in gray. Image size: 5 × 5 nm^2. (c) SPA–LEED pattern (T = 110 K, E = 81.3 eV). On the right hand side, the pattern is superimposed with the corresponding calculated LEED pattern. The unit cells of two mirror domains are depicted in blue and red. The inset shows the area around the specular spot of the β-phase at an electron energy of E = 51.3 eV. (d) Structure model of a full monolayer of QA on the Ag(100) surface in the β-phase. The unit cell corresponds to the red unit cell in (c) and depicts a different domain from the one that is shown in (b). It can be translated into the domain depicted in (b) by mirroring at the plane along $\mathbf{a}_1$ and rotating it by 90° (structure models of all four domains can be found in the Supporting Information). STM and SPA–LEED measurements yield the small unit cell given by the vectors $\mathbf{b}_1$ and $\mathbf{b}_2$. The large unit cell (composed of the small ones) takes into account the chirality (indicated by the colors yellow and green) of the molecules and is therefore twice as large as the small one. For detailed explanations, see text. The adsorption sites were chosen arbitrarily. All molecules on the corners of the unit cell are on identical adsorption sites.

molecular arrangement within these domains is shown in Figure 4b.

Figure 4c shows a SPA–LEED pattern of the β-phase. As expected from the STM images, the diffraction pattern is highly symmetric and consists of sharp spots. In contrast to the α-phase, no broadening of the spots can be detected. The analysis was carried out as described above and yielded a simulated diffraction pattern that accounts for all the observed spots and fits the experimental pattern. The corresponding superstructure matrix is

$$\mathbf{M}_\beta = \begin{pmatrix} 4 & 3 \\ -5 & 3 \end{pmatrix}$$

This corresponds to a unit cell with b_1 = 14.445 Å, b_2 = 16.848 Å, and α = 112.2° with α being the angle between $\mathbf{b}_1$ and $\mathbf{b}_2$. Similar to the α-phase, this superstructure also exhibits two mirror domains, both of which have two rotational domains, which is in agreement with the STM results. The unit cell contains two molecules, and the vector $\mathbf{b}_2$, which corresponds to the direction of the long axes of the molecules, is rotated by 31° with respect to the [10] direction of the substrate (32° for the α-phase for comparison). All the elements of the matrix are integers, which reveals that the structure is commensurate.

A structure model of the β-phase is shown in Figure 4d. The molecular arrangement was derived from STM images. The molecules arrange in dimers that form periodically indented and parallel chains. Evidently, the two molecules of a dimer have to be of the same handedness (RR or LL) in order to form two hydrogen bonds between them. However, because of the periodic offsets within the chains, it is impossible to form two hydrogen bonds between neighboring dimers. In order to form at least one hydrogen bond, it is necessary to switch the handedness periodically from dimer to dimer (yielding RRLL or LLRR). However, this leads to a structure with two different enantiomers on the corners of the unit cell that is derived from LEED and STM (cf. Figure 4d). Thus, the size of the unit cell in the direction of $\mathbf{b}_1$ has to be doubled if the chirality is accounted for. The fact that neither the STM nor the SPA–LEED images indicate this larger unit cell can be explained as follows: the differences in the geometric structures between the two enantiomers are very small with respect to identical parts, and the expected additional LEED spots are thus very weak. Apparently, the LEED images do not resolve these spots and hence cannot distinguish between the two enantiomers and yield the smaller unit cell. As noted in Section 3.1.1, for the α-phase, we could distinguish between the two enantiomers in STM images. However, for the β-phase, we were not able to achieve this.

It is interesting to note that the orientation of the vector $\mathbf{b}_2$, which corresponds to the direction of the long axis of the molecule, differs by only 1° (3.3%) for the two phases (α and β). This shows that the orientation of the molecules with respect to the substrate is identical before and after the phase transition. Furthermore, a comparison of the unit cells reveals that this is also true for the molecular density. In the β-phase, it is reduced by only 1.08% with respect to the α-phase. However, the number of hydrogen bonds per molecule is reduced by a factor of 0.75 compared to that in the α-phase.

3.2. QA/Cu(111). We turn to the results for QA on the Cu(111) surface. Section 3.2.1 deals with the structure of the full monolayer directly after the deposition at RT. We will call it α'-phase. In Section 3.2.2, we describe the structure of a full monolayer of QA on Cu(111) after annealing, named β'-phase. The structural order of the β'-phase is significantly limited by kinetic limitations. Section 3.2.3 describes our results for submonolayer coverages prior to and after annealing. Because of the lower coverages, the results after annealing differ from those of the full monolayer.

3.2.1. QA/Cu(111)—α′-Phase (Complete Monolayer). Figure 5a shows an STM image of a layer with a coverage of roughly 0.95 ML, which was obtained directly after deposition at RT. Similar to QA on Ag(100), the molecules form homochiral parallel chains because of intermolecular hydrogen bonds. Because of the higher symmetry (sixfold instead of fourfold) of the Cu(111) surface, every chain exhibits one of six distinct orientations instead of four [as on Ag(100)]. However, the structure appears to be significantly more disordered than its counterpart on Ag(100). On Cu(111), the chains do not form large ordered domains, and there are

https://dx.doi.org/10.1021/acs.jpcc.0c07850
J. Phys. Chem. C 2020, 124, 24861−24873

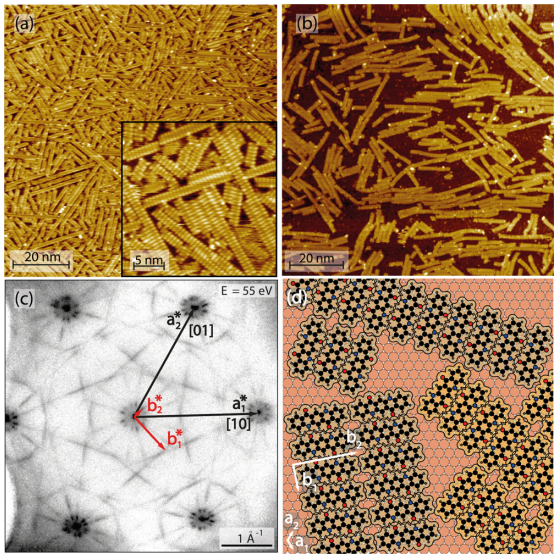

Figure 5. Complete monolayer of QA on the Cu(111) surface in the α'-phase. (a) Overview image at a coverage of θ = 0.95 ML (U_{Bias} = −1.5 V, I = 0.25 nA). Image size: 100 × 100 nm^2. The inset shows a zoom-in of the structure. Image size: 25 × 25 nm^2. (b) Overview image at a coverage of θ = 1.40 ML. It shows the growth of QA chains in the second layer on top of the monolayer of the α'-phase. Image size: 100 × 100 nm^2. (c) SPA−LEED image at a coverage of θ = 0.50 ML (T = 110 K, E = 55 eV). The superstructure is almost identical to the one observed for the complete monolayer except that the vector $\mathbf{b}_2^*$ is ca. 50% shorter (cf. Figure 7b and text). (d) Structure model of QA on Cu(111) in the α'-phase. The model encompasses three symmetry-equivalent chain directions.

even single chains that have no parallel neighboring chains at all. The high amount of only small stripelike domains leads to a high density of uncovered surface areas between the domains. We believe that this growth behavior is due to the stronger substrate−adsorbate interactions compared to those on Ag(100). Such stronger interactions support the nucleation of new chains but inhibit the ordering of the chains into larger domains and hence, in total, lead to more disorder. When molecules are deposited onto a full monolayer of QA at RT, a second layer begins to form on the top. This is illustrated in Figure 5b. The STM image shows that the molecules form the same kind of chains in the second layer. However, in contrast to the chains of the monolayer, the chains in the second layer are slightly bent and adopt fully arbitrary azimuthal orientations. This is likely due to smaller vertical interactions between the molecules in the second layer and the first layer in comparison to the interactions across the monolayer/Cu(111) interface.

A representative LEED pattern of the monolayer structure is shown in Figure 5c. It consists of six pairs of sharp spots around the specular and first-order spots of the substrate that correspond to the distance b_2 between neighboring chains. The rest of the pattern is made up of streaks, which indicates the lack of correlation between neighboring chains. The displayed pattern was actually recorded at a submonolayer coverage (θ = 0.50 ML) using the SPA−LEED instrument. However, it can be considered as a representative for the full monolayer too because the patterns are almost identical. We will discuss this LEED pattern in more detail later. A corresponding structure model is shown in Figure 5d. For the superstructure matrix and the corresponding structure parameters, we refer to Table 1. Except for the much smaller size of domains, the α'-phase on Cu(111) is very similar to the α-phase of QA on Ag(100). As on Ag(100), the straight segments of the chains need to be enantiopure in order to form two intermolecular hydrogen bonds between neighboring molecules. However, on Cu(111), the chains contain much more defects because of a higher amount of molecules of the "wrong handedness".

3.2.2. β'-Phase (Complete Monolayer). Similar to the α-phase on Ag(100), the α'-phase on Cu(111) transforms upon annealing at $T \geq$ 400 K. However, for QA on Cu(111), the preparation of an ordered complete monolayer of the same quality as on Ag(100) was more difficult. We believe that this is due to larger kinetic barriers at high coverages, which in turn are due to the larger QA/Cu(111) interactions. The best results were achieved after annealing at 500 K for 15 min and subsequent cooling to RT. These will be presented in the following.

An STM image of the β'-phase at a coverage of θ = 0.95 ML is shown in Figure 6a. It shows an area with a gradual transition from an ordered structure (left side), which, however, contains a large amount of small holes and larger defects, to a disordered structure composed of chainlike aggregates (right side). The molecular arrangement within the ordered structure can be seen in Figure 6b, and a corresponding structure model is shown in Figure 6d. The structure consists of parallel molecular chains, which are held together by hydrogen bonds. However, here (in contrast to the α'-phase), the chains consist of two regularly alternating segments. One segment is a dimer that consists of two molecules of the same handedness which are connected via two hydrogen bonds (LL or RR). The second segment is given by two molecules with different handednesses (LR or RL). Both molecules of this segment form only one hydrogen bond with their outer next neighbors because they have a different handedness from these. This implies that the handedness switches three times between two dimers of the LL and RR types (LLRLRR or RRLRLL). One defect that occurs quite regularly is that only a single molecule instead of two is located between two dimers (RRLRR or LLRLL). This leads to a gap in the direction of the long QA axis between two adjacent chains, which causes uncovered Cu patches apparent as the "holes" with a characteristic S-shape. These are indicated by the blue circles in Figure 6a,d.

A SPA-LEED pattern of this structure and a corresponding simulation are shown in Figure 6c. The spots of the first and second orders (corresponding to $\mathbf{b}_1^*$ and $\mathbf{b}_2^*$) are very weak, whereas the spots of higher orders are intense. Some of these spots are elongated, which are explained by the fact that they consist of two or more spots that are very close to each other (cf. Figure 6c). The analysis yielded a unit cell which is in good agreement with the structure deduced from the STM images. The corresponding superstructure matrix is

$$\mathbf{M}_{\beta'} = \begin{pmatrix} 6.5 & 0.8 \\ 3.8 & 11.3 \end{pmatrix}$$

We estimate that the error margin for all elements of the matrix is ±0.2. The matrix corresponds to a unit cell with b_1 = (15.6 ± 0.2) Å, b_2 = (25.3 ± 0.2) Å, and α = (94 ± 1)° with α being the angle between $\mathbf{b}_1$ and $\mathbf{b}_2$. The length b_1

https://dx.doi.org/10.1021/acs.jpcc.0c07850
J. Phys. Chem. C 2020, 124, 24861−24873

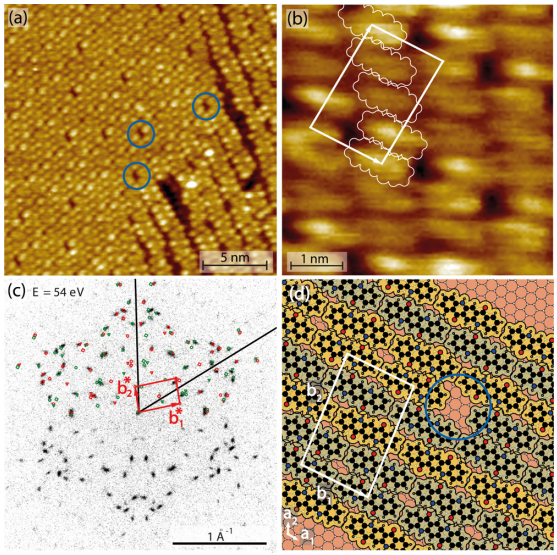

Figure 6. Complete monolayer of QA on the Cu(111) surface in the β'-phase. (a) Overview image at a coverage of θ = 0.95 ML (U_{Bias} = −1.5 V, I = 0.25 nA). Image size: 21 × 21 nm^2. The blue circles mark a common type of defect that can also be seen in (d) on the right-hand side. (b) Close-up of the structure (U_{Bias} = −1.5 V, I = 0.25 nA). Image size: 5 × 5 nm^2. It shows a domain symmetry-equivalent to the one shown in (a). The unit cell determined from the STM image is depicted in white. (c) SPA−LEED image at a coverage of θ = 1 ML (T = 214 K, E = 54 eV). The upper half of the image is superimposed with a simulation of the diffraction pattern. The corresponding unit cell is depicted in red and corresponds to the matrix given in the text. The long black lines point toward first-order spots of the substrate. (d) Structure model of QA on Cu(111) in the β'-phase. The blue circle marks a certain kind of defect, which can be seen in (a). The image in (a) depicts a different mirror domain, which leads to the mirrored shape of the defects. The white lines mark the unit cell. The handedness of the molecules was determined by the position of the molecules relative to their next neighbors in the chain (adjacent molecules connected by hydrogen bonds). Offsets in the direction of $\mathbf{b_1}$ between two molecules cause changes of the handedness along the chains. The displayed unit cell does not take into account the handedness of the molecules. The small deviation in the shape of the unit cell compared to that indicated in (b) is due to the distortion of the STM image.

matches the length of the molecule, and the length b_2 corresponds to 4 times the width of the molecule.

Overall, there are two aspects in which the β'-phase differs from the α'-phase: the disordered assembly of mostly straight and homochiral chains has transformed into ordered domains. In contrast to the α'-phase, these are made up by heterochiral (not homochiral) chains with periodic offsets. However, the orientation of the individual molecules with respect to the substrate remains nearly the same (within 4°).

3.2.3. QA/Cu(111)—Submonolayer Coverage. We turn to our results for submonolayer coverages of QA on Cu(111) directly after deposition at RT and after subsequent annealing at 600 K. After annealing at 400 or 500 K and subsequent cooling to RT, various chainlike structures were observed. For annealing at 600 K, a single structure prevailed, which did not change upon further annealing, and we will focus on this structure below.

We start with the phase which was present on the surface directly after deposition. An STM image at a coverage of θ = 0.40 ML is shown in Figure 7a. As on Ag(100), the

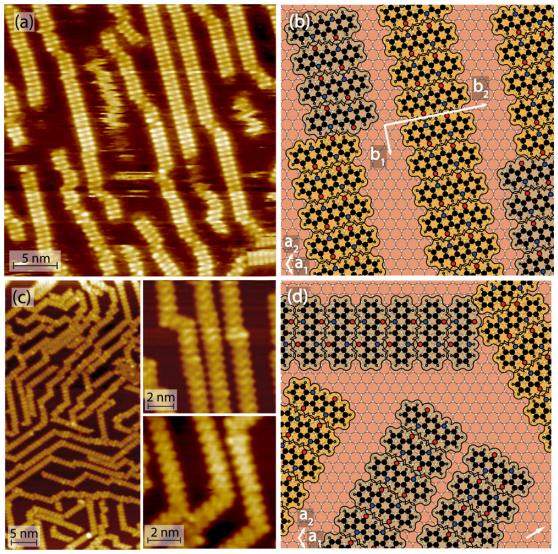

Figure 7. Submonolayer structures of QA on the Cu(111) surface after deposition at RT (a,b) and after annealing at 600 K (c,d). (a) STM image (U_{Bias} = −1.5 V, I = 0.35 nA) at a coverage of θ = 0.50 ML. (b) Structure model corresponding to (a). The average unit cell was determined from a SPA-LEED image and is indicated in white. The length b_2 varies with coverage. (c) STM images (U_{Bias} = −1.5 V, I = 0.25 nA) at a coverage of θ = 0.50 ML after annealing at 600 K for 15 min. The two smaller images show chains in the same direction, which consist of different enantiomers. (d) Structure model corresponding to (c). Each chain adopts one out of three directions that correspond to the main directions of the substrate ([10], [01], and [11]). The individual chains are homochiral, but all chains in all three directions can be made up of both enantiomers. The arrow in the bottom right corner indicates the [12] direction of the substrate.

submonolayer structure differs from the structure of the full monolayer mainly by a larger average distance between neighboring chains. Here, the distance between neighboring chains varies strongly. It was measured for 50 pairs of neighboring chains and ranges from 24 to 53 Å with the average distance being (37 ± 7) Å (the error margin denotes the standard deviation). This is presumably caused by similar long-range repulsive interactions that were deduced before for QA on Ag(100). The intermolecular distance within a chain was obtained from averaging over ∼100 distances and is (6.4 ± 0.1) Å. This value is within the margin of error identical to the corresponding value for QA on Ag(100). This reveals that the main driving forces for the formation of QA chains on Cu(111) directly after deposition at RT are the intermolecular hydrogen bonds between neighboring molecules.

Similar to the α'-phase, the submonolayer of QA on Cu(111) appears significantly more disordered than its counterpart on Ag(100) because the chains on Cu(111) contain significantly more defects than those on Ag(100). The most typical defect is an offset of a molecule with respect to its neighboring molecule in the direction of $\mathbf{b_2}$ (cf. the structure model in Figure 7b). These defects appear quite often; we

https://dx.doi.org/10.1021/acs.jpcc.0c07850
J. Phys. Chem. C 2020, 124, 24861−24873

were not able to find a single chain without such defects. The longest defect-free distance within a chain, which we could find, was 280 Å, which corresponds to a segment of 40 QA molecules. For QA on Ag(100), these defects were also observed, but they were comparatively very rare. A defect of this type occurs whenever the handedness of the molecules along the chain changes. This leads to an offset perpendicular to the chain, which preserves at least one hydrogen bond between the two neighbors of the opposite handednesses. The higher amount of defects on Cu(111) compared to Ag(100) is likely due to the stronger substrate−adsorbate interactions because they make the flipping of the molecules and diffusion less likely and therefore prevent the healing of defects.

A SPA-LEED pattern of QA on the Cu(111) surface at a coverage of roughly θ = 0.50 ML is shown in Figure 5c. As noted above, the LEED pattern is very similar to that of the full monolayer of the α'-phase. These two patterns only differ in the length of the vector $\mathbf{b}_2^*$. The pattern mainly contains two prevalent features. One is a set of 12 spots around the specular spot and the first-order spots of the substrate that are given by the vector $\mathbf{b}_2^*$. Compared to the rest of the diffraction pattern, the $\mathbf{b}_2^*$ spots are relatively sharp. However, they clearly show a radial broadening and the corresponding higher-order spots are not visible. The other prevalent feature is given by the streaks that make up the rest of the diffraction pattern. The lack of sharp spots of higher orders is an indicator for a high amount of lateral disorder, which is in agreement with the STM results. The analysis of the pattern turned out to be rather difficult, and it was not possible to derive the averaged unit cell from the LEED pattern alone, but additional information from STM was required. However, it was possible to determine the lengths of the two vectors of the unit cell from SPA−LEED. The orientation of the vector $\mathbf{b}_2$ with respect to the substrate was determined from the few sharp spots in the diffraction pattern. The angle α between the two vectors was obtained from the STM images. This led to a unit cell with b_1 = (7.0 ± 0.3) Å, b_2 = (23.2 ± 1.0) Å, and α = (90 ± 1)°. The corresponding superstructure matrix is

$$\mathbf{M}_{\mathrm{Cu}}^{\mathrm{sub}} = \begin{pmatrix} 2.1 & -1.0 \\ 7.9 & 9.9 \end{pmatrix}$$

We estimate the errors to be ±0.1 for the elements of the first row and ±0.3 for those of the second row. A structure model is given in Figure 7b. It shows the straight chains and the noted defects. The structure differs from that of the full monolayer of the α'-phase only by the value of b_2, which is elongated by a factor of 1.4. Consequently, the same symmetry aspects apply. Notably, the vector $\mathbf{b}_2$ of the unit cell (cf. Figure 7b) corresponds to an average distance vector between neighboring chains because these local distances vary.

Again, this structure changes upon annealing. In Figure 7c, an STM image at a coverage of θ = 0.45 ML after annealing at 600 K for 15 min is shown. At first glance, the structure appears rather disordered. The image shows that this structure consists of molecular chains too. However, many of these chains are neither straight over long distances nor parallel to neighboring chains. Remarkably, the chains and molecules no longer exhibit six but only three distinct azimuthal orientations with respect to the substrate, and the chains contain regular kinks with an angle of 120°. From this observation and a corresponding LEED pattern (not shown), we conclude that the chains are oriented along the [10] direction and the long axes of the molecules along the [12] direction of the substrate.

A structure model is shown in Figure 7d. The internal structure of the chains is the same as that of the chains prior to the annealing. However, they are rotated with respect to their orientation prior to annealing and are now aligned with the [10] direction of the substrate. A further difference concerns the long-range order of the structure. Prior to annealing, the chains formed domains that consisted of many parallel chains. After annealing, the amount of parallel chains has significantly decreased, and the structure appears more like an assembly of individual chains. Another important difference, which contributes to an increased disorder, is given by the high number of 120° kinks of the chains. An example showing such a 120° kink is given in the top right corner of the structure model in Figure 7d. The STM image on the upper right-hand side in Figure 7c shows the typical S-shape of the molecules that was discussed above and reveals that the chains are homochiral here as in the α'-structure. However, the image on the lower right-hand side in Figure 7c shows a chain of the same azimuthal orientation where the handedness is flipped. This implies that homochiral chains in all three directions can consist of both enantiomers. We believe that this is due to the fact that the chains are oriented along the high-symmetry [10] direction of the Cu(111) substrate. Consequentially, upon mirroring of the chains at a plane in the [10] direction, the molecules will change their handedness, but they maintain their adsorption configurations. Hence, chains of both types of enantiomers are energetically equivalent.

4. FINAL DISCUSSION

The structures of QA investigated in this work, as well as those of QA on Ag(111) reported by Wagner et al.,[30] result from a subtle interplay between intermolecular interactions and substrate−adsorbate interactions. An overview of the structure parameters of QA on Ag(100), Cu(111), and Ag(111) and in the α^{I}-QA polymorph of the bulk phase is given in Table 1.

4.1. Formation of Homochiral Chains and Domains.

The formation of homochiral chains, which is very typical for QA, occurs directly upon the deposition at RT and is induced by the intermolecular interactions, where each molecule forms two hydrogen bonds to its next neighbors. We believe that the substrate has little to no influence on the internal structure of these chains because it is identical within the margins of error on all three metal substrates and in the α^{I}-QA polymorph. The azimuthal orientation of the chains, however, is influenced by the substrate because on all investigated substrates, the chains do not arrange randomly but arrange along distinct orientations. This is also supported by the fact that the chains in the second layer, where the interactions to the QA layer below are weaker [as reported here for Cu(111)], adopt arbitrary orientations. Furthermore, the azimuthal orientation of the QA molecules and of the chains is a criterion to distinguish between the enantiomers. Chains that consist of different enantiomers (R or L) exhibit different orientations ($+\gamma$ and $-\gamma$) with respect to the ⟨10⟩ directions of the surfaces, which lead to large enantiopure domains of these chains on both the Ag(100) and Ag(111) surfaces. This result is remarkable because during and directly after deposition, a homogeneous and statistical mixture of both enantiomers is expected. In order to separate and to form large enantiopure domains, the molecules need a high mobility because of diffusion. However, it seems unlikely that diffusion alone is

https://dx.doi.org/10.1021/acs.jpcc.0c07850
J. Phys. Chem. C 2020, 124, 24861−24873

responsible for such a separation process because especially at high coverages (~1 ML), there is not much space between the molecules and the lateral motion is hindered. Hence, we would expect plenty of molecules of the "wrong handedness" that are trapped in the large enantiopure domains during the separation process. As we did not observe many of such defects in the α-phase on Ag(100), we propose that on Ag(100), the molecules can change their handedness by a rotation around their long axes at RT (L ↔ R). This "flipping" of a surface-adsorbed molecule to change its handedness is no uncommon process and was observed for molecules of a similar size before.[56,57] This mechanism allows the formation of enantiopure domains even at high coverages.

On Cu(111), however, kinetic barriers play an even more pronounced role. Directly after deposition at RT, the monolayer on Cu(111) consists mostly of individual chains (or only very small domains) rather than large homochiral domains. The chains on Cu(111) also contain a higher amount of defects (offsets due to changes in handedness of the molecules) than their counterparts on Ag(100). These phenomena are compatible with a lower likelihood of chiral segregation of the molecules after deposition in comparison to the Ag surfaces. This would indicate that the diffusion and/or the ability of QA to rotate around the long axis are reduced on Cu(111) compared to the Ag(100) and Ag(111) surfaces.

In our present model, hydrogen bonds between the N−H and ketone groups of QA play a decisive role. One may of course question whether a coordination of the molecules by metal atoms supplied from substrate steps (Ag or Cu) could alternatively or additionally be relevant. This applies in particular to the phases obtained after annealing (β and β'), which we will discuss below. Indeed, metal-coordinated N atoms located in heterocycles (i.e., between R−N=R′ groups) or at terminal groups have been frequently observed.[58,59] However, here, we have an R−NH−R′ group, and the formation of a metal−N bond would require a preceding deprotonation of the N atom, which is unlikely. In addition, metal-coordinated bonds are longer than the hydrogen bonds proposed here for which we derive a length from the N to the O of (2.7 ± 0.1) Å. For the N−Cu−O bond length, we estimate 3.9−4.4 Å.[60,61] Hence, a N−Cu−O coordination would not fit into our structure models.

4.2. Temperature-Induced Phase Transition. The chainlike structures, formed directly after deposition on Ag(100), Ag(111), and Cu(111), are thermodynamically not stable but only metastable because they transform irreversibly upon annealing. They are stabilized by kinetic barriers that are partly given by the intermolecular hydrogen bonds, which are activated and opened during the annealing. However, this is likely not the only reason for the barriers, as will be explained further below. Generally, the α- and α'-phases of QA on these three surfaces that form prior to the annealing are mainly determined by the intermolecular interactions (i.e., intermolecular hydrogen bonds), while the β-phases, formed after annealing, are more strongly determined by the substrate−adsorbate interactions. This is deduced from the fact that on Ag(100) and on Ag(111), the β-phases are both commensurate. Upon the phase transitions, the overall number of hydrogen bonds is reduced, but in the commensurate structures, all molecules occupy one of two distinct adsorption sites which are generally related to a gain in binding energy.[47] This is supposed to lead to an energetically more favorable situation overall. However, the fact that the two β-phases on Ag(100) and on Ag(111) are structurally almost identical (cf. Table 1) shows that the intermolecular interactions still play an important role (we note that the agreement of the b_1 values to the third decimal place in Table 1 is likely coincidental).

The phases of QA on Cu(111) differ significantly from those on the two Ag surfaces, but the phase transition ($\alpha' \rightarrow \beta'$) occurs for likely similar reasons. At low coverages, the chains reorient along the high-symmetry directions of the Cu(111) surface upon annealing at 600 K. The full monolayer transforms into a heterochiral, 2D, and long-range ordered structure (the β'-phase), which exhibits only 5/8 as many hydrogen bonds as the α'-phase. We propose that the phase transitions of the submonolayer and the full monolayer of QA on Cu(111) are both driven by an increase of the substrate−adsorbate interactions, as will be discussed for the Ag(100) surface below.

A further interesting aspect regarding the phase transitions of QA on Ag(100), Ag(111), and Cu(111) concerns the azimuthal orientation of the molecules on the surfaces before and after the phase transitions. On Ag(100), the azimuthal orientations of the molecules in the α- and β-phases are identical within the margins of error, revealing that the molecules already adopt their preferred azimuthal orientations in the metastable α-phase. The same behavior can be observed for the phase transitions of full monolayers of QA on the Ag(111)[30] surface ($\alpha \rightarrow \beta$) and on the Cu(111) surface ($\alpha' \rightarrow \beta'$). On Ag(100) and Ag(111), because of the high mobility of the molecules at RT, it is plausible that the molecules adopt their preferred azimuthal orientation upon deposition. In comparison, the mobility on Cu(111) is reduced. Hence, the above result reveals that the molecules may still rotate in the plane of the Cu(111) surface to adopt the most favorable azimuthal orientation upon deposition. Interestingly, the six preferred symmetry-equivalent azimuthal orientations of QA chains on Ag(111) are the same as those of QA on Cu(111). This indicates that the local sixfold geometry is the main determining factor for the azimuthal orientation of QA, despite the different lattice constants and chemical reactivities of the two substrates.

We come to the central question regarding the phase transitions ($\alpha \rightarrow \beta$ and $\alpha' \rightarrow \beta'$) that we have not fully discussed yet. Considering the high mobility of the molecules on Ag(100) and Ag(111) and the fact that they can change their handedness at RT, we question why the β-phases do not form directly upon deposition. Because the β-phases are stable and do not transform back to the α-phases, they are energetically favored. We suggest that the energy gain related to the formation of the β-phases is explained by an increase of the molecule/surface bonding possibly involving a small reconstruction of the top Ag layer of the Ag surfaces. Such a reconstruction, involving small lateral and vertical displacements of the atoms in the top layers, is feasible because the β-phases exhibit commensurate structures. Reconstructions of the first layer of the substrate by adsorption of a flat-lying organic molecule were observed before and were reported, for example, by Held et al.[62−64] A change in the molecule/surface bonding related to different phases was reported as well, for example, by Kilian et al.[27] and may contribute to the kinetic barrier. We note that the change in the molecule/surface bond may also have an indirect influence on the intermolecular hydrogen bonds.

Now, we explain that there must exist kinetic barriers that prevent the direct formation of the β-phases upon the

https://dx.doi.org/10.1021/acs.jpcc.0c07850
J. Phys. Chem. C 2020, 124, 24861−24873

deposition at RT. The β-phases do not form instantaneously because the formation of two hydrogen bonds at the end of a chain of molecules to molecules arriving on the surface favors the formation of the α-phases. Hence, a nucleation of chains with the intermolecular arrangement of the α-phase precludes the further growth of this phase. A transition to the β-phases would require that one-quarter of the hydrogen bonds of the α-phases have to be opened. This constitutes a kinetic barrier that must be overcome in order to form the β-phases on Ag(100) and Ag(111). A similar process may be present on Cu(111). In contrast to the α-phases which can be grown on the clean surfaces, the β-phases can only form from a disordered phase of QA molecules upon cooling. On Ag(100), the disordered phase can be obtained either by annealing the as-grown α-phase or by deposition at elevated temperatures (i.e., larger than 430 K). Therefore, the formation of the β-phases only occurs when the molecules can settle into this phase in a concerted manner. This process includes that the molecules bind to the surface more strongly as in the α-phases. The difference in the bonding of the QA molecules to the surfaces in the two phases should be distinguishable in photoemission[27] or vibrational spectroscopies.

Finally, we comment again on the possibility that the β-phases are formed by metal-coordinated bonds, which form because of the diffusion of substrate metal atoms at the elevated temperatures. As noted for the α-phases, such bonds are sterically not compatible with our current structure models of the β-phases, and hence, we consider this possibility as unlikely.

4.3. Comparison of the Substrate Surfaces. The structures of QA and their temperature-dependent behavior on Ag(100) and Ag(111) are very similar, but they differ significantly from those of QA on Cu(111). We have already mentioned the reduced mobility of QA on the Cu(111) surface, which we explain by a stronger corrugation of the QA/Cu(111) bonding potential related to stronger QA/Cu(111) interactions. Besides this, there are further differences between the behavior of QA on the surfaces. On Ag(100), annealing a submonolayer of QA results in island formation of the closely packed commensurate phase. On Cu(111), however, a layer of QA with a similar coverage behaves differently. Upon annealing, the molecular chains alter their orientation with respect to the substrate but mostly remain separated from other chains. Moreover, the annealed full monolayer of QA on Cu(111) exhibits a significant amount of disorder. In addition, many of our experimental attempts to prepare it resulted in disordered structures. This demonstrates that the rearrangement of QA molecules on the Cu(111) surface is significantly inhibited by kinetic barriers even at high temperatures. Furthermore, upon annealing QA on the Ag(100) surface, the diffraction pattern vanishes at about 470 K and it reappears at about 430 K upon cooling. Differently, the diffraction pattern of QA on the Cu(111) surface does not vanish completely during annealing at comparable temperatures (T = 500 K). Upon heating, it loses intensity and changes gradually with time. All these differences between QA on the Cu(111) surface and QA on the Ag(100) and Ag(111) surfaces can be consistently explained by a stronger bonding of QA on the Cu(111) surface compared to the Ag surfaces.

5. CONCLUSIONS

In summary, we have investigated the adsorption and ordering of QA on Ag(100) and Cu(111) directly after deposition at RT and after annealing. On both surfaces, we found homochiral domains of metastable chainlike structures after deposition. These are mainly a consequence of intermolecular hydrogen bonds and are stabilized by kinetic barriers related to the required opening of the hydrogen bonds. The heterochiral structures that form after annealing have a reduced density of hydrogen bonds and are more strongly dominated by the substrate−adsorbate interactions. We suggest that the phase transition on Ag(100) is associated with a change of the molecule/surface bond and a small reconstruction of the first layer of the substrate. A similar situation might presumably be present on Cu(111). On the Ag(100) and Ag(111) surfaces, the homochiral chain formation upon deposition reveals a high mobility and the activation of the rotation around the long molecular axis of QA allowing a change of the handedness. In contrast, these degrees of freedom are reduced on the Cu(111) surface. We attribute these differences to the stronger bonding between QA and the Cu(111) surface compared to that on the Ag surfaces.

Similar to many other prochiral molecules on surfaces,[28] QA on Ag(100) and Cu(111) as well as QA on Ag(111)[30] forms structures that are given by the subtle balances of different forces and that undergo phase transitions upon annealing. The observed phase transitions transform homochiral into heterochiral structures, which is an aspect that is not uncommon for structures of prochiral molecules on surfaces.[28] In the case of QA on Ag(100), Ag(111), and Cu(111), the initial formation of the homochiral structures is mainly driven by intermolecular hydrogen bonds. The heterochiral structures are thermodynamically more stable because of stronger substrate−adsorbate interactions and form upon annealing the as-grown and kinetically trapped chainlike structures via a disordered intermediate phase.

■ ASSOCIATED CONTENT

Supporting Information

The Supporting Information is available free of charge at https://pubs.acs.org/doi/10.1021/acs.jpcc.0c07850.

All four symmetry-equivalent domains of the β-phase of QA on Ag(100) (PDF)

■ AUTHOR INFORMATION

Corresponding Author

Moritz Sokolowski − *Institut für Physikalische und Theoretische Chemie der Universität Bonn, 53115 Bonn, Germany;* orcid.org/0000-0001-5991-3910; Phone: +49 (0) 228/73-2507; Email: sokolowski@pc.uni-bonn.de; Fax: + 49 (0) 228/73-9358

Authors

Niklas Humberg − *Institut für Physikalische und Theoretische Chemie der Universität Bonn, 53115 Bonn, Germany*

Rémi Bretel − *Université Paris-Saclay, CNRS, Institut des Sciences Moléculaires d'Orsay, 91405 Orsay, France*

Alexander Eslam − *Institut für Physikalische und Theoretische Chemie der Universität Bonn, 53115 Bonn, Germany*

Eric Le Moal − *Université Paris-Saclay, CNRS, Institut des Sciences Moléculaires d'Orsay, 91405 Orsay, France*

Complete contact information is available at:

https://dx.doi.org/10.1021/acs.jpcc.0c07850
J. Phys. Chem. C 2020, 124, 24861−24873

The Journal of Physical Chemistry C pubs.acs.org/JPCC Article

https://pubs.acs.org/10.1021/acs.jpcc.0c07850

Notes

The authors declare no competing financial interest.

■ ACKNOWLEDGMENTS

Financial support by the Deutsche Forschungsgemeinschaft (DFG) under project So407/6-3 is acknowledged. Rémi Bretel is thankful for the financial support from the French National Research Agency through a PhD grant (contract no. M-Exc-ICO ANR-16-CE24-0003), from the German Academic Exchange Service (DAAD) through a long-term research grant, and from the University of Paris-Saclay in France through a training research grant. We thank N. Rohbom for providing us with his self-written plug-in for the software Fiji.

■ REFERENCES

(1) Wang, C.; Dong, H.; Hu, W.; Liu, Y.; Zhu, D. Semiconducting π-conjugated Systems in Field-Effect Transistors: A Material Odyssey of Organic Electronics. *Chem. Rev.* **2012**, *112*, 2208−2267.
(2) Facchetti, A. Semiconductors for Organic Transistors. *Mater. Today* **2007**, *10*, 28−37.
(3) Shahnawaz, S.; Sudheendran Swayamprabha, S.; Nagar, M. R.; Yadav, R. A. K.; Gull, S.; Dubey, D. K.; Jou, J.-H. Hole-transporting Materials for Organic Light-Emitting Diodes: An Overview. *J. Mater. Chem. C* **2019**, *7*, 7144−7158.
(4) Kulkarni, A. P.; Tonzola, C. J.; Babel, A.; Jenekhe, S. A. Electron Transport Materials for Organic Light-Emitting Diodes. *Chem. Mater.* **2004**, *16*, 4556−4573.
(5) Hains, A. W.; Liang, Z.; Woodhouse, M. A.; Gregg, B. A. Molecular Semiconductors in Organic Photovoltaic Cells. *Chem. Rev.* **2010**, *110*, 6689−6735.
(6) Głowacki, E. D.; Leonat, L.; Irimia-Vladu, M.; Schwödiauer, R.; Ullah, M.; Sitter, H.; Bauer, S.; Sariciftci, N. S. Intermolecular Hydrogen-bonded Organic Semiconductors - Quinacridone versus Pentacene. *Appl. Phys. Lett.* **2012**, *101*, 023305.
(7) Głowacki, E. D.; Irimia-Vladu, M.; Kaltenbrunner, M.; Gsiorowski, J.; White, M. S.; Monkowius, U.; Romanazzi, G.; Suranna, G. P.; Mastrorilli, P.; Sekitani, T.; et al. Hydrogen-Bonded Semiconducting Pigments for Air-Stable Field-Effect Transistors. *Adv. Mater.* **2013**, *25*, 1563−9.
(8) Jeong, Y. J.; Jeon, J.; Lee, S.; Kang, M.; Jhon, H.; Song, H. J.; Park, C. E.; An, T. K. Development of Organic Semiconductors based on Quinacridone Derivatives for Organic Field-Effect Transistors: High-Voltage Logic Circuit Applications. *IEEE J. Electron Devices Soc.* **2017**, *5*, 209−213.
(9) Jeon, J.; Jhon, H.; Kang, M.; Song, H. J.; An, T. K. Quinacridone-quinoxaline-based Copolymer for Organic Field-Effect Transistors and its High-Voltage Logic Circuit Operations. *Org. Electron.* **2018**, *56*, 1−4.
(10) Kanbur, Y.; Coskun, H.; Głowacki, E. D.; Irimia-Vladu, M.; Sariciftci, N. S.; Yumusak, C. High Temperature-Stability of Organic Thin-Film Transistors based on Quinacridone Pigments. *Org. Electron.* **2019**, *66*, 53−57.
(11) Berg, D.; Nielinger, C.; Mader, W.; Sokolowski, M. Quinacridone Organic Field Effect Transistors with significant Stability by Vacuum Sublimation. *Synth. Met.* **2009**, *159*, 2599−2602.
(12) Wang, C.; Wang, S.; Chen, W.; Zhang, Z.; Zhang, H.; Wang, Y. A diphenylamino-substituted Quinacridone Derivative: Red Fluorescence based on Intramolecular Charge-Transfer Transition. *RSC Adv.* **2016**, *6*, 19308−19313.
(13) Cunha, M. P. d.; Do, T. T.; Yambem, S. D.; Pham, H. D.; Chang, S.; Manzhos, S.; Katoh, R.; Sonar, P. A Triphenylamine Substituted Quinacridone Derivative for solution processed Organic Light Emitting Diodes. *Mater. Chem. Phys.* **2018**, *206*, 56−63.
(14) Hwang, K. H.; Kim, D. H.; Choi, M. H.; Han, J. P.; Moon, D. K. Effect of Side Chain Position and Conformation of Quinacridone - Quinoxaline based conjugated Polymers on Photovoltaic Properties. *J. Ind. Eng. Chem.* **2016**, *34*, 66−75.
(15) Sung, H. A.; Kim, D. H.; Lee, T. H.; Choi, M. H.; Lee, E. J.; Moon, D. K. Effect of conjugated 2D-side groups on Quinacridone-based Copolymers to adjust deep HOMO level for Photovoltaics. *J. Ind. Eng. Chem.* **2017**, *46*, 304−314.
(16) Dunst, S.; Karner, E.; Coppola, M. E.; Trimmel, G.; Irimia-Vladu, M. Comparison of the Solution and Vacuum-Processed Quinacridones in Homojunction Photovoltaics. *Monatsh. Chem.* **2017**, *148*, 863−870.
(17) Wang, C.; Zhang, Z.; Wang, Y. Quinacridone-based π-conjugated electronic materials. *J. Mater. Chem. C* **2016**, *4*, 9918−9936.
(18) Lomax, S. Q. Phthalocyanine and Quinacridone Pigments: Their History, Properties and Use. *Stud. Conserv.* **2005**, *50*, 19−29.
(19) Labana, S. S.; Labana, L. L. Quinacridones. *Chem. Rev.* **1967**, *67*, 1−18.
(20) Faulkner, E. B.; Schwartz, R. J. *High Performance Pigments*; Wiley-VCH, 2009.
(21) Zollinger, H. *Color Chemistry; Syntheses, Properties, and Applications of Organic Dyes and Pigments*; WILEY-VCH: Weinheim, 2003.
(22) Panina, N.; Leusen, F. J. J.; Janssen, F. F. B. J.; Verwer, P.; Meekes, H.; Vlieg, E.; Deroover, G. Crystal Structure prediction of Organic Pigments: Quinacridone as an example. *J. Appl. Crystallogr.* **2007**, *40*, 105−114.
(23) Paulus, E. F.; Leusen, F. J. J.; Schmidt, M. U. Crystal Structures of Quinacridones. *CrystEngComm* **2007**, *9*, 131−143.
(24) Potts, G. D.; Jones, W.; Bullock, J. F.; Andrews, S. J.; Maginn, S. J. The Crystal Structure of Quinacridone: An archetypal pigment. *J. Chem. Soc., Chem. Commun.* **1994**, 2565−2566.
(25) Ernst, K.-H. Molecular Chirality at Surfaces. *Phys. Status Solidi B* **2012**, *249*, 2057−2088.
(26) Raval, R. Chiral Expression from molecular Assemblies at Metal Surfaces: Insights from Surface Science Techniques. *Chem. Soc. Rev.* **2009**, *38*, 707−721.
(27) Kilian, L.; Hauschild, A.; Temirov, R.; Subach, S.; Schöll, A.; Bendounan, A.; Reinert, F.; Lee, T.-L.; Tautz, F.; Sokolowski, M.; et al. Role of Intermolecular Interactions on the Electronic and Geometric Structure of a Large π-Conjugated Molecule Adsorbed on a Metal Surface. *Phys. Rev. Lett.* **2008**, *100*, 136103.
(28) Dutta, S.; Gellman, A. J. Enantiomer Surface Chemistry: Conglomerate versus Racemate Formation on Surfaces. *Chem. Soc. Rev.* **2017**, *46*, 7787−7839.
(29) Brock, C. P.; Schweizer, W. B.; Dunitz, J. D. On the Validity of Wallach's Rule: On the Density and Stability of Racemic Crystals compared with their Chiral Counterparts. *J. Am. Chem. Soc.* **1991**, *113*, 9811−9820.
(30) Wagner, T.; Györök, M.; Huber, D.; Zeppenfeld, P.; Głowacki, E. D. Quinacridone on Ag(111): Hydrogen Bonding versus Chirality. *J. Phys. Chem. C* **2014**, *118*, 10911−10920.
(31) Trixler, F.; Markert, T.; Lackinger, M.; Jamitzky, F.; Heckl, W. M. Supramolecular Self-Assembly initiated by Solid-Solid Wetting. *Chem.—Eur. J.* **2007**, *13*, 7785−7790.
(32) Eberle, A.; Nosek, A.; Büttner, J.; Markert, T.; Trixler, F. Growing low-dimensional Supramolecular Crystals directly from 3D Particles. *CrystEngComm* **2017**, *19*, 1417−1426.
(33) Cun, H.; Wang, Y.; Yang, B.; Zhang, L.; Du, S.; Wang, Y.; Ernst, K.-H.; Gao, H.-J. Homochiral Recognition among Organic Molecules on Cu(110). *Langmuir* **2010**, *26*, 3402−3406.
(34) Lin, F.; Zhong, D. Y.; Chi, L. F.; Ye, K.; Wang, Y.; Fuchs, H. Temperature-tuned Organic Monolayer Growth: N, N′-di(n-butyl)-Quinacridone on Ag(110). *Phys. Rev. B: Condens. Matter Mater. Phys.* **2006**, *73*, 235420.
(35) Qiu, D.; Ye, K.; Wang, Y.; Zou, B.; Zhang, X.; Lei, S.; Wan, L. In Situ Scanning Tunneling Microscopic Investigation of the Two-Dimensional Ordering of Different Alkyl Chain-Substituted Quinacridone Derivatives at Highly Oriented Pyrolytic Graphite/Solution Interface. *Langmuir* **2003**, *19*, 678−681.

(36) Shi, D. X.; Ji, W.; Lin, X.; He, X. B.; Lian, J. C.; Gao, L.; Cai, J. M.; Lin, H.; Du, S. X.; Lin, F.; et al. Role of Lateral Alkyl Chains in Modulation of Molecular Structures on Metal Surfaces. *Phys. Rev. Lett.* **2006**, *96*, 226101.
(37) Yang, B.; Wang, Y.; Cun, H.; Du, S.; Xu, M.; Wang, Y.; Ernst, K.-H.; Gao, H.-J. Direct Observation of Enantiospecific Substitution in a Two-Dimensional Chiral Phase Transition. *J. Am. Chem. Soc.* **2010**, *132*, 10440−10444.
(38) Schindelin, J.; Arganda-Carreras, I.; Frise, E.; Kaynig, V.; Longair, M.; Pietzsch, T.; Preibisch, S.; Rueden, C.; Saalfeld, S.; Schmid, B.; et al. Fiji: An Open-Source Platform for Biological-Image Analysis. *Nat. Methods* **2012**, *9*, 676−682.
(39) Conrady, A. E. Decentred Lens-Systems. *Mon. Not. R. Astron. Soc.* **1919**, *79*, 384−390.
(40) Bayersdorfer, P. *Spot-Plotter*, version 1.2; University of Würzburg, 2008.
(41) Nečas, D.; Klapetek, P. Gwyddion: An open-source Software for SPM Data Analysis. *Cent. Eur. J. Phys.* **2011**, *10*. DOI: 10.2478/s11534-011-0096-2
(42) Image-Metrology. *Scanning Probe Image Processor*, version 4.8.7; SPIP: Hørsholm, Denmark, 2006.
(43) Budden, A. S. Graphics Layout Engine 4.2. 2010, http://glx.sourceforge.net/.
(44) Allen, F. H.; Kennard, O.; Watson, D. G.; Brammer, L.; Orpen, A. G.; Taylor, R. Tables of Bond Lengths determined by X-ray and Neutron Diffraction. Part 1. Bond Lengths in Organic Compounds. *J. Chem. Soc., Perkin Trans. 2* **1987**, S1−S19.
(45) Bondi, A. Van der Waals Volumes and Radii. *J. Phys. Chem.* **1964**, *68*, 441−451.
(46) Lüftner, D.; Refaely-Abramson, S.; Pachler, M.; Resel, R.; Ramsey, M. G.; Kronik, L.; Puschnig, P. Experimental and Theoretical Electronic Structure of Quinacridone. *Phys. Rev. B: Condens. Matter Mater. Phys.* **2014**, *90*, 075204.
(47) Hooks, D. E.; Fritz, T.; Ward, M. D. Epitaxy and Molecular Organization on Solid Substrates. *Adv. Mater.* **2001**, *13*, 227−241.
(48) Lukas, S.; Witte, G.; Wöll, C. Novel Mechanism for Molecular Self-Assembly on Metal Substrates: Unidirectional Rows of Pentacene on Cu(110) Produced by a Substrate-Mediated Repulsion. *Phys. Rev. Lett.* **2001**, *88*, 028301.
(49) Schiffrin, A.; Reichert, J.; Auwärter, W.; Jahnz, G.; Pennec, Y.; Weber-Bargioni, A.; Stepanyuk, V. S.; Niebergall, L.; Bruno, P.; Barth, J. V. Self-aligning Atomic Strings in Surface-supported Biomolecular Gratings. *Phys. Rev. B: Condens. Matter Mater. Phys.* **2008**, *78*, 035424.
(50) Pennec, Y.; Auwärter, W.; Schiffrin, A.; Weber-Bargioni, A.; Riemann, A.; Barth, J. V. Supramolecular Gratings for Tuneable Confinement of Electrons on Metal Surfaces. *Nat. Nanotechnol.* **2007**, *2*, 99.
(51) Schiffrin, A.; Reichert, J.; Pennec, Y.; Auwärter, W.; Weber-Bargioni, A.; Marschall, M.; Dell'Angela, M.; Cvetko, D.; Bavdek, G.; Cossaro, A.; et al. Self-Assembly of L-Methionine on Cu(111): Steering Chiral Organization by Substrate Reactivity and Thermal Activation. *J. Phys. Chem. C* **2009**, *113*, 12101−12108.
(52) Schiffrin, A.; Riemann, A.; Auwärter, W.; Pennec, Y.; Weber-Bargioni, A.; Cvetko, D.; Cossaro, A.; Morgante, A.; Barth, J. V. Zwitterionic Self-assembly of L-methionine Nanogratings on the Ag(111) Surface. *Proc. Natl. Acad. Sci. U.S.A.* **2007**, *104*, 5279−5284.
(53) Padmore, T.; Thornton, G.; Padmore, H. The Surface Electronic Structure of Ag(001) and Ag(111) Studied with Multichannel Detection Angle-Resolved Photoemission. *Vacuum* **1988**, *38*, 261−265.
(54) Simic-Milosevic, V.; Heyde, M.; Nilius, N.; Nowicki, M.; Rust, H.-P.; Freund, H.-J. Substrate-mediated Interaction and Electron-induced Diffusion of Single Lithium Atoms on Ag(001). *Phys. Rev. B: Condens. Matter Mater. Phys.* **2007**, *75*, 195416.
(55) Weast, R. C. *CRC Handbook of Chemistry and Physics*; CRC Press, Cleveland, 1974.
(56) Weigelt, S.; Busse, C.; Petersen, L.; Rauls, E.; Hammer, B.; Gothelf, K. V.; Besenbacher, F.; Linderoth, T. R. Chiral Switching by Spontaneous Conformational Change in Adsorbed Organic Molecules. *Nat. Mater.* **2006**, *5*, 112−117.
(57) Liu, N.; Darling, G. R.; Raval, R. Dynamic Chiral Flipping within Strongly Chemisorbed molecular Monolayers at Surfaces. *Chem. Commun.* **2011**, *47*, 11324−11326.
(58) Dong, L.; Gao, Z. A.; Lin, N. Self-assembly of Metal−Organic Coordination Structures on Surfaces. *Prog. Surf. Sci.* **2016**, *91*, 101−135.
(59) Zhang, J.; Shchyrba, A.; Nowakowska, S.; Meyer, E.; Jung, T. A.; Muntwiler, M. Probing the Spatial and Momentum Distribution of confined Surface States in a Metal Coordination Network. *Chem. Commun.* **2014**, *50*, 12289−12292.
(60) Classen, T.; Fratesi, G.; Costantini, G.; Fabris, S.; Stadler, F. L.; Kim, C.; de Gironcoli, S.; Baroni, S.; Kern, K. Templated Growth of Metal−Organic Coordination Chains at Surfaces. *Angew. Chem., Int. Ed.* **2005**, *44*, 6142−6145.
(61) Umbach, T. R.; Bernien, M.; Hermanns, C. F.; Sun, L. L.; Mohrmann, H.; Hermann, K. E.; Krüger, A.; Krane, N.; Yang, Z.; Nickel, F.; et al. Site-specific Bonding of Copper Adatoms to Pyridine End Groups Mediating the Formation of two-dimensional Coordination Networks on Metal Surfaces. *Phys. Rev. B: Condens. Matter Mater. Phys.* **2014**, *89*, 235409.
(62) Stellwag, C.; Held, G.; Menzel, D. The Geometry of ordered Benzene Layers on Ru(001). *Surf. Sci.* **1995**, *325*, L379−L384.
(63) Held, G.; Bessent, M. P.; Titmuss, S.; King, D. A. Realistic Molecular Distortions and Strong Substrate Buckling induced by the Chemisorption of Benzene on Ni(111). *J. Chem. Phys.* **1996**, *105*, 11305−11312.
(64) Zheleva, Z. V.; Eralp, T.; Held, G. Complete Experimental Structure Determination of the p(3 × 2)pg Phase of Glycine on Cu(110). *J. Phys. Chem. C* **2012**, *116*, 618−625.

https://dx.doi.org/10.1021/acs.jpcc.0c07850
J. Phys. Chem. C 2020, 124, 24861−24873

Supporting Information:

Hydrogen Bonded One-Dimensional Chains of Quinacridone on Ag(100) and Cu(111): The Role of Chirality and Surface Bonding

Niklas Humberg,[†] Rémi Bretel,[‡] Alexander Eslam,[†] Eric Le Moal,[‡] and Moritz Sokolowski*,[†]

†*Institut für Physikalische und Theoretische Chemie der Universität Bonn, Wegelerstrasse 12, 53115 Bonn, Germany*

‡*Université Paris-Saclay, CNRS, Institut des Sciences Moléculaires d'Orsay, 91405, Orsay, France.*

E-mail: sokolowski@pc.uni-bonn.de

Phone: +49 (0) 228 / 73-2507. Fax: + 49 (0) 228 / 73 - 9358

The image in Figure 1 shows a structure model of the β-phase of quinacridone (QA) on the Ag(100) surface that is formed after annealing at 500 K. The model shows all four symmetry equivalent domains and illustrates how the chirality of the molecule changes between the different symmetry equivalent domains.

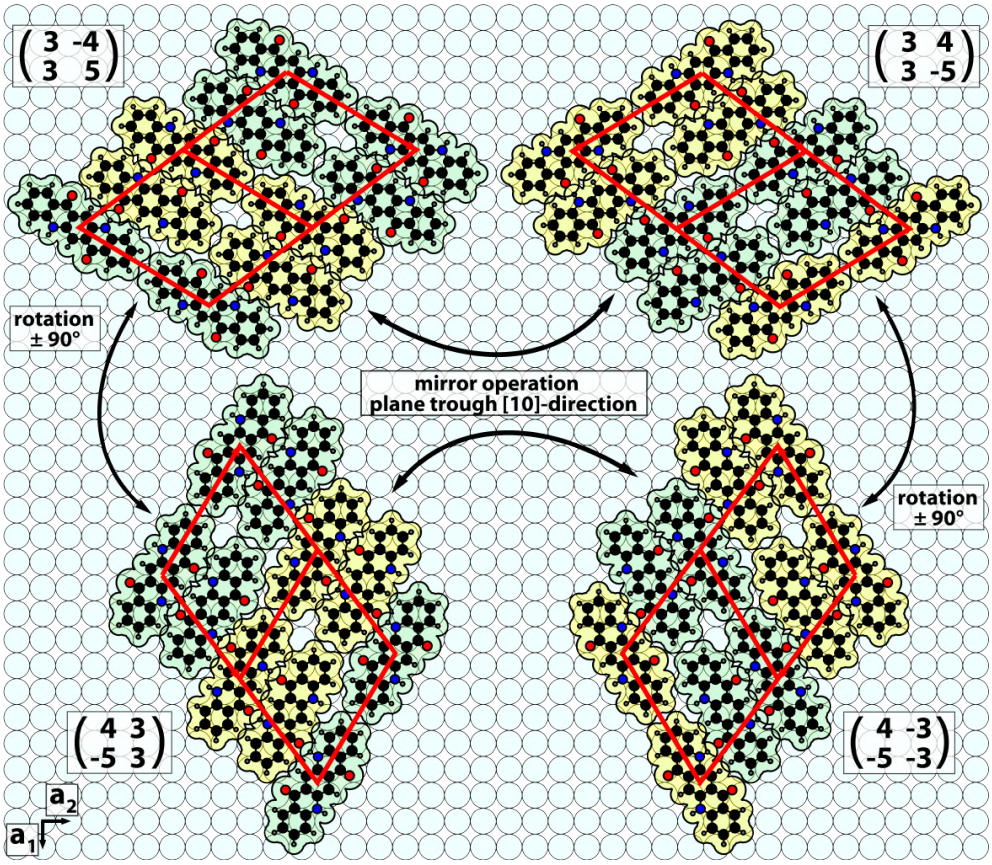

Figure S1: Structure model of the β-phase of QA on the Ag(100) surface. The model shows all four symmetry equivalent domains and the corresponding superstructure matrices. The black arrows indicate that the domains can be transformed into each other by a rotation of 90°, a mirror operation at a plane through the [10]-direction or a combination of the two. The unit cells are indicated in red. A single unit cell does not describe correctly the chirality of the molecules. This is the unit cell that we obtained from the STM and LEED experiments (cf. text of article). A doubled unit cell correctly describes the chirality and is therefore twice as long in the direction of b_1.

Correction to "Hydrogen Bonded One-Dimensional Chains of Quinacridone on Ag(100) and Cu(111): The Role of Chirality and Surface Bonding"

Niklas Humberg,[†] Rémi Bretel,[‡] Alexander Eslam,[†] Eric Le Moal,[‡] and Moritz Sokolowski*,[†]

[†]*Institut für Physikalische und Theoretische Chemie der Universität Bonn, Wegelerstrasse 12, 53115 Bonn, Germany*

[‡]*Université Paris-Saclay, CNRS, Institut des Sciences Moléculaires d'Orsay, 91405, Orsay, France.*

E-mail: sokolowski@pc.uni-bonn.de

Phone: +49 (0) 228 / 73-2507. Fax: + 49 (0) 228 / 73 - 9358

We report that in our paper[1] all the tunneling currents are too large by a factor of 10. However, this error has no ramifications regarding our interpretation of the data or the conclusions we draw from it. Specifically this means that range of tunneling current that were used in our expriments is 20 - 40 pA and not 200 - 400 pA as previously stated.

References

(1) Humberg, N.; Bretel, R.; Eslam, A.; Le Moal, E.; Sokolowski, M. Hydrogen-Bonded One-Dimensional Chains of Quinacridone on Ag(100) and Cu(111): The Role of Chirality and Surface Bonding. *The Journal of Physical Chemistry C* **2020**, *124*, 24861–24873.

A.2 "Growth of Hydrogen Bonded Molecular Aggregates on a Thin Alkali Halide Layer: Quinacridone on KCl/Ag(100)"

by Niklas Humberg, Qinmin Guo, Thomas Bredow and Moritz Sokolowski

published in: Physical Chemistry C **2023** 127(49), including Supporting Information.

DOI: https://doi.org/10.1021/acs.jpcc.3c04402

THE JOURNAL OF PHYSICAL CHEMISTRY C
A JOURNAL OF THE AMERICAN CHEMICAL SOCIETY

pubs.acs.org/JPCC Article

Growth of Hydrogen-Bonded Molecular Aggregates on a Thin Alkali Halide Layer: Quinacridone on KCl/Ag(100)

Niklas Humberg, Qinmin Guo, Thomas Bredow, and Moritz Sokolowski*

Cite This: J. Phys. Chem. C 2023, 127, 23814−23826 Read Online

ACCESS | Metrics & More | Article Recommendations | Supporting Information

ABSTRACT: Thef formation of self-assembled aggregates and domains of quinacridone (QA) on epitaxial KCl layers on the Ag(100) surface was investigated by scanning tunneling microscopy. If QA is deposited onto incomplete KCl layers that do not cover the complete Ag(100) surface, the QA molecules diffuse off the KCl islands and adsorb on the bare Ag surface instead. This is attributed to the high mobility of QA on KCl and the small Ehrlich-Schwoebel barrier of QA at KCl island edges on Ag(100). On KCl layers that completely cover the Ag(100) surface, the growth of QA depends on the thickness, namely, the number of monoatomic layers (ML), of the KCl layer. We find that ordered linear chains, held together by strong hydrogen bonds, and compact islands of these chains can be grown on thin KCl layers on Ag(100) for thicknesses of up to about three ML of KCl. This is attributed to attractive long-range dispersion forces between the QA molecules and the underlying Ag substrate through the KCl layer. These contribute to the adsorption energy of QA and support the adsorption of QA in a flat-lying geometry. For thicker KCl films, the attractive dispersion forces are not relevant, and hence, only nucleation of three-dimensional QA clusters occurs because the intermolecular interactions overbalance the QA/KCl interactions.

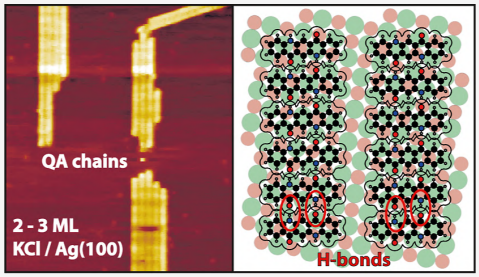

1. INTRODUCTION

Molecular self-assembly of organic molecules on metal surfaces is considered a method to create molecular nanostructures. By making use of specific physical and chemical properties of the molecules, e.g., their ability to form hydrogen bonds (H-bonds), these structures can be tailored to fit specific needs.[1−3] Considerable research effort has been put into the self-assembly of one-dimensional molecular chains or wires in recent years because these aggregates are not only interesting for probing the fundamentals of physics at interfaces but also for applications in a wide range of technological aspects.[4−6] Recently, the molecule 5,12-dihydro-quino[2,3-*b*]acridine-7,14-dione (quinacridone, QA; for structure formula, see below) has attracted interest because one-dimensional molecular chains of QA are ideal objects to investigate electronic and excitonic effects in quantum confined systems.[7−9] QA ($C_{20}H_{12}N_2O_2$) exhibits four isomers, of which in this work only the linear transisomer (see below) was considered. It contains two keto- and two secondary amine-groups, which are capable of forming intermolecular H-bonds. These H-bonds are the dominant structure-determining factor in the most known crystal structures of QA.[10]

One-dimensional chains of QA have been investigated on Ag(111),[11] Ag(100), and Cu(111),[12] and on graphene and MoS_2.[13,14] These studies have shown that QA does indeed form molecular chains on the named surfaces and that the extended QA structures can be tuned by sample temperature, coverage, or deposition rate. However, since the adsorption and bonding to metal surfaces change the properties of the molecules, the observation of the unperturbed electronic and excitonic states is prohibited there. A solution to this problem is the insertion of epitaxial layers of alkali halides (AH), which decouple the molecules from the metal surface.[15] A specific advantage of AH is that films can be prepared with distinct thicknesses and exhibit a large electronic band gap from thicknesses of two monolayers onward.[15,16] Epitaxial AH layers of LiCl,[17] NaCl,[15,18−20] KBr,[21,22] KCl,[23] LiF,[24] KF,[25] and RbCl[17] have been investigated on different metal surfaces. Recently, NaCl and KCl layers on Ag and Au surfaces have been used to measure STM-induced molecular luminescence,[26,27] tip-enhanced photoluminescence spectroscopy,[28,29] and the energy-selected fluorescence of single molecules on a surface.[30]

While the decoupling of individual organic molecules from the metallic substrate by layers of AH has been achieved, the preparation of ordered structures of organic molecules on AH layers through self-assembly remains challenging. One reason is that AH layers on metals often follow the Vollmer-Weber

Received: June 30, 2023
Revised: October 24, 2023
Accepted: October 24, 2023
Published: November 30, 2023

https://doi.org/10.1021/acs.jpcc.3c04402
J. Phys. Chem. C 2023, 127, 23814−23826

growth mode. Because of this, some areas of the metal substrate remain bare, and the molecules diffuse downward from the AH layer to the metal substrate. Another problem is the fact that on insulating layers, the adsorption energy (E_{ads}) of organic molecules is usually small compared to that on metal surfaces, which often leads to dewetting or nonwetting on AH layers.[31] So far, only a few reports of self-assembled domains of flat-lying molecules on AH layers have been reported, for example, PTCDA/KCl/Ag(100),[23] hexahydroxytriphenylene on KCl(100),[32] iron(II) phthalocyanine on NaCl/Cu(111),[33] and CuOEP/NaCl/Ag(111).[34] To the best of our knowledge, on AH layers, self-assembled molecular chains consisting of flat-lying molecules that are connected by H-bonds have not been reported yet. We note, however, that during the finalization of this work, Bretel et al. published data on a very similar system.[35] Finally, we mention that recently, a slightly different topic in this context has also become of interest, namely the growth of new hybrid structures of organic molecules and AH molecules.[36−38]

In this work, we report the growth of QA chains on KCl layers on Ag(100). Our findings indicate that QA has a small E_{ads} on KCl, which leads to a high mobility that enables the molecules to diffuse from incomplete KCl layers onto bare areas of the Ag surface. Furthermore, on KCl layers completely covering the Ag surface, which can be prepared by choosing optimized preparation parameters, it was observed that, depending on the thickness of the KCl layer, QA forms either chains of flat-lying molecules or bulk-like three-dimensional (3D) clusters. We discuss that the lateral ordering of QA molecules on the KCl layer depends on a subtle balance between E_{ads} of QA and the intermolecular interactions, whereby E_{ads} contains a contribution related to the Ag substrate and is therefore influenced by the KCl layer thickness. Our investigations show that, for a small range of KCl layer thicknesses, the self-assembly of one-dimensional QA chains can successfully be achieved.

2. EXPERIMENTAL SECTION

The experiments were carried out in an ultrahigh vacuum chamber with a base pressure of 2×10^{-10} mbar. The measurements were conducted by using a beetle-type scanning tunneling microscope (STM, type UHV 300) from RHK Technology. Furthermore, a microchannel plate low energy diffraction (MCP-LEED) instrument from OCI Vacuum Microengineering Inc. was used in order to check the prepared KCl layers for structural quality. A quadrupole mass spectrometer (QMS) of the type PRISMA from the company Pfeiffer Vacuum served to monitor the evaporation of QA and KCl. The Ag(100) crystal was cleaned by repeated sputtering with Ar^+ ions with energies of 1 keV and sample currents of 7−9 μA for 30 min and subsequent annealing at 700 K for 1 h. Afterward, the good structural quality of the Ag surface was confirmed by LEED.

KCl was evaporated from a home-built evaporator at crucible temperatures of ca. 870 K, while the sample was held at a temperature of 400 K. Several sample temperatures were tested, and it was found that at 400 K, large and smooth wetting layers covering the complete surface had formed. In contrast, deposition or annealing for 15 min after deposition at 500 K led to partial dewetting of the KCl layer and the formation of KCl islands that were several layers thick. The deposition rate was roughly 0.1 ML min^{-1}, where 1 ML corresponds to a nominal single atomic KCl layer completely covering the Ag(100) surface. The evaporated amount of KCl was monitored by integrating the QMS signal of the K^+ ion (m/z = 39 u) over time. The mass of KCl molecules (m/z = 74.5 u) was also observable in the mass spectra. However, the signal of the K^+ ion was chosen because it was more intense due to fragmentation. The average thickness θ_{KCl} of the KCl layers in numbers of monolayers was determined by using the integrated QMS signal and comparing it to that of a reference layer with a small nominal thickness (<2 ML) determined by STM.

Obviously, the local thickness of the KCl film in individual STM images is not guaranteed to be identical with the average thickness due to spatial variations. However, in our experiments, a systematic change in the growth behavior of the QA in correlation with the nominal (i.e., the averaged) KCl film thickness was observed. Hence, we propose that this latter value is meaningful for the interpretation of the STM results, although small local variations of the thickness may apply.

The QA was purified by gradient sublimation[39] and evaporated from a home-built evaporator at crucible temperatures of 670−720 K with a deposition rate of roughly 0.5 ML min^{-1}, while the sample was held at a temperature of 300 K. The deposition process was monitored by measuring and integrating the QMS signal of a QA fragment (m/z = 128 u, m(QA) = 312 u). The coverage θ_{QA} was calculated by comparing the integrated QMS signal to a reference that refers to a complete layer (1 ML) of a commensurate structure of QA on Ag(100), the so-called β-phase.[12]

Prior to the STM experiments, the KCl layer was checked by the MCP-LEED to ensure the presence of a well-ordered KCl layer showing sharp LEED spots. The reported QA structures were not observable by LEED because of very low QA coverages or a lack of highly ordered QA structures. All STM images were recorded in the constant-current mode at room temperature. The STM tip was a self-cut Pt/Ir (90:10) wire, and the bias voltage refers to the sample, while the tip was at ground potential. Most images were recorded with negative bias voltage (U_{Bias}) imaging occupied states and small currents (I_{set}) below 10 pA in order to minimize tip-sample interactions. Under these conditions, stable tunneling without much noise was routinely possible. The images were processed using the program SPIP.[40] If not stated otherwise, the processing included filtering out horizontal, vertical, or nondirectional noise and an adjustment of the contrast. Additionally, the distortion of the STM images of QA structures on KCl was corrected with parameters that were obtained from images of the KCl layer with atomic resolution, recorded under similar tunneling conditions, using the surface unit cell corresponding to the bulk KCl crystal structure.[41]

The structure models were drawn with the free software Graphics Layout Engine[42] and Adobe Illustrator.[43] The displayed hard sphere models of QA use bond lengths[41] and van der Waals radii[44] from the literature.

Quantum-chemical calculations, namely density functional theory (DFT) calculations, were performed with CRYSTAL17 version 1.0.2,[45] applying the PBE functional[46] augmented with D3 dispersion corrections.[47] The pob-tzvp-rev2 basis sets developed for solid-state calculations were employed.[48] In preliminary calculations, it was found that improved structural results are obtained after setting the empirical s8 parameter to zero. The KCl(100) surface was modeled with a three-layer 8×12 super cell slab. In the E_{ads} calculations, all atom positions were fully relaxed; only the lattice vectors were fixed

https://doi.org/10.1021/acs.jpcc.3c04402
J. Phys. Chem. C 2023, 127, 23814−23826

to the bulk-optimized values. The basis-set superposition error was corrected by the counterpoise method.[49] We calculated single molecules, dimers, and trimers of QA on KCl. The latter served as a model for the investigation of chains of QA molecules. Larger ensembles could not be calculated due to computational limitations given by the system size.

3. RESULTS

First, we report on the growth of KCl layers on the Ag(100) surface. Then, we present the growth of QA structures on incomplete and complete KCl layers and discuss how their thickness influences the growth of QA.

3.1. Growth of KCl on Ag(100). Layers of KCl on the Ag(100) surface have been investigated previously.[23] Here, we add some important details from additional observations. An STM image of KCl on the Ag(100) surface is shown in Figure 1. The overview STM image shows a wetting layer of 2 ML of KCl with several islands of 1 ML of KCl on top of it (upper half) and a region of the bare Ag substrate (lower half), which are separated by the edge of the KCl wetting layer. The KCl wetting layer typically consists of large patches that grow across Ag step edges, projecting the step edges onto the KCl layer. This growth mode leaves large areas of the Ag(100) substrate uncovered. This indicates a high mobility of KCl on Ag(100) and a low Ehrlich-Schwoebel barrier between the KCl wetting layer and the bare Ag surface at 400 K, as was pointed out previously by Müller et al.[23]

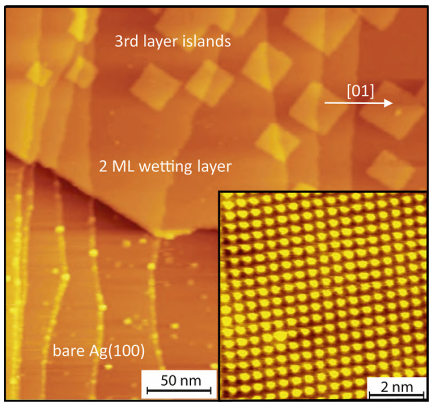

Figure 1. STM image (U_{Bias} = 3.9 V, I_{set} = 100 pA) of a KCl layer on the Ag(100) surface. The image shows a KCl wetting layer (2 ML, upper half) with several quadratic islands on top of it and a bare Ag surface (lower half). The white arrow indicates the [01] direction of KCl and the Ag(100) surface. The inset shows a close-up of the KCl layer with atomic resolution. The bright protrusions correspond to the Cl^- ions.

Usually, the small quadratic islands on top of the wetting layer are evenly distributed, but large areas without such islands, i.e., up to 150 × 150 nm in size, can also be found. The distribution and density of such islands vary even for identical preparation parameters. The structure of KCl is incommensurate with respect to the Ag(100) surface, but the two-dimensional (2D) unit cell vectors of the Ag(100) surface and those of the Cl^-(100) and K^+(100) surface unit cells exhibit the same azimuthal orientations, as illustrated in Figure 2. Distances of (4.6 ± 0.1) Å between the Cl^- ions were measured in STM images with atomic resolution (see the inset of Figure 1). This is in good agreement with the value deduced from LEED investigations by Müller et al.[23] and that of the bulk KCl crystal structure.[41]

Müller et al. originally proposed that the KCl wetting layer exhibits a thickness of only one atomic KCl layer.[23] However, we measured heights between the KCl wetting layer and the bare Ag substrate between 310 and 350 pm (U_{Bias} = −2.0 V, I_{set} = 100 pA), whereas Müller et al. reported heights of only 250 pm (U_{Bias} = 0.84 V, I_{set} = 12 pA). For the quadratic islands of the top layer, we found heights of roughly 140 pm (at the same tunneling conditions), whereas Müller et al. reported smaller heights of 120 pm. Examples of measured height profiles across such step edges can be found in figure S2 of the Supporting Information. The discrepancies are due to the different polarities of the bias voltage. Indeed, we found that for varying negative U_{Bias}, the apparent height of the wetting layer is constant, while for positive U_{Bias}, it is strongly dependent on U_{Bias}. This presumably makes the negative polarity (that was used here) more suitable for the determination of the layer heights. A similar observation of varying apparent heights at positive U_{Bias} was made by Guo et al. for NaCl/Cu(100)[50] and by Sun et al. for NaCl on Au(111).[51] Guo et al. explained their results by electrons tunneling from the tip into image potential states at distinct bias voltages. Within the scope of the present work, we did not investigate this phenomenon in further detail and use arguments based on a suppression of the tunneling from the Ag into the tip by the KCl layers.

The distance between (100) KCl lattice planes amounts to 314.5 pm.[41] The step height measured by STM for a single atomic layer of KCl on Ag(100) is expected to be smaller than this value because of the suppression of tunneling by the large band gap of KCl. Our values measured for the wetting layer heights (310−350 pm) are hence too large to be explained by a single KCl layer. In addition, the heights of the quadratic islands (140 pm) are less than half of the wetting layer height. Thus, we conclude that the quadratic islands on top of the wetting layer are of monoatomic height (1 ML) and that the wetting layer consists of 2 ML. This is also supported by other results from the literature. Cabailh et al. found that for NaCl on Ag(100), single ML islands can grow at low temperatures, but at elevated temperatures, the growth of 2 ML thick islands is always preferred.[52] However, standing wave experiments found that even at low temperatures KCl on Ag(100) forms a 2 ML wetting layer.[53] A detailed hard-sphere model of the wetting layer, and the quadratic islands is displayed in Figure 2.

The KCl film growth likely proceeds via the adsorption and diffusion of KCl molecules on the Ag substrate, where the Ag surface steps play an important role. We propose that the KCl molecules adsorb on the lower terrace close to a Ag step edge oriented in the preferred ⟨10⟩ direction (for the definition of [10] and [01] see Figure 2) in an upright position. As reported in ref 54, the local negative charge at the lower terrace side of the Ag step edges, related to the Smoluchowski effect, leads to KCl molecules pointing to the vacuum by their anions, while the cations are oriented toward the Ag surface. Subsequent to the decoration of the Ag steps by KCl molecules, the growth continues on both the lower and upper terraces. Because the upright standing molecules exceed the step edge in height, they serve as a nucleus for further growth on the lower and upper terraces (compare side views in Figure 2). Hence, the growth of the 2 ML wetting layer continues with additional molecules in an upright orientation on both sides of the steps. The

https://doi.org/10.1021/acs.jpcc.3c04402
J. Phys. Chem. C 2023, 127, 23814−23826

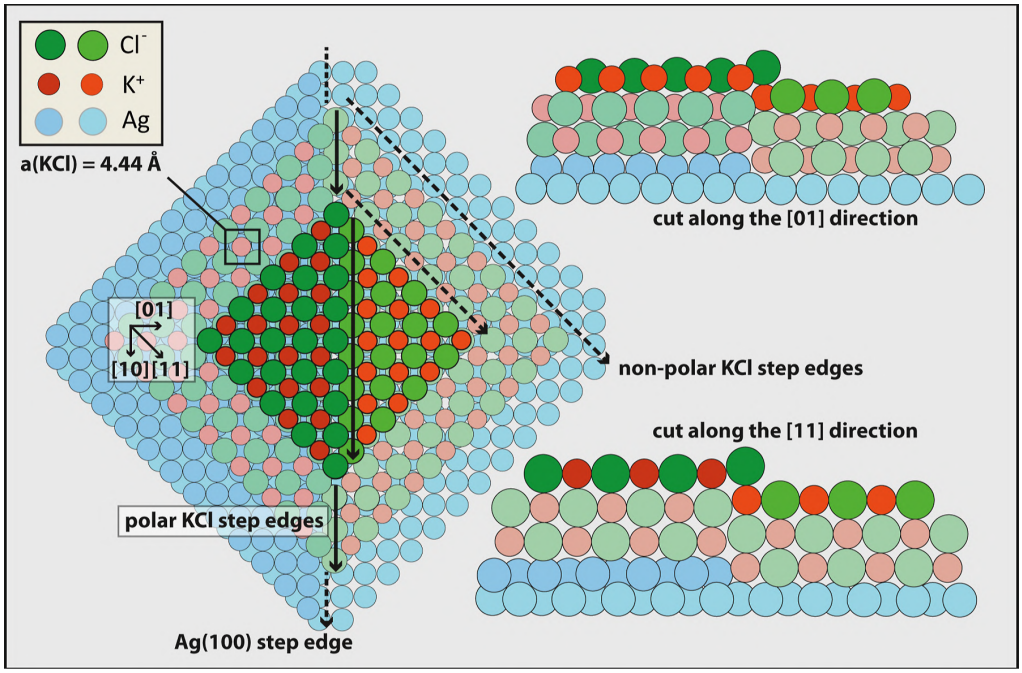

Figure 2. Structure model of thin KCl layers on the Ag(100) surface with one top-down view and two different side views. The model shows a 2 ML wetting layer (faint colors) that grows across a Ag step edge in the ⟨10⟩ direction with a quadratic island on top (full colors) consisting of one atomic layer. The Ag step edge is replicated onto the KCl layer and leads to polar step edges consisting only of Cl^- ions. The step edges in the ⟨11⟩ direction, which limit the wetting layer, and the quadratic islands consist of alternating ions and are therefore nonpolar. The KCl exhibits a quadratic unit cell with the same azimuthal orientation as the unit cell of the underlying Ag(100), and the length of the KCl unit cell vectors is 4.44 Å.

quadratic KCl islands on top of the wetting layer nucleate in the form of a decoration of the replicated Ag step edge by a row of upright standing KCl molecules in the ⟨10⟩ direction. The nucleation at step edges is concluded from the observation that the majority of the quadratic islands have a replicated Ag step edge crossing their center (see Figure 2). The growth of the quadratic islands then continues with flat-lying KCl molecules because the apparent height of the quadratic islands is too small for a KCl double layer.

Lastly, the interesting fact that the Ag step edges are replicated by the KCl layer is addressed. For the KCl layer thicknesses that we studied (≤6 ML), the replicated step edges appeared sharp, similar to the step edges on the bare Ag(100) surface (see Figure 1, upper half). For thicker layers, a so-called "carpet growth mode" may also be expected. This was previously observed for NaCl on the vicinal Ag(19, 1, 1) surface by Kramer et al.[55] but was not observed for our system. The replicated step edges are preferably oriented along the ⟨10⟩ direction of the Ag(100) substrate, which is the most favored direction for the Ag steps. This implies that the replicated KCl step edges are polar because, in the ⟨10⟩ direction, a KCl step edge consists of only Cl^- ions (see Figure 2). This is in contrast to the step edges that typically limit the KCl wetting layer and the quadratic islands on top of it, which are oriented along the ⟨11⟩ direction and consist of alternating ions leading to nonpolar step edges (see Figure 2). This difference of the steps will be important in the context of the nucleation of QA structures at step edges.

3.2. Nonwetting of QA on Incomplete KCl Layers. The results in this section concern the case in which QA (θ_{QA} = 0.5 ML) was deposited onto a partial KCl layer, which did not completely cover the Ag(100) surface. This was achieved by annealing the KCl layer (θ_{KCl} = 6 ML) after deposition for 15 min at 500 K, which caused partial dewetting. As a consequence, some areas of the Ag substrate were covered by very thick KCl layers (θ_{KCl} > 6 ML, no STM measurements possible), while other areas were covered by thin KCl layers ($\theta_{KCl} \leq$ 3 ML) or were completely bare of KCl. A corresponding STM image is displayed in panel (a) of Figure 3; it was recorded two h after the deposition. The image shows a step edge with a 500 pm height, which separates the bare Ag(100) surface (right-hand side) from a KCl island (left-hand side). A corresponding height profile of the step edge is shown in panel (b) of the figure. The height of 500 pm indicates that this step edge is three KCl layers high. Zooming into an area on the KCl layer shows that it is without any QA molecules on top of it, and it was possible to scan the layer with atomic resolution (see Figure S1 of the Supporting Information). One could argue that this is due to removing the QA molecules from the KCl layer in the process of scanning, which is a common and well-known phenomenon for STM.[56,57] However, this can be excluded here because the KCl layer always appeared clean during the first scan, and there was no particularly high noise in the tunneling current, which is typically seen when the STM tip is dragging molecules across the surface.

Looking at the Ag surface in panel (c) of Figure 3 reveals that it is densely covered with QA molecules. A structure formula for QA is displayed in panel (d) of the figure. This QA layer is disordered and consists of chain-like structures with

https://doi.org/10.1021/acs.jpcc.3c04402
J. Phys. Chem. C 2023, 127, 23814−23826

The Journal of Physical Chemistry C pubs.acs.org/JPCC Article

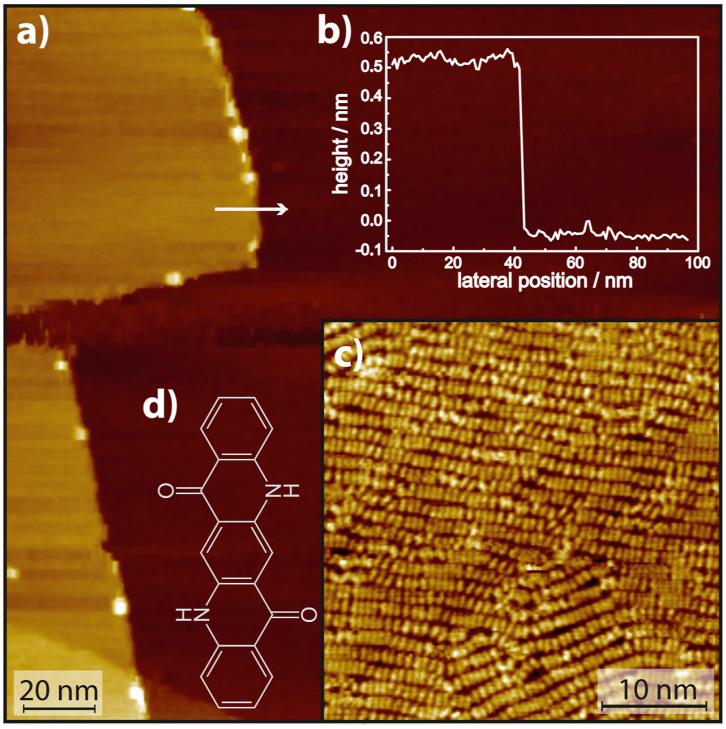

Figure 3. Medium coverage of QA (θ_{QA} = 0.5 ML) on a thick KCl layer (θ_{KCl} = 6 ML), which does not completely cover the Ag(100) surface. (a) STM image (U_{Bias} = −1.5 V, I_{set} = 8 pA). On the left side, there are two KCl islands with a thickness of three monoatomic layers; the dark area on the right side corresponds to the QA-covered Ag surface. A height profile along the white arrow is shown in panel (b). Panel (c) shows a close-up (U_{Bias} = −1.5 V, I_{set} = 8 pA) of a small excerpt of the dark area. It shows an assembly of QA molecules on the Ag(100) surface similar to that of the α-phase that is observed on a pure Ag(100) surface[12] but which is more disordered here. A structure formula of the molecule QA is displayed in panel (d).

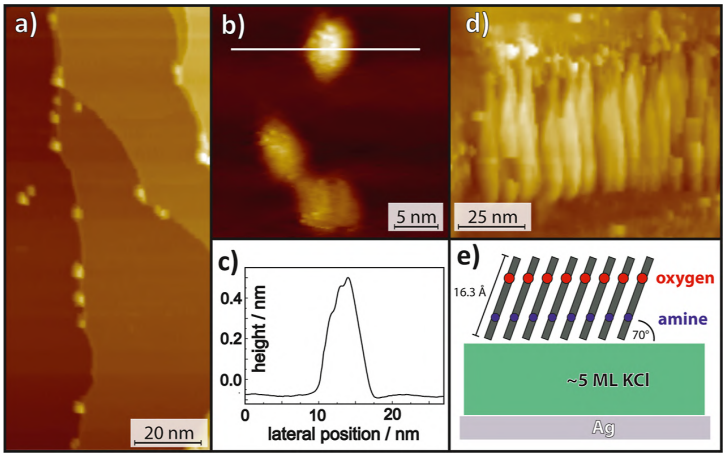

Figure 4. Growth of QA on thick KCl layers (θ_{KCl} = 5 ML), which completely cover the Ag(100) surface. (a) Constant current STM images (U_{Bias} = −1.5 V, I_{set} = 10 pA) of a small coverage (θ_{QA} = 0.05 ML). It shows several substrate step edges and several bright protrusions that are mainly located at the step edges of the substrate, which are replicated by the KCl layer. (b) Close-up showing three QA clusters. (c) A height profile along the line in panel (b) crossing one of the clusters. (d) Constant current STM image (U_{Bias} = −3 V, I_{set} = 10 pA) of a medium QA coverage (θ_{QA} = 0.5 ML). It shows elongated clusters that start at a KCl step edge and grow along the vertical axis of the image. (e) Schematic structure model for the molecular orientation. The model, including the angle of the molecules with respect to the KCl layer, is based on a similar structure that was found on SiO_2.[59] This parallel configuration of the molecules may seem energetically less favorable due to the close proximity of functional groups of the same charge compared to one with alternating keto and amine groups. But it is in agreement with the γ-phase of bulk-QA[10] and the structure that was found on SiO_2.[59] For further details, see the text.

https://doi.org/10.1021/acs.jpcc.3c04402
J. Phys. Chem. C 2023, 127, 23814−23826

many defects and kinks; however, very few of the chains are straight. These disordered structures have strong similarities with the α-phase that was previously observed for QA on the bare Ag(100) surface.[12] The α-phase consists of long, straight parallel chains of molecules that are connected via four H-bonds each. The noted disordered structures were commonly observed on the bare Ag patches between KCl islands by STM, and additionally, LEED images (see Figure S3 of the Supporting Information) exhibited smeared-out spots corresponding to those of the previously observed α-phase,[12] indicating that a significant fraction of the surface is covered by this disordered structure.

We explain the clean KCl layer and the formation of the disordered structures by diffusion-transport of the molecules from the KCl layer to the Ag surface. This leads to a lateral compression of the chains that formed on the Ag surface. The compression does not occur if QA (θ_{QA} = 1.2−1.5 ML) is deposited directly onto the pure Ag(100) surface.[12] This indicates that the compression is caused by the subsequent diffusion of QA from the KCl islands into the formerly nucleated QA chains on the Ag surface. This effective diffusion transport indicates a small diffusion barrier for QA on KCl and a small Ehrlich-Schwoebel barrier for QA across the KCl/Ag island edges. The transport mechanism over the step edge is possibly a "log-roll" mechanism, i.e., one with the long edge of the molecule parallel to the step edge, which was suggested for pentacene and several other molecules in a theoretical work by Goose et al.[58]

3.3. Clusters of QA on Complete Thicker KCl Layers. In the following, we report on QA on a thick and complete KCl layer of about 5−6 ML. Panel (a) of Figure 4 shows an STM image for small coverage (θ_{QA} = 0.05 ML). The image shows a typical Ag(100) surface with several step edges. The entire surface is covered homogeneously by KCl, and the step edges of the Ag substrate are replicated by the KCl layer. The QA is visible in the form of several round or ellipsoidal protrusions, which we assign on the basis of their height profile in panel (c) to small clusters of QA. These clusters are predominantly located at the replicated Ag step edges, but a few of them are found on the KCl terraces as well. In panel (b), a close-up of three clusters is displayed, with a corresponding height profile across one of the clusters in panel (c). This reveals that the clusters are of similar size and are of (5 ± 1) Å in apparent height and between 30 and 80 Å in both lateral dimensions. The close-up in panel (b) also shows that the clusters exhibit a substructure that might correspond to individual molecules standing upright on their long edge.

If a higher coverage of QA (e.g., θ_{QA} = 0.5 ML) is deposited on such a KCl layer, large elongated clusters are observed, which are shown in panel (d) of Figure 4. These clusters are about (12 ± 2) Å in height, up to 100 Å in width, and of variable length. Their apparent height exceeds that expected for flat-lying molecules, raising the question of how internal molecular assembly within these clusters could be. Previously conducted X-ray diffraction experiments by Scherwitzl et al.,[59] as well as Berg et al.,[39] on QA films on SiO_2 found two different phases with upright standing QA molecules. One was present at smaller nominal thicknesses and was assigned to an interface-near, substrate-induced thin-film phase.[59] The other phase was prevalent for thick QA films and is therefore not considered here. The thin film phase may potentially explain the observed structures. A model of this thin film phase is illustrated in panel (e) of Figure 4. It shows molecules standing on their short edge, which are tilted by 20° with respect to the surface normal according to ref. 59. The flat sides face one another, allowing for $\pi-\pi$ interactions. It is not possible to determine the exact geometric heights of the molecular clusters by STM, especially not in the case of an insulating layer underneath them. However, the apparent height of the observed elongated clusters of (12 ± 2) Å is within a reasonable range of what would be expected for QA molecules standing upright on their short edge, which is roughly 15 Å for a tilted hard-sphere model of the molecule.

The smaller apparent heights of the further above-described clusters at a small QA coverage (5 Å, see Figure 4a) cannot be explained by the same structure model but with one where the molecules are standing upright on their long instead of their short axis. Here, a height of ca. 7 Å would be expected. The upright orientations of both structures agree with those found for other molecules on AH layers. For example, for pentacene on KBr and KCl,[60] on both surfaces, two different kinds of domains were reported, consisting of pentacene molecules standing on their long and short edges, respectively.

It has been brought to our attention by one referee that the clusters could also be composed of a mixture of KCl and QA molecules similar to those mentioned in the introduction but of 3D character. Although we cannot exclude this from the experimental side, we consider this possibility less likely, as no 2D hybrid structures of QA and KCl on the Ag(100) surface (similar to those of PTCDA and KCl reported in ref. 38) were observed at low coverages of KCl.

3.4. Domain and Chain Growth of QA on Thin KCl Layers. Finally, we will present results for QA on a thin KCl layer of 2−3 ML. Panel (a) of Figure 5 shows an STM image

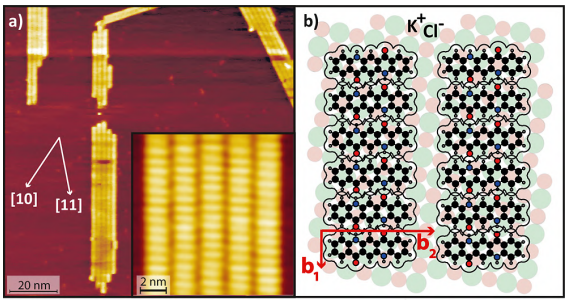

Figure 5. QA on a thin KCl layer. (a) STM image (U_{Bias} = −3 V, I_{set} = 10 pA) of QA/KCl/Ag(100). The entire Ag(100) surface is covered by this thin KCl layer (θ_{KCl} = 2.5 ML), and the QA coverage is very small ($\theta_{QA} \approx$ 0.05 ML). The two white arrows depict the [10] and [11] directions of the KCl(100) surface/Ag(100) interface. The image shows that the QA forms small domains of parallel chains. The molecular arrangement within the chains is displayed in the inset (U_{Bias} = −1.5 V, I_{set} = 10 pA), and a corresponding structure model is displayed in (b). The color code of the atoms is as follows: black = carbon, gray = hydrogen, blue = nitrogen, and red = oxygen.

for a small coverage ($\theta_{QA} \approx$ 0.05 ML) of QA on 2−3 ML KCl on Ag(100); a corresponding structure model is displayed in panel (b). The QA molecules form small domains of parallel chains consisting of many parallel QA molecules bordering one another with their long edges. As for the chains of QA on Ag(100) in the α-phase,[12] the motif for the formation of molecular chains are the intermolecular H-bonds between neighboring molecules that form between the keto-group of

https://doi.org/10.1021/acs.jpcc.3c04402
J. Phys. Chem. C 2023, 127, 23814−23826

one molecule and the amine-group of a second molecule. This implies that all molecules within one chain have the same chirality because, otherwise, they would not be able to form H-bonds between one another. The model displayed in (b) shows the ideal case of a QA domain with an ordered structure, where one unit cell, defined by the vectors $\mathbf{b}_1$ and $\mathbf{b}_2$, describes the complete domain. However, the STM images show that the chains are often offset with respect to one another in the direction of $\mathbf{b}_1$ in an irregular manner. This means that there is no correlation or only a small correlation between the chains of the same domain in the direction of $\mathbf{b}_1$. This was already observed for QA on Ag(100), where the correlation in particular decreases with increasing distance between neighboring chains.[12]

The analysis of the STM images yields an intermolecular distance within the chains of $b_1 = (6.6 \pm 0.2)$ Å. Within the margin of error, this value is identical with the intermolecular distance for QA/Ag(100) in the α-phase, showing that the length of the H-bonds remains unaltered by the insulating KCl layer with respect to the Ag(100) surface. The interchain distance for QA/KCl/Ag(100) is determined to be $b_2 = (20.0 \pm 0.5)$ Å. Comparing this value to the situation of QA/Ag(100) is not straightforward because on Ag(100), the interchain distance depends on the coverage. When we compare it to the chain distance on Ag(100), for the α-phase at its maximum coverage, this distance is larger on QA/KCl/Ag(100) by 3.6 Å (22%). A potential reason for this is that for QA on Ag(100) the layer is laterally compressed due to the high E_{ads}, leading to a smaller interchain distance.

The chains adapt four distinct symmetry-equivalent azimuthal orientations (only two are visible in Figure 5). Analysis of the STM images yields that the chains are rotated by $(33 \pm 3)^\circ$ with respect to the ⟨10⟩ direction of the Ag substrate. This was determined by measuring the angle of the QA chains with respect to the step edges of the quadratic KCl-islands, which have a known azimuthal orientation with respect to the Ag(100) substrate. Within the margin of error, the azimuthal orientations are identical to those of QA chains on the clean Ag(100) surface, which are rotated by $(31.2 \pm 0.5)^\circ$ with respect to the ⟨10⟩ direction. Whether the azimuthal orientation of the chains on KCl is given by the Ag substrate that interacts with the QA molecules across the KCl layer or by the surface of the KCl layer itself will be discussed in Section 4. The most prominent difference between the QA structures on KCl/Ag(100) and clean Ag(100) is that, on KCl/Ag(100), QA forms small domains where there is almost no space between neighboring chains. Contrary to this, on clean Ag(100) at coverages below 1 ML, the chains are isolated and maximize the distance to their neighbors. This can lead to distances between the chains of up to 60 Å. This phenomenon was explained by a substrate-mediated long-range repulsive interaction between the chains, which is induced by charge density waves in the surface electrons.[12] This repulsive interaction is no longer present on the KCl layer because, due to the larger distance, no electronic interactions between the QA molecules and the Ag surface electrons can occur. In the absence of this repulsive interaction between chains, the attractive van der Waals interactions between neighboring chains cause the formation of compact domains.

So far, only compact domains of QA on flat KCl terraces without steps have been considered. In Figure 6, STM images of QA on the thin KCl layer with polar and nonpolar step edges are displayed in panel (a) and a close-up of polar step edges in panel (b). The two step edges in the bottom right and bottom left of panel (a) correspond to quadratic KCl islands in the topmost layer (nonpolar steps), and the two step edges running diagonally through the center of the image are Ag step edges that are replicated by the KCl layer (polar steps). As can be seen in panel (a), several QA chains have nucleated at the nonpolar step edges of KCl islands in the topmost layer. The chains are marked with the letters A and B. There are long chains that are several nanometers long as well as very short chains that consist, judging by their lengths, of only 2−3 molecules. Their azimuthal directions are identical with those of the chains and domains on terraces that are not attached to step edges. Therefore, we conclude that the nonpolar step edges of KCl are favorable starting points for the growth of QA chains, but that the azimuthal directions of the chains are determined by the underlying substrate in combination with intermolecular interactions (see Section 4.3). However, the observation of compact domains of QA chains in Figure 5 shows that step edges are not required for the growth of chains. On smooth areas without any step edges, the compact domains form because they are more stable than individual chains. At step edges, it is possible to observe individual chains because they are stabilized by the step edges.

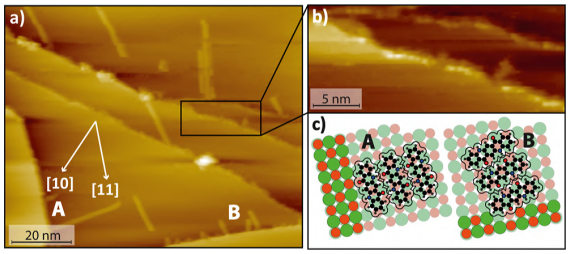

Figure 6. Growth of QA (θ_{QA} = 0.05 ML) chains at KCl step edges on a complete thin KCl layer (θ_{KCl} = 2.5 ML). (a) Constant current STM image (U_{Bias} = −3.5 V, I_{set} = 10 pA) of QA/KCl/Ag(100). Several chains starting at nonpolar KCl step edges are visible. The two white arrows indicate the ⟨10⟩ and ⟨11⟩ directions of the Ag(100) and KCl surfaces. (b) Close-up of two polar step edges. It can be seen that the upper as well as the lower part of the step edge is decorated by QA molecules. (c) Models of QA chains at nonpolar KCl step edges. The letters A and B refer to the same situations in (a).

Candidate structure models for the start of the chain growth at nonpolar KCl step edges are displayed in panel (c). The models take into account the azimuthal orientations of the QA chains with respect to the KCl step edges and consider the local charges of the KCl layer and the single QA molecules. In both models A and B, the QA molecule located closest to the KCl step edge is adsorbed with one of its oxygen atoms on top of a K^+ ion and close to another K^+ ion in the KCl step edge. In model B, a QA molecule replaced two ions of the KCl island edge. We propose that this may occur because this replacement maximizes E_{ads} at the step edge by Coulombic interactions between the oxygen atoms and the K^+ ions. A similar scenario was already observed, for example, for PTCDA at KCl(100) step edges.[61]

A close-up of two polar step edges is displayed in panel (b). There are bright protrusions on the upper as well as the lower terrace side of each step edge. This shows that the polar step edges are decorated by QA molecules that do not form molecular chains. This might be because the adsorption geometry of QA molecules at polar step edges differs from that

https://doi.org/10.1021/acs.jpcc.3c04402
J. Phys. Chem. C 2023, 127, 23814−23826

The Journal of Physical Chemistry C pubs.acs.org/JPCC Article

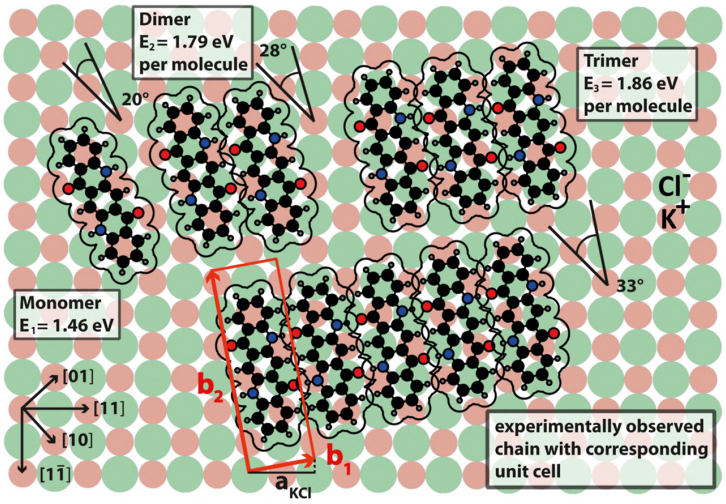

Figure 7. Structure Models of QA on KCl(100). The upper part of the image shows the DFT calculated adsorption geometries of a single QA molecule on the left side (E_1 = 1.46 eV), a QA dimer in the middle (E_2 = 1.79 eV per molecule), and a trimer on the right side (E_3 = 1.86 eV per molecule). The lower half of the image shows a chain of five QA molecules with azimuthal orientation, which was determined from STM experiments for long chains. The unit cell that was derived from the STM images of domains (see Figure 5) is displayed in red.

at nonpolar steps, for example, by an upright adsorption geometry of the QA on its long edge, which does not support chain growth.

4. DISCUSSION

4.1. Possible Charging of the QA Molecules. First, we address whether the QA molecules are charged on the KCl layer because some organic molecules on epitaxial insulating layers on metal surfaces are charged via charge transfer from the metal (although no cases are known on KCl).[62−65] In our STM images, the QA molecules always appeared as featureless, identical rods. Not a single molecule with a different contrast or submolecular resolution was observed. Thus, at present, we have no experimental evidence that the molecules are charged, and we hence interpret our results so far on the basis of uncharged molecules, which is compatible with all findings.

4.2. Energetic Considerations Concerning the Wetting. As a first interesting result, we discuss that the growth of QA on KCl depends on the thickness of the underlying KCl layer. Thin KCl layers (2−3 ML) support the growth of chains of flat-lying molecules, while thicker KCl layers (4−6 ML) lead to nonwetting and the formation of 3D QA clusters. We suppose that the latter KCl layers are thick enough to suppress the attraction between the Ag substrate and the QA molecules. This means that the growth of flat-lying molecular QA chains on KCl is per se not favored because E_{ads} of QA on KCl is too small in relation to the sublimation enthalpy (H_{sub}) of QA crystals. Thus, nonwetting and the formation of 3D bulk-like structures are preferred on thick KCl films. A potential reason for the small E_{ads} of QA on KCl is a geometric mismatch between the partial charges of the QA molecules and the charged ions in the KCl layer that leads to only a small electrostatic attraction between the molecule and the KCl surface. Recent publications on substituted helicene molecules on ionic Suzuki surfaces have illustrated the importance of such a geometric matching of opposite charges across the interface between the molecules and the surface with respect to E_{ads} and the resulting adsorption configuration of the molecules.[66,67] The electrostatic interaction between QA and the KCl lattice is discussed in further detail in Section 4.3.

The above assessment that flat-lying QA has a low E_{ads} is supported by our DFT calculations for QA on a semi-infinite KCl(100) surface. In the following, E_n (n = 1, 2, and 3) will denote the calculated E_{ads} per molecule of a mono-, di-, and trimer, respectively (for an illustration, see Figure 7). Our value for E_1 of a calculated QA monomer on KCl is 1.46 eV, with only a small share of the dispersion energy (E_{disp}) of 0.71 eV (i.e., ∼ 50%). We compare this value for E_1 to that of an isolated PTCDA molecule on KCl or NaCl, which is known to form ordered structures of flat-lying molecules on the named surfaces.[23,68] Theoretical DFT calculations by Hochheim and Bredow yielded adsorption energies in the range of 2.5−2.7 eV for PTCDA on NaCl and KCl, depending on the used basis set.[69] DFT calculations by Aldahhak et al. yielded adsorption energies of 2.9 and 2.5 eV for PTCDA on NaCl and KCl, respectively.[70] All calculated values for PTCDA on KCl and NaCl are larger by a factor of at least 1.7 than the E_1 = 1.46 eV of QA on KCl, although both molecules exhibit a similar footprint size. The larger value of E_{ads} for PTCDA on KCl is presumably related to a better geometric match between the partial charges in the PTCDA molecule and the charges on the KCl surface than is the case for QA on KCl.

To the best of our knowledge, values of H_{sub} of QA cannot be found in the literature. However, Scherwitzl et al. reported the desorption energy for QA on the SiO_2 surface as 2.1 eV,[71] which was derived from the zero-order thermal desorption spectra of QA multilayers. This value should be close to the H_{sub}. Furthermore, the lattice energies of different QA crystal structures, which should also be close to H_{sub}, were calculated by Panina et al. using the program Accelrys Polymorph Predictor and are in the range of 2.1−2.3 eV.[72] Our own calculations yielded a value of H_{sub} = 2.54 eV. In order to compare these values to the calculated E_{ads} of QA on KCl, it is necessary to look at small ensembles of QA molecules on KCl in order to include the intermolecular interactions which contribute to E_{ads}. Therefore, we also calculated a QA dimer

https://doi.org/10.1021/acs.jpcc.3c04402
J. Phys. Chem. C 2023, 127, 23814−23826

(E_2 = 1.79 eV per molecule) and a trimer (E_3 = 1.86 eV per molecule) on KCl. These values indicate that at a chain length of three, E_{ads} per molecule already approaches a maximum; i.e., it will not significantly increase further for longer chains. Hence, the comparison shows that E_3 = 1.86 eV, which includes the intermolecular interactions, is only between 73% and 90% of H_{sub} of QA (2.1−2.54 eV). As a consequence, the formation of bulk-like 3D aggregates is energetically favored over that of QA chains and domains on KCl.

Growth scenarios similar to the one observed here are reported in the literature, e.g., the methoxy functionalized *para*-quaterphenylene on NaCl and KCl layers on a glass substrate forms domains with upright molecules as well as fiber-like crystallites with lying molecules without the formation of a wetting layer.[73] Furthermore, the adsorption of *para*-hexaphenyl on KCl, NaCl, and KBr shows a similar behavior of nonwetting.[74,75] Other authors also report metastable domains that dewet post-deposition or at specific coverage thresholds, e.g., for PTCDA/NaCl,[68] PTCDA/KCl,[76] or hexamethoxytriphenylene on KBr.[77] A coexistence of two types of domains, one consisting of flat-lying molecules and the other consisting of standing molecules, was reported for a triphenylene derivative on KBr.[78] These examples point to small interfacial adsorption energies, which seem to be typical for organic molecules on layers of wide band gap materials such as KCl and which often lead to dewetting or nonwetting.[31]

The observed wetting of QA on thin KCl films implies that an additional force needs to be present that stabilizes the growth of flat-lying QA chains. We suppose that this attractive force is provided by the underlying Ag substrate in the form of van der Waals dispersion forces over a long range. These decrease with distance and, hence, the KCl film thickness. Indeed, in a theoretical study, Robledo and co-workers[79] showed that E_{ads} of benzene on 1, 2, and 3 monoatomic layers of NaCl on Cu(100) decrease with increasing thickness of the NaCl layer. The corresponding adsorption energies were reported as −1.3 eV, −0.75 eV, −0.48 eV, and −0.35 eV for 0, 1, 2, and 3 NaCl layers, respectively, and attributed to van der Waals dispersion forces that contribute to E_{ads} by −0.3 eV to −0.5 eV. The potential of these dispersion forces decreases with the distance z between the benzene and the NaCl/Cu(111) interface, i.e., the NaCl film thickness, proportional to z^{-3}. Since benzene exhibits only roughly 20% of the size of QA, we expect that such van der Waals dispersion forces between the QA molecules and the Ag substrate are even larger than the former. Furthermore, it was reported by Guo et al.[61] that the diffusion barrier of PTCDA on KCl on Ag(100) depends on the thickness of the KCl layer. This effect was also attributed to the Ag substrate. Lastly, for copper-octaethyl phorphyrin on 1−3 ML thick NaCl films on Ag(100) and Ag(111), an STM work by Ramoino et al.[34] showed that E_{ads} decreased with increasing NaCl layer thickness. On the basis of our results and the above examples from the literature, we conclude that attractive van der Waals forces also stabilize the QA structures on KCl layers of 1−3 ML thickness but that these are too weak for KCl layers of thicknesses above 3 ML to cause an effect there. Hence, within the kinetic limitations, the variation of E_{ads} with the KCl layer thickness determines whether the QA molecules form 2D domains and chains of flat-lying molecules or condense into bulk-like 3D aggregates.

Lastly, we comment on the mobility of QA on the KCl layers. Both the fact that the QA molecules are able to diffuse off the KCl islands and the formation of molecular chains and chain-like clusters show that the mobility of QA on KCl at 300 K is high. This is conceivable in view of the small values of E_{ads} of the single QA molecule on the KCl surface, and it fits further to the earlier observation that QA exhibits already a high mobility on the Ag(100) and Cu(111) surfaces,[12] although E_{ads} is larger there. The deduced low Ehrlich-Schwoebel barrier of QA at the KCl/KCl and KCl/Ag(100) steps is also plausible in view of the low E_{ads} of QA on KCl. This conclusion is supported by the theoretical work of Goose et al., who showed that for organic molecules, a roughly linear correlation between E_{ads} and the Ehrlich-Schwoebel barrier exists.[58]

4.3. Adsorption Geometries and Azimuthal Orientations. An interesting question concerns the understanding of the adsorption geometry of single QA molecules and chains of QA molecules with respect to the KCl surface. For this purpose, we again consider our DFT calculations for the QA monomer, dimer, and trimer on KCl in detail. Calculated structures are illustrated in the upper half of Figure 7. A structure model of a QA chain derived from STM data (see Figure 5) with a corresponding unit cell is shown in the lower half of the figure. Interestingly, the mono-, di-, and trimer exhibit different azimuthal orientations of 20, 28, and 33° with respect to the KCl ⟨10⟩ direction, respectively. The azimuthal orientation of the trimer is identical with that of the experimentally observed chains. As the DFT calculations were performed on a KCl half-space (without Ag), this agreement indicates that the azimuthal orientation is a consequence of the direct interactions between the KCl and QA molecules. Hence, the fact that the above-noted azimuthal orientations of QA chains on KCl/Ag(100) and Ag(100) are identical is likely a coincidence.

To understand the different azimuthal orientations of the calculated mono-, di-, and trimers, we look at their adsorption geometries in more detail. In the following, the notation E_0^n (n = 1, 2, and 3) denotes the site energies per molecule of an aggregate with n molecules, i.e., the direct interactions between the KCl surface and the QA molecules without the intermolecular interactions. Differently, E_n denotes the adsorption energy, including the site energy and the intermolecular interactions. We note that in our notation, more positive values of the energies refer to more tightly bonded molecules. The monomer shown in Figure 7 is located on the most favorable adsorption site found by DFT, with E_1 = 1.46 eV. (Note that $E_1 = E_0^1$.) The central carbon ring and the two nitrogen atoms are on 4-fold hollow sites, the two oxygen atoms are on bridge sites, and the two outer aromatic carbon rings are on top of K^+-ions. Small deviations from this adsorption site lead to a significant decrease in E_1. For instance, a rotation by ±8° (see Figure S4 of the Supporting Information) or a translation along the short molecular axis of QA decreases E_1 by up to 0.2 and 0.7 eV, respectively. This indicates that we have a very distinct and favorable adsorption site for a single QA molecule.

The calculated structure of the dimer (E_2 = 1.79 eV) shows an unexpected feature. The two molecules are shifted with respect to each other in the direction of the long molecular axes. Such an offset was never observed for longer QA chains by STM. The likely reason for this shift is a maximization of the interactions of the QA with the KCl surface because the shift yields a C_2 symmetry; i.e., both molecules come onto equivalent adsorption sites. The azimuthal orientation of the

https://doi.org/10.1021/acs.jpcc.3c04402
J. Phys. Chem. C 2023, 127, 23814−23826

dimer differs by 8° from that of the monomer, which can be understood as follows. The rotation provides a more favorable adsorption site for the second molecule. As seen from Figure 7, both molecules of the dimer sit on sites very similar to that of the monomer. The energy cost of the rotation was estimated by DFT (see Figure S4 of the Supporting Information) and is $2 \times \Delta E_{rot} = 2 \times 0.2$ eV = 0.4 eV, resulting in a site energy for the dimer of $E_0^2 = E_0^1 - \Delta E_{rot} = (1.46 - 0.2)$ eV = 1.26 eV. In the alternative situation where the second molecule was placed parallel to the monomer without a rotation, it would be on an unfavorable site with an energy cost of ΔE_{trans} = 0.7 eV, yielding $E_0^2 = (1.46-0.7)$ eV = 0.76 eV.

By DFT, we also calculated the interaction energy E_{NN}^2 between the two QA molecules of the dimer, which is comprised of H-bonds and van der Waals dispersion interactions. This yielded a value of E_{NN}^2 = 0.42 eV per molecule, with a share of the dispersion energy $E_{disp}^{NN} = 0.12$ eV. The remaining value of (0.42 − 0.12) eV = 0.30 eV has to be attributed to the intermolecular H bonds. (As E_{NN}^2 relates to one molecule sharing two H-bonds with its neighbor, 0.30 eV is the energy of one H-bond.) It is comparable to typical values for H-bonds of the type N−H···O. For example, the energy of the H-bonds between ammonia and water is 0.24 eV.[80]

The molecules in the trimer (E_3 = 1.86 eV per molecule) are further rotated by 5° with respect to the ones of the dimer, but they do not exhibit the same kind of offset. The azimuthal orientation of the trimer is in agreement with that of the experimentally observed chains. The calculated interaction energy for the trimer is $E_{NN}^3 = 0.59$ eV ($E_{disp}^{NN} = 0.14$ eV) per molecule. Hence, the average site energy E_0^3 can be calculated by subtracting E_{NN}^3 from the calculated value of E_{ads} of the trimer: $E_0^3 = (1.86-0.59)$ eV = 1.27 eV. The value for E_0^3 is smaller than the ones for E_0^2 and E_0^1, showing that longer chains include molecules with less favorable adsorption sites. The intermolecular interactions for longer QA chains E_{NN}^∞ can be estimated by E_{NN}^3. In the trimer, the average coordination number is $\frac{4}{3}$, but in an infinitely long chain, it would be 2. Hence, the intermolecular interactions in long chains can be estimated as $E_{NN}^\infty = 2\frac{3}{4} \cdot E_{NN}^3 = \frac{3}{2} \cdot E_{NN}^3 = 0.79$ eV. All calculated values are summarized in Table 1.

Table 1. Values for the Adsorption Energy E_n per Molecule Obtained From the DFT Calculations for Small QA Aggregates and the Extrapolated Infinitely Long Chain on KCl[a]

	monomer	dimer	trimer	∞ chain
γ/°	20	28	33	33
coordination number	0	1	$\frac{4}{3}$	2
E_n per molecule/eV	1.46	1.79	1.86	≲1.86
E_0^n per molecule/eV	1.46	1.37	1.27	1.07
E_{disp} per molecule/eV	0.71	0.70	0.70	0.70
E_{NN}^n per molecule/eV	not applicable	0.42	0.59	0.79

[a]In addition, the table shows the interaction energy per molecule of the cluster of length n between two next neighboring QA molecules, E_{NN}^n, the angle γ between the long axis of the QA molecules and the ⟨10⟩ direction of the KCl, the average site energy, E_0^n, and the dispersion energy between the QA molecules and the KCl surface, E_{disp}, which is contained in E_0^n. The following formulas were used: $E_0^2 = E_2 - E_{NN}^2$, $E_0^3 = E_3 - E_{NN}^3$, and $E_0^\infty = E_\infty - E_{NN}^\infty$. For more details, see the text.

Overall, our DFT results show that small chains of QA molecules (2 and 3 molecules) adapt orientations that differ from those of the monomer. The reason is that the continuation of the growth with the azimuthal angle of the monomer leads to unfavorable adsorption sites in terms of electrostatic interactions for the additional QA molecules in the chain. Hence, the dimer and trimer rotate with respect to the monomer in order to maximize the average interaction with the KCl surface. Our DFT results indicate that this rotation is relevant up to a chain length of about three molecules because calculated chains of three molecules exhibit approximately the same orientation as the long chains observed by STM.

A potential reason why the final azimuthal orientation is the most favorable may be the following. A projection of the vector $\mathbf{b}_1$ onto the KCl [11] direction yields a length that corresponds to the KCl bulk lattice constant. Thus, the spacing between the centers of molecules in the [11] direction (horizontal in Figure 7) also corresponds to the KCl lattice constant, as indicated in Figure 7. A consequence of this spacing between the molecules, their geometry, and their azimuthal orientation is that the oxygen atoms, which possess the highest local charge of the molecule, fall on sites between the anions and cations, i.e., in between the rows of alternating K^+ and Cl^- ions in the [$\bar{1}$1] direction. (We note that the molecular geometry does not allow us to place both O atoms on K^+ top sites.) This geometry is also in agreement with that from DFT calculations because the oxygen atoms in the calculated mono-, di-, and trimer are on similar adsorption sites. Hence, the oxygen atoms avoid the on-top positions on K^+ and Cl^- ions, optimizing E_{ads}. These observations further support the conclusion that the azimuthal orientation of the QA chains is determined by their interactions with KCl and not by the underlying Ag surface. We note that the situation at the KCl step edge (see Figure 6) is different from that on terraces. The molecules in the chains that grow at the KCl step edges may be translationally shifted with respect to those on terraces due to the strong Coulombic interactions between the terminal molecules and the ions in the step edge.

The adsorption geometries also play an important role in the question of whether all chains of QA on KCl in a domain have the same chirality. As said, individual chains need to be homochiral to allow the formation of intermolecular H-bonds. For domains composed of parallel chains, this aspect is not so obvious. However, if two chains had the same azimuthal orientation γ with respect to the KCl ⟨10⟩ direction but consisted of different enantiomers, they would comprise molecules on different individual adsorption sites and therefore exhibit different E_{ads}. Hence, for a change of the handedness of molecules, we would expect a change in the azimuthal orientation ($\gamma \rightarrow -\gamma$) of a chain. Therefore, we conclude that all domains with the same azimuthal orientation consist of the same enantiomer.

5. CONCLUSIONS

In summary, we have investigated the adsorption and ordering of quinacridone (QA) on the Ag(100) surface. We found that there is a relationship between the thickness of the KCl layer and the ordering of the QA molecules. On thick KCl layers (4−6 ML), we observed a nonwetting of the QA molecules and a formation of clusters that share similarities in their structure with known QA crystal structures. The nonwetting is attributed to the small adsorption energy of QA on KCl that

https://doi.org/10.1021/acs.jpcc.3c04402
J. Phys. Chem. C 2023, 127, 23814−23826

results from a structural mismatch between partial charges in the hydrogen-bonded QA chains and the ions of the KCl surface. In contrast, on thin KCl layers (2−3 ML), we found small domains of flat-lying parallel QA chains and individual chains that nucleated at KCl step edges. We propose that these aggregates are stabilized by long-range dispersion interactions through the thin KCl layers between the molecules and the Ag(100) substrate. By coincidence, these chains exhibit the same azimuthal orientations as QA chains on the bare Ag(100) surface[12] and also the intermolecular distance of (6.6 ± 0.2) Å is the same due to the strong intermolecular interactions of 0.79 eV per molecule. However, DFT calculations reveal that the chain orientation is a consequence of the interaction between the KCl surface and the QA.

Overall, our work shows that the lateral ordering of QA molecules on thin KCl layers of Ag(100) is determined by a subtle balance between the adsorption energy and intermolecular interactions. Furthermore, it shows that for a narrow range of KCl layer thicknesses, the self-assembly of molecular chains via H-bonds on alkali halide layers on metal surfaces is possible. This may be attractive for the investigation of the electronic and excitonic properties of 1D organic structures.

■ ASSOCIATED CONTENT

Supporting Information

The Supporting Information is available free of charge at https://pubs.acs.org/doi/10.1021/acs.jpcc.3c04402.

The Supporting Information contains additional STM data on the clean KCl film on Ag(100), a LEED image of QA on KCl on Ag(100), a plot of the calculated relative adsorption energy of the QA molecule on the KCl(100) surface upon rotation (PDF)

■ AUTHOR INFORMATION

Corresponding Author

Moritz Sokolowski − *Clausius-Institut für Physikalische und Theoretische Chemie der Universität Bonn, 53115 Bonn, Germany;* orcid.org/0000-0001-5991-3910; Phone: +49 (0) 228/73-2507; Email: sokolowski@pc.uni-bonn.de; Fax: + 49 (0) 228/73−9358

Authors

Niklas Humberg − *Clausius-Institut für Physikalische und Theoretische Chemie der Universität Bonn, 53115 Bonn, Germany;* orcid.org/0009-0007-6197-5740

Qinmin Guo − *Clausius-Institut für Physikalische und Theoretische Chemie der Universität Bonn, 53115 Bonn, Germany;* Present Address: The State Key Laboratory of Refractories and Metallurgy, Wuhan University of Science and Technology, Wuhan 430081, China; orcid.org/0000-0003-4184-7577

Thomas Bredow − *Clausius-Institut für Physikalische und Theoretische Chemie der Universität Bonn, 53115 Bonn, Germany*

Complete contact information is available at: https://pubs.acs.org/10.1021/acs.jpcc.3c04402

Notes

The authors declare no competing financial interest.

■ ACKNOWLEDGMENTS

Financial support by the Deutsche Forschungsgemeinschaft (DFG) under project So407/6-3 and the research training group 2591 is acknowledged. We thank Rémi Bretel and Eric Le Moal from the Université Paris-Saclay for a helpful discussion of the results and for informing us about their results on QA on KCl/Cu(111) prior to publication.

■ REFERENCES

(1) Ariga, K.; Nishikawa, M.; Mori, T.; Takeya, J.; Shrestha, L. K.; Hill, J. P. Self-assembly as a key player for materials nanoarchitectonics. *Sci. Technol. Adv. Mater.* **2019**, *20*, 51−95.

(2) Goronzy, D. P.; Ebrahimi, M.; Rosei, F.; Arramel; Fang, Y.; De Feyter, S.; Tait, S. L.; Wang, C.; Beton, P. H.; Wee, A. T. S.; et al. Supramolecular Assemblies on Surfaces: Nanopatterning, Functionality, and Reactivity. *ACS Nano* **2018**, *12*, 7445−7481.

(3) Amadi, E. V.; Venkataraman, A.; Papadopoulos, C. Nanoscale self-assembly: concepts, applications and challenges. *Nanotechnology* **2022**, *33*, 132001.

(4) Garnett, E.; Mai, L.; Yang, P. Introduction: 1D Nanomaterials/Nanowires. *Chem. Rev.* **2019**, *119*, 8955−8957.

(5) Zhou, G.; Xu, L.; Hu, G.; Mai, L.; Cui, Y. Nanowires for Electrochemical Energy Storage. *Chem. Rev.* **2019**, *119*, 11042−11109.

(6) Goktas, N. I.; Wilson, P.; Ghukasyan, A.; Wagner, D.; McNamee, S.; LaPierre, R. R. Nanowires for energy: A review. *Sci. Technol. Adv. Mater.* **2018**, *5*, 041305.

(7) Cahlík, A.; Hellerstedt, J.; Mendieta-Moreno, J. I.; Švec, M.; Santhini, V. M.; Pascal, S.; Soler-Polo, D.; Erlingsson, S. I.; Výborný, K.; Mutombo, P.; et al. Significance Of Nuclear Quantum Effects In Hydrogen Bonded Molecular Chains. *ACS Nano* **2021**, *15*, 10357−10365.

(8) Kanbur, Y.; Coskun, H.; Głowacki, E. D.; Irimia-Vladu, M.; Sariciftci, N. S.; Yumusak, C. High Temperature-Stability of Organic Thin-Film Transistors based on Quinacridone Pigments. *Org. Electron.* **2019**, *66*, 53−57.

(9) Daniel Głowacki, E.; Leonat, L.; Irimia-Vladu, M.; Schwödiauer, R.; Ullah, M.; Sitter, H.; Bauer, S.; Serdar Sariciftci, N. Intermolecular Hydrogen-bonded Organic Semiconductors - Quinacridone versus Pentacene. *Appl. Phys. Lett.* **2012**, *101*, 023305.

(10) Paulus, E. F.; Leusen, F. J. J.; Schmidt, M. U. Crystal Structures of Quinacridones. *CrystEngComm* **2007**, *9*, 131−143.

(11) Wagner, C.; Forker, R.; Fritz, T. On the Origin of the Energy Gain in Epitaxial Growth of Molecular Films. *J. Phys. Chem. Lett.* **2012**, *3*, 419−424.

(12) Humberg, N.; Bretel, R.; Eslam, A.; Le Moal, E.; Sokolowski, M. Hydrogen-Bonded One-Dimensional Chains of Quinacridone on Ag(100) and Cu(111): The Role of Chirality and Surface Bonding. *J. Phys. Chem. C* **2020**, *124*, 24861−24873.

(13) Trixler, F.; Markert, T.; Lackinger, M.; Jamitzky, F.; Heckl, W. M. Supramolecular Self-Assembly initiated by Solid-Solid Wetting. *Chem.—Eur. J.* **2007**, *13*, 7785−7790.

(14) Eberle, A.; Nosek, A.; Büttner, J.; Markert, T.; Trixler, F. Growing low-dimensional Supramolecular Crystals directly from 3D Particles. *CrystEngComm* **2017**, *19*, 1417−1426.

(15) Repp, J.; Meyer, G.; Stojković, S. M.; Gourdon, A.; Joachim, C. Molecules on Insulating Films: Scanning-Tunneling Microscopy Imaging of Individual Molecular Orbitals. *Phys. Rev. Lett.* **2005**, *94*, 026803.

(16) Kiguchi, M.; Inoue, H.; Saiki, K.; Sasaki, T.; Iwasawa, Y.; Koma, A. Electronic structure of alkali halide−metal interface: LiCl(001)/Cu(001). *Surf. Sci.* **2003**, *522*, 84−89.

(17) Loppacher, C.; Zerweck, U.; Eng, L. M. Kelvin probe force microscopy of alkali chloride thin films on Au(111). *Nanotechnology* **2004**, *15*, S9−S13.

(18) Bennewitz, R.; Barwich, V.; Bammerlin, M.; Loppacher, C.; Guggisberg, M.; Baratoff, A.; Meyer, E.; Güntherodt, H. J. Ultrathin

films of NaCl on Cu(111): a LEED and dynamic force microscopy study. *Surf. Sci.* **1999**, *438*, 289−296.
(19) Pivetta, M.; Patthey, F.; Stengel, M.; Baldereschi, A.; Schneider, W.-D. Local work function Moiré pattern on ultrathin ionic films: NaCl on Ag(100). *Phys. Rev. B* **2005**, *72*, 115404.
(20) Ploigt, H.-C.; Brun, C.; Pivetta, M.; Patthey, F.; Schneider, W.-D. Local work function changes determined by field emission resonances: NaCl/Ag(100). *Phys. Rev. B* **2007**, *76*, 195404.
(21) Reniers, F.; Fairbrother, D.; Wu, S.; Lipkowski, J. On the electrochemical adsorption of KBr on gold (100); a LEED−Auger study. *Surf. Sci.* **1999**, *433*−*435*, 12−16.
(22) Loppacher, C.; Zerweck, U.; Eng, L. M.; Gemming, S.; Seifert, G.; Olbrich, C.; Morawetz, K.; Schreiber, M. Adsorption of PTCDA on a partially KBr covered Ag(111) substrate. *Nanotechnology* **2006**, *17*, 1568−1573.
(23) Müller, M.; Ikonomov, J.; Sokolowski, M. Structure of Epitaxial Layers of KCl on Ag(100). *Surf. Sci.* **2011**, *605*, 1090−1094.
(24) Braun, K.-F.; Farias, D.; Fölsch, S.; Rieder, K.-H. Fractal growth of LiF on Ag(111) studied by low-temperature STM. *Surf. Sci.* **2000**, *454*−*456*, 750−754.
(25) Kikas, A.; Kisand, V.; Käämbre, T.; Ruus, R.; Nõmmiste, E.; Hirsimäki, M.; Valden, M.; Kukk, E.; Aksela, H.; Aksela, S. Insulating properties of ultrathin KF layers on Cu(100): Resonant Auger spectroscopy. *Surf. Sci.* **2005**, *584*, 49−54.
(26) Doppagne, B.; Chong, M. C.; Lorchat, E.; Berciaud, S.; Romeo, M.; Bulou, H.; Boeglin, A.; Scheurer, F.; Schull, G. Vibronic Spectroscopy with Submolecular Resolution from STM-Induced Electroluminescence. *Phys. Rev. Lett.* **2017**, *118*, 127401.
(27) Schultz, J. F.; Li, S.; Jiang, S.; Jiang, N. Optical scanning tunneling microscopy based chemical imaging and spectroscopy. *J. Phys.: Condens. Matter* **2020**, *32*, 463001.
(28) Yang, B.; Chen, G.; Ghafoor, A.; Zhang, Y.; Zhang, Y.; Zhang, Y.; Luo, Y.; Yang, J.; Sandoghdar, V.; Aizpurua, J.; et al. Sub-nanometre resolution in single-molecule photoluminescence imaging. *Nat. Photonics* **2020**, *14*, 693−699.
(29) Imada, H.; Imai-Imada, M.; Miwa, K.; Yamane, H.; Iwasa, T.; Tanaka, Y.; Toriumi, N.; Kimura, K.; Yokoshi, N.; Muranaka, A.; et al. Single-molecule laser nanospectroscopy with microelectron volt energy resolution. *Science* **2021**, *373*, 95−98.
(30) Marquardt, C.; Paulheim, A.; Hochheim, M.; Bredow, T.; Sokolowski, M. Homogeneous and inhomogeneous line shape of the electronic excitation of a single molecule on a surface. *Phys. Rev. B* **2021**, *104*, 045415.
(31) Burke, S. A.; Topple, J. M.; Grütter, P. Molecular dewetting on insulators. *J. Phys.: Condens. Matter* **2009**, *21*, 423101.
(32) Bocquet, F.; Nony, L.; Mannsfeld, S. C. B.; Oison, V.; Pawlak, R.; Porte, L.; Loppacher, C. Inhomogeneous Relaxation of a Molecular Layer on an Insulator due to Compressive Stress. *Phys. Rev. Lett.* **2012**, *108*, 206103.
(33) Scarfato, A.; Chang, S.-H.; Kuck, S.; Brede, J.; Hoffmann, G.; Wiesendanger, R. Scanning tunneling microscope study of iron(II) phthalocyanine growth on metals and insulating surfaces. *Surf. Sci.* **2008**, *602*, 677−683.
(34) Ramoino, L.; von Arx, M.; Schintke, S.; Baratoff, A.; Güntherodt, H. J.; Jung, T. Layer-selective epitaxial self-assembly of porphyrins on ultrathin insulators. *Chem. Phys. Lett.* **2006**, *417*, 22−27.
(35) Bretel, R.; Le Moal, S.; Oughaddou, H.; Le Moal, E. Hydrogen-bonded one-dimensional molecular chains on ultrathin insulating films: Quinacridone on KCl/Cu(111). *Phys. Rev. B* **2023**, *108*, 125423.
(36) Hieulle, J.; Peyrot, D.; Jiang, Z.; Silly, F. Engineering two-dimensional hybrid NaCl−organic coordinated nanoarchitectures on metal surfaces. *Chem. Commun.* **2015**, *51*, 13162−13165.
(37) Skomski, D.; Abb, S.; Tait, S. L. Robust Surface Nano-Architecture by Alkali−Carboxylate Ionic Bonding. *J. Am. Chem. Soc.* **2012**, *134*, 14165−14171.
(38) Guo, Q.; Huang, M.; Lu, S.; Cao, G. Ionic compound mediated rearrangement of 3, 4, 9, 10-perylene tetracarboxylic dianhydride molecules on Ag(100) surface. *Nanotechnology* **2015**, *26*, 275603.
(39) Berg, D.; Nielinger, C.; Mader, W.; Sokolowski, M. Quinacridone Organic Field Effect Transistors with significant Stability by Vacuum Sublimation. *Synth. Met.* **2009**, *159*, 2599−2602.
(40) *Scanning Probe Image Processor*, version 4.8.7.0. Image-Metrology, Hørsholm, Denmark, 2009.
(41) Weast, R. C. *CRC Handbook of Chemistry and Physics*, 55th ed.; CRC Press: Cleveland, Ohio, U.S., 1974; pp F202−F203.
(42) Pugmire, C.; Budden, A. S.; Grozin, A. G.; Rohde, A.; Jeffries, B.; Brendes, C.; Parfitt, D.; Edmondson, E.; Struyf, J.; Abbott, L. et al. Graphics Layout Engine, version 4.2, 2010, https://glx.sourceforge.io/(accessed Oct 20, 2023).
(43) *Adobe Illustrator CS5*, version 15.0.3. Adobe Inc., San Jose, California, U.S., 2010.
(44) Bondi, A. Van der Waals Volumes and Radii. *J. Phys. Chem.* **1964**, *68*, 441−451.
(45) Dovesi, R.; Erba, A.; Orlando, R.; Zicovich-Wilson, C. M.; Civalleri, B.; Maschio, L.; Rérat, M.; Casassa, S.; Baima, J.; Salustro, S.; et al. Quantum-mechanical condensed matter simulations with CRYSTAL. *Wiley Interdiscip. Rev.: Comput. Mol. Sci.* **2018**, *8*, No. e1360.
(46) Perdew, J. P.; Burke, K.; Ernzerhof, M. Generalized Gradient Approximation Made Simple. *Phys. Rev. Lett.* **1996**, *77*, 3865−3868.
(47) Grimme, S.; Ehrlich, S.; Goerigk, L. Effect of the damping function in dispersion corrected density functional theory. *J. Comput. Chem.* **2011**, *32*, 1456−1465.
(48) Vilela Oliveira, D.; Laun, J.; Peintinger, M. F.; Bredow, T. BSSE-correction scheme for consistent gaussian basis sets of double- and triple-zeta valence with polarization quality for solid-state calculations. *J. Comput. Chem.* **2019**, *40*, 2364−2376.
(49) Boys, S.; Bernardi, F. The calculation of small molecular interactions by the differences of separate total energies. Some procedures with reduced errors. *Mol. Phys.* **1970**, *19*, 553−566.
(50) Guo, Q.; Qin, Z.; Liu, C.; Zang, K.; Yu, Y.; Cao, G. Bias dependence of apparent layer thickness and Moiré pattern on NaCl/Cu(001). *Surf. Sci.* **2010**, *604*, 1820−1824.
(51) Sun, X.; Felicissimo, M. P.; Rudolf, P.; Silly, F. NaCl multi-layer islands grown on Au(111)-22×3 probed by scanning tunneling microscopy. *Nanotechnology* **2008**, *19*, 495307.
(52) Cabailh, G.; Henry, C. R.; Barth, C. Thin NaCl films on silver (001): island growth and work function. *New J. Phys.* **2012**, *14*, 103037.
(53) Le Moal, S.; Krieger, I.; Kremring, R.; Weiß, S.; Yang, X.; Tautz, F. S.; Silly, M.; Borisov, A. G.; Sokolowski, M.; Le Moal, E. Core-level binding energy shifts in ultrathin alkali-halide films on metals: KCl on Ag(100). *J. Phys. Chem. C*, **2023**.
(54) Kiguchi, M.; Entani, S.; Saiki, K.; Inoue, H.; Koma, A. Two types of epitaxial orientations for the growth of alkali halide on fcc metal substrates. *Phys. Rev. B* **2002**, *66*, 155424.
(55) Kramer, J.; Tegenkamp, C.; Pfnür, H. The growth of NaCl on flat and stepped silver surfaces. *J. Phys.: Condens. Matter* **2003**, *15*, 6473−6483.
(56) Böhringer, M.; Schneider, W.-D.; Berndt, R. Scanning tunneling microscope-induced molecular motion and its effect on the image formation. *Surf. Sci.* **1998**, *408*, 72−85.
(57) Meyer, G.; Zöphel, S.; Rieder, K. H. Manipulation of atoms and molecules with a low temperature scanning tunneling microscope. *Appl. Phys. A: Mater. Sci. Process.* **1996**, *63*, 557−564.
(58) Goose, J. E.; First, E. L.; Clancy, P. Nature of step-edge barriers for small organic molecules. *Phys. Rev. B* **2010**, *81*, 205310.
(59) Scherwitzl, B.; Röthel, C.; Jones, A. O. F.; Kunert, B.; Salzmann, I.; Resel, R.; Leising, G.; Winkler, A. Idiosyncrasies of Physical Vapor Deposition Processes from Various Knudsen Cells for Quinacridone Thin Film Growth on Silicon Dioxide. *J. Phys. Chem. C* **2015**, *119*, 20900−20910.
(60) Neff, J. L.; Milde, P.; Pérez León, C.; Kundrat, M. D.; Eng, L. M.; Jacob, C. R.; Hoffmann-Vogel, R. Epitaxial Growth of Pentacene

https://doi.org/10.1021/acs.jpcc.3c04402
J. Phys. Chem. C 2023, 127, 23814−23826

on Alkali Halide Surfaces Studied by Kelvin Probe Force Microscopy. *ACS Nano* **2014**, *8*, 3294−3301.
(61) Guo, Q.; Paulheim, A.; Sokolowski, M.; Aldahhak, H.; Rauls, E.; Schmidt, W. G. Adsorption of PTCDA on Terraces and at Steps Sites of the KCl(100) Surface. *J. Phys. Chem. C* **2014**, *118*, 29911−29918.
(62) Cochrane, K. A.; Schiffrin, A.; Roussy, T. S.; Capsoni, M.; Burke, S. A. Pronounced polarization-induced energy level shifts at boundaries of organic semiconductor nanostructures. *Nat. Commun.* **2015**, *6*, 8312.
(63) Hollerer, M.; Lüftner, D.; Hurdax, P.; Ules, T.; Soubatch, S.; Tautz, F. S.; Koller, G.; Puschnig, P.; Sterrer, M.; Ramsey, M. G. Charge Transfer and Orbital Level Alignment at Inorganic/Organic Interfaces: The Role of Dielectric Interlayers. *ACS Nano* **2017**, *11*, 6252−6260.
(64) Hurdax, P.; Hollerer, M.; Puschnig, P.; Lüftner, D.; Egger, L.; Ramsey, M. G.; Sterrer, M. Controlling the Charge Transfer across Thin Dielectric Interlayers. *Adv. Mater. Interfaces* **2020**, *7*, 2000592.
(65) Hurdax, P.; Kern, C. S.; Boné, T. G.; Haags, A.; Hollerer, M.; Egger, L.; Yang, X.; Kirschner, H.; Gottwald, A.; Richter, M.; et al. Large Distortion of Fused Aromatics on Dielectric Interlayers Quantified by Photoemission Orbital Tomography. *ACS Nano* **2022**, *16*, 17435−17443.
(66) Hoff, B.; Gingras, M.; Peresutti, R.; Henry, C. R.; Foster, A. S.; Barth, C. Mechanisms of the Adsorption and Self-Assembly of Molecules with Polarized Functional Groups on Insulating Surfaces. *J. Phys. Chem. C* **2014**, *118*, 14569−14578.
(67) Barth, C.; Gingras, M.; Foster, A. S.; Gulans, A.; Félix, G.; Hynninen, T.; Peresutti, R.; Henry, C. R. Two-Dimensional Nanostructured Growth of Nanoclusters and Molecules on Insulating Surfaces. *Adv. Mater.* **2012**, *24*, 3228−3232.
(68) Burke, S. A.; Ji, W.; Mativetsky, J. M.; Topple, J. M.; Fostner, S.; Gao, H.-J.; Guo, H.; Grütter, P. Strain Induced Dewetting of a Molecular System: Bimodal Growth of PTCDA on NaCl. *Phys. Rev. Lett.* **2008**, *100*, 186104.
(69) Hochheim, M.; Bredow, T. Adsorption-induced changes of intramolecular optical transitions: PTCDA/NaCl and PTCDA/KCl. *J. Comput. Chem.* **2015**, *36*, 1805−1811.
(70) Aldahhak, H.; Schmidt, W.; Rauls, E. Adsorption of PTCDA on NaCl(100) and KCl(100). *Surf. Sci.* **2013**, *617*, 242−248.
(71) Scherwitzl, B.; Lassnig, R.; Truger, M.; Resel, R.; Leising, G.; Winkler, A. Adsorption, desorption, and film formation of quinacridone and its thermal cracking product indigo on clean and carbon-covered silicon dioxide surfaces. *J. Chem. Phys.* **2016**, *145*, 094702.
(72) Panina, N.; Leusen, F. J. J.; Janssen, F. F. B. J.; Verwer, P.; Meekes, H.; Vlieg, E.; Deroover, G. Crystal Structure prediction of Organic Pigments: Quinacridone as an example. *J. Appl. Crystallogr.* **2007**, *40*, 105−114.
(73) Balzer, F.; Sun, R.; Parisi, J.; Rubahn, H.-G.; Lützen, A.; Schiek, M. Epitaxial growth of a methoxy-functionalized quaterphenylene on alkali halide surfaces. *Thin Solid Films* **2015**, *597*, 104−111.
(74) Yoshimoto, N.; Sato, T.; Saito, Y.; Ogawa, S. Epitaxial Relationships of Para-Sexiphenyl Thin Films on Alkali Halide Substrates. *Mol. Cryst. Liq. Cryst.* **2004**, *425*, 1−10.
(75) Frank, P.; Hernandez-Sosa, G.; Sitter, H.; Winkler, A. Search for a wetting layer in thin film growth of para-hexaphenyl on KCl(001). *Thin Solid Films* **2008**, *516*, 2939−2942.
(76) Dienel, T.; Loppacher, C.; Mannsfeld, S.; Forker, R.; Fritz, T. Growth-Mode-Induced Narrowing of Optical Spectra of an Organic Adlayer. *Adv. Mater.* **2008**, *20*, 959−963.
(77) Hinaut, A.; Lekhal, K.; Aivazian, G.; Bataillé, S.; Gourdon, A.; Martrou, D.; Gauthier, S. NC-AFM Study of the Adsorption of Hexamethoxytriphenylene on KBr(001). *J. Phys. Chem. C* **2011**, *115*, 13338−13342.
(78) Hinaut, A.; Pujol, A.; Chaumeton, F.; Martrou, D.; Gourdon, A.; Gauthier, S. An NC-AFM and KPFM study of the adsorption of a triphenylene derivative on KBr(001). *Beilstein J. Nanotechnol.* **2012**, *3*, 221−229.
(79) Robledo, M.; Pacchioni, G.; Martín, F.; Alcamí, M.; Díaz-Tendero, S. Adsorption of Benzene on Cu(100) and on Cu(100) Covered with an Ultrathin NaCl Film: Molecule−Substrate Interaction and Decoupling. *J. Phys. Chem. C* **2015**, *119*, 4062−4071.
(80) Emamian, S.; Lu, T.; Kruse, H.; Emamian, H. Exploring Nature and Predicting Strength of Hydrogen Bonds: A Correlation Analysis Between Atoms-in-Molecules Descriptors, Binding Energies, and Energy Components of Symmetry-Adapted Perturbation Theory. *J. Comput. Chem.* **2019**, *40*, 2868−2881.

https://doi.org/10.1021/acs.jpcc.3c04402
J. Phys. Chem. C 2023, 127, 23814−23826

Supporting Information:

Growth of Hydrogen Bonded Molecular Aggregates on a Thin Alkali Halide Layer: Quinacridone on KCl/Ag(100)

Niklas Humberg,[†] Qinmin Guo,[†,‡] Thomas Bredow,[†] and Moritz Sokolowski[*,†]

[†]*Clausius Institut für Physikalische und Theoretische Chemie der Universität Bonn, Wegelerstrasse 12, 53115 Bonn, Germany*

[‡]*present address: The State Key Laboratory of Refractories and Metallurgy, Wuhan University of Science and Technology, Wuhan 430081, China*

E-mail: sokolowski@pc.uni-bonn.de

Phone: +49 (0) 228 / 73-2507. Fax: + 49 (0) 228 / 73 - 9358

Figure S1 shows a small scale STM image of on island of KCl on Ag(100) with atomic resolution. This was a preparation during which QA was evaporated onto the KCl, however all the molecules diffused from the KCl islands to patches of the bare Ag(100) surface. The KCl island was 3 monoatomic KCl layers in height.

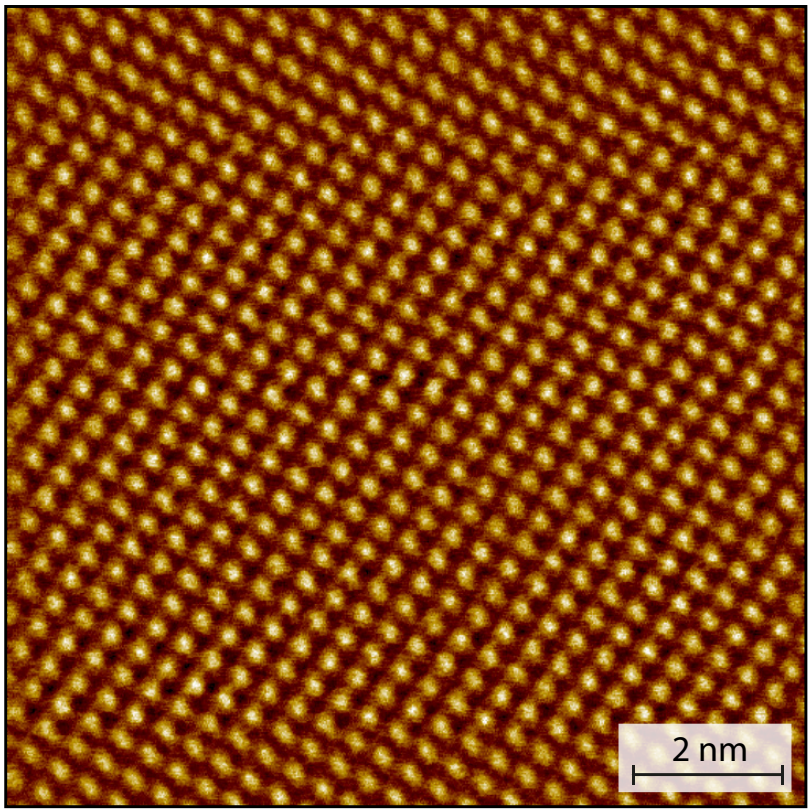

Figure S1: STM image ($U_{\mathrm{Bias}} = -3.5\,\mathrm{V}$, $I_{\mathrm{set}} = 10\,\mathrm{pA}$) of KCl on Ag(100). The bright protrusions correspond to the Cl^- ions.

Figure S2 shows line profiles measured at step edges in STM images for KCl on Ag(100).

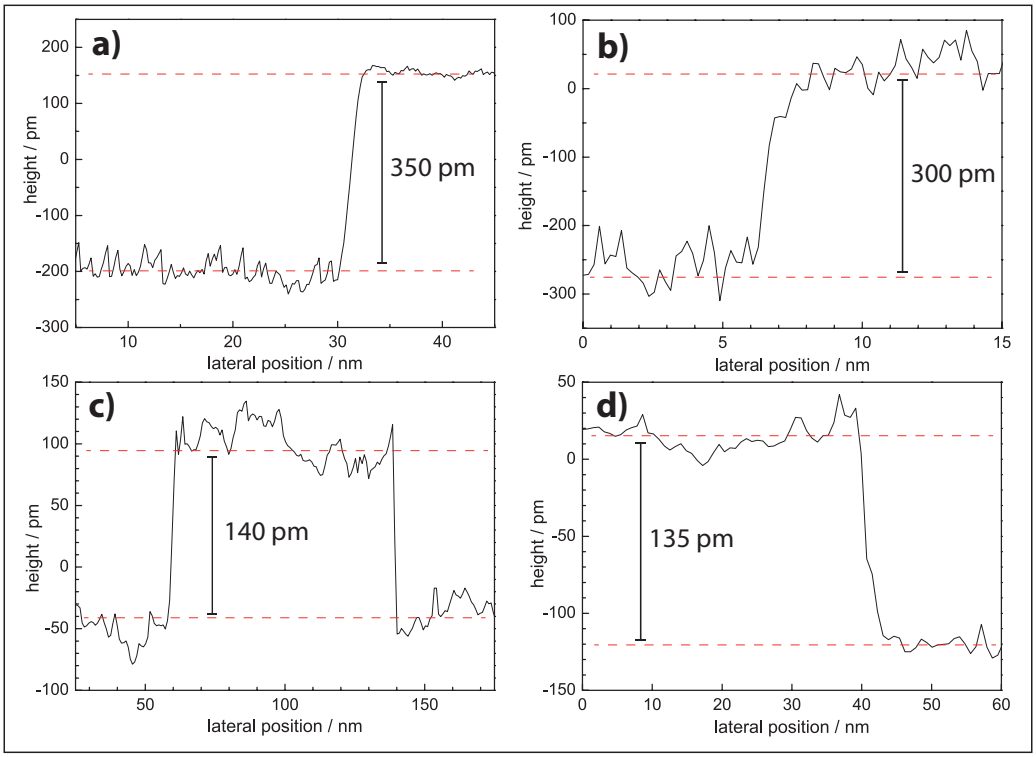

Figure S2: Line profiles extracted from STM images ($U_{\mathrm{Bias}} = -2\,\mathrm{V}$, $I_{\mathrm{set}} = 100\,\mathrm{pA}$) of KCl on Ag(100). Panels a) and b) show Ag-KCl step edges between the Ag substrate and the KCl wetting layer. Panels c) and d) show KCl-KCl step edges between the second and third monoatomic KCl layer. The dashed red lines indicate the average terrace heights between which the height of the KCl layer was measured.

Figure S3 shows a LEED image of QA on KCl on Ag(100). In this preparation the KCl layer had dewetted and hence there are KCl islands and patches of bare Ag present on the surface. The QA has diffused from the KCl islands to the Ag and formed a very disordered α-phase. The image shows the 8 spots that are given by the distance between neighboring chains (defined by the vector $\mathbf{b_2^*}$) and the smeared out spots that are given by the intermolecular distance within the chains (defined by the vector $\mathbf{b_1^*}$). This diffraction pattern has very low intensity spots and is very diffuse due to the large amount of disorder mentioned above.

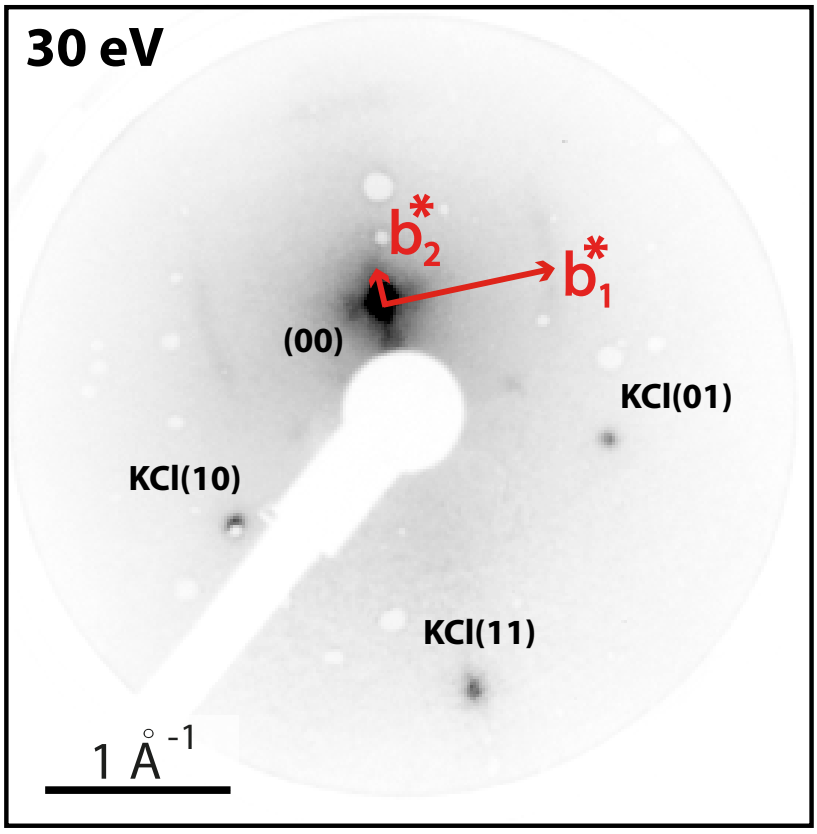

Figure S3: LEED image (electron energy = 30 eV, T = 300 K) of QA on KCl on Ag(100).

Figure S4 shows the calculated relative adsorption energy of a single QA molecule on the KCl(100) surface with respect to its azimuthal angle while the center of the molecule is fixed. The angle 0° corresponds to the most favorable calculated adsorption geometry.

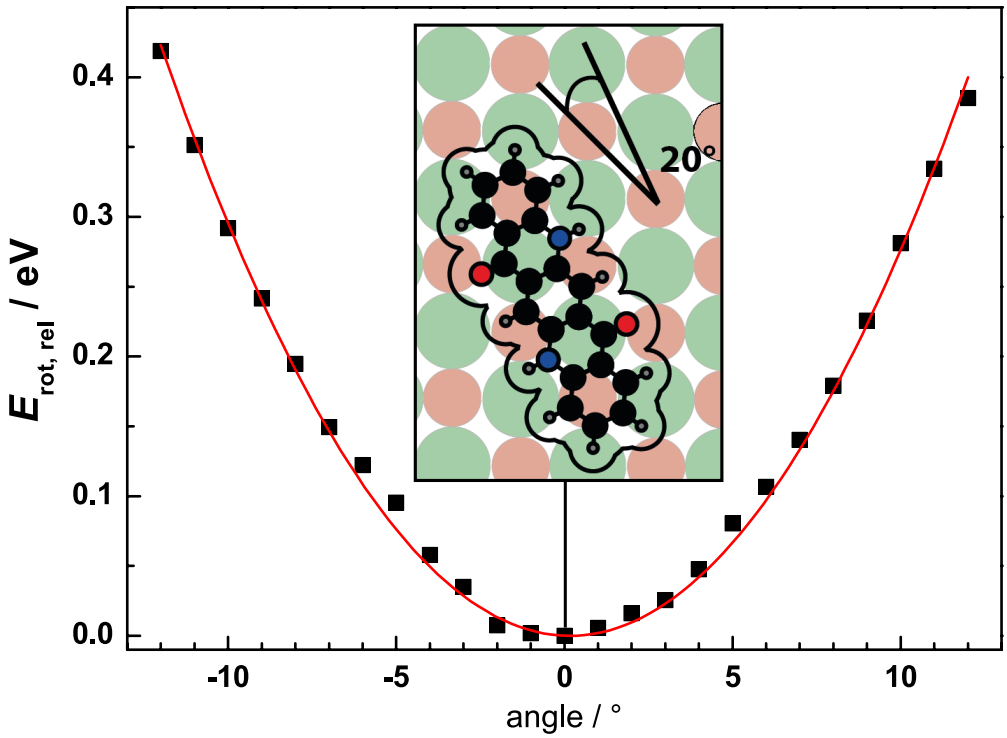

Figure S4: DFT calculated relative adsorption energy of a single QA molecule on KCl with respect to its azimuthal angle. The molecule was kept fixed at the same position and was rotated around its C_2 axis. The inset shows a model of the calculated most favorable adsorption site for a single QA molecule that corresponds to the minimum of the curve.

A.3 "Directed Growth of Quinacridone on a Vicinal Ag(35 1 1) Surface"

by Niklas Humberg, Lukas Grönwoldt and Moritz Sokolowski

published in: Beilstein J. Nanotechnol. **2024**, 15, 556-568, including Supporting Information.

DOI: https://doi.org/10.3762/bjnano.15.48

BEILSTEIN JOURNAL OF NANOTECHNOLOGY

Directed growth of quinacridone chains on the vicinal Ag(35 1 1) surface

Niklas Humberg, Lukas Grönwoldt and Moritz Sokolowski*

Full Research Paper

Open Access

Address:
Clausius-Institut für Physikalische und Theoretische Chemie der Universität Bonn, Wegelerstrasse 12, 53115 Bonn, Germany

Email:
Moritz Sokolowski* - sokolowski@pc.uni-bonn.de

* Corresponding author

Keywords:
Ag(100); intermolecular hydrogen bonds; one-dimensional aggregates; organic nanostructures; quinacridone; step-molecule interactions; vicinal surface

Beilstein J. Nanotechnol. **2024,** *15,* 556–568.
https://doi.org/10.3762/bjnano.15.48

Received: 16 February 2024
Accepted: 03 May 2024
Published: 21 May 2024

Associate Editor: S. A. Claridge

Abstract

The formation of self-assembled domains and chains of monomolecular width of quinacridone (QA) on the vicinal Ag(35 1 1) surface was investigated by scanning tunneling microscopy and low-energy electron diffraction. The focus was on the influence of the steps on the QA structures and their preferential azimuthal orientations with the aim of achieving a selective orientation. After deposition at a sample temperature of 300 K, QA forms the same kind of molecular chains as on the nominally flat Ag(100) surface because of strong intermolecular hydrogen bonds, which we reported in a previous publication [Humberg, N.; Bretel, R.; Eslam, A.; Le Moal, E.; Sokolowski, M. *J. Phys. Chem. C* **2020,** *124,* 24861–24873]. The vicinal surface leads to one additional chain orientation, which is parallel to the Ag step edges. However, most chains nucleate on the Ag terraces between steps with four distinct azimuthal orientations that are identical to those on Ag(100), and which are determined by the interactions with the (100) surface. At 300 K, the chains grow across the Ag steps, which do not break the azimuthal chain orientations. In contrast, during the deposition at sample temperatures of 400 and 500 K, the nucleation of the chains takes place at the Ag step edges. Hence, these have a strong influence on the azimuthal orientation of the molecules, resulting in a preferential growth of the chains in two of the four azimuthal orientations. We explain this by the adaptation of favorable adsorption sites, which involve the replacement of Ag atoms by QA molecules with specific azimuthal orientations at the step edges.

Introduction

A versatile and powerful method to create nanostructures on surfaces is the self-assembly of atoms and molecules. Here, the physical and chemical properties of the substrate and the adsorbate are the key that can be tuned to create nanostructures that fit specific needs [1-4]. A research focus over the recent years has been the self-assembly of molecules or atoms into one-dimensional (1D) linear aggregates. They allow for electron transport along the long axes of the 1D aggregates, while a confinement effect is present along their short axes. Hence, they are considered as building blocks for new generations of devices for computing, photovoltaics, thermoelectrics, and energy storage [5-7]. Furthermore, one-dimensional aggregates

Beilstein J. Nanotechnol. 2024, 15, 556–568.

are also used for gas sensing and carbon-capturing materials [8,9].

A group of surfaces that is very appealing for the growth of 1D structures are vicinal surfaces [10] because the step edges break the rotational symmetry of the surface further and add a periodic 1D grating, which can be used to direct the growth of nanostructures of adsorbates. The adsorption at step edges, as opposed to that on the terraces in between, is often favored because the additional interactions between the adsorbate and the atoms of the step edge contribute to the adsorption energy E_{ads}. This step decoration can be exploited to grow 1D chain-like structures of adsorbates that otherwise tend to form two-dimensional (2D) domains on flat terraces. Examples are atoms forming 1D metallic chains [11-15] and organic molecules forming 1D chains at step edges of vicinal metal surfaces at a low coverage, for example, PTCDA on Au(433) and Au(778) [16], a 1:1 mixture of PTCDI and 1,4-bis(2,4-diamino-1,3,5-triazine)benzene on Au(11 11 12) [17], and nickel-tetraphenylporphyrin on Au (788) [18].

Here, we report on the growth of an organic molecule, namely 5,12-dihydroquino[2,3-*b*]acridine-7,14-dione (quinacridone, QA), which forms 1D chains on flat metal surfaces already per se, on a vicinal Ag(100) surface. We describe how the presence of the step edges influences the azimuthal orientations of the chains. QA is a good candidate for such experiments because strong intermolecular hydrogen bonds (H-bonds) [19] support the growth of long 1D chains of parallel oriented QA molecules, both in bulk crystals and on surfaces.

It has been shown by Głowacki et al. that QA exhibits promising properties for applications in electronic and optoelectronic devices [20,21]. In particular, they found a hole mobility of 0.1 $cm^2 \cdot V^{-1} \cdot s^{-1}$ and a photocurrent of about 1 $mA \cdot cm^{-2}$. These observations were both attributed to a close packing of the molecules due to strong intermolecular H-bonds. The empirical formula of QA is $C_{20}H_{12}N_2O_2$, and a structural formula and a hard-sphere model of QA are displayed in Figure 1b. The self-assembly of QA has already been investigated on some nominally flat surfaces such as Ag(111) [22], Ag(100) and Cu(111) [23], and graphene and MoS_2 [24,25]. These studies have shown that QA grows in long one-dimensional chains connected by H-bonds. The chains exhibit a small set of distinct orientations, which are determined by the underlying substrates on all these surfaces. Furthermore, chains of QA have also been observed on insulating layers of KCl grown on Ag(100) or Cu(111) [19,26].

In this work, we report the growth of QA on the vicinal Ag(35 1 1) surface. The central question of this work was whether the unidirectional step edges influence the azimuthal orientations of the QA chains with respect to those that were observed on the nominally flat Ag(100) surface [23]. We found that the azimuthal orientations are identical to those on Ag(100), but, at elevated temperatures, the periodic step edges lead to a preferential growth of two distinct orientations out of four. Furthermore, we observed the growth of one, hitherto not described, azimuthal chain orientation parallel to the Ag step edges.

Experimental

The experiments were conducted in an ultrahigh vacuum chamber with a base pressure of 2×10^{-10} mbar equipped with a beetle-type scanning tunneling microscope (STM, type UHV 300) from RHK Technology, a microchannel plate low-energy diffraction (MCP-LEED) instrument from OCI Vacuum Microengineering Inc., and a quadrupole mass spectrometer (QMS) of the type PRISMA from Pfeiffer Vacuum. The vicinal Ag(35 1 1) crystal was obtained from MaTecK and cleaned by repeated cycles of sputtering and subsequent annealing at 700 K for 45 min. We tested whether a variation of the annealing temperatures between 500 and 800 K has an influence on the step distribution of the surface. However, no significant influence on the step distribution was observed. The purified QA [28] was evaporated from a custom-built evaporator at a crucible temperature of 720 K, while the sample was held at different temperatures between 300 and 500 K in order to test the role of the growth temperature. The deposition process was monitored by the QMS, and the integrated QMS signal was used to calculate the QA coverage θ_{QA}. It is given in numbers of monolayers (ML) of the α-phase, as explained in detail in [23]. A more detailed description of the experimental procedures can be found in [23].

The LEED measurements were performed at 300 K with beam currents below 10 nA and electron energies (E) between 30 and 200 eV. Note that the reported diffraction patterns are distorted due to the MCP geometry. All STM images were recorded at room temperature. As a tip, we used a self-cut Pt/Ir (90:10) wire. The bias voltage (U_{Bias}) refers to the sample, and the tunneling current (I) was at a constant value in the range of 10–50 pA. We usually adjusted the scanning plane parallel to the (35 1 1) plane of our sample in order to optimize the contrast of the images. The images were processed with the program SPIP [29], which included filtering out noise and an adjustment of the contrast. Additionally, to some images, a Prewitt or Roberts filter for edge enhancement was applied in order to enhance the visibility of the step edges.

The structure models were drawn with the free software Graphics Layout Engine [30]. The shown hard-sphere models

Beilstein J. Nanotechnol. **2024,** *15,* 556–568.

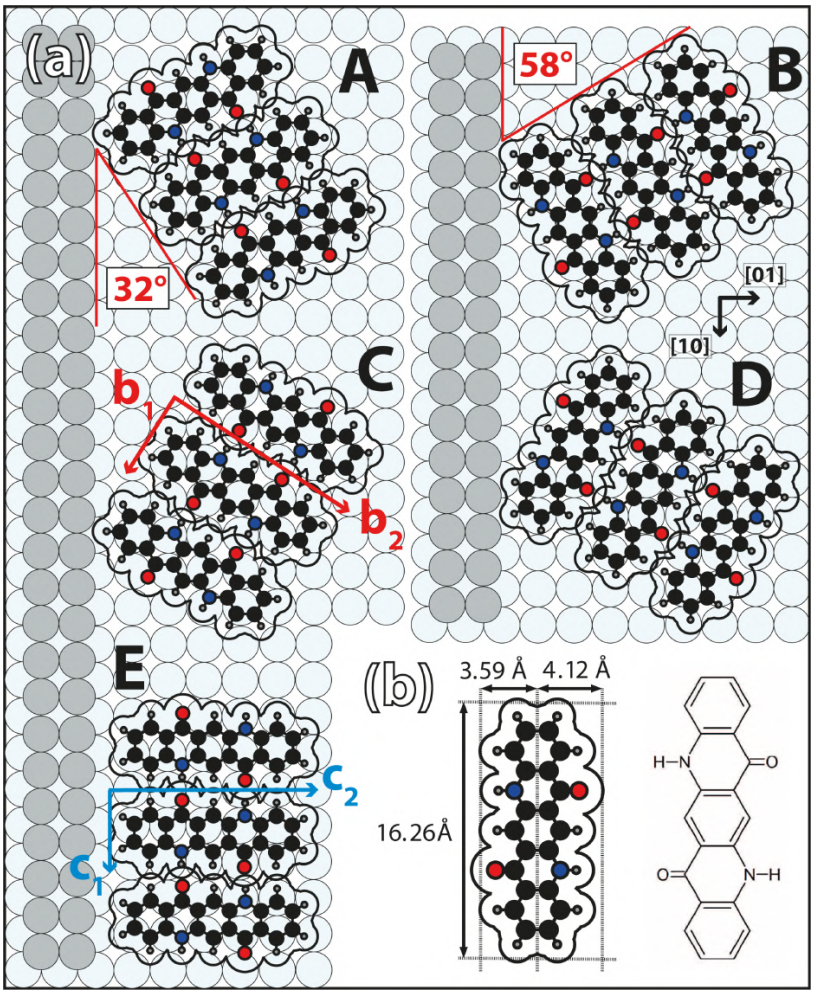

Figure 1: (a) Models of the five observed azimuthal QA chain orientations, A–E, relative to the unidirectional step edges of the Ag(35 1 1) surface. The four orientations A–D are identical to those that were already observed on the nominally flat Ag(100) surface [23]. The chain directions A and C, as well as B and D, exhibit equivalent adsorption sites because of a mirror symmetry. Note that the adsorbed molecules in A(C) and B(D) are of the same chirality R(L). For the chain orientation E there exists the energetically equivalent chain with molecules of the opposite chirality. The color code of the atoms is: black = carbon, gray = hydrogen, blue = nitrogen, and red = oxygen. (b) Structural formula and hard-sphere model with dimensions of QA. The nominal van der Waals radii used for the molecular models were taken from [27].

of QA use bond lengths [31] and van der Waals radii [27] from the literature.

Results and Discussion

The Ag(35 1 1) surface

The Ag(35 1 1) surface is vicinal (i.e., tilted by an angle of 2.3°) with respect to the Ag(100) surface. The step direction is along the [10] direction. In this work, we use the 2D unit cell of the Ag(100) terraces for reference. The corresponding [10] and [01] unit cell vectors are illustrated in Figure 1. These two orientations correspond to the [011] and the $[01\bar{1}]$ directions of the bulk crystal structure, respectively. In the LEED images (reciprocal space), the labels [10] and [01] also refer to the corresponding directions in real space and those of the reciprocal unit cell vectors.

On average, the steps are separated by a length of $\Lambda = 50.5$ Å or 17.5 atom rows. Regarding possible QA chains (see, e.g., Figure 1) on this surface, this means that up to three chains, parallel to an adjacent step edge, would fit on a terrace (one chain is 16.5 Å in width). A QA chain that is oriented perpendicular to the step edges would consist of seven molecules on one terrace (the intermolecular distance within a QA chain is 6.6 Å).

Beilstein J. Nanotechnol. 2024, 15, 556–568.

An STM image of the Ag(35 1 1) surface is shown in Figure S1a of Supporting Information File 1. The STM image reveals that the Ag steps are not regularly spaced. Instead, the distribution of the terrace widths is very broad. The step distribution that was obtained by evaluating STM images with an Python script reported by Bastidas et al. [32] is shown in Figure S1b in Supporting Information File 1. On the left-hand side of the STM image (Figure S1, Supporting Information File 1), the average distance between the steps is only 20 Å (seven atom rows), which is less than half of the expected terrace width of 50.5 Å. At the same time, the surface also exhibits flat areas with wide terraces of up to 300 Å in width. This can also be seen in the STM image. A similar type of step width distribution was also found for various other surfaces, for example, Cu(11*n*) [33] with n = 5, 9, 17, and Si(100) as well as Si(111) [34]. These aspects are of importance for the formation of QA structures on Ag(35 1 1), which will be reported below.

Deposition at 300 K

In many aspects, the growth of QA on Ag(35 1 1) is very similar to its growth on the nominally flat Ag(100) surface [23]. Upon deposition at a sample temperature of 300 K, QA forms the same kind of parallel chains of molecules that are connected via H-bonds, which can only be formed between molecules of the same handedness [23] on the surface. Hence, the chains are homochiral, and chains of the same azimuthal orientation consist of the same enantiomers. Like on Ag(100), the distance between the chains, b_2, depends on the coverage as they repel one another because of a substrate-mediated interaction. The intermolecular distance along the chains is $b_1 = 6.6 \pm 0.2$ Å, and is, within the margins of error, identical to the distance on Ag(100) [23] (see Figure 1). The chains exhibit four distinct azimuthal orientations, which are identical to the ones that we observed previously on the nominally flat Ag(100) surface [23] and will be named A–D in the following. Models of the four chain directions A–D relative to the direction of the step edges of the Ag(35 1 1) surface are illustrated in Figure 1. Because of the interactions at the step edges, only the chains A and C, as well as the chains B and D are energetically equivalent because of a remaining mirror plane perpendicular to the steps (see Figure 1). This is in contrast to the ideal (100) surface, where all four orientations are equivalent because of the additional rotational symmetry.

An STM image of the QA chains on Ag(35 1 1) is displayed in Figure 2a. It shows domains of parallel chains belonging to one of the azimuthal orientations A and D. This is an example of a common observation we made: In most areas of the surface with unidirectional step edges of not too small distance, these two out of the four orientations A–D were preferentially observed. However, we do not deduce yet that the orientations A and D are generally preferred over B and C because the statistics acquired from STM images are insufficient for reliable conclusions, although the images were deliberately collected from different regions of the sample. A corresponding LEED image is displayed below in Figure 3a and shows spots corresponding to the four azimuthal orientations with similar intensities. This shows that, on average, all four orientations are present on the surface with equal probability.

Growth across steps

A particularly striking observation from the STM image in Figure 2a is that, at step edges, the QA chains on the lower terrace very often continue at the exact position of the step edge where a chain on the upper terrace ends. For a coverage of 0.8 ML, this occurs in about 90% of all cases when a QA chain reaches a Ag step edge. At lower coverages, this phenomenon is less likely (at 0.45 ML only about 70%). When QA chains continue across the step, in about 50% of all cases a visible gap or break in the chain (discontinuity) can be seen (red circles in Figure 2a), while in the other 50% of all cases, it looks as if the chain grows undistorted across the Ag step (light blue circles). For a closer look, a zoom-in onto chains at Ag step edges with molecular resolution is displayed in the inset. The blue circle highlights a chain that grows across the step edge with all individual molecules being distinguishable. The red circle shows a chain with a discontinuity in the periodic structure, leading to a lateral offset between the two parts of the chain at the step edge. The chain in the middle of the inset (not marked by a circle) grows continuously across the Ag step, but three molecules close to the step edge appear slightly rotated with respect to the other molecules of the chain. This is an example of a slight distortion of the azimuthal orientations of the molecules in the chain, which we have observed frequently for chains growing continuously across Ag steps. In the literature, it has also been reported that linear molecules can bend when crossing a step edge [35,36]. We suppose that this is not the case here because the QA molecule is shorter and stiffer because of its planar structure. The above observation shows that the intermolecular H-bonds are capable of stabilizing the growth of QA chains across Ag step edges. The reason why the chains grow only occasionally continuously across the step edges will be discussed below. A similar observation of molecular chains that are formed by H-bonds and grow across step edges was made for 2,6-naphthalene-dicarboxylic acid (NDCA) on a vicinal Ag(110) surface [37].

From the above observations, conclusions about the chain growth can be drawn. The fact that the four azimuthal chain orientations A–D are present on the surface with equal probability indicates that, at 300 K, the nuclei of the chains start growing on the terraces where all four orientations are energeti-

Beilstein J. Nanotechnol. **2024,** *15,* 556–568.

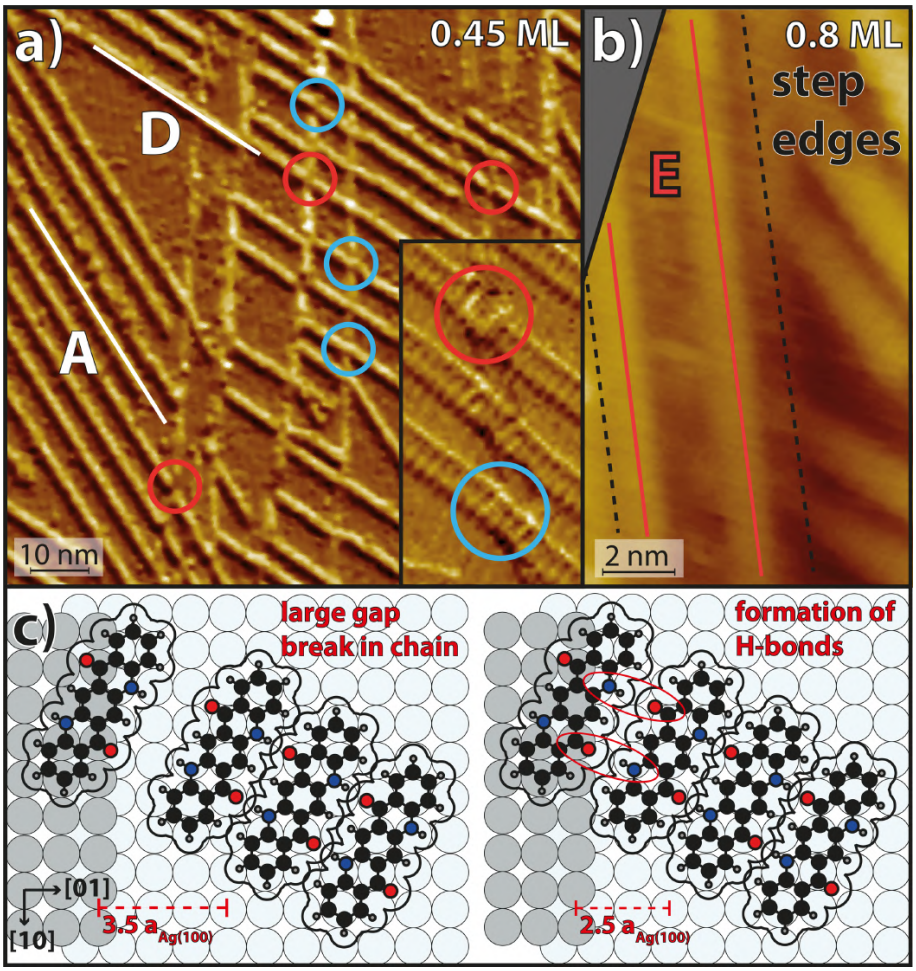

Figure 2: QA on the Ag(35 1 1) surface deposited at a sample temperature of 300 K. (a) STM image (U_{Bias} = −1.55 V, I = 40 pA) showing many parallel QA chains with the two azimuthal orientations A and D. The left-hand side of a step edge corresponds to its upper terrace and the right-hand side to its lower terrace. The red and blue circles highlight cases in which there is a break in a chain at a step edge and where the chains appears to grow seamlessly over the step edge, respectively. The inset shows an image at a different sample position of three QA chains at a Ag step edge, which was chosen for the high molecular resolution. (b) Small-scale STM image (U_{Bias} = 1.5 V, I = 25 pA) showing two of the four azimuthal orientations A and D, as well as two chains in the new orientation E (red lines). The black dashed lines indicate the positions of the step edges. (c) Models of chain growth at Ag step edges. These illustrate that the chains that nucleated on the lower terrace may statistically end in two positions with respect to the step edge. The left-hand side shows the case where the gap between the molecules on the upper and lower terrace is too large to allow for the formation of H-bonds. The right-hand side shows the case where the chain is one Ag lattice constant closer to the step edge, which allows for the formation of H-bonds across the step.

cally equivalent, and not at the steps. The chain nuclei grow at both of their ends until both step edges of a terrace are reached. For an explanation of the continuous or distorted growth of the chains across the steps, we propose the following model: We note that, because of the specific orientation and size of the molecules, the distance between the ends of the chains and the step edge can vary by one Ag(100) lattice constant ($a_{Ag(100)}$ = 2.89 Å [31]). This is illustrated by the two models in Figure 2c. We suppose that the adsorption of a QA molecule at the step edge on the upper/lower terrace induces a local change in the electron density at the step edge. This favors a specific adsorption site of a second QA molecule with the same chirality and azimuthal orientation at the step edge on the lower/upper terrace. Hence, the growth of the QA chain continues at a nearest position of the step edge where the chain on the upper/lower terrace ends. If both molecules come close enough to the step edge (see the two cases in Figure 2c), intermolecular H-bonds may form across the step, and the chain continues in an undistorted structure. In the alternative case, a small gap between the two molecules close to the step is formed.

Beilstein J. Nanotechnol. **2024,** *15,* 556–568.

New step-induced orientation

Another interesting observation is that, on Ag(35 1 1), a fifth azimuthal orientation exists, which is parallel to the Ag step edges. This orientation will be labeled E from now on. It does not occur on the nominally flat Ag(100) surface. This indicates that, on large terraces, the orientation E is less favorable than A–D, but it is stabilized by the step edges of the vicinal surface. A model of a chain with orientation E is illustrated in Figure 1a. Two chains of this orientation E on one terrace are highlighted by red lines in the STM image in Figure 2b. These kinds of chains were observed rarely by STM and were, in particular, never observed by STM on terraces wider than 50 Å. Nevertheless, a LEED image (discussed below) shows additional spots that need to be explained by this chain orientation. The LEED image indicates that even domains of several parallel chains (at least five or more) of orientation E are present. This difference between the STM and LEED data is again attributed to the fact that the STM images sampled only a limited region on the sample where such domains were not present. Furthermore, the fact that the chains of orientation E are parallel and close to the Ag step edges (as seen in Figure 2b) might have caused that they are difficult to image by STM and were, hence, overlooked.

We now discuss the corresponding features in the LEED images in detail. A LEED image of QA with a coverage of θ_{QA} = 0.65 ML is illustrated in Figure 3a. It is very similar to that of the α-phase of QA/Ag(100) but contains additional spots. The α-phase is defined as the phase of parallel QA chains

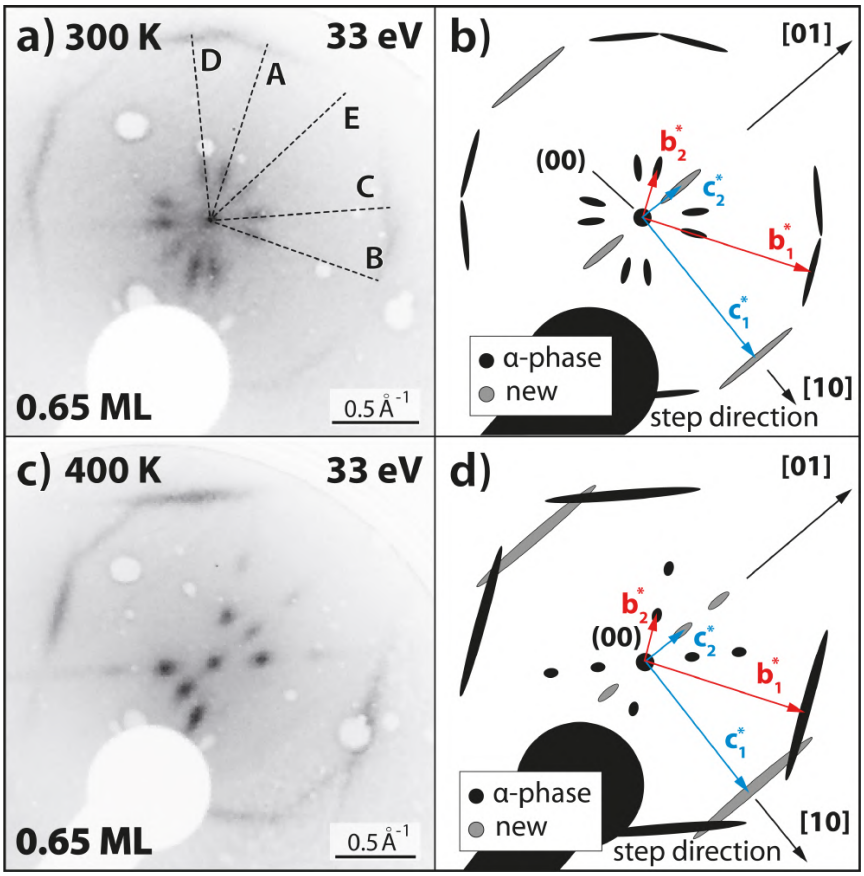

Figure 3: (a) LEED image (E = 33 eV, T = 300 K) of the region around the specular spot of 0.65 ML QA on Ag(35 1 1) after deposition at a sample temperature of 300 K. Note that the sample was rotated with respect to the normal incidence geometry. The diffraction pattern is very similar to the one of the QA α-phase on Ag(100) but contains additional spots that correspond to the new chain orientation E. The black dashed lines indicate the five azimuthal chain orientations. (b) Schematic drawing of the LEED pattern in panel (a). It shows the observed spots and the unit cell vectors of orientations A and E. (c) Same as (a) but for θ_{QA} = 0.65 ML and a deposition at 400 K. The diffraction pattern is very similar to the one in panel (a). However, it is missing two sets of spots corresponding to orientations B and D. (d) Schematic drawing of the observed LEED pattern in panel (c) containing all the observed spots and the corresponding unit cells. Both LEED images were measured under an in-phase condition for the specular spot with respect to monoatomic Ag steps [38]. This causes that the spots are sharp and not broadened because of the Ag steps. The scale bars for the LEED images are only approximately valid because of the distortion caused by the MCP geometry.

Beilstein J. Nanotechnol. 2024, 15, 556–568.

at a coverage of θ_{QA} = 1.0 ML, at which the distance b_2 between the chains is minimal [23]. The model of the diffraction pattern in Figure 3b shows the spots of the known α-phase diffraction pattern in black and the new spots in gray. The reciprocal vectors of the α-phase and those of the new orientation E are depicted in red and light blue, respectively. The spot described by the vector $\mathbf{c}_1^*$ of orientation E corresponds to the intermolecular distances within the chains. This spot is also oriented in the [10] direction of the substrate, which confirms that the chain orientation E is indeed parallel to the Ag step edges. The other new spot, which is described by the vector $\mathbf{c}_2^*$, corresponds to the distance between neighboring QA chains in orientation E. The length c_2^* is identical to b_2^*, which means that the distance c_2 between the chains of orientation E is identical to the distance b_2 between neighboring chains of domains of the other orientations. This distance is $c_2 = b_2 = 25 \pm 2$ Å and, hence, amounts to roughly half of the average terrace width (for the definition of $\mathbf{c_1}$ and $\mathbf{c_2}$ see Figure 1). This implies that only two chains of orientation E would fit onto one average terrace at this coverage. But from the sharpness of the spots, we conclude that these stem from domains of several parallel chains of orientation E, which have formed either on large terraces or even extend across the steps over several neighboring terraces. However, the spots given by the vector $\mathbf{c}_2^*$ are still more smeared out (broader by 25%) than those from the α-phase, given by $\mathbf{b}_2^*$. This can be explained by the fact that the domains of orientation E in the direction perpendicular to the chains are smaller than those of the other four orientations A–D.

The formation of similar one-dimensional structures parallel to the step edges of a vicinal crystal has been observed before, for example, PTCDA on Au(433) and Au(778) [16], a 1:1 mixture of PTCDI and 1,4-bis(2,4-diamino-1,3,5-triazine)benzene on Au(11 11 12) [17], α-6T on Ag(441) [39], and nickel tetraphenylporphyrin on Au (788) [18].

Deposition at 400 K

Interestingly, after the deposition of QA onto Ag(35 1 1) at an elevated sample temperature of 400 K, the resulting QA structures have changed significantly. The LEED images (Figure 3c,d) show that the layer still consists of domains of parallel chains, but only the orientations A, C, and E are present. Moreover, the spots are smaller, sharper, and more intense than their counterparts in Figure 3a. This shows that the structures are less disordered and the domains (in the direction perpendicular to the chains) are larger than the ones after deposition at 300 K.

Corresponding STM images of different resolutions and sizes and a corresponding structure model are displayed in Figure 4. They show domains of parallel chains in the orientations A and C, as well as in the orientation E, which is parallel to the Ag step edges. The intermolecular distance within the chains remained unchanged for all azimuthal orientations at 6.6 ± 0.2 Å. The biggest difference from the structures after deposition at 300 K is the absence of the orientations B and D, which confirms above LEED results. This symmetry break can only be explained by the step edges and is a strong indication that, at 400 K, the nucleation of the chains proceeds now from the Ag step edges. The molecules in chains of orientations A and C (which exhibit equivalent adsorption geometries at the Ag step edges, see Figure 1) adapt more favorable adsorption sites than those in orientations B and D. Hence, the nuclei of orientations A and C are more stable. In addition, it may be possible that the increased mobility of the QA molecules causes short chains of orientations B and D to dissolve and integrate into the step-stabilized chains with the orientations A and C, instead.

A potential explanation for the higher stability of nuclei of orientations A and C may be that, at 400 K, Ag atoms can thermally detach from the Ag step edges. This enables the QA molecules to find a thermodynamically more stable adsorption geometry at the step edges in orientations A and C, possibly including a replacement of Ag atoms in the step edges by a part of the molecule. Indeed, a closer look at the STM image (see Figure 4c) shows a periodic zig-zag pattern of the Ag step edges (indicated by the black dashed lines). This is induced by the starting points of QA chains that replace some of the Ag atoms in the step edge in order to maximize the interactions between the molecules and the step edge. This is similar to the situation of PTCDA molecules at KCl, NaCl, or KBr step edges [40-42]. A corresponding structure model of QA chains at Ag step edges is displayed in Figure 4d. Furthermore, the STM image shows several small protrusions where the QA chains end at the Ag step edge. We assign these to small clusters of the Ag atoms that were expelled from the step edges by the QA molecules.

Another interesting difference from the structures after deposition at 300 K is that, after the deposition at 400 K, there are more chains with orientation E parallel to the step edges (highlighted by the red line in Figure 4b). Most small terraces (width < 50 Å) inspected by STM had at least one chain with orientation E close to the upward-pointing step edge. The higher abundance of orientation E after deposition at 400 K is also confirmed by LEED because the corresponding spot is more intense and sharper (see Figure 3). The growth of chains in orientation E parallel to the step edges is favored at elevated temperatures because, for these chains, the intermolecular H-bonds are not distorted by the steps. In addition, the chains are stabilized by the long-range dispersion interactions of the QA with the atoms of the step edge.

Beilstein J. Nanotechnol. **2024,** *15,* 556–568.

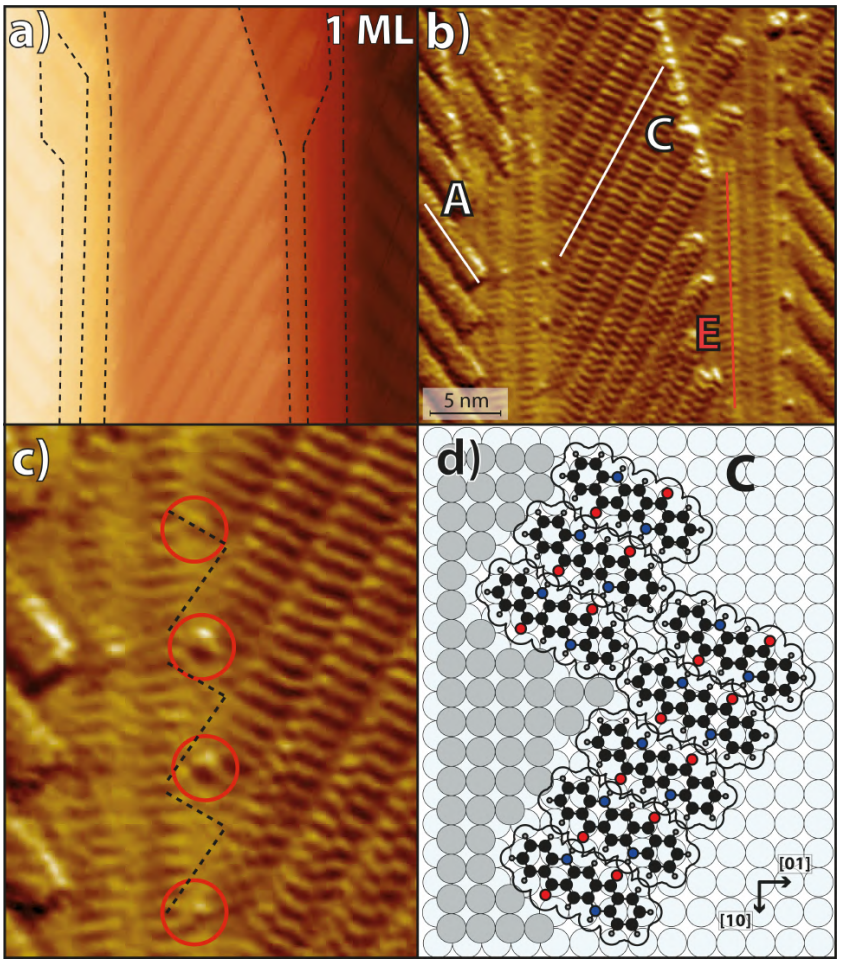

Figure 4: (a) STM image (U_{Bias} = −1.5 V, I = 25 pA) of QA on the Ag(35 1 1) surface deposited at a sample temperature of 400 K. It shows an area with several step edges running vertically through the image, which are highlighted by the dashed black lines. (b) The same STM image as in panel (a) with a Prewitt filter for better visibility of the QA structures. The image shows domains of parallel QA chains with the three orientations A, C, and E. (c) Zoom-in onto the STM image in panel (b) showing the QA chains at step edges. (d) Structure model of chains in orientation C at a step corresponding to panel (c). The black dashed lines mark the Ag step edges and the red circles highlight small circular protrusions that are assigned to small Ag clusters.

A further observation is that, after deposition at 400 K, no cases of chains continuously growing across Ag step edges could be observed anymore. The reason is that now the growth of the chains begins at the step edges, and the QA molecules at the start of the chains exhibit a strong bond to the Ag atoms of the step edges. Hence, they cannot provide H-bonds for chain growth across the steps. A second reason is that now the orientation E is significantly more prevalent than after deposition at 300 K, and these chains block other chains from growing across the steps.

Overall, these results show that the higher temperature of 400 K has led to the preferred formation of the three chain orientations A, C, and E, which are thermodynamically more stable than the orientations B and D.

Deposition at 500 K

Last, we discuss the structure of QA after deposition at 500 K. From our previous work regarding QA on Ag(100), we know that the elevated temperature induces an irreversible phase transition into a heterochiral and commensurate structure, the so-called β-phase [23]. This phase is also obtained after deposition at 500 K and subsequent cooling to 300 K. This preparation was chosen here. The β-phase also consists of parallel molecular chains of QA dimers as the α-phase, but with periodic indents along the chains. The molecules in the domains of the

Beilstein J. Nanotechnol. **2024,** *15,* 556–568.

β-phase exhibit the same azimuthal orientations as those in the α-phase. We find that the β-phase also forms on Ag(35 1 1), and the domains of the β-phase on Ag(35 1 1) will also be labeled A–D.

A corresponding LEED image (θ_{QA} = 0.65 ML) and a simulation are displayed in Figure 5a and Figure 5b, respectively. The spot positions in the LEED image are identical to those of the LEED image of QA on Ag(100) and, in principle, all four domains are seen. However, a striking difference is that, here, there is a very prominent inequivalence regarding the spot intensities. Half of the spots have significantly less intensity than the other half, which means that two domains of the β-phase are more prevalent than the other two domains. These are the domains A and C. This shows that, at 500 K, the growth of the β-phase also begins at the step edges, which leads to the observed preferential growth of two domains. This is in agreement with the above results regarding the growth of QA at 400 K and supports the scenario that the growth of QA chains starts at the Ag step edges at elevated temperatures.

All spots of the LEED pattern are very sharp. Hence, the corresponding domains are significantly larger than the average terrace width of 50 Å. A coherent continuation of the domains

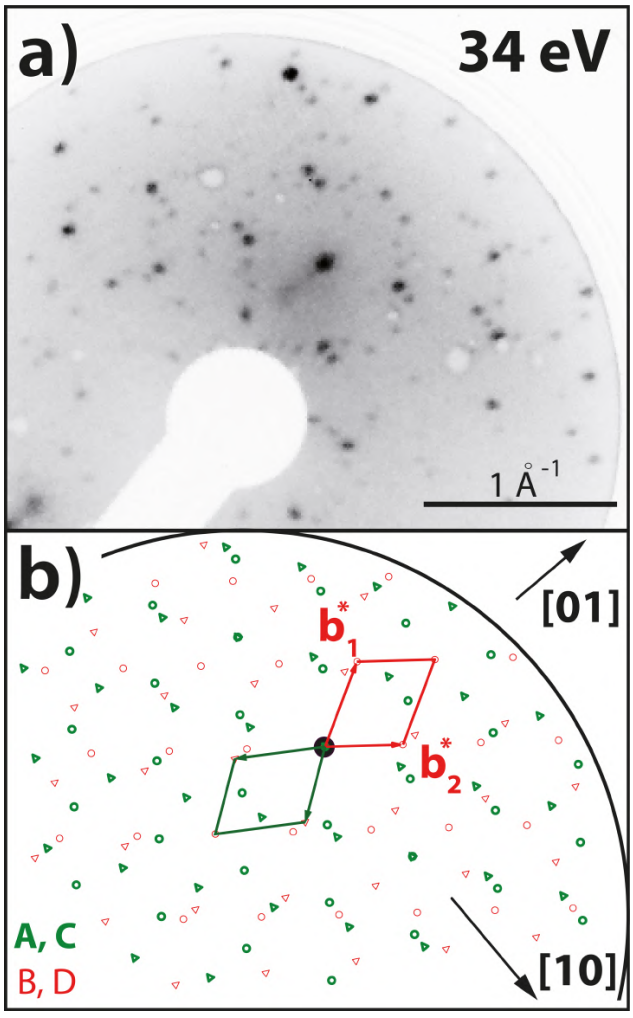

Figure 5: (a) LEED image (*E* = 33 eV, *T* = 300 K) of the β-phase of 0.65 ML QA on Ag(35 1 1) after deposition at a sample temperature of 500 K and subsequent cooling to 300 K. The diffraction pattern is very similar to the one of the QA β-phase on Ag(100) but exhibits a clear anisotropy. Roughly half of the spots are more intense than the other half. This LEED image was measured under an in-phase condition for the specular spot with respect to monoatomic Ag steps. (b) Simulated LEED pattern of the β-phase. The spots that are thicker and green correspond to the more intense spots in the diffraction pattern, which correspond to orientations A and C. The step direction is in the [10] direction, as before.

Beilstein J. Nanotechnol. 2024, 15, 556–568.

across the Ag step is very unlikely. As stated above, the terrace width distribution of the Ag(35 1 1) surface is rather broad with terrace widths of up to 300 Å. Thus, we conclude that the β-phase predominantly forms on those large terraces. This is also supported by the STM results, which show that large terraces were completely covered by one of the four β-phase domains (not shown). Furthermore, in areas of the sample where many step edges are very close to each other and the terraces are very small (below 50 Å), no QA molecules were observed on the terraces. This indicates that the molecules diffused off the small terraces onto larger ones because the space on the small terraces is not sufficient to form the β-phase. One may also ask whether this preference of the β-phase for large terraces leads to a step bunching on the substrate surface in order to increase the size of the terraces. However, we could not find any evidence that the terrace width distribution changed significantly after the preparation of the β-phase.

As already postulated above, we assume that, upon adsorption at the step edges, the QA molecules replace Ag atoms in order to maximize their adsorption energy. The nuclei of orientations A and C are more stable; thus, the growth of the corresponding domains is favored compared to that of the orientations B and D. Nevertheless, the orientations B and D are still present on the surface to some minor extent, which can possibly be explained by domains that nucleate and grow on large terraces and not at steps.

Final Discussion

Energetic considerations regarding chains parallel to the steps

The chain orientation E is not present on the nominally flat Ag(100) surface [23], which means that it must be induced by the step edges of the vicinal surface. On Ag(35 1 1), chains of orientations E were mainly observed close to step edges, that is, the far end of the molecule was within 20 Å. Remarkably, we do not find any step decorations by the QA molecules with their long axis close and parallel to the steps. Nevertheless, the step edges play an important role in the formation of chains of orientation E. The absence of chains with orientation E on the nominally flat surface shows that orientation E is energetically less favorable than the orientations A–D in terms of direct interactions between the QA molecules and the Ag(100) surface. This means that the nuclei with orientation E are less stable than those with orientations A–D on terraces. However, if chains of orientation E grow parallel to step edges, they are additionally stabilized because, owing to the close proximity, every molecule in the chain is subject to attractive dispersion interactions with the Ag step edge. This is not the case for orientations A–D, which grow away from the step edges. A model of such a chain of orientation E at a step edge is illustrated in Figure 1a.

A second aspect that favors the growth of chains with orientation E on small terraces is that, because they are parallel to the step edges, they can grow without encountering any distortions at Ag steps, as is the case for long chains of the orientations A–D in areas with a high density of unidirectional steps. Nevertheless, on the small terraces, the formation of chains with orientation E may be kinetically inhibited because of a lack of space, which hinders the diffusion of the molecules to the growing endpoints of the chains. This is supported by the fact that an increased mobility of QA molecules (i.e., during deposition at a sample temperature of 400 K instead of 300 K) promotes the formation of chains with orientation E.

QA chain growth across Ag step edges

As stated above, at 300 K, the QA chains are capable of growing continuously across Ag step edges. This brings forth some interesting aspects, which we discuss here. A chain across step edges without a significant break and intact intermolecular H-bonds requires some structural flexibility in the molecules and/or the intermolecular bonds. We suppose that QA molecules cannot bend in the plane of the π systems because of the annulated carbon rings. In contrast, H-bonds are mainly of electrostatic nature and, thus, have a pronounced flexibility in bond lengths and angles, which supports intermolecular bonds across step edges. Similar molecular chains that are connected by H-bonds and grow across monoatomic step edges without a break were observed before for NDCA on a vicinal Ag(110) surface by Schnadt et al. [37]. They found that the slight distortion of the chains at step edges leads only to a minor energy loss (below 0.1 eV), which is energetically still more favorable than a scenario in which no H-bonds are formed across the step edges. We propose that a similar situation is present here.

Another interesting question concerns the angle between the QA chains and the step edges. Schnadt et al. found that the self-assembly across step edges crucially depends on the azimuthal orientations of the chains relative to the step edges [37]. The chains of NDCA grow along the [10] direction of the substrate and are, thus, orthogonal to the direction of the step edges, which are oriented along the [01] direction. Density functional theory calculations have shown that the NDCA chains do not cross the step edges if they are rotated away from the close-packed rows [37]. In contrast, in our case, no chains grow across the step edges at a 90° angle. The QA chains continuously grow across the step edges in the four azimuthal orientations A–D, resulting in angles of 32° and 58° between the chains and the Ag step edges. Hence, such a strict selection of the

Beilstein J. Nanotechnol. 2024, 15, 556–568.

azimuthal angle of the chains, similar to the one found by Schnadt et al., does not apply to QA.

Anisotropic β-phase

Now we discuss an interesting aspect regarding the β-phase on Ag(35 1 1), namely the fact that the minority orientations B and D are present on the surface after the deposition at 500 K, although chains with these orientations could not be observed after the deposition at 400 K (see Figure 3c and Figure 4). This can be explained by the stability of the different QA phases. After the deposition at 500 K and subsequent cooling, the β-phase domains of orientations B and D have formed on the large terraces in addition to the majority domains with orientations A and C. The transition from a disordered phase after deposition at 500 K to the ordered β-phase occurs at about 450 K. These domains are more stable than the single chains with the same orientations B and D of the α-phase because of their commensurate nature. Hence, they do not completely transform into the domains of orientations A and C.

One might also ask whether annealing the sample at 500 K for a longer time, or several consecutive annealing steps at 500 K, might further change the ratio in favor of orientations A and C. This was not the case. We observed the same intensity ratio between the stronger and weaker spots in the LEED pattern after every preparation and several consecutive annealing cycles. This can be explained by the fact that, at 500 K, the β-phase again dissolves into a disordered phase and only forms again upon cooling [23]. Hence, the cooling rate may be relevant for the ratio between orientations A/C and B/D in the β-phase, but this was not investigated, yet.

Comparison to literature

Last, we discuss some similarities and differences between our results and some that were published previously. One similarity to other molecular systems is the growth of the QA chains with orientation E, which grow along the Ag step edges. Such a behavior was found for a few other organic molecules on different vicinal metal surfaces [17,18]. This shows that the contribution of the interactions between the atoms of the step edges and the organic molecules to the adsorption energy of the molecules is a common and important motif for the adsorption and self-assembly of organic molecules on stepped surfaces. We note, however, that the orientations of the QA molecules with respect to the steps at 300 K are unusual. Many examples from the literature that report on the decoration of steps by organic molecules found that the molecules adsorb in a flat-lying configuration with their long axis parallel to the step edges [43-45]. In some cases, an adsorption of upright standing molecules at steps was also found [45,46]. Here, the QA molecules are either oriented with their short edge parallel to the steps or at an angle of 32° or 58° with respect to the step direction. A stark difference to the examples described in the above publications is that, here, the Ag step edges also cause the preferential growth of QA chains or commensurate domains with distinct step-selected orientations at elevated temperatures. A similar phenomenon has, to the best of our knowledge, not been reported, so far.

Another phenomenon that was reported by Schmitt et al. [47] for PTCDA on vicinal Ag(100) surfaces is the faceting of the Ag substrate surface that is induced by the adsorption of the molecules. They found that the adsorption of PTCDA leads to the formation of Ag facets, which are usually not stable on the bare surface and are induced by the adsorption of PTCDA. However, within the scope of the present work, we did not observe any faceting of the Ag(35 1 1) surface. This is because the adsorption energy of QA is likely significantly smaller than the one of PTCDA on Ag surfaces.

Conclusion

We found that, at room temperature (RT), the growth of QA on the vicinal Ag(35 1 1) surface is, in general, very similar to its growth on the nominally flat Ag(100) surface. QA forms molecular homochiral chains with four distinct symmetry-equivalent orientations that are connected via H-bonds (α-phase). At RT, the growth of the chains begins on the Ag terraces, and the unidirectional step edges do not have any influence on the azimuthal orientations of the chains. Furthermore, the QA chains grow across the steps. We also found one azimuthal chain direction that does not exist on Ag(100) and is parallel to the unidirectional step edges of the vicinal surface. This is explained by the fact that the growth in this direction is additionally stabilized by the dispersion interactions between the QA molecules and the atoms of the Ag step edges, which overcompensates the lower site energy of the molecules on the terraces in this orientation.

After deposition at 400 K, only two of the above four azimuthal orientations are observed. Furthermore, the deposition at 500 K leads to heterochiral chains in a commensurate structure (β-phase) that also exhibits a strong anisotropy, that is, two domains are favored over the other two. In both situations, the preferential growth of specific orientations at 400 and 500 K is caused by a growth start of the QA structures at the Ag step edges at elevated temperatures. Thus, the step edges have a strong influence on the azimuthal orientations of the QA structures because adsorption sites at the Ag step edges of molecules in two distinct azimuthal orientations out of four are favored.

Overall, the azimuthal orientations of one-dimensional QA chains can be influenced by step edges on vicinal surfaces. Our

Beilstein J. Nanotechnol. 2024, 15, 556–568.

work is of importance for the general understanding of the interactions between organic molecules and metallic step edges and may be helpful for the preparation of one-dimensional organic structures with a global preferential orientation on surfaces.

Supporting Information

The Supporting Information features an STM image of the bare Ag(35 1 1) surface and a corresponding step edge distribution.

Supporting Information File 1

Terrace width distribution on Ag(35 1 1)
[https://www.beilstein-journals.org/bjnano/content/supplementary/2190-4286-15-48-S1.pdf]

Acknowledgements

We thank A. J. Kny and M. Specht for experimental support.

Funding

Financial support by the Deutsche Forschungsgemeinschaft (DFG) under project So407/6-3 and the research training group 2591 is acknowledged.

Author Contributions

Niklas Humberg: conceptualization; formal analysis; investigation; visualization; writing – original draft; writing – review & editing. Lukas Grönwoldt: formal analysis; investigation; visualization. Moritz Sokolowski: conceptualization; funding acquisition; project administration; resources; supervision; writing – review & editing.

ORCID® iDs

Niklas Humberg - https://orcid.org/0009-0007-6197-5740
Lukas Grönwoldt - https://orcid.org/0009-0003-0722-2431
Moritz Sokolowski - https://orcid.org/0000-0001-5991-3910

Data Availability Statement

The data that supports the findings of this study is available from the corresponding author upon reasonable request.

References

1. Ariga, K.; Nishikawa, M.; Mori, T.; Takeya, J.; Shrestha, L. K.; Hill, J. P. *Sci. Technol. Adv. Mater.* **2019,** *20,* 51–95. doi:10.1080/14686996.2018.1553108
2. Goronzy, D. P.; Ebrahimi, M.; Rosei, F.; Arramel; Fang, Y.; De Feyter, S.; Tait, S. L.; Wang, C.; Beton, P. H.; Wee, A. T. S.; Weiss, P. S.; Perepichka, D. F. *ACS Nano* **2018,** *12,* 7445–7481. doi:10.1021/acsnano.8b03513
3. Amadi, E. V.; Venkataraman, A.; Papadopoulos, C. *Nanotechnology* **2022,** *33,* 132001. doi:10.1088/1361-6528/ac3f54
4. Ren, H.; Wu, L.; Tan, L.; Bao, Y.; Ma, Y.; Jin, Y.; Zou, Q. *Beilstein J. Nanotechnol.* **2021,** *12,* 1140–1150. doi:10.3762/bjnano.12.85
5. Garnett, E.; Mai, L.; Yang, P. *Chem. Rev.* **2019,** *119,* 8955–8957. doi:10.1021/acs.chemrev.9b00423
6. Zhou, G.; Xu, L.; Hu, G.; Mai, L.; Cui, Y. *Chem. Rev.* **2019,** *119,* 11042–11109. doi:10.1021/acs.chemrev.9b00326
7. Goktas, N. I.; Wilson, P.; Ghukasyan, A.; Wagner, D.; McNamee, S.; LaPierre, R. R. *Appl. Phys. Rev.* **2018,** *5,* 041305. doi:10.1063/1.5054842
8. Patzsch, J.; Babu, D. J.; Schneider, J. J. *Beilstein J. Nanotechnol.* **2017,** *8,* 1135–1144. doi:10.3762/bjnano.8.115
9. Imran, M.; Motta, N.; Shafiei, M. *Beilstein J. Nanotechnol.* **2018,** *9,* 2128–2170. doi:10.3762/bjnano.9.202
10. Tegenkamp, C. *J. Phys.: Condens. Matter* **2009,** *21,* 013002. doi:10.1088/0953-8984/21/1/013002
11. Ahn, J. R.; Yeom, H. W.; Yoon, H. S.; Lyo, I.-W. *Phys. Rev. Lett.* **2003,** *91,* 196403. doi:10.1103/physrevlett.91.196403
12. Crain, J. N.; Kirakosian, A.; Altmann, K. N.; Bromberger, C.; Erwin, S. C.; McChesney, J. L.; Lin, J.-L.; Himpsel, F. J. *Phys. Rev. Lett.* **2003,** *90,* 176805. doi:10.1103/physrevlett.90.176805
13. Crain, J. N.; Himpsel, F. J. *Appl. Phys. A: Mater. Sci. Process.* **2006,** *82,* 431–438. doi:10.1007/s00339-005-3365-3
14. Schwingenschlögl, U.; Schuster, C. *EPL* **2008,** *81,* 26001. doi:10.1209/0295-5075/81/26001
15. Gurlu, O.; Adam, O. A. O.; Zandvliet, H. J. W.; Poelsema, B. *Appl. Phys. Lett.* **2003,** *83,* 4610–4612. doi:10.1063/1.1630383
16. Kröger, J.; Néel, N.; Jensen, H.; Berndt, R.; Rurali, R.; Lorente, N. *J. Phys.: Condens. Matter* **2006,** *18,* S51–S66. doi:10.1088/0953-8984/18/13/s04
17. Cañas-Ventura, M. E.; Xiao, W.; Wasserfallen, D.; Müllen, K.; Brune, H.; Barth, J. V.; Fasel, R. *Angew. Chem., Int. Ed.* **2007,** *46,* 1814–1818. doi:10.1002/anie.200604083
18. Fatayer, S.; Prieto, M. J.; Landers, R.; de Siervo, A. *Surf. Sci.* **2022,** *723,* 122105. doi:10.1016/j.susc.2022.122105
19. Humberg, N.; Guo, Q.; Bredow, T.; Sokolowski, M. *J. Phys. Chem. C* **2023,** *127,* 23814–23826. doi:10.1021/acs.jpcc.3c04402
20. Głowacki, E. D.; Leonat, L.; Irimia-Vladu, M.; Schwödiauer, R.; Ullah, M.; Sitter, H.; Bauer, S.; Serdar Sariciftci, N. *Appl. Phys. Lett.* **2012,** *101,* 023305. doi:10.1063/1.4736579
21. Głowacki, E. D.; Irimia-Vladu, M.; Kaltenbrunner, M.; Gsiorowski, J.; White, M. S.; Monkowius, U.; Romanazzi, G.; Suranna, G. P.; Mastrorilli, P.; Sekitani, T.; Bauer, S.; Someya, T.; Torsi, L.; Sariciftci, N. S. *Adv. Mater. (Weinheim, Ger.)* **2013,** *25,* 1563–1569. doi:10.1002/adma.201204039
22. Wagner, T.; Györök, M.; Huber, D.; Zeppenfeld, P.; Głowacki, E. D. *J. Phys. Chem. C* **2014,** *118,* 10911–10920. doi:10.1021/jp502148x
23. Humberg, N.; Bretel, R.; Eslam, A.; Le Moal, E.; Sokolowski, M. *J. Phys. Chem. C* **2020,** *124,* 24861–24873. doi:10.1021/acs.jpcc.0c07850
24. Trixler, F.; Markert, T.; Lackinger, M.; Jamitzky, F.; Heckl, W. M. *Chem. – Eur. J.* **2007,** *13,* 7785–7790. doi:10.1002/chem.200700529
25. Eberle, A.; Nosek, A.; Büttner, J.; Markert, T.; Trixler, F. *CrystEngComm* **2017,** *19,* 1417–1426. doi:10.1039/c6ce02348g
26. Bretel, R.; Le Moal, S.; Oughaddou, H.; Le Moal, E. *Phys. Rev. B* **2023,** *108,* 125423. doi:10.1103/physrevb.108.125423
27. Bondi, A. *J. Phys. Chem.* **1964,** *68,* 441–451. doi:10.1021/j100785a001
28. Berg, D.; Nielinger, C.; Mader, W.; Sokolowski, M. *Synth. Met.* **2009,** *159,* 2599–2602. doi:10.1016/j.synthmet.2009.09.017

Beilstein J. Nanotechnol. **2024,** *15,* 556–568.

29. *Scanning Probe Image Processor,* version 4.8.7.0; Image-Metrology: Hørsholm, Denmark, 2009.
30. Graphics Layout Engine, version 4.2. https://glx.sourceforge.io/ (accessed Oct 20, 2023).
31. Weast, R. C. *CRC Handbook of Chemistry and Physics,* 55th ed.; CRC Press: Cleveland, Ohio, USA, 1974; pp F202–F203.
32. Bastidas, J. M. P.; Auras, S. V.; Juurlink, L. B. F. *Appl. Surf. Sci.* **2021,** *567,* 150821. doi:10.1016/j.apsusc.2021.150821
33. Néel, N.; Maroutian, T.; Douillard, L.; Ernst, H.-J. *Phys. Rev. Lett.* **2003,** *91,* 226103. doi:10.1103/physrevlett.91.226103
34. Yagi, K.; Minoda, H.; Degawa, M. *Surf. Sci. Rep.* **2001,** *43,* 45–126. doi:10.1016/s0167-5729(01)00013-9
35. Hlawacek, G.; Puschnig, P.; Frank, P.; Winkler, A.; Ambrosch-Draxl, C.; Teichert, C. *Science* **2008,** *321,* 108–111. doi:10.1126/science.1159455
36. Palczynski, K.; Herrmann, P.; Heimel, G.; Dzubiella, J. *Phys. Chem. Chem. Phys.* **2016,** *18,* 25329–25341. doi:10.1039/c6cp05251g
37. Schnadt, J.; Rauls, E.; Xu, W.; Vang, R. T.; Knudsen, J.; Lægsgaard, E.; Li, Z.; Hammer, B.; Besenbacher, F. *Phys. Rev. Lett.* **2008,** *100,* 046103. doi:10.1103/physrevlett.100.046103
38. Horn-von Hoegen, M. *Z. Kristallogr.* **1999,** *214,* 684–721. doi:10.1524/zkri.1999.214.11.684
39. Wagner, T.; Fritz, D. R.; Rudolfová, Z.; Zeppenfeld, P. *Surf. Sci.* **2018,** *667,* 17–24. doi:10.1016/j.susc.2017.09.008
40. Guo, Q.; Paulheim, A.; Sokolowski, M.; Aldahhak, H.; Rauls, E.; Schmidt, W. G. *J. Phys. Chem. C* **2014,** *118,* 29911–29918. doi:10.1021/jp509663s
41. Karacuban, H.; Koch, S.; Fendrich, M.; Wagner, T.; Möller, R. *Nanotechnology* **2011,** *22,* 295305. doi:10.1088/0957-4484/22/29/295305
42. Loppacher, C.; Zerweck, U.; Eng, L. M.; Gemming, S.; Seifert, G.; Olbrich, C.; Morawetz, K.; Schreiber, M. *Nanotechnology* **2006,** *17,* 1568–1573. doi:10.1088/0957-4484/17/6/006
43. Matos, J.; Kara, A. *J. Phys.: Condens. Matter* **2016,** *28,* 445001. doi:10.1088/0953-8984/28/44/445001
44. Gavioli, L.; Fanetti, M.; Pasca, D.; Padovani, M.; Sancrotti, M.; Betti, M. G. *Surf. Sci.* **2004,** *566–568,* 624–627. doi:10.1016/j.susc.2004.05.123
45. Glöckler, K.; Seidel, C.; Soukopp, A.; Sokolowski, M.; Umbach, E.; Böhringer, M.; Berndt, R.; Schneider, W.-D. *Surf. Sci.* **1998,** *405,* 1–20. doi:10.1016/s0039-6028(97)00888-1
46. Hauschild, A.; Temirov, R.; Soubatch, S.; Bauer, O.; Schöll, A.; Cowie, B. C. C.; Lee, T.-L.; Tautz, F. S.; Sokolowski, M. *Phys. Rev. B* **2010,** *81,* 125432. doi:10.1103/physrevb.81.125432
47. Schmitt, S.; Schöll, A.; Umbach, E. *Surf. Sci.* **2016,** *643,* 59–64. doi:10.1016/j.susc.2015.07.017

BEILSTEIN JOURNAL OF NANOTECHNOLOGY

Supporting Information

for

Directed growth of quinacridone chains on the vicinal Ag(35 1 1) surface

Niklas Humberg, Lukas Grönwoldt and Moritz Sokolowski

Beilstein J. Nanotechnol. **2024,** *15,* 556–568. doi:10.3762/bjnano.15.48

Terrace width distribution on Ag(35 1 1)

In Figure S1a, a typical STM image of the clean Ag(35 1 1) surface is shown. It can be seen that the step edges are not evenly distributed with the nominal terrace width of 50.5 Å. Instead, there are areas on the surface where many step edges are very close together. For example, on the left-hand side of the image, there are six step edges within a distance of roughly 120 Å. This means that the average terrace width in this area is only 20 Å, which is less than half of the terrace width of the ideal Ag(35 1 1) surface. At the same time, there are also very large terraces on the surface. In Figure S1, the large terrace is 270 Å in width, which is more than five times of the ideal terrace width.

The terrace width distribution is displayed in Figure S1b. It shows a dominant peak at around $n = 10$ atoms rows (= 28.9 Å). For larger terrace widths, it follows a decay that can be roughly described by a geometric distribution, which is indicative of non-interacting steps [1]. However, for small terrace widths (less than ten rows) it exhibits a drastic decline, which shows that there is a repulsive interaction between the steps for very small terrace widths.

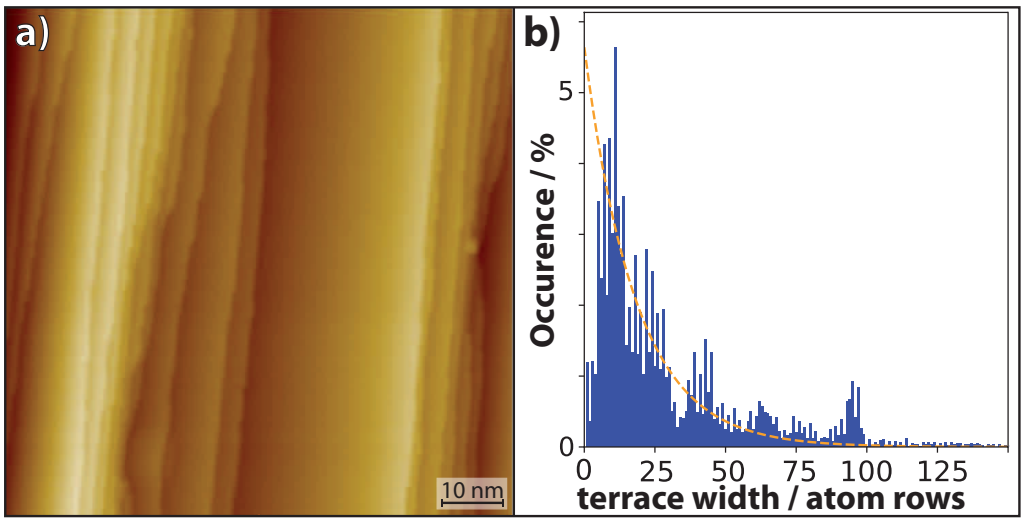

Figure S1: Step morphology of the Ag(35 1 1) surface. **(a)** STM image (U_{Bias} = +1.5 V, I = 25 pA). **(b)** Terrace width distribution. It was obtained by evaluating four large-scale STM images with a Python script by Bastidas et al. [2]. The local peaks at $n > 25$ are due to the fact that, because of the finite number of evaluated STM images, individual large terraces are oversampled by the script because it analyzes every horizontal line of the image. The orange dashed line corresponds to a fit by a geometric distribution, that is, occurrence $\propto p^n$, with n denoting the number of rows per terrace and p being the probability for two adjacent atomic rows at the same height level.

References

1. Busch, H.; Henzler, M. *Surf. Sci.* **1986**, *167*, 534–548. doi:10.1016/0039-6028(86)90722-3.

2. Bastidas, J. M. P.; Auras, S. V.; Juurlink, L. B. *Appl. Surf. Sci.* **2021**, *567*, 150821. doi:10.1016/j.apsusc.2021.150821.

A.4 "An X-Ray Standing Wave Analysis of Phosphorene on the Au(111) Surface"

by Niklas Humberg, Anna J. Kny, Morris Mühlpointner, Anja Haags, Sergey Soubach, David Duncan, Tien-Lin Lee, and Moritz Sokolowski

Manuscript and Supporting Information prepared for publication. Last edited on May 28, 2024.

An X-Ray Standing Wave Analysis of Phosphorene on the Au(111) Surface

Niklas Humberg[1], Anna J. Kny[1], Morris Mühlpointner[1], Anja Haags[2], Sergey Soubach[2], David Duncan[3], Tien-Lin Lee[3], and Moritz Sokolowski*,[1]

[1]Clausius Institut für Physikalische und Theoretische Chemie, Universität Bonn, Wegelerstr. 12, 53115 Bonn, Germany
[2]Forschungszentrum Jülich, Peter Grünberg Institut (PGI-3), 52425 Jülich, Germany
Jülich Aachen Research Alliance (JARA), Fundamentals of Future Information Technology, 52425 Jülich, Germany
[3]Diamond Light Source, Didcot OX11 0DE, UK

Email: Sokolowski@pc.uni-bonn.de

Abstract

The epitaxial growth of phosphorus on the Au(111) surface has been considered as a candidate for the synthesis of a layer of P with a buckled graphene-like structure. The formation of a (5×5) superstructure is observed by low energy electron diffraction and scanning tunneling microscopy and is commonly referred to as "blue phosphorus" or "blue phosphorene". Its structural details are interesting because they contribute to the fundamental understanding of the growth of 2D materials at metal interfaces. In addition, the structural investigations made so far provide different and conflicting models for this structure. Earlier models propose the growth of a pure buckled P layer. More recently, the formation of a P-Au network with Au ad-atoms interlinking aggregates of 9 P atoms has been found. Here, we report an analysis of the (5×5)P/Au(111) superstructure by photoelectron spectroscopy and the normal incidence x-ray standing wave (NIXSW) technique. NIXSW is especially suited to determine vertical bonding distances of adsorbates at surfaces. We find a structure where the P atoms are at two heights ("layers") which are 3.53 Å and 2.48 Å above the Au-surface, with a ratio of P atoms per area of about 1 : 2.4 for the top layer with respect to the bottom layer. For the bottom layer, two types of P atoms (39% : 61%) can be discerned from their different photoemission binding energies. The smaller fraction (39%) is attributed to P atoms linked to Au ad-atoms. This fact and additional conclusions from the Au7f photoemission spectra strongly support the P-Au network model. However, our analysis also provides an independent determination of the heights of the P atoms with respect to the Au surface.

1 Introduction

Blue phosphorus or blue phosphorene (blue P) is understood as a free standing 2D-layer of phosphorous with a buckled honeycomb structure [1]. Its existence has been proposed on theoretical grounds first, and it has attracted attention because of its predicted electronic properties [2] that differ from single layers of black phosphorus [3], which is also puckered but exhibits a rectangular unit cell. Different experimental approaches to prepare blue P by molecular beam epitaxy of P_2 molecules onto different substrate surfaces have been made, e.g., Au(111) [1, 4–9] or Au(111) [10]. The Au(111) surface has been most commonly used. It lends itself to this purpose because of its hexagonal symmetry and the low chemical reactivity of Au that is promising for growth of a decoupled P layer. Remarkably, the deposition of P onto the Au(111) surface held at 250° C leads very reproducibly to a commensurate (5×5) superstructure in a self-terminating growth process. This was reported by several groups [1, 4–9].

Evidently, there arises the question of the structural details of such a P layer on Au(111) and its possible resemblance to the proposed structure of blue P. A number of different experimental investigations were performed, mainly by scanning tunneling microscopy (STM) [1, 4–9], and in one case also by an analysis of the energy dependence of the spot intensities in low energy electron diffraction (LEED) [7]. Several theoretical investigations were undertaken using density functional theory (DFT) [1, 6, 8]. Interestingly, these studies partly arrived at different and conflicting results.

Earlier models proposed a buckled structure comprised of a top and bottom layer which contain 12 and 20 P atoms (32 atoms in total) per unit cell of a (5×5) superstructure on the Au surface [1, 5, 6]. We will refer to this model as the "double layer" (DL) model in the following. More recently, a buckled layer with 6 and 12 P atoms in the top and bottom layer (18 P atoms in total) and 9 additional Au ad-atoms in the bottom layer between the P atoms was derived [7, 11]. This structure is better described as a Au-P network structure, instead of an epitaxial P layer. It will be referred to as the "Au-P network". A schematic representation of both models is given in Figure 1. The averaged vertical distances of the P atoms in the top and bottom layers with respect to the averaged height

of the Au atoms in the surface layer are summarized in Table 1 for both models . The Au-P network model exhibits a higher symmetry (2D space group $p6m$) compared to the DL model, which exhibits only a mirror plane along the long diagonal of the unit cell (2D space group cm). The buckling, i.e., the difference between highest and lowest vertical atom positions, of the Au surface (0.30 Å) and the P layers (0.30 Å and 0.70 Å for the bottom and P top layer) is much stronger for the DL model compared to that of the Au-P network model. For the latter, the buckling of the Au surface amounts to only 0.14 Å and is negligible for the P layers (< 0.05 Å for both the bottom and top P layer). We will use these two models in the following to guide the analysis of our experimental data.

Clearly, a profound difference exists between the proposed models. This is relevant in terms of the resemblance of the structure of the (5×5)P/Au(111) to the ideal structure a blue P layer. Moreover, from a more general point of view, it is of interest for understanding the growth mechanism of this phosphorus layer on Au(111). Specifically, the Au-P network model requires that Au ad-atoms are expelled from the Au surface at terrace or steps sites into the P layer. Evidently, this situation asks for an investigation by further, so far not applied, experimental techniques and motivated the normal incidence x-ray standing wave (NIXSW) analysis that is reported here. NIXSW has proven as a very powerful technique for the analysis of the structure of epitaxial layers (s. e.g., ref. [12]). This is due to its specific strength, namely that NIXSW can provide vertical positions of atoms in relation with their chemical nature derived from photoemission spectra [13]. One important principle of NIXSW is that species that are discernible by different binding energies of their orbitals in photoemission spectra are located at different vertical heights with respect to the surface. However, as we will report, for the (5×5)P/Au(111) structures, we encounter a different and counterintuitive situation. Two P species with experimentally non-discernible binding energies are found at two different heights, while two P species with different binding energies are at the same height. As we will report, this aspect made the evaluation of the NIXSW data challenging.

Before we come to our results, we briefly describe the growth of the (5×5) structure of P/Au(111). The clean Au(111) surface exhibits the well known $(22 \times \sqrt{3})$ reconstruction with a herringbone-like arrangement of pairs of discommensuration lines [14, 15]. Upon the deposition of small quantities of P onto this surface at 250°C, this reconstruction transforms into a different P related reconstruction, which exhibits a lateral periodic length that is comparable to the distance between pairs of discommensuration lines on the clean Au(111) surface ($\sim$ 70 Å) [14, 15]. This has been observed by STM by other authors [4] and by ourselves [16] using LEED. Both reconstructions can be identified by characteristic, but different patterns of satellite spots around the integer LEED spots of the Au(111) surface. The details of the P induced change in the reconstruction will be reported elsewhere. When the P coverage increases further, large domains of the (5×5) structure grow. This is evidenced by the appearance of sharp LEED spots at the (5×5) positions, while the satellite spots, which are related to the reconstruction, vanish.

Table 1: Overview of structural parameters of the double layer (DL) and Au-P network model proposed for the (5×5) structure of P on Au(111) which are illustrated in Fig. 1. The table displays the distances of the top and bottom P layers with respect to the Au(111) surface layer (averaged vertical positions). The numbers in the brackets (...) denote the number of P atoms in the respective layers within the (5×5) unit cell. Δd_{12} denotes the difference in the averaged heights of the P atoms in the two P layers ("buckling"). The numerical values were calculated from the data of refs. [5] and [7]. Hereby, the x,y,z-coordinates of the structure in ref. [5] were made available to the authors by E. Golias. The position of the extended (111) Bragg-plane is calculated at a position 0.14 Å below the surface plane for the DL model, meaning that the surface undergoes and outward relaxation by 0.14 Å. Differently, for the P-Au-network model, the extended (111) Bragg plane coincides with the average surface plane.

	DL model[1, 5, 6]	**Au-P network**[7, 8]
top layer	3.60 Å (12)	3.50 Å (6)
bottom layer	2.40 Å (20)	2.40 Å (12)
Δd_{12}	1.20 Å	1.10 Å

2 Results

2.1 Photoemission of the Au4f orbital

Before we turn to the NIXSW results, we discuss photoemission spectra of the Au4f orbital, because these provide valuable insight straightaway. In addition, these spectra relate our data to published results, where photoemission spectra have been also reported [1, 5, 6]. Figure 2 shows the photoemission spectra of the Au4$f_{\frac{7}{2}}$ component for the clean Au(111) surface (bottom) and for the surface with a (5×5)P superstructure (top). Importantly, both spectra have been measured under exactly identical experimental conditions.

The spectrum of the clean surface consists of two overlapping peaks at different binding energies (E_B), namely, a surface related peak ($E_B = 83.63$ eV) and a bulk related peak ($E_B = 83.94$ eV) at higher binding energy. This peak assignment was earlier reported, e.g., in ref. [17]. In our case, the bulk related peak is slightly smaller than the bulk related peak which is a matter of the detailed photoemission conditions. The bulk peak is shifted by 0.31 eV to higher binding energies. This is worth a comment, as one would intuitively expect a smaller screening of the photohole for the surface atoms and, thus, a higher binding energy of the surface peak (final state effect). Instead, here the revers order of the binding energies is explained by an initial state effect that is given by the narrowing of the d-band in the surface layer [17, 18].

As seen in Figure 2, the spectrum can well be fitted by a superposition of two lines with equal shape, which is close to that

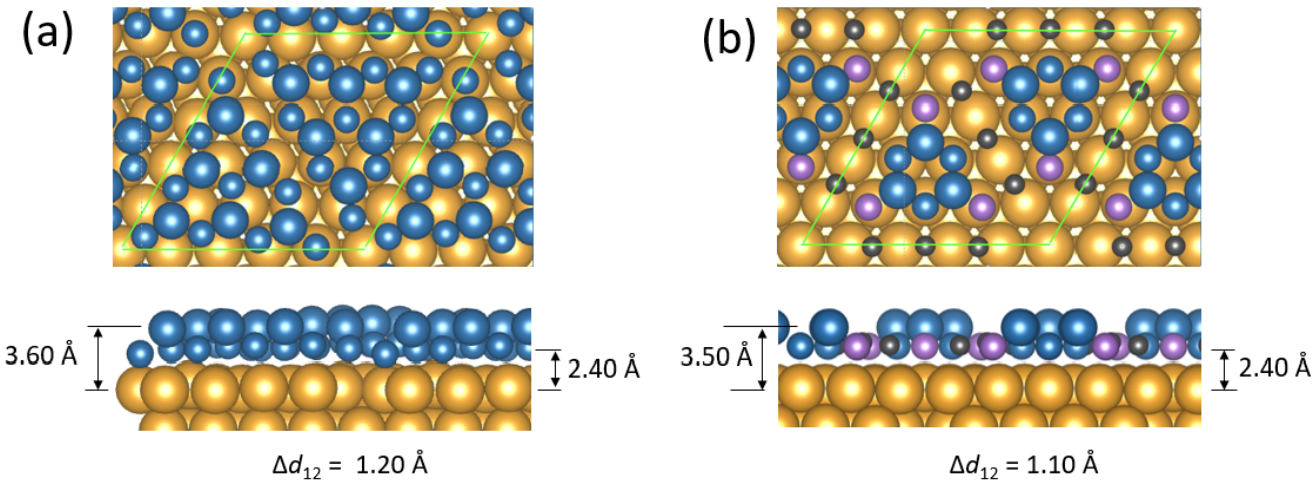

Figure 1: Schematic ball-and-stick models in top and side views of structures proposed for the (5×5)P/Au(111) structure with indicated unit cells (green lines). (a) Double layer (DL) model [1, 5, 6]; (b) Au-P network model [7, 8]. Blue and violet: P atoms; the small/large spheres resemble atoms of the bottom/top layer. Yellow and brown (small spheres): Au atoms in the surface and Au ad-atoms. In panel (b) the violet P atoms are two-fold coordinated with Au ad-atoms (brown), while the blue P atoms (small spheres) are coordinated to only one Au-ad-atom. The drawings were produced from the coordinates of the structures in refs. [5] and [7]. The marked distances are calculated as the differences between averaged vertical heights of the atoms belonging to the respective layers and the Au surface.

of a Lorentzian. The full width at half maximum (FWHM) is very similar for both lines and amounts to 0.39 eV and 0.35 eV for the surface and bulk component, respectively. The fit yields an area ratio of the surface to bulk component of $\chi_{\mathrm{Au}} = 1.31$. This value is smaller than the ratio observed by other authors ($\chi_{\mathrm{Au}} = 2.6 - 2.8$) [19]. This is partly explained by the less surface sensitive photon energy used here (180 eV instead of 135 eV [19]) and partly by differences in the emission geometries and acceptance angles of the electron analyzers.

The Au4$f_{\frac{7}{2}}$ spectrum of the (5×5)P/Au(111) structure is significantly different from that of the clean surface (s. Fig. 2). There is one broad peak with a maximum that is shifted to a higher binding energy ($E_{\mathrm{B}} = 84.0$ eV) with respect to the surface related peak of the clean surface ($E_{\mathrm{B}} = 83.63$ eV). This change in the spectrum shape reveals the chemical bonding of the surface Au atoms to the adsorbed P atoms and was also observed by Zhang *et al.* before [6]. The question is whether distinctly different species of Au atoms can be identified and determined from the spectrum. For this purpose we fitted the spectrum by two lines resembling the clean Au surface and the Au bulk atoms, using exactly the same parameters as before for the clean surface (shape, FWHM, and positions of the peaks) plus new additional lines with a shape and FWHM corresponding to that of the surface peak of the clean surface, but with adjustable positions and heights. The reasoning for choosing the same shape and width as that of the surface peak this is given by the plausible assumption that the chemically different new species of Au atoms are equally well defined by their structural and chemical environment as the Au atoms in the surface layer of the clean Au surface. Some validation of this approach is given in hindsight by the good overall fit of the spectrum we obtained.

We found that that two additional lines (1 and 2 at $E_{\mathrm{B}} = 84.11$ and 84.35 eV) are sufficient to fit the experimental spectrum (s. Fig. 2). Hereby, the area of the component 2 is slightly larger than component 1. The area ratio of the components 2 and 1 amounts to 1.22. We emphasize that this fit by *two* additional lines is not unique; the spectrum can be equally well fitted by only one additional line which is then of much larger width. However, it turns out that the fit by two additional lines can plausibly be interpreted in view of the P-Au network model and the following structural results from NIXSW.

The fitted areas of the 4 Au components (1, 2, bulk, and surface) in the spectrum of the (5×5)P/Au(111) structure result to relative values of 28%, 35%, 33%, and 4%. The component resembling the clean Au surface is strongly reduced (only 4% of the total intensity), and the respective intensity is shifted to the new components 1 and 2 at larger binding energies. This small residual intensity of the clean-surface component at its original position is possibly related to small areas of the surface that remained bare between (5×5)P domains due to surface defects.

A plausible working hypothesize is that the two components 1 and 2 stem from two species of Au atoms in two different bonding geometries with respect to the P atoms. The area ratio of the sum of these surface components 1 and 2 with respect to the bulk component, i.e., $\chi_{\mathrm{P}} = ([1] + [2]) : [\mathrm{bulk}]$, is calculated as $\chi_{\mathrm{P}} = 1.9$. It is considerably larger than the respective ratio for the clean surface, $\chi_{\mathrm{Au}} = [\mathrm{surface}] : [\mathrm{bulk}] = 1.31$, we reported above. This indi-

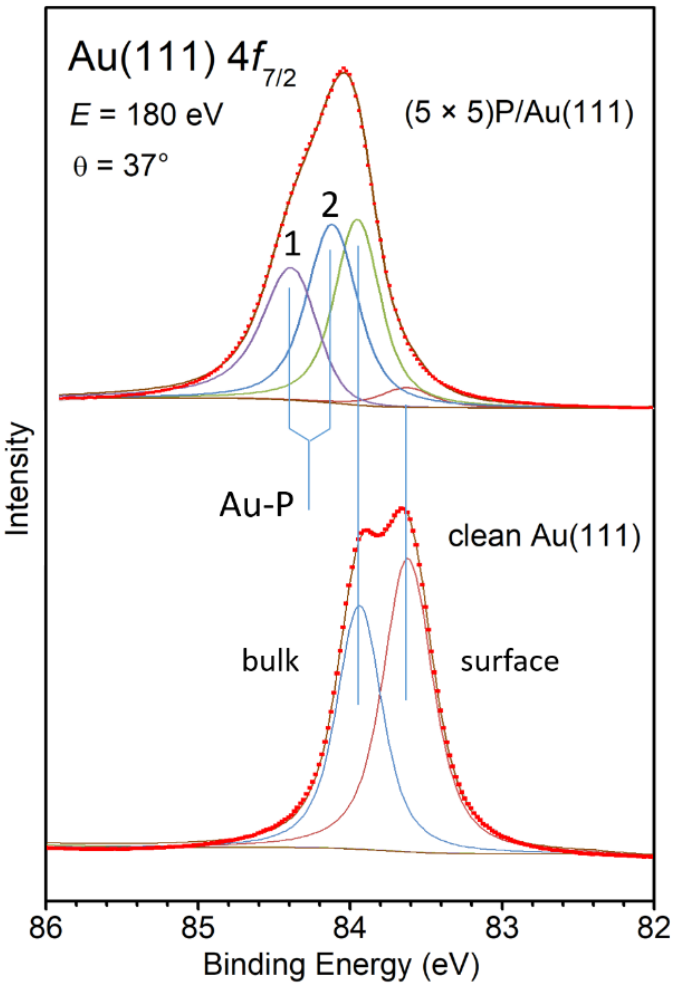

Figure 2: Photoemission spectra of the Au4f orbital of the clean Au(111) surface (bottom) and the $p(5 \times 5)$P/Au(111) structure (top). Only the 7/2 component is displayed, the 5/2 component is located 3.67 eV to higher binding energies and hence outside the spectral range. Both spectra were fitted by a sum of peaks representing different chemical components. The spectrum of the clean surface and is composed of two components, one representing the surface atoms (E_B= 83.63 eV) and one representing the bulk atoms (E_B= 83.94 eV). The spectrum at the top shows the P covered surface and is fitted by the same components as that of the clean surface plus two additional components (marked by 1 and 2) that are assigned to two species of Au atoms bonded to P. The spectra were recorded at 180 eV photon energy for an average emission angle $\theta = 37°$ with respect to the surface normal and included data within a range of the angular emission of $\pm 5°$. For further details see text.

cates that the two components 1 and 2 cannot stem from a single topmost (now P covered) Au layer alone, because then one would expect a similar ratio as for the clean surface, namely $\chi_P \approx \chi_{Au} = 1.31$. Hence, more than 25 Au atoms per (5×5) unit cell appear to contribute to the peaks 1 and 2 and are thus involved in the formation of the (5×5)P/Au(111) structure. This result speaks for the Au-P network model where additional Au ad-atoms are present on top of the Au surface layer and in between the P atoms of the bottom layer. It stands against the DL model, because there the Au/P interface exhibits the density of Au atoms of the ideal Au surface. A natural assignment of the peaks 1 and 2 within the Au-P network would be to the 25 Au atoms in the surface layer below the Au-P network (peak 2) and the 9 Au ad-atoms within the P network (peak 1). Hereby, we suppose that the Au atoms in the surface layer yield the peak 2 at smaller binding energy due to a better screening of the photohole, while the peak 1 at larger binding energies corresponds tot eh Au ad-atoms. The expected stoichiometric ratio of the two types of Au atoms in the Au-P network model is 25/9 = 2.78. This expected ratio compares to an experimentally observed area ratio [2] : [1] = 1.22. However, this by more than a factor of 2 smaller experimental value can be rationalized by the attenuation of the photoelectrons, which are emitted from the 25 Au atoms in the topmost complete Au layer (peak 2), by the Au-P network composed of 9 Au ad-atoms and the 18 P atoms.

In order to support this interpretation quantitatively, we estimate the attenuation factor q for the Au-P network double layer (comprising 9 Au and 18 P atoms) for our specific experimental conditions. We assume that q has a similar value as q for of a pure complete layer of Au atoms. In other words, we assume that the layer of 18 P atoms plus 9 Au atoms leads to a similar attenuation as a layer of 25 Au atoms per (5×5) unit cell. Of course, this assumption neglects that P and Au atoms have different cross sections for the attenuation of the photoelectrons and it neglects the small difference in the atom densities. However, the strength of the assumption is that it correctly accounts for all experimental factors (in particular the grazing emission geometry and the width of the detection cone of the analyzer). As we consider these factors as more relevant for q than the ratio of the cross sections, we rely on this approximation.

Here q is understood as the percentage of photoelectrons that are transmitted without scattering by one layer of Au atoms. We calculate q from the spectrum of the clean sample, whereby we assume that the surface component in the spectrum of the clean sample represents one layer of Au atoms per (5×5) unit cell. This means that we neglect the small compression by 4% of the clean surface due to the reconstruction and consider layers of Au atoms of equal surface density. Then, χ_{Au} = [surface] : [bulk] is related to q by a geometric sum representing the emission of the surface layer with respect to the attenuated emission of all bulk layers:

$$\chi_{Au} = \frac{1}{\sum_{i=1}^{\infty} q^i} = \frac{1-q}{q} . \qquad (1)$$

This yields an attenuation factor $q = 0.43$ from the experimental value of $\chi_{Au} = 1.31$.

Now we come back to the observed ratio of the two Au components, [2] : [1] = 1.22 measured for the phosphorus covered surface. We correct the bulk component by the value of $q = 0.43$. Doing this, we obtain the expected ratio [2] : [1] as

$q \times 25/9 = 0.43 \times 2.78 = 1.19$ for the Au-P network model. This is in good agreement with the experimental value 1.22. Thus, the ratio [2] : [1] is well understood.

In conclusion, the Au-P network model explains the Au4f photoemission spectrum and, in particular, two aspects in a quantitative manner. Firstly, the fact that $\chi_{\mathrm{P}} = 1.9$ is significantly larger than $\chi_{\mathrm{Au}} = 1.31$ is understood due the contribution of the Au ad-atoms in addition to the top Au layer that is chemically interacting with the P atoms. Secondly, the ratio [2] : [1] of the two discernible chemically modified Au components can be quantitatively interpreted in view of the model.

2.2 Photoemission of the P2p orbital

Figure 3 compares two photoemission spectra of the P2p orbital of the (5×5)P/Au(111) structure, which were recorded at photon energies in the hard and soft x-ray energy range, respectively. For the spectrum recorded at a photon energy of 280 eV the experimental resolution is higher and the contributing peaks are thus better resolved. This spectrum served us to develop a "fitting model" which was then used for the analysis of the spectra recorded in the hard x-ray range at the Au(111) Bragg condition for the NIXSW measurements. This will be described below. Both spectra show essentially the same line shape, although the features are more washed out in the hard x-ray spectrum. As demonstrated in Figure 3, both spectra can be fitted by a superposition of the same two doublets, although, for the hard x-ray spectrum, larger FWHM had to be used.

For the moment, we focus on the better resolved spectrum in the soft x-ray energy range. The P2p spectrum of a single species is a doublet consisting of two lines with an intensity ratio of 2 : 1, representing the final states of the photohole for a spin of $\frac{3}{2}$ and $\frac{1}{2}$. Here, two of such doublets superpose, whereby the one of lower intensity ($\sim 33\%$ of the total intensity) is shifted by 0.28 eV to smaller E_{B} values. As described in detail in the experimental section below, we fitted both doublets by two asymmetric Lorentzian lines with the same energy difference and intensity ratio of the two lines, and equal line shapes and widths. A superposition of two of such doublets fits the observed spectrum (s. Fig. 3) and defines our "fitting model" for the further analysis. For practical reasons we name the two components as "main" (the larger at higher E_{B}) and "sub" (the smaller at lower E_{B}) in the following.

P2p photoemission spectra of this line shape were also reported in refs. [5] and [6]. The appearance of two components in the spectrum demonstrates that P atoms in at least two different chemical environments can be distinguished. Importantly, the spectrum remains unchanged for a decrease in the P coverage. We observed the same spectrum, when the P coverage was significantly smaller (as estimated from the total intensity of the spectrum), e.g., only about 25% with respect to that of Figure 3. Hence we can exclude that the

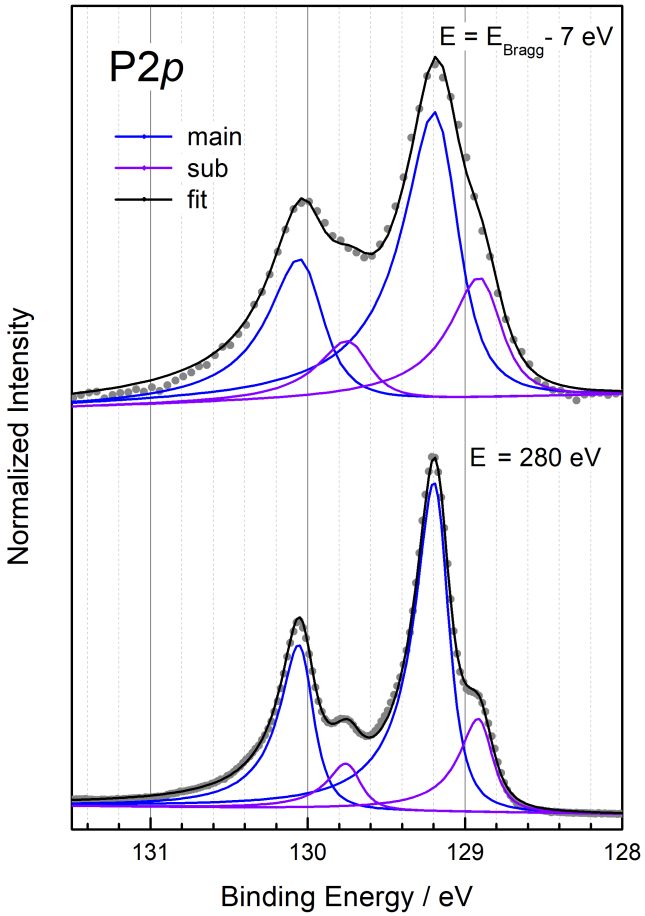

Figure 3: Photoemission spectra of the P2p orbital for an excitation in the hard x-ray energy range (2621 eV, top) and in the soft x-ray energy range (280 eV, bottom). Both spectra were fitted by two doublets with identical spin orbit splitting, intensity ratio, and FWHM. The two doublets correspond to two chemically discernible phosphorus components which are named main and sub. The photon energy for the hard x-ray spectrum was 7 eV below the Bragg energy of the Au(111) reflection, which safeguards that the intensity ratio of the components is not subject to standing wave field effects.

smaller component "sub" is related to overdosing of P and the nucleation of an additional layer on top of the (5×5) structure. We discuss this aspect, because a third layer of P on top of a double layer (comprised of a bottom and top layer) was indeed postulated from STM images by Zhang *et al.* [6]. In addition, Golias *et al.* [5] observed that the sub-components gained intensity beyond the level seen in Figure 3, when P was deposited at room temperature.

In conclusion, this means that an additional, third layer or additional atoms of P on top of the (5×5) structure may form and contribute to the spectrum, but that this can be excluded for our preparation and the present spectrum. The obvious question is how the two components ("main" and "sub") relate to the different P atoms in the structure models discussed above. The answer to this question is provided by the following NIXSW analysis.

2.3 NIXSW analysis

2.3.1 P2p orbital

Figure 4 shows four photoemission spectra of the P2p orbital as examples for the spectra evaluated in the NIXSW analysis as a function of photon energy at the Au(111) Bragg reflection. For all spectra the same fitting model from above with two components (main and sub) was applied. Figure 4 demonstrates the good quality of the fit by the model for four spectra selected from the complete set of spectra over the scan range of the photon energy of 10 eV around the Bragg energy. Only very close to the Bragg energy (i.e., at $E - E_{\mathrm{Bragg}} = -0.56$ eV), the indentation at the center of the experimental spectrum is not perfectly reproduced by the fit. However, this small difference, of so far unknown origin, did not have an impact on the results obtained in the further evaluation. The corresponding yield curves ($Y(E)$) are displayed in Figure 5. These are computed from the intensities of the two fitted components (main and sub). In addition, we also fitted the yield curve of the total intensity of the P2p spectrum, which is named "region" in the following. It corresponds to the sum of the former two components within the statistical error.

The yield curves were fitted according the theory of NIXSW as described in the experimental section below. They were normalized such that the extrapolated intensities far away from the Bragg energy equal to 1 [20]. The fits of all three yield curves (main, sub, and region) are of very good quality (s. Fig. 5). The fitted coherent fractions (f_{c}) and positions (p_{c}) are tabulated in table 2.

For the smaller component sub, the fit yields $f_{\mathrm{c}}^{\mathrm{sub}} = 0.750 \pm 0.013$ and $p_{\mathrm{c}}^{\mathrm{sub}} = 0.054 \pm 0.004$. The value of the coherent fraction is high and indicates that the corresponding phosphorus species are located within a narrow vertical distribution centered at one vertical height with respect to the Au surface. From the coherent position ($p_{\mathrm{c}}^{\mathrm{sub}}$) the corresponding average height is calculated at $d_{\mathrm{c}}^{\mathrm{sub}} = (n + p_{\mathrm{c}}) \times d_{\mathrm{Au}_{(111)}} = 2.482 \pm 0.009$ Å for a plausible integer value of $n = 1$. The value of $d_{\mathrm{c}}^{\mathrm{sub}}$ is by 0.082 Å larger than the height of the bottom P layer (2.40 Å) given by both the DL and the Au-P network model (s. Tab. 1). However, the still close agreement indicates that the respective P atoms are in a small distance to to the first Au layer and hence contribute to the bottom layer. This finding constitutes a first corner stone for the interpretation of the P2p spectrum. The remaining P atoms are resembled by the main component. Surprisingly, its coherent fraction $f_{\mathrm{c}}^{\mathrm{main}}$ is much smaller than $f_{\mathrm{c}}^{\mathrm{sub}}$ (23% instead of 75%). This immediately reveals that the main component does not stem from P atoms at one single height, i.e., one single layer, but contains contributions of atoms at at least two different heights. The alternative explanation that $f_{\mathrm{c}}^{\mathrm{main}}$ is small due to a very broad distribution of the vertical positions is not plausible and hence dismissed. This aspect yields the second corner stone for the analysis.

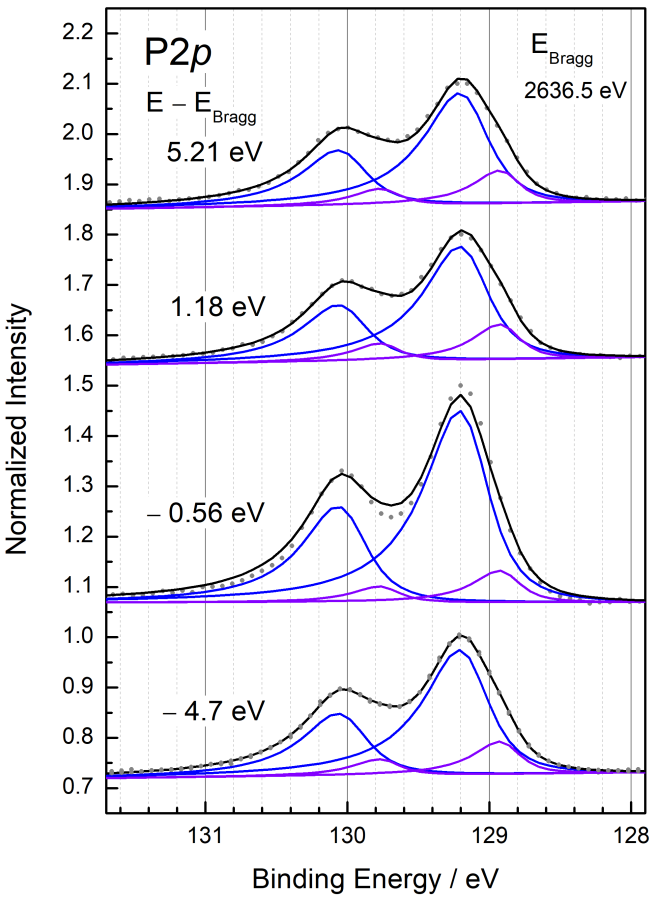

Figure 4: A set of four exemplary photoemission spectra of the of P2p orbital for different photon energies close to the Bragg condition of the Au(111) reflection ($E_{\mathrm{Bragg}}^{(111)} = 2636.5$ eV). The spectra were fitted by two components (main/blue and sub/violett) with parameters that were fixed to values obtained from fitting the spectra displayed in Fig. 3. The spectra in the above figure were computed by summing-up spectra from 19 NIXSW runs recorded on different sample positions.

However, before expanding on this this aspect further, we comment on $f_{\mathrm{c}}^{\mathrm{region}}$ and $p_{\mathrm{c}}^{\mathrm{region}}$. For this purpose it is helpful to visualize the situation in the complex plane (Argand diagram). The Argand vector (vector, for short in the following) of a species j of atoms is defined as

$$\mathbf{F}_{\mathrm{c}}^{j} = f_{\mathrm{c}}^{j} \cdot \exp\left(i\, 2\pi\, p_{\mathrm{c}}^{j}\right). \tag{2}$$

For our experimental results, the situation is shown in Figure 7 below. As the yield curve of region is the sum of the yield curves of main and sub a sum rule holds for the corresponding vectors:

$$\mathbf{F}_{\mathrm{c,exp}}^{\mathrm{region}} = \gamma_{\mathrm{main}} \cdot \mathbf{F}_{\mathrm{c,exp}}^{\mathrm{main}} + \gamma_{\mathrm{sub}} \cdot \mathbf{F}_{\mathrm{c,exp}}^{\mathrm{sub}} \tag{3}$$

where $\mathbf{F}_{\mathrm{c,exp}}^{\mathrm{main}}$ and $\mathbf{F}_{\mathrm{c,exp}}^{\mathrm{sub}}$ are the vectors of the yield curves of the main and sub components. Here, the subscript "exp" indexes the experimentally determined vectors with respect to those obtained by fitting later on. The coefficients γ_{main} and

Table 2: Experimentally determined coherent fractions f_c and positions p_c of the (5×5)P/Au(111) structure for different orbitals, Bragg reflections ((111) and (222)), and components. The vertical heights were calculated according to: $d_c = (n + p_c) \times d_{Au(111)}$ with with $d_{Au(111)} = 2.355$ Å and $d_{Au(222)} = d_{Au(111)}/2$, using the given values of n. The values for the P2p orbital were obtained from the yield curves shown in Figure 5; those of the P1s orbital are from Figure 6 (below). Note that all d_c values, except the one related to the sub component, correspond to averaged heights of different P species and are thus not meaningful on themselves.

orbital	**Bragg reflection**	**component**	f_c	p_c	n	d_c (Å)
P2p	(111)	region	0.349 ± 0.005	0.085 ± 0.002	1	2.556 ± 0.005
		main	0.233 ± 0.007	0.131 ± 0.006	1	2.664 ± 0.014
		sub	0.750 ± 0.013	0.054 ± 0.004	1	2.482 ± 0.009
P1s	(111)	region	0.246 ± 0.013	0.095 ± 0.012	1	2.579 ± 0.028
	(222)	region	0.761 ± 0.023	0.077 ± 0.005	2	2.536 ± 0.006

γ_{sub} can be identified by the molar fractions of the contributing species, as long as attenuation effects of the photoelectron yields can be neglected. If attenuation effects play a role, the coefficients must be considered as "effective" molar fractions. In either case, $\gamma_{main} + \gamma_{sub} = 1$ holds. Because of its importance in the present context, the sum rule is explained in more detail in the supporting information.

As a consequence of eq. (3), $\mathbf{F}_{c,exp}^{region}$ must be located on the line that spans from $\mathbf{F}_{c,exp}^{main}$ to $\mathbf{F}_{c,exp}^{sub}$. As seen in Figure 7, this is well fulfilled and proves the consistency of the decomposition of the NIXSW spectra into spectra of two components. Furthermore, the lever rule $\gamma_{main} \cdot (\mathbf{F}_{c,exp}^{main} - \mathbf{F}_{c,exp}^{region}) = -\gamma_{sub} \cdot (\mathbf{F}_{c,exp}^{sub} - \mathbf{F}_{c,exp}^{region})$ holds. From Figure 7 we hence read $\gamma_{main} : \gamma_{sub} = 75\% : 25\%$, which means that about one quarter of the P atoms contribute to the sub and three quarters to the main component.

As said above, from the small value of f_c^{main} we have to conclude that the two components (main and sub) contributing to the P2p spectrum (Fig. 3) cannot correspond in a one-to-one manner to two layers of P atoms at two different heights, but that the stronger component main comprises atoms that are located at, at least, two different heights. This finding is unusual, because commonly different structural, and hence chemically different, locations of atoms are reflected by different binding energies of their respective photoemission peaks which allows to discern them in the NIXSW analysis. However, in the present situation, the difference in the binding energies is apparently too small to allow one to spectrally resolve the different components contributing to the main component. We will deal with this aspect again when we discuss the chemical bonding of the P atoms.

The small value of the coherent fraction of the main component, i.e., the magnitude of $\mathbf{F}_{c,exp}^{main}$, can be explained if we assume that the measured yield curve is a superposition of yield curves from different species at different heights, in analogy to the situation for $\mathbf{F}_{c,exp}^{region}$ (s. eq. (3)). At least two species, corresponding to two so far unknown vectors $\mathbf{F}_c^{main1}$ and $\mathbf{F}_c^{main2}$, are required. Again the sum rule holds:

$$\mathbf{F}_{c,exp}^{main} = \gamma_{main1} \cdot \mathbf{F}_c^{main1} + \gamma_{main2} \cdot \mathbf{F}_c^{main2}, \qquad (4)$$

where $\mathbf{F}_c^{main1}$ and $\mathbf{F}_c^{main2}$ are the vectors of the two components contributing to the yield curves. As a consequence, a vector of small magnitude, i.e., coherent fraction (as it is observed), can result from two vectors of about equal coherent fractions with an opening angle of $\sim \pi$ between them, which corresponds to a vertical displacement of $\sim d_{Au(111)}/2$.

2.3.2 P1s orbital

In order to gain further information and determine $\mathbf{F}_c^{main1}$ and $\mathbf{F}_c^{main2}$ we measured the yield curve for the Au(222) Bragg reflection. The idea behind this strategy is that the coherent positions are multiplied by a factor of 2 when going from the (111) to the (222) reflection which leads a different, but predictable, superposition of $\mathbf{F}_c^{main1}$ and $\mathbf{F}_c^{main2}$.
We use the P1s orbital (E_B= 2.149 keV) instead of the P2p orbital because, at this high photon energy of the (222) reflection (E_{Bragg} = 5.273 keV), the photoelectron yield of the P2p orbital is too small to yield data with suitable statistics. The P1s spectra show only one peak with a width of about 1 eV ($\sim$ 0.5 eV for the P2p orbital) due the smaller lifetime of the photohole. Unlike the P2p spectra, the P1s spectra thus do not permit a separation into different components. Consequently, we evaluated only the integrated intensities of the spectra after subtraction of a Shirley background. The derived yield curves correspond hence to those indexed above by "region" and comprise all P components ($\mathbf{F}_c^{sub}$, $\mathbf{F}_c^{main1}$ and $\mathbf{F}_c^{main2}$). For simplicity, the superscript "region" is waived here for simplicity. For a additional cross-check, the yield curve of the Au(111) reflection was measured again using the P1s instead of the P1p orbital. Figure 6 displays the data and the fits. The respective coherent fractions and positions are included in Table 2, and the corresponding vectors are displayed in Figure 7. As expected, the shape of the yield curve of the (111) reflection measured for the P1s orbital (s. Fig. 6)

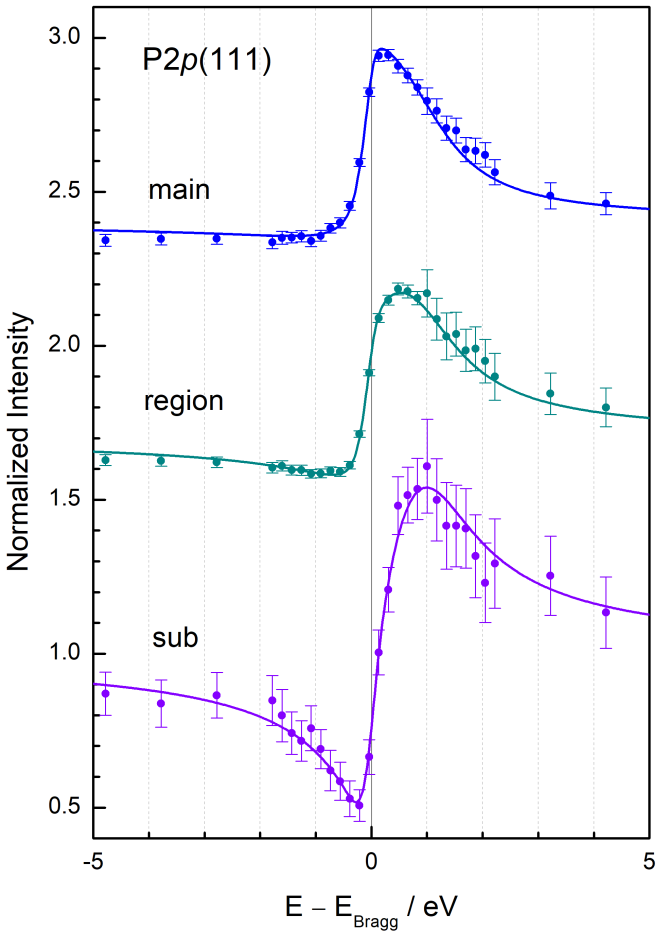

Figure 5: Photoemission yield curves of different components (main and sub) and of the integrated intensities (region) of the P2p orbital for the (111) Bragg reflection and theoretical fits (lines). The curves are vertically displaced against each other by a value of 0.75 for clarity. The corresponding fitted values of f_c and p_c values are given in table 2.

agrees with that of the total intensity of the P2p orbital (region), which is shown in Figure 5 above. However, the fitted coherent fraction and position differ slightly. This is unexpected and likely due to the smaller statistics of the P1s data compared to the P2p data. Hence, for the further analysis we did not include data from the (111) reflection recorded for the P1s orbital.

As expected, the shape of yield curve of the (111) reflection measured for the P1s orbital (see Fig. 6) agrees with that of the total intensity of the P1p orbital ("region"), which was shown in Figure 5 above. However, the fitted coherent fraction and position differ slightly. Because of its better statistics and its higher coherent fraction we consider the coherent fraction and position derived from the P2p orbital as more reliable. We thus do not include data from the (111) reflection recorded for the P1s orbital in our further analysis.

As expected, the yield curve of the (222) reflection (s. Fig. 6) differs considerably from the yield curves for the region recorded for the (111) reflection (s. Figs. 5 and 6). This is also evidenced by the fitted coherent fractions and positions (s. Tab. 2). This is a consequence of the increase of the coherent positions of the contributing vectors by a factor of two at the higher order (222) reflection compared to the (111) reflection which results in the different superpositions.

2.3.3 *Analysis of* $\mathbf{F}_c^{\text{main}}$

We now come back to the analysis of $\mathbf{F}_{c,\text{exp}}^{\text{main}\,(111)}$ that was determined from the P2p(111) yield curve. We restate what we theoretically expect on the basis of the sum rule for the (111) and (222) reflections:

$$\mathbf{F}_c^{\text{main},\,(111)} = \gamma_{\text{main1}} \cdot \mathbf{F}_c^{\text{main1},\,(111)} + \gamma_{\text{main2}} \cdot \mathbf{F}_c^{\text{main2},\,(111)}\,, \tag{5}$$

$$\mathbf{F}_c^{\text{region},\,(222)} = \gamma_{\text{main1}} \cdot \mathbf{F}_c^{\text{main1},\,(222)} + \gamma_{\text{main2}} \cdot \mathbf{F}_c^{\text{main2},\,(222)} + \gamma_{\text{sub}} \cdot \mathbf{F}_c^{\text{sub},\,(222)}\,. \tag{6}$$

Hereby, the vectors of the (222) reflection are related to those of the (111) reflection by multiplying the coherent positions by a factor of 2 and reducing the coherent fraction by a factor factor $\xi_{(111)/(222)}$:

$$\mathbf{F}_c^{(222)} = \xi_{(111)/(222)}\, f_c^{(111)} \cdot \exp\left(i\, 2\pi\, 2 \cdot p_c^{(111)}\right). \tag{7}$$

Generally, the factor $\xi_{(111)/(222)}$ is smaller than 1 and also depends on $f_c^{(111)}$. It can be compiled for a specific distribution of the vertical heights of the emitters. For instance, for a Gaussian height distribution, the equation $f_c^{(222)} = \left(f_c^{(111)}\right)^4$ holds, as shown in ref. [21].

As the distribution of the vertical height is unknown, we approximate $\xi_{(111)/(222)} = 1$. Of course this is a simplifying approximation; however, it served for our purpose. As a consequence, the last vector in eq. (6), $\mathbf{F}_c^{\text{sub},\,(222)}$, can be calculated from the known value of $\mathbf{F}_c^{\text{sub},\,(111)}$ by eq. (7).

Because the eqs. (5) and (6) are valid for the real and imaginary parts of the complex numbers, we have *four* equations in total, which apply to *five* unknown quantities, namely γ_{main1}, and the real and imaginary parts of both $\mathbf{F}_c^{\text{main1}}$ and $\mathbf{F}_c^{\text{main2}}$. For simplicity, we do not index the vectors referring to the (111) reflection here and below. We note that γ_{main2} is known, as $\gamma_{\text{main2}} = 1 - \gamma_{\text{main1}} - \gamma_{\text{sub}}$ holds, and γ_{sub} was determined above. Nevertheless, we are still short of information to independently determine all quantities from the data. We hence make the further plausible assumption that the magnitudes, i.e., the coherent fractions, of $\mathbf{F}_c^{\text{main1}}$ and $\mathbf{F}_c^{\text{main2}}$, namely f_c^{main1} and f_c^{main2}, are equal to $f_c^{\text{sub}} = 0.75$, which was experimentally determined (s. above). This assumes that the

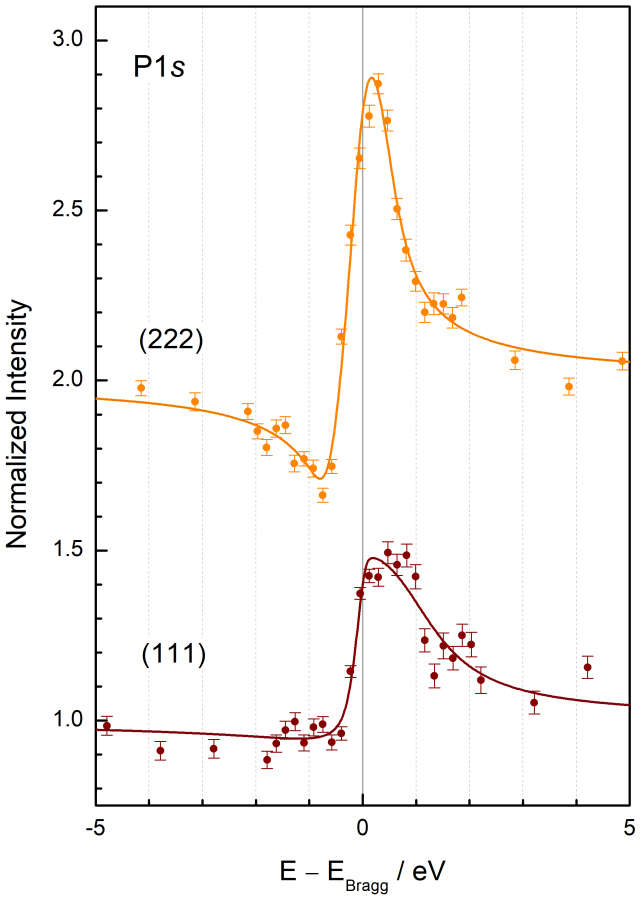

Figure 6: Photoemission yield curve of the integrated intensities (corresponding to that marked by region in Fig. 5) of the P1*s* orbital for the (222) and (111) Bragg reflections and theoretical fits (lines). The curves are vertically displaced by a value of 1.0 for clarity. The corresponding fitted values f_c and p_c values are given in table 2. The Bragg condition of the Au(222) reflection is fulfilled at a photon energy of $E_{\mathrm{Bragg}}^{(222)} = 5273$ eV.

reduction of the coherent fractions from the ideal value of 1 by static and dynamical disorder is the same for all three P species. This assumption implies that the vertical distributions of the three emitters with respect to their respective averaged heights are similar, which is plausible for models with defined P layers. As a consequence, we are left with only *three* unknown quantities now, namely p_c^{main1}, p_c^{main2}, and γ_{main1}.

To our knowledge, there exists no simple way to obtain these quantities in a direct manner from the above equations (5) and (6). Hence, we determined these by trial and error and calculated the values of $\mathbf{F}_{\mathrm{c,exp}}^{\mathrm{main},(111)}$ and $\mathbf{F}_{\mathrm{c,exp}}^{\mathrm{region},(222)}$ (left side of eqs. (5) and (6)) from anticipated quantities of p_c^{main1}, p_c^{main2}, and γ_{main1} until the experimental values were fitted best. This fit in the Argand diagram was performed by eye. Figure 7 illustrates this in the complex plane; the derived quantities are given in Table 3. In Figure 7, the open larger circles represent the experimentally determined vectors; the small filled circles

Table 3: Coherent positions p_c, referring to the (111) reflection, respective vertical heights d_c, and molar fractions γ of the three phosphorus components obtained from the analysis (fitting) of the complete data set as described in the text. $d_c = (1+p_c)\times d_{\mathrm{Au(111)}}$ with $d_{\mathrm{Au(111)}} = 2.355$ Å. As described in the text, all coherent fractions were assumed to be equal and set to the value measured for the sub component ($f_c^{\mathrm{sub}} = 0.75$)

component		p_c	d_c (Å)	γ
main1	top layer	0.497 ± 0.002	3.526 ± 0.005	27%
main2	bottom layer	0.053 ± 0.002	2.480 ± 0.005	44%
sub		0.053 ± 0.002	2.480 ± 0.005	28%

correspond to the fitted vectors. The size of the circles for the experimental data was chosen such that it covers the area given by the statistical error bars of the experimental data points.[1]

We find that there are two contributions to $\mathbf{F}_{\mathrm{c,exp}}^{\mathrm{main}}$, namely $\mathbf{F}_c^{\mathrm{main1}}$ and $\mathbf{F}_c^{\mathrm{main2}}$ with molar fractions $\gamma_{\mathrm{main1}} = 27\%$ and $\gamma_{\mathrm{main2}} = 44\%$; the remaining P atoms contribute to $\mathbf{F}_c^{\mathrm{sub}}$ ($\gamma_{\mathrm{sub}} = 28\%$). Notably, in the complex plane, $\mathbf{F}_c^{\mathrm{main2}}$ and $\mathbf{F}_c^{\mathrm{sub}}$ fall onto to each other within the uncertainty of the analysis (s. Fig. 7). This reveals that the respective P atoms are within the statistical error at the same height.

In summary, we find that 72% (44% + 28%) of the P atoms are located between 2.480 ± 0.005 Å above the Au surface and resemble the bottom layer. Two chemically different types of P atoms (main2 and sub) contribute to this layer. The smaller fraction of P atoms (27%) are 1.046 Å ± 0.010 Å further away from the surface, at 3.526 ± 0.005 Å, and form the top layer.

2.3.4 Evaluation of $(1\bar{1}1)$ *reflection*

We also performed NIXSW scans on the $(1\bar{1}1)$ reflection using the P1*s* orbital. This reflection is inclined versus the surface normal and hence provides information on the lateral arrangement of the P atoms. A non-zero value for the coherent position ($f_c^{(1\bar{1}1)}$) is possible for this reflection, because the structure is commensurate. First, we calculated the values using the coordinates for the P atoms given by the two models. The principal procedure to calculate $f_c^{(hkl)}$ and $p_c^{(hkl)}$ for an inclined Bragg reflection is described, e.g., in ref. [21]. The values have to be averaged over possible different rotational domains. There are three of these for the DL structure, whereas there exists only one for the Au-P network model (see above). For the DL model we calculated $f_{\mathrm{c,\,DL}}^{(1\bar{1}1)} = 0.105$ and $p_{\mathrm{c,\,DL}}^{(1\bar{1}1)} = 0.332$ and for the Au-P model $f_{\mathrm{c,\,Au-P}}^{(1\bar{1}1)} = 0.475$ and $p_{\mathrm{c\,Au-P}}^{(1\bar{1}1)} = 0.300$. The smaller value of $f_{\mathrm{c\,DL}}^{(1\bar{1}1)}$ for the DL model can be understood in view of its smaller symmetry and the

[1] We note that, fitting *all* experimentally determined vectors ($\mathbf{F}_{\mathrm{c,exp}}^{\mathrm{main}}$, $\mathbf{F}_{\mathrm{c,exp}}^{\mathrm{sub}}$, $\mathbf{F}_{\mathrm{c,exp}}^{\mathrm{region,exp}}$, and $\mathbf{F}_{\mathrm{c,exp}}^{(222)}$) at the same time, gave an additional accuracy to the analysis, and yielded a fitted coherent position p_{sub} slightly smaller than $p_{\mathrm{sub,exp}}$ by -0.01 (s. Fig. 7). The impact on γ_{sub}, which was determined earlier from eq. (3) was, however, negligible.

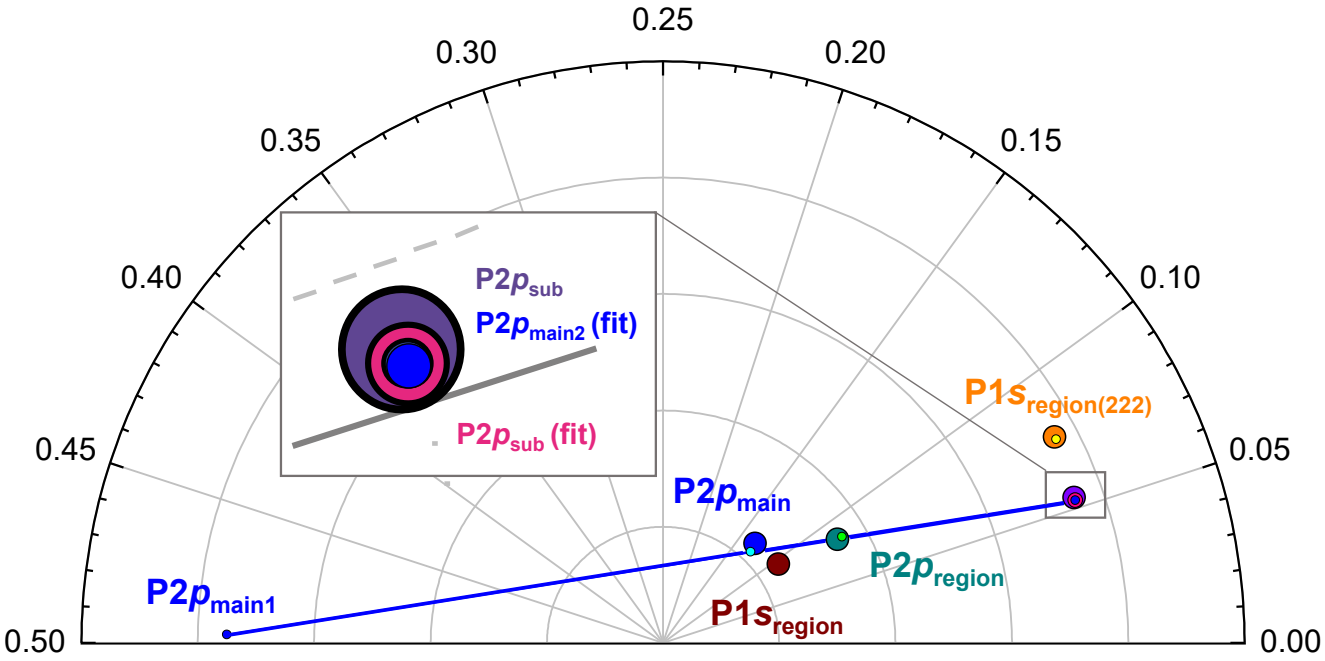

Figure 7: Argand diagram of the five experimentally obtained vectors (large circles) and corresponding fitted values (small points). All vectors refer to the (111) reflection with one exception referring to the (222) reflection as marked. The sizes of the larger circles representing the experimental vectors were chosen such that they cover the range of the statistical error bars. The inset shows the experimentally determined vector of the sub component (P2p_{sub}, violet) and the fitted vector (P2p_{sub}(fit), pink); in addition the fitted vector of the main2 component (P2p_{main2}(fit), blue) is shown; it falls on top of P2p_{sub}(fit) within the statistical error bars.

higher number of P atoms within the (5×5) unit cell (32 instead of 18). The $p_{\mathrm{c}}^{(1\bar{1}1)}$ values of both model are however rather similar and do not allow a further discrimination.
From four evaluated yield curves of the total intensity of the P1s orbital (not shown) we obtained $f_{\mathrm{c}}^{(1\bar{1}1)} = 0.483 \pm 0.030$ and $p_{\mathrm{c}}^{(1\bar{1}1)} = 0.250 \pm 0.003$. Comparison of this experimental value to those that would be expected for the DL and Au-P network models, yields a better agreement with the Au-P model. The latter model, in particular explains the experimental value of $f_{\mathrm{c}}^{(1\bar{1}1)} = 0.483$, whereas this is not provided by the DL model. Hence, the result for the $(1\bar{1}1)$ reflection also supports the Au-P model.

3 Discussion

We start by comparing the obtained heights with those given by the DL and Au-P-network models (s. Tab. 1). We find a value for the height of the top layer (3.526 Å) that lies between the values predicted by the two models, i.e., at 26% of their difference. The height of the bottom layer (2.480 Å) is by about 0.08 Å (3.3%) above those of the bottom layers of both models, for which are given at identical values.[2] As a consequence, the experimentally determined height difference between the top and bottom layer, i.e., the "buckling" (1.046 Å ± 0.010 Å), is smaller than that proposed by the Au-P-network model by 0.05 Å and smaller than that of the DL-network model by 0.15 Å. The DL and Au-P-network model predict that 37.5%, respectively 33% of all P atoms are in the top layer, while we find only 27%, given that attenuation effects for the photoelectrons by the top layer can be neglected.[3]

Hence, the vertical arrangement of the P atoms of the (5×5)P/Au(111) differs from those given by the two models. It is instructive to visualize the comparison by an Argand diagram. This is done in Figure 8. Both models and the data from our NIXSW analysis are represented by a respective line, which spans from the the vector (marked by the filled circle) representing the top layer (on the left) to the vector representing the bottom layer (on the right). All coherent fractions of the experimental vectors are 0.75; for the vectors of the models, coherent fractions of 1.0 were used for simplicity. (Using smaller f_{c} values would not lead to principal differences.) As a consequence of the sum rule, the respective lines resemble the possible locations of the the respective vectors that can result for the regions, $\mathbf{F}_{\mathrm{c}}^{\mathrm{region}}$ upon a variation of the stoichiometric

[2]Note that we refer to the averaged height values.

[3]We note that a relaxation of the Au top layer in direction of the vacuum by 0.14 Å was obtained by DFT for the DL model [5]. If this is accounted, it should be added to the heights given for the DL modell, as the NIXSW heights refer to the position of the extended lattice plane. No relaxation was present for the Au-P network model.

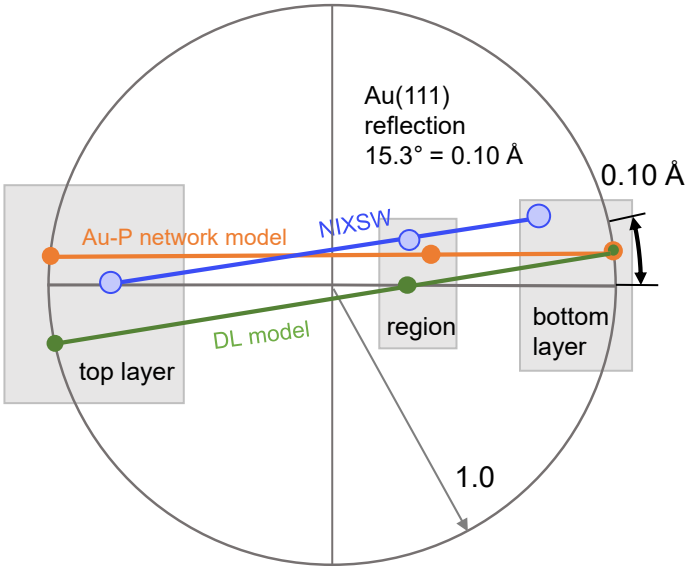

Figure 8: Argand diagram of values obtained from the present NIXSW analysis (s. Tab. 3) in comparison with those expected for DL and the Au-P network model. The lines from the vector of the bottom layer to that of the top layer represent the possible positions for the vector of the region upon a variation of relative occupation of the two layers.

ratios, i.e., relative occupancy numbers of the layers. Figure 8 shows that the lines of both models and the NIXSW data differ significantly from each other, both in their positions and slopes, whereby the differences are beyond the error bars of the data. Hence, none of the two models is directly verified by the layer heights obtained from the NIXSW data. Much more, a revision of the layer heights is suggested. Here the high accuracy of the NIXSW method for the determination of bonding heights comes into play, which is partly due to the fact that heights are measured modulo the lattice constant $d_{(hkl)}$.

Evidently, in any case, the line has to pass through the position of the experimentally most reliable determined vector $\mathbf{F}_{\mathrm{c,exp}}^{\mathrm{region}}$. As said, this is not the case for both models and this demonstrates clearly that none of the two models is in full agreement with our data. However, for the Au-P network model the line by passes the respective position at a smaller distance than the line of the DL model. We take this as an indication that this model is more appropriate and discuss it further in view of our data.

For this purpose we consider a modified Au-P network model, where the layer heights are adjusted to the values determined by our NIXSW data. Can we then find further arguments from our experiment supporting that this model is principally correct? A strong argument is given by the fact that, within the P-Au network model, one can identify two different species of P atoms in the bottom layer. These two species may explain the presence of two chemically different components (main2 and sub). The situation is illustrate in Figure 1 above. Namely, 6 of the 12 P atoms of the bottom layer (blue color), which are within the six-membered rings, are coordinated to two P atoms (of the top layer) and one Au ad-atom in the bottom layer, while the other 6 P atoms (violet color) are coordinated to one P atom (of the top layer) and two Au ad-atoms in the bottom layer. We tentatively assign the first P species to the main2 component and the second to the sub component. Here, we argue that for the P atoms that are coordinated to two electron rich Au ad-atoms the photohole is better screened. This is reflected by the smaller binding energy of the sub component versus that of the main2 component.

On the other hand, the P atoms contributing to the main1 and main2 components are both located in the six-membered rings. This may be the reason that the respective photoemission peaks have within the energy resolution identical binding energies. This interpretation implies that the lateral coordination of the P atoms is primary decisive for the respective binding energies of their photoemission peaks, and to only lesser extent their vertical distance to the underlying Au surface, which alternatively may have an impact on the binding energy through the screening of the photohole by surface electrons. Admittedly, a similar interpretation would be also possible in the frame of the DL model, as there the P atoms also have different coordination numbers (s. Fig. 1). However, from inspecting the lateral arrangement of the P atoms in this model, the variation of the local coordination of the P atoms appears less distinct, and hence such a clear splitting of the photoemission peaks into two species at different binding energies, as we observed, is not so plausible there.

Finally, we recall that the Au-P network model also provides an interpretation for the Au7f photoemission spectrum. It explains the unexpectedly strong contribution of the chemically modified Au atoms ($\chi_{\mathrm{P}} = 1.9$) by an incomplete Au layer (given by the 9 Au ad-atoms) on top of the first complete Au surface layer. No such explanation is provided by the DL model, where the topmost Au layer exhibits an equal atom density as the underlying bulk layers. In view of the Au-P network model, the peak 1 of the Au7f spectrum (at higher binding energy) corresponds to the 9 Au ad-atoms that are coordinated between two P atoms in the bottom layer, which represent the sub component of the P peak at smaller binding energy with respect to the main1 and main 2 components. The peak 2 in the Au7f spectrum corresponds to the topmost complete Au layer.

In summary, we find that both, the Au7f photoemission spectra, and the NIXSW data, can be consistently and plausibly explained by the Au-P network model, when the bonding heights are revised. An experimental finding that, however, differs from the model is the fact that the NIXSW data assigns only 27% of the P atoms to the top layer, whereas the Au-P network model requires that one third of all P atoms are in the top layer. Of course the attenuation of the photoelectrons of the bottom layer by the top layer may play a role. However, this biases the intensity of the top layer, mak-

ing the discrepancy of the corrected ratios even larger. One explanation may be that the top layer was more strongly subject to photodesorption during the NIXSW experiment than the bottom layer and the number of P atoms in this layer was therefore diminished. A further aspect of our data that differs from the expectation of the Au-P network model is that the predicted stoichiometric ratio of the two P atoms in the bottom layer is 1 : 1, whereas we find $\gamma_{\mathrm{sub}} : \gamma_{\mathrm{main2}} = 0.64 : 1$. This difference may be due to statistical errors in the data evaluation and/or again an inequivalent attenuation of the photoelectrons of the respective emitters due to angular effects with respect to the top layer.

Before closing, we briefly discuss an alternative interpretation that is also compatible with our data and motivated by the observation that, at low coverages, P atoms are substitutionally embedded in the first Au layer. As mentioned in the introduction, these give rise to a surface reconstruction of the same length scale but with different structure as the Au herringbone reconstruction. As the NIXSW experiment can distinct vertical heights only modulo the lattice spacing, i.e., in our case $d_{\mathrm{Au(111)}}$, it is also compatible with the data that the P atoms of the sub component are located at $d_{\mathrm{c}} = p_{\mathrm{c}} \times d_{\mathrm{Au(111)}}$, instead of $d_{\mathrm{c}} = (1+p_{\mathrm{c}}) \times d_{\mathrm{Au(111)}}$. This corresponds to a height of 0.145 Å with respect to the center of the first complete Au layer (surface layer). This conclusion is also motivated for the sub component by its shift to smaller binding energies (due to screening) with respect to the component main1. This would imply that more than 28% of the P atoms are embedded in the first Au layer forming a mixed layer, a situation similar to that found for Ag silicenes [12]. We estimate more than 28%, because due to attenuation effects the stoichiometry will be underrepresented by the respective coherent fraction. However, we consider this possibility as rather unlikely, because such a structure would likely not be commensurate with the Au(111), as it is observed. Hence, this alternative explanations is dismissed.

4 Conclusions

From normal incidence x-ray standing wave and photoemission we find evidence that the (5×5)P/Au(111) is described by a Au-P-network model that is very close to the one proposed by Tian *et al.* [7, 11]. However, a revision of the vertical heights appears to be required. The P atoms are located at two different heights (top and bottom layer). Hereby, our data gives some evidence, although only indirectly, that the P atoms in the bottom layer are connected by Au ad-atoms as it was proposed by Tian *et al.*. The top layer is slightly closer to the bottom layer as predicted by the Au-P network model, and the resulting buckling is only 1.043 Åinstead of 1.10 Å. The height of the P atoms in the bottom layer is by about 0.08 Å larger with respect to the height that was earlier determined [7, 11]. From our data we further obtain a complete interpretation of the photoemission spectra of the P2p and the Au4f orbitals.

5 Experimental details

5.1 Sample preparation

The sample preparation and recording of the photoemission spectra for the chemical analysis and for the normal incidence x-ray standing wave (NIXSW) analysis were performed under ultra-high-vacuum at the beamline I09 of the Diamond Light source at Didcot/GB. The Au(111) surface was prepared by Ar ion sputtering and subsequent annealing at 550°C for about 30 min. The P superstructure was prepared by subliming black phosphorus from a small glass crucible at a temperature of about 400°C, while the Au sample was held at 250°C. Subsequently, low energy diffraction (LEED) showed the pattern of a (5×5) superstructure with sharp and distinct spots which we observed within the energy range of from 22 to 66 eV. As far as we can judge from the visual inspection of the LEED patterns, the intensity ratios of the LEED spots corresponded to that reported by Golias *et al.* [5] and by Tian *et al.* [7]. In particular, the $(\frac{1}{5}, 0)$ and $(0, \frac{1}{5})$ spots exhibited characteristic very small intensities. This indicates that we prepared the same phase of P on Au(111) as the former authors. The satellites from the Au(111) herringbone reconstruction were not seen any more for the layers analyzed here.

5.2 Photoelectron spectroscopy

The soft and hard x-ray photoemission spectra were recorded using a hemispherical analyzer operated in angle integrated mode. The full acceptance cone of the analyzer was $\theta_{\mathrm{cone}} = 56°$. The axis of the analyzer was perpendicular to the direction of the photon beam and in the plane of the polarization of the photons. Using soft x-rays at photon energies of 180 eV and 280 eV, spectra of the Au4f and the P2p orbitals were recorded with high energy resolution and high statistics. The P2p spectra served for the identification and assignment of different chemical components of P and the development of "fitting models" for the NIXSW data that were recorded at higher photon energies (hard x-rays) and which were of lower resolution. For the soft x-ray spectra the surface normal was rotated towards the axis of the analyzer such that the axis of the analyzer, and hence the center of the acceptance cone, was at angles of θ of 60° and 20° with respect to the surface normal, yielding a grazing (surface sensitive) and a closer to normal (bulk sensitive) emission geometry.

For the NIXSW analysis, the spectra were recorded at photon energies (E) close to the Bragg energies of the (111) and (222) reflections of Au, i.e., $E_{\mathrm{Bragg}} = 2636.5$ eV and 5273 eV, respectively. Here, the (111) direction of the sample was close to the opposite direction of the incident photon beam (normal incidence). For recording the intensity of the reflected x-ray beam ($R(E)$) on a fluorescent screen it was tilted by $-3°$

out of the exact normal incidence position (defined by the x-ray beam) in the direction away from the analyzer, yielding a Bragg angle of 87°. For this geometry, photoelectrons recorded in the emission cone of the analyzer exhibit emission angles with respect to the surface normal of $\theta = 65°$ to 90°. The experimental geometry for the NIXSW experiments is further described in ref. [21].

Due to its small binding energy, the cross section of the P2p orbital at photon energies corresponding to the Bragg energy of the Au(111) reflection is small and individual spectra are hence of low statistics. In order to allow a decomposition of the spectra measured for the NIXSW analysis into the contributions of different chemical components by fitting a sum of the components to the spectra, we hence summed-up the photoemission spectra at respective photon energies from 19 individual NIXSW scans. Beam degradation of the sample was not drastic, but observable, i.e., during the recording of one NIXSW scan, the spectrum of the P2p orbital lost about 15% of its intensity. Thus, in order to minimize effects from beam degradation, all NIXSW scans (comprising 29 photoemission spectra each) were recorded on fresh spots on the sample. Hereby, care was taken that all selected sample spots provided reflectivity curves of same shape and height.

For the NIXSW scans using the P1s orbital which were done at the (222), (111), and $(1\bar{1}1)$ reflections, we proceeded in a similar manner and summed photoemission spectra at individual photon energies of 5, 3 and 4 NIXSW scans, respectively. Because of the higher binding energy of the P1s orbital ($E_\mathrm{B} = 2.149$ keV), the cross sections of the P1s orbital at the respective Bragg energies was sufficiently high that this small number of scans provided a sufficient statistics.

5.3 Data analysis

The photoemission spectra were fitted under the software CasaXPS [22]. Empirically, we found that asymmetric Lorentzian line shapes convoluted by a Gaussian (line-shape "TLA" in CasaXPS) in combination with a linear background described the spectra of the P2p orbital best. Two components were fitted to the P2p spectrum ("main" and "sub"). For both of them we used a doublet of two peaks with a fixed spin orbit splitting of 0.85 eV, identical FWHM, and an ideal intensity ratio of 2 between the P2$p_{\frac{3}{2}}$ and P2$p_{\frac{1}{2}}$ peaks. The yield curves ($Y(E)_\mathrm{main/sub}$) were computed from the areas of the fitted components versus the photon energy E. For the P1s orbital, the resolution did not permit to discriminate different components; hence, the total intensities were obtained from integration over the region of the spectra after background subtraction and evaluated. The same procedure was used for computing the total intensities of the P2p orbital.

When fitting the P2p spectra recorded for varying photon energies during an NIXSW run, we found by trial and error that a very small systematic correction of up to −120 meV (at the high energy end of the spectral series) in the binding energy of the P2$p_{\frac{3}{2}}$ orbital had to be implemented in the fits. If this energy correction was not made, some intensity (≈ 20%) of the fitted main component was erroneously transferred to the sub component for spectra recorded at photon energies above the Bragg energy. This resulted in nonphysical yield curves of both components that deviated systematically from theoretically predicted yield curves (see below). We suppose that the shift is related to a small systematic deviations of the true photon energies from the preset values when the monochromator was scanned in energy. The effect appears to be specifically relevant for the spectrum of the P2p orbital because it is composed of two significantly overlapping doublets (main and sub) which both consist of two rather narrow lines (FWHM ∼ 0.25 eV). For another recent NIXSW analysis involving 2p orbitals we refer to ref. [23].

The experimentally obtained NIXSW yield curves ($Y(E)$) were fitted by the theoretically predicted curves using the program Torricelli [20] according to the following formula:

$$\begin{aligned} Y(E) = 1 &+ S_\mathrm{R}\sqrt{R(E)} \\ &+ 2\,|S_\mathrm{I}|\,R(E)\,f_\mathrm{c}\,\cos\left(\eta(E) - 2\,\pi\,p_\mathrm{c} + \psi\right)\,. \end{aligned} \tag{8}$$

Here f_c and p_c are the coherent fraction and position. $\eta(E)$ denotes the photon energy dependent phase, and $R(E)$ the reflectivity. The parameters $S_\mathrm{R}, S_\mathrm{I}$, and ψ are the "non-dipolar correction" parameters which take account of the difference between the measured electron yield $Y(E)$ and the intensity of the standing x-ray wave field at the position of the emitting atom [13]. These arise when the dipole approximation for the photoelectron yield becomes invalid at higher photon energies where the photon wavelength is no more large with respect to the extension of the emitting orbital. In that situation, the momentum of the photon biases the electron emission. As a result of the detection geometry, the reflected photon wave contributes stronger to the signal than the incoming. Statistical errors were treated as described in ref. [20].

5.4 Non-dipolar corrections

For the P2p orbital the non-dipolar corrections were taken into account. However, presently, there exists no established formula for these corrections. An approximation was suggested by Nelson *et al.* [24] (see alternatively ref. [13], p. 206). It is implemented in the program Torricelli [20]. Using the correction, we obtained f_c and p_c values close to those obtained without correction, namely within about twice the range given by the statistical uncertainty. For the P1s orbital we have also fitted the yield curves of the (111) and (222) reflections with and without non-dipolar corrections Above, corrected values were reported always. For the (111) reflection, the corrections are not relevant, because the orbital is small with respect to to the x-ray wavelength. For the (222) reflection, the correction parameters were used according to the description in ref. [20]. Hereby, the averaged emission angle of the photoelectrons was

Table 4: Overview on the non-dipolar correction parameters used for the fitting of the experimental yield curves according to eq. 8. For the computation of the parameters S_R, S_I, and ψ from δ_p, δ_d, and γ, we refer to ref. [20].

orbital	E (eV)	δ_p	δ_d	γ
P2p	2636.5	−1.38740	1.24605	0.71527
P1s	2636.5	−0.52621	1.55875	0.25807
	5273	−1.48245	1.19590	1.125514

set to 76°. The corrections reduced the values of f_c and p_c for the (222) reflection by about 10%. For reference purpose the correction parameters are reported in Table 4.

6 Acknowledgement

We are grateful to E. Golias for sending us the coordinates of their structure model published in ref. [5]. We acknowledge support by Diamond Light Source (Didcot, GB) and in particular by the team of the beamline I09. We thank M. Buchta and A. Grüneis for experimental hints, and C. Kumpf for discussions during the evaluation. The project was further supported by the Deutsche Forschungsgemeinschaft (DFG) under the project SO-407/6-3 and through the DFG research training group 2591.

References

[1] J. L. Zhang, S. T. Zhao, C. Han, Z. Z. Wang, S. Zhong, S. Sun, R. Guo, X. Zhou, C. D. Gu, K. Di Yuan, Z. Y. Li, and W. Chen, "Epitaxial Growth of Single Layer Blue Phosphorus: A New Phase of Two-Dimensional Phosphorus", Nano Letters **16**, 4903 (2016).

[2] H. T. Nguyen-Truong, "Optical absorption and excitation spectra of monolayer blue phosphorene", Journal of Physics-Condensed Matter **32** (2020).

[3] J. Lu, J. Yang, A. Carvalho, H. Liu, Y. Lu, and C. H. Sow, "Light–Matter Interactions in Phosphorene", Accounts of Chemical Research **49**, 1806 (2016).

[4] J.-P. Xu, J.-Q. Zhang, H. Tian, H. Xu, W. Ho, and M. Xie, "One-Dimensional Phosphorus Chain and Two-Dimensional Blue Phosphorene Grown on Au(111) by Molecular-Beam Epitaxy", Physical Review Materials **1**, 061002 (2017).

[5] E. Golias, M. Krivenkov, A. Varykhalov, J. Sanchez-Barriga, and O. Rader, "Band Renormalization of Blue Phosphorus on Au(111)", Nano Letters **18**, 6672 (2018).

[6] W. Zhang, H. Enriquez, Y. F. Tong, A. Bendounan, A. Kara, A. P. Seitsonen, A. J. Mayne, G. Dujardin, and H. Oughaddou, "Epitaxial Synthesis of Blue Phosphorene", Small **14** (2018).

[7] H. Tian, J. Q. Zhang, W. K. Ho, J. P. Xu, B. W. Xia, Y. P. Xia, J. Fan, H. Xu, M. H. Xie, and S. Y. Tong, "Two-Dimensional Metal-Phosphorus Network", Matter **2**, 111 (2020).

[8] J. L. Zhang, S. Zhao, S. Sun, H. Ding, J. Hu, Y. Li, Q. Xu, X. Yu, M. Telychko, J. Su, C. Gu, Y. Zheng, X. Lian, Z. Ma, R. Guo, J. Lu, Z. Sun, J. Zhu, Z. Li, and W. Chen, "Synthesis of Monolayer Blue Phosphorus Enabled by Silicon Intercalation", ACS Nano **14**, 3687 (2020).

[9] M. Gruenewald, M. Schaal, I. Karadzhov, L. Brill, J. Domke, P. Grimm, F. Otto, J. Picker, P. M. Simon, H. Tamm, T. Fritz, and R. Forker, "Blue Phosphorene on Au(111) as a Decoupling Layer for Organic Epitaxially Grown Films", Phys. Rev. Mater. **6**, 015601 (2022).

[10] C. He, S. Xu, X. Dong, C. He, X. Hu, G. Liu, and H. Xu, "Step-guided epitaxial growth of blue phosphorene on vicinal ag(111)", Phys. Rev. Mater. **7**, 034003 (2023).

[11] S. Zhao, J. L. Zhang, W. Chen, and Z. Y. Li, "Structure of Blue Phosphorus Grown on Au(111) Surface Revisited", Journal of Physical Chemistry C **124**, 2024 (2020).

[12] J. T. Kuechle, A. Baklanov, A. P. Seitsonen, P. T. P. Ryan, P. Feulner, P. Pendem, T.-L. Lee, M. Muntwiler, M. Schwarz, F. Haag, J. Barth V, W. Auwaerter, D. A. Duncan, and F. Allegretti, "Silicene's pervasive surface alloy on Ag(111): a scaffold for two-dimensional growth", 2D Materials **9** (2022).

[13] J. Zegenhagen and A. Kazimirov, eds., *The X-ray Standing Wave Technique - Principles and Applications, in Series on Synchrotron Radiation Techniques and Applications, vol. 7* (World Scientific, NewJersey, 2013).

[14] A. Sandy, S. Mochrie, D. Zehner, K. Huang, and D. Gibbs, "Structure and Phases of the Au(111) Surface - X-ray-scattering Measurements", Physical Review B **43**, 4667 (1991).

[15] M. Corso, L. Fernández, F. Schiller, and J. E. Ortega, "Au(111)-Based Nanotemplates by Gd Alloying", ACS Nano **4**, 1603 (2010).

[16] M. Mühlpointner, "Investigations on the Evolution of Blue Phosphorus Films on the Au(111) Surface", MSc thesis (Universität Bonn, 2023).

[17] P. Citrin, G. Wertheim, and Y. Baer, "Core-Level Binding Energy and Density of States from Surface Atoms of Gold", Physical Review Letters **41**, 1425 (1978).

[18] B. Johansson and N. Martensson, "Core-Level Binding-Energy Shifts for the Metallic Elements", Physical Review B **21**, 4427 (1980).

[19] A. Chaudhuri, T. J. Lerotholi, D. C. Jackson, D. P. Woodruff, and V. Dhanak, "Local Methylthiolate Adsorption Geometry on Au(111) from Photoemission Core-Level Shifts", Phys. Rev. Lett. **102**, 126101 (2009).

[20] F. C. Bocquet, G. Mercurio, M. Franke, G. van Straaten, S. Weiss, S. Soubatch, C. Kumpf, and F. S. Tautz, "TORRICELLI: A software to determine atomic spatial distributions from normal incidence x-ray standing wave data", Computer Physics Communications **235**, 502 (2019).

[21] S. Weiß, I. Krieger, T. Heepenstrick, S. Soubatch, M. Sokolowski, and F. S. Tautz, "Determination of the adsorption geometry of PTCDA on the Cu(100) surface", Phys. Rev. B **96**, 075414 (2017).

[22] N. Fairley, *CasaXPS, version 2.3.16*, Casa Software Ltd, Bay House, 5 GrosvenorTerrace, Teignmouth, Devon TQ14 8NE, United Kingdom.

[23] S. Le Moal, I. Krieger, R. Kremring, S. Weiß, X. Yang, S. Soubatch, F. S. Tautz, M. Silly, A. G. Borisov, M. Sokolowski, and E. Le Moal, "Core-Level Binding Energy Shifts in Ultrathin Alkali-Halide Films on Metals: KCl on Ag(100)", The Journal of Physical Chemistry C **127**, 24253 (2023).

[24] E. J. Nelson, J. C. Woicik, P. Pianetta, I. A. Vartanyants, and J. W. Cooper, "Quadrupole effects in core and valence photoelectron emission from crystalline germanium measured via a spatially modulated x-ray interference field", Phys. Rev. B **65**, 165219 (2002).

Supporting Information

Sum Rule

For the evaluation of NIXSW data a sum rule applies and is most helpful. If a yield curve is obtained by integrating the intensity over the total spectral region of a specific orbital ("region") and is given by a superposition of yield curves of different species (j), the corresponding Argand vector $\mathbf{F}_{\mathrm{c}}^{\mathrm{region}}$ (s. eq. (2)) is given by a weighted sum of the argand vectors $\mathbf{F}_{\mathrm{c}}^{j}$ that correspond to the K yield curves of the individual species:

$$\mathbf{F}_{\mathrm{c}}^{\mathrm{region}} = \sum_{j=1}^{K} \gamma_j \cdot \mathbf{F}_{\mathrm{c}}^{j} \,. \tag{9}$$

γ_j are the molar fractions of the contributing species, i.e., $\gamma_j = N_j/N$, where N is the total number of emitters and N_j the number of emitters contributing to the component j.

Strictly speaking, the sum rule is only valid as long as attenuation effects of the photoelectron yield can be neglected (s. below.) The sum rule is formally analogue to the definition of the center of mass and reduces to the "lever rule" for the case of two species. It is useful as it relates the vectors of different components with each other by their molar fractions.

The sum rule results from two aspects, namely the normalization of the experimental yield curves ($Y(E)_{hkl}$) during the evaluation and the independent superposition of the photoelectron yields of the N individual emitters (i) to the total photoemission intensity.

Let us consider the first aspect which is given by the normalization of all yield curves in the evaluation according to eq. (8). During the fitting of the theoretical curve to the experimental data, the experimental data is normalized to 1 for photon energies (E) far away from the Bragg condition, i.e., where $R(E) = 0$ holds (s. eq. (8). This is provided by the fitting tool, e.g., by Torricelli.[20] This holds for all yield curves which are evaluated, i.e., for the one of the integrated intensity ($Y(E)_{hkl}^{\mathrm{region}}$) and also for those of any of the individual

components (j) that contribute ($Y(E)^j_{hkl}$) to the total intensity.

Under the condition that all emitters contribute equally to the photoemission intensity it follows that the the normalized yield curve of the integrated intensity is obtained from the normalized yield curves of the individual components when these are weighted by their individual molar fractions γ_j. Hence it holds:

$$Y(E)^{\text{region}}_{hkl} = \sum_{j=1}^{K} \gamma_j \cdot Y(E)^j_{hkl} \,. \tag{10}$$

The assumption that the photoemission cross sections of all emitters, contributing to the orbital under consideration are equal is usually a good approximation for hard x-ray photoemission. However, for a sample with several layers, as it is the case here, this is only true to the extent that the intensities of photoelectrons of emitters at lower heights are not attenuated by atoms at larger heights. Alternative, the coefficients γ_j have to be interpreted as effective molar fractions.

Finally, we need to understand, how eq. (10) implies eq. (9). For this purpose it is sufficient to validate that the vectors $\mathbf{F}_\text{c}$ relates in a linear manner to the emitting species, i.e., in other words, that

$$\mathbf{F}_\text{c}^{\text{region},\,(hkl)} = \mathbf{F}_\text{c} \left(\sum_{j=1}^{K} \gamma_j \cdot Y(E)^j_{hkl} \right) = \sum_{j=1}^{K} \gamma_j \cdot \mathbf{F}_\text{c}(Y(E)^j_{hkl}) \,. \tag{11}$$

holds. Then, the sum rule eq. (9) follows from eq. (10). For demonstrating eq. (11), we recall that the normalized yield curve $Y(E)^j_{hkl}$ is given by a summation of the contributions of the individual emitters:

$$Y(E)^j_{hkl} = \frac{1}{N_j} \sum_{i=1}^{N_j} \left[1 + S_\text{R} \sqrt{R(E)} + 2\,|S_\text{I}|\, R(E)\, \cos\left(\eta(E) - 2\,\pi\, z_i / d_{hkl} + \psi\right) \right] . \tag{12}$$

Here the definitions from above apply and z_i denotes the height of the emitter i versus the

Bragg plane (hkl) moduo $d_{(hkl)}$. Eq. (12) can be rewritten:

$$Y(E)^{j}_{hkl} = 1 + S_{\mathrm{R}}\sqrt{R(E)} + 2\,|S_{\mathrm{I}}|\,R(E)\,\Re\left\{\exp\left(i\,(\eta(E)+\psi)\right)\,\left[\frac{1}{N_j}\sum_{i=1}^{N_j}\exp\left(-i\,2\,\pi\,z_i/d_{hkl}\right)\right]\right\}. \tag{13}$$

Here $\Re\{\dots\}$ denotes the real part of a complex number. Now, we use the definition of the coherent fraction f_{c}^{j} and position p_{c}^{j} and, in addition, eq. (2) for the vector $\mathbf{F}_{\mathrm{c}}^{j,\,(hkl)}$. Then the term in square brackets is equivalent to:

$$\frac{1}{N_j}\sum_{i=1}^{N_j}\exp\left(-i2\,\pi\,z_i/d_{hkl}\right) = f_{\mathrm{c}}^{j,\,(hkl)}\exp\left(-i\,2\pi\,p_{\mathrm{c}}^{j,\,(hkl)}\right) = \overline{\mathbf{F}_{\mathrm{c}}^{j,\;(hkl)}}\,, \tag{14}$$

where the bar denotes the complex conjugate. Hence we receive the basic formula relating the normalized yield curve and the vector:

$$Y(E)^{j}_{hkl} = 1 + S_{\mathrm{R}}\sqrt{R(E)} + 2\,|S_{\mathrm{I}}|\,R(E)\,\Re\left\{\exp\left(i\,(\eta(E)+\psi)\right)\,\overline{\mathbf{F}_{\mathrm{c}}^{j,\,(hkl)}}\right\}. \tag{15}$$

We use this and calculate:

$$\sum_{j=1}^{K}\gamma_j\cdot Y(E)^{j}_{hkl} = 1+S_{\mathrm{R}}\sqrt{R(E)}+2\,|S_{\mathrm{I}}|\,R(E)\,\Re\left\{\exp\left(i\,(\eta(E)+\psi)\right)\,\sum_{i=1}^{N_j}\gamma_j\cdot\overline{\mathbf{F}_{\mathrm{c}}^{j,\,(hkl)}}\right\}. \tag{16}$$

whereby we have exploited that $\sum_{i=j}^{K}\gamma_j = 1$. On the the other end, by the same definition, it must hold that:

$$\begin{aligned}\sum_{j=1}^{K}\gamma_j\cdot Y(E)^{j}_{hkl} &= Y(E)^{\mathrm{region}}_{hkl}\\ &= 1 + S_{\mathrm{R}}\sqrt{R(E)} + 2\,|S_{\mathrm{I}}|\,R(E)\,\Re\left\{\exp\left(i\,(\eta(E)+\psi)\right)\,\overline{\mathbf{F}_{\mathrm{c}}^{\mathrm{region},\,(hkl)}}\right\}.\end{aligned} \tag{17}$$

From comparison of eqs. (16) and (17) we retrieve the sum rule, i.e., eq. (10).

B Experimental details

This chapter serves to illustrate and explain some important details regarding the preparation of the samples, the evaluation of the data, and the technical constructions of machine parts that were needed for the experiments. Section B.1 discusses the influence of different annealing temperatures on the monoatomic step edges of the Ag(100) surface. In Section B.2 different methods to determine the QA coverage are explained, which can be used to obtain a reference for the calibration of the QMS integrals. Lastly, the technical constructions of a filament current chopper for SPA-LEED measurements, a Ag evaporator, and a transfer fork for the wobble stick in the STM chamber are explained in Sections B.3, B.4, and B.5, respectively.

B.1 Testing of lower temperatures for the annealing of Ag(100)

As mentioned in Chapter 4.2, annealing the Ag crystals at 850 K or higher for 30 to 60 minutes leads to the formation of Ag clusters and curved step edges. This phenomenon does not cause any issues for LEED experiments, but it can be very disruptive for the investigation of organic structures on surfaces by STM. That is because it complicates differentiating between Ag clusters and clusters of organic molecules that may form on the surface during or after deposition. Hence, it was tested whether annealing at a lower temperature reduces the formation of such Ag clusters. The results of these experiments are presented in this section.

Figure B.1 shows STM images of the Ag(100) surface after annealing for 60 minutes at 850 K and 700 K in panel a) and b), respectively. The STM images show that, after annealing the crystal at 850 K, there are a lot of bright protrusions, which are about between 2 Å and 5 Å in apparent height and which are preferably located at Ag step edges. These protrusions are assigned to small clusters of Ag atoms. An alternative explanation could be that these protrusions are small clusters of carbon, which has segregated from the bulk of the Ag crystal to the surface during annealing. Such segregation of carbon to the surfaces is a well-known phenomenon and has been reported for example for nickel surfaces [276, 277]. However, it is unlikely that the observed protrusions consist of carbon atoms because carbon would be expected to form 2D ordered layers (graphene) instead of clusters because the most stable form of carbon is graphite. The STM image (Fig. B.1a) also shows that the monoatomic step edges of the surface exhibit many concave curves. This is a consequence of the cluster formation because the clusters are not mobile and pin the step edges to a distinct location.

In contrast, after annealing at 700 K, the step edges are very straight and the amount of Ag clusters is significantly lower (Fig. B.1b). This effect is explained by the reduced mobility of the atoms at the lower temperature, which inhibits the formation of the thermodynamically more stable

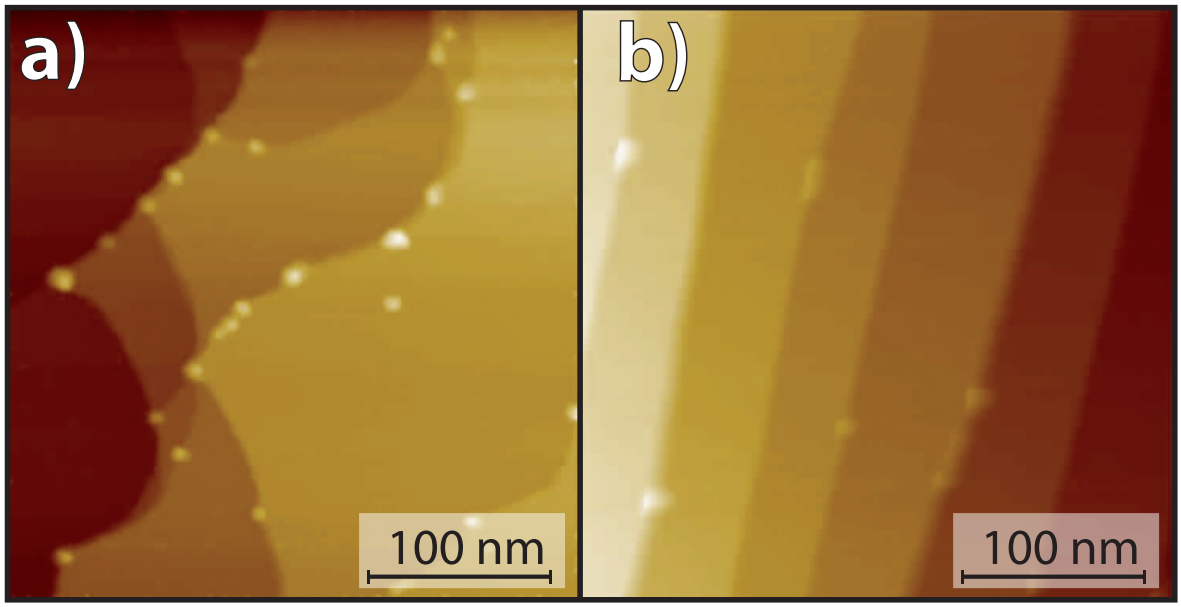

Figure B.1: *STM images ($U_B = -1.5\,V$, $I_{tun} = 25\,pA$) of the clean Ag(100) surface.* ***a)*** *The Ag(100) surface after annealing at 850 K. It can be seen that there are many small round protrusions, which are assigned to small clusters of Ag. The step edges are very curvy and often pinned at such clusters.* ***b)*** *The surface after annealing at 700 K. The step edges are mostly straight and a significantly smaller amount of Ag clusters is observed.*

Ag clusters. Of course, the extent to which this phenomenon occurred did vary strongly with the location on the sample. Furthermore, the two images were handpicked in order to illustrate the impact of the temperature during annealing. Nevertheless, the consideration of many STM images that were recorded over periods of several months does indeed confirm the observation: On average, the amount of Ag clusters and curvy step edges was significantly lower after using an annealing temperature of only 700 K than it was for one of 850 K. This means that the annealing temperature of 700 K is better suited than the one of 850 K for STM measurements on the Ag(100) surface.

B.2 Calibration of the QMS integrals

In many cases, the correct determination of the coverage of an organic adsorbate is not an easy feat. One way to determine the coverage of an organic or inorganic layer on a surface is by using the relative QMS integrals from the deposition. However, this method works only under the assumption that the sticking factor does not depend on the coverage and it requires a reference integral of a known corresponding coverage. This section will illustrate two methods to obtain such a reference integral for the case of QA on Ag(100) and Cu(111).

One very straightforward way to determine the coverage is by evaluating large-scale STM images with less than 1 ML of QA by pixel counting. This works under the assumption that all observed molecules are adsorbed on the surface in a flat-lying configuration. An example of this is illustrated in Figure B.2. Panel a) shows a normal STM image of QA on Cu(111). In panel b) an

intensity threshold was chosen in such a way that all pixels corresponding to QA chains are assigned a gray value of 0 (white) and the remaining pixels are assigned a gray value of 255 (black). The pixels were counted with the image processing software ImageJ [278]. With the amount of black and white pixels N_{255}^{pix} and N_{0}^{pix}, the coverage θ_{QA} can be calculated (the result is given as decimal portion of 1):

$$\theta_{\mathrm{QA}} = \frac{N_{0}^{\mathrm{pix}}}{N_{255}^{\mathrm{pix}} + N_{0}^{\mathrm{pix}}}. \tag{B.1}$$

The determination of the coverage of an organic layer with SPA-LEED is usually not trivial, but in this case, a special quality of the α-phase of QA on metal surfaces can be utilized. A typical SPA-LEED image with a corresponding line profile of the QA α-phase on Ag(100) are displayed

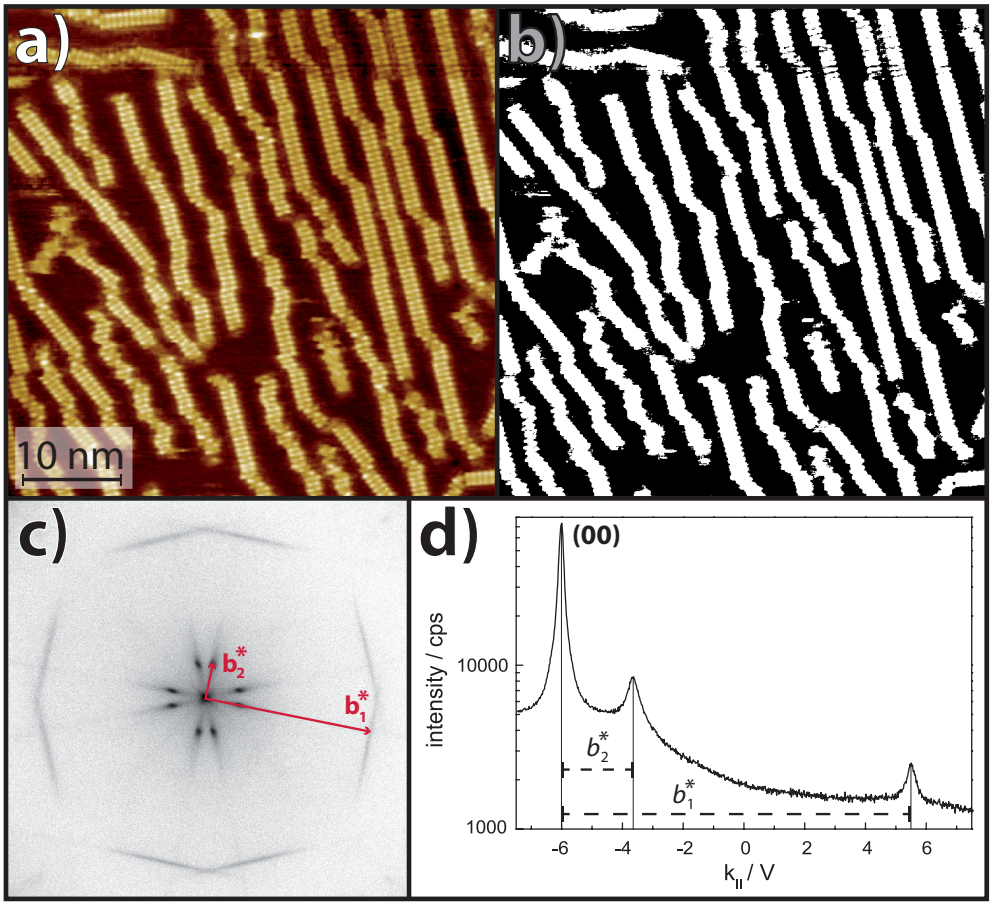

Figure B.2: *Exemplary illustration of how the QA coverage was determined with STM and SPA-LEED.* ***a)*** *STM image ($U_{\mathrm{B}} = -1.5\,\mathrm{V}$, $I_{\mathrm{tun}} = 35\,\mathrm{pA}$) of QA chains on the Cu(111) surface.* ***b)*** *The same image as in panel a), but all pixels above a certain intensity threshold were attributed to QA chains and colored white, and the remaining pixels were attributed to the bare substrate and colored black. The coverage can be calculated by counting the white pixels.* ***c)*** *SPA-LEED image ($T = 110\,\mathrm{K}, E = 53.1\,\mathrm{eV}$) of the area around the specular spot of QA on Ag(100) in the α-phase.* ***d)*** *A line profile along the vector $\mathbf{b_1^*}$. The ratio between the reciprocal lengths b_1^*, b_2^* of the vectors $\mathbf{b_1^*}$, $\mathbf{b_2^*}$ can be used to calculate the coverage θ_{QA}. For more information, see text.*

in panels c) and d) of Figure B.2, respectively. As discussed in Chapter 5.1.1, the average distance between neighboring chains b_2 increases with decreasing coverage while the intermolecular distance b_1 within the chains is defined by the strong H-bonds and therefore constant for all coverages. In a simple model, which assumes that the chains are equally spaced, a $b_2 \sim \theta_{QA}^{-1}$ correlation is expected. With this correlation and the known distance $b_2^{\theta_{QA}=1}$ for a full ML, it is straightforward to calculate an unknown coverage if the distance between neighboring chains is known from SPA-LEED investigations:

$$\theta_{QA} = \frac{b_2^{\theta_{QA}=1}}{b_2}. \tag{B.2}$$

It is not known per se how accurate the assumed correlation between θ_{QA} and b_2 is. All STM images at coverages below 1 ML show an equal spacing between neighboring chains. But it cannot be excluded that there may be small jumps in b_2 at distinct coverages. However, overall this method to determine QA coverages from SPA-LEED images yields accurate results with an estimated error of $\Delta\theta_{QA} = 0.1$. With high enough statistics, the results from the STM images are estimated to be slightly more accurate with an error of $\Delta\theta_{QA} = 0.05$. The SPA-LEED method to determine the coverage can be used for coverages between about 0.5 and 1.0 ML. For smaller coverages, the intensity of the spots in the diffraction pattern is too small and smeared out. The STM method can be used to determine coverages between 0.0 and 1.0 ML. However, for very low coverages (< 0.2 ML) it is especially important to acquire high statistics because local variations of the coverage may cause a significant error.

B.3 Current chopper for SPA-LEED measurements

In order to investigate the phase transition between the α- and the β-phase of QA on Ag(100), SPA-LEED experiments at elevated temperatures were conducted. A potential problem that may arise during such experiments is that the current flowing through the filament, which is located directly behind the sample, induces a magnetic field. Thus, the electrons that are scattered at the sample experience an additional unquantifiable deflection caused by the magnetic field. According to a review by Horn-von-Hoegen, the presence of magnetic or electrostatic alternating current (AC) stray field is very disruptive to SPA-LEED measurements because it would cause to electron beam to oscillate with the given frequency. However, constant magnetic or electrostatic fields are not problematic because they usually only lead to a small shift of the spots without a change of the spot profile [75]. Nevertheless, within the scope of the present thesis a so-called current chopper was designed and constructed in cooperation with R. Paulig in order to minimize all potential influence of the magnetic field. This was particularly important for temperature-dependent measurements of line profiles (cf. Chapter 5.4) where a temperature-dependent movement of the superstructure spots is very disruptive.

The basic principle of this current chopper is to make use of pulse heating and gated detection. That means that the heating of the sample is achieved by heating pulses (heating periods) that are followed without delay by voltage and current-free pauses (measurement periods), during which

electrons can be collected without the influence of a magnetic field. This concept was first put into practice on Si(111) by Kury *et al.* in 2004 [279]. There, the Si sample was heated with direct current sample heating, which causes very strong magnetic fields around the sample that in addition can be very inhomogeneous. Hence, in that case, the observed influence of the magnetic field on the LEED pattern is particularly strong.

The program WinSPA [223] can be run in a mode in which it generates and outputs a transistor-transistor logic (TTL) signal of a periodic rectangular step function alternating between 0 V and 5 V. This signal defines the heating and measurement periods. The frequency of the periodic step function can be chosen between roughly 100 – 1000 Hz and the ratio between the heating and measurement periods can be adjusted between 0.2 – 0.8. Usually, a frequency of 100 Hz with a measurement ratio of 0.5 was used, i.e., the heating and measurement periods were both 5 milliseconds. This TTL signal is fed into the current chopper, which is located between the power supply and the heating filament in the electric circuit. The chopper has a field-effect transistor (FET) switch that periodically opens (at 5 V) and closes (at 0 V) the circuit according to the received TTL signal.

The influence of the magnetic field on the SPA-LEED images was systematically tested by recording 2D images and line profiles through the specular spot at different temperatures of up to 500 K. The positions, profile shapes, and FWHMs of the spots were compared between images recorded without gated detection and those that were recorded with gated detection. Overall, it was found that the influence of the magnetic field on the SPA-LEED images was negligible. No changes in the profile shape or the FWHM of the specular spot were found. Only a small displacement of the spots ($\leq$ 0.1 V) could be observed. These observations are in line with the statements in the review by Horn-von-Hoegen that constant magnetic fields are not problematic for SPA-LEED measurements [75].

B.4 Construction of an Ag evaporator

In order to investigate the influence of Ag atoms on the observed QA structures on Ag(100), experiments were conducted in which Ag atoms were deposited into the observed QA structures (cf. Chapter 5.1.3). For these experiments, a Ag evaporator was constructed. The Ag evaporator was designed by M. Specht and assembled and tested by T. Bald within the scope of his bachelor's thesis [235]. A schematic drawing of the evaporator is given in Figure B.3.

The evaporator is divided into three parts: a CF63 flange on which the entire structure is mounted, a support structure consisting of three rods made of stainless steel that carries the oven, and the oven itself, which is electrically isolated from the rest of the evaporator. The oven consists of a crucible that is made of a titanium-zirconium-molybdenum (TZM) alloy allowing it to endure temperatures of up to 2600°C [280], is 22 mm in length, and has an opening with a diameter of 4 mm. For the temperature measurement, a type K thermocouple is screwed to the outer wall of the crucible. The front compartment of the crucible contains a small Ag sample from the laboratory supply with a weight of about 4 g and the back compartment with a diameter of 7.5 mm gives

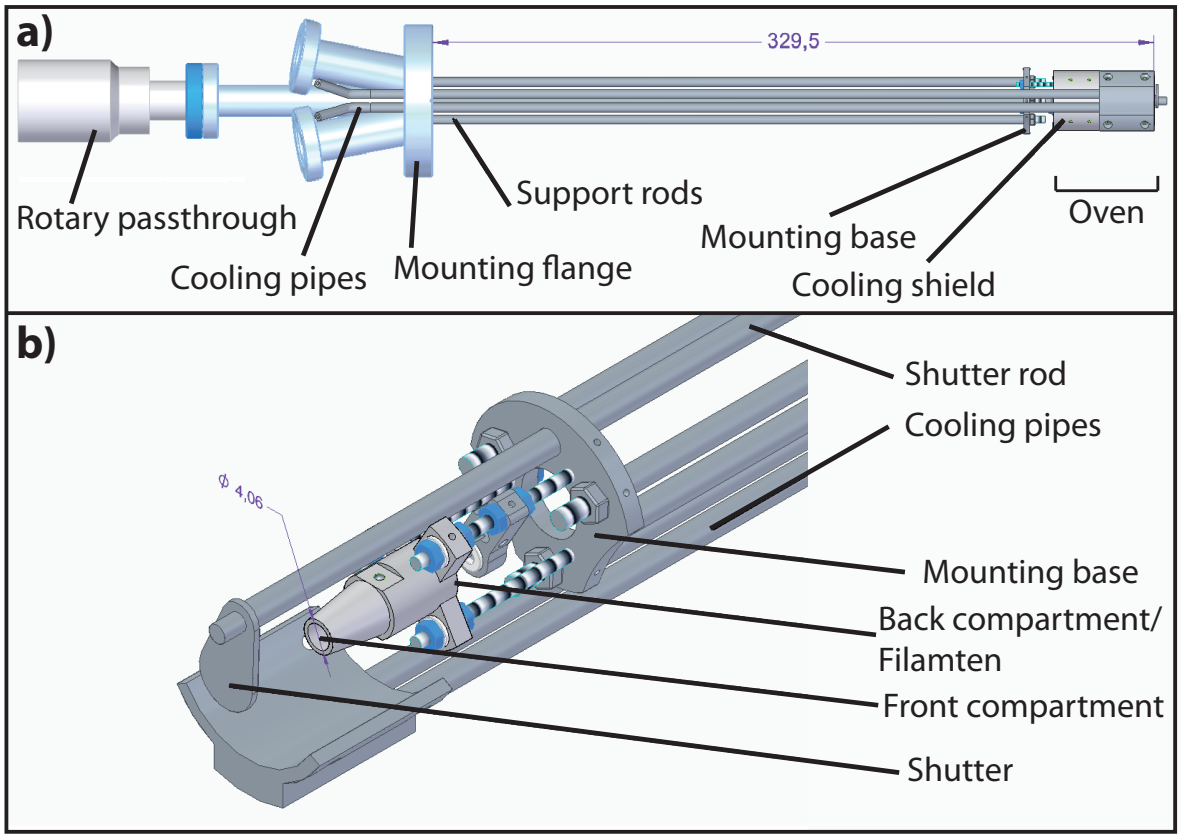

Figure B.3: *Technical drawing of the Ag evaporator.* ***a)*** *Top view of the whole evaporator. On the right-hand side is the oven (see panel b) and its cooling shield. It is mounted on a DN63 mounting flange via 3 metal rods.* ***b)*** *Side view onto the front of the evaporator. It shows the crucible that is mounted on the mounting base. The front compartment of the crucible contains the Ag and the shutter in front of it can be used to interrupt the atom beam.A 100 W filament in the back compartment is used to heat the entire crucible. The rods that are colored with a striation are threaded. Both drawings were taken from ref. [235]*

.

room for a 100 W filament that is able to heat the crucible to up to 1200 K. In order to prevent the rest of the evaporator and its surroundings from heating up too much, the oven is also equipped with a cooling shield that is cooled by a constant flow of water. Furthermore, the shield prevents the evaporation of Ag in unwanted directions. It has a hole with a diameter of 4 mm at the front that acts like a pinhole and restricts the evaporated Ag atoms into a beam that is directed at the sample.

The three rods of the support structure are welded to the CF63 flange on its vacuum side. The two pipes of the water line for the cooling shield are fed through the flange and welded vacuum-tight. Additionally, three CF16 flanges are welded to the CF63 flange. Those are used for a rotary feed-through for opening and closing the shutter, an electric feed-through for the filament and the temperature measurements, and a vacuum mount for pumping. The whole evaporator is 330 mm in length, which also defines how far it protrudes into the vacuum chamber. A more in-depth description of the evaporator, the thermal properties, and information regarding the deposition

rate and deposition distribution is not given in the present thesis but can be found in the bachelor's thesis by T. Bald [235].

B.5 Construction of a transfer fork for the wobble stick

Within the scope of the present thesis, a transfer fork for a new wobble stick (ZWS150 from VACGEN, 150 mm linear travel, and 15° angular movement) was developed and constructed because the bellow of the old wobble stick broke and became leaky. Technical drawings of the wobble stick and the transfer fork are shown in Figure B.4. All parts of the transfer fork (described below) are made of aluminum. The metal aluminum was used because it is softer and more flexible than for example stainless steel. The flexibility allows the user to adjust the fork a little bit after construction so that it has a firm grip on the sample holder. Furthermore, the fact that aluminum is softer than stainless steel prevents the fork from damaging experimental parts in the chamber that are made out of stainless steel, for example, the STM table.

The transfer fork consists of three parts. The first part is a cylinder that fits over the end of the wobble stick and is screwed to it via 4 M2 screws. It has a small hole that prevents air from getting trapped in there, which might cause a micro leak. The second part is a small metal rod with a diameter of 5 mm that is jammed into a hole of the same size on the opposite side of the cylinder. The other side of the rod has a 2.02 mm wide and 15 mm deep slot. The last part is the actual fork, which fits into the slot of the metal rod and is screwed to it with 2 M2 screws. The fork is 2 mm thick and has two arms that are separated from each other by a circular cutout with a radius of 9.5 mm. At the front of the fork, there is a half-circular cutout with a radius of 11.35 mm that is used to grab the same holder in the UHV chamber. The two cutouts are connected by a 2 mm wide gap in order to make the two arms more flexible. This gives some leeway for bending the two arms so that the grip between the fork and the sample holder can be adjusted to personal preference. When bending the two arms outside of the vacuum chamber, it is important to keep in mind that the grip between the fork and the sample holder will be tighter in the vacuum because the air acts as a lubricant and reduces the friction between the two parts.

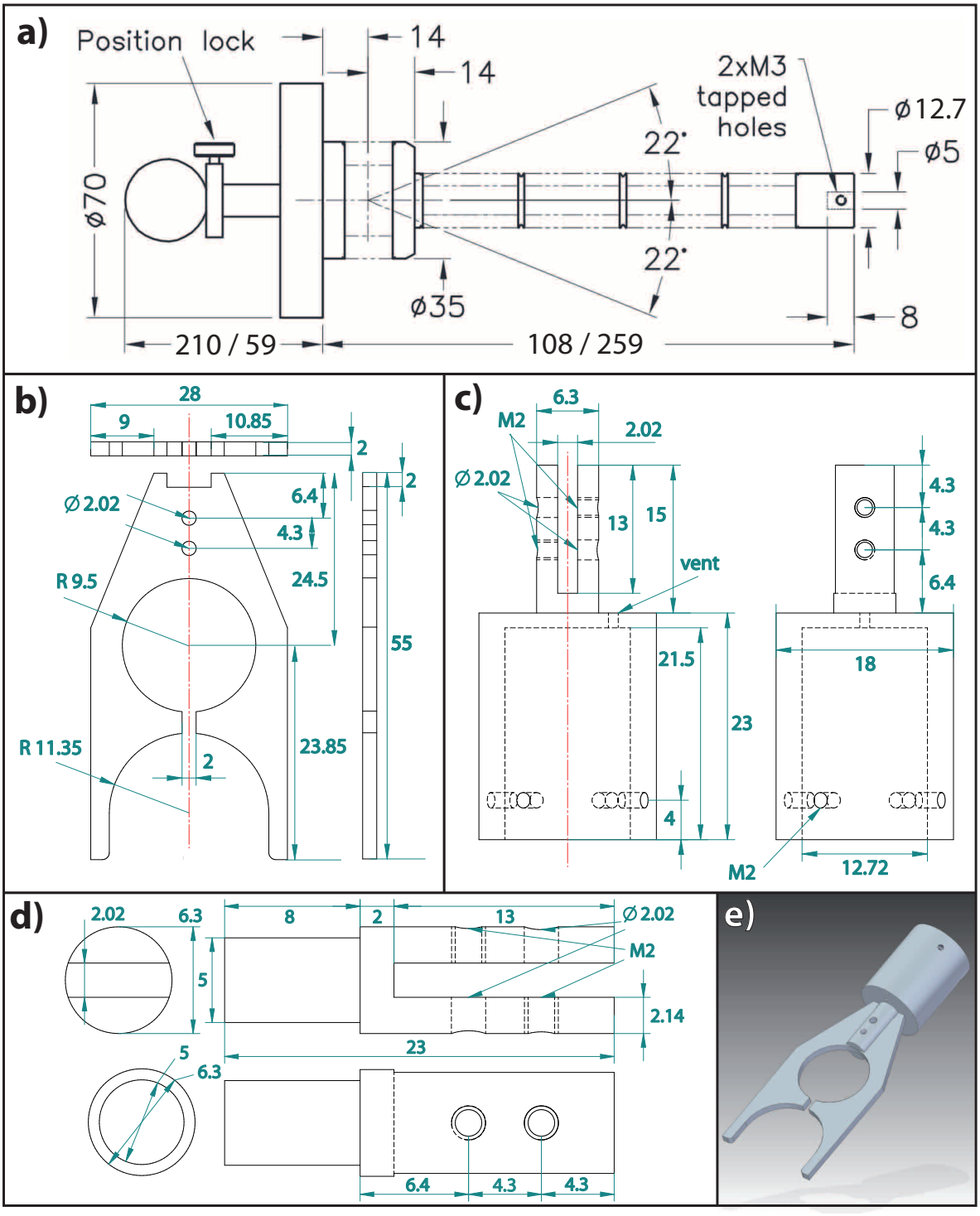

Figure B.4: *Construction of a transfer fork for a new wobble stick.* ***a)*** *Technical drawing of the ordered wobble stick.* ***b)*** *Technical Drawing of the transfer fork.* ***c)*** *Technical Drawing of the cylinder and the small rod that are used to attach the transfer fork to the wobble stick.* ***d)*** *Technical drawing of only the small rod.* ***e)*** *Image of all three parts put together.*

C Additional quinacridone phases

C.1 Additional phases on Ag(100)

In this section, two phases of QA on Ag(100) in addition to those described in Chapter 5 will be presented in Sections C.1.1 and C.1.3, respectively. In addition, an interesting anisotropic phase, which is similar to the α-phase, will be discussed in Section C.1.2.

The first additional phase of QA will be named the γ-phase. It was only observed in coexistence with the β-phase after annealing the α-phase at 500 K for 15 minutes. Furthermore, it was only observed on one specific Ag(100) crystal in the SPA-LEED chamber and could not be prepared on the other Ag(100) crystals. Nevertheless, the phase will be discussed here because it shows some interesting kinetic and thermodynamic properties and may be very similar to a phase that R. Priya observed on Ag(110) [81].

The second additional QA phase was observed only once after annealing a QA layer from the previous day at 550 K for 15 minutes. Although this phase was only observed once and was not reproduced again, it will be discussed here because it corresponds to a double layer of two different phases, which may yield some interesting insight regarding the interfacial interactions between QA and the Ag substrate.

C.1.1 The γ-phase

As mentioned above, the γ-phase was only observed in coexistence with the β-phase after annealing the α-phase at 500 K for 15 minutes. Interestingly, this phase was only observed on one Ag(100) crystal that was used in the SPA-LEED chamber within the scope of the bachelor's thesis of T. Bald [235] and the focusing laboratory course of J. Roth [237]. During SPA-LEED experiments that were conducted previously on a different Ag(100) crystal [281, 282] and all STM experiments that were conducted within the scope of the present thesis on Ag(100), this phase was never observed. In the following, the structure of the γ-phase, its thermodynamic and kinetic properties, and potential reasons for the fact that it was only present on one crystal will be discussed.

A SPA-LEED image of a mixture of the β- and γ-phase is displayed in Figure C.1. It consists of many sharp and intense spots. Roughly half of the spots belong to the already known β-phase (cf. Chapter 5.1.1), the other half belongs to the new γ-phase. The upper left and right quadrants are superimposed with simulations of the pure β- and γ-phase, respectively. The bottom right quadrant is superimposed with the simulations of both phases. The combined simulation of both phases accounts for all observed spots and no systematic elimination of spots can be observed. The analysis of the diffraction pattern yields that the γ-phase is also commensurate making it

likely that the γ-phase is a structure in the first layer. It exhibits a quadratic unit cell with the parameters $b_1 = b_2 = 21.93\,\text{Å}$, and $\alpha = 90°$ and the corresponding superstructure matrix is:

$$\mathbf{M}_\gamma = \begin{pmatrix} 3 & 7 \\ -7 & 3 \end{pmatrix}.$$

The vectors $\mathbf{b_1}$ and $\mathbf{b_2}$ are rotated by 23° with respect to the Ag⟨10⟩ direction. Interestingly, R. Priya found a unit cell with very similar dimensions (the lengths of the unit cell deviate by about 3%), which is also commensurate, for QA on Ag(110) after annealing [81]. This indicates that the molecular arrangement within these two structures may be identical, or at least very similar.

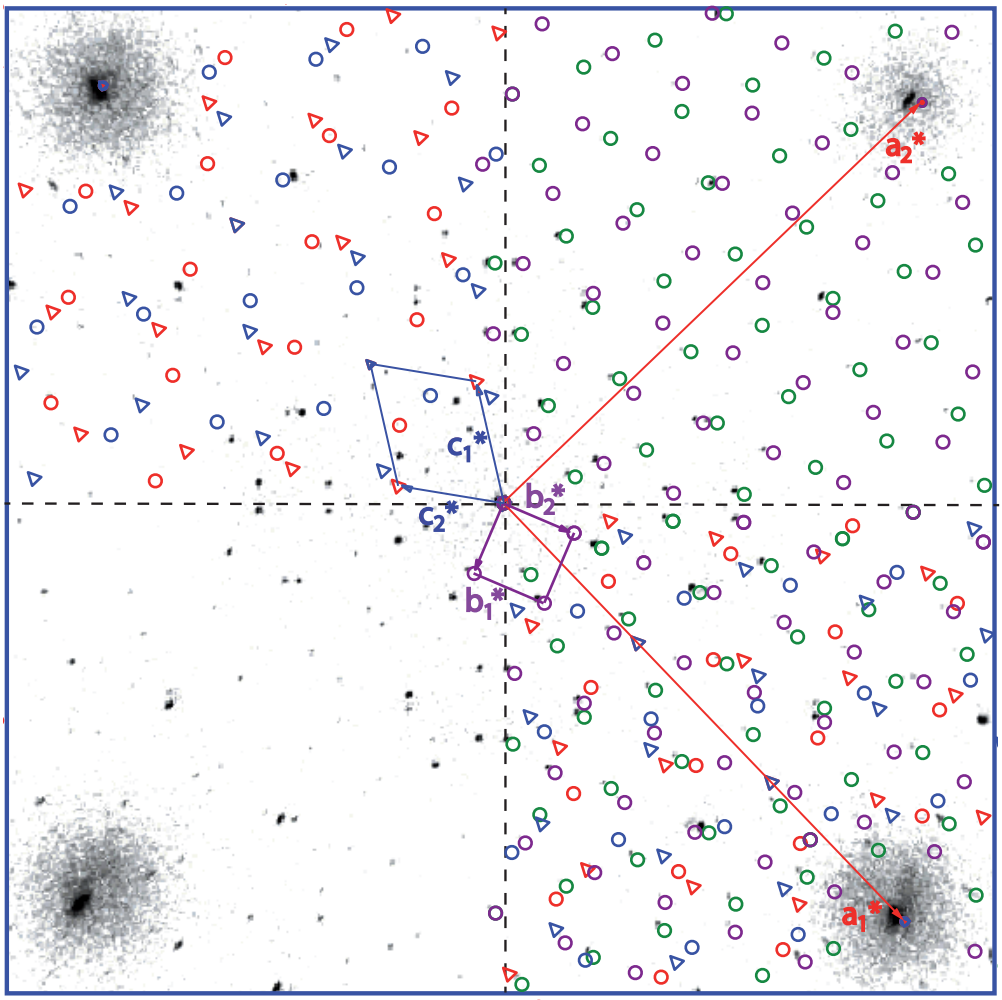

Figure C.1: *Distortion corrected SPA-LEED image ($T = 110\,\text{K}, E = 53.1\,\text{eV}$) of of a mixture of the β- and γ-phase on Ag(100). The upper left and right quadrants of the image are superimposed with simulated spots of the β- and γ-phase, respectively. The bottom right quadrant is superimposed with the simulated spots of both phases and the bottom left quadrant shows the diffraction pattern without a simulation. The simulated spots of the β-phase are red and blue, while the ones of the γ-phase are violet and green. This figure was taken from ref. [237] and slightly modified. The distortion was corrected with the help of a python routine by J. Roth [237].*

Unfortunately, the arrangement of the QA molecules in the unit cell can only be guessed, since no STM (or other methods that yield this information) experiments were conducted on the γ-phase. Two possible structure models are illustrated in Figure C.2. The structure in panel a) is based on a structure that was suggested by R. Priya for the annealed phase of QA on Ag(110). It is very similar to the homochiral chains in the α-phase, but it contains periodic offsets caused by molecules of the opposite handedness (RRLRR or LLRLL). Because of the periodic offsets, in this kind of chain only $\frac{4}{3}$ H-bonds per molecule are formed (the α-phase on Ag(100) has 2 H-bonds per molecule). The unit cell contains three molecules and roughly 30% of the substrate is not covered by molecules resulting in a molecule density of $0.0062\,\text{Å}^{-2}$. This is only 70% of the molecular density in the β-phase ($0.0089\,\text{Å}^{-2}$).

An alternative structure model for the γ-phase on Ag(100) with 4 molecules per unit cell is displayed in panel b) of Figure C.2. Here, every molecule forms 1.25 H-bonds on average and the molecule density is $0.0083\,\text{Å}^{-2}$, which is almost identical to that of the β-phase ($0.0089\,\text{Å}^{-2}$). Interestingly, the structure of this model consists of the same kind of chains as the β′-phase that was observed after annealing QA on the Cu(111) surface (LLRLRR or RRLRLL, cf. Figure 5.6), but here neighboring chains are shifted by one molecule with respect to one another in the direction of the chains. That means that in contrast to the β′-phase, here the dimers of neighboring chains are not directly adjacent anymore. This leads to one small S-shaped hole in the molecular structure per unit cell. The same kind of hole occurs in the β′-phase as defects [224]. The structure model (Fig. C.2b) has molecules of different chiralities on the corners, which means that, strictly speaking, it is not the true unit cell of the proposed structure. However, similar to the β-phase (cf. Chapter 5.1.1, page 39) on Ag(100), it can be assumed that the structure factors of the two QA enantiomers are very similar, and hence they cannot be distinguished by SPA-LEED.

Considering the fact that the γ-phase exists after annealing in coexistence with the β-phase but never as a pure phase, the model in panel b) seems more plausible. The structure in panel a) is basically the α-phase with an offset every three molecules due to molecules of the opposite handedness and with a different azimuthal orientation. This implies that the chains in this phase are less favorable than the ones of the α-phase in terms of the number of H-bonds and the azimuthal orientation. It is unlikely that the commensurate nature of the proposed phase (i.e., every third molecule exhibits the same adsorption site) can overcompensate for this energy loss. And since the α-phase is not the thermodynamically most stable structure, a phase that is energetically less favorable than it is unlikely to exist after annealing at 500 K. Furthermore, it was observed that at lower coverages the spots of the β-phase are more pronounced than the ones of the γ-phase and the spots of the γ-phase become more pronounced for coverages slightly below 1 ML [235, 237], which supports the model with the higher molecule density. Moreover, the structure in panel b) shares some similarities with the β-phase regarding their molecular arrangements.

The kinetic properties of the transition between the β- and γ-phase of QA were investigated by J. Roth within the scope of his focusing laboratory course [237]. When left at RT, over time the intensity of the γ-spots decreases and that of the β-spots increases until they reach the maximum

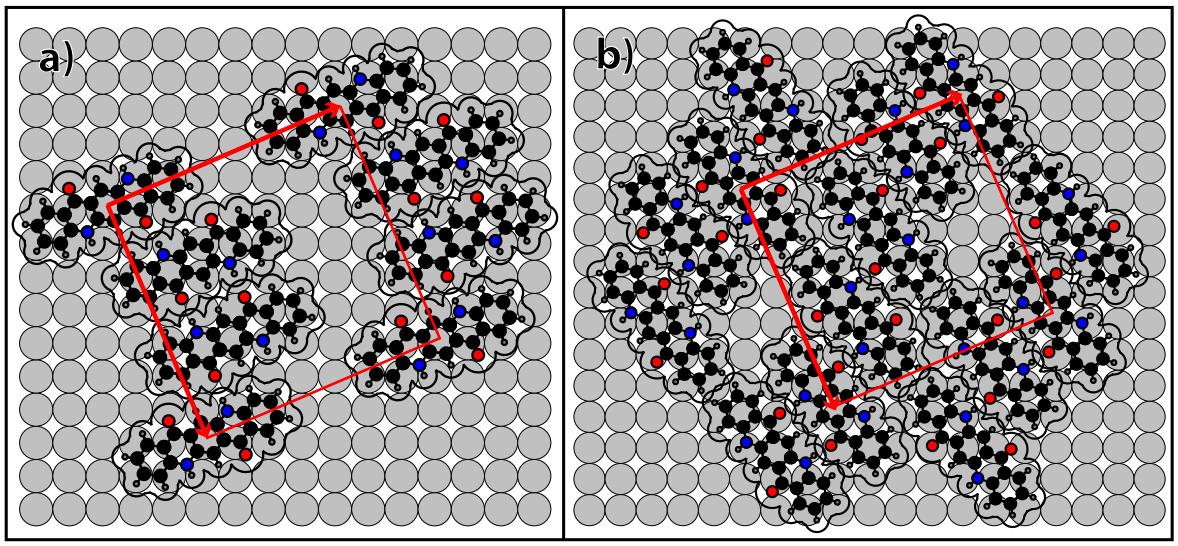

Figure C.2: *Two suggestion for structure models for the γ-phase on Ag(100).* ***a)*** *A model with three molecules per unit cell. Each molecule forms $\frac{4}{3}$ H-bonds on average and the molecule density is 0.0062 Å^{-2}. Te structure consists of homochiral dimers that are connected by a single QA molecule of the opposite handedness.* ***b)*** *A structure model with four molecules per unit cell. Each molecule forms 1.25 H-bonds on average and the molecule density is 0.0083 Å^{-2}. The structure consists of the same kind of chains as the β′-phase on Cu(111), but neighboring chains are offset by one molecule with regard to one another. The unit cell does not consider the different chiralities of the QA molecules. For more information, see text.*

intensity after about 20 hours. This shows that the γ-phase is not stable at RT and slowly transforms back into the β-phase. The intensity of the β-spots increases twice as fast as the intensity of the γ-spots decreases. Since a transition via an unordered phase would have the opposite effect, this indicates a direct 1:1 conversion between the two phases. Interestingly, this phase transition is reversible. After annealing at 475 K, the intensity of the γ-spots has increased again and the one of the β-spots has decreased. This shows that the γ-phase is the preferred structure at elevated temperatures, while the β-phase is preferred at RT. A possible explanation is that the β-phase is thermodynamically slightly more stable than the γ-phase, but the γ-phase is preferred at higher temperatures due to entropic differences between the two phases.

Lastly, it is interesting to ask the question of why it was only possible to prepare the γ-phase in the one specific experimental setup. Three ideas were considered and will be briefly discussed in the following.

(i) The γ-phase is a mixed phase of PTCDA and QA, which is caused by an unintended co-deposition of PTCDA during the evaporation of QA due to the close proximity of the two evaporators. However, the temperature in the PTCDA evaporator remained well below its sublimation temperature during the evaporation of QA. Furthermore, the deliberate deposition of PTCDA into the mixed β- and γ-phase did not lead to an increase in the intensity of the γ-spots. Hence, this possibility is dismissed.

(ii) The γ-phase is a mixed phase of indigo and QA due to thermal decomposition of QA into indigo during the evaporation, which was found by Scherwitzl *et al.* [79, 80]. This was checked by monitoring the masses of the molecule beam with the QMS during deposition and the masses only corresponding to indigo could not be observed. Hence, this possibility can also be excluded. The possible decomposition of QA is discussed in more detail in Appendix D.

(iii) The γ-phase is caused by systematic defects of the used Ag(100) crystal. This may for example be in the form of facets with a different geometry that are caused for example by a miscut or a macroscopic damage. In different experiments, an anisotropic α-phase of QA was observed on the same crystal (cf. Section C.1.2), which further supports the assessment that the crystal surface exhibits some sort of unusual geometry, e.g., an unusually high step density.

C.1.2 Anisotropic α-phase on Ag(100)

Similar to the observation of the γ-phase (cf. Section C.1.1), there is a second phenomenon that was only observed on the same crystal. Within the scope of the bachelor's thesis of T. Bald [235] an anisotropy in the α-phase of QA on Ag(100) was found. A corresponding SPA-LEED image is displayed in panel a) of Figure C.3. The positions of the spots are identical to those of the normal α-phase (see Fig. 5.1), which means that the phase consists of the same chains with the same four distinct azimuthal orientation. The difference is that two sets of spots are significantly more intense than the other two sets of spots. That means that two azimuthal orientations of the chains are preferred over the other two. This is very counterintuitive because all four azimuthal orientations are symmetry equivalent on an ideal Ag(100) surface. Thus, it was concluded that the crystal that was used for these experiments exhibited some kind of macroscopic damage, which led to an anisotropy of the Ag(100) surface causing the observed and very unusual behavior of the QA molecules.

Furthermore, annealing this structure at 425 K for 10 minutes leads to an even more interesting effect, which can be seen in the corresponding SPA-LEED image in panel b) of Figure C.3. The other two sets of spots are now more intense and the angle between the specular spot and two superstructure spots has increased by 15° (indicated in red). That means that now the other two azimuthal directions of the chains are preferred and additionally all azimuthal chain orientations have changed by 7.5°. A satisfactory explanation for this behavior could not be found. In his thesis, T. Bald explained this with a complex interplay of several factors. He proposed a miscut of the sample that lead to a high density of steps in [11] direction, at which the chain growth of two distinct orientations is preferred at RT due to the strong interactions between the step edges and the QA molecules. After annealing, azimuthal orientations that are more parallel to the step edges are preferred because this enables the formation of longer chains and thus more H-bonds. Hence, step edge nucleation was considered to be less relevant at high temperature. A more in-depth explanation of this theory can be found in his thesis [235].

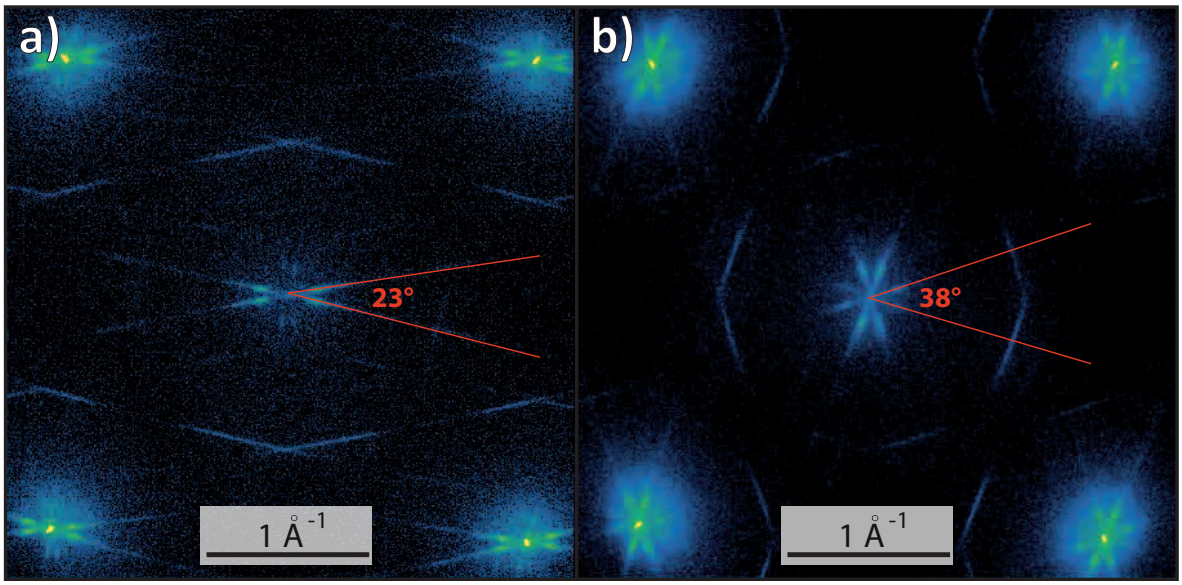

Figure C.3: *Two SPA-LEED ($T = 110\,\mathrm{K}, E = 53.1\,\mathrm{eV}$) images showing the anisotropy of the α-phase on Ag(100). It is important to note that this anisotropy only occurred on one specific Ag(100) crystal and does not reflect the diffraction pattern of the normal α-phase.* ***a)*** *Diffraction pattern after preparation at a sample temperature of 350 K.* ***b)*** *Diffraction pattern after annealing at 425 K for 10 minutes. The figure was copied from ref. [235] and slightly modified.*

However, under consideration of the results for QA on the vicinal Ag(35 1 1) surface (cf. Chapter 7.1), this explanation does not seem plausible. There, it was found that at RT the QA chains nucleate on the Ag terraces at RT, and all four azimuthal orientations grow with equal probability. At elevated sample temperatures (> 400 K), the nucleation preferably occurs at the step edges, which leads to a preferential growth of distinct orientations. Hence, it is more likely that the favored orientations of the QA chains that T. Bald observed after annealing at 425 K are caused by the interactions between the QA molecules and the Ag steps. However, the reasons for the preferential growth of the two other azimuthal orientations at RT are unclear.

C.1.3 A double-layer phase on Ag(100)

In this section, a SPA-LEED image of a QA phase on Ag(100), which turned out to be an annealed double layer during the analysis, will be presented and discussed. This phase was only observed once and was not reproduced. Nevertheless, this phase is interesting because the proposed molecular arrangement of this phase (discussed below) differs from those of the other QA structures that were discussed in the present work, which yields additional insights into the intermolecular interactions. The circumstances under which this phase was observed are very specific. A QA layer that was supposed to be a full ML of the β-phase (the actual coverage is discussed below) was heated in steps of 10 K up to a temperature of 500 K in order to record line profiles across the β-spots at every temperature step (cf. Chapter 5.4). On the next morning, the SPA-LEED image only contained diffuse intensity. Hence, in an attempt to induce a phase transition back into the β-phase, the sample was annealed at 550 K for 15 minutes. The resulting diffraction pattern is illustrated in Figure C.4 and will be discussed in the following.

The diffraction pattern in Figure C.4 is very complex and consists of sharp spots, smeared-out spots, and very long smeared-out lines. The analysis turned out to be rather difficult and no single unit cell was found that can explain the pattern. Thus, the observed diffraction pattern is explained as a consequence of a QA double layer in which the first and the second layer exhibit different structures. The two unit cells are given by the vectors $\mathbf{b_1^*}$, $\mathbf{b_2^*}$ (first layer, blue) and $\mathbf{c_1^*}$, $\mathbf{c_2^*}$ (second layer, red). Both unit cells do not correspond to a structure that is already known, such as the α- or β-phase. The left-hand side of the SPA-LEED image is superimposed with the spots of the corresponding simulations. The upper quadrant only contains simulated spots of the second layer, whereas the lower quadrant contains simulated spots corresponding to both layers.

First, the structure of the second layer will be discussed because the corresponding spots are more intense than the ones of the first layer. It can be seen that the majority of the observed spots and the lines of the diffraction pattern are accounted for by the simulated red spots (second layer). The red unit cell corresponds to a real space unit cell with the vectors $\mathbf{c_1}$, $\mathbf{c_2}$ with lengths of $c_1 = (6.4 \pm 0.4)$ Å and $c_2 = (17.4 \pm 0.4)$ Å, and $\alpha = (96 \pm 2)^\circ$. This unit cell and a suggested corresponding arrangement of the QA molecules are illustrated on the left-hand side of the inset in the top right of Figure C.4. The corresponding superstructure matrix is:

$$\mathbf{M}^{\mathbf{Ag(100)}}_{\mathbf{c_1},\mathbf{c_2}} = \begin{pmatrix} 1.0 \pm 0.1 & 2.0 \pm 0.1 \\ 5.6 \pm 0.1 & -2.1 \pm 0.1 \end{pmatrix}.$$

The unit cell and the corresponding structure model in the inset of Figure C.4 show that the structure of the second QA layer consists of molecular chains similar to those in the α-phase. This is in good agreement with the results for the structures of QA in the second layer on Ag(100) and Cu(111), which were presented in Chapter 5.3. As was explained there, the structures of QA in the second molecular layer always consist of 1D molecular chains, even after annealing at 500 K. The reason for that is that the formation of the β-phase is only favored on metal substrates where the loss of H-bonds can be overcompensated by stronger interactions between the molecules and the metal substrate. In the second layer, this is not the case, which is why the formation of molecular chains with two H-bonds per molecule is preferred there.

Now the structure of the first QA layer will be discussed. The simulated blue spots that correspond to the blue unit cell, which is given by the vectors $\mathbf{b_1^*}$, $\mathbf{b_2^*}$, account for some of the remaining spots. The observed spots that are not described by one of the unit cells can be explained by multiple scattering; an example is illustrated by the green arrows. The blue unit cell corresponds to a real space unit cell with the vectors $\mathbf{b_1}$, $\mathbf{b_2}$ with lengths of $b_1 = (9.9 \pm 0.4)$ Å and $b_2 = (10.6 \pm 0.4$ Å), and $\alpha = 99 \pm 2^\circ$. The corresponding superstructure matrix is

$$\mathbf{M}^{\mathbf{Ag(100)}}_{\mathbf{b_1},\mathbf{b_2}} = \begin{pmatrix} 3.0 \pm 0.1 & -1.7 \pm 0.1 \\ 1.2 \pm 0.1 & 3.5 \pm 0.1 \end{pmatrix}.$$

A structure model of the first QA layer is illustrated on the right-hand side in the inset of Figure C.4. The QA molecules are arranged in chains with an offset for each molecule. That means

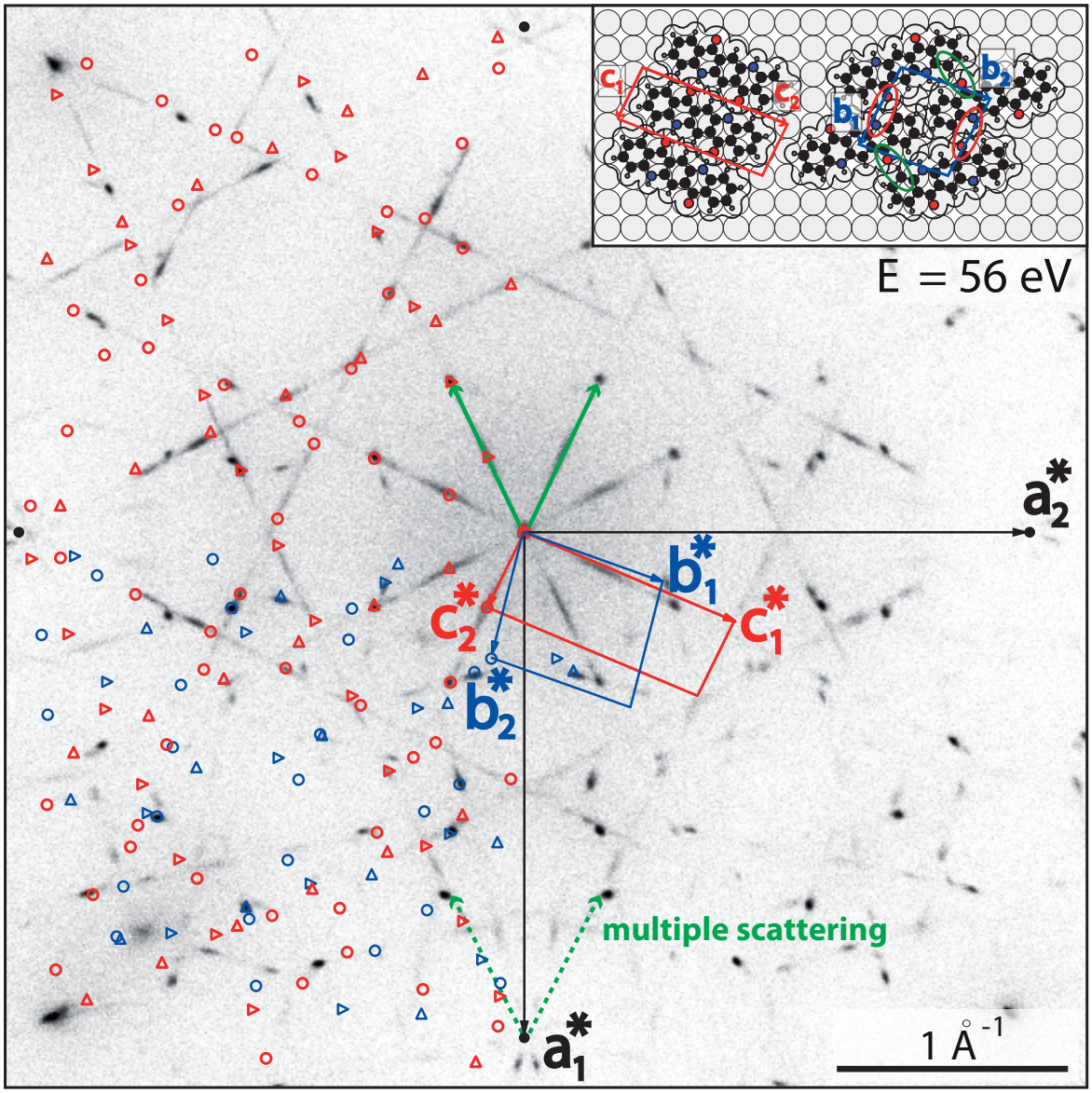

Figure C.4: *An unknown phase of QA on Ag(100) that was only observed once and was not reproduced. It was observed after the β-phase was annealed stepwise to 500 K in order to investigate the behavior of the β-phase at increased temperature (cf. Chapter 5.4). After about 14 hours, the SPA-LEED pattern consisted only of diffuse intensity and the SPA-LEED pattern which is shown here appeared after annealing the sample again at 550 K for 15 minutes. The image was not deskewed. The diffraction pattern is a combination of sharp spots and smeared-out lines and is explained by a combination of two unit cells in the first and the second layer, which are illustrated in red(second layer) and blue (first layer). The left-hand side of the SPA-LEED image is superimposed with a corresponding simulated diffraction pattern. The simulation is able to reproduce the majority of the spots, but cannot account for some rather strong spots that are further outward from the specular spot. These spots can be explained by multiple scattering; an example of multiple scattering around the [10]-spot is illustrated by the dashed green lines. The full green lines shows the corresponding unit cell vectors around the specular spot. The inset shows the resulting unit cells and proposed candidate QA structure models.*

that every molecule only forms one intermolecular H-bond of the type N–H$\cdots$O (indicated by the red ellipses). Additionally, each molecule is also involved in the formation of one H-bond of the significantly weaker type C–H$\cdots$O (indicated by the green ellipses). Consequently, the handedness within the chains alternates with every molecule. The molecule density of the first layer is $0.0095\,\text{Å}^{-2}$, which is slightly higher ($\sim$6%) than the one in the β-phase ($0.0089\,\text{Å}^{-2}$), which helps to compensate for energy loss due to the lower amount of H-bonds. The reason why the first QA layer forms this phase and not the known β-phase is likely caused by the fact that a second QA layer was present during annealing. This second layer constitutes a supply of additional QA molecules and exerts an additional pressure onto the first QA layer. That means that molecules in the second layer may also be able to squeeze into the first layer during annealing. These two aspects lead to the formation of a different structure with a larger molecule density. The reason why this structure was not reproduced is likely due to the fact that the coverage of the layer was underestimated, and it was assumed to be not larger than 1 ML. Hence, the attempts to reproduce this structure were conducted at coverages that were not sufficient for its formation.

C.2 Additional phases on Cu(111)

In this chapter, two additional structures, which were observed after depositing and annealing QA on the Cu(111) surface, will be discussed. Here, some of the structures contain molecules that show smaller apparent lateral sizes than that of the QA molecule. This is likely explained by a thermally induced decomposition of the QA molecules into indigo. It is important to note this decomposition was not observed for the β′-phase on Cu(111), which was discussed in Chapter 5.2 (page 46). This difference can likely be explained by different annealing times and/or differences in the QA coverage.

C.2.1 Phase after annealing of a QA multilayer

In this section, a phase, which was only observed after annealing a QA layer ($\theta_{QA} > 1$ ML) on Cu(111) at 500 K for 15 minutes, will be discussed. Corresponding STM images are shown in panels a) and b) of Figure C.5. The STM images show that this structure also consists of domains of parallel molecular chains, but with only three azimuthal orientations, which are aligned with the $\langle 10 \rangle$ direction of the Cu(111) substrate. The domains are very small and only consist of 3 – 5 parallel chains. Furthermore, the molecules are tilted by 30° with respect to the direction of the chain. A corresponding SPA-LEED image is displayed in panel c). It consists of two sets of 6 spots, which form two hexagons around the specular spot. These spots are the only superstructure spots that are visible in the diffraction pattern and they are rather weak and broad, which is likely caused by the small domain size of the organic layer. The analysis of the SPA-LEED image yielded a unit cell with $b_1 = (6.9 \pm 0.1)$Å and $b_2 = (13.8 \pm 0.2)$ Å, which are in good agreement with

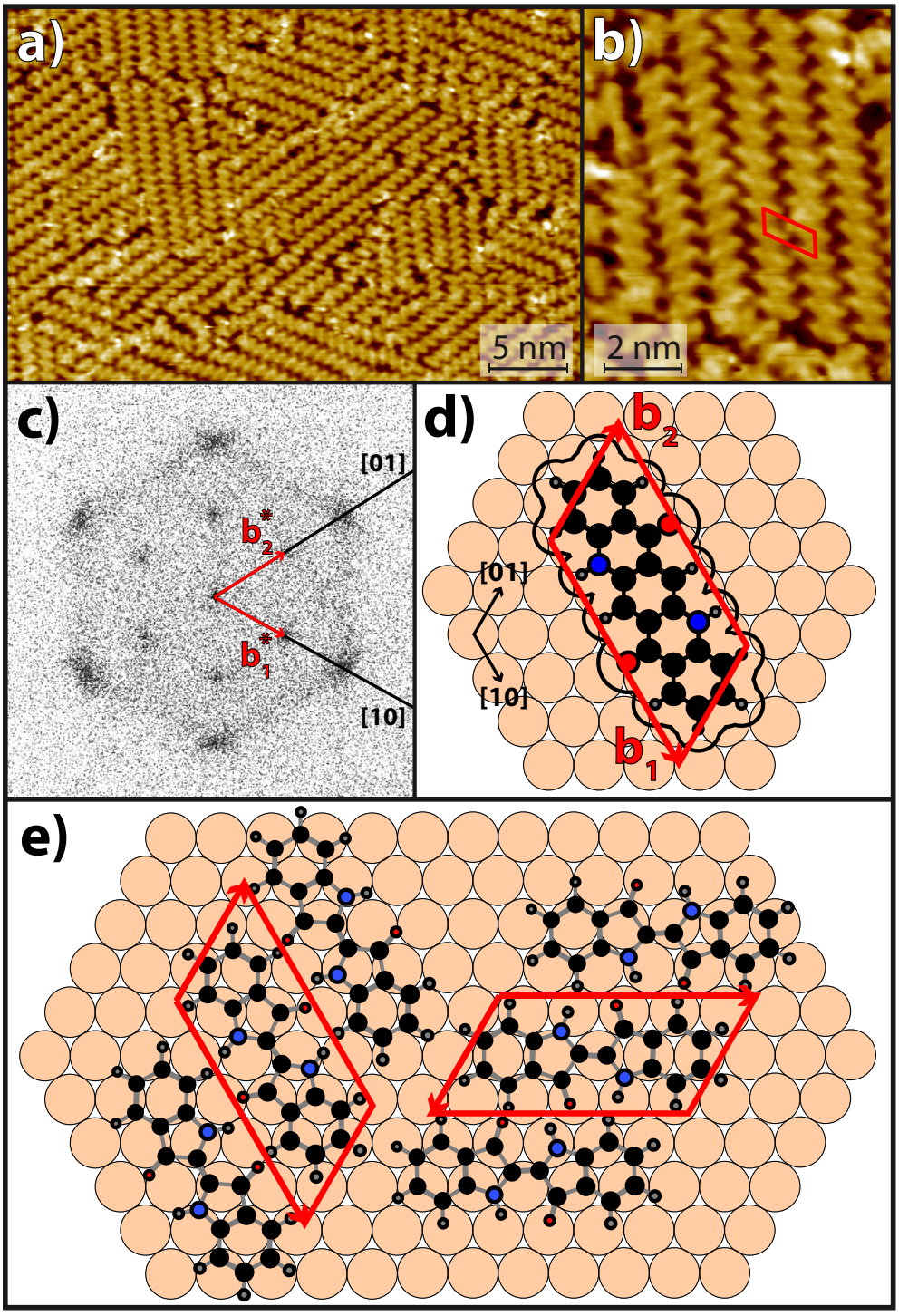

Figure C.5: *Phase that was observed on Cu(111) after a layer of QA ($\theta_{QA} > 1$ ML) was annealed at 500 K for 15 minutes.* ***a)*** *large scale STM image ($U_B = -1.5$ V, $I_{tun} = 25$ pA) of the structure.* ***b)*** *Zoom in on the structure for a better look at the molecular arrangement. A unit cell is depicted in red.* ***c)*** *SPA-LEED image ($T = 300$ K, $E = 30$ eV) showing the area around the specular spot. This image was recorded by R. Bretel within the scope of his PhD thesis [93]. The $\langle 10 \rangle$ direction of the substrate and the proposed reciprocal unit cell vectors of the superstructure are indicated in black and red, respectively.* ***d)*** *A structure model showing the corresponding real space unit cell and a QA molecule. It can be seen that the unit cell is too small to fit a single QA molecule.* ***e)*** *Proposed structure model for chains of indigo on Cu(111).*

the corresponding lengths in the STM images. The angle between the two vectors $\mathbf{b_1}$ and $\mathbf{b_2}$ is $\alpha = 120°$. The corresponding superstructure matrix is:

$$\mathbf{M}^{\mathbf{Cu(111)}}_{\mathbf{b_1},\mathbf{b_2}} = \begin{pmatrix} 5.4 \pm 0.1 & 0 \\ 0 & 2.7 \pm 0.1 \end{pmatrix}.$$

A corresponding structure model showing the real space unit cell and a QA molecule is shown in panel d) of Figure C.5. This model shows that the unit cell is smaller than a single QA molecule in both dimensions. Thus, the observed unit cell can only be explained by a molecule that is smaller than QA. A potential candidate molecule is the organic dye indigo (shown in the inset of panel b) of Figure D.1) because it was reported by Scherwitzl *et al.* that QA can thermally crack during evaporation, which leads to a mixture of QA and indigo on the surface [79]. The indigo molecule would fit nicely into the unit cell because both its width and its length are smaller by about 15% than those of the QA molecule. Hence, it is likely that the observed structure (cf. Fig. C.5) consists of indigo molecules.

The structure of indigo on Cu(111) was already reported by Villagomez *et al.* [128], which is also summarized in Appendix D.1.2. They found that indigo also forms molecular chains that are connected via intermolecular H-bonds. Each molecule is involved in the formation of 4 H-bonds and the structure has 2 H-bonds per molecule. After annealing a full ML of indigo at 400 K, they found closely packed molecular chains with a intermolecular distance of $b_1 = (7.1 \pm 0.2)$Å, a distance between chains of $b_2 = (15.0 \pm 0.2)$ Å, and an angle between the two vectors of about $\alpha = 90°$. These lengths are only slightly larger (by up to 8%) than the above-mentioned ones that were observed for the structure that is shown in Figure C.5. Considering this, a structure that consists of molecular indigo chains, similar to the one observed by Villagomez *et al.*, may be a possible explanation for the observed structure. However, the angle between the two unit cell vectors of the structure that was observed in the present thesis is considerably larger ($\alpha = 120°$). Hence, it is concluded that the chains here have a periodic alteration of the handedness (RLRL), which also causes a periodic indent in the chains. A corresponding structure model is shown in panel e) of Figure C.5. It shows two mirror equivalent chains of indigo that are oriented along the same main axis of the Cu(111) substrate. This structure was not observed by Villagomez *et al.* [128]. A potential reason for that may be that, similar to the β-phase of QA on Ag(100), the structure that was observed here only forms upon annealing at about 500 K. Every molecule in this structure is only involved in the formation of two H-bonds between NH- and CO-groups and the structure has one such H-bond per molecule. But similar to the β-phase on Ag(100), this loss of binding energy may possibly be overcompensated by stronger substrate-adsorbate interactions.

The possibility of a decomposition of QA into indigo during the evaporation or on the surface through a catalytic reaction and the structures of indigo on Cu(111) will be discussed in more detail in Section D.

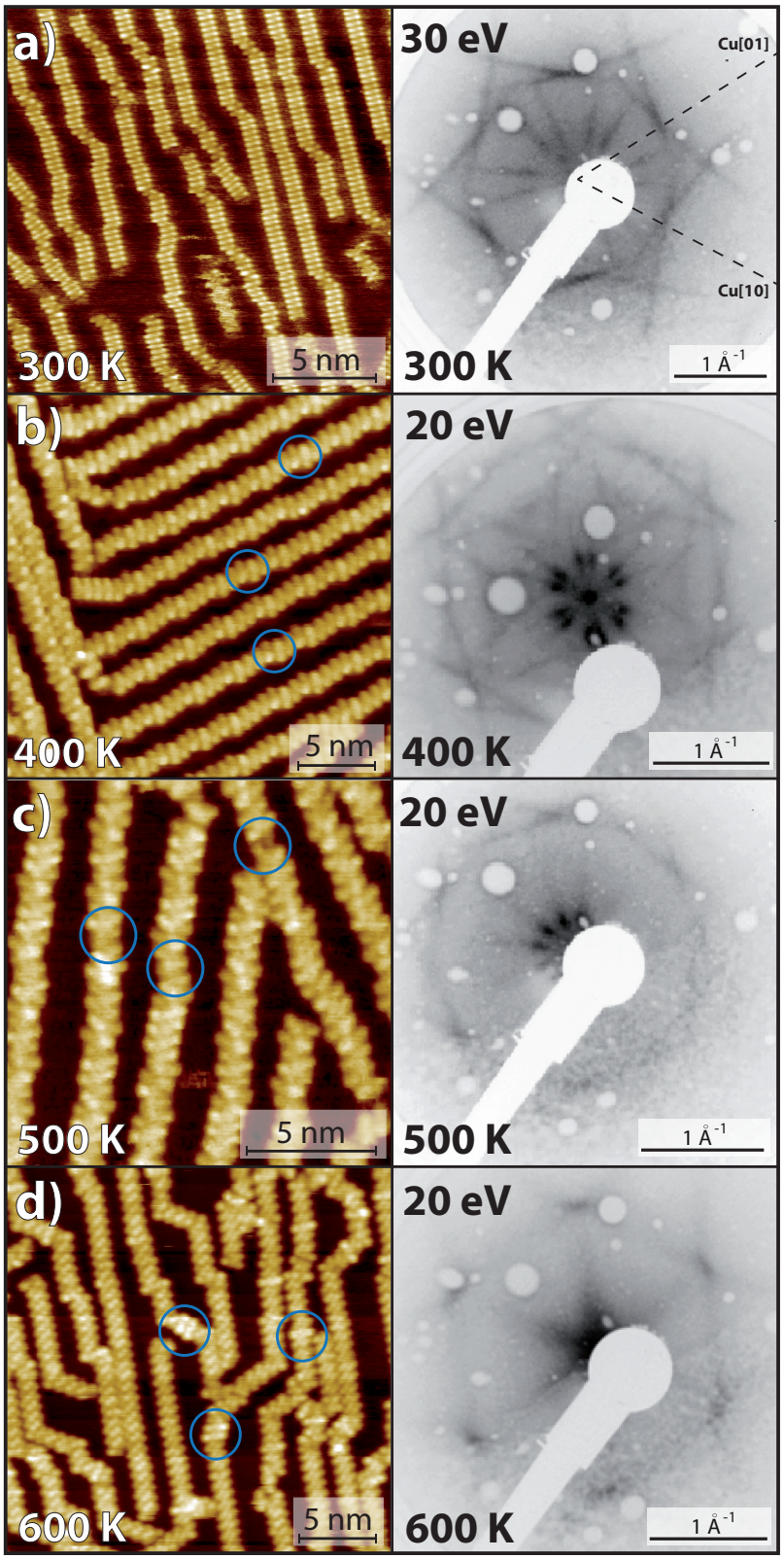

Figure C.6: *STM and LEED images of different chain-like structures of QA on Cu(111). Panel* ***a)*** *shows 0.5 ML of the typical α′-phase and panels* ***b)***, ***c)***, *and* ***d)*** *show the same layer after annealing the sample at 400 K, 500 K, and 600 K for 15 minutes, respectively. All images were recorded at RT. The blue circles in panels b), c), and d) highlight distinct features in the chains, for more information see text.*

C.2.2 Several QA chain structures at medium coverage

Now, different chain structures of QA on Cu(111) after different annealing steps will be addressed. Similar structures were not observed on Ag(100), which is likely due to the fact that the interactions between the QA molecules and the metal substrate are stronger on the Cu(111) surface.

Figure C.6 shows STM and LEED images that correspond to the different structures of a QA layer with a coverage of 0.5 ML QA on the Cu(111) surface after annealing at different temperatures. Panel a) shows images of a phase that is in principle identical to the α'-phase that is shown in panel a) of Figure 5.6 (page 48), but at a lower coverage. It consists of parallel molecular chains with six distinct azimuthal orientations (as discussed in Chapter 5.2 and Appendix A.1).

Panel b) of the figure shows an STM and a LEED image of the same layer after annealing at 400 K for 15 minutes. The STM and LEED images show that the chains are now rotated by $(9 \pm 2)^\circ$ with respect to the azimuthal angles of the chains after deposition at 300 K. Furthermore, the STM image reveals that the internal structure of the molecular chains is now also different. Instead of straight chains where every molecule exhibits two H-bonds to the neighboring QA molecules, the chains here consist of homochiral molecule pairs (RR/LL, examples are indicated by blue circles). These do not exhibit an offset and there are two H-bonds between the two QA molecules within the pair. These pairs are connected by either one or two QA molecules with alternating handedness which leads to periodic offsets in the chains (RRLRLL/LLRLRR and RRLRR/LLRLL). The case in which the homochiral pairs have two molecules between them (RRLRLL/LLRLRR) leads to chains that are very similar to the chains that the β'-phase of a full ML of QA on Cu(111) is comprised of (described in detail in Appendix A.1).

The structure after annealing at 500 K for 15 minutes, which is shown in panel c) of Figure C.6, still consists of molecular chains with the same six azimuthal orientations as the ones after annealing at 400 K (panel b), which was confirmed by STM and LEED. However, now the chains are more curved and the internal structure of the chains appears to be more chaotic. It was not possible to clearly determine the molecular arrangement within these chains from the STM images. Furthermore, it appears as if some of the molecules are smaller than the rest (13 Å vs. 16 Å, examples are highlighted by blue circles). The LEED images also point to a stronger disorder because the intensities are lower and the spots more smeared-out than the ones of the LEED image after annealing at 400 K.

Lastly, after annealing at 600 K for 15 minutes, a structure that differs significantly from the above three structures emerges, which does not further change upon annealing at even higher temperatures. Corresponding STM and LEED images are shown in panel d) of Figure C.6. This structure consists of chains with only three azimuthal orientations, which are also aligned along the $\langle 10 \rangle$ direction of the Cu(111) substrate, which means that a distinct azimuthal orientation can no longer be attributed to only one of the two chiralities. The molecules exhibit a characteristic S-shape, which was also observed for chains of QA on Ag(100) (cf. Chapter 5.1.1, page 35). Within an individual chain, the handedness of the S-shapes stays constant. This indicates that each chain is still completely homochiral with 2 H-bonds per molecule. A more detailed description of this

structure can be found in Appendix A.1. In this publication, the structure was attributed to chains of QA. However, after a more thorough analysis of more data, it was found that the width of the chains is only (13.5 ± 0.5) Å, which is significantly smaller than the length of a hard-sphere model of the QA molecule (16.3 Å). Moreover, the STM images show that the chains also contain molecules that are visibly wider than the rest of the chains (17.0 Å vs. 13.5 Å). Such molecules are highlighted by blue circles. Thus, it is more likely that the chains after annealing at 600 K consist of indigo molecules that are the product of a catalytic decomposition of QA. Furthermore, the smaller molecules in the chains after annealing at 500 K may also be indigo molecules.

The above-discussed structure is similar to the structures of indigo on Cu(111) that were observed by Villagomez *et al.* [128] by STM. Both structures consist of homochiral molecular chains. However, the structures that were observed here exhibit three distinct azimuthal chain orientations that are oriented along the $\langle 10 \rangle$ directions of the substrate, while those observed by Villagomez *et al.* exhibit six azimuthal chain orientations, which are rotated by $\pm 9.5^\circ$ with respect to the $\langle 10 \rangle$ directions of the substrate. This difference may be explained by the fact that Villagomez *et al.* deposited indigo directly instead of QA and that here the structures were annealed at a higher temperature (600 K vs. 400 K). The higher sample temperature may lead to a slight reconstruction of the first Cu layer, similar to the situation of the β-phase of QA on Ag(100), which favors the chain growth along the $\langle 10 \rangle$ directions of the Cu substrate.

Overall, the results of this section have shown that a sub-monolayer of the α'-phase of QA on Cu(111) undergoes phase transitions at 400 K, 500 K, and 600 K into different structures consisting of molecular chains. The structure after annealing at 600 K is thermodynamically stable and does not change further upon annealing at higher temperatures. The two structures that were observed after annealing at 400 K and 500 K, are metastable structures that are stabilized by the strong interaction with the substrate. Furthermore, the phase transition likely involves a catalytic decomposition of QA into indigo. However, in order to confirm this more experiments (for example by XPS) are required. These results are in stark contrast to similar situations for QA on Ag(100). There, if a sub-monolayer of QA is annealed at 500 K for 15 minutes, it forms large domains of the commensurate and closely packed β-phase, while leaving the rest of the substrate completely uncovered. This difference can be explained by the fact that the mobility of the QA molecules on Cu(111) is significantly smaller than on Ag(100), which hinders the formation of closely packed 2D domains.

D Possible decomposition of quinacridone into indigo during the evaporation

A publication by Scherwitzl *et al.* postulates a thermal decomposition of QA into indigo during the evaporation of QA [79]. This phenomenon leads to an unwanted deposition of indigo resulting in a mixture of QA and indigo on the surface. Hence, within the scope of the present thesis, it was very important to critically review all the data regarding the question of whether the observed structures may partially or completely be composed of indigo. Section D.1 of this chapter will summarize the important aspects of the decomposition that was found by Scherwitzl *et al.* and will also present the structures of indigo on Cu(111), which was investigated by Villagomez *et al.* [128]. Afterwards, in Section D.2 it will be discussed if and to what degree a decomposition of QA into indigo may have occurred within the experiments reported in the present thesis.

D.1 Literature overview

D.1.1 Decomposition of quinacridone during evaporation

Scherwitzl *et al.* conducted TDS experiments on a carbon-covered SiO_2 surface after the deposition of QA [79]. For $m/z = 128$, which corresponds to the most prominent fragment of QA ($C_{10}H_8^+$), they found a single desorption peak at roughly 500 K. However, for a different mass of $m/z = 76$, which also corresponds to a fragment of QA, they found an additional peak at 420 K. From this, they concluded that there was a second more weakly bonded molecule with a different desorption behavior present on the surface, despite the fact that only pure QA was loaded into the evaporator. A full mass scan in the range of $m/z = 35 - 150$ revealed two different cracking patterns. One belonged to QA and the other was assigned to indigo. Thus, they concluded that indigo is the product of a thermal decomposition of QA during evaporation.

In order to investigate this decomposition further, the authors also conducted experiments with different kinds of evaporators. They compared an evaporator where the QA was in an open glass crucible (no collisions before leaving the crucible) with an evaporator where the glass crucible had a small effusion hole at the front (estimated 400 collisions before leaving the crucible). They found that the deposition with the open crucible led to only a single desorption peak at 500 K (i.e., only QA was adsorbed on the surface), while the use crucible with the small effusion hole caused the second peak at 420 K to appear (i.e., QA and indigo were adsorbed on the surface). From these results, the authors concluded that the decomposition of QA is thermally activated by the collisions with the hot walls of the crucible, which also means that the decomposition of QA during evaporation is dependent on the type of evaporator.

D.1.2 Indigo on Cu(111)

The structures of indigo on the Cu(111) surface were investigated by Villagomez *et al.* [128]. Similar to QA, the indigo molecule is prochiral, which means that upon adsorption on a surface, it forms two different enantiomers. Another similarity to QA is the fact that the indigo molecule contains the same functional chemical groups and is thus prone to the formation of intermolecular H-bonds. On Cu(111), indigo forms domains of parallel molecular chains after the deposition at RT. A corresponding STM image is shown in panel a) of Figure D.1. The indigo molecules in the chains are connected by intermolecular H-bonds. Each molecule is involved in the formation of four H-bonds and the chains exhibit two H-bonds per molecule, which means that the chains of indigo are also homochiral. The chains of indigo adapt six distinct orientations that are rotated by $(\pm 9.5 \pm 0.5)^\circ$ with respect to the $\langle 10 \rangle$ direction of the Cu(111) substrate. The intermolecular distance within the chains amounts to (7.0 ± 0.2) Å and the distance between neighboring chains is (19.0 ± 0.5) Å.[1] The domains are very small and only consist of 3 – 7 parallel chains, which results in many small patches of bare Cu. Overall, the arrangement of the chains looks very similar to the one of 1 full ML QA on Cu(111) after deposition at 300 K (cf. panel a) of Fig. 5.6 on page 48). STM images of individual indigo molecules are shown in the inset. It can be seen that the indigo molecules appear as two lobes that are clearly separable.

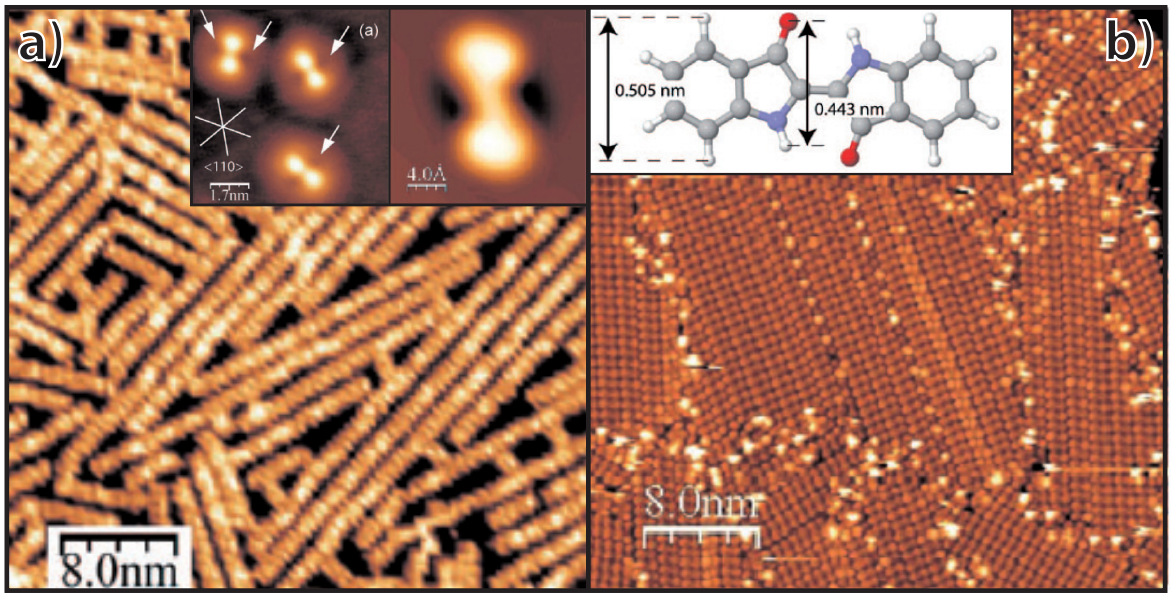

Figure D.1: *The structure of indigo on Cu(111). The images were copied from the corresponding publication by Villagomez et al. and slightly modified [128]. All images were taken at a sample temperature of 5 K.* ***a)*** *STM image ($U_B = 2.0\,V$, $I_{tun} = 10\,pA$) of indigo on Cu(111) after the deposition at 300 K. The inset shows an STM image ($U_B = -0.3\,V$, $I_{tun} = 10\,pA$) of three individual indigo molecules (left side) and a calculated STM image of a single indigo molecule (right side).* ***b)*** *STM image ($U_B = 0.6\,V$, $I_{tun} = 11\,pA$) of a full ML indigo on Cu(111) after annealing at 400 K. The inset shows a model of an indigo molecule with dimensions for the width.*

[1] Note that, similar to the chains of QA, the interaction between neighboring chains is repulsive. Hence, the distance between neighboring chains is dependent on the coverage.

After annealing a ML of indigo on Cu(111) at 400 K, the structure looks in principle very similar to the one described above but is more ordered. A corresponding STM image is shown in panel b) of Figure D.1. The chains are now longer on average and the domains consist of up to 10 parallel chains. The azimuthal orientations of the chains are the same as the one after deposition at 300 K. Furthermore, the structure is now more closely packed; the distance between the chains here only amounts to (15.0 ± 0.2), which is very close to the *van der Waals* length of an indigo molecule. A more in-depth description of this system can be found in the corresponding publication [128].

D.2 Own Results

Now, it will be discussed if and to what degree the decomposition of QA into indigo and potential structures of indigo on the surfaces may have played a role in the experiments that were conducted within the scope of the present thesis.

The first aspect that needs to be addressed is the dependency of the decomposition on the kind of evaporator. Within the experiments of the present thesis, QA was always evaporated from an open glass crucible. That means the amount of collisions with the hot walls of the crucible that the molecules experience before reaching the sample is minimal. Hence, the likelihood of QA undergoing a thermally induced decomposition is very small. Furthermore, the mass spectra during the deposition of QA did not contain a significant amount of signals that could not be assigned to fragments of QA. An example of a mass spectrum that was recorded during the evaporation of QA is shown in panel a) of Figure D.2. A mass spectrum that was recorded by Scherwitzl *et al.*, which shows the partial decomposition of QA into indigo, is illustrated in panel b). The comparison of the two spectra shows that the majority of the peaks that Scherwitzl *et al.* assigned to a fragment of only indigo could not observed during the evaporation of QA within the scope of the experiments of the present thesis. Thus, the choice evaporator and the mass spectra do not point towards a potential decomposition of QA during the evaporation.

Nevertheless, it is important to critically review all the data with the aspect of a potential decomposition in mind. First, the structures that are present on the surfaces after deposition without annealing will be addressed. For LEED images, potential hints towards a decomposition of QA might be the coexistence of two phases or a single mixed phase with a unit cell of a size that can not be explained by an arrangement of only QA molecules. However, a coexistence of two phases after deposition at RT was never observed and the sizes of the unit cells were always in very good agreement with the size of the QA molecules. In STM images, the main criterion to identify indigo molecules is the fact that the indigo molecule is shorter than the QA molecule by roughly 2 Å. Furthermore, the indigo molecule is visible as two lobes that are clearly distinguishable, while the QA molecule appears as a single ellipsoid protrusion. In all STM images that were recorded after deposition at RT, molecules of two different sizes were *never* observed, which would be expected in the case of a partial decomposition of QA. Furthermore, the observed molecules did not appear as two separate protrusions as would be expected for indigo molecules [128]. Thus, from this,

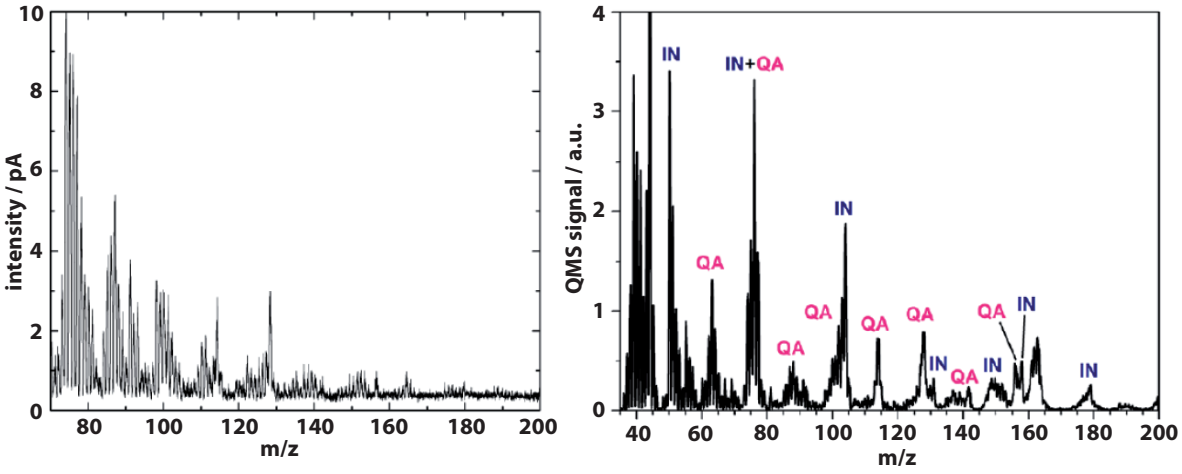

Figure D.2: a) *QMS spectrum of QA during the evaporation that was recorded within the scope of the present thesis.* ***b)*** *QMS spectrum of QA during the evaporation that was recorded by Scherwitzl et al. [79]. The different peaks are assigned to QA, indigo (IN) or a combination of both.*

it can be concluded that the structures that were observed on Ag(100) and Cu(111) after deposition *without* subsequent annealing, consist purely of QA molecules. This also implies that no decomposition of QA occurred during deposition.

The above arguments do not exclude to possibility of the decomposition of QA into indigo completely. One could also imagine that such a decomposition takes place on the metal surfaces during annealing, where the metal substrate could even act as a catalyst for this decomposition. The structures of QA on Ag(100) did not show any signs of indigo molecules. However, on Cu(111), several STM images showed structures consisting of molecules of two different lengths after annealing at 500 K and 600 K. The corresponding structures were discussed in more detail in Sections C.2.1 and C.2.2. This indicates that a catalytic decomposition of QA into indigo may be achieved on a Cu surface at elevated temperatures. Furthermore, the fact that a similar observation could not be made on Ag(100), indicates that this decomposition is a catalytic reaction that is enabled by the Cu(111) surface. This is a very interesting aspect to investigate further, for example with XPS.

E Structure parameters of different QA phases

In this chapter, some of the most important structure parameters for the QA structures on various surfaces that were investigated in the present work, and for those QA structures that have been reported in literature, are summarized. In figure E.1, polar diagrams of the azimuthal chain orientations of QA chains on different metal substrates and insulating layers are displayed.

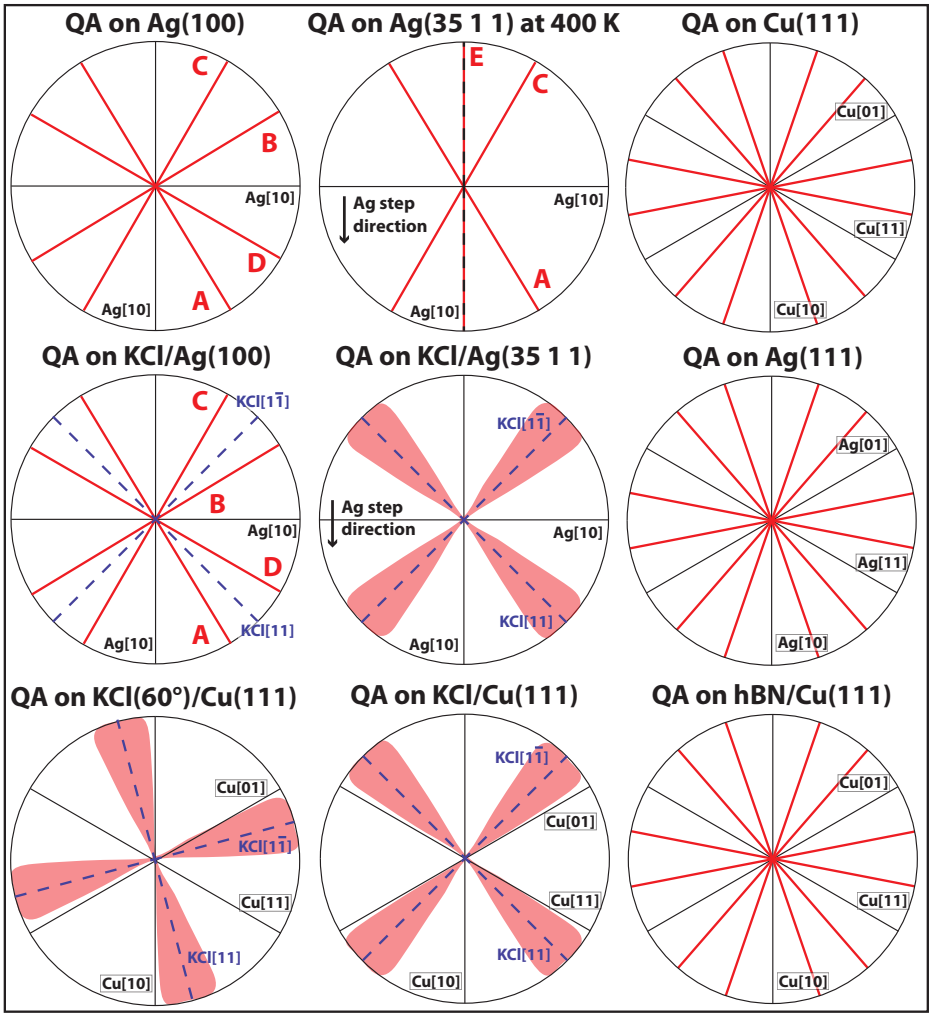

Figure E.1: *Polar diagrams of the in-plane azimuthal orientation of the QA chains on different substrates. The red lines or cones correspond to the azimuthal QA chain orientations. The values for QA on Ag(111) and KCl/Cu(111) were taken from ref. [15] and [240], respectively. For QA on KCl/Cu(111), two cases are shown, which differ from each other by the azimuthal orientation of the KCl layer with respect to the Cu(111) substrate. Note that for KCl on Cu(111), one Cu-KCl step edge in the KCl[10] direction is aligned with the [10] direction of the Cu(111) surface [240].*

Table E.1 shows an overview over the structure parameters of the common QA structures that were observed within the scope of the present thesis, and of those that were reported in literature. It includes the superstructure matrices, and the lengths, the area and the angles of the unit cells of all observed QA structures.

Table E.1: *Overview of the structure parameters of QA on Ag(100), KCl/Ag(100), KCl/Ag(35 1 1), Cu(111), and hBN/Cu(111), those of QA on Ag(111), which were obtained by Wagner et al. [15], those of QA on Ag(110), which were obtained by Priya et al. [81], those of KCl/Cu(111), which were obtained by Bretel et al., and those of the* $(1\bar{1}2)$ *plane of the* α^{I}*-QA polymorph[14]. All surface structures belong to the space group P2. The angle between the vectors* $\mathbf{b_1}$ *and* $\mathbf{b_2}$ *is called* α*, Z denotes the number of molecules per unit cell, and the area of the unit cells is named A. Errors of the matrix entries are given in the text. For the calculation of the vector lengths of the unit cells, the lattice constants at 300 K for Cu (3.597 Å) and Ag (4.079 Å) were used [241].*

	Ag(100)			**Cu(111)**		**Ag(111)** [15]		$\boldsymbol{\alpha^{\mathrm{I}} - \mathbf{QA}}$ [14]
	α-phase	β-phase	γ-phase	α'-phase	β'-phase	α^*-phase	β^*-phase	$(1\bar{1}2)$-plane
M	$\begin{pmatrix} 2 & 1.25 \\ -3 & 4.80 \end{pmatrix}$	$\begin{pmatrix} 4 & 3 \\ -5 & 3 \end{pmatrix}$	$\begin{pmatrix} 3 & 7 \\ -7 & 3 \end{pmatrix}$	$\begin{pmatrix} 2.1 & -1.0 \\ 5.6 & 7.1 \end{pmatrix}$	$\begin{pmatrix} 6.5 & 0.8 \\ 3.8 & 11.3 \end{pmatrix}$	$\begin{pmatrix} 3 & 2 \\ -1.5 & 6 \end{pmatrix}$	$\begin{pmatrix} 5 & 5 \\ -1 & 5 \end{pmatrix}$	not applicable
b_1 / Å	6.8 ± 0.1	14.445	21.93	7.0 ± 0.3	15.6 ± 0.2	7.0 ± 0.5	14.445	6.9
b_2 / Å	16.4 ± 0.1	16.848	21.93	16.6 ± 1.0	25.3 ± 0.2	20.0 ± 0.2	16.088	16.9
α / °	90 ± 1	112.2	90	90 ± 1	94 ± 1	90	111.1	110.3
Z	1	2	3 or 4[a]	1	4	1	2	1
A / Å^2	111.5 ± 0.2	225.4	484.4	116 ± 10	395 ± 15	142.1	216.8	109.2

	Ag(110) [81] [b]			**KCl**			**hBN**
	$\alpha^{\dagger}$-phase	$\beta_1^{\dagger}$-phase	$\beta_2^{\dagger}$-phase	Ag(100)	Cu(111) [240]	Ag(35 1 1)	Cu(111)
M	$\begin{pmatrix} 1 & -2 \\ 3 & 4 \end{pmatrix}$	$\begin{pmatrix} 2 & -0.3 \\ 0 & 4.6 \end{pmatrix}$	$\begin{pmatrix} 5 & -3 \\ 2 & 7 \end{pmatrix}$	n.d.[c]	n.d.[c]	n.d.[c]	n.d.[c]
b_1 / Å	7.0	8.3 ± 0.2	21.8	6.6 ± 0.2	$6.4 - 6.8$	6.5 ± 0.2	6.8 ± 0.2
b_2 / Å	16.8	13.2 ± 0.2	21.8	20.0 ± 0.5	n.d.	16.5 ± 0.5	17.0 ± 0.5
α / °	98	97 ± 2	90	90 ± 1	$91 - 97$	96 ± 1.0 [d]	90 ± 2
Z	1	1	3 or 4	1	1	1	1
A / Å^2	117.9	107.7 ± 0.2	483.4	132 ± 8	n.d.	107 ± 7	116 ± 7

[a] Two possible structures of the γ-phase contain 3 or 4 molecules per unit cell and are discussed in section C.1.1

[b] These are preliminary results that are not published yet.

[c] The superstructure matrices of the QA structures with respect to the metal substrate were not determined.

[d] Most STM pictures did not show molecular resolution. Thus, it is possible that a wider range of angles exists, similar to the QA chains on KCl/Cu(111) [240].

Bibliography

[1] G. Zhou, L. Xu, G. Hu, L. Mai, and Y. Cui, "Nanowires for Electrochemical Energy Storage", Chem. Rev. **119**, 11042 (2019).

[2] N. I. Goktas, P. Wilson, A. Ghukasyan, D. Wagner, S. McNamee, and R. R. LaPierre, "Nanowires for energy: A review", Appl. Phys. Rev. **5**, 041305 (2018).

[3] J. Chuancheng, Z. Lin, Y. Huang, and X. Duan, "Nanowire Electronics: From Nanoscale to Macroscale", Chem. Rev. **119**, 9074 (2019).

[4] R. K. Daniels, M. D. Arnold, Z. E. Heywood, J. B. Mallinson, P. J. Bones, and S. A. Brown, "Brainlike Networks of Nanowires and Nanoparticles: A Change of Perspective", Phys. Rev. Appl. **20**, 034021 (2023).

[5] J. Gu, Y. Shen, S. Tian, Z. Xue, and X. Meng, "Recent Advances in Nanowire-Based Wearable Physical Sensors", Biosensors **13** (2023).

[6] J. Patzsch, D. J. Babu, and J. J. Schneider, "Hierarchically structured nanoporous carbon tubes for high pressure carbon dioxide adsorption", Beilstein J. Nanotechnol. **8**, 1135 (2017).

[7] M. Imran, N. Motta, and M. Shafiei, "Electrospun one-dimensional nanostructures: a new horizon for gas sensing materials", Beilstein J. Nanotechnol. **9**, 2128 (2018).

[8] A. B. Asha and R. Narain, "Chapter 15 - Nanomaterials properties", in *Polymer Science and Nanotechnology*, edited by R. Narain (Elsevier, 2020), pp. 343–359.

[9] Y. S. Zhao, H. Fu, A. Peng, Y. Ma, D. Xiao, and J. Yao, "Low-Dimensional Nanomaterials Based on Small Organic Molecules: Preparation and Optoelectronic Properties", Adv. Mater. **20**, 2859 (2008).

[10] H. Yu, D. Y. Kim, K. J. Lee, and J. H. Oh, "Fabrication of One-Dimensional Organic Nanomaterials and Their Optoelectronic Applications", J. Nanosci. Nanotechnol. **14**, 1282 (2014).

[11] M. B. Ross, C. A. Mirkin, and G. C. Schatz, "Optical Properties of One-, Two-, and Three-Dimensional Arrays of Plasmonic Nanostructures", J. Phys. Chem. C **120**, 816 (2016).

[12] M. Bellingeri, A. Chiasera, I. Kriegel, and F. Scotognella, "Optical properties of periodic, quasi-periodic, and disordered one-dimensional photonic structures", Opt. Mater. **72**, 403 (2017).

[13] E. Roduner, "Size matters: why nanomaterials are different", Chem. Soc. Rev. **35**, 583 (2006).

[14] E. F. Paulus, F. J. J. Leusen, and M. U. Schmidt, "Crystal Structures of Quinacridones", CrystEngComm **9**, 131 (2007).

[15] T. Wagner, M. Györök, D. Huber, P. Zeppenfeld, and E. D. Głowacki, "Quinacridone on Ag(111): Hydrogen Bonding versus Chirality", J. Phys. Chem. C **118**, 10911 (2014).

[16] A. Eberle, A. Nosek, J. Büttner, T. Markert, and F. Trixler, "Growing low-dimensional Supra-molecular Crystals directly from 3D Particles", CrystEngComm **19**, 1417 (2017).

[17] F. Trixler, T. Markert, M. Lackinger, F. Jamitzky, and W. M. Heckl, "Supramolecular Self-Assembly initiated by Solid-Solid Wetting", Chem. - Eur. J. **13**, 7785 (2007).

[18] E. D. Głowacki, L. Leonat, M. Irimia-Vladu, R. Schwödiauer, M. Ullah, H. Sitter, S. Bauer, and N. Serdar Sariciftci, "Intermolecular Hydrogen-bonded Organic Semiconductors - Quinacridone versus Pentacene", Appl. Phys. Lett. **101**, 023305 (2012).

[19] E. D. Głowacki, M. Irimia-Vladu, M. Kaltenbrunner, J. Gsiorowski, M. S. White, U. Monkowius, G. Romanazzi, G. P. Suranna, P. Mastrorilli, T. Sekitani, S. Bauer, T. Someya, L. Torsi, and N. S. Sariciftci, "Hydrogen-Bonded Semiconducting Pigments for Air-Stable Field-Effect Transistors", Adv. Mater. **25**, 1563 (2013).

[20] J. Jeon, H. Jhon, M. Kang, H. J. Song, and T. K. An, "Quinacridone-quinoxaline-based Copolymer for Organic Field-Effect Transistors and its High-Voltage Logic Circuit Operations", Org. Electron. **56**, 1 (2018).

[21] Y. Jeong, J. Jeon, S. Lee, M. Kang, H. Jhon, H. J. Song, C. E. Park, and T. K. An, "Development of Organic Semiconductors based on Quinacridone Derivatives for Organic Field-Effect Transistors: High-Voltage Logic Circuit Applications", IEEE J. Electron Devices Soc. **5**, 209 (2017).

[22] Y. Kanbur, H. Coskun, E. D. Głowacki, M. Irimia-Vladu, N. S. Sariciftci, and C. Yumusak, "High Temperature-Stability of Organic Thin-Film Transistors based on Quinacridone Pigments", Org. Electron. **66**, 53 (2019).

[23] D. Berg, C. Nielinger, W. Mader, and M. Sokolowski, "Quinacridone Organic Field Effect Transistors with significant Stability by Vacuum Sublimation", Synth. Met. **159**, 2599 (2009).

[24] D. Saadi, F. Mayr, C. Yumusak, D. Wielend, M. Cobet, B. Kahraman, C. V. Irimia, Y. Kanbur, M. Bednorz, K. Kotwica, A. Ben Fredj, S. Romdhane, M. C. Scharber, N. S. Sariciftci, and M. Irimia-Vladu, "N,N'-Substituted quinacridones for organic electronic device applications", Mater. Adv. **4**, 2214 (2023).

[25] C. Wang, S. Wang, W. Chen, Z. Zhang, H. Zhang, and Y. Wang, "A diphenylamino-substituted Quinacridone Derivative: Red Fluorescence based on Intramolecular Charge-Transfer Transition", RSC Adv. **6**, 19308 (2016).

[26] M. Pilz da Cunha, T. T. Do, S. D. Yambem, H. D. Pham, S. Chang, S. Manzhos, R. Katoh, and P. Sonar, "A Triphenylamine Substituted Quinacridone Derivative for solution processed Organic Light Emitting Diodes", Mater. Chem. Phys. **206**, 56 (2018).

[27] H. Min, I. S. Park, and T. Yasuda, "cis-Quinacridone-Based Delayed Fluorescence Emitters: Seemingly Old but Renewed Functional Luminogens", Angew. Chem. Int. Ed **60**, 7643 (2021).

[28] K. H. Hwang, D. H. Kim, M. H. Choi, J. P. Han, and D. K. Moon, "Effect of Side Chain Position and Conformation of Quinacridone - Quinoxaline based conjugated Polymers on Photovoltaic Properties", J. Ind. Eng. Chem. **34**, 66 (2016).

[29] H. A. Sung, D. H. Kim, T. H. Lee, M. H. Choi, E. J. Lee, and D. K. Moon, "Effect of conjugated 2D-side groups on Quinacridone-based Copolymers to adjust deep HOMO level for Photovoltaics", J. Ind. Eng. Chem. **46**, 304 (2017).

[30] S. Dunst, E. Karner, M. Coppola, G. Trimmel, and M. Irimia-Vladu, "Comparison of the Solution and Vacuum-Processed Quinacridones in Homojunction Photovoltaics", Monatsh. Chem. **148**, 863 (2017).

[31] C. Wang, Z. Zhang, and Y. Wang, "Quinacridone-based π-conjugated Electronic Materials", J. Mater. Chem. C **4**, 9918 (2016).

[32] J. Mizuguchi and T. Senju, "Solution and Solid-State Spectra of Quinacridone Derivatives as Viewed from the Intermolecular Hydrogen Bond", J. Phys. Chem. B **110**, 19154 (2006).

[33] J. Repp, G. Meyer, S. M. Stojković, A. Gourdon, and C. Joachim, "Molecules on Insulating Films: Scanning-Tunneling Microscopy Imaging of Individual Molecular Orbitals", Phys. Rev. Lett. **94**, 026803 (2005).

[34] R. Adhikari, J. Brox, S. Massicot, M. Ruppel, N. Jux, H. Marbach, and H.-P. Steinrück, "Structure and Conformation of Individual Molecules upon Adsorption of a Mixture of Benzoporphyrins on Ag(111), Cu(111), and Cu(110) Surfaces", ChemPhysChem **24**, e202300355 (2023).

[35] A. Mugarza, R. Robles, C. Krull, R. Korytár, N. Lorente, and P. Gambardella, "Electronic and magnetic properties of molecule-metal interfaces: Transition-metal phthalocyanines adsorbed on Ag(100)", Phys. Rev. B **85**, 155437 (2012).

[36] M. S. Baviloliaei and L. Diekhöner, "Molecular self-assembly at nanometer scale modulated surfaces: trimesic acid on Ag(111), Cu(111) and Ag/Cu(111)", Phys. Chem. Chem. Phys. **16**, 11265 (2014).

[37] M. Smerieri, L. Vattuone, D. Costa, F. Tielens, and L. Savio, "Self-Assembly of (S)-Glutamic Acid on Ag(100): A Combined LT-STM and Ab Initio Investigation", Langmuir **26**, 7208 (2010).

[38] M. Müller, J. Ikonomov, and M. Sokolowski, "Structure of Epitaxial Layers of KCl on Ag(100)", Surf. Sci. **605**, 1090 (2011).

[39] S. Joshi, D. Ecija, R. Koitz, M. Iannuzzi, A. P. Seitsonen, J. Hutter, H. Sachdev, S. Vijayaraghavan, F. Bischoff, K. Seufert, J. V. Barth, and W. Auwärter, "Boron Nitride on Cu(111): An Electronically Corrugated Monolayer", Nano Lett. **12**, 5821 (2012).

[40] C. Brülke, T. Heepenstrick, N. Humberg, I. Krieger, M. Sokolowski, S. Weiß, F. S. Tautz, and S. Soubatch, "Long Vertical Distance Bonding of the Hexagonal Boron Nitride Monolayer on the Cu(111) Surface", J. Phys. Chem. C **121**, 23964 (2017).

[41] S. S. Labana and L. L. Labana, "Quinacridones", Chem. Rev. **67**, 1 (1967).

[42] A. Inc., *Graphics Layout Engine 4.2*, http://glx.sourceforge.net/, 2010.

[43] A. Bondi, "Van der Waals Volumes and Radii", J. Phys. Chem. **68**, 441 (1964).

[44] J. Mizuguchi, T. Sasaki, and K. Tojo, "Refinement of the crystal structure of 5,7,12,14-tetrahy-dro[2,3-b]-quinolinoacridine (γ-form), $C_{20}H_{12}N_2O_2$, at 223 K", Z. Kristallogr. N. Cryst. **217**, 249 (2002).

[45] C. F. H. and S. R. W., "Vacuum sublimation and crystallography of quinacridones", J. Appl. Crystallogr. **4**, 506 (1971).

[46] S. Q. Lomax, "Phthalocyanine and quinacridone pigments: their history, properties and use", Stud. Conserv. **50**, 19 (2005).

[47] E. B. Faulkner and R. J. Schwartz, *High Performance Pigments* (Wiley-VCH, 2009).

[48] P. Pollak, "New routes in the synthesis of quinacridone pigments", Progress in Organic Coatings **5**, 245 (1977).

[49] Merck, *Aniline*, `https://www.sigmaaldrich.com/DE/de/product/sial/242284`, Accessed: 2024-04-30.

[50] Merck, *Diethyl succinate*, `https://www.sigmaaldrich.com/DE/de/product/mm/800680`, Accessed: 2024-04-30.

[51] GESTIS, *Quinacridone*, `https://gestis.dguv.de/data?name=491348&lang=en`, Accessed: 2024-06-03.

[52] H. Zollinger, *Color Chemistry; Syntheses, Properties, and Applications of Organic Dyes and Pigments* (WILEY-VCH, Weinheim, 2003).

[53] N. Panina, F. J. J. Leusen, F. F. B. J. Janssen, P. Verwer, H. Meekes, E. Vlieg, and G. Deroover, "Crystal Structure prediction of Organic Pigments: Quinacridone as an example", J. Appl. Crystallogr. **40**, 105 (2007).

[54] G. D. Potts, W. Jones, J. F. Bullock, S. J. Andrews, and S. J. Maginn, "The Crystal Structure of Quinacridone: An archetypal pigment", J. Chem. Soc., Chem. Commun., 2565 (1994).

[55] T. E. Gorelik, C. Czech, S. M. Hammer, and M. U. Schmidt, "Crystal structure of disordered nanocrystalline α^{II}-quinacridone determined by electron diffraction", CrystEngComm **18**, 529 (2016).

[56] K. Momma and F. Izumi, "*VESTA3* for three-dimensional visualization of crystal, volumetric and morphology data", J. Appl. Crystallogr. **44**, 1272 (2011).

[57] E. Karl-Heinz, "Molecular Chirality at Surfaces", Phys. Status Solidi B **249**, 2057 (2012).

[58] R. Raval, "Chiral expression from molecular assemblies at metal surfaces: insights from surface science techniques", Chem. Soc. Rev. **38**, 707 (2009).

[59] C. P. Brock, W. B. Schweizer, and J. D. Dunitz, "On the Validity of Wallach's Rule: On the Density and Stability of Racemic Crystals compared with their Chiral Counterparts", J. Am. Chem. Soc. **113**, 9811 (1991).

[60] S. Dutta and A. J. Gellman, "Enantiomer Surface Chemistry: Conglomerate versus Racemate Formation on Surfaces", Chem. Soc. Rev. **46**, 7787 (2017).

[61] G. Binnig, H. Rohrer, C. Gerber, and E. Weibel, "Surface Studies by Scanning Tunneling Microscopy", Phys. Rev. Lett. **49**, 57 (1982).

[62] R. Wiesendanger, *Scanning Probe Microscopy and Spectroscopy - Methods and Applications* (Cambridge University Press, 1994).

[63] K. W. Kolasinski, *Surface Science - Foundations of Catalysis and Nanoscience*, Second Edition (WILEY-VCH, Weinheim, 2008).

[64] D. P. Woodruff and T. A. Delchar, *Modern Techniques of Surface Science* (University Press, Cambridge, 1999).

[65] C. J. Chen, *Introduction to Scanning Tunneling Microscopy* (Oxford University Press, Mar. 2021).

[66] J. Tersoff and D. R. Hamann, "Theory of the scanning tunneling microscope", Phys. Rev. B **31**, 805 (1985).

[67] C. J. Chen, "Tunneling matrix elements in three-dimensional space: The derivative rule and the sum rule", Phys. Rev. B **42**, 8841 (1990).

[68] P. K. Hansma and J. Tersoff, "Scanning tunneling microscopy", J. Appl. Phys. **61**, R1 (1987).

[69] D. Lüftner, S. Refaely-Abramson, M. Pachler, R. Resel, M. G. Ramsey, L. Kronik, and P. Puschnig, "Experimental and Theoretical Electronic Structure of Quinacridone", Phys. Rev. B **90**, 075204 (2014).

[70] L. Gross, N. Moll, F. Mohn, A. Curioni, G. Meyer, F. Hanke, and M. Persson, "High-Resolution Molecular Orbital Imaging Using a *p*-Wave STM Tip", Phys. Rev. Lett. **107**, 086101 (2011).

[71] P. Hapala, G. Kichin, C. Wagner, F. S. Tautz, R. Temirov, and P. Jelínek, "Mechanism of high-resolution STM/AFM imaging with functionalized tips", Phys. Rev. B **90**, 085421 (2014).

[72] C. Davisson and L. H. Germer, "The Scattering of Electrons by a Single Crystal of Nickel", Nature **119**, 558 (1927).

[73] C. H. Schmitz, "On-surface synthesis of one- and two-dimensional polymers: polyamide films on Ag(111)", PhD thesis (Universität Bonn, 2011).

[74] W. Moritz and M. Hove, *Surface Structure Determination by LEED and X-rays* (Cambridge University Press, Aug. 2022).

[75] M. Horn-von Hoegen, "Growth of semiconductor layers studied by spot profile analysing low energy electron diffraction", Z. Kristallogr. – Cryst. Mater. **214**, 684 (1999).

[76] J. Ikonomov, *MCPDeskew*, Universität Bonn, 2010.

[77] G. Ertl and J. Küppers, *Low Energy Elctrons and Surface Chemistry*, 2nd (Wiley-VCH, Weinheim, 1985).

[78] A. R. Eberle, "Growing low-dimensional supramolecular crystals via Organic Solid-Solid Wetting Deposition: physico-chemical basis, structure analysis, and doping of graphene", PhD thesis (Universität München, 2018).

[79] B. Scherwitzl, C. Röthel, A. O. F. Jones, B. Kunert, I. Salzmann, R. Resel, G. Leising, and A. Winkler, "Idiosyncrasies of Physical Vapor Deposition Processes from Various Knudsen

Cells for Quinacridone Thin Film Growth on Silicon Dioxide", J. Phys. Chem. C **119**, 20900 (2015).

[80] B. Scherwitzl, R. Lassnig, M. Truger, R. Resel, G. Leising, and A. Winkler, "Adsorption, desorption, and film formation of quinacridone and its thermal cracking product indigo on clean and carbon-covered silicon dioxide surfaces", J. Chem. Phys. **145**, 094702 (2016).

[81] R. Priya, Philipps-Universität Marburg, Surface and Interface Science, *personal communication*, 2023.

[82] R. Priya, W. Wu, K. Jin, and P. Jakob, "Homo- and Heterochiral Phases of Quinacridone Monolayers on Ag(110) and Ag(111)", DPG Tagung, Session O28, Dresden (2023).

[83] H. Cun, Y. Wang, B. Yang, L. Zhang, S. Du, Y. Wang, K.-H. Ernst, and H.-J. Gao, "Homochiral Recognition among Organic Molecules on Cu(110)", Langmuir **26**, 3402 (2010).

[84] F. Lin, D. Y. Zhong, L. F. Chi, K. Ye, Y. Wang, and H. Fuchs, "Temperature-tuned Organic Monolayer Growth: N, N′-di(n-butyl)-Quinacridone on Ag(110)", Phys. Rev. B **73**, 235420 (2006).

[85] F. Lin, Z. Fang, S. Qu, S. Huang, W. Song, L. Chi, and X. Zhu, "Homogeneous Epitaxial Growth of N,N ′-di(n-butyl)quinacridone Thin Films on Ag(110)", J. Nanosci. Nanotechnol. **10**, 7162 (2010).

[86] D. Qiu, K. Ye, Y. Wang, B. Zou, X. Zhang, S. Lei, and L. Wan, "In Situ Scanning Tunneling Microscopic Investigation of the Two-Dimensional Ordering of Different Alkyl Chain-Substituted Quinacridone Derivatives at Highly Oriented Pyrolytic Graphite/Solution Interface", Langmuir **19**, 678 (2003).

[87] D. X. Shi, W. Ji, X. Lin, X. B. He, J. C. Lian, L. Gao, J. M. Cai, H. Lin, S. X. Du, F. Lin, C. Seidel, L. F. Chi, W. A. Hofer, H. Fuchs, and H.-J. Gao, "Role of Lateral Alkyl Chains in Modulation of Molecular Structures on Metal Surfaces", Phys. Rev. Lett. **96**, 226101 (2006).

[88] X. Yang, Z. Mu, Z. Wang, X. Zhang, J. Wang, and Y. Wang, "STM Study on Quinacridone Derivative Assemblies: Modulation of the Two-dimensional Structure by Coadsorption with Dicarboxylic Acids", Langmuir **21**, 7225 (2005).

[89] X. Yang, J. Wang, X. Zhang, Z. Wang, and Y. Wang, "STM Study on 2D Molecular Assemblies of Luminescent Quinacridone Derivatives: Structure Fine-tuned by Introducing Bulky Substitutes and Co-adsorption with Monofunctional/Bifunctional Acid", Langmuir **23**, 1287 (2007).

[90] B. Yang, Y. Wang, H. Cun, S. Du, M. Xu, Y. Wang, K.-H. Ernst, and H.-J. Gao, "Direct Observation of Enantiospecific Substitution in a Two-Dimensional Chiral Phase Transition", J. Am. Chem. Soc. **132**, 10440 (2010).

[91] C. Yang, J. Zhu, X. Wu, H. Zhang, F. Lin, and Z. Fang, "Self-Assembly of N,N′-Di(n-butyl)-1,3,8,10-tetramethylquinacridone Governed by Metallic Surface Features of a Ag(110) Substrate", J. Phys. Chem. C **125**, 10151 (2021).

[92] X. B. He, J. M. Cai, D. X. Shi, Y. Wang, and H.-J. Gao, "Epitaxial Growth of Quinacridone Derivative on Ag(110) Studied by Scanning Tunneling Microscopy", J. Phys. Chem. C **112**, 7138 (2008).

[93] R. Bretel, "Design and study of low dimensional systems decoupled from metallic surfaces for nano-optics", PhD thesis (Université Paris-Saclay, CNRS, Institut des Sciences Moléculaires, 2021).

[94] A. P. H. J. Schenning and E. W. Meijer, "Supramolecular electronics; nanowires from self-assembled π-conjugated systems", Chem. Commun., 3245 (2005).

[95] E. Barrigón, M. Heurlin, Z. Bi, B. Monemar, and L. Samuelson, "Synthesis and Applications of III–V Nanowires", Chem. Rev. **119**, 9170 (2019).

[96] N. Oncel, "Atomic chains on surfaces", J. Phys.: Condens. Matter **20**, 393001 (2008).

[97] A. G. Syromyatnikov, S. V. Kolesnikov, A. M. Saletsky, and A. L. Klavsyuk, "Formation and properties of metallic atomic chains and wires", Phys.-Usp. **64**, 671 (2021).

[98] S. Fölsch, P. Hyldgaard, R. Koch, and K. H. Ploog, "Quantum Confinement in Monatomic Cu Chains on Cu(111)", Phys. Rev. Lett. **92**, 056803 (2004).

[99] S. Loth, S. Baumann, C. P. Lutz, D. M. Eigler, and A. J. Heinrich, "Bistability in Atomic-Scale Antiferromagnets", Science **335**, 196 (2012).

[100] C. F. Hirjibehedin, C. P. Lutz, and A. J. Heinrich, "Spin Coupling in Engineered Atomic Structures", Science **312**, 1021 (2006).

[101] P. Gambardella, M. Blanc, H. Brune, K. Kuhnke, and K. Kern, "One-dimensional metal chains on Pt vicinal surfaces", Phys. Rev. B **61**, 2254 (2000).

[102] P. Gambardella and K. Kern, "Ni growth on vicinal Pt(111): low temperature exchange and formation of ordered surface alloys", Surf. Sci. **475**, L229 (2001).

[103] P. Gambardella, A. Dallmeyer, K. Maiti, M. C. Malagoli, W. Eberhardt, K. Kern, and C. Carbone, "Ferromagnetism in one-dimensional monatomic metal chains", Nature **416**, 301 (2002).

[104] N. Zaki, D. Potapenko, P. D. Johnson, and R. M. Osgood, "Atom-wide Co wires on Cu(775) at room temperature", Phys. Rev. B **80**, 155419 (2009).

[105] J. Schoiswohl, F. Mittendorfer, S. Surnev, M. G. Ramsey, J. N. Andersen, and F. P. Netzer, "Chemical Reactivity of Ni-Rh Nanowires", Phys. Rev. Lett. **97**, 126102 (2006).

[106] J. Guo, Y. Mo, E. Kaxiras, Z. Zhang, and H. H. Weitering, "Formation of monatomic Fe chains on vicinal Cu(111) surfaces: An atomistic view", Phys. Rev. B **73**, 193405 (2006).

[107] J. H. G. Owen, K. Miki, and D. R. Bowler, "Self-assembled nanowires on semiconductor surfaces", J. Mater. Sci. **41**, 4568 (2006).

[108] A. Baski, K. Saoud, and K. Jones, "1-D nanostructures grown on the Si(5 5 12) surface", Appl. Surf. Sci. **182**, Proceedings of the International Workshop on Nanomaterials, 216 (2001).

[109] S. Hasegawa, "Quasi-one-dimensional metals on semiconductor surfaces with defects", Journal of Physics: Condensed Matter **22**, 084026 (2010).

[110] D. H. Wei, C. L. Gao, K. Zakeri, and M. Przybylski, "Pd Atomic Chain Formation as a Result of Submonolayer Deposition of 3*d* Metals on Pd(110)", Phys. Rev. Lett. **103**, 225504 (2009).

[111] L. Yan, M. Przybylski, Y. Lu, W. H. Wang, J. Barthel, and J. Kirschner, "Fabrication and uniaxial magnetic anisotropy of Co nanowires on a Pd(110) surface", Appl. Phys. Lett. **86**, 102503 (2005).

[112] F. J. Himpsel and J. E. Ortega, "Edge state and terrace state for Cu on W(331) and W(110)", Phys. Rev. B **50**, 4992 (1994).

[113] S. M. York and F. M. Leibsle, "Co nanowire arrays on N-terminated Cu(110) surfaces", Phys. Rev. B **64**, 033411 (2001).

[114] M. Koepf, F. Chérioux, J. A. Wytko, and J. Weiss, "1D and 3D surface-assisted self-organization", Coord. Chem. Rev. **256**, 2872 (2012).

[115] C. Wang, H. Zhang, and L. Chi, "Covalently Bonded Organic Structures via On-Surface Synthesis", in *Supramolecular Chemistry on Surfaces* (John Wiley & Sons, Ltd, 2022) Chap. 7.

[116] Z. Chen, A. Narita, and K. Müllen, "Graphene Nanoribbons: On-Surface Synthesis and Integration into Electronic Devices", Adv. Mater. **32**, 2001893 (2020).

[117] D. G. de Oteyza, A. García-Lekue, M. Vilas-Varela, N. Merino-Díez, E. Carbonell-Sanromà, M. Corso, G. Vasseur, C. Rogero, E. Guitián, J. I. Pascual, J. E. Ortega, Y. Wakayama, and D. Peña, "Substrate-Independent Growth of Atomically Precise Chiral Graphene Nanoribbons", ACS Nano **10**, 9000 (2016).

[118] C. Moreno, M. Paradinas, M. Vilas-Varela, M. Panighel, G. Ceballos, D. Peña, and A. Mugarza, "On-surface synthesis of superlattice arrays of ultra-long graphene nanoribbons", Chem. Commun. **54**, 9402 (2018).

[119] L. Talirz, H. Söde, T. Dumslaff, S. Wang, J. R. Sanchez-Valencia, J. Liu, P. Shinde, C. A. Pignedoli, L. Liang, V. Meunier, N. C. Plumb, M. Shi, X. Feng, A. Narita, K. Müllen, R. Fasel, and P. Ruffieux, "On-Surface Synthesis and Characterization of 9-Atom Wide Armchair Graphene Nanoribbons", ACS Nano **11**, 1380 (2017).

[120] J. Cai, P. Ruffieux, R. Jaafar, M. Bieri, T. Braun, S. Blankenburg, M. Muoth, A. P. Seitsonen, M. Saleh, X. Feng, K. Müllen, and R. Fasel, "Atomically precise bottom-up fabrication of graphene nanoribbons", Nature **466**, 470 (2010).

[121] L. Talirz, P. Ruffieux, and R. Fasel, "On-Surface Synthesis of Atomically Precise Graphene Nanoribbons", Adv. Mater. **28**, 6222 (2016).

[122] A. Narita, X.-Y. Wang, X. Feng, and K. Müllen, "New advances in nanographene chemistry", Chem. Soc. Rev. **44**, 6616 (2015).

[123] L. Lafferentz, F. Ample, H. Yu, S. Hecht, C. Joachim, and L. Grill, "Conductance of a Single Conjugated Polymer as a Continuous Function of Its Length", Science **323**, 1193 (2009).

[124] D. Zhong, J.-H. Franke, S. K. Podiyanachari, T. Blömker, H. Zhang, G. Kehr, G. Erker, H. Fuchs, and L. Chi, "Linear Alkane Polymerization on a Gold Surface", Science **334**, 213 (2011).

[125] Z. Hao, J. Zhang, M. Xie, X. Li, L. Wang, Y. Liu, K. Niu, J. Wang, L. Song, T. Cheng, H. Zhang, and L. Chi, "From n-alkane to polyacetylene on Cu (110): Linkage modulation in chain growth", Sci. China: Chem. **65**, 733 (2022).

[126] L. Giovanelli, R. Pawlak, F. Hussein, O. MacLean, F. Rosei, W. Song, C. Pigot, F. Dumur, D. Gigmes, Y. Ksari, F. Bondino, E. Magnano, E. Meyer, and S. Clair, "On-Surface Synthesis of Unsaturated Hydrocarbon Chains through C-S Activation", Chem. - Eur. J. **28**, e202200809 (2022).

[127] Z. Yang, C. Lotze, K. J. Franke, and J. I. Pascual, "Metal–Organic Superlattices Induced by Long-Range Repulsive Interactions on a Metal Surface", J. Phys. Chem. C **125**, 18494 (2021).

[128] C. J. Villagomez, O. Guillermet, S. Goudeau, F. Ample, H. Xu, C. Coudret, X. Bouju, T. Zambelli, and S. Gauthier, "Self-assembly of enantiopure domains: The case of indigo on Cu(111)", J. Chem. Phys. **132**, 074705 (2010).

[129] G. Chakraborty, I.-H. Park, R. Medishetty, and J. J. Vittal, "Two-Dimensional Metal-Organic Framework Materials: Synthesis, Structures, Properties and Applications", Chem. Rev. **121**, 3751 (2021).

[130] M. Dudev, J. Wang, T. Dudev, and C. Lim, "Factors Governing the Metal Coordination Number in Metal Complexes from Cambridge Structural Database Analyses", J. Phys. Chem. B **110**, 1889 (2006).

[131] V. M. Santhini, C. Wäckerlin, A. Cahlík, M. Ondráček, S. Pascal, A. Matěj, O. Stetsovych, P. Mutombo, P. Lazar, O. Siri, and P. Jelínek, "1D Coordination π–d Conjugated Polymers with Distinct Structures Defined by the Choice of the Transition Metal: Towards a New Class of Antiaromatic Macrocycles", Angew. Chem., Int. Ed. **60**, 439 (2021).

[132] S. Tait, A. Langner, N. Lin, S. Stepanow, C. Rajadurai, M. Ruben, and K. Kern, "One-Dimensional Self-Assembled Molecular Chains on Cu(100): Interplay between Surface Assisted Coordination Chemistry and Substrate Commensurability", J. Phys. Chem. C **111**, 10982 (2007).

[133] J. Ren, D.-L. Bao, L. Dong, L. Gao, R. Wu, L. Yan, A. Wang, J. Yan, Y. Wang, Q. Huan, J.-T. Sun, S. Du, and H.-J. Gao, "Lattice-Directed Construction of Metal–Organic Molecular Wires of Pentacene on the Au(110) Surface", J. Phys. Chem. C **121**, 21650 (2017).

[134] X. Yu, Q. Sun, M. Liu, W. Du, Y. Liu, L. Cai, Z. Zha, J. Pan, F. Kang, W. Gao, D. Yang, X. Qiu, and W. Xu, "Lattice-Directed Selective Synthesis of Acetylenic and Diacetylenic Organometallic Polyynes", Chem. Mater. **34**, 1770 (2022).

[135] S. Lukas, G. Witte, and C. Wöll, "Novel Mechanism for Molecular Self-Assembly on Metal Substrates: Unidirectional Rows of Pentacene on Cu(110) Produced by a Substrate-Mediated Repulsion", Phys. Rev. Lett. **88**, 028301 (2001).

[136] J. V. Barth, "Molecular Architectonic on Metal Surfaces", Annu. Rev. Phys. Chem. **58**, 375 (2007).

[137] A. Schiffrin, A. Riemann, W. Auwärter, Y. Pennec, A. Weber-Bargioni, D. Cvetko, A. Cossaro, A. Morgante, and J. V. Barth, "Zwitterionic Self-assembly of L-methionine Nanogratings on the Ag(111) Surface", Proc. Natl. Acad. Sci. **104**, 5279 (2007).

[138] A. Schiffrin, J. Reichert, W. Auwärter, G. Jahnz, Y. Pennec, A. Weber-Bargioni, V. S. Stepanyuk, L. Niebergall, P. Bruno, and J. V. Barth, "Self-aligning Atomic Strings in Surface-supported Biomolecular Gratings", Phys. Rev. B **78**, 035424 (2008).

[139] Q. Chen and N. V. Richardson, "Enantiomeric interactions between nucleic acid bases and amino acids on solid surfaces", Nat. Mater. **2**, 324 (2003).

[140] F. Klappenberger, M. E. Cañas-Ventura, S. Clair, S. Pons, U. Schlickum, Z.-R. Qu, H. Brune, K. Kern, T. Strunskus, C. Wöll, A. Comisso, A. De Vita, M. Ruben, and J. V. Barth, "Conformational Adaptation in Supramolecular Assembly on Surfaces", ChemPhysChem **8**, 1782 (2007).

[141] F. Klappenberger, M. E. Cañas-Ventura, S. Clair, S. Pons, U. Schlickum, Z.-R. Qu, T. Strunskus, A. Comisso, C. Wöll, H. Brune, K. Kern, A. De Vita, M. Ruben, and J. V. Barth, "Does the Surface Matter? Hydrogen-Bonded Chain Formation of an Oxalic Amide Derivative in a Two- and Three-Dimensional Environment", ChemPhysChem **9**, 2522 (2008).

[142] Z. Yang, C. Lotze, M. Corso, S. Baum, K. J. Franke, and J. I. Pascual, "Direct Imaging of the Induced-Fit Effect in Molecular Self-Assembly", Small **15**, 1804713 (2019).

[143] J. Lipton-Duffin, J. Miwa, S. G. Urquhart, G. Contini, A. Cossaro, L. Casalis, J. V. Barth, L. Floreano, A. Morgante, and F. Rosei, "Binding Geometry of Hydrogen-Bonded Chain Motif in Self-Assembled Gratings and Layers on Ag(111)", Langmuir **28**, 14291 (2012).

[144] J. Reichert, A. Schiffrin, W. Auwärter, A. Weber-Bargioni, M. Marschall, M. Dell'Angela, D. Cvetko, G. Bavdek, A. Cossaro, A. Morgante, and J. V. Barth, "L-Tyrosine on Ag(111): Universality of the Amino Acid 2D Zwitterionic Bonding Scheme?", ACS Nano **4**, 1218 (2010).

[145] L. Cheng, "Role of Hydrogen Bonding in the Formation of Adenine Chains on Cu(110) Surfaces", Materials **9**, 1016 (2016).

[146] J. V. Barth, J. Weckesser, G. Trimarchi, M. Vladimirova, A. De Vita, C. Cai, H. Brune, P. Günter, and K. Kern, "Stereochemical Effects in Supramolecular Self-Assembly at Surfaces: 1-D versus 2-D Enantiomorphic Ordering for PVBA and PEBA on Ag(111)", J. Am. Chem. Soc. **124**, 7991 (2002).

[147] J. Schnadt, E. Rauls, W. Xu, R. T. Vang, J. Knudsen, E. Lægsgaard, Z. Li, B. Hammer, and F. Besenbacher, "Extended One-Dimensional Supramolecular Assembly on a Stepped Surface", Phys. Rev. Lett. **100**, 046103 (2008).

[148] J. Kröger, N. Néel, H. Jensen, R. Berndt, R. Rurali, and N. Lorente, "Molecules on vicinal Au surfaces studied by scanning tunnelling microscopy", J. Phys.: Condens. Matter **18**, S51 (2006).

[149] M. E. Cañas-Ventura, W. Xiao, D. Wasserfallen, K. Müllen, H. Brune, J. V. Barth, and R. Fasel, "Self-Assembly of Periodic Bicomponent Wires and Ribbons", Angew. Chem., Int. Ed. **46**, 1814 (2007).

[150] S. Fatayer, M. J. Prieto, R. Landers, and A. de Siervo, "Coverage-dependent study of nickel tetraphenyl-porphyrin on Au(332) and Au(788)", Surf. Sci. **723**, 122105 (2022).

[151] O. Bauer, G. Mercurio, M. Willenbockel, W. Reckien, C. Heinrich Schmitz, B. Fiedler, S. Soubatch, T. Bredow, F. S. Tautz, and M. Sokolowski, "Role of functional groups in surface bonding of planar π-conjugated molecules", Phys. Rev. B **86**, 235431 (2012).

[152] J. Repp, G. Meyer, S. Paavilainen, F. E. Olsson, and M. Persson, "Scanning Tunneling Spectroscopy of Cl Vacancies in NaCl Films: Strong Electron-Phonon Coupling in Double-Barrier Tunneling Junctions", Phys. Rev. Lett. **95**, 225503 (2005).

[153] S. Mohr, T. Xu, T. Döpper, M. Laurin, A. Görling, and J. Libuda, "Molecular Orientation and Structural Transformations in Phthalic Anhydride Thin Films on MgO(100)/Ag(100)", Langmuir **31**, 7806 (2015).

[154] C. Schuschke, M. Schwarz, C. Hohner, T. N. Silva, and J. Libuda, "Phosphonic Acids on Well-Ordered CoO Surfaces: The Binding Motif Depends on the Surface Structure", J. Phys. Chem. C **122**, 16221 (2018).

[155] A. Matković, A. Çiçek, M. Kratzer, B. Kaufmann, A. Thomas, Z. Chen, O. Siri, C. Becker, and C. Teichert, "Growth morphologies of dihydro-tetraaza-acenes on c-plane sapphire", Surf. Sci. **678**, 128 (2018).

[156] S. Freund, A. Hinaut, N. Marinakis, E. C. Constable, E. Meyer, C. E. Housecroft, and T. Glatzel, "Comparing a porphyrin- and a coumarin-based dye adsorbed on NiO(001)", Beilstein J. Nanotechnol. **10**, 874 (2019).

[157] D. A. Duncan, J. H. K. Pfisterer, P. S. Deimel, R. G. Acres, M. Fritton, P. Feulner, J. V. Barth, and F. Allegretti, "Formation of a thermally stable bilayer of coadsorbed intact and deprotonated thymine exploiting the surface corrugation of rutile TiO2(110)", Phys. Chem. Chem. Phys. **18**, 20433 (2016).

[158] C. Brülke, T. Heepenstrick, I. Krieger, B. Wolff, X. Yang, A. Shamsaddinlou, S. Weiß, F. C. Bocquet, F. S. Tautz, S. Soubatch, and M. Sokolowski, "Quantitative analysis of the electronic decoupling of an organic semiconductor molecule at a metal interface by a monolayer of hexagonal boron nitride", Phys. Rev. B **99**, 121404 (2019).

[159] F. Schulz, R. Drost, S. K. Hämäläinen, and P. Liljeroth, "Templated Self-Assembly and Local Doping of Molecules on Epitaxial Hexagonal Boron Nitride", ACS Nano **7**, 11121 (2013).

[160] C. Simbrunner, G. Hernandez-Sosa, M. Oehzelt, T. Djuric, I. Salzmann, M. Brinkmann, G. Schwabegger, I. Watzinger, H. Sitter, and R. Resel, "Epitaxial growth of sexithiophene on mica surfaces", Phys. Rev. B **83**, 115443 (2011).

[161] Y. Li, Y. Li, Y. Wei, W. Shen, S. Wu, C. Hu, X. Hu, R. Zimmerleiter, M. Hohage, and L. Sun, "Reflectance and fluorescence spectroscopy of ultrathin PTCDI-C_5 films on muscovite mica", Synth. Met. **228**, 105 (2017).

[162] P. Rahe, M. Nimmrich, A. Greuling, J. Schütte, I. G. Stará, J. Rybáček, G. Huerta-Angeles, I. Starý, M. Rohlfing, and A. Kühnle, "Toward Molecular Nanowires Self-Assembled on an Insulating Substrate: Heptahelicene-2-carboxylic acid on Calcite ($10\bar{1}4$)", J. Phys. Chem. C **114**, 1547 (2010).

[163] M. Kittelmann, P. Rahe, M. Nimmrich, C. M. Hauke, A. Gourdon, and A. Kühnle, "On-Surface Covalent Linking of Organic Building Blocks on a Bulk Insulator", ACS Nano **5**, 8420 (2011).

[164] R. Bennewitz, V. Barwich, M. Bammerlin, C. Loppacher, M. Guggisberg, A. Baratoff, E. Meyer, and H.-J. Güntherodt, "Ultrathin films of NaCl on Cu(111): a LEED and dynamic force microscopy study", Surf. Sci. **438**, 289 (1999).

[165] M. Pivetta, F. Patthey, M. Stengel, A. Baldereschi, and W.-D. Schneider, "Local work function Moiré pattern on ultrathin ionic films: NaCl on Ag(100)", Phys. Rev. B **72**, 115404 (2005).

[166] H.-C. Ploigt, C. Brun, M. Pivetta, F. Patthey, and W.-D. Schneider, "Local work function changes determined by field emission resonances: NaCl/Ag(100)", Phys. Rev. B **76**, 195404 (2007).

[167] E. L. Moal, M. Müller, O. Bauer, and M. Sokolowski, "Misfit driven azimuthal orientation of NaCl domains on Ag(100)", Surf. Sci. **603**, 2434 (2009).

[168] S. Katano and Y. Uehara, "In Situ Observation of Atomic-Scale Growth of a NaCl Thin Crystal on Au(111) by Scanning Tunneling Microscopy", J. Phys. Chem. C **124**, 20184 (2020).

[169] A. J. Weymouth, M. Persson, and F. J. Giessibl, "Revealing buckling of an apparently flat monolayer of NaCl on Pt(111)", Phys. Rev. B **105**, 035412 (2022).

[170] X. Tan, J. Pan, J. Feng, Z. Zhang, M. Liu, D. Ma, and X. Qiu, "One-Dimensional Periodic Buckling at a Symmetry-Incompatible Heterointerface of the NaCl(001) Monolayer on Ir(111)", J. Phys. Chem. C **127**, 6109 (2023).

[171] C. Loppacher, U. Zerweck, and L. M. Eng, "Kelvin probe force microscopy of alkali chloride thin films on Au(111)", Nanotechnology **15**, S9 (2003).

[172] F. Reniers, D. Fairbrother, S. Wu, and J. Lipkowski, "On the electrochemical adsorption of KBr on gold (100); a LEED–Auger study", Surf. Sci. **433-435**, 12 (1999).

[173] C. Loppacher, U. Zerweck, L. M. Eng, S. Gemming, G. Seifert, C. Olbrich, K. Morawetz, and M. Schreiber, "Adsorption of PTCDA on a partially KBr covered Ag(111) substrate", Nanotechnology **17**, 1568 (2006).

[174] T. Leoni, L. Nony, E. Zaborova, S. Clair, F. Fagès, F. Para, A. Ranguis, C. Becker, and C. Loppacher, "Stereoisomeric selection upon adsorption: A structural and optical study of curcuminoid derivatives on ultrathin films of KCl on Au(111) and on bulk KCl(001)", Phys. Rev. B **104**, 205415 (2021).

[175] K.-F. Braun, D. Farias, S. Fölsch, and K.-H. Rieder, "Fractal growth of LiF on Ag(111) studied by low-temperature STM", Surf. Sci. **454-456**, 750 (2000).

[176] V. Romankov and J. Dreiser, "Morphology of ultrathin lithium fluoride deposited on Ag(100): Dendrites versus islands", Phys. Rev. B **104**, 195401 (2021).

[177] A. Kikas, V. Kisand, T. Käämbre, R. Ruus, E. Nõmmiste, M. Hirsimäki, M. Valden, E. Kukk, H. Aksela, and S. Aksela, "Insulating properties of ultrathin KF layers on Cu(100): Resonant Auger spectroscopy", Surf. Sci. **584**, 49 (2005).

[178] A. Bera and K. Morgenstern, "In Situ Growth and Bias-Dependent Modification of NaBr Ionic Layers on Ag(111)", J. Phys. Chem. C **126**, 10610 (2022).

[179] G. Cabailh, C. R. Henry, and C. Barth, "Thin NaCl films on silver (001): island growth and work function", New J. Phys. **14**, 103037 (2012).

[180] S. A. Burke, J. M. Topple, and P. Grütter, "Molecular dewetting on insulators", J. Phys.: Condens. Matter **21**, 423101 (2009).

[181] E. Le Moal, M. Müller, O. Bauer, and M. Sokolowski, "Stable and metastable phases of PTCDA on epitaxial NaCl films on Ag(100)", Phys. Rev. B **82**, 045301 (2010).

[182] F. Rossel, M. Pivetta, F. Patthey, E. Ćavar, A. P. Seitsonen, and W.-D. Schneider, "Growth and characterization of fullerene nanocrystals on NaCl/Au(111)", Phys. Rev. B **84**, 075426 (2011).

[183] Y. Wang, J. Kröger, R. Berndt, and H. Tang, "Molecular Nanocrystals on Ultrathin NaCl Films on Au(111)", J. Am. Chem. Soc. **132**, 12546 (2010).

[184] F. Balzer, R. Sun, J. Parisi, H.-G. Rubahn, A. Lützen, and M. Schiek, "Epitaxial growth of a methoxy-functionalized quaterphenylene on alkali halide surfaces", Thin Solid Films **597**, 104 (2015).

[185] N. Yoshimoto, T. Sato, Y. Saito, and S. Ogawa, "Epitaxial Relationships of Para-Sexiphenyl Thin Films on Alkali Halide Substrates", Mol. Cryst. Liq. Cryst. **425**, 1 (2004).

[186] P. Frank, G. Hernandez-Sosa, H. Sitter, and A. Winkler, "Search for a wetting layer in thin film growth of para-hexaphenyl on KCl(001)", Thin Solid Films **516**, 2939 (2008).

[187] S. A. Burke, W. Ji, J. M. Mativetsky, J. M. Topple, S. Fostner, H.-J. Gao, H. Guo, and P. Grütter., "Strain Induced Dewetting of a Molecular System: Bimodal Growth of PTCDA on NaCl", Phys. Rev. Lett. **100**, 186104 (2008).

[188] T. Dienel, C. Loppacher, S. C. B. Mannsfeld, R. Forker, and T. Fritz, "Growth-Mode-Induced Narrowing of Optical Spectra of an Organic Adlayer", Adv. Mater. **20**, 959 (2008).

[189] A. Hinaut, K. Lekhal, G. Aivazian, S. Bataillé, A. Gourdon, D. Martrou, and S. Gauthier, "NC-AFM Study of the Adsorption of Hexamethoxytriphenylene on KBr(001)", J. Phys. Chem. C **115**, 13338 (2011).

[190] L. Gross, F. Mohn, N. Moll, P. Liljeroth, and G. Meyer, "The Chemical Structure of a Molecule Resolved by Atomic Force Microscopy", Science **325**, 1110 (2009).

[191] Q. Guo, A. Paulheim, M. Sokolowski, H. Aldahhak, E. Rauls, and W. G. Schmidt, "Adsorption of PTCDA on Terraces and at Steps Sites of the KCl(100) Surface", J. Phys. Chem. C **118**, 29911 (2014).

[192] L. Ramoino, M. von Arx, S. Schintke, A. Baratoff, H.-J. Güntherodt, and T. Jung, "Layer-selective epitaxial self-assembly of porphyrins on ultrathin insulators", Chem. Phys. Lett. **417**, 22 (2006).

[193] C. Barth, M. Gingras, A. S. Foster, A. Gulans, G. Félix, T. Hynninen, R. Peresutti, and C. R. Henry, "Two-Dimensional Nanostructured Growth of Nanoclusters and Molecules on Insulating Surfaces", Adv. Mater. **24**, 3228 (2012).

[194] B. Hoff, M. Gingras, R. Peresutti, C. R. Henry, A. S. Foster, and C. Barth, "Mechanisms of the Adsorption and Self-Assembly of Molecules with Polarized Functional Groups on Insulating Surfaces", J. Phys. Chem. C **118**, 14569 (2014).

[195] M. Robledo, G. Pacchioni, F. Martín, M. Alcamí, and S. Díaz-Tendero, "Adsorption of Benzene on Cu(100) and on Cu(100) Covered with an Ultrathin NaCl Film: Molecule–Substrate Interaction and Decoupling", J. Phys. Chem. C **119**, 4062 (2015).

[196] B. Doppagne, M. C. Chong, H. Bulou, A. Boeglin, F. Scheurer, and G. Schull, "Electrofluorochromism at the single-molecule level", Science **361**, 251 (2018).

[197] H. Imada, K. Miwa, M. Imai-Imada, S. Kawahara, K. Kimura, and Y. Kim, "Real-space investigation of energy transfer in heterogeneous molecular dimers", Nature **538**, 364 (2016).

[198] W. Steurer, S. Fatayer, L. Gross, and G. Meyer, "Probe-based measurement of lateral single-electron transfer between individual molecules", Nature Communications **6**, 8353 (2015).

[199] I. Swart, T. Sonnleitner, and J. Repp, "Charge State Control of Molecules Reveals Modification of the Tunneling Barrier with Intramolecular Contrast", Nano Letters **11**, 1580 (2011).

[200] C. J. Villagomez, T. Zambelli, S. Gauthier, A. Gourdon, S. Stojkovic, and C. Joachim, "STM images of a large organic molecule adsorbed on a bare metal substrate or on a thin insulating layer: Visualization of HOMO and LUMO", Surf. Sci. **603**, 1526 (2009).

[201] K. Kaiser, L.-A. Lieske, J. Repp, and L. Gross, "Charge-state lifetimes of single molecules on few monolayers of NaCl", Nat. Commun. **14**, 4988 (2023).

[202] M. Hollerer, D. Lüftner, P. Hurdax, T. Ules, S. Soubatch, F. S. Tautz, G. Koller, P. Puschnig, M. Sterrer, and M. G. Ramsey, "Charge Transfer and Orbital Level Alignment at Inorganic/Organic Interfaces: The Role of Dielectric Interlayers", ACS Nano **11**, 6252 (2017).

[203] P. Hurdax, M. Hollerer, P. Puschnig, D. Lüftner, L. Egger, M. G. Ramsey, and M. Sterrer, "Controlling the Charge Transfer across Thin Dielectric Interlayers", Adv. Mater. Interfaces **7**, 2000592 (2020).

[204] W. Auwärter, "Hexagonal boron nitride monolayers on metal supports: Versatile templates for atoms, molecules and nanostructures", Surf. Sci. Rep. **74**, 1 (2019).

[205] N. Krane, C. Lotze, G. Reecht, L. Zhang, A. L. Briseno, and K. J. Franke, "High-Resolution Vibronic Spectra of Molecules on Molybdenum Disulfide Allow for Rotamer Identification", ACS Nano **12**, 11698 (2018).

[206] K. A. Cochrane, A. Schiffrin, T. S. Roussy, M. Capsoni, and S. A. Burke, "Pronounced polarization-induced energy level shifts at boundaries of organic semiconductor nanostructures", Nat. Commun. **6**, 8312 (2015).

[207] X. Yang, I. Krieger, D. Lüftner, S. Weiß, T. Heepenstrick, M. Hollerer, P. Hurdax, G. Koller, M. Sokolowski, P. Puschnig, M. G. Ramsey, F. S. Tautz, and S. Soubatch, "On the decoupling of molecules at metal surfaces", Chem. Commun. **54**, 9039 (2018).

[208] B. Yang, G. Chen, A. Ghafoor, Y. Zhang, Y. Zhang, Y. Zhang, Y. Luo, J. Yang, V. Sandoghdar, J. Aizpurua, Z. Dong, and J. G. Hou, "Sub-nanometre resolution in single-molecule photoluminescence imaging", Nat. Photonics **14**, 693 (2020).

[209] H. Imada, M. Imai-Imada, K. Miwa, H. Yamane, T. Iwasa, Y. Tanaka, N. Toriumi, K. Kimura, N. Yokoshi, A. Muranaka, M. Uchiyama, T. Taketsugu, Y. K. Kato, H. Ishihara, and Y. Kim, "Single-molecule laser nanospectroscopy with microelectron volt energy resolution", Science **373**, 95 (2021).

[210] B. Doppagne, M. C. Chong, E. Lorchat, S. Berciaud, M. Romeo, H. Bulou, A. Boeglin, F. Scheurer, and G. Schull, "Vibronic Spectroscopy with Submolecular Resolution from STM-Induced Electroluminescence", Phys. Rev. Lett. **118**, 127401 (2017).

[211] J. F. Schultz, S. Li, S. Jiang, and N. Jiang, "Optical scanning tunneling microscopy based chemical imaging and spectroscopy", J. Phys.: Condens. Matter **32**, 463001 (2020).

[212] S. Jiang, T. Neuman, R. Bretel, A. Boeglin, F. Scheurer, E. Le Moal, and G. Schull, "Many-Body Description of STM-Induced Fluorescence of Charged Molecules", Phys. Rev. Lett. **130**, 126202 (2023).

[213] C. Marquardt, A. Paulheim, M. Hochheim, T. Bredow, and M. Sokolowski, "Homogeneous and inhomogeneous line shape of the electronic excitation of a single molecule on a surface", Phys. Rev. B **104**, 045415 (2021).

[214] A. Paulheim, M. Müller, C. Marquardt, and M. Sokolowski, "Fluorescence spectroscopy of PTCDA molecules on the KCl(100) surface in the limit of low coverages: site selection and diffusion", Phys. Chem. Chem. Phys. **15**, 4906 (2013).

[215] I. Kossev, "Rastertunnelmikroskopische Untersuchungen zur Selbstorganisation und molekularen Erkennung von Tetralactam-Makrocyclen auf Oberflächen", PhD thesis (Universität Bonn, 2007).

[216] M. Sterrer, Universität Graz, Surface Science, *personal communication*, 2019.

[217] M. Mühlpointner, "Investigations on the Growth of KCl-Films on the Ag(100) Surface via SPA-LEED", BSc thesis (Universität Bonn, 2021).

[218] C. Marquardt, "Optical investigations on PTCDA on KCl(100): superradiant aggregates and single molecules", PhD thesis (Universität Bonn, 2019).

[219] C. Brülke, "Structural and electronic decoupling of a large organicmolecule from a metal surface by a single layer ofhexagonal boron nitride", PhD thesis (Universität Bonn, 2021).

[220] RHK Technology, *XPMPro, 2.0.1.5*, Chicago, United States of America.

[221] D. Nečas and P. Klapetek, "Gwyddion: An open-source Software for SPM Data Analysis", Cent. Eur. J. Phys. **10** (2011).

[222] Image-Metrology, *Scanning Probe Image Processor, 4.8.7*, Hørsholm, Denmark.

[223] P. Kury, *WinSPA Software V2.1.93*, 2022.

[224] N. Humberg, R. Bretel, A. Eslam, E. Le Moal, and M. Sokolowski, "Hydrogen-Bonded One-Dimensional Chains of Quinacridone on Ag(100) and Cu(111): The Role of Chirality and Surface Bonding", J. Phys. Chem. C **124**, 24861 (2020).

[225] S. Weigelt, C. Busse, L. Petersen, E. Rauls, B. Hammer, K. Gothelf, F. Besenbacher, and T. Linderoth, "Chiral Switching by Spontaneous Conformational Change in Adsorbed Organic Molecules", Nat. Mater. **5**, 112 (2006).

[226] N. Liu, G. R. Darling, and R. Raval, "Dynamic Chiral Flipping within Strongly Chemisorbed molecular Monolayers at Surfaces", Chem. Commun. **47**, 11324 (2011).

[227] D. E. Hooks, T. Fritz, and M. D. Ward, "Epitaxy and Molecular Organization on Solid Substrates", Adv. Mater. **13**, 227 (2001).

[228] Y. Pennec, W. Auwärter, A. Schiffrin, A. Weber-Bargioni, A. Riemann, and J. V. Barth, "Supramolecular Gratings for Tuneable Confinement of Electrons on Metal Surfaces", Nat. Nanotechnol. **2**, 99 (2007).

[229] A. Schiffrin, J. Reichert, Y. Pennec, W. Auwärter, A. Weber-Bargioni, M. Marschall, M. Dell'Angela, D. Cvetko, G. Bavdek, A. Cossaro, A. Morgante, and J. V. Barth, "Self-Assembly of L-Methionine on Cu(111): Steering Chiral Organization by Substrate Reactivity and Thermal Activation", J. Phys. Chem. C **113**, 12101 (2009).

[230] C. Stellwag, G. Held, and D. Menzel, "The Geometry of ordered Benzene Layers on Ru(001)", Surf. Sci. **325**, L379 (1995).

[231] G. Held, M. P. Bessent, S. Titmuss, and D. A. King, "Realistic Molecular Distortions and Strong Substrate Buckling induced by the Chemisorption of Benzene on Ni(111)", J. Chem. Phys. **105**, 11305 (1996).

[232] Z. V. Zheleva, T. Eralp, and G. Held, "Complete Experimental Structure Determination of the p(3×2)*pg* Phase of Glycine on Cu(110)", J. Phys. Chem. C **116**, 618 (2012).

[233] J. L. Neff, H. Söngen, R. Bechstein, P. Maass, and A. Kühnle, "Long-Range Order Induced by Intrinsic Repulsion on an Insulating Substrate", J. Phys. Chem. C **119**, 24927 (2015).

[234] L. Dong, Z. Gao, and N. Lin, "Self-assembly of Metal–Organic Coordination Structures on Surfaces", Prog. Surf. Sci. **91**, 101 (2016).

[235] T. Bald, "Test of an Ag Evaporator and the Effects of Ag Deposition on Quinacridone Superstructureson the Ag(100)-surface", BSc thesis (Universität Bonn, 2021).

[236] P. W. Voorhees, "The theory of Ostwald ripening", J. Stat. Phys. **38**, 231 (1985).

[237] J. P. Roth, "SPA-LEED Investigation on Phases of Quinacridone on the Ag(100)Surface at High Coverages", lab report: focusing laboratory course (Universität Bonn, 2022).

[238] B. Persson, "Ordered structures and phase transitions in adsorbed layers", Surf. Sci. Rep. **15**, 1 (1992).

[239] L. Kilian, A. Hauschild, R. Temirov, S. Subach, A. Schöll, A. Bendounan, F. Reinert, T.-L. Lee, F. Tautz, M. Sokolowski, and E. Umbach, "Role of Intermolecular Interactions on the Electronic and Geometric Structure of a Large π-Conjugated Molecule Adsorbed on a Metal Surface", Phys. Rev. Lett. **100**, 136103 (2008).

[240] R. Bretel, S. Le Moal, H. Oughaddou, and E. Le Moal, "Hydrogen-bonded one-dimensional molecular chains on ultrathin insulating films: Quinacridone on KCl/Cu(111)", Phys. Rev. B **108**, 125423 (2023).

[241] R. C. Weast, *CRC Handbook of Chemistry and Physics* (CRC Press, Cleveland, 1974).

[242] A. Husseen, "Alkali-Halide Thin Films: Growth, Structure and Reactivity upon Electron Irradiation", PhD thesis (Université Paris-Saclay, 2018).

[243] D. M. Roessler and W. C. Walker, "Electronic Spectra of Crystalline NaCl and KCl", Phys. Rev. **166**, 599 (1968).

[244] N. O. Lipari and A. B. Kunz, "Energy Bands for KCl", Phys. Rev. B **4**, 4639 (1971).

[245] Q. Guo, Z. Qin, C. Liu, K. Zang, Y. Yu, and G. Cao, "Bias dependence of apparent layer thickness and Moiré pattern on NaCl/Cu(001)", Surf. Sci. **604**, 1820 (2010).

[246] X. Sun, M. P. Felicissimo, P. Rudolf, and F. Silly, "NaCl multi-layer islands grown on Au(111)-$(22 \times \sqrt{3})$ probed by scanning tunneling microscopy", Nanotechnology **19**, 495307 (2008).

[247] M. Hochheim and T. Bredow, "Adsorption-induced changes of intramolecular optical transitions: PTCDA/NaCl and PTCDA/KCl", J. Comput. Chem. **36**, 1805 (2015).

[248] H. Aldahhak, W. Schmidt, and E. Rauls, "Adsorption of PTCDA on NaCl(100) and KCl(100)", Surf. Sci. **617**, 242 (2013).

[249] J. E. Goose, E. L. First, and P. Clancy, "Nature of step-edge barriers for small organic molecules", Phys. Rev. B **81**, 205310 (2010).

[250] Q. Li, X. Zou, M. Liu, J. Sun, Y. Gao, Y. Qi, X. Zhou, B. I. Yakobson, Y. Zhang, and Z. Liu, "Grain Boundary Structures and Electronic Properties of Hexagonal Boron Nitride on Cu(111)", Nano Lett. **15**, 5804 (2015).

[251] D. Kumar, J. Hellerstedt, B. Lowe, and A. Schiffrin, "Mesoscopic 2D molecular self-assembly on an insulator", Nanotechnology **34**, 205601 (2023).

[252] C. Brülke, O. Bauer, and M. M. Sokolowski, "The influence of an interfacial hBN layer on the fluorescence of an organic molecule", Beilstein J. Nanotechnol. **11**, 1663 (2020).

[253] D. M. Zimmermann, K. Seufert, L. Đorđević, T. Hoh, S. Joshi, T. Marangoni, D. Bonifazi, and W. Auwärter, "Self-assembly and spectroscopic fingerprints of photoactive pyrenyl tectons on hBN/Cu(111)", Beilstein J. Nanotechnol. **11**, 1470 (2020).

[254] C. Tegenkamp, "Vicinal surfaces for functional nanostructures", J. Phys.: Condens. Matter **21**, 013002 (2008).

[255] K. Hermann, *Surface Explorer*, `http://surfexp.fhi-berlin.mpg.de/`, Accessed: 2023-10-17.

[256] J. M. P. Bastidas, S. V. Auras, and L. B. Juurlink, "A Python script to automate STM image analysis for stepped surfaces", Appl. Surf. Sci. **567**, 150821 (2021).

[257] L. Grönwoldt, "Investigation of the step distribution on the Ag(35 1 1) surface using STM and LEED", lab report: focusing laboratory course (Universität Bonn, 2023).

[258] N. Humberg, Q. Guo, T. Bredow, and M. Sokolowski, "Growth of Hydrogen-Bonded Molecular Aggregates on a Thin Alkali Halide Layer: Quinacridone on KCl/Ag(100)", J. Phys. Chem. C **127**, 23814 (2023).

[259] N. Néel, T. Maroutian, L. Douillard, and H.-J. Ernst, "From Meandering to Faceting, Is Step Flow Growth Ever Stable?", Phys. Rev. Lett. **91**, 226103 (2003).

[260] K. Yagi, H. Minoda, and M. Degawa, "Step bunching, step wandering and faceting: self-organization at Si surfaces", Surf. Sci. Rep. **43**, 45 (2001).

[261] H. Busch and M. Henzler, "Quantitative evaluation of terrace width distributions from LEED measurements", Surf. Sci. **167**, 534 (1986).

[262] M. Giesen and G. S. Icking-Konert, "Step-Step Interaction Energy on Cu(111) Vicinal Surfaces", Surf. Rev. Lett. **06**, 27 (1999).

[263] R. Kaplan, "LEED study of the stepped surface of vicinal Si (100)", Surf. Sci. **93**, 145 (1980).

[264] B. Olshanetsky and A. Shklyaev, "Leed studies of vicinal surfaces of silicon", Surf. Sci. **82**, 445 (1979).

[265] M. Müller, "Optische Spektroskopie von PTCDA auf Alkalihalogenidoberflächen: vereinzelte Moleküle und Monolagen", PhD thesis (Universität Bonn, 2011).

[266] J. Kramer, C. Tegenkamp, and H. Pfnür, "The growth of NaCl on flat and stepped silver surfaces", J. Phys.: Condens. Matter **15**, 6473 (2003).

[267] A. Riemann, S. Fölsch, and K. H. Rieder, "Epitaxial growth of alkali halides on stepped metal surfaces", Phys. Rev. B **72**, 125423 (2005).

[268] M. Cañas-Ventura, W. Xiao, P. Ruffieux, R. Rieger, K. Müllen, H. Brune, and R. Fasel, "Stabilization of bimolecular islands on ultrathin NaCl films by a vicinal substrate", Surf. Sci. **603**, 2294 (2009).

[269] J. L. Zhang, S. Zhao, C. Han, Z. Wang, S. Zhong, S. Sun, R. Guo, X. Zhou, C. D. Gu, K. D. Yuan, Z. Li, and W. Chen, "Epitaxial Growth of Single Layer Blue Phosphorus: A New Phase of Two-Dimensional Phosphorus", Nano Letters **16**, 4903 (2016).

[270] E. Golias, M. Krivenkov, A. Varykhalov, J. Sánchez-Barriga, and O. Rader, "Band Renormalization of Blue Phosphorus on Au(111)", Nano Letters **18**, 6672 (2018).

[271] W. Zhang, H. Enriquez, Y. Tong, A. Bendounan, A. Kara, A. P. Seitsonen, A. J. Mayne, G. Dujardin, and H. Oughaddou, "Epitaxial Synthesis of Blue Phosphorene", Small **14**, 1804066 (2018).

[272] "Two-Dimensional Metal-Phosphorus Network", Matter **2**, 111 (2020).

[273] J. L. Zhang, S. Zhao, S. Sun, H. Ding, J. Hu, Y. Li, Q. Xu, X. Yu, M. Telychko, J. Su, C. Gu, Y. Zheng, X. Lian, Z. Ma, R. Guo, J. Lu, Z. Sun, J. Zhu, Z. Li, and W. Chen, "Synthesis of Monolayer Blue Phosphorus Enabled by Silicon Intercalation", ACS Nano **14**, 3687 (2020).

[274] M. Gruenewald, M. Schaal, I. Karadzhov, L. Brill, J. Domke, P. Grimm, F. Otto, J. Picker, P. M. Simon, H. Tamm, T. Fritz, and R. Forker, "Blue phosphorene on Au(111) as a decoupling layer for organic epitaxially grown films", Phys. Rev. Mater. **6**, 015601 (2022).

[275] J.-P. Xu, J.-Q. Zhang, H. Tian, H. Xu, W. Ho, and M. Xie, "One-dimensional phosphorus chain and two-dimensional blue phosphorene grown on Au(111) by molecular-beam epitaxy", Phys. Rev. Mater. **1**, 061002 (2017).

[276] J. Shelton, H. Patil, and J. Blakely, "Equilibrium segregation of carbon to a nickel (111) surface: A surface phase transition", Surf. Sci. **43**, 493 (1974).

[277] J. M. Blakely, J. S. Kim, and H. C. Potter, "Segregation of Carbon to the (100) Surface of Nickel", J. Appl. Phys. **41**, 2693 (1970).

[278] C. A. Schneider, W. S. Rasband, and K. W. Eliceiri, "NIH Image to ImageJ: 25 years of image analysis", Nature Methods **9**, 671 (2012).

[279] P. Kury, P. Zahl, M. Horn-von Hoegen, C. Voges, H. Frischat, H.-L. Günter, H. Pfnür, and M. Henzler, "Chopped sample heating for quantitative profile analysis of low energy electron diffraction spots at high temperatures", Rev. Sci. Instrum. **75**, 4911 (2004).

[280] American Elements, *TZM Molybdenum Alloy*, `https://www.americanelements.com/tzm-molybdenum-alloy`, Accessed: 2023-09-08.

[281] A. Eslam, "Strukturanalyse dünner Chinacridon-Filme auf der Ag(100)- und Cu(111)-Oberfläche: Hochaufgelöste Beugung langsamer Elektronen", MSc thesis (Universität Bonn, 2018).

[282] N. Humberg, "Strukturaufklärung epitaktischer Schichten von Chinacridon auf der Ag(100)-Oberfläche", MSc thesis (Universität Bonn, 2018).

List of abbreviations

General Abbreviations

1D	one-dimensional
2D	two-dimensional
3D	three-dimensional
AC	alternating current
AFM	atomic force microscopy
CT	charge transfer
CVD	chemical vapor deposition
DFT	density functional theory
et al.	lat: et alii, et aliae, et alia = and others
fcc	face-centered cubic
FET	field-effect transistor
FWHM	full width at half maximum
HOMO	highest occupied molecular orbital
H-bond	hydrogen bond
IDCT	interfacial dynamical charge transfer
IPS	image potential state
IR	infrared
LDOS	local density of states
LEED	low-energy electron diffraction
LUMO	lowest unoccupied molecular orbital
ML	monolayer
MCP-LEED	microchannel plate low-energy electron diffraction
NIXSW	normal incidence X-ray standing wavefield
OFET	organic field-effect transistor
OLED	organic light-emitting diode
OPV	organic photovoltaic
OSWD	organic solid-solid wetting deposition
PID	proportional–integral–derivative
POL	point-on-line
RT	room temperature
R and L	handedness of QA molecules on surfaces
SI	supporting information

SPA-LEED	spot profile analysis low-energy electron diffraction
STM	scanning tunneling microscopy
STS	scanning tunneling spectroscopy
TDS	thermal desorption spectroscopy
TTL	transistor-transistor logic
QMS	quadrupol mass spectrometer
UHV	ultra-high vacuum
UPS	ultraviolet photoelectron spectroscopy
XPS	X-ray photoelectron spectroscopy

Chemical Abbreviations

AH	alkali halide
CuOEP	copper-octaethyl porphyrin
GNR	graphene nanoribbon
hBN	hexagonal boron nitride
HOPG	highly oriented pyrolytic graphite
PTCDA	3,4,9,10-perylene tetracarboxylic dianhydride
KCl	potassium chloride
PTCDI	3,4,9,10-perylene tetracarboxylic diimide
QA	quinacridone
SnPc	tin phthalocyanine
TZM	titanium-zirconium-molybdenum

Parameters and Variables

a, b	spacings of a two-dimensional lattice
$\mathbf{b_1^*}$	first reciprocal lattice vector of the adsorbate structure unit cell
$\mathbf{b_2^*}$	second reciprocal lattice vector of the adsorbate structure unit cell
b_1^*	length of $\mathbf{b_1^*}$
b_2^*	length of $\mathbf{b_2^*}$
$\mathbf{b_1}$	first real lattice vector of the adsorbate structure unit cell
$\mathbf{b_2}$	second real lattice vector of the adsorbate structure unit cell
b_1	length of $\mathbf{b_1}$
b_2	length of $\mathbf{b_2}$
$b_2^{\theta_{QA}=1}$	distance between neighboring chains for a full ML of QA on Ag(100) in the α-phase
$\mathbf{c_1^*}$	first reciprocal lattice vector of the second layer adsorbate structure unit cell
$\mathbf{c_2^*}$	second reciprocal lattice vector of the second layer adsorbate structure unit cell
$\mathbf{c_1}$	first real lattice vector of the second layer adsorbate structure unit cell
$\mathbf{c_2}$	second real lattice vector of the second layer adsorbate structure unit cell
c_1	length of $\mathbf{c_1}$
c_2	length of $\mathbf{c_2}$

d	the distance between the sample and the STM tip
e	the elementary charge
E	the energy
E_{kin}	the kinetic energy
E_{ads}	adsorption energy
E_{B}	shift between the Fermi levels of STM tip and sample caused by the bias voltage
E_{disp}	dispersion energy
$E_{\mathrm{F,s}}$	the Fermi level of the sample
$E_{\mathrm{F,t}}$	the Fermi level of the STM tip
E_n	calculated adsorption energy per molecule for small QA chains ($n = 1, 2, 3$) on KCl
$\mathbf{G}$	two-dimensional reciprocal lattice vactor
$\hbar$	the reduced Planck constant
H_{sub}	sublimation enthalpy
I_{tun}	tunneling current during STM measurements
$\boldsymbol{k_0}$	wave vector of a incident electron wave in LEED
$\boldsymbol{k_{ij}}$	wave vector of a scattered electron wave in LEED
$\mathbf{k}_{\|\|}$	component of momentum parallel to the surface of a scattered electron
m	mass
m_{e}	mass of an electron
N_0^{pix}	number of pixels with a gray value of 0
N_{255}^{pix}	number of pixels with a gray value of 255
p	pressure in the vacuum chamber
$\mathbf{r_0}$	position of the center of the STM tip
S_{n}	phase with respect to monoatomic Ag step edge for spots of the order n.
T_{tun}	the transmission coefficient for tunneling
U_{B}	bias voltage applied to the STM sample
V_0	height of the potential barrier for tunneling
z_{c}	the charge number
α	angle between the two unit cell vectors of a superstructure unit cell
γ	azimuthal angle between the long axis of QA and the [10]-direction
θ_{KCl}	nominal coverage/thickness of the KCl layer
θ_{QA}	coverage/thickness of the QA layer
λ_{e}	*de Broglie* wavelength of an electron
μ_{r}	the permeability
φ	scattering angle in LEED at which constructive interference occurs
Φ_{s}	work function of the sample
Φ_{t}	work function of the STM tip
Ψ	wave function

Phases of QA

α phase consisting of QA chains on Ag(100)
α_d the α-phase with a lot of defects that are induced by heating
β commensurate QA phase on Ag(111)
γ QA phase that coexists with the β-phase on Ag(111)
δ mixed phase between the α-phase and a disordered 2D gas phase on Ag(100)
ε mixed phase between the ordered α- and the ordered β-phase on Ag(100)
λ mixed phase between the α-phase and an unknown disordered phase on Ag(100)
α' phase consisting of QA chains on Cu(111)
β' commensurate QA phase on Cu(111)
γ' heterochiral QA phase on Cu(111) that was only rarely observed
α^* phase consisting of QA chains on Ag(111)
β^* commensurate QA phase on Ag(111)
α_B^I the bulk α^I crystal structure of QA
α_B^{II} the bulk α^{II} crystal structure of QA
β_B the bulk β crystal structure of QA
γ_B the bulk γ crystal structure of QA
$\alpha^\dagger$ phase consisting of QA chains on Ag(110) [81]
$\beta_1^\dagger$ phase after annealing on Ag(110) [81]
$\beta_2^\dagger$ phase after annealing on Ag(110) [81]

List of figures

Acknowledgements

In closing, I would like to express my sincere gratitude to all people who have academically or emotionally supported me during the intensive work for the present thesis:

- Professor Dr. Moritz Sokolowski, for giving me the opportunity to work on my thesis in his group. His continuous support and invaluable advice, as well as the many fruitful scientific discussions, have been of great help to me during my PhD study.
- Professor Dr. Meike Stöhr (Universität Groningen, Netherlands/Fachhochschule Graubünden, Chur, Switzerland), for agreeing to be co-referee for the present thesis.
- Dr. Rémi Bretel (Université Paris-Saclay, France), for the good collaboration during the STM experiments on QA/Cu(111) and QA/hBN/Cu(111) during his stays here in Bonn as an exchange PhD student. I am also grateful to him and Dr. Eric Le Moal (Université Paris-Saclay, France) for many fruitful scientific discussions, which helped me with my interpretation of the data.
- Prof. Dr. Thomas Bredow, for supporting my work with theoretical density functional theory calculations regarding the adsorption of quinacridone molecules on KCl.
- All members of the Organic Films group, for providing a pleasant and productive working atmosphere and always being ready to help with technical or scientific problems and questions. In particular, I would like to thank my colleagues Anna J. Kny and Dr. Christine Brülke for a good collaboration at the UHV experiments, as well as Timon Bald, Jannik Roth, and Lukas Grönwoldt for their careful experimental work within the scope of their bachelor thesis and focusing laboratory course. My special thanks goes to Martin Specht for his excellent technical support and always being able to provide quick solutions for all sorts of technical problems.
- David Duncan and Tien-Lin Lee at the Diamond Light Source (Didcot, UK) for their technical and scientific support.
- All staff members of the mechanics and electronics workshops of the Clausius Institut für Physikalische und Theoretische Chemie, for their quick and reliable support. In particular, I would like to thank Rolf Paulig for the development and construction of a current chopper for the SPA-LEED experiment. I would also like to thank Tony Hanfland for supplying me with liquid helium for the low temperature STM experiments.
- Knut Hintzen, for his help with all IT related problems.
- The Deutsche Forschungsgemeinschaft, for financial support.
- Finally, I would like to express my deepest gratitude to my family, my girlfriend, and my friends for their continuous emotional support and encouragement throughout the years of work. I could not have done it without you!

Eidesstattliche Erklärung

Hiermit versichere ich an Eides statt, dass ich die vorliegende Dissertation “One-dimensional aggregates of the organic dye quinacridone on metallic and dielectric surfaces” persönlich, selbstständig und ohne Benutzung anderer als der angegebenen Hilfsmittel angefertigt habe, die benutzten Quellen kenntlich gemacht sind und die Arbeit nicht anderweitig als Dissertation eingereicht ist. Als kumulative Dissertation ist die vorliegende Arbeit an den nachfolgenden Stellen veröffentlicht:

- Niklas Humberg, Rémi Bretel, Alexander Eslam, Eric Le Moal, and Moritz Sokolowski, "Hydrogen-Bonded One-Dimensional Chains of Quinacridone on Ag(100) and Cu(111): The Role of Chirality and Surface Bonding", J. Phys. Chem. C **124**, 45, 24861–24873 (2020).
  DOI: https://doi.org/10.1021/acs.jpcc.0c07850
- Niklas Humberg, Qinmin Guo, Thomas Bredow, and Moritz Sokolowski, "Growth of Hydrogen-Bonded Molecular Aggregates on a Thin Alkali Halide Layer: Quinacridone on KCl/Ag(100)", J. Phys. Chem. C **127**, 49, 23814–23826 (2023).
  DOI: https://doi.org/10.1021/acs.jpcc.3c04402
- Niklas Humberg, Lukas Grönwoldt, Moritz Sokolowski, "Directed Growth of Quinacridone Chains on the Vicinal Ag(35 1 1) Surface", Beilstein J. Nanotechnol. **2024**, 15, 556-568.
  DOI: https://doi.org/10.3762/bjnano.15.48

Bonn, Juni 2024

(Hans Niklas Humberg)